

Improving contrast for the detection of archaeological vegetation marks using optical remote sensing techniques.

by

David Stott

**Submitted in accordance with the requirements
for the degree of Doctor of Philosophy.
School of Computing, University of Leeds**

January 2017

The candidate confirms that the work submitted is his/her own, except where work which has formed part of jointly authored publications has been included. The contribution of the candidate and the other authors to this work has been explicitly indicated on the following page. The candidate confirms that appropriate credit has been given within the thesis where reference has been made to the work of others.

This copy has been supplied on the understanding that it is copyright material and that no quotation from the thesis may be published without proper acknowledgement.

©2017 The university of Leeds and David Stott.

Declarations

Some parts of the work presented in this thesis have been published in the following articles:

Chapter 4 is contains some work published in these papers:

Stott, D. Boyd, D, Beck, A. Cohn A. 2013. Hyperspectral Detection Dynamics of Archaeological Vegetation Marks and Enhancement Using Full Waveform LiDAR Data. *IGARSS proceedings 2013, Melbourne, Australia* Stott, D., Boyd, D.S., Beck, A. and

Cohn, A.G., 2015. Airborne LiDAR for the detection of archaeological vegetation marks using biomass as a proxy. *Remote Sensing*, 7(2), pp.1594-1618.

These pertain to the use of full-waveform and multi-temporal LiDAR for the detection of archaeological vegetation marks expressed as biomass variations considered in this chapter. The data analyses were conducted by the author, with contributions to the text of the paper from the author and co-authors.

Chapter 3 contains work published in this conference paper:

David Stott, Anthony Beck, Doreen S. Boyd and Anthony Cohn. 2013. Understanding hyperspectral detection dynamics: Analysis and characterisation of archaeological vegetation marks using continuum removed reflectance spectroscopy. *Archaeological Prospection: Proceedings of the 10th International Conference - Vienna May 29th - June 2nd 2013*

The use of continuum removal considered in chapter 3 is presented in this paper. The data collection and analyses were principally undertaken by the author, with the assistance of Doreen Boyd and Anthony Beck, with contributions to the text of the paper from the author and co-authors

Abstract

Airborne archaeological prospection in arable crops relies on detecting features using contrasts in the growth of the overlying crop as a proxy. This is possible because the composition of the soil in the features differs from the unmodified subsoil, and this exerts influence on the state of the crop. This influence is expressed as changes in crop canopy density, structure, and in periods of resource constraint, variations in vegetation stress and vigour. These contrasts are dynamic, and vary temporally with local weather, and spatially with variations in drift geology and land use. This means that the archaeological features have no unique spectral signature usable for classification. Rather, contrast is expressed as relative, local variation in the crop.

The extent to which the features are detectable using a particular technique is dependant on the strength of the contrast and the ability of the sensor to resolve it. Current practice relies heavily on photography in the visible spectrum, but other sensors and processing techniques have the potential to improve our ability to resolve subtle contrasts. This is important, as it affords the opportunity to extend the detection temporally and in soil types not normally considered conducive to detection.

This work uses multi-temporal spectro-radiometry and ground-based survey to study contrast at two sites in southern England. From these measurements leaf area index, vegetation indices, the red-edge position, chlorophyll fluorescence and continuum removal of foliar absorption features were derived and compared to evaluate contrast. The knowledge gained from the ground-based surveys was used to inform the analysis of the airborne surveys. This included the application of vegetation indices to RGB cameras, the use of multi-temporal and full-waveform LiDAR to detect biomass variations, and the use of various techniques with hyper-spectral imaging spectroscopy. These methods provide a demonstrable improvement in contrast, particularly in methods sensitive to chlorophyll fluorescence, which afford the opportunity to record transient and short term contrasts that are not resolved by other sensors.

Acknowledgements

My supervisors. Dr Anthony Beck conceived of the DART project, provided many hours of entertaining debate and constant friendship. Professor Anthony Cohn kept me in touch with reality. Professor Doreen Boyd provided valuable input on remote sensing and access to the equipment.

My fellow students on the DART project. Rob Fry for all that driving, ranting, raving and geophysics. Dan Boddice for constant reassurance. Laura Pring for an engineer's perspective.

The DART investigators. Chris Gaffney, Keith Wilkinson, Armin Schmidt and Nicole Metje for asking valuable questions.

The DART consortium and consultants For their timely and friendly advice, including: Rog Palmer, Dave Cowley, Bob Evans, Bill Hanson, Keith Challis, Cameron Neylon, Roger Boyle, Ionna Otlean, Derek Magee, Pete Horne, Anthony Crawshaw, Graham Ferrier and others

My colleagues at the School of Computing, Specifically: Dr Dave Harrison for explaining patiently how computers work and many hours of good geeky company. Dr Ian Hales, Dr Duane Carey and Nicole Kerrison for their support and friendship. Judi Drew and Teresa Honore for making everything happen. Everybody else for creating a warm collegiate atmosphere.

The Landowners at the Royal Agricultural University and Thornhill Estates, and their agents, as without access to the fields none of this could of happened. At the RAU Tony Norris and Tom Overbury accommodated our every whim. At Thornhill Tim and Vicky Dickens were a great help.

NERC ARSF and FSF for providing data and advice, especially Gary Llewellyn, Ben Taylor and Alisdair Mac Arthur.

The AARG community for providing a freindly forum for discussion, debate and advice. Oscar Aldred, Michael Doneus, Geert Verhoeven, Veronique De Laet, Anthony Corns, and Wlodzimierz Raczkowski all asked good questions. John Wells is inspirational.

The contributors to FOSS projects used in this work, including Numpy, Scipy, Matplotlib, Quantumn GIS, GRASS GIS, SAGA, GDAL, Fiona, Shapely, Monteverdi, Inkscape, GIMP, Texmaker and many others.

And finally Lou Felding, who not only provided me with continual love, encouragement and support, but also rectified a few oblique APs.

List of Abbreviations

ABA – Abscisic Acid
ADC – Analogue to Digital Converter
AIS – Airborne Imaging Spectroscopy
ALS – Airborne Laser Scanning
ARI – Anthocyanin Reflectance Index
ARSF – Airborne Remote Sensing Facility
ASD – Analytical Spectral Devices
ATM – Airborne Thematic Mapper
ATP – Adenosine Triphosphate
AVIRIS – Airborne Visible Infrared Imaging Spectrometer
AWC – Available Water Capacity
BDRF – Bi-Directional Reflectance Factor
BNA – Band Normalised by Area
BRDF – Bi-Directional Reflectance Distribution Function
CARI – Chlorophyll Absorption Ratio Index
CASI – Compact Airborne Spectroscopic Imager
CCD – Charge Coupled Device
CEC – Cation Exchange Capacity
CFA – Colour Filter Array
CMOS – Complementary Metal Oxide Semiconductor
CRI – Carotenoid Reflectance Index
CSM – Canopy Surface Model
DART – Detection of Archaeological Residues using Remote Sensing Techniques
DDCF – Diddington Clay Field
DDPF – Diddington Pasture Field
DDT1 – Diddington Transect 1s
DSM – Digital Surface Model
DTM – Digital Terrain Model
ExG – Excess Green index
ExR – Excess Red index
ExGR – Excess Green minus Excess Red index
EMD – Earth Movers Distance
FC – Field Capacity
FW – Full-Waveform
FWHM – Full Width at Half Maximum

GA – Green Angle
GBS – Green Blue Slope
GNSS – Global Navigation Satellite Systems
GR – Green Red ratio
GRS – Green Red Slope
HER – Historic Environment Records
HHCC – Harnhill Cherry Copse
HHQF – Harnhill Quarry Field
HIS – Hue Saturation Intensity
IFOV – Instantaneous Field of View
IMU – Inertial Measurement Unit
LAI – Leaf Area Index
LRM – Local Relief Model
MCARI – Modified Chlorophyll Absorption Index
MSI – Moisture Stress Index
MSR – Modified Simple Ratio
MSAVI – Modified Soil Adjusted vegetation Index
MSRVI – Modified Soil Rssitant Vegetation Index
MTBVI – Multi-wavelength Twin Band Vegetation Index
MTVI – Modified Triangular Vegetation Index
NADPH – Nicotinamide Adenine Dinucleotide Phosphate
NDGBI – Normalised Difference Green Blue Index
NDGRI – Normalised Difference Green Red Index
NDII – Normalised Difference Infrared Index
NDRBI – Normalised Difference Red Blue Index
NDLI – Normalised Difference Lignin
NDVI – Normalised Difference Vegetation Index
NDWI – Normalised Difference Water Index
NERC – National Environmental Research Council
NIR – Near Infrared
NMP – National Mapping Program
NPCI – Normalised Photochemical Carotenoid Index
NPQ – Non-Photochemical Quenching
NPQI – Normalised Phaeophytinization Index
PAR – Photosynthetically Active Radiation
PCA – Principal Components Analysis

PRI – Photochemical Reflectance Index
PRSI – Plant Senescence Reflectance Index
PS – Photosystem
PSMD – Potential Soil Moisture Deficit
PWP – Permanent Wilt Point
RB – Red Blue ratio
REIP – Red Edge Inflection Position
RDVI – Renormalized Difference Vegetation Index
RGB – Red Green Blue
RR – Residual Relief
RTK – Real-Time Kinematic
SAVI – Soil Adjusted Vegetation Index
SFM – Structure from Motion
SIPI – Structure Insensitive Photochemical Index
SMD – Soil Moisture Deficit
SVI – Simple Vegetation Index
SWIR – Shortwave Infrared
TBVI – Two Band Vegetation Index
TLS – Terrestrial Laser Scanning
TVI – Triangular Vegetation Index
UAV – Unmanned Aerial Vehicles
VARI – Visible Atmospheric Resistant Index
VIC – Vegetation Index Contrast
VIS – visible
VREI – Vogelmann Red Edge Index
WBI – Water Band Index

Contents

1	Introduction	1
1.1	Summary	1
1.2	Motivation	3
1.2.1	Why?	3
1.2.2	The problem	4
1.2.2.1	What are vegetation marks?	4
1.2.2.2	How are they detected?	5
1.3	The thesis: Improving detection	7
1.3.1	Ground-based survey	8
1.3.2	Airborne laser scanning	8
1.3.3	RGB images	9
1.3.4	Airborne imaging spectroscopy	9
1.3.5	Contributions	9
2	Background	11
2.1	Introduction	11
2.2	Archaeological features: What are they? How do we find them?	12
2.2.1	What are archaeological features?	12
2.2.2	Archaeological formation processes	12
2.2.3	Archaeological remote sensing	15
2.2.3.1	Contrast	15
2.3	Archaeological vegetation marks	16
2.3.1	Causation	16
2.3.2	Plants and soil	16
2.3.2.1	Water	16
2.3.2.2	Drought stress	17
2.3.2.3	Feed-forwarding and developmental effects.	18
2.3.2.4	Soil hardness and porosity	18

2.3.2.5	Nutrients	19
2.3.3	How archaeological formation processes change the soil	20
2.3.4	Vegetation mark expression	22
2.3.4.1	Crops	23
2.3.5	Weather	25
2.3.5.1	Soil moisture deficit	25
2.3.6	Soils	25
2.4	Remote sensing of vegetation properties	26
2.4.1	Principles of remote sensing	26
2.4.1.1	The electromagnetic spectrum in the optical domain	26
2.4.1.2	Sensors	27
2.4.1.3	Platforms	29
2.4.1.4	Displaying images	29
2.5	Optical properties of vegetation	30
2.5.1	Photosynthesis	30
2.5.1.1	Pigments	32
2.5.1.2	Fluorescence	33
2.5.2	Foliar Biochemicals	35
2.5.2.1	Canopy water content	35
2.5.2.2	Lignin and cellulose	35
2.5.2.3	Nitrogen	36
2.6	Hyper-spectral vegetation analysis techniques	36
2.6.1	Vegetation Indices	36
2.6.1.1	Three band indices	39
2.6.1.2	Red-edge indices	40
2.6.1.3	Water content indices	41
2.6.1.4	Leaf pigment sensitive indices	42
2.6.2	The red-edge	44
2.6.2.1	The red-edge and fluorescence	45
2.6.3	Fluorescence indices	46
2.6.4	Continuum removal	47
2.7	Related work: The detection of vegetation marks	49
2.7.1	Aerial photography	49
2.7.1.1	Observer directed oblique photography: A tried and tested technique	49
2.7.1.2	Systematic vertical photography	51

2.7.1.3	Recent developments	52
2.7.2	Multi and hyper-spectral approaches to vegetation mark detection	53
2.7.2.1	Indices	53
2.7.2.2	Principal component analysis	55
2.7.2.3	The red-edge	55
2.7.2.4	Fluorescence and other methods	56
2.7.2.5	Evaluating contrast	56
2.8	Conclusions	57
3	From the ground up: Fieldwork	59
3.1	Introduction	59
3.2	The study sites	60
3.2.1	Site selection	60
3.2.1.1	Transects	61
3.2.1.2	DDT1 (Diddington Transect 1)	62
3.2.1.3	Diddington Clay field (DDCF)	62
3.2.1.4	Harnhill Quarry Field (HHQF)	63
3.2.1.5	Harnhill Cherry Copse (HHCC)	65
3.2.1.6	Weather conditions	65
3.3	Background: Field measurement of vegetation marks	66
3.4	Methodology	67
3.4.1	Field spectroscopy	67
3.4.1.1	Data collection	68
3.4.1.2	Data preparation	69
3.4.1.3	Data analysis	69
3.4.2	Ground cover	74
3.4.2.1	Data collection	76
3.4.2.2	Image analyses	76
3.4.3	Biomass: Leaf area index and crop height	76
3.4.3.1	Measuring crop height	76
3.4.3.2	Growth stage	76
3.4.3.3	Leaf Area Index	76
3.4.4	Analysis Methodology	77
3.5	Results	77
3.5.1	Diddington Clay Field	78
3.5.2	Diddington Transect 1	80

3.5.2.1	June-July 2011	80
3.5.2.2	August 2011-June 2012	86
3.5.3	Harnhill Quarry field	86
3.5.3.1	September 2011-March 2012	86
3.5.3.2	March-August 2012	88
3.5.4	Harnhill Cherry Copse	89
3.6	Evaluation of methods	95
3.6.1	Biomass	95
3.6.2	Vegetation indices	95
3.6.3	The MTBVI	96
3.6.4	Chlorophyll fluorescence and the red-edge inflection point	96
3.6.5	Continuum Removal	99
3.7	Conclusions	101
3.7.1	The nature of archaeological vegetation marks	101
3.7.1.1	When are vegetation marks detectable?	101
3.7.1.2	How are the vegetation marks expressed	103
3.7.2	Implications for airborne survey	103
4	Airborne laser scanning	105
4.1	Introduction	105
4.2	Background	106
4.2.1	What is airborne laser scanning?	106
4.2.1.1	Operating principles of the sensor	106
4.2.1.2	Spectral properties	106
4.2.1.3	Full waveform ALS	107
4.2.2	Lidar for sensing crop properties	107
4.2.2.1	Terrestrial lidar	107
4.2.2.2	Airborne lidar	109
4.2.3	ALS in archaeological prospection	109
4.2.3.1	Topographic archaeological ALS techniques	109
4.2.3.2	Archaeological soil and vegetation mark detection using ALS	111
4.3	Methodology	112
4.3.1	Data Collection	112
4.3.2	Analysis rationale	114
4.3.3	Full-waveform analysis	115

4.3.4	Multi-temporal crop biomass modelling	115
4.3.4.1	Residual relief contrast enhancement	117
4.3.4.2	Analysis of contrast	118
4.4	Results	119
4.4.1	Summary	119
4.4.2	Full-waveform	119
4.4.3	Crop Surface Model	119
4.4.4	Residual relief	121
4.5	Discussion and further work	121
4.6	Conclusions	127
5	Getting the most out of RGB images	130
5.1	Introduction	130
5.2	Background	131
5.2.1	What are RGB images and how are they made?	131
5.2.2	RGB cameras as multispectral sensors	132
5.2.3	RGB methods for vegetation analysis	132
5.2.3.1	Simple indices	133
5.2.3.2	Normalised difference indices	133
5.2.3.3	Slope derived indices	134
5.2.3.4	Chromatic transformations	135
5.3	Methodology	136
5.3.1	Data collection and preparation	136
5.3.1.1	Data preparation	137
5.3.2	Data analysis	137
5.4	Results	140
5.4.1	Diddington Clay Field	140
5.4.2	Diddington Transect 1	140
5.4.3	Harnhill Quarry Field	144
5.4.4	Harnhill Cherry Copse	144
5.5	Discussion	147
5.5.1	Do RGB ratios improve contrast?	147
5.5.2	Do RGB ratios correct for illumination differences?	148
5.6	Conclusions	148

6	Airborne imaging spectroscopy	151
6.1	Introduction	151
6.2	Background	152
6.2.1	How the scanners work	152
6.2.2	AIS and archaeology	152
6.3	Methodology	153
6.3.1	Data	153
6.3.1.1	Data Processing	153
6.3.2	Data analyses	154
6.3.2.1	Vegetation Indices	154
6.3.2.2	Fluorescence Indices	154
6.3.2.3	The Red-edge	156
6.3.2.4	The MTBVI	156
6.3.2.5	Continuum Removal	156
6.4	Results	156
6.4.1	Summary	156
6.4.2	Diddington Clay Field	157
6.4.2.1	2011	157
6.4.2.2	2012	158
6.4.3	Diddington Transect 1	159
6.4.3.1	2011	159
6.4.3.2	2012	160
6.4.4	Harnhill Cherry Copse	161
6.4.4.1	2011	161
6.4.4.2	2012	161
6.4.5	Harnhill Quarry field	162
6.4.5.1	2011	162
6.4.5.2	2012	163
6.5	Discussion	164
6.5.1	Resolution	164
6.5.2	Further work	165
6.6	Conclusions	166
7	Conclusions	167
7.1	Introduction	167
7.2	Evaluation of results	168

7.2.1	How are vegetation marks expressed?	168
7.2.1.1	Detecting environmental adaptation	169
7.2.1.2	Detecting short-term stress responses	169
7.2.1.3	Detecting long-term damage	170
7.2.2	Limitations	171
7.3	Further work	172
7.3.1	Optimising contrast in the airborne datasets	172
7.3.1.1	Local optimisation	172
7.3.1.2	Data fusion	173
7.3.2	Designing better systems	175
7.3.2.1	Extending the spectral range	177
	Bibliography	179
	Appendices	219
	Appendix A Data and code	220
A.1	Data	220
A.2	Code	220
A.3	Spectral analyses	220
A.4	Raster Analyses	221
A.5	ALS data	222
A.6	RGB images	222
	Appendix B Transect survey results	223
B.1	Transect Survey conditions	223
	227	

List of Figures

1.1	Archaeological vegetation marks	3
1.2	Spectra showing temporal variation in vegetation mark expression	4
2.1	Formation processes	13
2.2	The electromagnetic spectrum	27
2.3	Leaf structure and optical properties	31
2.4	Chlorophyll absorption spectra	32
2.5	Linear extrapolation of the red-edge inflection point	46
2.6	Foliar absorption features used for continuum removal	48
2.7	Example of band normalised by area continuum removed spectra	50
2.8	Performance of indices from Agapiou et al. (2012)	54
3.1	Location of DART project study sites	61
3.2	Location of DDT1 transects and archaeological features	63
3.3	Location of DDCF transects and archaeological features	64
3.4	Location of HHQF transects and archaeological features	64
3.5	Location of HHCC transects and archaeological features	65
3.6	Potential soil moisture deficits at the study sites	66
3.7	Derivation of vegetation coverage using the <i>EXG – EXR</i> method.	75
3.8	Summary of results from DDCF	78
3.9	Performant methods from Diddington Clay Field 24/07/2012	79
3.10	Photograph of DDCF, July 2012	80
3.11	Summary of results from DDT1	81
3.12	Photograph of cropmarks in DDT1 14/06/2011	82
3.13	Photograph of cropmarks in DDT1 29/06/2011	82
3.14	Performant methods from Diddington Transect 1 08/06/2011	83
3.15	Performant methods from Diddington Transect 1 14/06/2011	85
3.16	Summary of results from HHQF	87
3.17	Performant methods from Harnhill Quarry field 20/06/2012	88

3.18	Transect Summary HHCC	90
3.19	Performant methods from Harnhill Cherry Copse 14/02/2012	91
3.20	Performant methods from Harnhill Cherry Copse 24/05/2012	92
3.21	Performant methods from Harnhill Cherry Copse 19/06/2012	93
3.22	Performant methods from Harnhill Cherry Copse 25/07/2012	94
3.23	Summary of performance of vegetation indices	96
3.24	MTBVI performance in wheat crops	97
3.25	MTBVI correlated with REIP	97
3.26	MTBVI correlated with fluorescence	98
3.27	Summary of performance of red-edge inflection point methods	98
3.28	Summary of performance of fluorescence indices	99
3.29	Summary of performance of continuum removal for the 470nm absorption feature	100
3.30	Summary of performance of continuum removal for the 670nm absorption feature	100
3.31	Summary of performance of continuum removal for the 970nm absorption feature	101
3.32	Summary of performance of continuum removal for the 1200nm absorp- tion feature	102
4.1	Leaf Area Index and Vegetation Height for HHQF, June 2012	114
4.2	Mean FW peaks from HHQF	116
4.3	Effects of filtering on bare soil DTM	117
4.4	Full waveform results for HHQF, June 2012.	120
4.5	CSM model results from HHQF, June 2012	122
4.6	CSM model results from DDT1, June 2011	123
4.7	CSM model results from HHCC, June 2012	124
4.8	Residual relief model results from HHQF, June 2012 DSM	125
4.9	Residual relief model results from HHQF, June 2011 CSM	126
4.10	Correlation between CSM, vegetation height and LAI	128
5.1	Spectral properties of vegetation and RGB cameras	132
5.2	Filters applied to an NDGRI image derived from 0.1m spatial resolution RGB photograph	138
5.3	Summary of contrast using different RGB analysis methods. DDCF	141
5.4	Summary of contrast using different RGB analysis methods. DDT1	142
5.5	Summary of contrast using different RGB analysis methods. HHQF	145

5.6	Summary of contrast using different RGB analysis methods. HHCC	146
5.7	Image comparing RGB image to NDGRI index	147
5.8	Image showing the ability of RGB ratios to correct for illumination variations. Diddington, 14/06/2011	149
6.1	Significant results from Diddington Clay Field 14/06/2011	157
6.2	Diddington Clay Field: MTBVI at 630nm & 769nm compared to RGB image	158
6.3	Significant results from Diddington Transect 1 14/06/2011	159
6.4	Significant results from Diddington Transect 1 27/06/2011	160
6.5	Harnhill Cherry Copse 27/06/2011 MTBVI & RGB image	161
6.6	Significant results from Harnhill Cherry Copse 23/03/2012	162
6.7	Significant results from Harnhill Quarry Field 20/06/2012	163
6.8	Comparison of spatial resolution between AIS image and aerial photo . . .	166
7.1	Summary of significant results	168
7.2	Suggested workflow for optimisation of hyperspectral datasets	173
7.3	Example of the optimisation workflow	174
7.4	Data fusion Harhill Quarry Field 20/06/2012	176
B.1	Transect vegetation properties DDCF 28/09/2011	227
B.2	Transect vegetation properties DDCF 23/01/2012	227
B.3	Spectra DDCF 23/01/2012	227
B.4	Vegetation indices DDCF 23/01/2012	227
B.5	Fluorescence Indices DDCF 23/01/2012	228
B.6	MTBVI DDCF 23/01/2012	228
B.7	Continuum removed metrics 470nm DDCF 23/01/2012	228
B.8	Continuum removed reflectance 470nm DDCF 23/01/2012	229
B.9	Continuum removed reflectance BNA 470nm DDCF 23/01/2012	229
B.10	Continuum removed metrics 670nm DDCF 23/01/2012	229
B.11	Continuum removed reflectance 670nm DDCF 23/01/2012	230
B.12	Continuum removed reflectance BNA 670nm DDCF 23/01/2012	230
B.13	Continuum removed metrics 970nm DDCF 23/01/2012	230
B.14	Continuum removed reflectance 970nm DDCF 23/01/2012	231
B.15	Continuum removed reflectance BNA 970nm DDCF 23/01/2012	231
B.16	Continuum removed metrics 1200nm DDCF 23/01/2012	231
B.17	Continuum removed reflectance 1200nm DDCF 23/01/2012	232

B.18	Continuum removed reflectance BNA 1200nm DDCF 23/01/2012	232
B.19	Transect vegetation properties DDCF 16/02/2012	232
B.20	Spectra DDCF 16/02/2012	233
B.21	Vegetation indices DDCF 16/02/2012	233
B.22	Fluorescence Indices DDCF 16/02/2012	233
B.23	MTBVI DDCF 16/02/2012	234
B.24	Continuum removed metrics 470nm DDCF 16/02/2012	234
B.25	Continuum removed reflectance 470nm DDCF 16/02/2012	234
B.26	Continuum removed reflectance BNA 470nm DDCF 16/02/2012	235
B.27	Continuum removed metrics 670nm DDCF 16/02/2012	235
B.28	Continuum removed reflectance 670nm DDCF 16/02/2012	235
B.29	Continuum removed reflectance BNA 670nm DDCF 16/02/2012	236
B.30	Continuum removed metrics 970nm DDCF 16/02/2012	236
B.31	Continuum removed reflectance 970nm DDCF 16/02/2012	236
B.32	Continuum removed reflectance BNA 970nm DDCF 16/02/2012	237
B.33	Continuum removed metrics 1200nm DDCF 16/02/2012	237
B.34	Continuum removed reflectance 1200nm DDCF 16/02/2012	237
B.35	Continuum removed reflectance BNA 1200nm DDCF 16/02/2012	238
B.36	Transect vegetation properties DDCF 20/03/2012	238
B.37	Spectra DDCF 20/03/2012	238
B.38	Vegetation indices DDCF 20/03/2012	239
B.39	Fluorescence Indices DDCF 20/03/2012	239
B.40	MTBVI DDCF 20/03/2012	239
B.41	Continuum removed metrics 470nm DDCF 20/03/2012	240
B.42	Continuum removed reflectance 470nm DDCF 20/03/2012	240
B.43	Continuum removed reflectance BNA 470nm DDCF 20/03/2012	240
B.44	Continuum removed metrics 670nm DDCF 20/03/2012	241
B.45	Continuum removed reflectance 670nm DDCF 20/03/2012	241
B.46	Continuum removed reflectance BNA 670nm DDCF 20/03/2012	241
B.47	Continuum removed metrics 970nm DDCF 20/03/2012	242
B.48	Continuum removed reflectance 970nm DDCF 20/03/2012	242
B.49	Continuum removed reflectance BNA 970nm DDCF 20/03/2012	242
B.50	Continuum removed metrics 1200nm DDCF 20/03/2012	243
B.51	Continuum removed reflectance 1200nm DDCF 20/03/2012	243
B.52	Continuum removed reflectance BNA 1200nm DDCF 20/03/2012	243
B.53	Transect vegetation properties DDCF 25/04/2012	244

B.54	Transect vegetation properties DDCF 16/05/2012	244
B.55	Spectra DDCF 16/05/2012	244
B.56	Vegetation indices DDCF 16/05/2012	245
B.57	Fluorescence Indices DDCF 16/05/2012	245
B.58	MTBVI DDCF 16/05/2012	245
B.59	Continuum removed metrics 470nm DDCF 16/05/2012	246
B.60	Continuum removed reflectance 470nm DDCF 16/05/2012	246
B.61	Continuum removed reflectance BNA 470nm DDCF 16/05/2012	246
B.62	Continuum removed metrics 670nm DDCF 16/05/2012	247
B.63	Continuum removed reflectance 670nm DDCF 16/05/2012	247
B.64	Continuum removed reflectance BNA 670nm DDCF 16/05/2012	247
B.65	Continuum removed metrics 970nm DDCF 16/05/2012	248
B.66	Continuum removed reflectance 970nm DDCF 16/05/2012	248
B.67	Continuum removed reflectance BNA 970nm DDCF 16/05/2012	248
B.68	Continuum removed metrics 1200nm DDCF 16/05/2012	249
B.69	Continuum removed reflectance 1200nm DDCF 16/05/2012	249
B.70	Continuum removed reflectance BNA 1200nm DDCF 16/05/2012	249
B.71	Transect vegetation properties DDCF 23/05/2012	250
B.72	Transect vegetation properties DDCF 26/06/2012	250
B.73	Spectra DDCF 26/06/2012	250
B.74	Vegetation indices DDCF 26/06/2012	250
B.75	Fluorescence Indices DDCF 26/06/2012	251
B.76	MTBVI DDCF 26/06/2012	251
B.77	Continuum removed metrics 470nm DDCF 26/06/2012	251
B.78	Continuum removed reflectance 470nm DDCF 26/06/2012	252
B.79	Continuum removed reflectance BNA 470nm DDCF 26/06/2012	252
B.80	Continuum removed metrics 670nm DDCF 26/06/2012	252
B.81	Continuum removed reflectance 670nm DDCF 26/06/2012	253
B.82	Continuum removed reflectance BNA 670nm DDCF 26/06/2012	253
B.83	Continuum removed metrics 970nm DDCF 26/06/2012	253
B.84	Continuum removed reflectance 970nm DDCF 26/06/2012	254
B.85	Continuum removed reflectance BNA 970nm DDCF 26/06/2012	254
B.86	Continuum removed metrics 1200nm DDCF 26/06/2012	254
B.87	Continuum removed reflectance 1200nm DDCF 26/06/2012	255
B.88	Continuum removed reflectance BNA 1200nm DDCF 26/06/2012	255
B.89	Transect vegetation properties DDCF 27/06/2012	255

B.90	Transect vegetation properties DDCF 24/07/2012	256
B.91	Spectra DDCF 24/07/2012	256
B.92	Vegetation indices DDCF 24/07/2012	256
B.93	Fluorescence Indices DDCF 24/07/2012	257
B.94	MTBVI DDCF 24/07/2012	257
B.95	Continuum removed metrics 470nm DDCF 24/07/2012	257
B.96	Continuum removed reflectance 470nm DDCF 24/07/2012	258
B.97	Continuum removed reflectance BNA 470nm DDCF 24/07/2012	258
B.98	Continuum removed metrics 670nm DDCF 24/07/2012	258
B.99	Continuum removed reflectance 670nm DDCF 24/07/2012	259
B.100	Continuum removed reflectance BNA 670nm DDCF 24/07/2012	259
B.101	Continuum removed metrics 970nm DDCF 24/07/2012	259
B.102	Continuum removed reflectance 970nm DDCF 24/07/2012	260
B.103	Continuum removed reflectance BNA 970nm DDCF 24/07/2012	260
B.104	Continuum removed metrics 1200nm DDCF 24/07/2012	260
B.105	Continuum removed reflectance 1200nm DDCF 24/07/2012	261
B.106	Continuum removed reflectance BNA 1200nm DDCF 24/07/2012	261
B.107	Transect vegetation properties DDT1 07/06/2011	261
B.108	Transect vegetation properties DDT1 08/06/2011	261
B.109	Spectra DDT1 08/06/2011	262
B.110	Vegetation indices DDT1 08/06/2011	262
B.111	Fluorescence Indices DDT1 08/06/2011	262
B.112	MTBVI DDT1 08/06/2011	263
B.113	Continuum removed metrics 470nm DDT1 08/06/2011	263
B.114	Continuum removed reflectance 470nm DDT1 08/06/2011	263
B.115	Continuum removed reflectance BNA 470nm DDT1 08/06/2011	264
B.116	Continuum removed metrics 670nm DDT1 08/06/2011	264
B.117	Continuum removed reflectance 670nm DDT1 08/06/2011	264
B.118	Continuum removed reflectance BNA 670nm DDT1 08/06/2011	265
B.119	Continuum removed metrics 970nm DDT1 08/06/2011	265
B.120	Continuum removed reflectance 970nm DDT1 08/06/2011	265
B.121	Continuum removed reflectance BNA 970nm DDT1 08/06/2011	266
B.122	Continuum removed metrics 1200nm DDT1 08/06/2011	266
B.123	Continuum removed reflectance 1200nm DDT1 08/06/2011	266
B.124	Continuum removed reflectance BNA 1200nm DDT1 08/06/2011	267
B.125	Transect vegetation properties DDT1 14/06/2011	267

B.126	Spectra DDT1 14/06/2011	267
B.127	Vegetation indices DDT1 14/06/2011	268
B.128	Fluorescence Indices DDT1 14/06/2011	268
B.129	MTBVI DDT1 14/06/2011	268
B.130	Continuum removed metrics 470nm DDT1 14/06/2011	269
B.131	Continuum removed reflectance 470nm DDT1 14/06/2011	269
B.132	Continuum removed reflectance BNA 470nm DDT1 14/06/2011	269
B.133	Continuum removed metrics 670nm DDT1 14/06/2011	270
B.134	Continuum removed reflectance 670nm DDT1 14/06/2011	270
B.135	Continuum removed reflectance BNA 670nm DDT1 14/06/2011	270
B.136	Continuum removed metrics 970nm DDT1 14/06/2011	271
B.137	Continuum removed reflectance 970nm DDT1 14/06/2011	271
B.138	Continuum removed reflectance BNA 970nm DDT1 14/06/2011	271
B.139	Continuum removed metrics 1200nm DDT1 14/06/2011	272
B.140	Continuum removed reflectance 1200nm DDT1 14/06/2011	272
B.141	Continuum removed reflectance BNA 1200nm DDT1 14/06/2011	272
B.142	Transect vegetation properties DDT1 29/06/2011	273
B.143	Spectra DDT1 29/06/2011	273
B.144	Vegetation indices DDT1 29/06/2011	273
B.145	Fluorescence Indices DDT1 29/06/2011	274
B.146	MTBVI DDT1 29/06/2011	274
B.147	Continuum removed metrics 470nm DDT1 29/06/2011	274
B.148	Continuum removed reflectance 470nm DDT1 29/06/2011	275
B.149	Continuum removed reflectance BNA 470nm DDT1 29/06/2011	275
B.150	Continuum removed metrics 670nm DDT1 29/06/2011	275
B.151	Continuum removed reflectance 670nm DDT1 29/06/2011	276
B.152	Continuum removed reflectance BNA 670nm DDT1 29/06/2011	276
B.153	Continuum removed metrics 970nm DDT1 29/06/2011	276
B.154	Continuum removed reflectance 970nm DDT1 29/06/2011	277
B.155	Continuum removed reflectance BNA 970nm DDT1 29/06/2011	277
B.156	Continuum removed metrics 1200nm DDT1 29/06/2011	277
B.157	Continuum removed reflectance 1200nm DDT1 29/06/2011	278
B.158	Continuum removed reflectance BNA 1200nm DDT1 29/06/2011	278
B.159	Transect vegetation properties DDT1 15/07/2011	278
B.160	SpectraDDT1 15/07/2011	278
B.161	Vegetation indices DDT1 15/07/2011	279

B.162	Fluorescence Indices DDT1 15/07/2011	279
B.163	MTBVI DDT1 15/07/2011	279
B.164	Continuum removed metrics 470nm DDT1 15/07/2011	280
B.165	Continuum removed reflectance 470nm DDT1 15/07/2011	280
B.166	Continuum removed reflectance BNA 470nm DDT1 15/07/2011	280
B.167	Continuum removed metrics 670nm DDT1 15/07/2011	281
B.168	Continuum removed reflectance 670nm DDT1 15/07/2011	281
B.169	Continuum removed reflectance BNA 670nm DDT1 15/07/2011	281
B.170	Continuum removed metrics 970nm DDT1 15/07/2011	282
B.171	Continuum removed reflectance 970nm DDT1 15/07/2011	282
B.172	Continuum removed reflectance BNA 970nm DDT1 15/07/2011	282
B.173	Continuum removed metrics 1200nm DDT1 15/07/2011	283
B.174	Continuum removed reflectance 1200nm DDT1 15/07/2011	283
B.175	Continuum removed reflectance BNA 1200nm DDT1 15/07/2011	283
B.176	Transect vegetation properties DDT1 24/08/2011	283
B.177	Spectra DDT1 24/08/2011	284
B.178	Vegetation indices DDT1 24/08/2011	284
B.179	Fluorescence Indices DDT1 24/08/2011	284
B.180	MTBVI DDT1 24/08/2011	285
B.181	Continuum removed metrics 470nm DDT1 24/08/2011	285
B.182	Continuum removed reflectance 470nm DDT1 24/08/2011	285
B.183	Continuum removed reflectance BNA 470nm DDT1 24/08/2011	286
B.184	Continuum removed metrics 670nm DDT1 24/08/2011	286
B.185	Continuum removed reflectance 670nm DDT1 24/08/2011	286
B.186	Continuum removed reflectance BNA 670nm DDT1 24/08/2011	287
B.187	Continuum removed metrics 970nm DDT1 24/08/2011	287
B.188	Continuum removed reflectance 970nm DDT1 24/08/2011	287
B.189	Continuum removed reflectance BNA 970nm DDT1 24/08/2011	288
B.190	Continuum removed metrics 1200nm DDT1 24/08/2011	288
B.191	Continuum removed reflectance 1200nm DDT1 24/08/2011	288
B.192	Continuum removed reflectance BNA 1200nm DDT1 24/08/2011	289
B.193	Transect vegetation properties DDT1 25/10/2011	289
B.194	Spectra DDT1 25/10/2011	289
B.195	Vegetation indices DDT1 25/10/2011	290
B.196	Fluorescence Indices DDT1 25/10/2011	290
B.197	MTBVI DDT1 25/10/2011	290

B.198	Continuum removed metrics 470nm DDT1 25/10/2011	291
B.199	Continuum removed reflectance 470nm DDT1 25/10/2011	291
B.200	Continuum removed reflectance BNA 470nm DDT1 25/10/2011	291
B.201	Continuum removed metrics 670nm DDT1 25/10/2011	292
B.202	Continuum removed reflectance 670nm DDT1 25/10/2011	292
B.203	Continuum removed reflectance BNA 670nm DDT1 25/10/2011	292
B.204	Continuum removed metrics 970nm DDT1 25/10/2011	293
B.205	Continuum removed reflectance 970nm DDT1 25/10/2011	293
B.206	Continuum removed reflectance BNA 970nm DDT1 25/10/2011	293
B.207	Continuum removed metrics 1200nm DDT1 25/10/2011	294
B.208	Continuum removed reflectance 1200nm DDT1 25/10/2011	294
B.209	Continuum removed reflectance BNA 1200nm DDT1 25/10/2011	294
B.210	Transect vegetation properties DDT1 17/11/2011	295
B.211	Transect vegetation properties DDT1 17/12/2011	295
B.212	Transect vegetation properties DDT1 23/01/2012	295
B.213	Transect vegetation properties DDT1 16/02/2012	296
B.214	Transect vegetation properties DDT1 20/03/2012	296
B.215	Transect vegetation properties DDT1 21/03/2012	296
B.216	Transect vegetation properties DDT1 23/04/2012	296
B.217	Transect vegetation properties DDT1 22/05/2012	297
B.218	Spectra DDT1 22/05/2012	297
B.219	Vegetation indices DDT1 22/05/2012	297
B.220	Fluorescence Indices DDT1 22/05/2012	298
B.221	MTBVI DDT1 22/05/2012	298
B.222	Continuum removed metrics 470nm DDT1 22/05/2012	298
B.223	Continuum removed reflectance 470nm DDT1 22/05/2012	299
B.224	Continuum removed reflectance BNA 470nm DDT1 22/05/2012	299
B.225	Continuum removed metrics 670nm DDT1 22/05/2012	299
B.226	Continuum removed reflectance 670nm DDT1 22/05/2012	300
B.227	Continuum removed reflectance BNA 670nm DDT1 22/05/2012	300
B.228	Continuum removed metrics 970nm DDT1 22/05/2012	300
B.229	Continuum removed reflectance 970nm DDT1 22/05/2012	301
B.230	Continuum removed reflectance BNA 970nm DDT1 22/05/2012	301
B.231	Continuum removed metrics 1200nm DDT1 22/05/2012	301
B.232	Continuum removed reflectance 1200nm DDT1 22/05/2012	302
B.233	Continuum removed reflectance BNA 1200nm DDT1 22/05/2012	302

B.234	Transect vegetation properties HHCC 29/09/2011	302
B.235	Spectra HHCC 29/09/2011	303
B.236	Vegetation indices HHCC 29/09/2011	303
B.237	Fluorescence Indices HHCC 29/09/2011	303
B.238	MTBVI HHCC 29/09/2011	304
B.239	Continuum removed metrics 470nm HHCC 29/09/2011	304
B.240	Continuum removed reflectance 470nm HHCC 29/09/2011	304
B.241	Continuum removed reflectance BNA 470nm HHCC 29/09/2011	305
B.242	Continuum removed metrics 670nm HHCC 29/09/2011	305
B.243	Continuum removed reflectance 670nm HHCC 29/09/2011	305
B.244	Continuum removed reflectance BNA 670nm HHCC 29/09/2011	306
B.245	Continuum removed metrics 970nm HHCC 29/09/2011	306
B.246	Continuum removed reflectance 970nm HHCC 29/09/2011	306
B.247	Continuum removed reflectance BNA 970nm HHCC 29/09/2011	307
B.248	Continuum removed metrics 1200nm HHCC 29/09/2011	307
B.249	Continuum removed reflectance 1200nm HHCC 29/09/2011	307
B.250	Continuum removed reflectance BNA 1200nm HHCC 29/09/2011	308
B.251	Transect vegetation properties HHCC 28/10/2011	308
B.252	Spectra HHCC 28/10/2011	308
B.253	Vegetation indices HHCC 28/10/2011	308
B.254	Fluorescence Indices HHCC 28/10/2011	309
B.255	MTBVI HHCC 28/10/2011	309
B.256	Continuum removed metrics 470nm HHCC 28/10/2011	309
B.257	Continuum removed reflectance 470nm HHCC 28/10/2011	310
B.258	Continuum removed reflectance BNA 470nm HHCC 28/10/2011	310
B.259	Continuum removed metrics 670nm HHCC 28/10/2011	310
B.260	Continuum removed reflectance 670nm HHCC 28/10/2011	311
B.261	Continuum removed reflectance BNA 670nm HHCC 28/10/2011	311
B.262	Continuum removed metrics 970nm HHCC 28/10/2011	311
B.263	Continuum removed reflectance 970nm HHCC 28/10/2011	312
B.264	Continuum removed reflectance BNA 970nm HHCC 28/10/2011	312
B.265	Continuum removed metrics 1200nm HHCC 28/10/2011	312
B.266	Continuum removed reflectance 1200nm HHCC 28/10/2011	313
B.267	Continuum removed reflectance BNA 1200nm HHCC 28/10/2011	313
B.268	Transect vegetation properties HHCC 17/12/2011	313
B.269	Transect vegetation properties HHCC 25/01/2012	314

B.270	Transect vegetation properties HHCC 14/02/2012	314
B.271	Spectra HHCC 14/02/2012	314
B.272	Vegetation indices HHCC 14/02/2012	315
B.273	Fluorescence Indices HHCC 14/02/2012	315
B.274	MTBVI HHCC 14/02/2012	315
B.275	Continuum removed metrics 470nm HHCC 14/02/2012	316
B.276	Continuum removed reflectance 470nm HHCC 14/02/2012	316
B.277	Continuum removed reflectance BNA 470nm HHCC 14/02/2012	316
B.278	Continuum removed metrics 670nm HHCC 14/02/2012	317
B.279	Continuum removed reflectance 670nm HHCC 14/02/2012	317
B.280	Continuum removed reflectance BNA 670nm HHCC 14/02/2012	317
B.281	Continuum removed metrics 970nm HHCC 14/02/2012	318
B.282	Continuum removed reflectance 970nm HHCC 14/02/2012	318
B.283	Continuum removed reflectance BNA 970nm HHCC 14/02/2012	318
B.284	Continuum removed metrics 1200nm HHCC 14/02/2012	319
B.285	Continuum removed reflectance 1200nm HHCC 14/02/2012	319
B.286	Continuum removed reflectance BNA 1200nm HHCC 14/02/2012	319
B.287	Transect vegetation properties HHCC 20/03/2012	320
B.288	Transect vegetation properties HHCC 22/03/2012	320
B.289	Spectra HHCC 22/03/2012	320
B.290	Vegetation indices HHCC 22/03/2012	320
B.291	Fluorescence Indices HHCC 22/03/2012	321
B.292	MTBVI HHCC 22/03/2012	321
B.293	Continuum removed metrics 470nm HHCC 22/03/2012	321
B.294	Continuum removed reflectance 470nm HHCC 22/03/2012	322
B.295	Continuum removed reflectance BNA 470nm HHCC 22/03/2012	322
B.296	Continuum removed metrics 670nm HHCC 22/03/2012	322
B.297	Continuum removed reflectance 670nm HHCC 22/03/2012	323
B.298	Continuum removed reflectance BNA 670nm HHCC 22/03/2012	323
B.299	Continuum removed metrics 970nm HHCC 22/03/2012	323
B.300	Continuum removed reflectance 970nm HHCC 22/03/2012	324
B.301	Continuum removed reflectance BNA 970nm HHCC 22/03/2012	324
B.302	Continuum removed metrics 1200nm HHCC 22/03/2012	324
B.303	Continuum removed reflectance 1200nm HHCC 22/03/2012	325
B.304	Continuum removed reflectance BNA 1200nm HHCC 22/03/2012	325
B.305	Transect vegetation properties HHCC 24/04/2012	325

B.306	Transect vegetation properties HHCC 24/05/2012	326
B.307	Spectra HHCC 24/05/2012	326
B.308	Vegetation indices HHCC 24/05/2012	326
B.309	Fluorescence Indices HHCC 24/05/2012	327
B.310	MTBVI HHCC 24/05/2012	327
B.311	Continuum removed metrics 470nm HHCC 24/05/2012	327
B.312	Continuum removed reflectance 470nm HHCC 24/05/2012	328
B.313	Continuum removed reflectance BNA 470nm HHCC 24/05/2012	328
B.314	Continuum removed metrics 670nm HHCC 24/05/2012	328
B.315	Continuum removed reflectance 670nm HHCC 24/05/2012	329
B.316	Continuum removed reflectance BNA 670nm HHCC 24/05/2012	329
B.317	Continuum removed metrics 970nm HHCC 24/05/2012	329
B.318	Continuum removed reflectance 970nm HHCC 24/05/2012	330
B.319	Continuum removed reflectance BNA 970nm HHCC 24/05/2012	330
B.320	Continuum removed metrics 1200nm HHCC 24/05/2012	330
B.321	Continuum removed reflectance 1200nm HHCC 24/05/2012	331
B.322	Continuum removed reflectance BNA 1200nm HHCC 24/05/2012	331
B.323	Transect vegetation properties HHCC 19/06/2012	331
B.324	Spectra HHCC 19/06/2012	332
B.325	Vegetation indices HHCC 19/06/2012	332
B.326	Fluorescence Indices HHCC 19/06/2012	332
B.327	MTBVI HHCC 19/06/2012	333
B.328	Continuum removed metrics 470nm HHCC 19/06/2012	333
B.329	Continuum removed reflectance 470nm HHCC 19/06/2012	333
B.330	Continuum removed reflectance BNA 470nm HHCC 19/06/2012	334
B.331	Continuum removed metrics 670nm HHCC 19/06/2012	334
B.332	Continuum removed reflectance 670nm HHCC 19/06/2012	334
B.333	Continuum removed reflectance BNA 670nm HHCC 19/06/2012	335
B.334	Continuum removed metrics 970nm HHCC 19/06/2012	335
B.335	Continuum removed reflectance 970nm HHCC 19/06/2012	335
B.336	Continuum removed reflectance BNA 970nm HHCC 19/06/2012	336
B.337	Continuum removed metrics 1200nm HHCC 19/06/2012	336
B.338	Continuum removed reflectance 1200nm HHCC 19/06/2012	336
B.339	Continuum removed reflectance BNA 1200nm HHCC 19/06/2012	337
B.340	Transect vegetation properties HHCC 25/07/2012	337
B.341	Spectra HHCC 25/07/2012	337

B.342	Vegetation indices HHCC 25/07/2012	338
B.343	Fluorescence Indices HHCC 25/07/2012	338
B.344	MTBVI HHCC 25/07/2012	338
B.345	Continuum removed metrics 470nm HHCC 25/07/2012	339
B.346	Continuum removed reflectance 470nm HHCC 25/07/2012	339
B.347	Continuum removed reflectance BNA 470nm HHCC 25/07/2012	339
B.348	Continuum removed metrics 670nm HHCC 25/07/2012	340
B.349	Continuum removed reflectance 670nm HHCC 25/07/2012	340
B.350	Continuum removed reflectance BNA 670nm HHCC 25/07/2012	340
B.351	Continuum removed metrics 970nm HHCC 25/07/2012	341
B.352	Continuum removed reflectance 970nm HHCC 25/07/2012	341
B.353	Continuum removed reflectance BNA 970nm HHCC 25/07/2012	341
B.354	Continuum removed metrics 1200nm HHCC 25/07/2012	342
B.355	Continuum removed reflectance 1200nm HHCC 25/07/2012	342
B.356	Continuum removed reflectance BNA 1200nm HHCC 25/07/2012	342
B.357	Transect vegetation properties HHCC 22/08/2012	343
B.358	Transect vegetation properties HHQF 27/06/2011	343
B.359	Transect vegetation properties HHQF 29/09/2011	343
B.360	Transect vegetation properties HHQF 16/11/2011	344
B.361	Transect vegetation properties HHQF 17/12/2011	344
B.362	Transect vegetation properties HHQF 25/01/2012	344
B.363	Transect vegetation properties HHQF 15/02/2012	345
B.364	Transect vegetation properties HHQF 21/03/2012	345
B.365	Transect vegetation properties HHQF 25/04/2012	345
B.366	Transect vegetation properties HHQF 24/05/2012	345

List of Tables

2.1	Table showing plant nutrients and symptoms of deficiency.	19
2.2	Typical density and rooting depth of arable crops	24
2.3	Table showing the properties of different sensors	30
2.4	Table summarizing common variants of the NDVI	37
2.5	Reflectance based fluorescence indices	47
2.6	Derivative based fluorescence indices	47
3.1	Properties of the ASD FieldSpec Pro instrument.	67
3.2	Vegetation indices used in this study	70
3.3	Absorption features used for continuum removal in this study	72
3.4	Metrics derived from continuum removed spectra	73
4.1	Table summarising RGB imagery used in this study. (* Note: 2011/06/14 Diddington only).	112
4.2	State of study sites during data acquisition.	113
5.1	Table summarising RGB imagery used in this study	136
6.1	Table showing hyper-spectral AIS surveys undertaken for this work	153
6.2	Vegetation indices used for the airborne data	155
6.3	MTBVI results from ground-based and airborne data	164
7.1	Correlation between methods for data fusion at HHQF 20/06/2012	175
B.1	Summary of surveys undertaken at DDCF	223
B.2	Summary of surveys undertaken at DDT1	224
B.3	Summary of surveys undertaken at HHQF	225
B.4	Summary of surveys undertaken at HHCC	226

Chapter 1

Introduction

1.1 Summary

This project examines means of improving the detection of subsurface archaeological features in arable areas using contrasting properties of the vegetation on the surface as a proxy for direct measurement of the properties of the soil. This is possible because the modification of soils by past human activity affects the resources available to the growing crop, and thus influences its health and development.

These effects have been widely used to map and characterise archaeological features since the early 20th century (e.g. Crawford 1923, St. Joseph 1945). However, acquiring data at the right time is problematic, as the temporal windows where the contrast in the vegetation is strong enough to detect the archaeological features are narrow and the contrasts are highly dynamic, varying spatially and temporally with local environmental conditions (Jones & Evans 1975, Allen et al. 1984, Evans & Catt 1987).

Recent work, using narrow band multi and hyper-spectral sensors that record images outside the visible spectrum has sought to extend these windows, as sensors that record reflectance in the near infrared region of the electromagnetic spectrum are more sensitive to variations in foliar biochemistry and vegetation structure than those that record broad-band reflectance in the visible spectrum (Challis et al. 2009, Bennett et al. 2011,

Verhoeven 2011, Aqduş et al. 2012, Verhoeven et al. 2013). While these studies have successfully developed means for improving contrast for detection, they have tended to focus on methods using reflectance at or near the *red-edge inflection point*. This provides a useful indication of both biomass and chlorophyll content. While these are proven indicators of stress and vigour in vegetation, they conflate long-term adaptation to environmental conditions and short-term responses to resource constraint by the crop.

This work contends that the temporal windows for the detection of archaeological vegetation marks can be extended by disambiguating the long-term and short term responses to differences in resource available to the crop canopy. This is demonstrated by the results of repeat, high-resolution ground-based measurement of reflectance and structural properties of crops over known archaeological features at four study sites in Southern England (chapter 3). Measurement of the physical properties indicated that biomass provided the most significant contrast in the long-term development of the crop, and methods sensitive to chlorophyll fluorescence were the most successful for detection of short-term responses to resource availability.

The subsequent chapters demonstrate that the knowledge gained from the ground-based work can be applied to three airborne sensors. Chapter 4 examines airborne laser scanning for the sensing of biomass variations, and demonstrates a novel, multi-temporal method for the detection of vegetation marks. Chapter 5 investigates methods for maximising contrast in vegetation canopies using imagery from visible light digital cameras. Chapter 6 evaluates whether the results of the ground-based survey can be applied to lower resolution hyper-spectral airborne imaging spectroscopy.

The results demonstrate that there is considerable scope for improving techniques for the detection of archaeological vegetation marks, particularly using locally optimised methods sensitive to short-term shortfalls in water availability in the crop canopy. However, the airborne hyper-spectral sensors used in this study lack the spatial resolution and temporal flexibility to make the most of these techniques. The final chapter of this work explores how these shortcomings can be overcome, and proposes the development of inexpensive aerial remote sensing platforms designed to maximise contrast in archaeological vegetation marks.

This work was undertaken as part of the DART project (Detecting Archaeological Residues using Remote Sensing Techniques), an AHRC and EPSRC funded interdisci-

plinary research project involving a broad consortium of organisations seeking to examine the dynamics of archaeological detection using airborne remote sensing and geophysical survey.

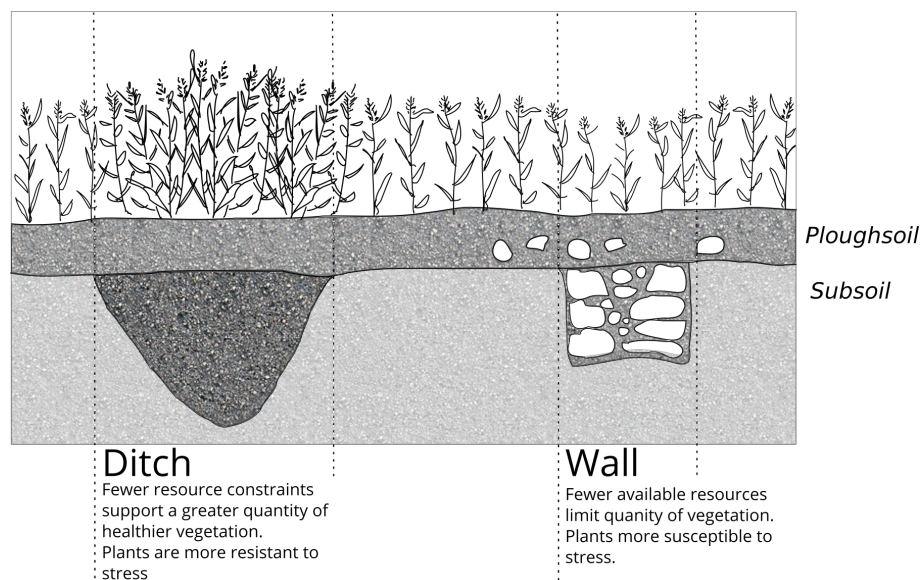


Figure 1.1: Archaeological vegetation marks are defined by differences in the structure and health of the vegetation caused by the material properties of the underlying soil.

1.2 Motivation

1.2.1 Why?

Archaeology is the study of past anthropogenic activity through material culture. This varies in scale from individual artefacts and ecofacts to entire landscapes altered by human actions. It enables us to study the lifestyles of past and present cultures, but more importantly is essential to understanding both human impact on the environment and the impact of changing environments on human societies (Renfrew & Bahn 1991, pp. 12–30). The evidence that allows us to study this is both fragile and fragmentary.

It is threatened by agricultural practices (Haldenby & Richards 2010), development (Kristiansen 2009) and environmental change (Chapman 2002, Murphy et al. 2009). To preserve and manage these finite resources effectively, either *in-situ* or by record it is essential to be able to rapidly identify and characterise areas of archaeological potential. This requires well-developed Historic Environment Records (HERs). Remote sensing

plays an essential role in the development of these records as it allows archaeological potential to be rapidly evaluated over large areas (Bewley 1993, Challis et al. 2008). However, with the increasing threats to the historic environment, caused by population growth and the rapidly changing environment, the pressure on the resources of bodies seeking to record and preserve it also increases. Improving the understanding of the detection of archaeological features will enable these bodies to make the best use of their limited resources.

1.2.2 The problem

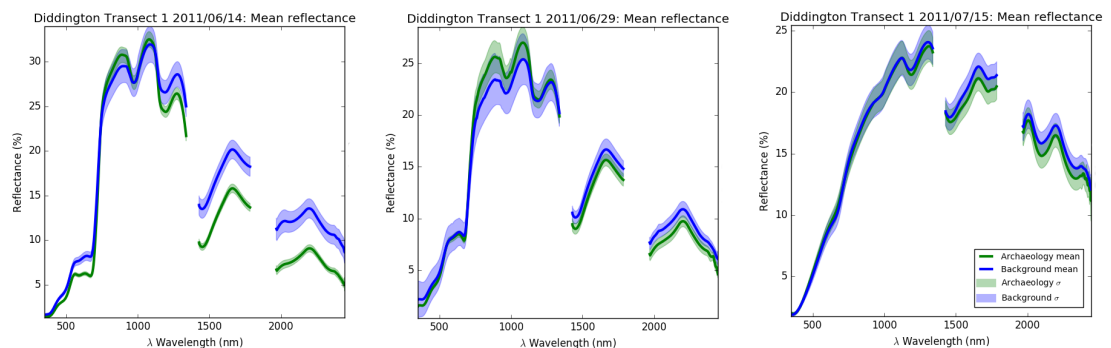


Figure 1.2: Spectra from Diddington transect 1, showing variation in vegetation mark expression in a mature wheat crop. *Left*: A fruiting crop. The archaeological features absorb more light in the visible and short-wave infra-red regions of the spectrum, and reflect more in the near infra-red. This is indicative of a greater quantity of healthier vegetation. *Middle*: Ripening crop. Less contrast is visible, as photosynthesis decreases. *Right*: Senescent crop. Reflectance in the visible and near infra-red is linear, as photosynthesis has ceased.

1.2.2.1 What are vegetation marks?

Vegetation marks are caused by localised modification of the soil in the archaeological features, meaning its properties contrast with those of the surrounding, unmodified subsoil. These modifications affect the composition, structure and chemistry of the soil in the features, which in turn affect the availability of water and nutrients to the crop. This influences the growth of the vegetation over the archaeological features. Where these are cut into the subsoil and filled with less compact, finer-grained material and inclusions of organic matter fewer constraints are placed on the growth of the vegetation (Scollar 1964, Jones & Evans 1975, Evans & Jones 1977, Stanjek & Fassbinder 1995). Conversely, where these modifications mean that there are compact inclusions such as stone struc-

tures, the roots cannot penetrate as deeply and fewer resources are available, meaning that resources are constrained over these features (figure 1.1) (Crawford 1923).

While the systematic mapping of archaeological features using these principles is well established in a number of countries (e.g. Bewley 1993, Bourgeois et al. 2002, Olesen 2004, Winton et al. 2010, Gojda 1997) there are a number of problems that limit its utility. Foremost among these are the temporal specificity and local variability of vegetation mark expression (figure 1.2). Contrast in vegetation marks is dependant on soil and weather conditions limiting individual plants in the crop from meeting their resource requirements from the soil (Jones & Evans 1975, Evans & Jones 1977). The conditions where these constraints occur are generally only of short duration, and in some drift geologies are infrequently detectable. This is particularly an issue in clay soils, which retain more water than free draining sands and gravels (Evans 2007).

There are three key aspects to the expression of contrast in the vegetation governed by the soil. The first of these are feedforward responses, which are long-term adaptations to environmental conditions, ensuring that the demand for water and other resources does not exceed supply by regulating growth (Passioura 2002). The second aspect are short-term responses to resource shortfalls, where the crop limits its demand for water by actively regulating its metabolism (Carter & Miller 1994, Genty et al. 1989). The third aspect are long-term expressions of stress expressed as differences in foliar biochemistry, a result of impaired synthesis of pigments, and in-extremis the death of foliar tissue (Chaves et al. 2002, Ashraf & Harris 2013).

1.2.2.2 How are they detected?

Most of the work undertaken by archaeologists in this area is conducted using observer directed, oblique aerial photography, where a photographer in a light aircraft records vegetation marks as they are seen (Riley 1987, pp. 41–47). While this technique is temporally responsive and inexpensive it is problematic. Only features observable to the naked eye are recorded, and given the high speed of the aircraft and the limits of human visual perception, is thus liable to omission through subjectively recording only the most apparent features (Hanson 2005, Brophy 2005). In addition, there is a tendency to bias in the record, as surveyors tend to focus their efforts on areas known to be productive. This leads to established sites being recorded in greater detail at the expense of discovering new ones in more 'difficult' areas (Bewley 2001, M. 2005, Palmer 2005). Some of these problems can be overcome by using systematic, vertical aerial surveys, where dedicated aircraft are

used to record overlapping coverage of entire regions. This mitigates the bias introduced by the observer, and provides more context to the observed features (Mills 2005, Palmer 2005, 2007). However, because these surveys require specially modified aircraft they are both more expensive and less temporally flexible than observer directed photography. In addition, despite the wide-spread use of these sensors the use of image processing techniques to enhance contrast is not widespread for these images beyond simple histogram optimisation.

Both of the above methods rely on broadband reflectance in the visible spectrum. While this is productive, the ability of these sensors to resolve subtle differences in vegetation properties is limited compared to narrow bandwidth hyper-spectral sensors that record in both the visible and near-infrared spectrum. Where a typical visible wavelength camera has three bands 100nm wide, a hyper-spectral sensor might possess hundreds 5nm wide or less. This enables the discrimination of greater contrast in the structure, pigmentation and metabolic processes of the vegetation, potentially extending the temporal window for detecting archaeological features (Beck, Wilkinson & Philip 2007, Verhoeven & Doneus 2011, Verhoeven 2008). While this has been comprehensively demonstrated in a number of studies, the use of these sensors is not widespread Beck (2011). There are a number of reasons for this. The expense and scarcity of the sensors means that they are generally accessible beyond research projects, and where they are accessible they may not be available at the right time. The processing, analysis and interpretation of the data is not trivial, and also requires considerable investment in specialised resources.

Approaches to utilising these sensors for archaeological detection tend to focus on well-known indices and data reduction techniques that emphasise specific foliar properties in the visible and near infra-red regions of the spectrum (e.g. Verhoeven 2011, Verhoeven et al. 2013, Doneus et al. 2014, Agapiou et al. 2010, Agapiou et al. 2013, Bennett et al. 2012, Bennett et al. 2013). These methods potentially conflate biomass, pigment absorption and metabolic processes, and are sensitive to long term adaptation to environmental conditions, rather than short term responses to variations in resource availability (Cho & Skidmore 2006). Developing methods that are sensitive to short term stress responses would enable detection of archaeological contrast is essential, as these responses occur before long-term adaptation to environmental conditions, and would expand the utility of these sensors by resolving contrasts that cannot be detected using other methods.

An advantage of the dedicated airborne survey platforms is that they can deploy multiple sensors at the same time, meaning that hyperspectral and vertical photographic and Airborne Laser Scanning (ALS) data can be collected simultaneously. Unlike the sensors discussed above, ALS is an active instrument, in that it measures the reflectance of energy emitted by the sensor and reflected by objects on the ground (Dubayah et al. 2000). ALS is widely used in archaeology for the detection of topographic features indicative of ruined structures and earthworks (Hesse 2010, Doneus & Briese 2006, Opitz & Cowley 2013), but is not widely used in for the investigation of archaeological cropmarks. It is, however, possible to use these sensors to measure crop structure, providing a more reliable measurement of biomass than spectral methods (Stott et al. 2013, 2015)

1.3 The thesis: Improving detection

The principal aim of this work is to investigate whether the temporal windows for detection of archaeological vegetation marks can be extended by optimising techniques for the application of each of three sensors considered in this work, namely ALS, RGB photography and hyper-spectral Airborne Imaging Spectroscopy (AIS). To do this requires an understanding of how the sensors work, what they record and how this can be used to detect contrast in vegetation marks.

To evaluate this each of three main aspects of vegetation mark expression were investigated:

- Long-term adaptation to resource availability through feedforward responses. These are expressed as variations in biomass, identified in the literature (Jones & Evans 1975) as the primary means of vegetation mark expression.
- Short term responses indicative of resource conservation such as chlorophyll fluorescence and ratios of chlorophyll to assistive pigments. These offer the greatest potential to extend detection, however they may be the hardest to detect given they are indicated by narrow spectral features.
- Stress, indicated by variations in foliar pigmentation. These are suggestive of long-term shortfalls in resource expression causing damage to the crop that cannot be mitigated by the two mechanisms above (Chaves et al. 2002).

Methods were first evaluated using multi-temporal ground-based survey of the physical and spectral properties of the vegetation in 2011 and 2012. The results of this work were then applied to inform analysis of the airborne data collected at much broader temporal intervals.

1.3.1 Ground-based survey

This was achieved by using intensive ground-based survey of the physical and spectral properties of the vegetation at high temporal, spectral and spatial resolutions at two study areas in the South of England: Diddington in Cambridgeshire and Harnhill in Gloucestershire. Diddington is located at the edge of the Fens, and spans free-draining sands and gravels and clays. Harnhill, located in the West of the country, generally receives more rainfall than Diddington, and contains both clay soils and shallow topsoils over limestone brash. These sites were chosen as they present a variety of conditions. At each site measurements were acquired over two known archaeological features, one in clay soils and the other on free-draining soils. The features were located by geophysical survey and trial excavation, and co-located with the monitoring equipment and geophysical surveys undertaken the University of Birmingham (Boddice 2015) and the University of Bradford (Fry 2014).

The results of the ground-based work showed that biomass variations were the strongest expressions of contrast, indicative of feed forward responses. Stress was observed only under the most extreme drought conditions, but where they were observed they tended to coincide with biomass variations. The greatest potential for temporally extending detection was encountered using locally optimised spectral indices sensitive to chlorophyll fluorescence. However, these indices depended on resolving narrow spectral features, and are only applicable to the AIS data. The application of chlorophyll fluorescence is novel for the detection of archaeological vegetation marks.

The methodology and results of this work are discussed in chapter 3.

1.3.2 Airborne laser scanning

Airborne laser scanning was used here to investigate the physical expression of vegetation marks through biomass variations. To do this a both full-waveform lidar and a novel, multi-temporal method for the detection of archaeological vegetation marks were investigated. This showed that the multi-temporal technique under ideal conditions provided better resolution of contrast expressed as biomass than both the full-waveform and aerial photography. This work was published in (Stott et al. 2015), and is explored in greater detail in chapter 4 of this work.

1.3.3 RGB images

RGB imaging is the most commonly applied method for detection of vegetation marks. However, to date relatively little effort has been expended in maximising contrast using the spectral properties of the vegetation, as the RGB images are treated as photographs rather than data. This is despite the fact RGB cameras are multi-spectral sensors and can be used to derive meaningful information on foliar properties. In this work methods used in precision agriculture for the detection of biomass and stress were applied to airborne RGB imagery. This demonstrated that these methods provide both a minor improvement in contrast, and additionally provide correction for differences in illumination caused by cloud cover. This work is detailed in chapter 5.

1.3.4 Airborne imaging spectroscopy

In chapter 6 the successful spectral methods evaluated in the ground-based work was applied to the airborne data. This work demonstrated that the methods identified as having the greatest potential, namely locally optimised narrow band indices sensitive short term adaptations, were applicable to the airborne data, despite the lower spectral resolution of the airborne data. However, the contrast detectable using the airborne sensors is limited by the low spatial resolution of the sensors. This is a limitation of the airborne systems accessible to this study, rather than the techniques themselves. Means of mitigating this using data fusion techniques and the development of systems capable of better resolving these contrasts are explored in the concluding chapter.

1.3.5 Contributions

The results of this work demonstrate that there is considerable potential to extend the capabilities of airborne remote sensing for the detection of archaeological vegetation marks through the application of methods novel to archaeological detection. These are, in order of their potential to improve contrast:

1. Narrow-band spectral techniques to detect short term responses to resource availability expressed by chlorophyll fluorescence. These methods provide contrast before it is detectable through biomass variation and stress, and offer considerable potential to extend the utility of hyper-spectral imaging for archaeology.
2. A multi-temporal ALS method for recording biomass variations in crop canopies. This provides the opportunity to record and characterise vegetation mark expres-

sion resulting from long-term feed forward responses to environmental conditions irrespective of illumination conditions.

3. Reflectance indices for improving contrast in RGB aerial photography. While these only provide minor improvements in the temporal ranges where contrast is detectable, the prevalence of these sensors and the large quantity of archival imagery means that this work has considerable impact.

Chapter 2

Background

2.1 Introduction

Past human activity modifies the structure and composition of the soil, which in turn influence the development and health of the vegetation above it. The contrast between the properties of the vegetation growing over concentrations of activity and elsewhere can be used as a proxy for the identification of the archaeology. These differences are temporally and spatially variable, and are theoretically caused by variations in resource availability in the soil to the crop. These differences may be the result of long-term developmental adaptation by the vegetation, or the result of short-term stress responses to sudden shortfalls (Chaves et al. 2002, Passioura 2002). These differences have long been used by archaeologists to detect buried archaeological features, and increasingly remote sensing techniques designed to monitor the growth and health of crops by exploiting the reflectance properties of crops inside and outside the visible spectrum. These techniques have been successfully applied to archaeological detection, but many approaches have focussed on data reduction and simple vegetation indices. While undeniably useful, these methods do not fully explore the potential of the sensors to provide fine-grained, detailed information about the crop. This information is key to understanding the expression of the vegetation marks, as it can be used to infer the causation of the vegetation marks, which in turn may allow us to extend the temporal periods where they can be detected (Beck 2011).

This chapter will discuss how we define archaeological features and the processes that form them. It will go on to explore these processes influence the growth of the vegetation and how this can be detected using remote sensing techniques. It will then discuss the current state of the art in the detection of archaeological vegetation marks.

2.2 Archaeological features: What are they? How do we find them?

2.2.1 What are archaeological features?

In this work the term *archaeological features* is used to denote the features we are looking for. In the arable landscapes considered here these are often discrete pockets of anthropogenically modified material that have survived continuous truncation from ploughing as they are either cut into the subsoil or are of sufficient depth to survive (Wilkinson et al. 2006, Haldenby & Richards 2010, Darvill 2014). The term *background* is used to describe areas outside these features, where subsoil is unmodified. The ploughsoil can be considered a separate cultural horizon covering the entire field, consisting of conflated material from the topsoil (or A-horizon), the subsoil, material from archaeological activity, and other anthropogenic additions resulting from agricultural practices such as manuring (Edgeworth 2014, Schofield 1989, Yorston et al. 1990).

Fundamentally, archaeological features are physical traces of past anthropogenic activity, and are direct evidence of how human beings modify their environments to fulfil their needs (Butzer 1982), be they basic in terms of shelter and food, such as settlements and their associated field systems, or ritual, for example religious monuments and mortuary structures. The majority of these features are not spectacular monuments, but the traces of small ditches, buried wall foundations, pits and postholes (Knapp & Ashmore 1999). Despite the ephemeral nature of these features they provide important knowledge about how people occupied and modified the landscape in the past.

2.2.2 Archaeological formation processes

Key to understanding detection are archaeological site formation processes. These are the sequence of events in the past that created the archaeological evidence that exists in the present. Essentially there are two types of events, subtractive events where material is removed, and additive events, where material is deposited (Harris et al. 1993). These

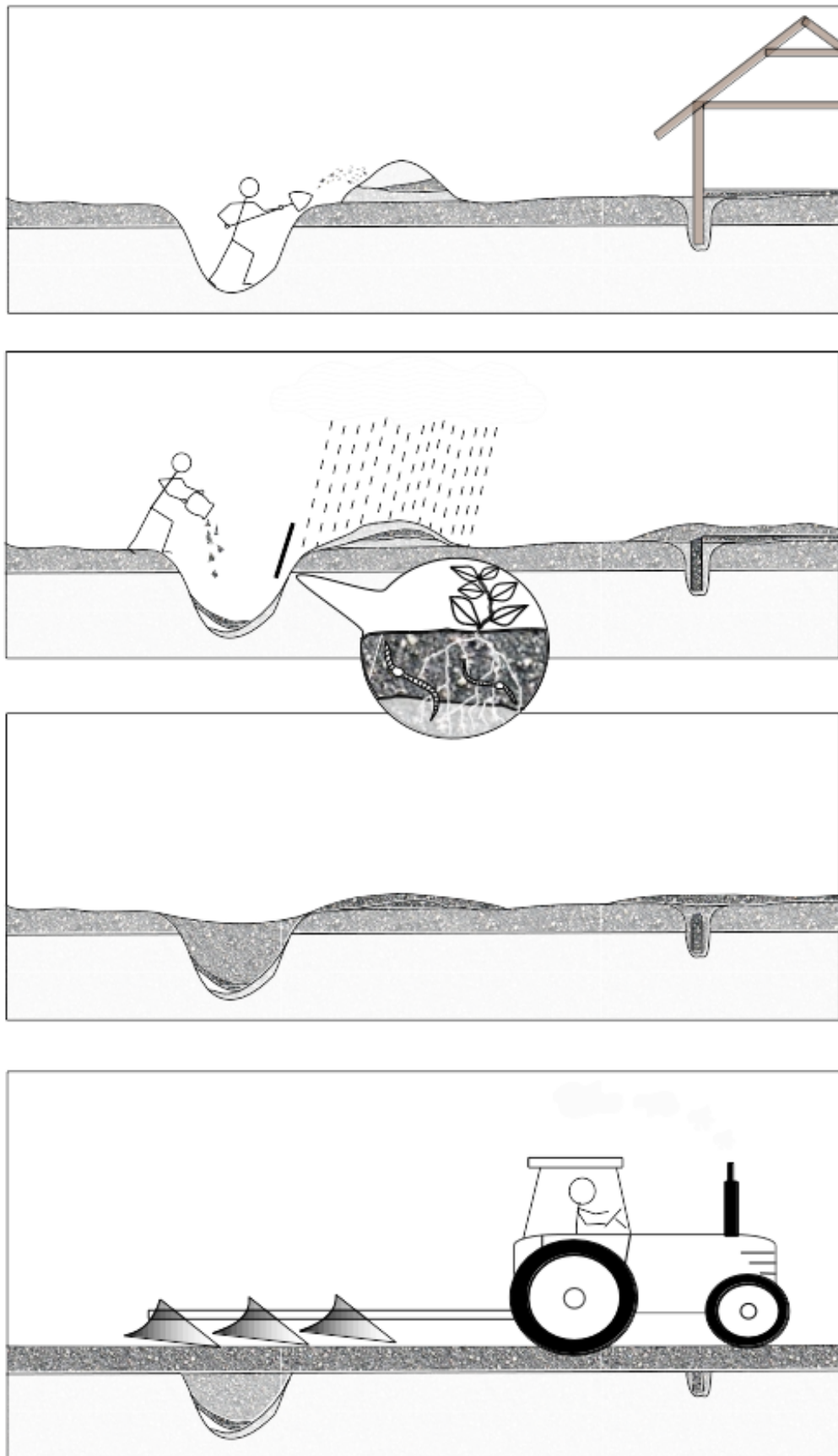


Figure 2.1: Schematic representation of typical archaeological site formation processes.

processes always maintain an equilibrium, as the material removed during subtractive events must be deposited somewhere else, and deposited material must always have been removed from somewhere else. This can vary in scale, from millimetres in the case of material mixed by the action of soil organisms (Matthews et al. 1997, Canti 2003, Atkinson 1957) to many kilometres in the case of natural processes such as windblown erosion and deposition (Schiffer 1996). During excavation archaeologists try to identify these events and remove them in chronological order so that deposits and the material associated with them can be dated in relation to each other (Harris et al. 1993; Carver 2013, 15-19).

An hypothetical sequence, typical of the sites considered for this project might be as follows (figure 2.1):

- In the past a field boundary is constructed. This consists of a ditch, cut through the topsoil and underlying subsoil. The material removed during the construction of the ditch is deposited adjacent to it to form a bank. During the lifetime of the boundary, exposed parent material from the sides of the ditch is washed into the base. At the same time vegetation becomes established within the ditch and on the bank. Decaying organic matter from this vegetation forms humus. This newly deposited material becomes conflated by the action of organisms and plant roots (bioturbation). The ditch slowly begins to fill with eroded material and organic matter.
- The hypothetical ditch is located near an area of human settlement. As the natural infill processes continue the ditch goes out of use, and becomes an attractive dumping ground for waste material. This results in the more rapid infilling of the ditch with human and animal waste, discarded artefacts, animal bone and other organic matter.
- The settlement is then abandoned. The ditch continues to infill by the processes of erosion and deposition. The deposits nearer the surface are conflated by bioturbation. These processes eventually lead to the ditch and bank being little more than a slight rise and depression visible on the ground surface.
- At some point this area is used for arable cultivation. It is ploughed using a mould-board plough, which truncates, inverts and redeposits the top 0.3m of soil. Successive ploughing events level the ground surface and further truncate the features until little or no topographic indication of the ditch and bank remain. The ploughing and subsequent harrowing and drilling conflate the material from the ditch surface

with the surrounding topsoil. Compaction and erosion caused by cultivation cause a gradual loss in volume of the topsoil, meaning that over time the plough cuts slightly deeper into the subsoil and archaeological deposits.

- During the present day nothing remains of the bank as it has been completely removed by ploughing. Some of the material truncated from the ditch and bank may remain in ploughsoil, mixed with the surrounding topsoil.

These processes mean that the material deposited in the feature differ markedly in structure and composition from the surrounding sterile subsoil (Lisá et al. 2015, Matthews et al. 1997). This difference allows us to identify the feature as contrasting with the surrounding material

2.2.3 Archaeological remote sensing

Archaeological remote sensing uses these differences to detect the feature. These can either be identified by direct measurement of the soil's electromagnetic properties, for example, electrical resistance, temperature, and soil reflectance (Scollar et al. 1990, Clark & Clark 2003, Gaffney & Gater 2006), or by proxy measurement of other properties influenced by these differences (Beck, Wilkinson & Philip 2007). Proxy measurement is important for the detection of features in arable areas, as cultivation practices mean it is seldom possible to measure these contrasts directly using optical techniques. Reflectance in the optical domain is from material in the top micrometer of the surface, and the crop and leaf litter both obscure the soil for much of the year (Huete 2005, Asner & Lobell 2000).

2.2.3.1 Contrast

The apparent contrast between the measurements recorded over the features and the background is used to interpret and identify the features. In the work considered here, the contrast is expressed in the growth of crops that are grown as monocultures. This means that the contrasts are expressed as differences in crops that are very similar. As such, there is no unique spectral signature that can be used to identify the archaeological features (Beck 2007). Instead, detection is contingent on subtle, relative variations in the growth of the crop. Because the properties of the background vary, even within the same field the expression of these contrasts is localised, and varies spatially with changes in soil composition, drainage and land use (Christensen 1974, Gojda & Hejcman 2012).

2.3 Archaeological vegetation marks

2.3.1 Causation

The causation of archaeological vegetation marks is the result of complex interactions between the properties of the soil, water movement and retention properties, temperature effects, and the vegetation itself (Scollar et al. 1990, pp. 50-75, Scollar 1964, Riley 1986). The vegetation marks occur when the difference between the subsoil and the fills of the feature are great enough to cause an observable effect on the development and health of the vegetation. In general, the fills of features such as pits and ditches are capable of supporting a greater density of healthier vegetation that is more resilient to stress induced by drought than the unmodified subsoil. Conversely, buried features that result in the compaction or deposition of hard material, such as buried walls and trackways cannot support as great a density of healthy vegetation, and are less resilient to stress (Crawford 1923, Evans & Jones 1977, Jones & Evans 1975).

2.3.2 Plants and soil

Plant roots are the means by which the plant interacts with the growth medium (in this case the soil). They are responsible for both the uptake of water, essential for both photosynthesis and the metabolic processes of the plant, and the uptake of dissolved nutrients (Raven & Edwards 2001, Russell et al. 1977). Water is thus the most important factor in the interactions between the plant and the soil, as a shortage means that the plant cannot make use of the nutrients in the soil even if these are in abundance (Barraclough 1989, Alam 1999, Hu & Schmidhalter 2005).

2.3.2.1 Water

Water content in the soil usable by the crop is measured using Available Water Capacity (AWC). This is a measure of the quantity of water available to the plant, and is defined by the difference between the water content at Field Capacity (FC) and at the Permanent Wilt Point (PWP):

$$AWC = \theta_{fc} - \theta_{pwp} \quad (2.1)$$

FC is defined as the bulk water content retained by the soil at -33 J/kg of negative hydraulic head. This is equivalent to the water content in the soil when drainage of excess water ceases and the rate of vertical movement through the profile is decreased (Veihmeyer & Hendrickson 1927). Typically this occurs 2-3 days after a rainfall event in pervious

soils. PWP is the minimal soil moisture that a plant requires not to wilt. At lower soil moisture content than this the plant wilts and cannot recover its turgidity. The physical definition of the PWP is water content at -1500 J/kg of negative hydraulic head. However, these values are not constant, and vary with the integrated effects of soil, vegetation and the atmospheric conditions (Richards 1928, Richards & Wadleigh 1952, Kramer et al. 1969). Conditions where soil moisture is approaching the PWP are known as a Soil Moisture Deficit (SMD). This is where cumulative evapotranspiration exceeds cumulative precipitation. The opposite situation to this is the Soil Moisture Surplus (SMS), where soil moisture is approaching or above the FC. The derivation of accurate SMD estimates can be complex, requiring detailed modelling of vegetation coverage, soil properties and weather conditions (Calder et al. 1983, Clark 2002).

2.3.2.2 Drought stress

Where there is a shortfall in water resources available to the plant it will attempt to mitigate these by regulating water losses. The primary mechanism for this is stomatal closure in response to decreasing soil water potential and leaf turgidity. Stoma are pores found on the epidermis of leaves that are used to control gas exchange during photosynthesis. CO₂ is an essential reactant in photosynthesis, so during daylight hours the stoma must be open for the plant to assimilate CO₂. The air spaces in the leaf are saturated with water vapour which escapes through the stoma (Bates & Hall 1981, Downton et al. 1988, Chaves et al. 2002). Thus the plant cannot photosynthesise without simultaneously losing water vapour, which is passively drawn up from the root system. By closing the stoma the plant can control these losses. This can be in response to temperature, humidity and losses caused by wind, but the roots also use Abscisic Acid (ABA) to induce stomatal regulation of leaf water losses in response to dehydration (Zhang & Davies 1989, Gowing et al. 1990). Closing the stoma means that gas exchange is also reduced, effectively limiting the rate of photosynthesis (Farquhar & Sharkey 1982). Thus, remote sensing techniques such as chlorophyll fluorescence (explored in detail below) that are sensitive to photosynthetic activity can in theory be used to detect drought stress in plants before there are physical and developmental effects (Zarco-Tejada et al. 2012). Stomatal closure is also temporally variable around the middle of the day, when there is the highest evaporative demand. The duration of this will increase with the severity of the drought (Tenhunen et al. 1984, Chaves et al. 2002). In the longer term there is a gradual decrease in demand for CO₂ as the activity of the various enzymes decrease. This leads to an eventual loss in chlorophyll content as the plant downgrades its demand for CO₂ to adapt to the changed circumstances. If drought conditions persist eventually damage occurs

to the photosynthetic apparatus of the plant, leading to a further decrease in chlorophyll content. This may be due to pigment degradation caused by degradation of thylakoids in chloroplasts or impaired synthesis of pigments (Kaiser 1987, Chaves et al. 2002, Ashraf & Harris 2013).

2.3.2.3 Feed-forwarding and developmental effects.

In addition, there is strong evidence that the roots of the plant provide sensory information to the plant that allow it to anticipate and respond to changing environmental conditions by sending inhibitory signals that regulate the growth and development of the plant before damage occurs due to resource constraint. This mechanism is known as feed-forward (Aiken & Smucker 1996, Krouk et al. 2011). Currently the role of the various enzymes and hormones potentially used as inhibitors to govern cell division, cell expansion, and leaf appearance are poorly understood (Demmig-Adams et al. 2014, Chew et al. 2014). However, it is clear that plants reduce Leaf Area Index (LAI) by inhibiting growth in the face of falling soil moisture conditions, before leaf water status is affected (Davies & Zhang 1991). These long-term, conservative responses to difficult growth conditions are not necessarily desirable in arable crops where high yields are desired, so their impact has been reduced over time by selective breeding out of these traits (Passioura 2002).

2.3.2.4 Soil hardness and porosity

There is also an apparent feed-forward response to soil hardness and porosity (White & Kirkegaard 2010). In compacted soils there is a marked decrease in LAI with increasing bulk density and a soil hardness. This is apparent from the growth of the first few leaves, at a time when the plant is under no resource constraint. This indicates that the feed-forward response is limiting growth in relation to how difficult it is for the roots to penetrate the soil, anticipating future shortfalls in resources (Passioura 2002, Oussible et al. 1992). Overly porous or poorly compacted soil can also have a deleterious effect on growth. This is possibly due to the roots preferentially following the pores, resulting in a reduced intake of water compared to more evenly distributed roots. This may be due to the roots in clumps effectively competing with each other, causing localised drying and hardening of the soil and thus affecting water uptake (Tardieu et al. 1992). Although excessive porosity is deleterious to growth under normal conditions it is advantageous in drought conditions as it allows roots to achieve greater depth more rapidly (Cornish 1993).

2.3.2.5 Nutrients

Plants require nutrients from the soil in addition to water, O₂ and CO₂. The nutrient uptake from the soil is through cation exchange, where roots pump H⁺ ions into the soil, displacing cations attached to negatively charged soil particles, making them available for uptake by the root. Nutrients are divided into three key groups according to the quantity the plant needs for healthy growth; primary macronutrients, secondary macronutrients, and micronutrients and trace minerals (Hopkins & Hner 1995, Barker & Pilbeam 2010), These, and the effects of deficiency are outlined in table 2.1.

Element	Required for	Deficiency symptoms
N	Proteins	Stunted or slow growth, chlorosis
K	Stomatal regulation, photosynthesis, cellulose	Necrosis, interveinal chlorosis, brown spotting disease, risk
P	Photosynthesis, biosynthesis.	Intense green colouration of leaves, necrosis, anthocyanin accumulation
S	Chloroplasts, amino acids	Yellowing leaves, stunted growth
Ca	Nutrient transport, enzyme activation	Stunting
Mg	Chlorophyll	Chlorosis
Si	Strength of cell walls	Lodging, disease and pest susceptibility
Fe	Photosynthesis	Chlorosis, necrosis
Mo	Amino acids, N metabolism	N deficiency
B	Pectins, cell division	Necrosis, stunting
Cu	Photosynthesis	Chlorosis
Mn	Photosynthesis	Discolouration, chlorosis
Na	Growth, metabolism, replacing K	Chlorosis, wilting, brown spots
Zn	Enzymes, DNA transcription	Stunted leaves
Ni	Nitrogen metabolism	Necrotic lesions
Cl	Osmosis, ionic balance	White spots
Co	Nitrogen fixation in legumes, Mo substitution	See N deficiency
Al	Fungicide	Root rot

Table 2.1: Table showing plant nutrients and symptoms of deficiency. After Hopkins & Hner (1995). Macronutrients are indicated by **bold** text.

Chlorosis is the inability of the plant to produce chlorophyll. This is indicated by pallid yellowish or yellow-white foliage. Necrosis, another key symptom of nutrient stress is indicated by the death of leaf tissue. The parts of the plant effected by nutrient deficiency are determined by mobility of the nutrient. Deficiency in mobile nutrients, such as N, P and K, will be evident in the older leaves first, as the plant can move these to where they are most needed in younger, still developing leaves. Less mobile nutrients, such as S, stay in older leaves, meaning that signs of deficiency are most evident in the younger leaves (Bukovac & Wittwer 1957, Alam 1999, Buhtz et al. 2010). In excess many of these nutrients are toxins and cause damage to the plant. For example, an excess of nitrogen can cause lodging in wheat, where the plant grows too quickly and is prone to damage from wind (Crook & Ennos 1995).

In general supplies of micronutrients are provided by the weathering of the substrate and mineralisation of decaying organic matter (White & Zasoski 1999). In natural ecosystems the supply of macro nutrients is effectively a closed loop, as cyclical processes remove and replenish nutrients, for example, in the nitrogen and phosphorous cycles (Galloway et al. 2004). In arable agriculture however, a large quantity of biomass, and thus embodied nutrients that would ordinarily be returned to the soil through ammonification are removed every time the crop is harvested (Stevenson 1965). This means these macronutrients must be replenished using fertilisers or rotation with nitrogen fixing crops and animals. Fertilisers are applied to the ground surface, meaning that to be available to the plant's root system there must be enough rainfall to carry the dissolved fertiliser into the soil. This is why during a drought crops will often exhibit symptoms of nutrient stress as well as obvious symptoms of drought stress (Barraclough 1989, Alam 1999, Hu & Schmidhalter 2005).

2.3.3 How archaeological formation processes change the soil

Soil structure is arguably the most important factor, as it greatly affects both the moisture movement through the soil and the ability of the plant's roots to forage for water and nutrients. Plants are dependant on water, both for metabolic processes and for the uptake of critical nutrients in solution. A less compact, more porous structure means that roots can penetrate to a greater depth, but also mean that water can move much more easily through the soil, effectively increasing the availability of water to the roots (Atwell 1990, Barken et al. 1987). In general, we would expect the fills of archaeological features to

be less compact, with a greater density of pores than the surrounding subsoils (Scollar et al. 1990, pp. 10–18, Stanjek & Fassbinder 1995). This is in part due to the formation processes of the features. Where features are in-filled deliberately, the infill material will typically be deposited in lumps of excavated material, resulting in a heterogeneous structure that is often used during excavation as a diagnostic characteristic of archaeological deposits. Where the feature has been open for some time the growth of vegetation results in bioturbation by roots and other soil organisms, again increasing the porosity of the fills (Grave & Kealhofer 1999, Johnson 2002, Wilkinson et al. 2009). Inclusions in the infill of the feature also affect the soil structure. Charcoal and other burned organic material is particularly important, as it creates porous structures that break down extremely slowly, to such an extent that 'biochar' is becoming increasingly used as a soil amendment to increase drought resistance in agricultural crops (Atkinson et al. 2010, Lehmann & Joseph 2009). Other persistent inclusions in the fills, such as bone and ceramics will also create pockets of porous material. The effects of these inclusions have been observed in the *Terras Petras* or 'black earths' of the Brazilian Amazon, where the long-term deposition of charcoal, bone and ceramics were used as soil amendments for extensive areas of cultivation in prehistory, resulting in persistent improved crop yields in the present day compared to the other soils in the area that are rapidly depleted after deforestation (Novotny et al. 2009, Glaser & Birk 2012).

Soil Composition. The growth of vegetation and the anthropogenic deposition of plant and animal waste increase the quantity of organic carbon in the soil. These are both typical components of the formation processes of the fills of the archaeological features. Organic carbon both increases soil porosity even after it decays, but also increases water retention in sandy soils, and improves the structural stability of clay soils (Donahue et al. 1972). In addition, the particle sizes of material filling the feature tend to be smaller and more evenly distributed than those in the surrounding subsoil (Scollar et al. 1990, 1–15, Strunk-Lichtenberg 1965). In addition to material deposited in the feature by human agency, the particle size of eroded material washed into the feature are smaller, as finer material can be carried further by water than coarser material. This is the origin of vegetation marks from geomorphological features such as relict stream channels and ice wedge polygons, as the finer particle sizes are washed into voids created by these geological processes (Shotton 1960, Christensen 1974, Svensson 1988). Finer particle sizes result in better water retention, as in the soil matrix they provide a greater surface area, slowing the percolation of water through the soil. This means that crops grown on these features have better resistance to drought than those growing on a more freely draining, coarse

particle sized background (Jones & Evans 1975, Evans & Catt 1987, Stanjek & Fassbinder 1995). Both clays and organic carbon improve the Cation Exchange Capacity (CEC) of the soil. CEC is the number of exchangeable cations per dry weight the soil can hold due to electrostatic charges that attract and hold ions (Liang et al. 2006). This reflects the ability of the soil to store nutrients that would otherwise be leached away.

Nutrients and mineral content in the archaeological features are also modified by human activity. The addition of ash, human and animal waste, by-products of manufacturing processes such as metalworking and tanning, and midden material all change the chemistry of the soil. It has been suggested that this is a significant factor in vegetation mark formation, but experimental results in work undertaken by Sharpe (2004) that attempted to correlate geophysical responses and vegetation mark formation with nutrient content proved inconclusive. Indeed, it has been suggested (Scollar et al. 1990, p. 66, Jones & Evans 1975) that the frequent application of phosphate and nitrate fertilisers effectively mask the differences in content of major nutrients, and that the difference in mineral content between archaeological fills and the background is comparatively minor due to leaching of nutrients over time (Wilson 1975, Wilson et al. 2008, Oonk et al. 2009, Nielsen & Kristiansen 2014). However, vegetation marks defined by symptomatic differences in nutrient content are not uncommon (Jones & Evans 1975). This is partially due to the likelihood that the fills of the archaeological features have a higher CEC, and thus have the capacity to retain nutrients for longer between fertiliser applications, but the moisture content of the soil is also critical, as the roots are dependant on water for the transportation of nutrients (Passioura 1983, Jaleel et al. 2009).

Temperature. Archaeological features are generally wetter and contain more organic carbon than the background soils. This makes them darker in colour than the surrounding background, meaning they have a lower albedo and higher thermal conductivity

2.3.4 Vegetation mark expression

In the section above we have discussed how plants interact with the soil, and how archaeological formation process change the soil. These changes influence the growth and development of the vegetation. To infer what is happening in the soil, and thus the likely presence of archaeological features we use the properties of the vegetation as a proxy. This is dependant on the interactions of many variables, including the properties of particular soils, the nature of the archaeology itself, land management practices and the weather. The conventional understanding of vegetation mark visibility is that these are stress and

vigour variations, however the feedforward mechanisms that allow plants to regulate their growth in response to soil conditions mean that we can expect to see expression in terms of LAI variation before stress and vigour variations are apparent, as these responses are the plant's means of regulating demand in step with environmental constraints. This is supported by the most thorough exploration of vegetation mark formation by (Jones & Evans 1975, Evans & Jones 1977), who propose that LAI is the most common form of expression. The increased LAI over the features in these marks mean that they appear darker green than the background, as a greater proportion of visible light is absorbed by the greater quantity of vegetation. In the near-infrared portion of the spectrum we expect to see an increase in reflectance. Contrast expressed as LAI also likely corresponds to variations in the height of the crop noted by many authors (Crawford 1923, St Joseph 1969, Riley 1944, Riley 1987, pp. 33–36, Wilson 1982, p. 54) meaning that under low solar zenith angles the marks can be defined by differences in highlight and shadow.

Stress and vigour variations, visible as changes in leaf colour to the naked eye are more likely the result of sudden, severe, stresses resulting in a loss in chlorophyll content as a response to prolonged stomatal closure. This may explain the vegetation marks noted by a number of authors (Wilson 1982, p.55, Riley 1986,(Riley 1987, pp. 31–33), Scollar et al. 1990, pp. 53–55) that are visible during a period of drought that disappear after rainfall events. Under extreme drought conditions there are also differences in the maturation of the crop, with the less stressed plants fruiting and reaching maturity more rapidly (Riley 1987, pp. 33–35, Darvill 1996). This leads to 'cropmark reversal', where positive vegetation marks are tonally lighter against the darker background of the rest of the crop. Similar responses can be observed in oilseed rape, lavender crops and poppies, where variations in flowering and ripening can define spectacularly colourful vegetation marks (Riley 1944, St. Joseph 1945, Hampton et al. 1977). Marks defined by lodging of crops, where excessive growth leads to weak stems and makes the crops prone to being knocked down by wind or heavy rain (Jones & Evans 1975, Wilson 1982, pp. 59-60, Stanjek & Fassbinder 1995) are relatively rare in the present day due to the prevalence of dwarf varieties since the green revolution (Passioura 2002).

2.3.4.1 Crops

Effectively in vegetation mark archaeology every plant in a crop canopy is a sensor (Wilson 1982, p. 56). This is a useful analogy, as each plant can be crudely construed as a pixel in an image. This is why cereal crops, with their high planting density, demonstrate the greatest clarity, as each individual plant is more likely to be influenced by

very localised soil conditions. At lower densities the portion of the plant's root structure growing in, and thus influenced by, the archaeological feature will be smaller. In addition, cereal crops are comparatively deep-rooted and reach maturity during the period of highest evaporative demand, making them both more likely to be affected by soil moisture deficits and to be able to forage for resources at depth. In general, winter cereal crops have deeper and more extensive root systems than spring sown crops due to their longer establishment phase. These can be up to twice the depth of similar spring sown crops (Thorup-Kristensen et al. 2009, White & Kirkegaard 2010, Sylvester-Bradley et al. 2008). This potentially makes winter crops more resistant to resource constraint, as they can draw upon water and nutrients from deeper in the soil. This also potentially makes them less conducive for vegetation mark formation in deep soils, as the plant can draw upon groundwater resources not available to shallow rooted crops. Table 2.2 illustrates planting densities and rooting depth for the four most common arable crops in the UK.

Crop	Spring wheat	Winter wheat	Oilseed Rape	Barley
Density (N/m^2)	200	100	24	300
Max root depth (m)	1.1	2.2	1.8	1.7

Table 2.2: Table indicating typical density and maximum depth of crops. This will vary dependant on local conditions. Adapted from Canadell et al. (1996), Barraclough (1989).

Oilseed rape, although deep rooted, is not as conducive for vegetation mark expression as cereal crops. This is partiality due to lower planting densities, but also the peak water demand of the crop is during the late winter and spring (Barraclough 1989, Berry et al. 2014), meaning that the this crop is less susceptible to moisture stress than cereals during the period of highest evapo-transpiration and lowest rainfall. Most vegetation marks recorded in oilseed rape are the result of variable flowering and ripening. Root crops, such as potatoes, swedes and turnips are less conducive to vegetation mark formation, as these crops can both store substantial reserves of water in their tubers, and are comparatively shallow rooted. Where these crops are growing over shallow walls or other hard features, however, vegetation marks may be detectable by wilting or leaf inversion.

2.3.5 Weather

2.3.5.1 Soil moisture deficit

SMD has long been used by archaeologists to predict vegetation mark formation. The general consensus is that PSMDs of 50mm or greater are indicative of a high likelihood of vegetation mark formation in free draining soils (Jones & Evans 1975, Evans & Jones 1977) and 150mm in clay soils (Evans 2007). PSMD is perhaps an overly simplistic indicator as crops have different moisture requirements over the course of their growth cycle. For example, the water requirements of wheat decline after heading and flowering, meaning that an PSMD in the spring and early summer will likely have the greatest impact on the crop, and thus the formation of vegetation marks. PSMD is a cumulative measure. As such the effects of short duration rainfall events will be obscured by an increasing deficit (Evans & Catt 1987, Scollar et al. 1990, pp. 63–74). The local drainage conditions are also an important factor that will influence soil moisture and are not taken into account by the PSMD calculations. This can be in the form of land drains, slope and the surface condition of the soil (Burt & Butcher 1985). Compact or very dry surfaces are less pervious to water so that precipitation will run off the ground surface rather than being absorbed into the soil matrix (Batey & McKenzie 2006).

2.3.6 Soils

The nature of the the subsoil is a critical in the formation of vegetation marks. Clay soils retain moisture over longer periods than free draining soils. This is because clays possess a greater surface area due to their small particle size. This creates greater surface tension between water and the soil. In theory, this makes them less conducive to vegetation mark formation than free-draining sands and gravels. This is traditionally explained (e.g. Riley 1987, Wilson 1982) by the larger water holding capacity that make water deficits develop more slowly. However, this could also be explained by there being less of a contrast between the moisture retention and holding capacity between the fills of the features and the surrounding subsoil (Evans 2007). This has led to clay soils being dismissed as unproductive by a number of archaeologists, who have historically focussed their attentions on areas that are known to be productive (Cowley & Dickson 2007, Grady 2007). Recently, however, there have been a number of researchers challenging this. A systematic ortho-photographic survey commissioned by the local authority in Bedfordshire in 1996 revealed extensive vegetation mark complexes in clay soils (Palmer 2007), and other surveys conducted in the East Midlands of England revealed large numbers of archaeological vegetation marks (Deegan 2007, Deegan & Foard 2013).

2.4 Remote sensing of vegetation properties

2.4.1 Principles of remote sensing

Remote sensing is the discipline of observing and measuring phenomena without actually being in physical contact with them. In the context considered here this involves measuring electromagnetic radiation emitted or reflected by objects, either using solar illumination in the case of passive remote sensing (such as RGB cameras and multi and hyper-spectral radiometers) or by using energy emitted by the sensor itself (lidar scanners). Different materials possess distinct patterns of absorption and reflectance. Equipped with an understanding of these properties we can use them to infer qualitative and quantitative information about the composition and state of these objects (Lillesand et al. 2004).

2.4.1.1 The electromagnetic spectrum in the optical domain

We classify the light returned by objects using the intensity of the light at the wavelength(s) that the sensor records. Figure 2.2 shows the classification of energy in the electromagnetic spectrum. The reflectance of a scene is calculated by using irradiance (the energy illuminating the scene) and radiance (the energy received by the sensor). The radiance recorded by the sensor is the result of complex interactions that occur between the illumination source, the target and the sensor. Radiance recorded by the sensor is the sum of mixed contributions contained within the Instantaneous Field of View (IFOV) of the sensor, and the medium through which the energy is travelling (Lillesand et al. 2004, pp. 4–39, Campbell & Wynne 2011, pp. 36–54. For example, when measuring a crop canopy the irradiate energy is reflected and absorbed by the crop canopy, any under-story vegetation and leaf litter, the soil, and the atmosphere between the sensor and the ground. To further complicate matters the texture and geometry of the object in relation to the light source and sensor are also important. To model this the Bi-Directional Reflectance Distribution Function (BRDF) is used (Nicodemus 1965, Torrance & Sparrow 1967, Schaepman-Strub et al. 2006). This is a four-dimensional function that returns a ratio of radiance to irradiance. Measuring and BRDF is difficult and time consuming, as it is also wavelength dependant because the relationship between the physical structure of the object and the wavelength defines the extent to which they are specular (mirror like) or lambertian (matte, or rough). For vegetation canopies, where the leaf angle distribution is heterogeneous and varies with the time of day and wind moving the canopy, BRDF is almost impossible to model comprehensively (Strahler 1997, Weiss & Baret 1999, Kumar et al. 2002). This is why measurements are ideally acquired as close as possible to

solar noon, as making the illumination angle as constant as possible greatly simplifies comparison between measurements (Liang & Strahler 1993, Sandmeier et al. 1998).

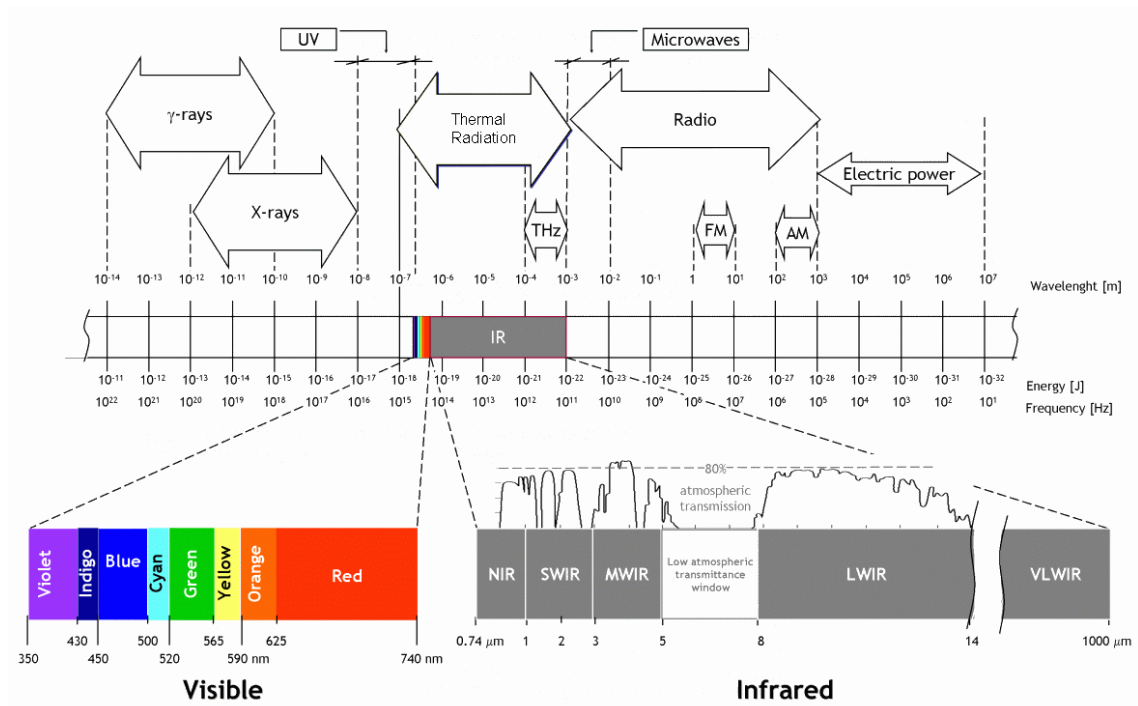


Figure 2.2: The electromagnetic spectrum. "Infrared spectrum" by Clemente Ibarra-Castanedo Licensed under Creative Commons Attribution-Share Alike 3.0 via Wikimedia Commons.

2.4.1.2 Sensors

The radiance at the sensor is recorded using arrays of photodetectors. These produce a voltage from the energy incident on each detector during the integration or exposure time, which is then converted to a value using an Analogue to Digital Converter (ADC). The measurement domain of the axes of the array of photodetectors varies with different sensor designs. On a panchromatic camera the x and y axes of the array are purely spatial (Leberl et al. 2003). On an RGB camera both axes are spatial, but the Bayer filter attached to the array means that each detector is also filtered spectrally (Bayer 1976, Malvar et al. 2004). On a push-broom hyper-spectral scanner the x domain of the sensor is spatial and the y axis is spectral, with the second spatial dimension being provided by the movement of the sensor (Gupta & Hartley 1997, Fricker & Rohrbach 2005). Separation of spectral properties at the sensor is achieved using a number of different techniques. The simplest is the application of filters to the photodetectors, as in RGB cameras. This limits the number of bands the sensor can record, so hyperspectral imagers tend to use diffraction

gratings or prisms to divide light of different wavelengths across the array (Hinnrichs & Massie 1997, Fisher et al. 1998, Yuen & Richardson 2010). The implications of different sensor designs are explored in detail later in the appropriate chapters.

Resolution is the ability of the sensor to resolve and discriminate between objects. This is commonly used to refer only to spatial resolution, but a sensor can be of very high spatial resolution and still lack the ability to resolve tonal differences between similar objects. The four principal properties of resolution are:

- **Spectral resolution** is an intrinsic property of the sensor that describes the ability of the sensor to resolve spectral differences between objects. This generally refers to the number of bands across the range of instrument's spectral sensitivity. The width of these bands is defined using the Full Width at Half Maximum (FWHM) of each band. This is the width of each band in wavelength units at half the maximum sensitivity of each band. Often the sensitivity of adjacent bands will overlap outside the FWHM (Woodcock & Strahler 1987, Pohl & Van Genderen 1998).
- **Radiometric resolution** is an intrinsic property that describes the ability of the sensor to resolve differences in reflectance within each band without adjusting exposure. This is often expressed as the bit-depth of the sensor. An 8-bit sensor can record 256 discrete values, whereas a 16 bit sensor can resolve 65536 values. An oft-repeated example of how this effects images is a scene that contains areas of snow and dark rock. The 8 bit sensor will saturate over the snow and be unable to resolve differences over the rock unless the integration time or gain is adjusted to record each area individually in separate images. The 16 bit sensor will be able to resolve detail in both areas simultaneously without adjusting exposure (Tucker 1980, Legleiter et al. 2002, Rama Rao et al. 2007).
- **Spatial resolution** is a term most used to describe the size of each pixel in an image that is widely used in the literature. In a sense this a term is a misappropriation. More properly, this should be referred to as ground sample distance. This is the size of the IFOV of each pixel of the sensor projected on the scene at a given distance. This is a combination of extrinsic and intrinsic properties, as the size of the detector array, the field of view of any optics used to project an image onto the array, and the distance of the sensor from the scene are all properties that govern this (Woodcock & Strahler 1987, Legleiter et al. 2002).
- **Temporal resolution** is the minimum time between measurements of the same area. For remote sensing this is largely extrinsic to the sensor, as it depends on how it is

deployed. For the airborne systems considered here this is largely irrelevant, but for satellite systems this is dependant on orbital geometry (Lillesand et al. 2004, pp. 45-49)

2.4.1.3 Platforms

The platform is means by which the sensor is deployed to cover the area of interest. The sensor and the platform together is here referred to as a system. These range in size and complexity, from kites and balloons (Smith et al. 2009, Verhoeven 2009) to dedicated aircraft and satellites (Mather & Koch 2011). The platform on which a sensor is deployed defines the spatial and temporal resolution of the system. Temporal resolution defines the ability of the system to acquire repeat measurements. For satellites this is easy to quantify, as temporal resolution is governed by the orbital geometry of the platform. These are often deployed in constellations, reducing the revisit time. For aircraft this is harder to quantify, as theoretically there few constraints on repeat flights over the same area (Lillesand et al. 2004, pp. 45-49). However, the highly specialised dedicated aircraft used for systematic airborne surveys are often in great demand, with users having to schedule surveys months in advance. The responsiveness of the system to changes in conditions on the ground is an important consideration for the recording of archaeological vegetation marks, as the temporal windows for data acquisition are relatively short.

2.4.1.4 Displaying images

One of the challenges in hyperspectral remote sensing is the large number of redundant bands. Successfully displaying this information in a way that represents the phenomena of interest is not trivial, as there is more information than can be represented on a single display. The data are displayed either as gray scale and pseudo-colour intensity images of single bands, or as colour composites, where different bands are mapped to the red, green and blue channels of the display, mimicking trichromatic human vision, and meaning that three distinct datasets can be displayed simultaneously. Where these correspond to reflectance in the red, green and blue regions of the visible spectrum this known as an *approximate true colour composite* (Porter & Duff 1984, D'Entremont & Thomason 1987). Where reflectance is used but one or more of the bands is not used to approximate RGB reflectance this is known as a *false colour composite* (Toet & Walraven 1996, Zhimin et al. 2002). A *pseudo-colour composite* incorporates either the products of reflectance or data from other sources, such as terrain models (Tajima 1983). If more information is required

Platform	Sensors	Spatial resolution	Revisit time	Availability	Cost km ²
Worldview 3 Satellite	multi-spectral imager	1.24m	<1 day	High	100s
NERC ARSF aircraft	Hyper-spectral, lidar, frame camera	1m	Limited by availability	Low	By grant application
Geomatics Group Aircraft	Hyper-spectral, lidar, frame camera	1m	Limited by availability	Low	1000s
Cessna	RGB oblique camera	<0.25m	<1 day	Medium	100s
UAV	RGB camera	<0.1m	<1 day	High	100s

Table 2.3: Table showing temporal properties and cost of platforms for airborne surveys.

to be displayed this can be performed using data fusion techniques. These are explored more fully in the final chapter of this work.

2.5 Optical properties of vegetation

Remote sensing techniques are used extensively for the characterisation and analysis of vegetation. The available literature exploring applications such as forestry, ecology, climate change monitoring, and precision agriculture is comprehensive. As such the optical properties of vegetation are well understood.

2.5.1 Photosynthesis

Photosynthesis is the means by which plants convert energy gained by absorbing light into sugars that provide the organism with the energy required for metabolic processes. The pigments fundamental to this process gives vegetation its most distinctive spectral absorption features. Between 70% and 90% of visible light falling on a leaf is absorbed by the main photosynthetic pigments, chlorophyll a and b. These pigments are located in chloroplast organelles. The highest concentration of chloroplasts is found in the densely packed palisade cells of the upper mesophyll. Below this the cells in the spongy meso-

phyll contain fewer chloroplasts. The cells here are much less dense, with many air voids that allow for gas and water vapour to diffuse through the leaf. The epidermis of the leaf is largely transparent (Blankenship 2008, Garab 1998).

In the NIR region of the spectrum little light is absorbed by the pigments, as the epidermis and palisade cells are largely transparent to light at these wavelengths. In the spongy mesophyll the many air-water interfaces cause scattering. About 5-10% of NIR radiation is absorbed by the tissues of the plant, and 40-60% is reflected. The remainder is transmitted through the leaf. The transmission and scattering of light at these wavelengths is important, as it is highly sensitive to variations in LAI and thus biomass (Fourty et al. 1996, Guyot et al. 1992). This is because vegetation canopies are not formed of a single layer of leaves, so the scattered and transmitted radiation is further reflected by the canopy. This phenomenon is described as leaf stacking in the literature. The steep increase in reflectance in the NIR region is one of the most characteristic spectral features of vegetation. The wavelength of the inflection point where reflectance increases in the far red or NIR is known as the Red Edge Inflection Position (REIP) (Boochs et al. 1990).

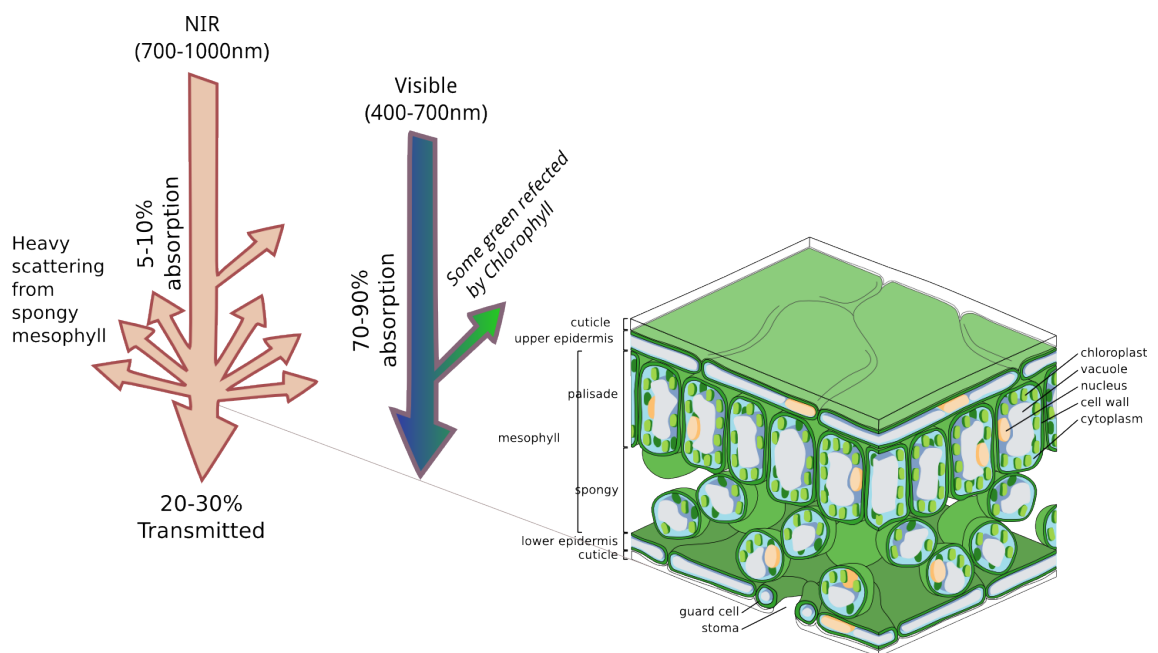


Figure 2.3: Leaf structure and optical properties. After Verhoeven (2011). Based on “Leaf Structure” by Zephyris Licensed under Creative Commons Attribution-Share Alike 3.0 via Wikimedia Commons.

2.5.1.1 Pigments

Chlorophyll molecules are embedded in the thylakoid membranes of chloroplasts. The main function of the chlorophyll molecules is to absorb light and transform the energy by resonance energy transfer to the reaction center of the photosystems. Plants contain two distinct chlorophyll molecules, chlorophylls a and b. Chlorophyll a has approximate absorption peaks at approximately 430nm and 662nm. Chlorophyll b has absorption maxima at approximately 453nm and 642nm. The reaction centres of photosystems I and II (PSI & PSII) contain varying quantities of chlorophyll a and b bonded to different protein structures (Mackinney 1941, Brown 1983, Nuijs et al. 1986). The photosystems have their own reaction centre chlorophyll pigments named after their peak absorption wavelengths in nanometres in the red region of the spectrum. These are P700 and P680 respectively. PSI and PSII function in series, with PSII acting first to produce Adenosine Triphosphate (ATP) by channelling an electron through a series of receptors to drive a proton pump. The electron is then passed to PSI, which uses light energy to channel the electron to ferredoxin, producing the enzyme Nicotinamide Adenine Dinucleotide Phosphate (NADPH). ATP and NADPH are then utilised in the light independent reactions of the Calvin cycle to generate carbohydrates (Blankenship 2008, Garab 1998).

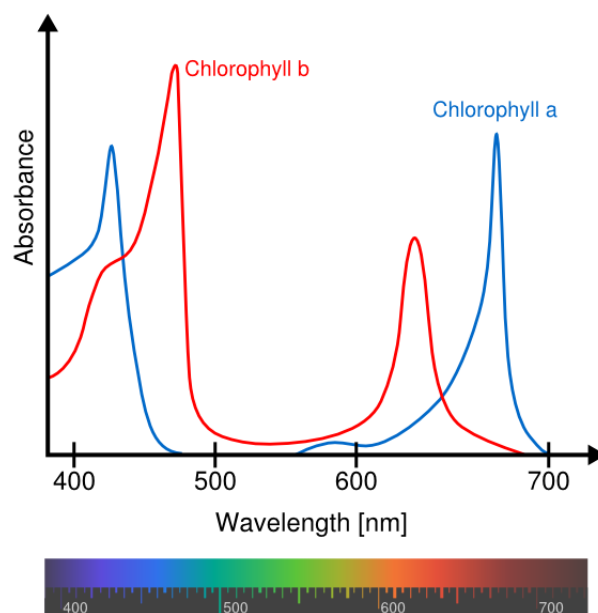


Figure 2.4: Chlorophyll absorption spectra. "Chlorophyll ab spectra-en" by M0tty. Licensed under Creative Commons Attribution-Share Alike 3.0 via Wikimedia Commons.

The REIP is used as an indicator of vegetation stress. In stressed vegetation it shifts towards the blue end of the spectrum, whereas in healthy vegetation it is generally located further towards the red portion of the spectrum, as increased chlorophyll content leads to a broadening of the absorption feature. This shift occurs in the region between 680nm and 760nm. A number of studies have suggested that this is strongly correlated with overall chlorophyll content at a leaf level (Curran et al. 1995, Horler et al. 1983), however, due to leaf stacking this is harder to quantify at the canopy level (Boochs et al. 1990). Water stress has also been suggested as influencing the shape of the red-edge, as water content affects the leaf structure, and therefore the scattering behaviour at longer wavelengths (Filella & Penuelas 1994). In addition a common stress response is for the chlorophyll *a/b* ratio to shift (Alberte et al. 1977, Jaleel et al. 2009). This is probably related to a lower ratio of occurrence of PSII to PSI (Ashraf & Harris 2013, Murata et al. 2007), explaining a shift in absorption towards shorter wavelengths. Methods for estimating the REIP are explored in depth in section 2.6.2.

Other pigments than chlorophylls also play an essential role in photosynthesis. Two different kinds of carotenoids, xanthophylls and carotenes. The xanthophyll cycle is responsible for non-photochemical quenching (NPQ), a mechanism by which prevents oxidative damage to pigments, lipids and proteins caused by an excess of chlorophylls in an excited state. With increasing light intensity the photosynthetic capacity of the leaf tends to saturate, creating an excess in the light energy absorbed by the pigments. NPQ dissipates this energy as heat through molecular vibration. As such, their presence and activity is implicitly related to the photosynthetic capacity of the plant. Carotenes, the orange pigment that give carrots their colour, extend the wavelength range of energy that the plant can absorb into the green region of the spectrum (Cogdell 1978). Carotenes are accessory pigments, so cannot harvest this energy directly. Instead, it must be passed to chlorophyll pigments. In addition, carotenes also act as antioxidant, protecting cellular tissues in the plant by absorbing energy from singlet oxygen. Carotenoids increase absorption in the blue and green regions of the spectrum, from 400-530nm. Kov et al. (2013) used continuum removal techniques to successfully characterise xanthophyll content in the region between 511nm-557nm.

2.5.1.2 Fluorescence

Chlorophyll fluorescence is light re-emitted after being absorbed by chlorophyll. Energy absorbed by the leaf will be either used as part of the photosynthetic process, emitted as heat due to NPQ or as light at a longer wavelength due chlorophyll fluorescence. Thus,

by measuring fluorescence information about the efficiency of the photochemistry can be inferred. In the pigment-protein complexes of the cells there are two distinct peaks, at 690nm and 740nm (Krause & Weis 1984, 1991, Schreiber et al. 1995, Maxwell & Johnson 2000). Fluorescence is a highly sensitive measure of stress, as adaptations to stressful conditions such as stomatal closure reduce the ability of the plant to metabolise normally, meaning that there is a potential imbalance between the absorption of energy and its use in photosynthesis (Downton et al. 1988, Flexas et al. 2002). Fluorescence can be used to measure short-term stress responses that occur before there are permanent changes in the pigment content or structure of the foliage. As such, it is a powerful tool for the identification of stress before other techniques can detect it. However, in highly stressed vegetation and high light levels there is a decline in fluorescence with photosynthesis, as the activation of the xanthophyll cycle and reduction in pigment contents reduce the photosynthetic capacity of the plant (Meroni et al. 2009, van der Tol et al. 2009). There is also a strong overall correlation between fluorescence and total chlorophyll content. Gitelson et al. (1999) found a linear relationship between chlorophyll content and fluorescence at 735nm, using the a ratio of reflectance at $\lambda 735/\lambda 700$.

Measuring Fluorescence in the field or lab is most often conducted using chlorophyll fluorometers. These are portable instruments that use a modulated light source with a detector tuned to detect excitation at the same modulation as the light source. The ratio $\frac{F_v}{F_m}$ is the most commonly used measure of efficiency of photosystem II, where F_v is the maximal fluorescence excited by the light source minus the minimal fluorescence of the dark-adapted leaf, and F_m is the maximal fluorescence (Schreiber et al. 1986, 1995). Unfortunately the measurement of fluorescence using remote sensing techniques is far from straightforward, as the amount of emitted radiation is small (1-2%) in relation to that absorbed and reflected by the vegetation canopy. One technique is to exploit gaps in the solar and atmospheric spectrum known as Fraunhofer lines. Because there is little or no light at these wavelengths from the sun, the extent to which they are filled indicates radiance derived from fluorescence. However, the Fraunhofer features are extremely narrow, requiring an instrument of extremely high spectral resolution (0.05-0.1nm) or complicated fitting methods for the unmixing of fluorescence derived radiance and from the edges of the Fraunhofer features (Carter et al. 1990, 1996, Meroni et al. 2009). Alternatively, reflectance based methods using indices of reflectance or derivative reflectance can be used. These use apparent reflectance and its derivatives at two or three wavelengths, one affected by fluorescence and at least one less affected. The latter is used to normalize the former. Apparent reflectance based methods cannot provide fluorescence estimates in

absolute physical units, but instead return Fluorescence in relation to reflectance (Meroni et al. 2009, Zarco-Tejada et al. 2012). Airborne and spaceborne measurement of fluorescence is complicated by heavy attenuation of light at these wavelengths by O₂ in the atmosphere between the target and the sensor.

2.5.2 Foliar Biochemicals

In addition to the photosynthetic and assistive pigments a number of other essential biochemicals are present in the vegetation canopy that may be detected optically. These have well defined absorption features that can be used for their estimation. These absorption features are broadened by multiple scattering. In addition, many compounds absorb light at similar wavebands, meaning that particular wavelengths in the reflectance spectrum are never uniquely related to a single chemical. Furthermore these absorption features may coincide with atmospheric absorption bands, making their use impractical outside laboratory environments (Curran 1989).

2.5.2.1 Canopy water content

Foliage contains a high proportion of water. Water content has a strong correlation with green biomass. In addition, it can be used to identify senescence and extreme stress and vigour variations. However, it is less useful for identifying subtle drought stress responses as these maintain leaf water content at great expense. Liquid water absorption features as a result of O-H bonds can be found at 970nm, 1200nm, 1450nm and 1950nm (Curran 1989, Peuelas et al. 1993). The features at 1450nm and 1950nm are most pronounced, but also coincide with atmospheric water vapour absorption bands that preclude their use. Thus the features at 970 and 1200m, although less pronounced are more useful. Associated with these are water vapour absorption features centred on 940nm and 1140nm (Clevers et al. 2008). This means that increased transpiration has the potential to broaden these features, as water vapour is released by the plant during photosynthesis. Thus, by using the width of these features stomatal closure can possibly be assessed.

2.5.2.2 Lignin and cellulose

Lignin and cellulose are organic polymers that make up the structure of plants, forming elements of cell walls and the vascular system. Thus they are an important indicator of biomass and dry weight. Lignin has absorption features centred on 1120nm, 1420nm, 1450nm, 1690nm, 1754nm, 1940nm, 2262nm and 2380nm (Curran 1989, Serrano et al. 2002). The bands centred on 1420nm and 1940nm are located in atmospheric absorption

peaks, making them impractical for use under field conditions. Cellulose has absorption features centred on 1490nm, 1540nm, 1780nm, 1820nm, 2100nm, 2270nm and 2350nm (Curran 1989, Nagler et al. 2003). Sensing of lignin and cellulose is important, as it enables refinement of biomass estimates by separating dry, dead matter from healthy green vegetation (Nagler et al. 2003).

2.5.2.3 Nitrogen

N is a component of chlorophyll and proteins, and is present in quickly growing, green vegetation. 1510nm, 1690nm, 2060nm, 2180nm, 2300nm, and 2350nm (Curran 1989, Jones et al. 2014).

2.6 Hyper-spectral vegetation analysis techniques

2.6.1 Vegetation Indices

Vegetation indices are the simplest and most widely used method of investigating vegetation properties in field and imaging spectroscopy. At their most basic these are ratios between the reflectance minima and maxima for known foliar absorption features, for example the Simple Vegetation Index (SVI, 2.2):

$$SVI = \frac{R_{NIR}}{R_{RED}} \quad (2.2)$$

This uses the increased absorption of light in the red band and increased reflectance of light in the infra-red band characteristic of vegetation. Bare soil will exhibit values in the SVI close to 1, with values increasing with the quantity of green vegetation.

Simple ratios such as the SVI are highly susceptible to changes in illumination geometry and intensity. Normalised Difference Vegetation Indices (NDVI, 2.3, Rouse et al. (1974)) are attempt to resolve this. As such it is a transformation of The SVI. There have been numerous attempts to correlate the NDVI with various foliar and biochemical quantities, such as biomass and chlorophyll content. However, if the NIR wavelength is outside the region potentially effected by the REIP (beyond 750nm) then it is less influenced by chlorophyll content and more influenced by LAI.

$$NDVI = \frac{R_{NIR} - RED}{R_{NIR} + R_{RED}} \quad (2.3)$$

NDVI and SVI were originally formulated as a broadband index for use with Landsat and other multi-spectral sensors, where the large bandwidths mean there is often a single red

and near infrared band. Adapting the the sensor for use with narrow-band, hyper-spectral sensors makes the choice of which bands to use more difficult. Several authors have suggested narrow band indices that emphasise particular elements of vegetation reflectance (table 2.4).

Red band	IR band	Rationale	Source
670	800	Biomass sensitive	Haboudane (2004)
705	750	Avoids saturation caused by senescent leaves and high chlorophyll a content	Gitelson et al. (1999)
694	760	Sensitive to chlorosis, less sensitive to LAI variations	Carter & Miller (1994)
695	805	Red-edge sensitive	Carter & Miller (1994)

Table 2.4: Table showing common wavelength derivation variants of the the NDVI.

However, the spectral properties of the vegetation canopy are a result of the combined reflectance of the crop, its state, and the soil and land management practices. From the point of view of detecting subtle variations in canopy properties using narrow-band NDVI each field is unique, and there is no universally applicable form of the NDVI in terms of band selection. In addition, the relationship between NDVI values and LAI shows a non linear relationship and saturates in dense canopies (Baret & Guyot 1991, Lillesaeter 1982). The Renormalized Difference Vegetation Index (RDVI, equation 2.4; Roujean & Breon (1995)) and Modified Simple Ratio (MSR, equation 2.5; Chen (1996)) are attempts to improve the accuracy of the NDVI at both high and low canopy densities by defining a more linear relationship.

$$RDVI = \frac{R_{800} - R_{670}}{\sqrt{R_{800} + R_{670}}} \quad (2.4)$$

$$MSR = \frac{\left(\frac{R_{800}}{R_{670}} - 1\right)}{\sqrt{\left(\frac{R_{800}}{R_{670}} + 1\right)}} \quad (2.5)$$

In sparse canopies and dry conditions indices can be distorted by contributions to reflectance from the soil, as this increases reflectance in the red region of the spectrum, where the greatest absorption from chlorophyll is expected. Several indices attempt to mitigate against this. The modified soil resistant vegetation index (equation 2.6) uses a band in the blue region of the spectrum, as reflectance from the soil is lower in this region, but absorption from chlorophylls and carotenoids is still high (Sims & Gamon 2002)

$$mSRVI = \frac{R_{750} - R_{445}}{R_{705} + R_{445}} \quad (2.6)$$

The soil adjusted vegetation index uses a constant (equation 2.7), L to correct for the influence of soil reflectance. The value of this constant varies with the LAI of the vegetation canopies in question between zero and one. At very low canopy densities a value of 1 is appropriate, for intermediate densities a value of 0.5 is used. In general a value of 0.5 is used, as this provides an adjustment factor suitable for a wide range of conditions Huete (1988).

$$SAVI = \frac{R_{NIR} - R_{RED}}{R_{NIR} + R_{RED} + L} (1 + L) \quad (2.7)$$

Optimising the value of L requires either *a priori* knowledge of the density of the vegetation or trial and error to identify the best value. The modified soil adjusted vegetation index (equation 2.8) attempts to mitigate for this by using the slope of the soil reflectance (Qi, Chehbouni, Huete, Kerr & Sorooshian 1994), where s is the slope of the soil line.

$$MSAVI = \frac{(R_{NIR} - R_{RED})(1 + L)}{R_{NIR} + R_{RED} + L} L = 1 - \frac{2s(R_{NIR} - R_{RED})(R_{NIR} - s * R_{RED})}{R_{NIR} + R_{RED}} \quad (2.8)$$

Again, MSAVI requires some prior knowledge, as the reflectance of the soil must be known to characterise s . This can vary considerably with changing soil moisture content. Qi, Kerr & Chehbouni (1994) applied a recursive solution to the derivation of the soil brightness correction factor, eliminating the need for its prior derivation. This index (MSAVI2, equation 2.9) has thus largely replaced MSAVI in common usage.

$$MSAVI2 = \frac{2R_{NIR} + 1 - \sqrt{(2R_{NIR} + 1)^2 - 8(R_{NIR} - R_{RED})}}{2} \quad (2.9)$$

2.6.1.1 Three band indices

Three band vegetation indices use reflectance in the green region of the spectrum to measure the depth of the chlorophyll absorption feature in the red region relative to the green and NIR reflectance peaks. Kim et al. (1994) developed the chlorophyll absorption ratio index (equation 2.10). The ratio of reflectance between reflectance at 550nm and 700nm is constant, regardless of leaf level differences of chlorophyll concentration. Thus, variations in chlorophyll content can be normalised for biomass.

$$CARI = \left(\frac{|a \cdot R_{670} + |R_{670}| + b|}{(a^2 + 1)^{0.5}} \right) \cdot \left(\frac{R_{700}}{R_{670}} \right) \quad (2.10)$$

Where $a = \frac{R_{700} - R_{550}}{150}$ and $b = R_{550} - (550a)$. This index was simplified by Daughtry et al. (2000) as the modified chlorophyll absorption index (MCARI, equation 2.11). Despite MCARI being designed as being responsive to chlorophyll it was found that LAI accounted for 60% of the variation of this index, despite there being no NIR component.

$$MCARI = ((R_{700} - R_{670}) - 0.2(R_{700} - R_{550})) \cdot \left(\frac{R_{700}}{R_{670}} \right) \quad (2.11)$$

Haboudane (2004) introduced two modifications of MCARI. MCARI1 (equation 2.12) introduces reflectance from a NIR wavelength to reduce sensitivity to chlorophyll effects and increase sensitivity to LAI variations. MCARI2 (equation 2.13) reduces contamination from soil reflectance by introducing a soil correction factor, optimised to preserve sensitivity to LAI as well as reducing sensitivity to the influence of chlorophyll.

$$MCARI1 = 1.2 [2.5(R_{800} - R_{670}) - 1.3(R_{800} - R_{550})] \quad (2.12)$$

$$MCARI2 = \frac{1.5 [2.5(R_{800} - R_{670}) - 1.3(R_{800} - R_{550})]}{\sqrt{(2R_{800} + 1)^2 - (6R_{800} - 5\sqrt{R_{670}}) - 0.5}} \quad (2.13)$$

Similar to the CARI based indices is the triangular vegetation index (TVI, equation 2.14). Conceptually the triangular area defined by the green peak, maximal chlorophyll absorption in the red, and the increased reflectance in the NIR will increase as a result of chlorophyll absorption and LAI (Broge & Leblanc 2001). However, increased chlorophyll

causes reduced reflectance in the green region, due both to slight absorption at these wavelengths by chlorophyll itself and the absorption of assistive carotenoid pigments. In addition, the NIR wavelength R_{750} chosen by the authors can be influenced by the REIP (Haboudane 2004).

$$TVI = 0.5 [120(R_{750} - R_{550}) - 200(R_{670} - R_{550})] \quad (2.14)$$

Haboudane (2004) adapted the TVI to make it more suitable for LAI estimation. By substituting the R_{750} used for TVI for R_{800} which is not influenced by pigment level changes and applying a scaling factor MTVI1 (equation 2.15 is thus more sensitive to biomass than the TVI. Like MCARI2, MTVI2 (equation 2.16 uses a soil correction factor.

$$MTVI1 = 1.2 [1.2(R_{800} - R_{550}) - 2.5(R_{670} - R_{550})] \quad (2.15)$$

$$MTVI2 = \frac{1.5 [1.2(R_{800} - R_{550}) - 2.5(R_{670} - R_{550})]}{\sqrt{(2R_{800+1})^2 - (6R_{800} - 5\sqrt{R_{670}}) - 0.5}} \quad (2.16)$$

2.6.1.2 Red-edge indices

Indices are also used to provide a relative indication of the REIP. The red-edge NDVI (equation 2.17, Gitelson & Merzlyak (1994)) and red-edge visible atmospheric resistant index (equation 2.18, (Gitelson, Kaufman, Stark & Rundquist 2002)) utilises the REIP to refine the NDVI in accordance with the state of the crop .

$$Red - edgeNDVI = \frac{R_{NIR} - R_{REIP}}{R_{NIR} + R_{REIP}} \quad (2.17)$$

$$Red - edgeVARI = \frac{R_{REIP} - R_{RED}}{R_{REIP} + R_{RED}} \quad (2.18)$$

R_{REIP} is the reflectance at the REIP. Both indices are suitable for the identification of stress and vigour variations. The modified red-edge normalized difference vegetation index (equation 2.19, Sims & Gamon (2002)) uses an extra band from the blue region of the spectrum to provide a correction for specular reflection of red light from leaves.

$$mNDVI_{705} = \frac{R_{750} - R_{705}}{R_{750} + R_{705} - 2R_{445}} \quad (2.19)$$

A simpler approach to defining differences in REIP related stress and vigour is to use ratios to attempt to capture the gradient of reflectance at the red-edge Vogelmann et al.

(1993) suggests two indices to achieve this. The first index (equation 2.20) is a simple ratio between R_{740} and R_{720} . This is problematic, as if the REIP is outside this range the index will be distorted. The second index (equation 2.21) mitigates this by using three wavelengths, so that curvature in the slope of reflectance is accounted for.

$$VOG1 = \frac{R_{740}}{R_{720}} \quad (2.20)$$

$$VOG2 = \frac{R_{734} - R_{747}}{R_{720} + R_{726}} \quad (2.21)$$

2.6.1.3 Water content indices

Water band indices exploit the properties of the water band absorption features to provide a relative estimate of canopy water content. The simplest of these is the Water Band Index (WBI, equation 2.22; Peuelas et al. (1993)), which is a simple ratio of the absorption minima and maxima of the 970nm absorption feature. The similar Moisture Stress Index (MSI, equation 2.23; Hunt Jr & Rock (1989)) uses the absorption feature at 1599nm, and reflectance unaffected by water at 819nm.

$$WBI = \frac{R_{900}}{R_{970}} \quad (2.22)$$

$$MSI = \frac{R_{1599}}{R_{819}} \quad (2.23)$$

In addition to the above simple reflectance ratios normalised difference water indices, similar conceptually to NDVI. The Normalized Difference Water Index (NDWI, equation 2.24; Gao (1995)) uses the well defined water absorption feature centred on 1240nm and reflectance at a reference wavelength unaffected by water content at 857nm. The Normalised Difference Infrared Index (NDII, equation 2.25, Hardisky et al. (1983)) uses water absorption at 1649 nm and reflectance at 819nm .

$$NDWI = \frac{R_{857} - R_{1242}}{R_{857} + R_{1241}} \quad (2.24)$$

$$NDII = \frac{R_{819} - R_{1649}}{R_{819} + R_{1649}} \quad (2.25)$$

2.6.1.4 Leaf pigment sensitive indices

Plants under nitrogen stress show an increase in the ratio of carotenoids to chlorophyll. Peuelas et al. (1994) developed the NPCI (equation 2.26) index to detect this, using a ratio of absorption at 430nm, associated with carotenoid absorption in relation to chlorophyll absorption at 680nm

$$NPCI = \frac{R_{680} - R_{430}}{R_{680} + R_{430}} \quad (2.26)$$

Penuelas et al. (1995) also developed the Structure Insensitive Photochemical Index (SIPI, equation 2.27) to be sensitive to changes in the changes in the ratio between carotenoids and chlorophyll, but use a band in the NIR to normalise reflectance in the blue and red regions. This makes the index less sensitive to biomass and vegetation structure.

$$PRI = \frac{R_{800} - R_{445}}{R_{800} + R_{680}} \quad (2.27)$$

Merzlyak et al. (1999) developed the Plant Senescence Reflectance Index (PSRI, equation 2.28) to track changes in crop ripening and senescence. This index also uses the ratio of carotenoids in relation to chlorophyll, using the relationship between maximal chlorophyll absorption at 680nm and carotenoid absorption at 500nm.

$$PSRI = \frac{R_{680} - R_{500}}{R_{750}} \quad (2.28)$$

Gitelson, Zur, Chivkunova & Merzlyak (2002) Developed the carotenoid reflectance indices CRI1 (equation 2.29) and CRI2 (equation 2.30). CRI1 uses absorption at 510nm, associated with carotenoid absorption in relation to the green peak of reflectance at 550nm. CRI2 uses absorption at 510nm in relation to maximal chlorophyll absorption at 700nm. This is sensitive to changes in the carotenoid to chlorophyll ratio

$$CRI1 = \frac{1}{R_{510}} - \frac{1}{R_{550}} \quad (2.29)$$

$$CRI2 = \frac{1}{R_{510}} - \frac{1}{R_{700}} \quad (2.30)$$

Barnes et al. (1992) derived the NPQI (Normalized Pheophytinization Index, equation 2.31), which is sensitive to changes in the chlorophyll a/b ratio, and should thus be

sensitive to vegetation stress.

$$NPQsI = \frac{R_{415} - R_{435}}{R_{415} + R_{435}} \quad (2.31)$$

Anthocyanin sensitive indices Anthocyanin reflectance indices are sensitive to new growth and senescence. Gitelson et al. (2001) developed the Anthocyanin reflectance indices (ARI1 and ARI2, equations 2.32 and 2.33).

$$ARI = \frac{1}{R_{550}} - \frac{1}{R_{700}} \quad (2.32)$$

$$ARI2 = R_{800} \left(\frac{1}{R_{510}} - \frac{1}{R_{700}} \right) \quad (2.33)$$

Light use efficiency indices Light use efficiency is related to non-photochemical quenching and the xanthophyll cycle, and is thus sensitive to short term changes in stress and vigour. The Photochemical Reflectance Index (PRI, equation 2.34) is sensitive to increases in apparent carotenoid content caused by a broadening of the chlorophyll absorption features (Gamon et al. 1992, 1997).

$$PRI = \frac{R_{531} - R_{570}}{R_{531} + R_{570}} \quad (2.34)$$

Biochemical sensitive indices Several indices have also been developed to exploit the absorption properties of non-photosynthetic biochemicals in the SWIR. The Cellulose Absorption index (equation 2.35) uses the absorption feature correlated with cellulose at 2100nm (Nagler et al. 2003). The Normalised Difference Lignin (NDLI, equation 2.36) and Nitrogen (NDNI, 2.37) use absorption at bands correlated with those chemicals in conjunction with an unrelated band at 1680nm (Melillo et al. 1982, Fourty et al. 1996, Serrano et al. 2002)

$$CAI = 0.5(R_{2000} + R_{2200}) - R_{2100} \quad (2.35)$$

$$NDLI = \frac{\log^1 R_{1754} - \log^1 R_{1680}}{\log^1 R_{1754} + \log^1 R_{1680}} \quad (2.36)$$

Nitrogen sensitive indices

$$NDNI = \frac{\log^1 R_{1510} - \log^1 R_{1680}}{\log^1 R_{1510} + \log^1 R_{1680}} \quad (2.37)$$

2.6.2 The red-edge

Deriving the position of the REIP requires identifying the inflection point between chlorophyll absorption in the red region of the spectrum and increased reflectance in the NIR region. For high resolution spectro-radiometers that record broadly contiguous spectra the simplest approach is to take the maximum of the first derivative of reflectance in the red-edge region (680nm-740nm). However, many imaging spectrometers lack the spectral resolution to use this technique reliably. Thus, the position of the red-edge must be extrapolated from the bands present in this region. One way to resolve this by linear interpolation using reflectance at four wavebands. Linear interpolation (equation 2.38) assumes that the red-edge can be simplified as a straight line between between the absorption maxima in the red region and the base of the shoulder of maximal reflectance in the NIR. Using the slope of this line the REIP then estimated using a simple linear equation (Clevers 1994, Guyot et al. 1992, Clevers et al. 2002).

$$REIP = 700 + 40 \left(\frac{(0.5[R_{670} + R_{780}]) - R_{700}}{R_{740} - R_{700}} \right) \quad (2.38)$$

Bonham-Carter (1988) use least-squares fitting of inverse Gaussian fitting technique to define the REIP from reflectance spectra, where the REIP is the midpoint of the ascending edge of the Gaussian curve,

$$REIP = R_s - (R_s - R_0) \exp - \left[\frac{(\lambda - \lambda_0)^2}{2\sigma^2} \right] \quad (2.39)$$

where R_s is the reflectance at the shoulder in the NIR, R_0 is the reflectance where $\lambda = \lambda_0$ and σ is the Gaussian shape parameter in nm, so that the REIP is equal to $\sigma + \lambda_0$. Both the inverse Gaussian and Linear interpolation methods use reflectance to derive the REIP. This can be problematic, as although reflectance in this region of the spectrum is dominated by chlorophyll related absorption, contributions from soil, shadow and other foliar biochemicals can distort the position of the REIP. These effects can be reduced using derivative spectra (Curran et al. 1991, Elvidge 1990), as the slight changes in reflectance related to foliar absorption are emphasised. (Dawson & Curran 1998) propose a method for deriving the red-edge position from derivative spectra using a Lagrangian interpolation

technique (equation 2.40):

$$REIP = \frac{A(\lambda_i + \lambda_{i+1}) + B(\lambda_{i-1} + \lambda_{i+1}) + C(\lambda_{i-1} + \lambda_i)}{2(A + B + C)} \quad (2.40)$$

where:

$$A = \frac{D_{\lambda(i-1)}}{(\lambda_{i-1} - \lambda_i)(\lambda_{i-1} - \lambda_{i+1})} \quad B = \frac{D_{\lambda(i)}}{(\lambda_i - \lambda_{i-1})(\lambda_i - \lambda_{i+1})} \quad C = \frac{D_{\lambda(i+1)}}{(\lambda_{i+1} - \lambda_{i-1})(\lambda_{i+1} - \lambda_i)} \quad (2.41)$$

and λ_i , is the wavelength of the maximum first derivative, and λ_{i+1} and λ_{i-1} are the wavelength of adjacent bands and D_{λ} is the first derivative of reflectance at these locations

Dawson & Curran (1998) suggest that this method is less computationally intensive than other methods based of fitting curves to the first derivative, but the interpolation The Lagrangian method is most suitable for coarsely sampled data (Clevers et al. 2002). For more contiguous data the maximum of the first derivative in this region is often used (Pinar & Curran 1996, Horler et al. 1983, Filella & Penuelas 1994), whether identified manually or through fitting.

2.6.2.1 The red-edge and fluorescence

When using derivative spectra several researchers have noted that there may be multiple peaks in reflectance in the first derivative (Boochs et al. 1990, Horler et al. 1983). These features are related to chlorophyll fluorescence, and may distort the estimation of the REIP, especially as fluorescence increases with stress, meaning that the red-edge position can be mis-identified at longer wavelengths (Zarco-Tejada et al. 2003, Smith et al. 2004). This is potentially mitigated by the linear interpolation method or inverse Gaussian fitting of reflectance (Clevers et al. 2002, Cho & Skidmore 2006). The linear extrapolation technique (Cho & Skidmore 2006, Cho et al. 2007, Cho, Skidmore & Atzberger 2008) disambiguates the red-edge position from multiple peaks caused by fluorescence. It achieves this by using the intercept of the slope of the first derivative on either side of the broader chlorophyll absorption feature derivative from the region:

$$REIP = \frac{-(c_1 - c_2)}{m_1 - m_2} \quad (2.42)$$

where c_1 and m_1 are the intercept and slope for the red side of the absorption feature, and c_2 and m_2 are the slope and intercept of the infra-red side. To derive the slope and derivative reflectance at two wavelengths on each side are required. Cho, Skidmore &

Atzberger (2008) suggest using wavelengths at 680nm and 694nm for the red and 724nm and 760nm for the infra-red to derive the slopes of these lines (figure 2.5).

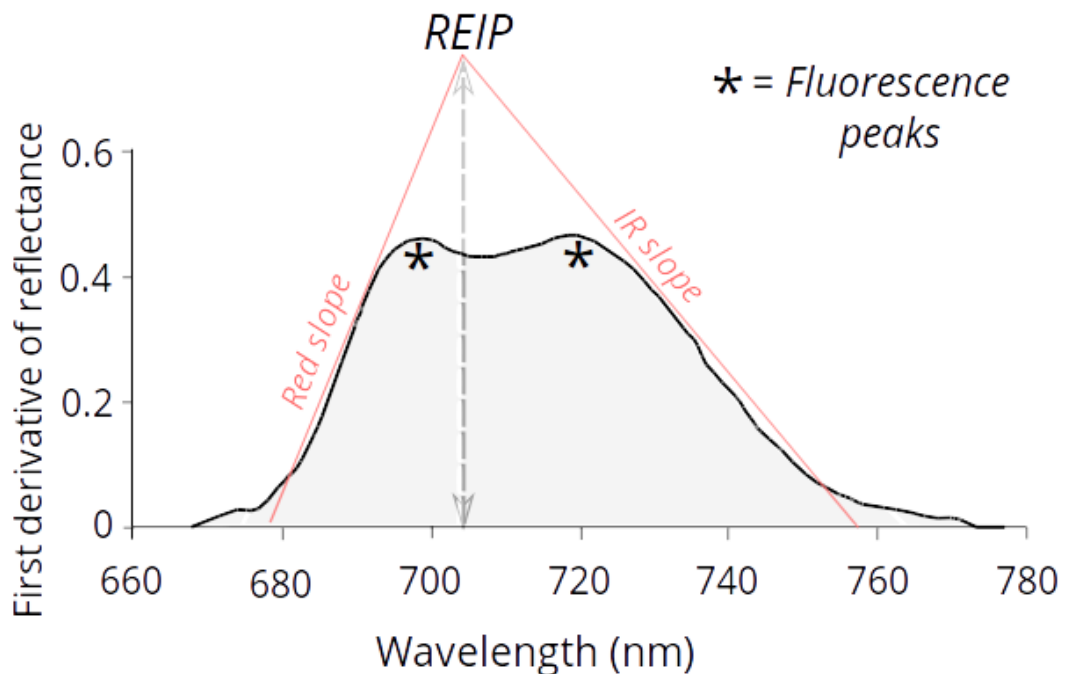


Figure 2.5: Linear extrapolation of the red-edge inflection point. After Cho & Skidmore (2006).

2.6.3 Fluorescence indices

As discussed above, the estimation of chlorophyll fluorescence under solar illumination is not straightforward. Methods exploiting Fraunhofer infilling are not considered here, as the sensors used in this work lack the spectral resolution to resolve them. Instead, reflectance based methods appropriate to the sensors are considered. These are indices based on reflectance (table 2.5) or the first derivative of reflectance (table 2.6).

Reflectance based indices work by using a ratio of on band affected by reflectance and one band less affected to normalise the shape of the reflectance curve. The derivative based methods use the first derivative of reflectance. Zarco-Tejada et al. (2003) propose that derivative methods are more suitable for detection of fluorescence, as these can potentially

Index	Source
$\frac{R_{680}}{R_{630}}$	Zarco-Tejada et al. (2000)
$\frac{R_{685}}{R_{630}}$	Zarco-Tejada et al. (2000)
$\frac{R_{685}}{R_{655}}$	Zarco-Tejada et al. (2000)
$\frac{R_{687}}{R_{630}}$	Zarco-Tejada et al. (2000)
$\frac{R_{690}}{R_{630}}$	Zarco-Tejada et al. (2000)
$\frac{R_{737}}{R_{700}}$	Gitelson et al. (1999)
$\frac{R_{740}}{R_{800}}$	Dobrowski et al. (2005)
$\frac{R_{685}}{R_{675}-R_{690}}$	Zarco-Tejada et al. (2000)
$\frac{R_{675}-R_{690}}{R_{683}^2}$	Zarco-Tejada et al. (2000)

Table 2.5: Reflectance based chlorophyll fluorescence indices.

Index	Source
$\frac{D_{705}}{D_{722}}$	Zarco-Tejada et al. (2003)
$\frac{D_{730}}{D_{706}}$	Zarco-Tejada et al. (2003)
$\frac{D_{686}-D_{710}}{D_{697}}$	Zarco-Tejada et al. (2000)
$\frac{D_{\lambda REIP}}{D_{720}}$	Zarco-Tejada et al. (2012)
$\frac{D_{\lambda REIP}}{D_{703}}$	Zarco-Tejada et al. (2003)
$\frac{D_{\lambda REIP}}{D_{\lambda REIP+12}}$	Zarco-Tejada et al. (2003)

Table 2.6: Derivative based chlorophyll fluorescence indices.

distinguish fluorescence from the reflectance properties of other foliar constituents. This is particularly important considering that the wavelengths associated with the REIP and fluorescence are closely located, causing the double peak in derivative spectra discussed above.

2.6.4 Continuum removal

Continuum removal is a method for the characterisation of absorption features. A continuum is fitted to the reflectance spectra, and the continuum removed reflectance is the difference between reflectance and this line, enabling the comparison of absorption properties from a common baseline (Clark & Roush 1984). The absorption depth is often normalised relative to the depth at the centre of the absorption feature (Band normalised by centre: BNC). Kokaly & Clark (1999)) or the overall area of the absorption feature (Band Normalised by Area: BNA. Curran et al. (2001)). This enables the comparison of absorption characteristics of foliar constituents, emphasising shifts in absorption proper-

ties such as the broadening of the feature, and reducing the influence of structural variation such as LAI and variations in illumination geometry (Curran et al. 2001, Cho et al. 2007).

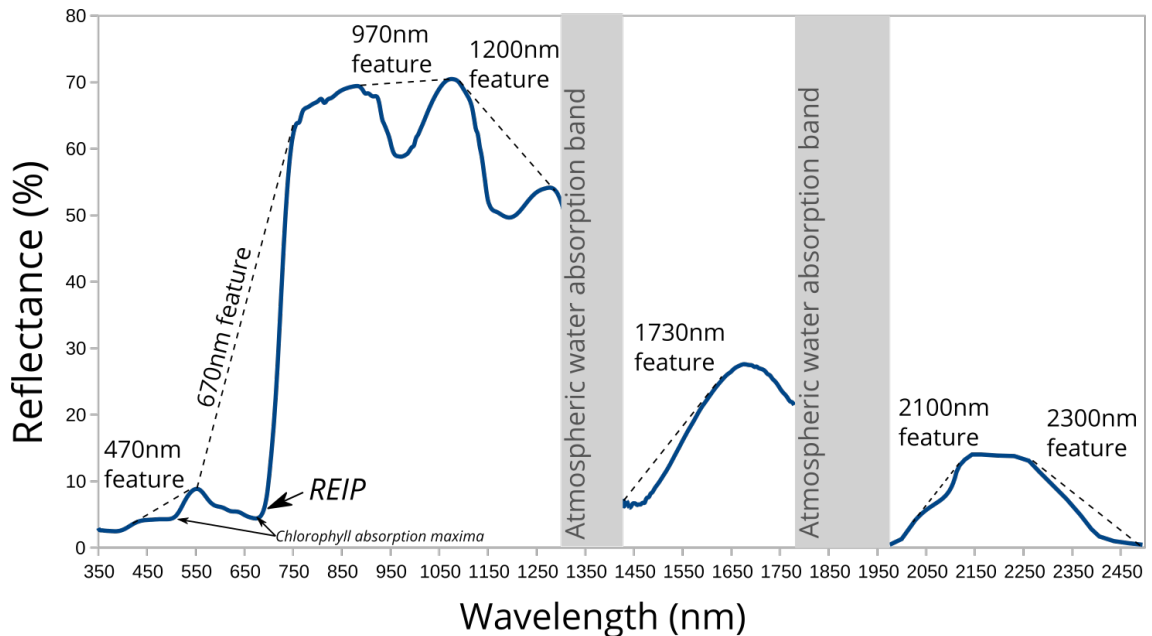


Figure 2.6: Foliar absorption features used for Continuum Removal. After Curran et al. (2001).

Continuum removal is widely applied for the identification of minerals in geological remote sensing. Kokaly & Clark (1999) proposed its use for the analysis of vegetation reflectance, examining continuum removed reflectance in absorption features centred on 1730nm, 2100nm and 2300nm in relation to three foliar biochemicals (nitrogen, lignin and cellulose) using stepwise linear regression, and found high R^2 values between continuum removed reflectance and biochemical. Curran et al. (2001) extended Kokaly and Clark's methodology to 12 other foliar biochemicals, finding that BNA normalisation produced the best results. Both studies were conducted on dried and ground leaves in a laboratory environment. Kokaly & Clark (1999) simulate AVIRIS spectra with varying degrees of influence from soil, atmospheric interferences, and leaf water content. It was found that with increasing water content quantitative estimation of biochemical content became less accurate. However, these results demonstrated that the errors were smaller than those encountered using derivative spectra of the same data. Noomen et al. (2006) used continuum removed reflectance to evaluate the impact of gas leaks in the soil in a greenhouse experiment demonstrating an improved ability to detect stress expressed as shifts in the visible spectrum. Cho et al. (2007) correlate continuum removed reflectance

with LAI and biomass using partial least squares regression for grassland canopies using both field and airborne imaging spectroscopy. At wavelengths previously associated with biomass the coefficient of determination for the continuum removed reflectance was significantly higher than reflectance and its first two derivatives. Clevers et al. (2008) used continuum removal techniques to estimate canopy water content for the 970nm and 1200nm absorption features. Unlike the other studies, that examined correlation between biochemical content and a single wavelength, the authors examined the area of the absorption features. Although this produced poor results when correlated with canopy water contents alone it has interesting implications for the work considered here, where contrast may be expressed by the actions of multiple, correlated, adjacent absorption features.

$$BNA = \frac{1 - \frac{R}{R_i}}{A} \quad (2.43)$$

$$BNC = \frac{1 - \frac{R}{R_i}}{1 - \frac{R_c}{R_{ic}}} \quad (2.44)$$

2.7 Related work: The detection of vegetation marks

2.7.1 Aerial photography

2.7.1.1 Observer directed oblique photography: A tried and tested technique

Observer directed aerial photography has been used for archaeological purposes since the last decades of the nineteenth century. As early as 1898 Giacomo Boni acquired aerial images of the Forum in Rome using a captive balloon (Ceraudo 2003). In the United Kingdom images were acquired from a hot-air balloon were of Stonehenge in 1916 (Barber 2014). The rapid development of aircraft, imaging technology and expertise during and after the World Wars led to aerial reconnaissance being more widely used, both for the recording of upstanding monuments and cropmark sites, and systematic aerial survey of archaeological heritage was increasingly employed in in England (Crawford 1923, Riley 1944, St. Joseph 1945, Crawford 1954), France (Agache 1962, 1964), Germany (Braasch 2014) and many other countries (Olesen 2004, Gojda 1997).

In essence this technique has changed little since, and utilises an observer directing a light aircraft to photograph features as they are seen (Riley 1987, Wilson 1982). These photographs are then geo-rectified to provide accurate spatial locations for the identified

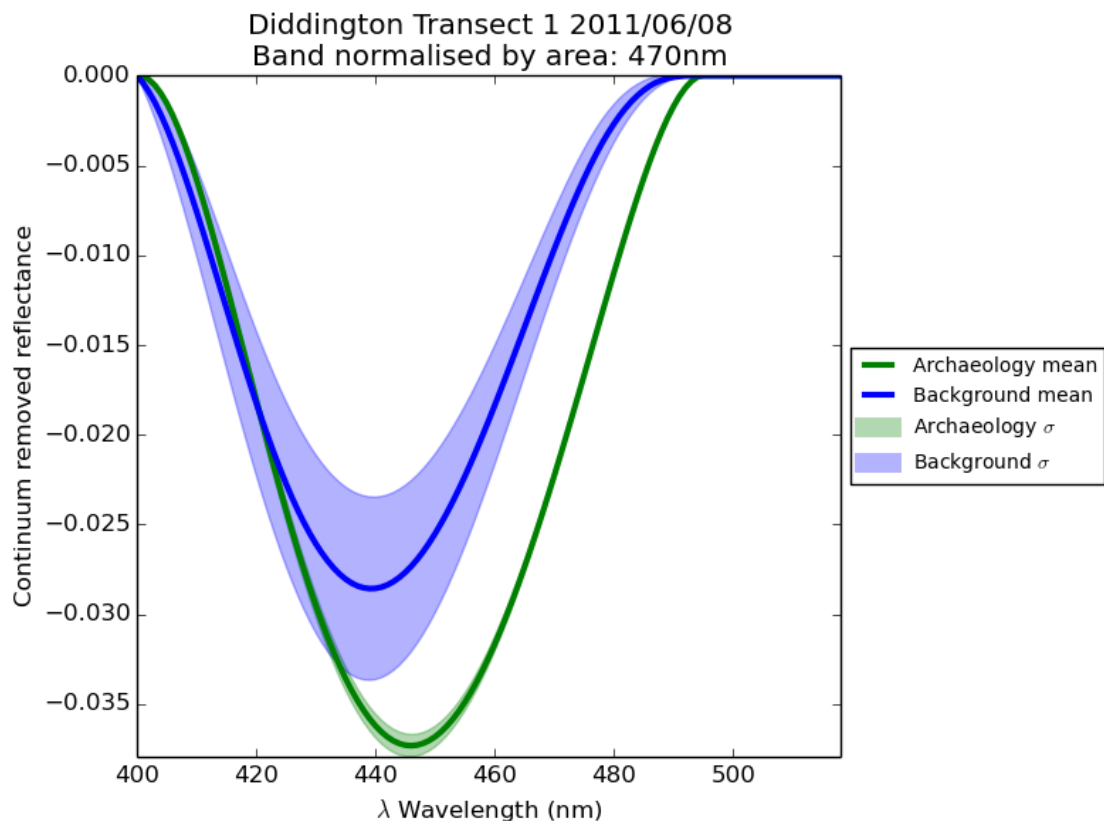


Figure 2.7: Example of band normalised by area continuum removed spectra for the 470nm absorption feature from Diddington T1, 8th of June 2011. Note the shift in both depth and breadth in the absorption feature between the archaeology and the background.

features. The features are then interpreted and transcribed from the rectified photographs as vectors, permitting their use in Geographic Information System (GIS) software packages for further analysis (Bewley 1999a, Doneus 2001).

The main advantage of this technique is its inexpensiveness and simplicity, as the technological requirements are comparatively low— even the most advanced consumer cameras are cheap when compared to the cost of dedicated mapping cameras. In addition, the aircraft used do not have to be especially modified for airborne survey. This means that the tools are widely available, and makes it possible for the technique to be particularly responsive to changing conditions (Riley 1987, pp. 48–50). This is important given the high degree of temporal variability in contrast between the archaeological features and the background, and enables more rapid deployment than dedicated survey systems. As a result of these advantages this technique has been the default methodology for curatorial

remote sensing in the United Kingdom, and is used extensively to populate both national and regional curatorial databases. An example of this is English Heritage's National Mapping Program (NMP), which seeks to systematically map the whole of England (Bewley 1999*b*, Grady 2007, Horne 2009).

The increasing availability of high-resolution, geo-rectified orthophotography in recent years has led to much discussion in the archaeological domain about the advantages of oblique photography compared to vertical photography. Arguments have been made that the human eye is more sensitive to subtle variation in the visible spectrum than conventional digital or analogue recording media, meaning that the observer can better detect features of interest from the air and focus recording on them (Wilson 1982, pp. 23–24,65). A further argument for observer directed oblique photography is that some features are only readily perceived from certain view angles due to the relationship between the sun, the sensor and the phenomena being recorded. However, due to the low-altitudes and oblique angles involved capturing enough control points for rectification can be problematic, leading to poor quality positional information (Palmer 2005).

Further criticisms focus on the bias introduced by the observer, who, due to the limited nature of human visual attention tend to focus on nodal, readily identifiable features and record little information about the context of the features, the surrounding landscape or features that are not as easily seen. In addition, these aerial survey campaigns have had a tendency to focus on known, productive areas or honeypots (Cowley 2002, Brophy 2005, Hanson 2005, Palmer 2005). This has led to the same areas being flown repeatedly, and tends to provide diminishing returns; further detail about known sites and features are recorded but few new features are being identified. This is largely due to this method recording only what the observer can see. In addition there is a tendency to focus on productive soils such as sands and gravels. Soils that are less conducive to cropmark formation such as clays are less intensively investigated (Palmer 2007, Cowley & Dickson 2007, Mills 2005).

2.7.1.2 Systematic vertical photography

It has thus been suggested that large scale, high spatial resolution vertical imagery provides a means to deal with these biases more effectively as whole landscapes are recorded (Doneus 1997, 2000, Palmer 2005). There is a concern that imagery acquired in this way is more expensive to acquire and less temporally flexible than traditional, oblique approaches. Whilst it is true that the cost per flight is higher the data covers a far greater

spatial extent. Less time is needed to process and georeference the imagery and there is also the possibility that the costs of data acquisition can be distributed between the archaeological community and other organisations. However, it has been suggested that the rapid repeated acquisition of high-spatial resolution satellite imagery afforded by platforms such as WorldView2 or GeoEye provides a solution to this problem. WorldView, for example can be tasked to revisit each location every day. In addition to imagery acquired specifically for archaeological prospection there is a quantity of archive aerial and satellite imagery that can be successfully utilised for the detection of archaeological activity (Palmer 2005, 2007).

2.7.1.3 Recent developments

Structure from motion Is a computer vision technique that enables the creation of both dense, three dimensional point clouds and georeferenced ortho-imagery from overlapping images. Unlike traditional photogrammetric recording high degrees of accuracy can be attained with consumer-grade, uncalibrated cameras. Recent developments in both open and propriety software have made the exploitation of the technique possible with very expertise, as they offer largely automated workflows. This has led to a profusion of recent studies espousing the use of this technique, both for documenting archaeological excavations and artefacts on the ground, and the recording of archaeological features from the air. Verhoeven & Vermeulen (2016) have recently further automated these workflows, using GNSS and inertial measurement to record the exterior orientation parameters for each image, greatly reducing the amount of time required for preprocessing.

The near infrared Reflectance in the near infrared region of the spectrum is more sensitive to vegetation marks than the visible spectrum, so methods recording reflectance in this region are desirable. Early applications used infrared sensitive films (Agache 1968, Tartaglia 1977, Hampton 1974), however most consumer grade digital cameras are sensitive to about 1100nm if the filters that block NIR light are removed and a filter is added to block light from the visible spectrum (Verhoeven et al. 2009). This has enabled the deployment of low cost infrared imagers for archaeological aerial photography. When used in conjunction with standard visible wavelength cameras this enables the derivation of vegetation indices such as NDVI highly sensitive to biomass and stress and vigour variations (Verhoeven 2008, Verhoeven et al. 2016). By using narrow bandwidth interference filters it is possible to constrain reflectance to very specific ranges of sensitivity, enabling the investigation of foliar constituents. By combining several adapted cameras Verhoeven & Doneus (2011) use the R_{700}/R_{800} ratio to reveal previously invisible archaeological

features by exploiting the gradient of reflectance near the red-edge.

2.7.2 Multi and hyper-spectral approaches to vegetation mark detection

Multi and hyperspectral AIS approaches to archaeological prospection have been exploited since the late 1970s. Early applications were limited to archaeological information detectable by coarse (50-30m) spatial resolution sensors, such as landscape characterisation (Hanson 1978) and large archaeological sites in the near east, where dense occupation of large settlements over centuries has created substantial changes to the reflectance of the soil of a scale. It is only in the past two decades that the spatial resolution of the sensors has been fine enough to resolve archaeological vegetation marks of a scale common in northern Europe. This limited early studies, such as that by Donoghue & Shennan (1988) using 3-5m multi-spectral data, to examining landscape features such as large irrigation ditches and relict stream channels in the Fenland of eastern England. This and a number of subsequent studies have demonstrated the utility of applying vegetation indices such as NDVI to vegetation mark detection.

2.7.2.1 Indices

Vegetation indices use the known spectral properties of vegetation to qualitatively discern differences in the state of the crop. As discussed above, the suitability of different indices for resolving archaeological vegetation marks at any given point in time is dependant on the conditions on the ground. (Agapiou et al. 2012) investigated this using multi-temporal field spectra recorded over a simulated archaeological feature on Cyprus. They compared broadband multi-spectral indices to narrowband, hyperspectral indices for the ability to resolve contrast, and found that the narrowband indices maximise the difference in contrast by up to 20%. In total 71 indices were compared. Figure 2.8 shows the best performing indices from this study.

In general soil adjusted biomass and red-edge sensitive indices, particularly SAVI (equation 2.7) performed best throughout the year. However in the later part of the year pigment sensitive indices improves. In addition, the performance of the PRI index was high on the 4th of March. This is possibly indicative of drought stress causing inversion of the cropmark through a variation in maturation.

2.7.2.2 Principal component analysis

With the increased availability of hyperspectral sensors with hundreds of bands there became a need to identify the bands that resolved the greatest contrast between archaeology and the background in highly redundant and auto-correlated data. A common approach to this is to use Principal Components Analysis (PCA) to identify wavelengths usable for band ratios or false colour composites (Almeida & Filho 2004). Challis et al. (2009) used this approach on Daedalus ATM and CASI data for two study sites in the Trent Valley in England, and found that the greatest contrast was identified in the ATM data at the band centered on the region 760nm-900nm. For the same areas finer spatial resolution CASI data shows the most variation in the band centred on 749nm. Bennett et al. (2013) use PCA found that bands in the region of 680-750nm exhibited the best contrast for identifying the archaeological features on grassland. Given the well understood spectral properties of vegetation this is unsurprising, as reflectance in the red-NIR range is heavily affected by chlorophyll content, REIP and biomass. This makes the application of PCA for identifying regions of contrast for vegetation mark detection largely redundant, as this is effectively performing data reduction to identify variation in the areas where we expect the most variation to be. In addition, if PCA is calculated for an entire scene rather than for smaller subsets of areas of cropland the result will be distorted, as the variations between the field, hedgerows, trackways, windbreaks and buildings will all be far greater than that within the field. PCA is also widely used as a visualisation technique to plot the the first three components of variation as false colour composites (Winterbottom & Dawson 2005, Aqduş et al. 2008, 2012, Bennett et al. 2013).

2.7.2.3 The red-edge

Few studies have studied the impact of deriving the REIP as an indicator of contrast other than using red-edge sensitive indices. (Verhoeven & Doneus 2011) proved the utility of the red-edge using the simple $R700/R800$ index for their work with NIR adapted cameras. It is suggested by the authors that the use of indices that make use of reflectance at the REIP such as the Red-edge NDVI and VARI (equations 2.17 and 2.18 are the most suited for the detection of vegetation marks, due to their sensitivity to both stress and biomass variations. Agapiou et al. (2013) demonstrated a variation of this index, $R800/R700$ provided improved contrast compared to NDVI indices. To identify the actual REIP position using hyper-spectral sensors Verhoeven et al. (2013) and Doneus et al. (2014) use the highest first derivative of the smoothed and interpolated spectra.

These studies demonstrate considerable utility for detection. However, as discussed above, the methods applied potentially conflate the REIP and contributions to reflectance from chlorophyll fluorescence (Cho & Skidmore 2006, Cho, Skidmore & Atzberger 2008). Thus, it may be the case that the increase in contrast gained from using metrics sensitive to the REIP are as much related to variations in fluorescence as a temporary response to stress as a change in pigment content resulting in a shift in the REIP. In addition, using techniques such as the maximum first derivative to identify the REIP may result in masking of contrast, as fluorescence can potentially cause a shift in the REIP unless this is taken into account.

2.7.2.4 Fluorescence and other methods

Fluorescence has not been exploited for vegetation mark detection, however, as discussed above some of the apparent success of methods using the REIP and PCA may in fact be related to chlorophyll fluorescence. For example, the 749nm band identified by Challis et al. (2009) as revealing the most contrast is related to fluorescence. Continuum removal has also been little explored in vegetation mark archaeology, although it has been applied to classification of contrasts in the reflectance of bare soil caused by large quantities of tile and pottery on Roman settlements (De Laet and Jordan, pers comm.). Doneus et al. (2014) approach detection by fitting probability density functions of known foliar properties of stressed and healthy vegetation to spectra, demonstrating that under the right circumstances these methods were capable of outperforming visible wavelength imaging.

2.7.2.5 Evaluating contrast

A number of studies have sought to quantify contrast for detecting archaeological vegetation marks. Cavalli et al. (2007) developed a separability index to evaluate contrast in multi-spectral images:

$$SI = \left(1 - \frac{\int D_a D_b dx}{\sqrt{\int D_a^2 dx \int D_b^2 dx}} \right) \times 100 \quad (2.45)$$

Where D_a is the frequency distribution of the pixels classified as archaeological features and D_b is that of the background. This provides an indication of the overlap between the two frequency distributions. Agapiou et al. (2012) evaluated contrast in different

vegetation indices using the following method:

$$VIC = \left(\left(\frac{VI_a}{VI_{amax}} \right) - \left(\frac{VI_b}{VI_{bmax}} \right) \right) \times 100 \quad (2.46)$$

Where Vegetation Index Contrast (*VIC*) is a ratio between the value of the index over the archaeological feature (VI_a) divided by the maximum value recorded over the whole growth season (VI_{amax}) and the value of the index over the background divided (VI_b) by the maximum value over whole growth season (VI_{bmax}). In subsequent work Agapiou et al. (2013) used Euclidean distance, Mahalanobis distance, and cosine similarity between pairs of reflectance observations to evaluate contrast.

These methods do not provide an indication of positive or negative correlation or indicators of statistical significance. In addition, both the separability index and the distance based methods are only suitable for reflectance measurements, and cannot be used for indices and other hyperspectral products. In remote sensing of vegetation T-tests are more commonly used to evaluate the ability of different methods to discriminate between classes (Castro-Esau et al. 2004, Cho, Sobhan, Skidmore & de Leeuw 2008, Colgan et al. 2012, Prospere et al. 2014), as these afford the ability to both examine the strength of the contrast and its significance.

Qualitative methods for evaluating contrast are used by a number of studies. A common method is to digitise the features visible in each method (Doneus et al. 2014, Bennett 2011, Bennett et al. 2011, 2013) and to use the number of features identified to evaluate contrast. This is problematic, as it does not indicate the strength or significance of the contrast and it is difficult to repeatedly interpret the features objectively

2.8 Conclusions

Vegetation mark expression is the result of complex interactions between the crop, soil and environmental conditions. Long-term adaptation by the crop to environmental conditions of contrast are the result of feed-forward responses, where the individual plants limit their growth to avoid depleting the available resources too quickly. These lead to a greater quantity of vegetation over the archaeological features, identified by a number of authors as the principle expression of vegetation mark expression (Riley 1944, Jones & Evans 1975, Evans & Jones 1977, Evans & Catt 1987). In addition, these feed-forward responses are probably responsible for differences in maturation. Differences in pigmen-

tation occur only when long-term resource deficiency effect the photosynthetic mechanisms of the crop. These are expressed first through protective mechanisms such as the xanthophyll cycle, but over time a reduction of chlorophyll and other pigments occurs. These have also been widely exploited in both visible wavelength photography and NIR spectroscopy for archaeological detection (e.g. Verhoeven et al. 2013, Doneus et al. 2014, Agapiou et al. 2010, Verhoeven & Doneus 2011). The short term expression of contrast resulting from water conservation responses indicated by chlorophyll fluorescence has great potential to improve the temporal windows for detection, as these responses occur before contrast is expressed in other methods, and may occur in otherwise healthy crops at times of peak insolation. Despite the potential of fluorescence for detection it has not been exploited for archaeological detection.

Chapter 3

From the ground up: Fieldwork

3.1 Introduction

This chapter evaluates the techniques used to investigate contrast using ground-based fieldwork. This work is key to developing an understanding of the formation and nature archaeological vegetation marks that can be applied to the deployment and interpretation of the airborne data. There are three principal reasons why this work informs the analysis of the airborne surveys; first, the ground-based work affords the opportunity to measure and observe the properties of the vegetation directly. Second, the cost of acquiring airborne measurements means that these are by necessity acquired with much lower temporal resolution, whereas the ground-based measurements can be acquired more frequently. Third, the ground-based spectral measurements can be acquired at higher spectral and spatial resolution, providing a more detailed dataset better able to detect and examine subtle contrasts than with the airborne sensors.

The main aims of this work were to identify how contrast was expressed under different conditions, and to identify the most effective means of detecting these contrast. To achieve this measurements were acquired at four study sites over two growth seasons at monthly intervals, covering a variety of different land uses and soil types.

The measurements taken were indicators of biomass and the spectral properties of the vegetation. Biomass has been identified as one of the main expressions of contrast in

archaeological vegetation marks, and was measured using different techniques appropriate to the developmental stage of the vegetation. For crops in the early growth stages an estimate of ground coverage was obtained using binary segmentation of digital camera images. For mature crops a canopy ceptometer was used to estimate Leaf Area Index (LAI). For all surveys the height of the vegetation above the ground surface was recorded. The spectral measurements were recorded using a high resolution field spectrometer. The vegetation indices and red-edge Inflection Point (REIP) methods discussed in the previous chapter were evaluated. In addition, methods for evaluating chlorophyll fluorescence and continuum removed reflectance for known foliar absorption features were evaluated. These methods are novel for vegetation mark detection, and respectively afford the opportunity to detect short-term expressions of contrast and investigate the shape and magnitude of absorption features.

Results from this work confirmed that the expression of contrast over time is complex, and no that single method is universally applicable. However, both indices sensitive to chlorophyll fluorescence and an optimised vegetation index utilising nearly adjacent wavelengths consistently outperformed other methods.

3.2 The study sites

The ground-based work was conducted at the two DART project study areas, Diddington in Cambridgeshire, and Harnhill in Gloucestershire (figure 3.1). Harnhill experiences higher rainfall than Diddington. Both sites contain areas of free draining and clay soils. This enables differences in rainfall and moisture retention properties to be investigated. The ground-based work is co-located with monitoring stations installed as part of the project by the University of Birmingham to monitor weather conditions and apparent soil water content (Boddice 2015), and the field surveys were conducted at the same time as geophysical surveys undertaken by the University of Bradford. These survey comprised twin probe and tomographic earth resistance survey and electromagnetic (EM) soil conductivity and magnetic susceptibility measurements (Fry 2014).

3.2.1 Site selection

Study areas were located so that measurements were recorded at one site on the clay and one site on the free draining soils. Archaeological features of interest were identified using HER searches and map regression to identify relict field boundaries. To confirm

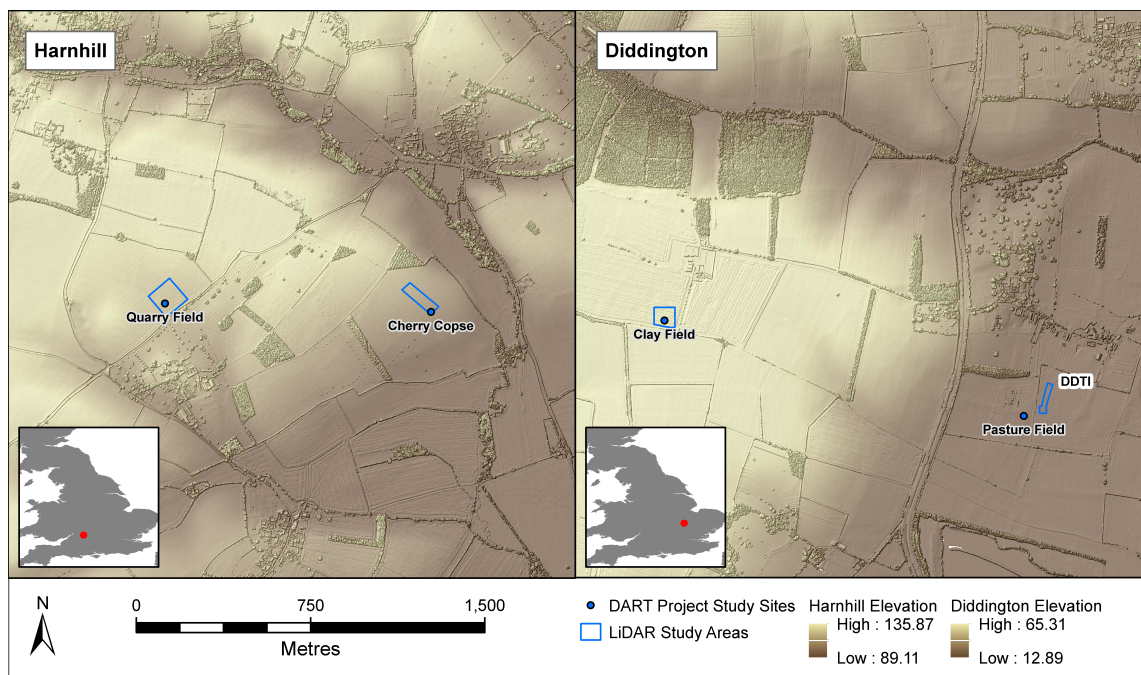


Figure 3.1: Locations of DART project study sites.

the locations of these features archaeological features small areas of fluxgate gradiometer magnetometer survey were undertaken using either a Bartington Grad 601-2 or a Geoscan FM256 collected at a 0.25m sample interval along 1m traverses and located using RTK GNSS in each field. The features thus identified were used for the statistical analysis of the vegetation marks, as features identified solely as vegetation marks from aerial photography survey risks confirmation bias. Magnetic anomalies interpreted as likely to be caused by archaeological and geological features were digitized as polygons using GIS software to produce an interpreted dataset used to classify subsequent airborne measurements.

3.2.1.1 Transects

To measure the properties of the vegetation 10-15m transects were located broadly orthogonally to the archaeological features, outside the areas where the crop had been disturbed by the installation of the monitoring equipment and the geophysical surveys. This length of transect was chosen to ensure that there were enough readings on either side of the feature to properly characterise the background, allowing for transitional effects on either side of the archaeological feature. The transects were located using RTK GNSS and total station surveys to ensure that they correspond to the features recorded by the geophysical survey. Where possible the transects were always recorded in the same locations. How-

ever, land management practices and other disturbance to the growing crop meant that the transects at Harnhill Cherry Copse and Diddington Transect 1 had to be relocated to acquire representative comparative measurements.

3.2.1.2 DDT1 (Diddington Transect 1)

Diddington Transect 1 is located in the field adjacent to the monitoring equipment installation, referred to as 'Diddington Pasture Field' (DDPF) elsewhere. The transect was located here as this area was under arable rotation, whereas DDPF was set-aside with areas of cover crops grown for pheasants, meaning it was not representative of arable landuse. The transect is located 75m to the North East of the monitoring equipment in DDPF.

The site is located on alluvial gravel terraces associated with the river Ouse. Using transcribed cropmark data from the Cambridge county council HER an extensive area of probable Iron Age to Romano-British settlement was located. The fluxgate gradiometer survey was then used to identify linear anomalies likely to represent the ditches forming part of a complex of enclosures associated with this settlement. Excavations of the ditch in DDPF for the installation of monitoring equipment revealed a ditch cut through the underlying river gravels to a depth of 1.1m from the surface sealed beneath 0.3m of compact, sandy silt subsoil, with a further 0.25-0.3m deep cultivation horizon above this. The fills of the ditch contained frequent inclusions of charcoal, animal bone and ceramics, indicating activity typical of settlements of this period. Although the ditch in DDT1 was not excavated fluxgate gradiometer survey and soil auger surveys indicate that it is similar to the excavated feature. Figure 3.2 shows the location of the transects in relation to the probable archaeological features.

3.2.1.3 Diddington Clay field (DDCF)

The site is located on alluvial gravel terraces associated with Oxford Clay series. Using transcribed cropmark data from the Cambridge county council HER a probable Iron Age to Romano British settlement was located. The fluxgate gradiometer survey was then used to identify linear anomalies likely to represent the ditches forming part of a complex of enclosures associated with this settlement, and probable ring gullies defining houses typical of this period. The location of a probable ditch, running approximately N-S was confirmed by soil coring and excavated for the installation of the monitoring equipment.

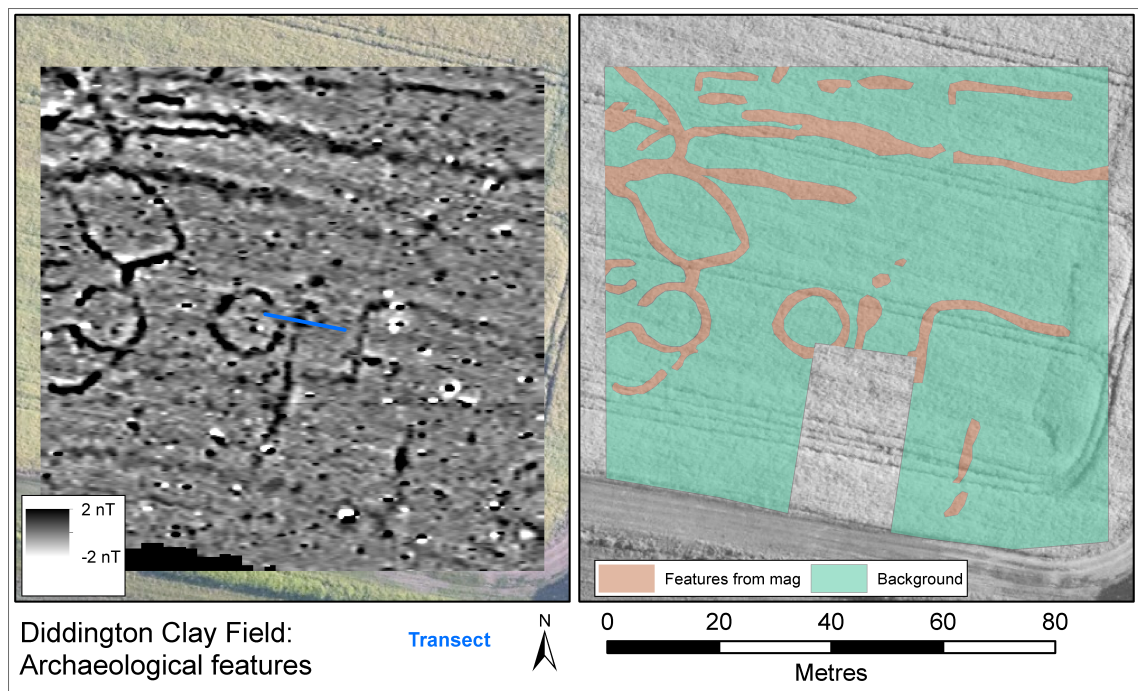


Figure 3.2: Location of transects in DDT1, showing fluxgate gradiometer survey and interpreted archaeological features.

This revealed a substantial 1.3m wide ditch cut into the clay 1.2m from the surface, located beneath a 0.3m deep cultivation horizon and 0.1-0.15m of clay subsoil. The fills of the ditch contained evidence of nearby human occupation, with frequent inclusions of charcoal, animal bone and ceramics. Figure 3.3 shows the location of the transects in relation to the potential archaeological features. The excavated ditch bisects the transect. In addition, at the west end of the transect intersects with an annular anomaly probably indicative of a round house associated with the settlement.

3.2.1.4 Harnhill Quarry Field (HHQF)

Harnhill Quarry field is located on Clayey Signet Member Drift geology. Analysis of historic Ordnance Survey mapping identified a field boundary last shown on the 1924 6-inch edition and absent from the 1947 RAF vertical aerial photography. Subsequent fluxgate gradiometer survey confirmed the location of this boundary and linear anomalies indicative of extensive open-field ridge and furrow cultivation associated with pre-enclosure medieval and later agriculture. Excavation of field boundary revealed a ditch containing clay drainage tiles related to an extant field drain, possibly inserted into the extant boundary ditch when it was in-filled. The ditch is 1.1m wide and cut 0.8m below the surface with clay drainage tile in the base. The fills of the ditch were comparatively sterile, with

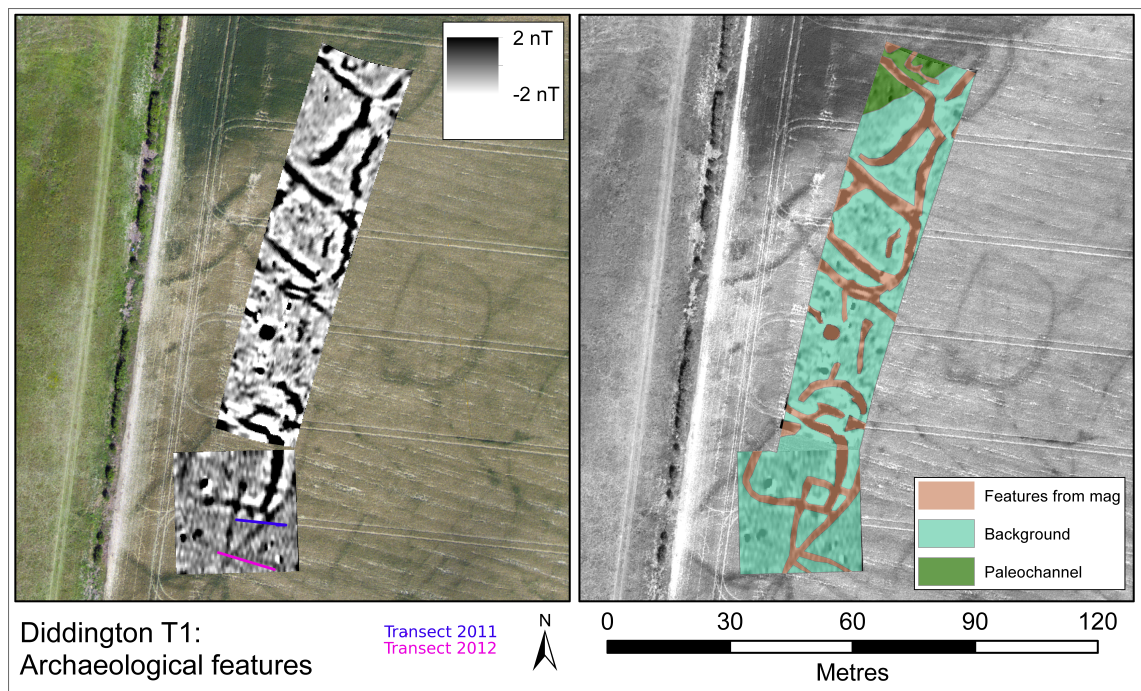


Figure 3.3: Location of transects in DDCF, showing fluxgate gradiometer survey and interpreted archaeological features

few inclusions indicative of anthropogenic activity. The transect is located over this ditch, and also intersects with a furrow from the medieval field systems (figure 3.4).

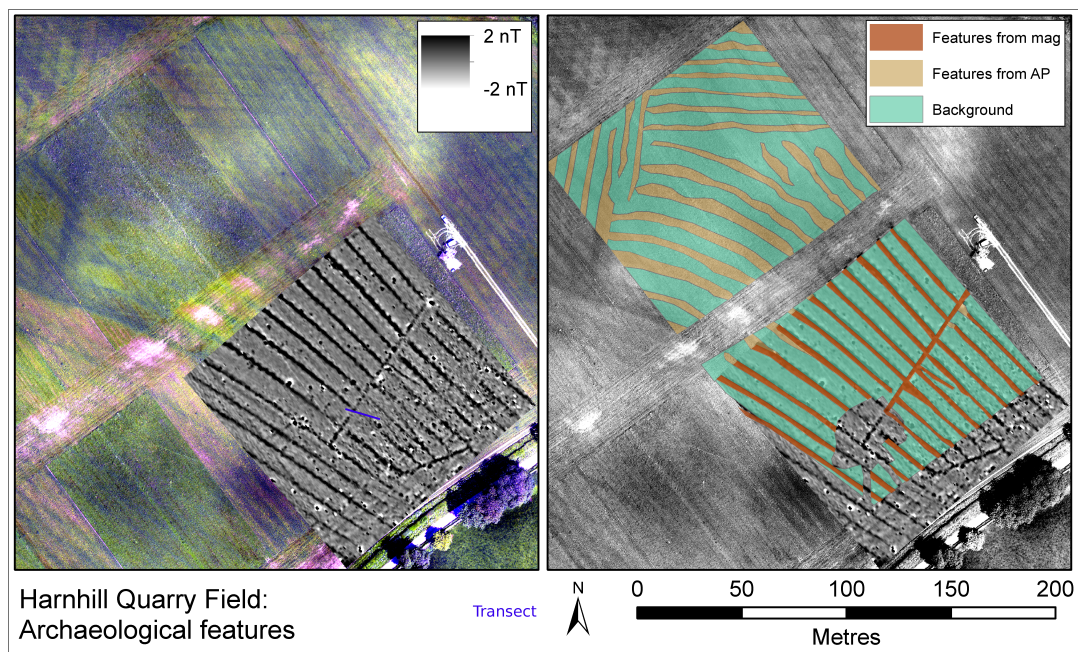


Figure 3.4: Location of transects in HHQF, showing fluxgate gradiometer survey and interpreted archaeological features.

3.2.1.5 Harnhill Cherry Copse (HHCC)

Harnhill Cherry Copse is located shallow (0.3m depth) silty clay soil overlying limestone cornbrash. A relict field boundary, extant until the 1930s, was identified using historic mapping and confirmed using fluxgate gradiometer survey. Coring and excavation revealed a substantial ditch cut directly into the limestone bedrock, 1.3m wide and cut to a depth of 1.1m deep below the ground surface, and possibly re-cut at least once. The fills of the ditch contained few indicators of anthropogenic activity. The ditch is the only detectable feature covered by the transect (fig 3.5).

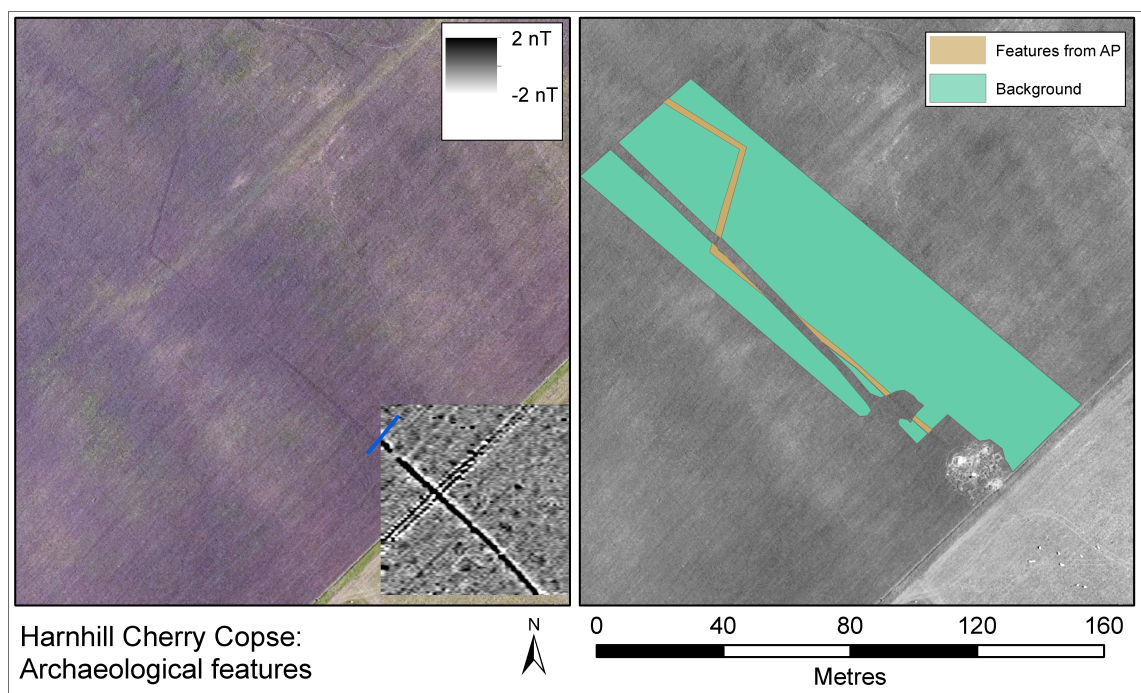


Figure 3.5: Location of transects in HHCC, showing fluxgate gradiometer survey and interpreted archaeological features.

3.2.1.6 Weather conditions

At both sites the dry summer of 2011 resulted in high Potential Soil Moisture Deficits (PSMD) being present over most of the growth season. This resulted in very high contrast in the vegetation marks at Diddington on the free draining soils. Conversely 2012 was one of the wettest years on record, with positive soil moisture deficits being present only intermittently.

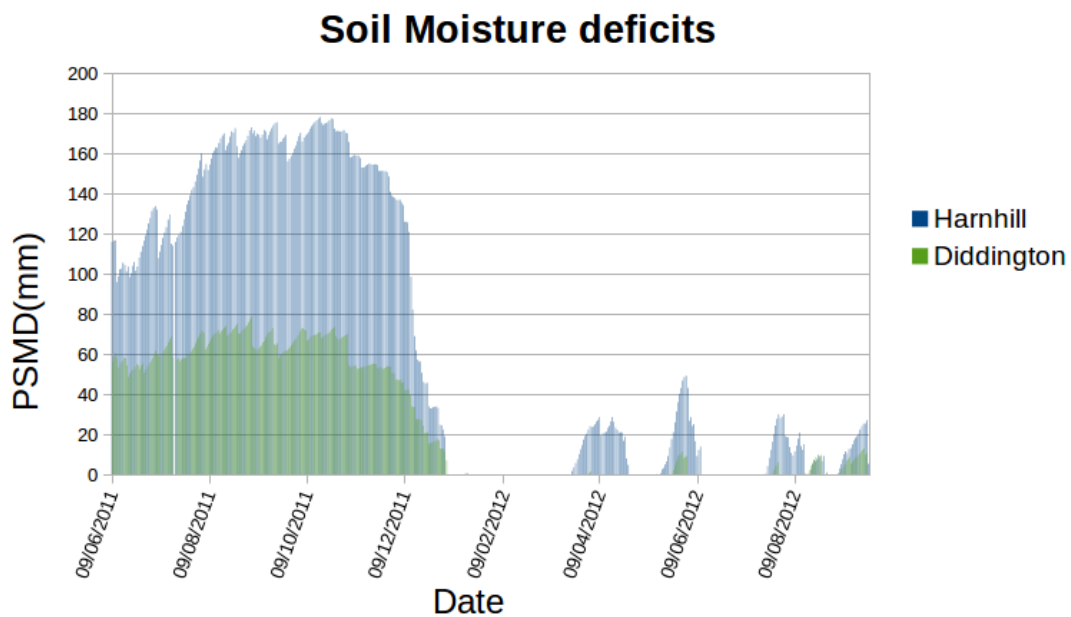


Figure 3.6: Potential Soil moisture Deficits at Diddington and Harnhill.

3.3 Background: Field measurement of vegetation marks

There have been few detailed multi-temporal field measurements of archaeological vegetation marks. Agapiou et al. (2010, 2012, 2013) used ground-based spectroradiometry using the GER 1500 instrument to record the reflectance properties over time for both actual and simulated archaeological features in Cyprus. This work largely considers the derivation of various vegetation indices for the detection of archaeological features, and the simulation of various multi-spectral sensor properties to identify optimal indices for detection. For both barley and wheat the authors demonstrated that the best contrast occurred during the booting stage of development, when the seed head begins to fill. This is when the water demand of the crop is at its highest (Jones & Evans 1975), so any variations in water availability in the soil are more likely to impact the crop. The authors suggest that this is most detectable using the red-edge region, and suggest a narrow band ratio of 800/700 (Agapiou et al. 2013). Other groups have conducted ground-based survey of vegetation marks, but the results of these studies have not been published (Verhoeven, Opitz pers. comm.)

Kalacska et al. (2009) examined the detection of mass graves using hyperspectral techniques, and used multi-temporal ground-based spectroscopic measurements of the ground cover to distinguish between a simulated grave filled with animal carcasses and an empty grave as a control over a 16 month period. To compare reflectance the authors used a clas-

Property	Value	Description
Measurement range	350-2500nm	The sensor measures from the visible to short-wave infrared
Sampling interval 350-1000nm	1.4nm	Measurement interval of the sensor
Sampling interval 1000-2500nm	2nm	
Spectral resolution (FWHM)@ 700nm	3nm	Full Width at Half Maximum
Spectral resolution (FWHM)@ 1400nm	10nm	
Spectral resolution (FWHM)@ 2100nm	12nm	
FWHM	3-12nm	Full Width at Half Maximum of sensor (spectral resolution)
IFOV	23 degrees	The nominal Instantaneous Field Of View of the instrument

Table 3.1: Properties of the ASD FieldSpec Pro instrument.

sifier to identify spectral features. While this approach was successful it has limited utility here, as the large differences in reflectance caused by re-vegetation of the infilled pits observed by the authors are not representative of the relatively subtle contrast considered here.

3.4 Methodology

3.4.1 Field spectroscopy

The core element of the ground-based fieldwork was the collection of spectra using the Analytical Spectral Devices (ASD) FieldSpec Pro spectroradiometer. This instrument collects spectroscopic data from the visible (VIS) to short-wave infrared (SWIR) regions of the electromagnetic spectrum, using a silicon photodiode array for the visible and near-infrared region and two separate cooled InGaAs photodiodes for the SWIR region (Analytical Spectral Devices 2002).

Table 3.1 details the properties of this instrument. Reflectance data is recorded by comparing the recorded spectra to that recorded over BaSO₄ panel immediately before recording the reflectance reading. This allows for the correction for local atmospheric conditions provided these remain relatively constant over the time taken between recording the reflectance from the panel and the reflectance measurement (Jackson et al. 1987,

Milton 1987, Milton et al. 2009). Taking these measurements in the field requires clear, cloudless conditions for optimal measurement. This is obviously problematic when undertaking readings in the United Kingdom, where there are very few cloudless days (Armitage et al. 2013). In addition, the geometry of the illumination should be as near vertical as possible to avoid complications caused by BDRF (Bi-Directional Reflectance Factor), meaning that ideally the measurements are recorded as near to solar noon as possible (Jacquemoud et al. 1992, Rollin et al. 2000). Recording measurements in the field also means that additional noise from atmospheric water vapour is introduced (McCoy 2005, Milton et al. 2009). These coincide with the joins between the different sensor arrays in the instrument, which further contribute to the noise in these regions. This means that the data from the regions between 1340-1420nm, 1788-2012nm, and 2414-2500nm are unusable. In addition, damage to the fibre-optic cable and poor calibration of the second SWIR sensor on this instrument meant that the data from 1800-2500nm suffered from a 5% signal loss and increased noise in this region.

The instrument records data to a laptop using the proprietary ASD RS 3.01 software package. This averages fifty reflectance measurements recorded by the instrument as a single measurement to assure stability. The raw data are interpolated to 1nm spectral resolution by the software. Unfortunately the un-interpolated measurements are not available from the instrument (Analytical Spectral Devices 2002).

3.4.1.1 Data collection

Where weather conditions allowed spectra were acquired using the ASD Fieldspec Pro along 10-15m GNSS located transects over archaeological features identified by the geophysical surveys. To take advantage of brief opportunities in weather conditions the instrument had to be able to be deployed rapidly at short notice, precluding the use of tripods or other static devices ordinarily employed to ensure optimal measurement. The measurements were recorded as frequently as measurement conditions allowed along the transect, generally 3-9 readings per metre, although where sub-optimal conditions afforded only a short measurement window this was restricted to a few readings on and off the feature. After each metre a reading was recorded from the white reference panel, and then a new white reference reading was taken to derive reflectance. The readings were taken using the probe at a height of approximately 1m above the crop surface, affording approximately a 0.4m measurement footprint. An audio recording device was used to record the location of each reading as this enabled a single operator to use both hands to control the instrument.

3.4.1.2 Data preparation

The data were downloaded and converted to ASCII text files using the ASD ViewSpec software. The data were then associated with their spatial information and imported to the HDF5 format. To reduce the effects of high-frequency noise, especially in the regions at 350-400nm and in the regions in the SWIR region, the data were smoothed using a univariate spline. Because the noise varied between the silicon and the two InGaAs arrays different smoothing parameters were used for each of these regions.

3.4.1.3 Data analysis

Spectral analyses were conducted using bespoke, open-source Python software developed by the author and making heavy use of the NumPy (Developers 2014), SciPy (Jones et al. 2001) and Matplotlib (Hunter et al. 2007) libraries. A fuller description of and links to the repositories containing this software can be found in Appendix A (page 220). This software was designed to be adaptable to different multi and hyper-spectral sensors of varying spectral properties, and work with spectra derived from both field spectroscopy and imaging spectrometers.

Vegetation Indices The 34 vegetation indices discussed in the previous chapter were implemented. These indices are correlated with well-understood foliar properties, and should provide insight into the nature of vegetation mark expression. The properties measured by these indices are summarised in table 3.2

In addition, because the results of the NDVI (equation 2.3, page 36) are highly variable dependant on the wavelengths selected, every permutation of this index from 650nm-750nm in the red and 700nm-850nm in the NIR was tested. This follows the work of Hansen & Schjoerring (2003) and Mutanga & Skidmore (2004), who tested a wide variety of band combinations for the assessment of nitrogen and biomass respectively, and found that narrow band indices in this region provided the best determination of these parameters. This range covers several important features, including chlorophyll fluorescence, the REIP, and the chlorophyll absorption features, and should show how the choice of wavelength affects contrast. This method is henceforth designated as the MTBVI (Multi-wavelength Twin Band Vegetation Index).

Index	Page	Sensitive to
SR 700 800	36	Biomass, red-edge
NDVI 705 750	36	red-edge
NDVI 700 800	36	Biomass, red-edge
NDVI 694 760	36	red-edge
NDVI 695 805	36	Biomass
NPCI	42	Chlorophyll
NPQI	43	Chlorophyll
RDVI	37	Chlorophyll, red-edge
SAVI	38	Biomass
MSAVI	39	Biomass
MSR	38	red-edge, biomass
MSRVI	38	red-edge, biomass
MDVI	40	red-edge, biomass
TVI	40	Chlorophyll, biomass
MTVI	40	Chlorophyll, biomass
MTVI2	40	Chlorophyll, biomass
VOG1	41	red-edge
VOG2	41	red-edge
PRSI	42	Senescence
PRI	43	Light use efficiency
SIPI	43	Light use efficiency
CARI	39	Chlorophyll, biomass
MCARI1	39	Chlorophyll, biomass
MCARI2	39	Chlorophyll, biomass
CRI1	42	Carotenoids
CRI2	42	Carotenoids
ARI1	43	Anthocyanins
ARI2	43	Anthocyanins
WBI	41	Canopy water content
NDWI	41	Canopy water content
MSI	41	Canopy water content
NDII	41	Canopy water content
NDNI	44	Nitrogen
NDLI	43	Lignin

Table 3.2: Vegetation indices used in this work, showing page references to definition and the foliar constituents the indices are correlated with.

Fluorescence. The reflectance indices outlined by Meroni et al. (2009) and Zarco-Tejada et al. (2012) for the qualitative characterisation of chlorophyll fluorescence were also derived. These are summarised in tables 2.5 and 2.6 (page 47). While purely qualitative these indices should enable the detection of fluorescence and an indication of its viability as a prospection technique, as fluorescence is highly responsive to short term stress responses to water constraint (Passioura 2002, Chaves et al. 2002). Contrast for these indices was evaluated using the same techniques as for the indices outlined above.

Red-edge Inflection Point The REIP sensitive is sensitive to both variations in vegetation stress and vigour and biomass. Other than the work of Verhoeven & Doneus (2011) and Verhoeven et al. (2013) it has not been extensively investigated for the detection of archaeological vegetation marks. Three different methods of deriving the REIP were tested. Linear interpolation (see page 44) is often used as a baseline methodology for comparison of REIP methods (for example, see Dawson & Curran (1998), Cho & Skidmore (2006) and Clevers et al. (2002)), so is included here. Lagrangian interpolation of the REIP (see page 45) is best suited for coarsely sampled data, so is included here as it may be useful for airborne data, particularly from the CASI sensor. To examine the extent to which the REIP is influenced by chlorophyll fluorescence the linear extrapolation technique (page 45) suggested by Cho & Skidmore (2006) was also tested.

Absorption feature characterisation. Continuum removal of key foliar absorption features were tested. This will enable the investigation of the combined effect of overlapping absorption features, for example, in the 670nm feature, where the effects of biomass, the REIP, chlorophyll and carotenoid content, fluorescence are all combined. By examining the the breadth, depth and area of the continuum removed absorption features it should be possible to examine the combined effects of multiple foliar and structural constituents of reflectance. By using normalisation by area (page 49) it should also be possible to identify shifts in absorption whilst reducing the effects of biomass (Curran et al. 2001).

During early testing of the methods to derive continuum removed spectra using pre-determined end members to derive the continua proved problematic. Firstly, it made the the method insensitive to broadening of the absorption features. This is important particularly for the water absorption features centred on 970nm and 1200nm, where an adjacent water-vapour absorption feature causes broadening. Second, if the continuum line is intercepted by reflectance at any point other than the end members this causes negative vales in the resultant continuum removed spectra. This makes comparison of the

area of the absorption feature overly sensitive to any narrowing of the feature.

To solve this some approaches, such as that used by the ENVI software suite use a convex hull to derive end members on absorption peaks for the entire spectral curve. This is not ideal for vegetation spectra, as the convex hull is defined by the smallest set, meaning that the continuum thus defined will often cover all absorption features between the visible and the near infrared, making the investigation of single absorption features difficult. To derive end-members in the work implemented here, a subset of reflectance for the general region of each absorption feature was first extracted. Then, the reflectance maxima on each side of the reflectance minima are determined. These are used to further refine the subset. Then, a convex hull is derived using the Quickhull algorithm (Barber et al. 1996). Assuming that the absorption feature is convex, the continuum is the simplex of the convex hull with the greatest distance in wavelengths between vertices. The refined end-members are then used to interpolate a straight line segment at the same wavelength intervals as the input data to be used as the continuum line.

Table 3.3 shows the initial definitions of the absorption features used for continuum removal. The SWIR from features 1400m-2500nm used in the studies by Kokaly & Clark (1999) and Curran et al. (2001) were not used here due to the sensor noise in this region.

Absorption Feature	Start	End	Correlated with
470nm	400	518	Chlorophyll (depth). Carotenoids (breadth)
680nm	548	800	Chlorophyll (breadth and depth). Carotenoids (left slope). red-edge (right slope). Biomass (depth).
970nm	880	1115	Water vapour (left slope). Canopy water content (depth). Biomass (depth)
1200nm	1080	1300	Water vapour (left slope). Canopy water content (depth). Biomass (depth)

Table 3.3: Initial definition of absorption features used in this study and the foliar constituents they are correlated with.

In addition to the continuum removed reflectance, additional metrics defining the absorption features were derived. These are defined in table 3.4

Metric	Description	Rationale
Start λ	Refined wavelength of the left end member	Shows variations in feature breadth
End λ	Refined wavelength of the right end member	Shows variations in feature breadth
Feature area	Area of the absorption feature	Shows variations in depth and breadth
Left TBVI	Two band vegetation index using the minima of the absorption feature and the maxima to the left of this	Shows the normalised gradient of reflectance of left slope of feature
Right TBVI	Two band vegetation index using the minima of the absorption feature and the maxima to the right of this =	Shows the normalised gradient of reflectance on the right of the absorption feature
Continuum gradient	Gradient of the continuum line	Shows the relative difference in height between the end-members, demonstrating the relationship between the reflectance peaks on either side of the feature
Continuum area	Area of the continuum removed absorption feature	Sensitive to breadth and depth, but normalised for comparison
Maximum feature depth	Continuum maximum removed band depth	Shows normalised feature depth
Maximum feature depth λ	Wavelength of the above	Sensitive to lateral shifts in absorption
Area left	Continuum removed area to the left of the feature minima	Shows variations in breadth and depth, sensitive to broadening of the left slope of the feature
Area right	Continuum removed area to the right of the minima	Shows variations in breadth and depth, sensitive to broadening of the left slope of the feature

Table 3.4: Metrics derived from continuum removed spectra for comparison.

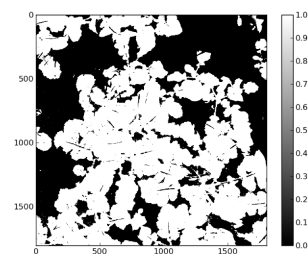
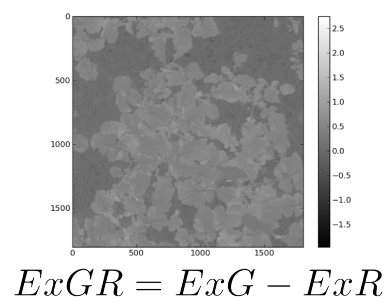
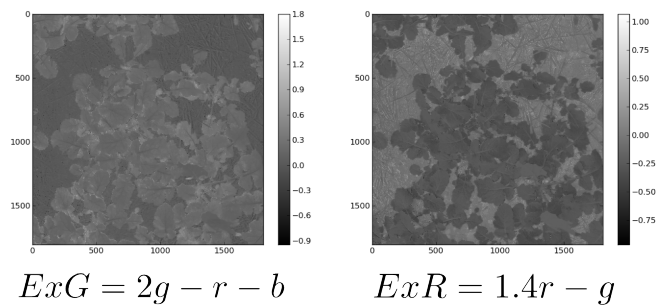
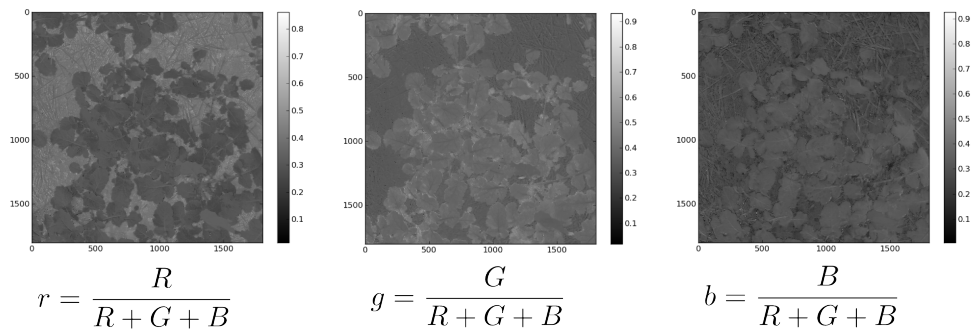
3.4.2 Ground cover

Near-vertical photography was acquired using a hand-held digital camera, both to record ground conditions where spectral and crop property measurements were recorded and to evaluate vegetation density and biomass during the early growth stages. This was necessary, as before the formation of a crop canopy, other methods, such as the canopy ceptometer are not suitable. Several approaches to solving this problem were tested during the early stages of the project, including using red filtered RGB and infra-red adapted cameras in conjunction to derive NDVI 2.3 images (Lebourgeois et al. 2008, Rabatel et al. 2011, Nijland et al. 2014). Although this worked well on test images it was too difficult to deploy in the field, as acquiring images with no parallax between cameras at close range proved impossible. As an alternative, mounting the camera on a tripod and changing the filtration to capture red and near infra-red image pairs was also tested. This resulted in fewer problems related to parallax, but under field conditions movement of the vegetation caused by wind resulted in errors in co-registration of pixels between images acquired at different times. As result, RGB images captured at a single point in time from a single viewpoint were deemed more practical, despite the reduced contrast between the vegetation and the background. Several methods are used in precision agriculture to discriminate vegetation from the soil and crop litter using RGB cameras. These are explored in greater depth in chapter 5. Of these the most effective for discriminating green vegetation is the $EXG - EXR$ (equation 3.1, figure 3.7) method (Meyer & Neto 2008, Romeo et al. 2013), where R, G and B are the red, green and blue bands in the RGB image.

$$EXG - EXR = \left(2 \frac{G}{R+G+B} - \frac{R}{R+G+B} - \frac{B}{R+G+B} \right) - \left(1.4 \frac{R}{R+G+B} - \frac{G}{R+G+B} \right) \quad (3.1)$$

The resultant image is thresholded to provide a binary distinction between vegetation and the background. Using a fixed value for this threshold is problematic, as changes in illumination and variance in the vegetation, background and sensor properties can shift the distribution of the histograms. Meyer & Neto (2008) resolve this by using Otsu's method to select an appropriate threshold value (Otsu 1975) for each image.

Source RGB image



Binary threshold

Figure 3.7: Derivation of vegetation coverage using the $EXG - EXR$ method.

3.4.2.1 Data collection

Data were acquired at each meter along the transect using either Canon Powershot S100 or Samsung GX10 digital cameras. Both cameras are ten megapixel sensors using optics with an approximate 74 degree IFOV. A hot-shoe mounted spirit level was used to ensure that the camera was pointing approximately on-nadir, and a measuring stick placed orthogonally to each metre along the transect was used to ensure correct framing. After acquisition the images were cropped to approximately 1x1m using the GNU Image Manipulation Program (Gimp (2008)).

3.4.2.2 Image analyses

The resultant images were then analysed to identify the proportion of each image covered by green vegetation. First the *EXG – EXR* was applied to the images and thresholded using Otsu's method using the Python programming language. These were then divided into 16 subsets establish variability across the area at close to the scale the other measurements were recorded, and from these percentage coverage was then derived.

3.4.3 Biomass: Leaf area index and crop height

3.4.3.1 Measuring crop height

Where significant growth of crop was present the height of the vegetation was measured along the transect. For the wheat crops considered here, this was measured to the highest point, generally the tip of the flag leaf. For oilseed rape this was measured to the top of the flower head. These readings were taken every 0.2-0.3m along the transect.

3.4.3.2 Growth stage

Growth stage was noted on the Feekes scale (Large 1954) for wheat crops. Additionally, for young crops the number of tillers, or shoots was noted as this is affected by changes in available soil moisture and compaction in the early growth stages. For oilseed rape the scale devised by Harper & Berkenkamp (1975) was used.

3.4.3.3 Leaf Area Index

In March 2012 the project acquired an Accupar LP-80 canopy ceptometer (Decagon Devices Inc. 2014). This instrument measures Photosynthetically Active Radiation (PAR), representing the portion of the spectrum in the 400-700nm region used for photosynthesis.

By comparing the quantity of PAR incident above the canopy to that below the canopy, the absorption of PAR by photosynthesis can be used to estimate LAI (Leaf Area Index) (Armbrust 1990, Welles & Cohen 1996, Cohen et al. 1997). The quantity of PAR absorbed by the crop canopy is directly linked to the productivity of the crop in terms of dry matter (Monteith & Moss 1977). The Accupar uses an above canopy sensor in conjunction with the below canopy sensor, which consists of a 1m long wand, with 80 sensors. measurements are averaged over 8 segments of the wand (Decagon Devices Inc. 2014). Additional parameters are leaf distribution, or χ , and the solar zenith angle, derived by the instrument using latitude and the time and date. χ is the ratio between the length of the horizontal and vertical axes of the spheroid defined by the leaf angle distribution of the crop. Based on the manufacturer's recommendations χ values of 1 were used for wheat crops, for oilseed rape a value of 2 was used (Decagon Devices Inc. 2014). Data were collected along transect at 0.2-0.3m intervals. To avoid the readings being distorted by the disturbance caused by the crop being trampled when taking measurements along the transects only the 4 segments from the furthest end of the below canopy sensor were used.

3.4.4 Analysis Methodology

The data collected from the transects was classified in to archaeology and background using the probable extents of the features detected from the magnetic survey. For each measure the two classes were analysed using a Welch's T-test Welch (1947), Zimmerman & Zumbo (1993). This method was chosen as there are comparatively few samples, and it could not be assumed that the variances of the samples were equal. The resultant T and P values provide an indication of the strength and statistical significance of the contrast respectively, and provide a useful metric for comparison between methods. Based on observation of contrast values in the field, contrast was determined as having a T value greater than 5 and a P value under the 95% confidence interval. This provides a meaningful indication of both the clarity and statistical significance of the contrast.

3.5 Results

A summary of the transect surveys undertaken and their results are presented in Appendix B (page 223), as space prevents exploring them in detail here. The results are ordered by transect and date. Absolute contrast is plotted using the T value in the summary plots for measurements of vegetation structure and density, the REIP, fluorescence indices, bench-

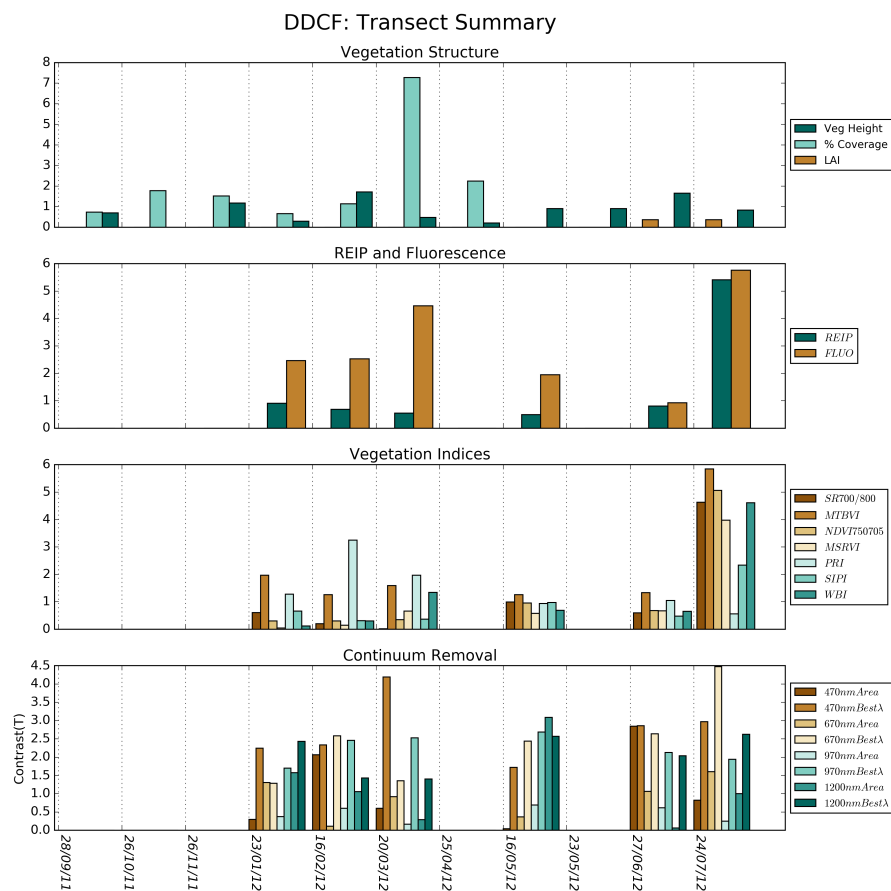


Figure 3.8: Summary of results from DDCF, showing the vegetation measurements a results of the analysis of field spectra.

mark vegetation indices identified from the literature as being performant for detection of archaeological vegetation marks as well as the best performing variable wavelength MT-BVI, and continuum removed metrics including feature area and the continuum removed wavelength displaying the greatest contrast.

3.5.1 Diddington Clay Field

Diddington Clay field was under wheat during the entire period of measurement. Little contrast was visible during most of the year (figure 3.8, possibly due to the soil moisture surplus and clay soils meaning that there was no resource constraint placed upon the growing crop. Biomass variations showed little contrast, except during March 2012, where a significant negative correlation between the archaeological feature and the vegetation coverage was observed. This indicates a reduction in overall biomass. In addition,

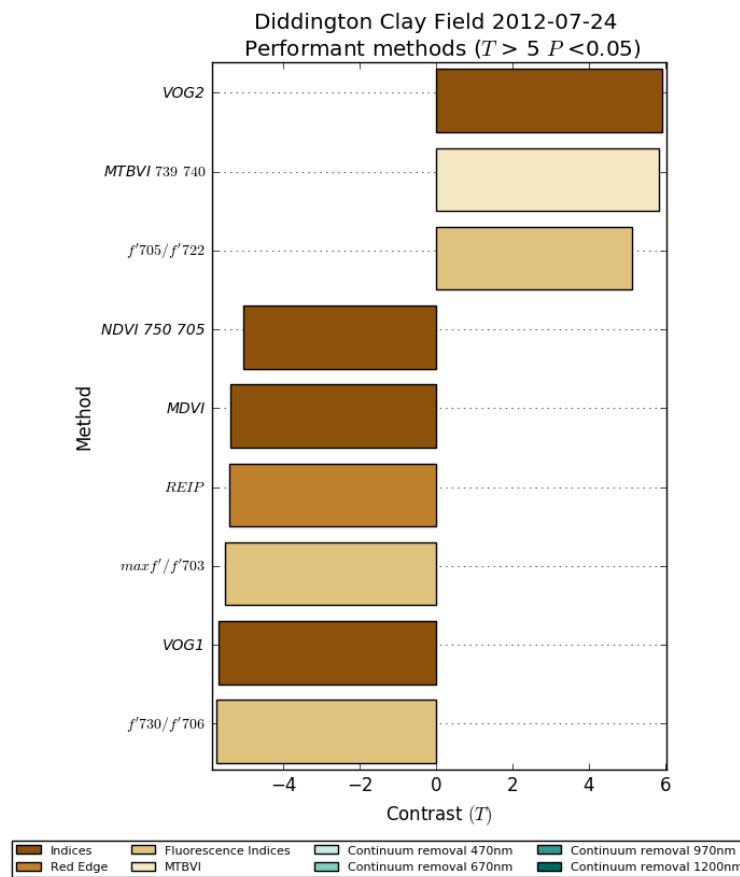


Figure 3.9: Performant methods from Diddington Clay field during July 2012. Fluorescence and red-edge indices detected the most contrast.

a positive correlation between fluorescence and the archaeological features suggests that the crop is more stressed than that growing over the background. This is curious, as generally for cut features such as ditches we expect an increase in biomass. This may reflect inhibitory responses to excess soil moisture over the feature (Passioura 2002), or delayed germination caused by encapsulation of the seed in the heavy clay.

The only other date where significant contrast was observed was the 24th of July 2012 (figure 3.9). On this date fluorescence and REIP sensitive measures demonstrated the most contrast, including the Vogelmann red-edge Index. Additionally, there is a strong negative correlation between continuum removed reflectance at 738nm. The MTBVI exhibits strongest contrast using adjacent bands at 739nm and 740nm, in the region of maximal fluorescence emission in the NIR, taking the spectral resolution of the sensor into account (Meroni et al. 2009).

These measures indicate that there is a significant difference between the photosynthetic activity in the crop growing over the archaeology and the background. The crop at this stage was ripening and at the early stages of senescence. The increase in contrast at wavelengths related to the REIP and fluorescence possibly indicates a subtle variation in maturation, with the more stressed vegetation growing on the background reaching senescence sooner than that growing over the archaeology (figures 3.10).



Figure 3.10: Photograph looking west along the transect in DDCF, showing that cropmark inversion is not visible to the naked eye.

3.5.2 Diddington Transect 1

3.5.2.1 June-July 2011

During this period the field was under winter wheat. A severe drought and significant PSMDs meant that significant vegetation marks were visible on the ground surface as both variations in the colour and height of the crop (figures 3.12 and 3.13). The height



Figure 3.11: Summary of results from DDT1, showing the vegetation measurements and results of the analysis of field spectra.

variations between the background and the archaeology were as much as 0.2m. This contributes to significant contrast expressed as biomass variations. The biomass variations are persistent, and remain significant event though the contrast in the spectral measurements changes over time.



Figure 3.12: Panoramic view of vegetation marks at Diddington transect 1, looking NE over enclosure ditches. The vegetation marks are visible as both variations in height and colour, with the crop over the ditches a deeper green than over the background.



Figure 3.13: Panoramic view of vegetation marks at Diddington transect 1, looking NW over enclosure ditches. The vegetation marks are visible as both variations in height and colour, where the crop over the ditches has reached maturity and is ripening and the crop between the ditches is retarded and is still green.

Using the REIP the greatest contrast is observed on the 8th of June, when the crop was still green, and decreases as the crop matures (figure 3.11). On all dates the performance of fluorescence indices is greater than that of the REIP. The greatest contrast in fluorescence is apparent on the 14th of June and decreases afterwards, suggesting that as drought and vegetation stress increase in severity the chlorophyll content of the crop is decreasing, either due to adaptation or damage Chaves et al. (2002).

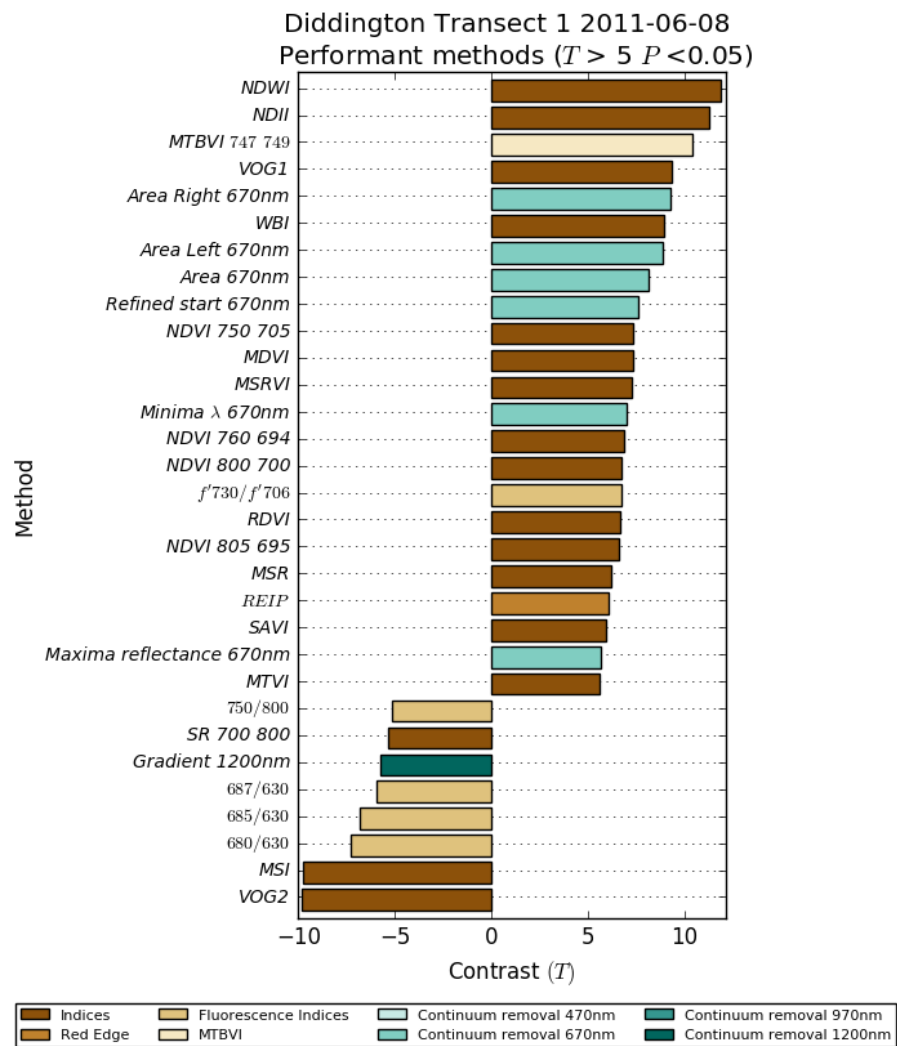


Figure 3.14: Performant methods from Diddington Transect 1 on the 14th of June 2011. Water sensitive indices, followed by those sensitive to chlorophyll fluorescence detect the most contrast.

The MTBVI values perform well compared to other indices on the 8th and 14th of June (figures 3.14 and 3.15), with wavelengths at 747nm and 749nm on the 8th of June and 712nm and 714nm on the 14th. 747nm is correlated with chlorophyll fluorescence, so the contrast at these wavelengths is likely a result of variations in short term stress and vigour. On the 14th of June the wavelengths are close to the mean REIP at 718.7nm. This means that although the contrast expressed in the REIP is weaker than other methods, the gradient of reflectance at the REIP is more sensitive. Other indices on these dates also demonstrated significant contrast. On the both 8th and the 14th of June the NDWI and NDII, sensitive to canopy water content expressed the most contrast. However, this is not reflected in the continuum removed spectra for the 970nm and 1200nm absorption features on the 8th of June. However, the readings from the 14th of June demonstrate a considerably better correlation between the water absorption indices and continuum removed spectra. It is possible that the readings from the 8th are anomalous, as significant noise is evident in the SWIR region of the spectra from this survey. This may be as a result of not allowing the instrument enough time to acclimatise before conducting the survey.

The results from the continuum removal during this period are mixed. On the 8th of June the strongest overall contrast was expressed in the 470nm BNA continuum removed absorption feature at the 484nm wavelength. This wavelength is at the edge of the absorption feature, and the strong negative correlation with the archaeological features in this region may indicate broadening of the 470nm feature, most likely due to the actions of assistive pigments such as xanthophylls and carotenoids (Gamon & Surfus 1999, Curran et al. 2001, Kov et al. 2013). Indeed, the continuum removed spectra indicate a significant narrowing of the absorption feature when comparing the archaeology to the background. On the 14th contrast is visible in the 470nm, 670nm and 1200nm features. On the 29th significant contrast is only recorded in continuum removed reflectance for the 470nm absorption feature. This again indicates an increase in the activity of assistive pigments as the crop senescences (Kov et al. 2013). Negative correlations with the archaeology in the 670nm and 1200nm features indicate that the crop over the archaeology has reached maturity and senescence sooner than the crop over the background. This phenomena is often described as 'cropmark inversion' (Riley 1987, Darvill 1996), which is normally detected using aerial photography as ripe crops over the archaeology appearing lighter in colour against a darker background of still ripening crop.

By the 15th of July the crop is senescent and photosynthetic activity has ceased largely ceased. Significant contrasts are detectable in the RDVI vegetation index and the MTBVI

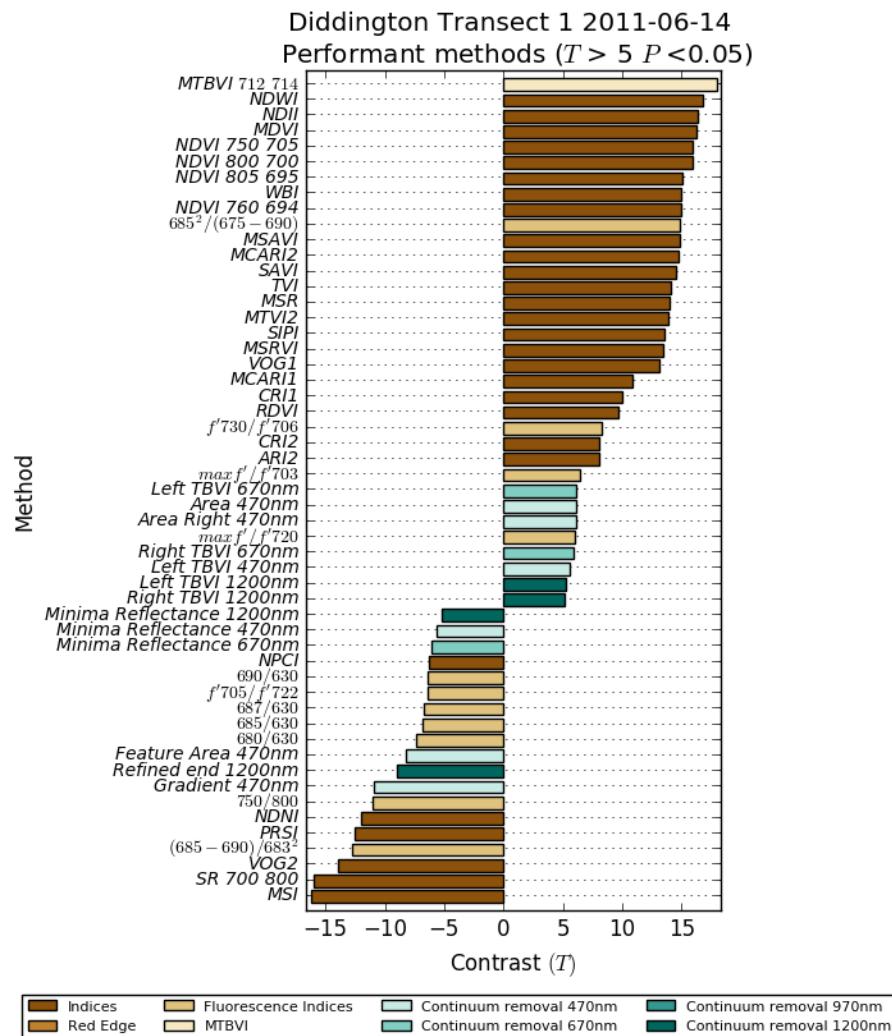


Figure 3.15: Performant methods from Diddington Transect 1 on the 14th of June 2011. A wide range of methods produced significant contrast.

at 735 and 736nm.

3.5.2.2 August 2011-June 2012

During this period the field was under oilseed rape. This crop is considered less conducive to vegetation mark formation than cereals, and, as opposed to the drought encountered during the 2011 growing season, this was one of the wettest on record. This meant comparatively little contrast was visible during this period. In addition, heavy predation of the crop mean the transect was moved during October 2011. While the same feature is covered, the shift in location may have resulted in reduced contrast over the feature. In addition, the density and height of the mature crop in June meant that after this point measurement had to be curtailed, as it was impossible to acquire measurements from the dense crop canopy.

Significant contrasts were detectable in February and May 2012. In February these were expressed most strongly in the MTBVI at wavelengths associated with fluorescence, and in the continuum removed spectra for the 970nm and 1200nm absorption features.

During May 2012 the contrast was most strongly expressed as variations in the PRI index and fluorescence. Interestingly, the contrast between fluorescence and the archaeological feature is positive, indicating that the vegetation is more stressed over the feature than the background. This is supported by a negative correlation with the 670nm, 970nm and 1200nm absorption features. However, this may be due to differences in reflectance caused by the flowering of the crop (Wang et al. 2004).

3.5.3 Harnhill Quarry field

3.5.3.1 September 2011-March 2012

During this period Quarry Field was left fallow. The field was under organic cultivation, meaning that there was a significant understory of clover and grasses that grew quickly after the crop had been harvested. While only one set of spectral measurements could be obtained during this period there was a significant variation in vegetation coverage over the winter. This is probably related to the increased temperature over the archaeological feature noted by an number of authors (Evans 2007, Scollar et al. 1990, pp. 22–25).

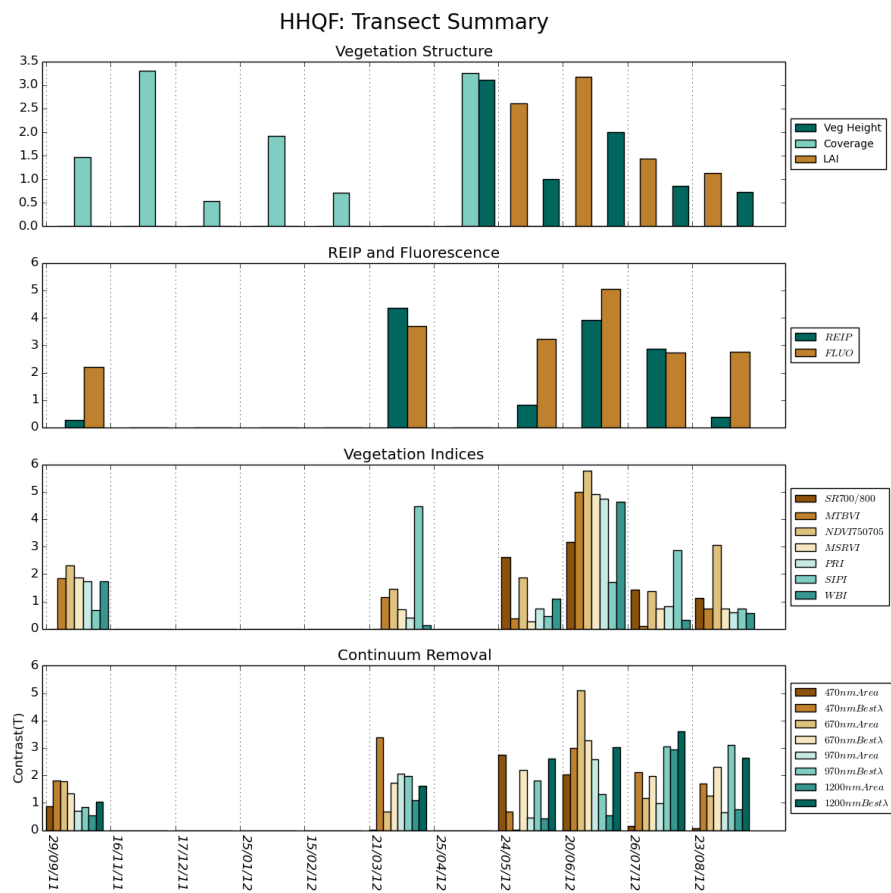


Figure 3.16: Summary of results from HHQF, showing the vegetation measurements and results of the analysis of field spectra.

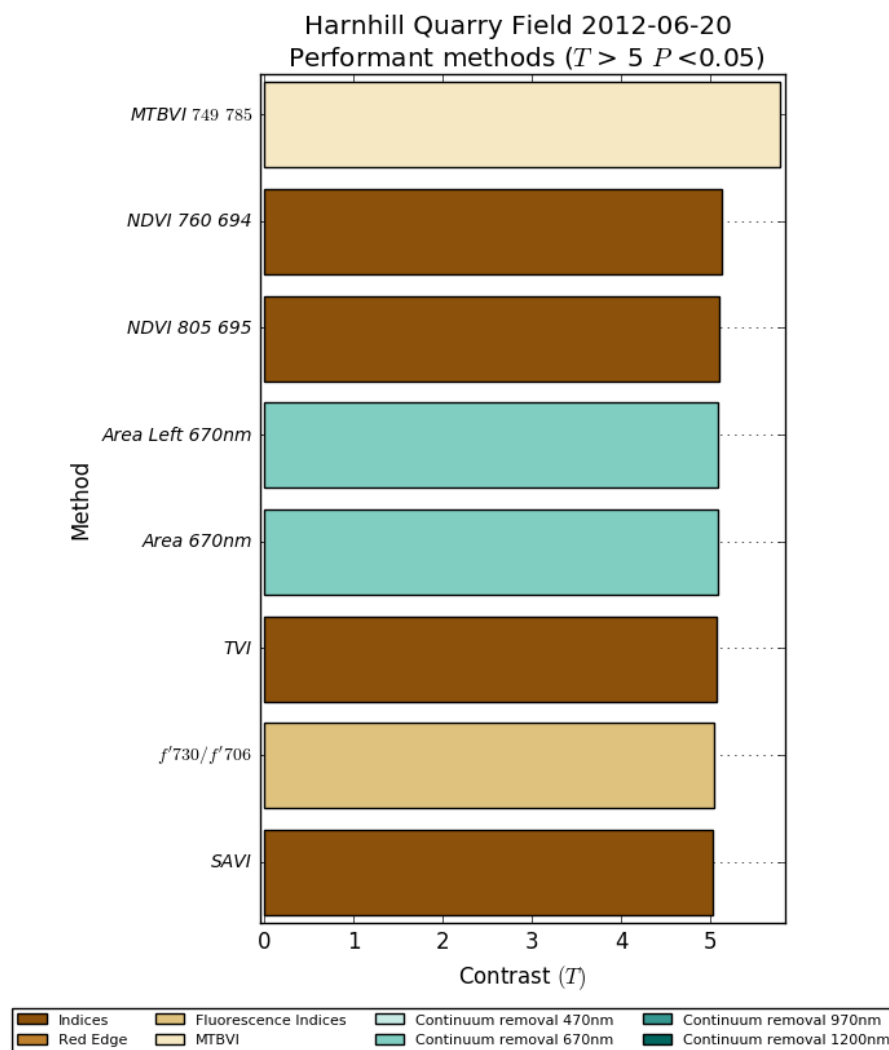


Figure 3.17: Performant methods from Harnhill Quarry Field June 2012. Measures related to fluorescence provide the best indications of contrast.

3.5.3.2 March-August 2012

In March 2012 the field was drilled with spring wheat. The March measurements were acquired over bare soil. These still demonstrate contrast in the vegetation indices and fluorescence ratios, as these record the gradient of reflectance between the darker plough soil over the archaeology and the lighter soil over the background. During the early growth of the crop significant variation in biomass was observed. In April variations in both vegetation height and coverage were significant. In May and June significant variations in LAI were observed. These decreased as the crop matured in July and August.

The spectral differences from the May survey were comparatively minor, with the greatest contrast evident as fluorescence. During the June survey the ditch was visible as a vegetation mark to the naked eye, and this is also the period of highest contrast in the spectral data (figure 3.17). The greatest contrast was recorded by the by the MTBVI at wavelengths 749nm and 785nm. 749nm is associated with fluorescence. In addition, significant contrasts are observed in generic and red-edge sensitive indices and continuum removal for the 670nm absorption feature. The $\frac{D_{730}}{D_{706}}$ fluorescence index demonstrates a positive relationship with the archaeological features, indicating that photosynthesis in the vegetation over the feature is being constrained to preserve water. This is in opposition to other stress indicators, including the REIP and continuum removed reflectance for the 670nm feature, which show that the vegetation over the features is healthier than that over the background. This may indicate a sudden shortfall in resources, which is not unexpected given the main feature considered is an active field drain. The 670nm absorption feature, correlated with biomass and chlorophyll content was the best performing continuum removal metric, in line with the contrast exhibited in the red-edge and biomass sensitive indices.

During July and August contrast decreased in the ripening and senescent crop. Subtle and statistically insignificant contrasts were observed in fluorescence and the REIP, with absorption in the 1200nm feature also indicating subtle contrasts.

3.5.4 Harnhill Cherry Copse

Cherry Copse was under pasture and hay meadow for much of the period considered here. Due to the the shallow soil over bedrock this field demonstrated the most frequent contrast of all the study sites, as the ditch represents a significant difference of root constraint to the background. Over the winter there was little contrast expressed as biomass variations, as the area was grazed by sheep, keeping the vegetation low. However, spectral contrasts were detectable, particularly in the water absorption feature at 1200nm. In February 2012 the contrast in the water absorption band was particularly strong. In addition there is a strong contrast related to fluorescence , and MTBVI at wavelengths associated with fluorescence (figure 3.19).

During March subtle but statistically insignificant contrasts were recorded in measures related to canopy water content. In April, May and June significant contrasts in biomass were recorded as the vegetation grew and became subject to resource constraint. These contrasts were significantly reduced during July when the field was mown. During May

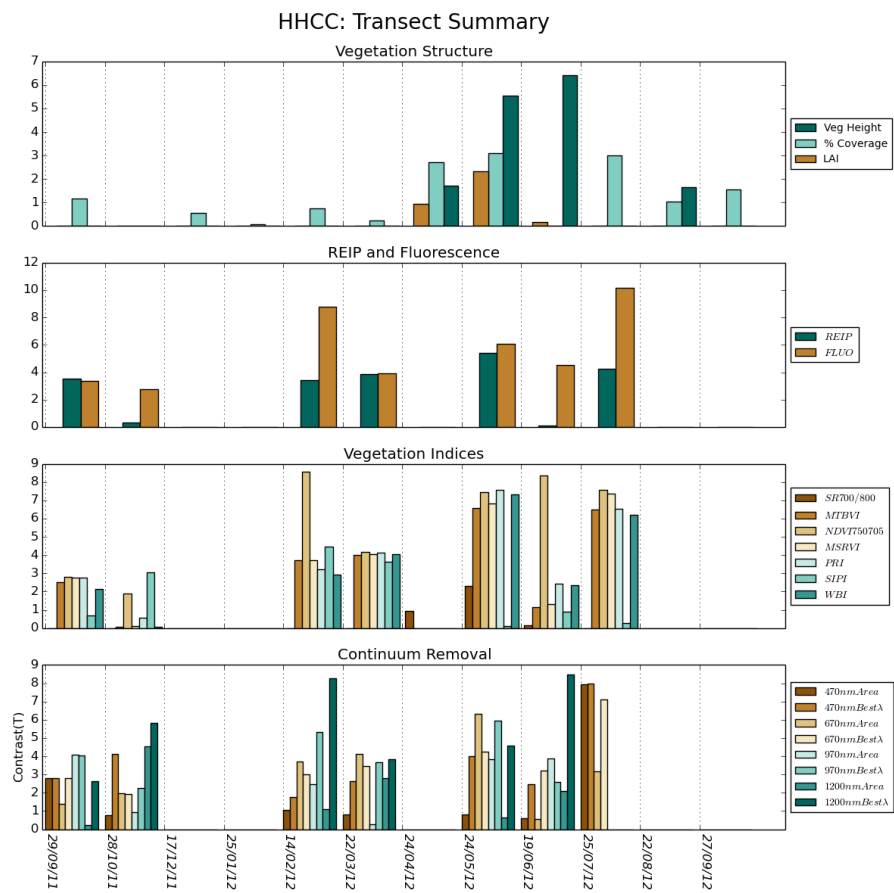


Figure 3.18: Summary of vegetation and field spectroscopy from Harnhill Cherry Copse.

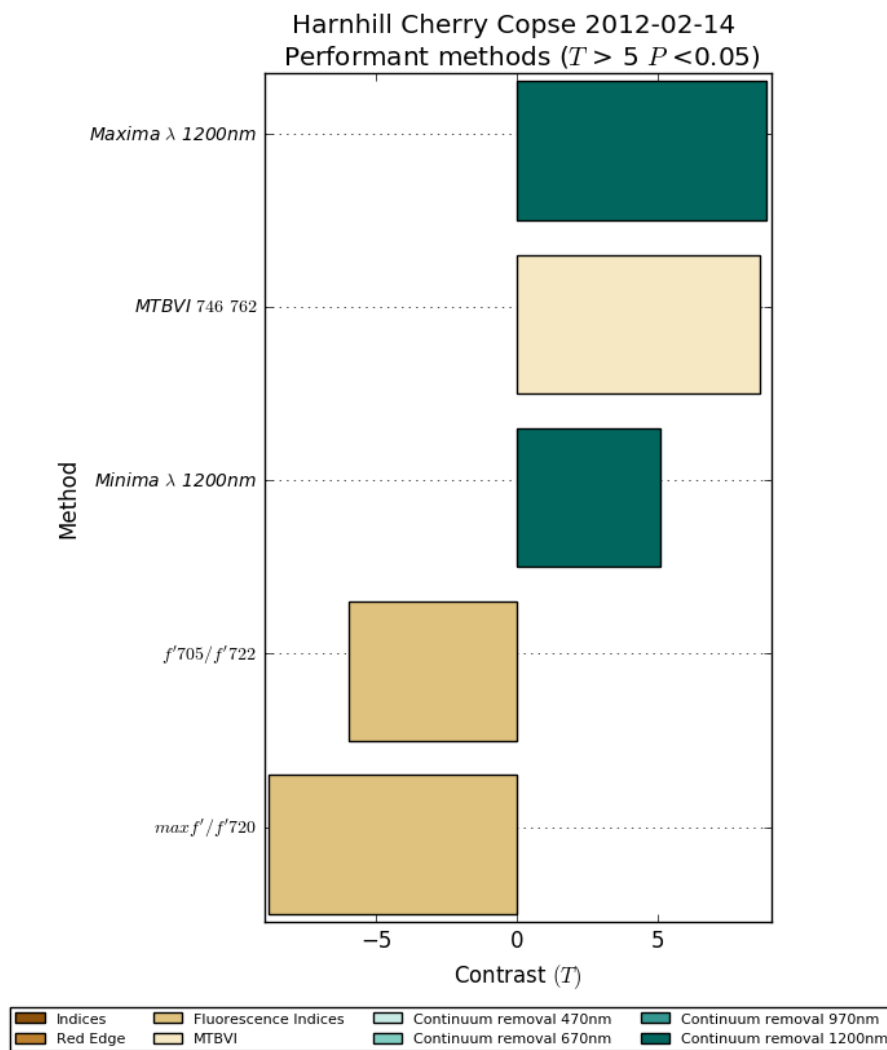


Figure 3.19: Performant methods from Harnhill Cherry Copse February 2012. Measures related to fluorescence provide the best indications of contrast.

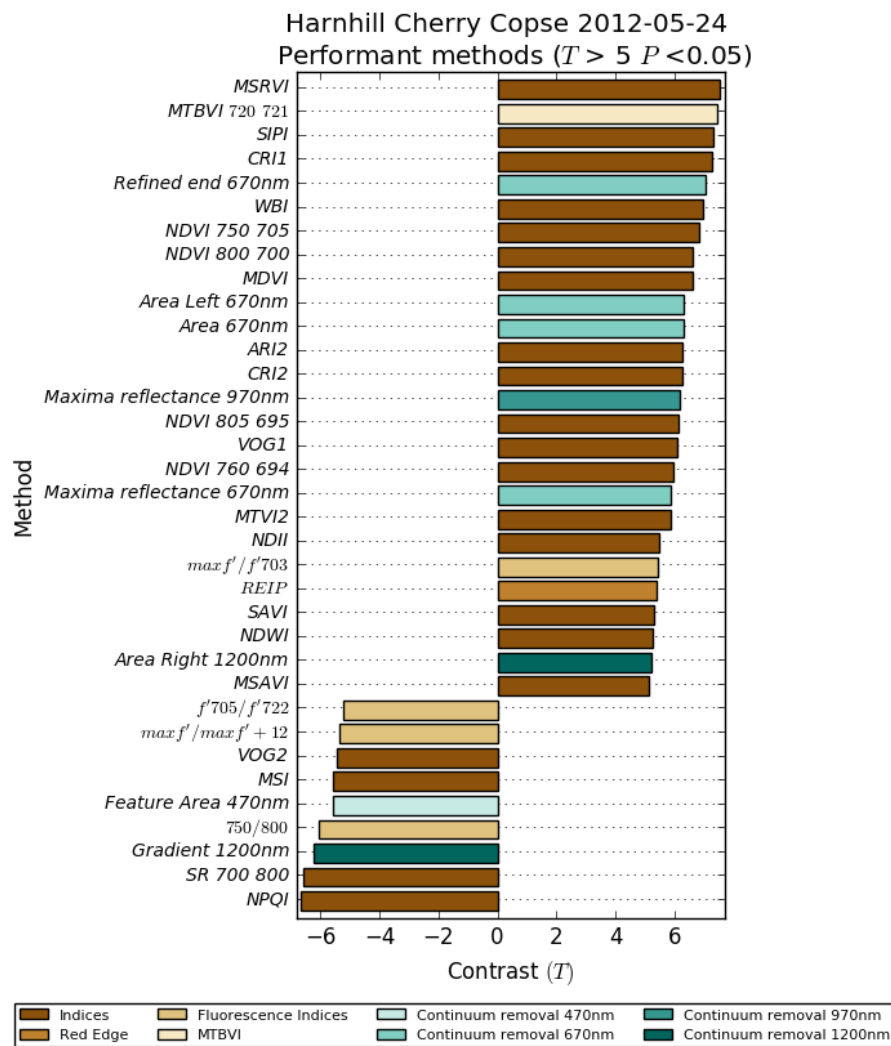


Figure 3.20: Performant methods from Harnhill Cherry Copse May 2012. Measures related to fluorescence provide the best indications of contrast.

significant contrasts were visible in the spectral data, with REIP sensitive measures indicating the greatest contrast. This includes the MSRVI and MTBVI at 720nm and 721nm. Significant contrasts in fluorescence indices and canopy water content, detected by continuum removal for the 970 and 1200nm absorption features were also observed (figure 3.20).

In June the contrast in biomass sensitive indices is reduced, despite a strong variation in the height of the vegetation. This is possibly due to saturation of many of these indices in the dense vegetation canopy. Little contrast was also visible in the REIP. However, in continuum removed reflectance for the 970nm and 1200nm absorption features using the feature area and reflectance maxima measures (figure 3.17). Additionally significant

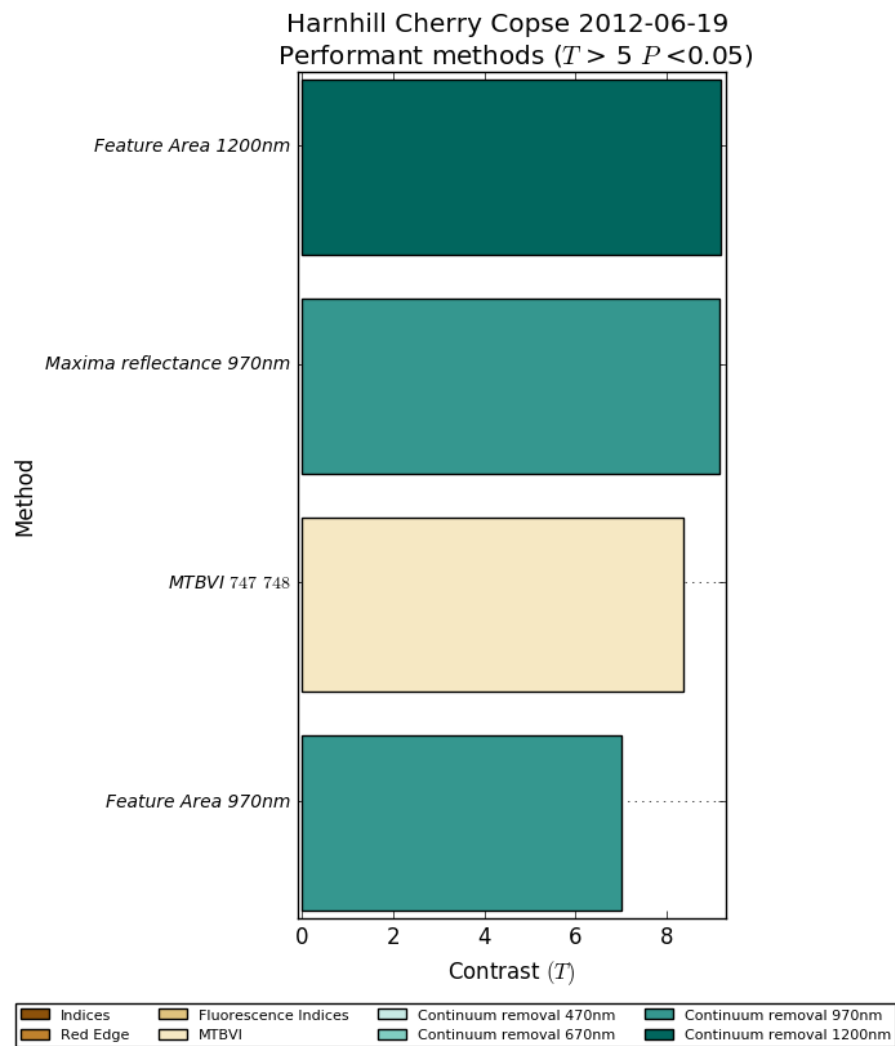


Figure 3.21: Performant methods from Harnhill Cherry Copse June 2012. Continuum removal metrics for the 670nm absorption features express the most contrast.

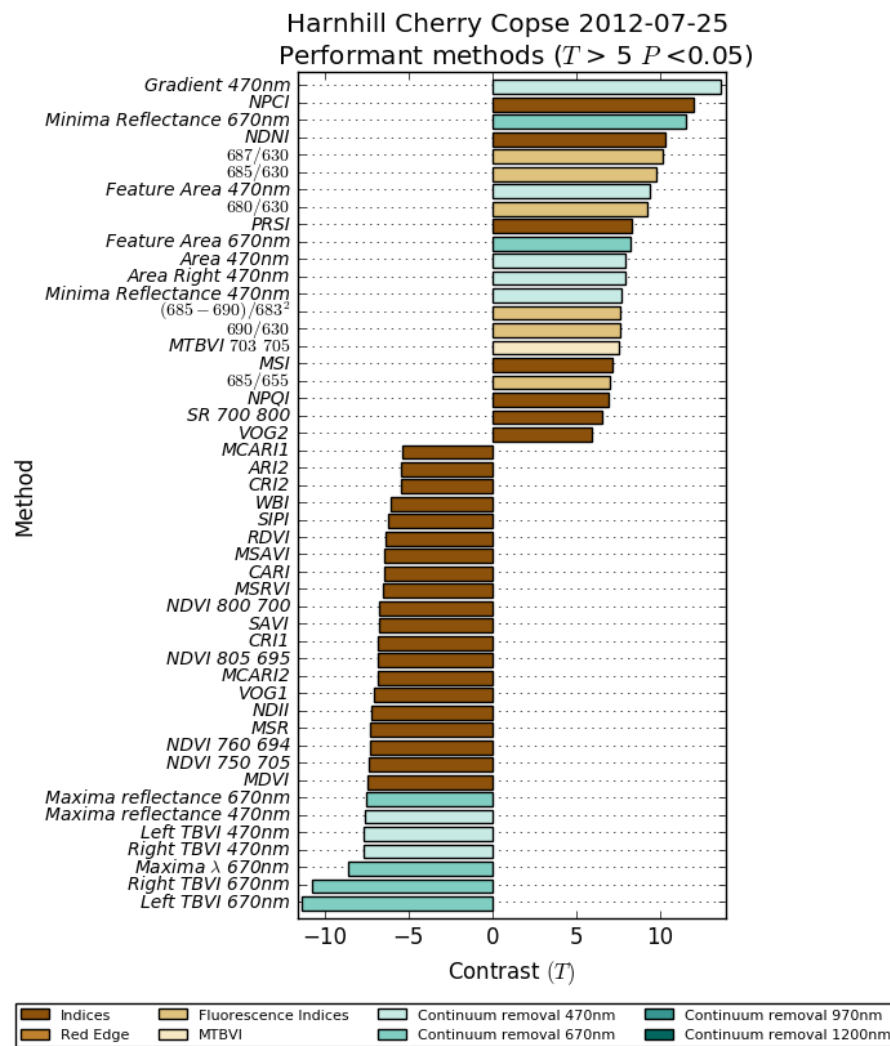


Figure 3.22: Performant methods from Harnhill Cherry Copse July 2012. Measures related to fluorescence provide the best indications of contrast.

contrasts were observable in the MTBVI at 747 and 748nm, wavelengths related to fluorescence. One possible explanation for the lack of contrast in the chlorophyll absorption measures is the large quantity of poppies flowering in the field at the time of survey. These will increase reflectance in the red region, which many of these methods rely on.

In July measurements were acquired shortly after the field was cut for hay. Over the ditch the vegetation recovered more quickly, leading to increased contrast in biomass sensitive indices, vegetation coverage and continuum removed reflectance in the 470 and 670nm absorption features (figure 3.22). There was a positive relationship between fluorescence and archaeology, and a negative relationship with the REIP. This indicates that the crop over the ditch is more stressed.

3.6 Evaluation of methods

3.6.1 Biomass

Variations in biomass are important, and represent a long-term adaptation to growth conditions (Passioura 2002). This can be seen in the results from DDT1, where on the 8th and 14th of June significant spectral contrasts were accompanied by variations in biomass. In the ripening and senescent crop the spectral contrasts were reduced, but the biomass variations remained. During the early growth stages the coverage estimates provided using RGB images also provide contrast, as at Diddington Clay Field during March 2012. It may be possible to exploit these contrasts in the spectral data, as the imaged pixel will conflate radiance from both the vegetation and the soil. Vegetation indices based on the red and infra-red portions of the spectrum perform poorly during this stage of crop development. This is likely due to the mixed contribution from the crop, soil and leaf litter (Nagler et al. 2000). During March 2012 at Diddington Clay Field the continuum removed spectra from the 470nm absorption feature shows better contrast than the other methods. Indices incorporating bands in the blue region of the spectrum, such as the NPCI also performed better.

These results confirm that biomass variations provide useful contrast that can be used for archaeological detection that can be potentially exploited in the airborne data. However, isolating contrast caused by biomass from other spectral features is problematic, as reflectance methods used to identify it are conflated with absorption features from pigments (Asrar et al. 1984, Baret & Guyot 1991, Carlson & Ripley 1997, Mutanga & Skidmore 2007) and emissions from fluorescence Cho et al. (2007).

3.6.2 Vegetation indices

The vegetation indices commonly used for archaeological detection perform consistently well, in particular red-edge sensitive indices and the various permutations of the NDVI (figure 3.23). These indices conflate the spectral effects of biomass and photosynthetic activity in the red and near infra-red regions of the spectrum. Indices designed for the detection of specific pigments and photochemicals perform less consistently. However, these indices provide can provide contrast when the more generic chlorophyll indices do not. This can be observed in the results from Diddington Transect 1 in March 2012, when indices sensitive to assistive pigments such as carotenoids, anthocyanin chlorophyll a and b provide statistically significant contrasts between the archaeology and the back-

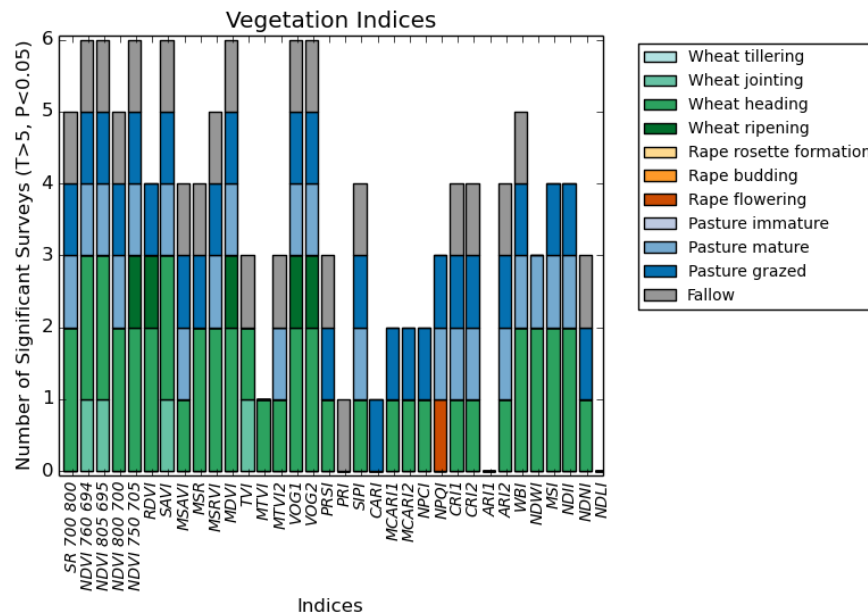


Figure 3.23: Performance of vegetation indices ranked by crop type and number of surveys where significant contrast was observed.

ground. Applying these indices to the airborne data is trivial and computationally cheap. Therefore it is suggested that for the airborne data all possible vegetation indices be derived.

3.6.3 The MTBVI

Predictably the MTBVI produces better results than the standard NDVI indices in a wider variety of conditions. However, rather than producing the best results using refined absorption minima and maxima, often the greatest contrast is recorded in ratios between nearly adjacent bands (figure 3.24) in the NIR region at wavelengths associated with the red-edge, for example at Diddington T1 14th June 2011 (figure 3.25) and chlorophyll fluorescence at Diddington T1 8th June 2011 (figure 3.26).

3.6.4 Chlorophyll fluorescence and the red-edge inflection point

While a number of red-edge sensitive indices provide good contrast, contrast in the red-edge position is generally less pronounced than that provided by the fluorescence indices, indicating that much of the contrast attributed to the REIP (for example, Doneus et al. 2014, Agapiou et al. 2013) in archaeological detection is likely conflated with chlorophyll fluorescence (Cho & Skidmore 2006). In particular, methods identified in these studies

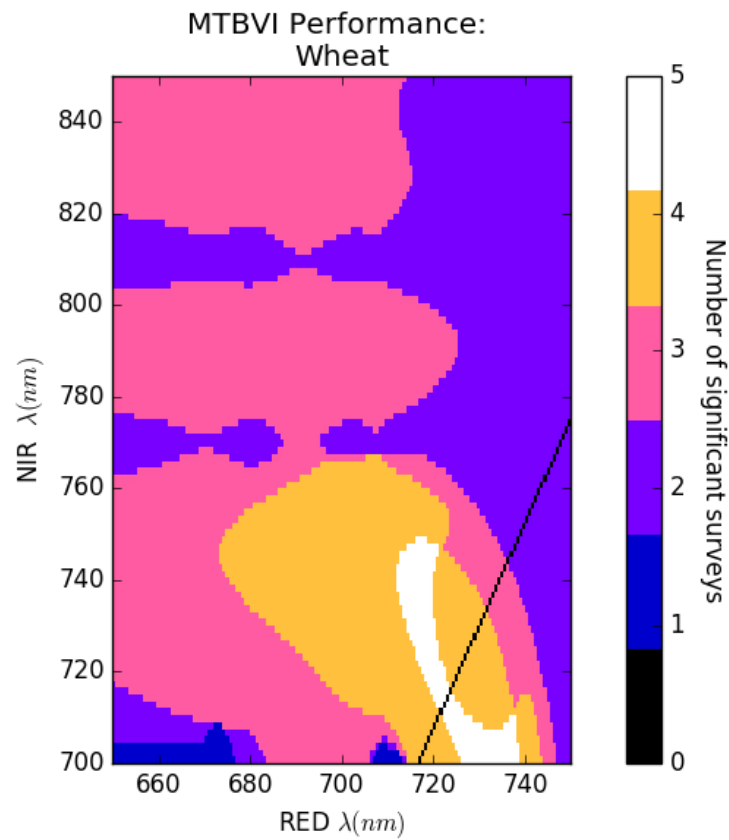


Figure 3.24: MTBVI performance in wheat crops.

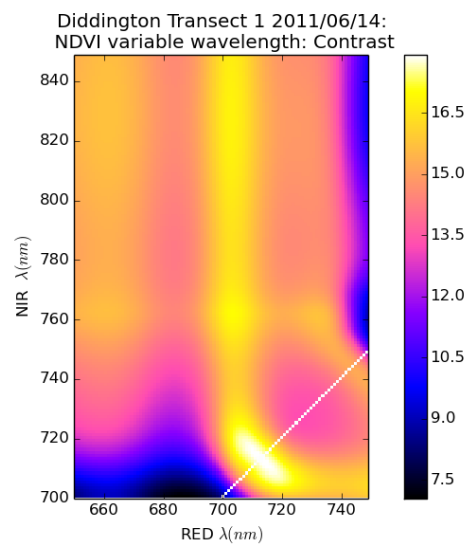


Figure 3.25: MTBVI correlated with REIP. DDT1 14/06/2011.

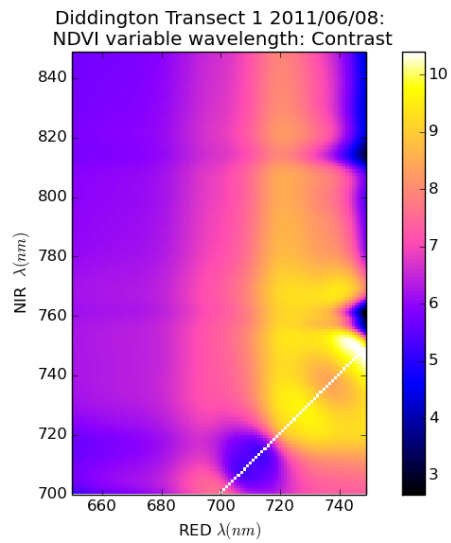


Figure 3.26: MTBVI correlated with fluorescence. DDT1 08/06/2011.

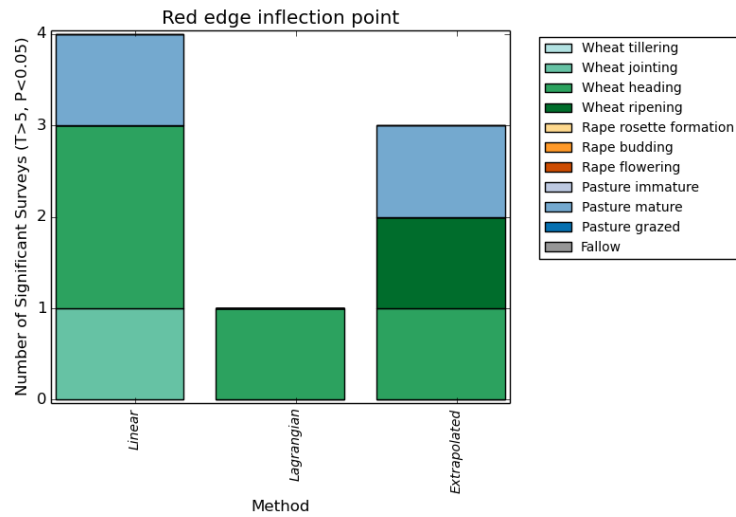


Figure 3.27: Performance of red-edge inflection point methods ranked by crop type and number of surveys where significant contrast was observed.

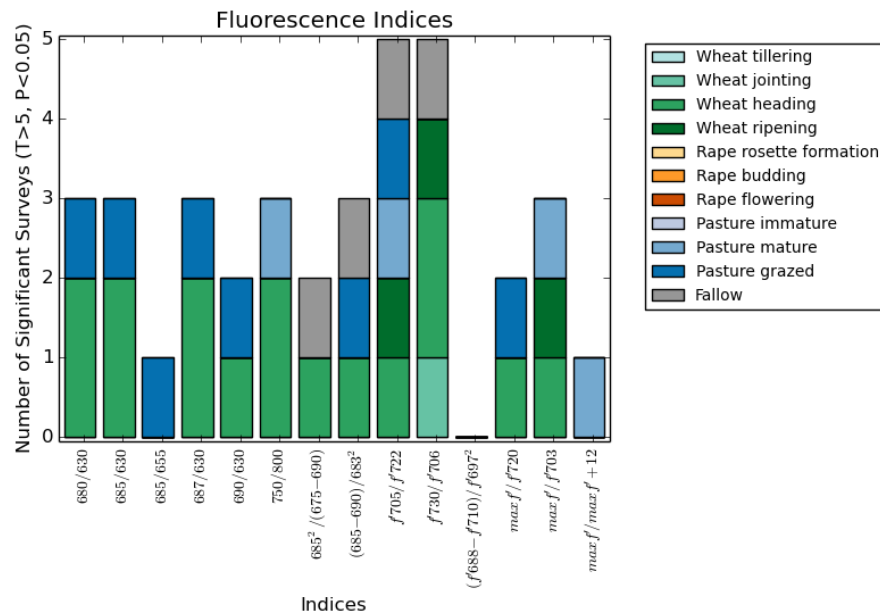


Figure 3.28: Performance of fluorescence indices ranked by crop type and number of surveys where significant contrast was observed.

using the maximum first derivative of reflectance are likely to instead identify fluorescence emissions (Zarco-Tejada et al. 2003, Smith et al. 2004, Cho & Skidmore 2006, Cho et al. 2007, Cho, Skidmore & Atzberger 2008).

The fluorescence indices perform well, with the $\frac{D_{730}}{D_{706}}$ and $\frac{D_{705}}{D_{722}}$ indices providing the most consistent contrast (figure 3.28), especially in during the later growth stages of cereal crops. Fluorescence is short-term response to a resource shortfall, and as such could be evident at times when little contrast is expressed in other ways. This is observable at DDCF during March 2012 and Harnhill Cherry Copse during February 2012.

3.6.5 Continuum Removal

Continuum removed reflectance for the 470nm (figure 3.29) and 670nm (figure 3.30) absorption features provided usable contrast under a wide variety of conditions. The 470nm feature proves most effective in senescent or chlorotic crops, as at Diddington Transect 1 on the 29th of June 2011, where it out performed other methods. This indicates the role of assistance pigments in stressed vegetation. In general where contrast is identified using the 670nm absorption feature using vegetation indices contrast is also recorded using the other methods such as the MTBVI and vegetation indices located in the same feature.

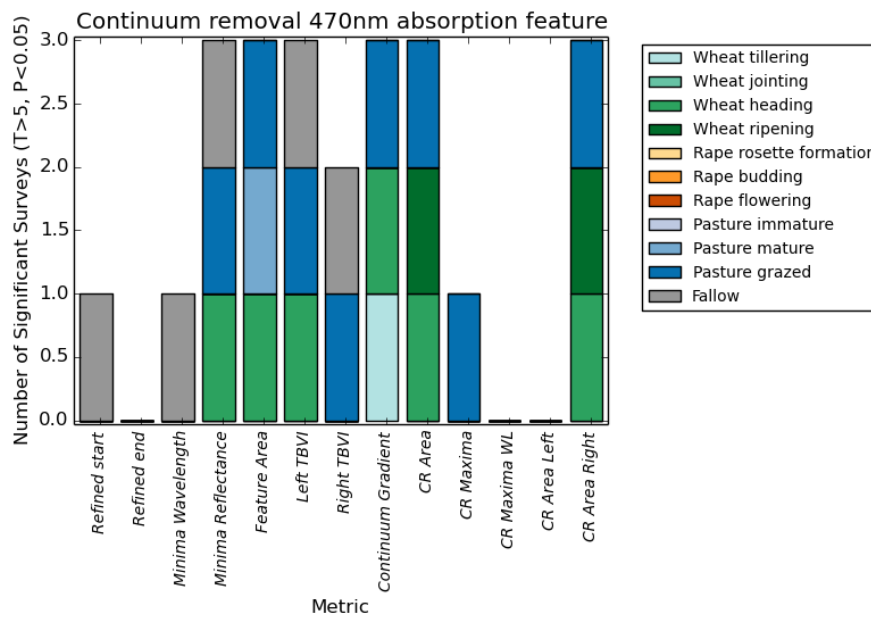


Figure 3.29: Performance of continuum removal for the 470nm absorption feature ranked by crop type and number of surveys where significant contrast was observed.

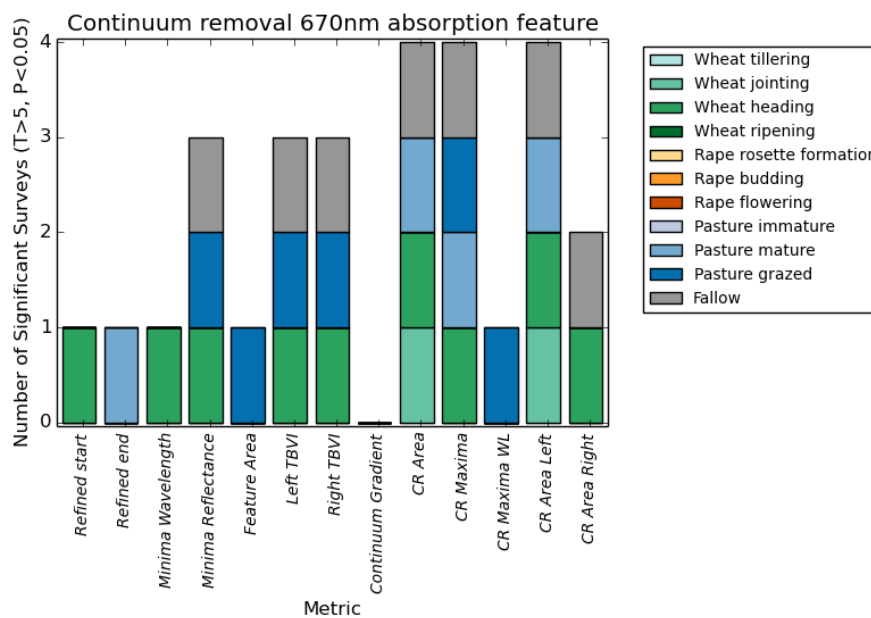


Figure 3.30: Performance of continuum removal for the 670nm absorption feature ranked by crop type and number of surveys where significant contrast was observed.

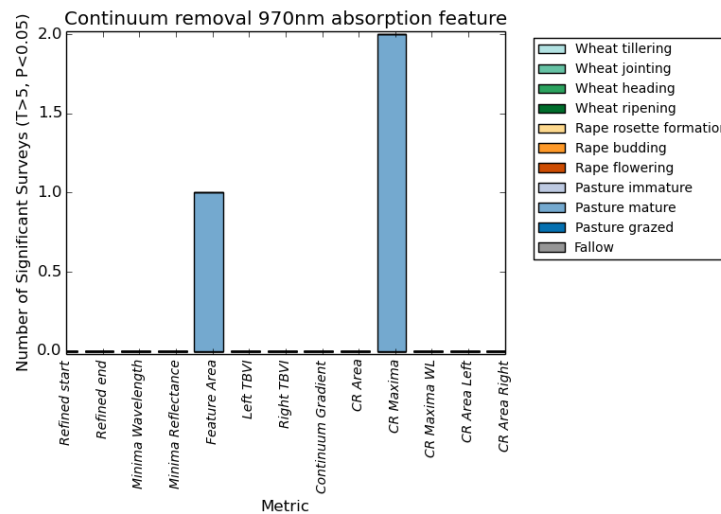


Figure 3.31: Performance of continuum removal for the 970nm absorption feature ranked by crop type and number of surveys where significant contrast was observed.

Continuum removal for the water absorption bands (figure 3.31 and 3.32) also provided statistically significant contrast under a wide variety of conditions. By using variable end-members the method is sensitive to the broadening of the feature, as well as the normalised depth of absorption. Often contrast is recorded in these features where little or no contrast is observed using other methods, for example at Harnhill Cherry Copse during December 2011 and February 2012. The 1200nm feature is, in general more effective than the 970nm feature.

3.7 Conclusions

3.7.1 The nature of archaeological vegetation marks

3.7.1.1 When are vegetation marks detectable?

While the data considered here is extensive, it is not enough to rigorously examine the conditions that cause cropmark formation with any statistical confidence. This is largely due to the differences between crops and seasons over the same features, meaning that comparison between different years and different sites is problematic. If further work of the same nature is undertaken in the future it is suggested that to mitigate this narrow strips of different crops are planted across the same linear feature on successive years. This will enable more exhaustive investigation of contrast under different land use conditions.

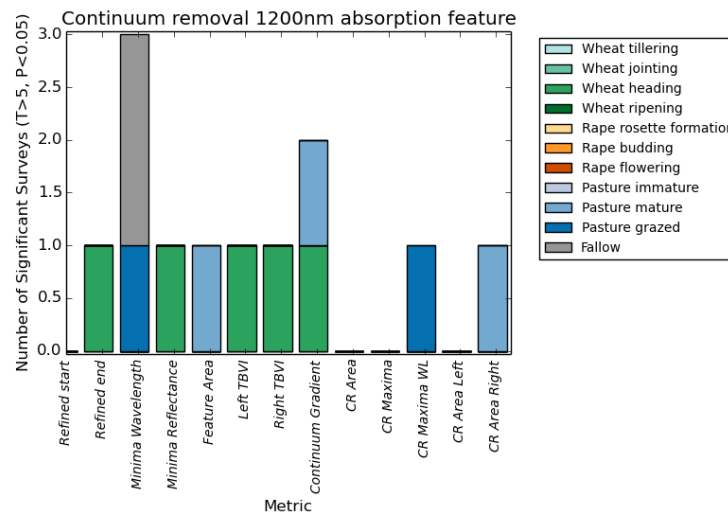


Figure 3.32: Performance of continuum removal for the 1200nm absorption feature ranked by crop type and number of surveys where significant contrast was observed.

Nonetheless, the results broadly confirm the existing understanding of when maximal contrast in vegetation marks develops. The strongest contrasts are observed in mature wheat crops on the free draining soils at Diddington during the drought of 2011. During the much wetter summer of 2012 little or no contrast is visible in the oilseed rape crop in the same area. Exceptions that confound this picture are observed at Harnhill Quarry Field, where despite the clay soil and wet weather, significant contrasts were observed. Additionally subtle contrasts were observable in the early growth stages of the oilseed rape crop at Diddington Transect 1 during February 2012 and in the grazed pasture at Harnhill Cherry Copse during March. These contrasts indicate that even early in the growing season the archaeological features influence the growth of the crop. This is to be most commonly expressed as increased biomass over the archaeological feature. It has been posited by Evans (2007) that this can be explained by differences in temperature resulting in early germination above the archaeological feature, but these contrasts were not observed until relatively late in the growth of winter crops. It may be that although this contrast is not visible above ground before this time the plants over the archaeology have a more developed root system, and are thus able to develop foliage more rapidly as solar irradiance increases (Passioura 1983). Diddington clay field during March 2012 presents the inverse of this situation, where there is a negative correlation between biomass and the archaeological feature. This may be explained by the higher clay content causing the seed to be enclosed in the drill slot, meaning the germination and early development of the seeds is retarded by a coating of compact wet clay (Evans 2007).

3.7.1.2 How are the vegetation marks expressed

As suggested by previous studies the strongest contrasts were observed in biomass. We have demonstrated that these contrasts are detectable in the early growth stages, and that these persist in mature crops into senescence, when contrast in the field spectroscopy is reduced. There are, however, many occasions where significant contrast is expressed in the spectral vegetation analyses but none is recorded in the physical properties of the crop. This is especially the case for the fluorescence indices and the MTBVI at wavelengths associated with fluorescence and the REIP. This is important, as fluorescence in particular indicates a short term response to a shortfall in resources, rather than the longer term adaptation to environmental constraints indicated by biomass and pigment content. The relationship between fluorescence and the archaeology is complex, as it demonstrates both a positive and negative correlation with the archaeological features. This would appear counter-intuitive, as we would expect the vegetation over the archaeological features to be generally less stressed than that over the background and thus demonstrate a negative correlation. Where there is a positive correlation between the features and fluorescence there is also an increase in biomass over the archaeological feature. This is likely a result of the greater quantity of vegetation, causing greater competition for resources. This effect can be observed in the data from Diddington T1 on the 14th of June 2011 and at Harnhill Quarry Field in June 2012.

3.7.2 Implications for airborne survey

The most performant methods for the detection of archaeological contrast were physical measurement of biomass, chlorophyll fluorescence and the MTBVI using near adjacent bands. In addition contrast in the early growth stages. The following chapters will evaluate how these methods can be applied to the airborne data. In chapter 4 measurement of crop biomass will be performed by introducing a novel method using multi temporal airborne laser scanning to estimate the height of the vegetation.

Chapters 5 and 6 will examine the use of visible wavelength aerial photography and airborne imaging spectroscopy respectively. These sensors represent the extremes of spatial and spectral resolution. The aerial photography represents very high spatial, but very low spectral resolution, whereas the ALS data provides greatest spectral resolution available in imaging sensors in this study at the expense of spatial resolution. The low, broadband spectral resolution of the RGB sensors implies lower contrast, as they omit the NIR wavelengths that provide. However, the relationship between reflectance in the red and green

bands of the RGB images should provide an indication of biomass, especially if contrast can be improved using RGB indices.

While the AIS data provide much higher spectral resolution compared to the aerial photography it may not be possible to replicate the results investigated here. The most consistently performant methods were fluorescence indices and the MTBVI using nearly adjacent wavelengths. This may not be applicable to the airborne data, which has lower spectral resolution than the field spectrometer. In addition the best spatial resolution attainable by the sensor is nominally 1m, close to the breadth of the features. This may reduce contrast compared to the ground-based data. This is compounded by the distance between the sensor and the ground, creating greater possibility for atmospheric interference (Jackson et al. 1983, Myneni & Asrar 1994).

Chapter 4

Airborne laser scanning

4.1 Introduction

In the previous chapter we demonstrated that variations in biomass, measured there using percent coverage, vegetation height and Leaf Area Index (LAI) provide the strongest contrast between the crop over the features and the background. This chapter explores how Airborne Laser Scanning (ALS) can be used for the for the detection of archaeological vegetation marks using these variations. While ALS is widely used for the detection and analysis of archaeological features defined by topographical variations it has not been widely used for cropmark detection. This chapter presents novel methods for using full waveform and discrete multi-temporal ALS data to map and characterise biomass variations related to archaeological vegetation marks. The multi-temporal approach uses two ALS derived surface models, one acquired between harvest and sowing, when there is no crop, and subtracting this from one acquired during the summer from a mature crop. This provides an estimate of height and density of the crop (Stott et al. 2015). The full waveform approaches examine the width and intensity of the returned pulse to estimate biomass in the crop. The results demonstrate that these approaches, in particular the multi-temporal crop surface model can provide significant and useful contrast for the identification of archaeological features, with a number of advantages over traditional passive methods for the detection of archaeological contrast. First, ALS measures the physical properties of the crop, and are thus not dependant on spectral contrast. Second,

because the method is active rather than passive it does not depend on external illumination conditions, which means that cloud cover and solar zenith angle are not critical for flight timing.

4.2 Background

4.2.1 What is airborne laser scanning?

4.2.1.1 Operating principles of the sensor

ALS uses lidar sensors to rapidly record large numbers of points. The sensor uses a light emitted by a pulse modulated laser to measure the time of flight to, and intensity of reflection from objects on the Earth's surface. Because the laser is modulated it is possible to differentiate between different pulses, making it possible to record multiple returns or reflections from the same pulse, enabling the measurement of the height of the canopy, under-storey vegetation and ground surface in a forest. Laser scanners use a rotating angled mirror to modify the angle of the laser as it leaves the scanner, thus enabling it to emit many pulses over a wide field of view. The angle of this mirror is encoded with each pulse, so that if the position and orientation of the scanner are known the time of flight for each return can be used to establish location of the pulse's interactions with the earth's surface. The position and orientation on airborne platforms are generally established using RTK GNSS (Real-Time Kinematic Global Navigation Satellite Systems) in conjunction with IMU (Inertial Measurement Unit) systems. The returning pulse is then encoded as a digital value by an ADC (Analogue Digital Converter) and recorded on digital storage media. In discrete lidar systems the returning pulse is recorded as a number of separate returns (Baltsavias 1999, Wehr & Lohr 1999, Vosselman & Maas 2010). In recent years advances in the speed and bandwidth of both the ADC and the storage media have facilitated the development of FW (Full-Waveform) laser scanners. These record the intensity of the returning pulse as a continuous waveform, enabling the recovery of more detailed and nuanced information than discrete systems (Persson et al. 2005, Wagner et al. 2008, Mallet & Bretar 2009a).

4.2.1.2 Spectral properties

With the exception of specialised sensors such as bathymetric (Wozencraft & Millar 2005) and multi-spectral lidar (Wallace et al. 2014), most laser scanners use light in the near-infrared region of the spectrum. Photo-detectors in this range are relatively inexpensive,

and the lasers can be of higher output power while remaining eye-safe than visible wavelengths.

4.2.1.3 Full waveform ALS

Full waveform scanners record intensity of the returning pulse over time. It is well established that via advanced processing methods such as signal decomposition or modelling (Höfle et al. 2012). FWF ALS data offers increased pulse detection reliability, accuracy and resolution and therefore improve the accuracy of topographic models. Furthermore, these data have been shown to provide additional information about the structure and physical backscattering properties of the objects they interact with (Mallet & Bretar 2009b). In particular, significant information on the roughness, slope and reflectivity of surface materials may be retrieved from full waveform data using both the range and intensity data. Differences in the properties of isolated returns, such as width, amplitude and cross-section, and their number have been illustrated for vegetation and ploughed fields versus roads or meadow areas and between grass and bare earth or between different roof materials, for example (Wagner et al. 2004). Common application of these data have been in forest studies, both at the level of the stand and the individual tree, for the estimation and modelling of forest properties (Dubayah et al. 2000) and tree species mapping (Heinzel & Koch 2011). However, it is commonly assumed that for studies other than that of forests, such as arable crops FWF ALS cannot be expected to enhance the information content already provided by the discrete return ALS data (Buddenbaum et al. 2013).

4.2.2 Lidar for sensing crop properties

ALS is used extensively for the detection of vegetation properties in forestry and habitat management. It is less widely utilised for the analysis of arable crops, partially due to the limited ability of the sensors to be able to resolve relatively subtle differences in the short crop (Cui et al. 2010). Thus applications of the technology for sensing crop properties in precision agriculture use Terrestrial Laser Scanning (TLS) at oblique angles to measure the properties of the crop.

4.2.2.1 Terrestrial lidar

These systems are often vehicle mounted, and use Gaussian decomposition to establish points which are part of the ground surface and those which are part of the crop canopy as the vehicle moves over the crop, as the inexpensive scanners used do not provide multiple returns. The height of the crop is then triangulated from these points (Ehlert et al. 2009).

Sources of error include obfuscation of the returning pulse by other plants, and over estimation of the crop height due to its geometry (Ehlert & Heisig 2013). Using active sensors in this manner presents a number of advantages for the evaluation of fruiting and ripening cereal crops over passive reflectance sensors, as the strong correlation between NDVI and other indices and biomass in a green crop becomes less robust in a senescent crop optical techniques (Long & McCallum 2013). The applications of these systems include weed detection (Andjar et al. 2013), biomass estimation in cereal and crops (Ehlert et al. 2008, Hosoi & Omasa 2009), and as a means of controlling feed rate on combine harvesters by estimating yield for both grain and straw during harvest (Saeys et al. 2009, Long & McCallum 2013).

The efficacy of these systems is improved by using intensity measurements in conjunction with structural parameters. Eitel et al. (2014) used terrestrial laser scanning to successfully evaluate both wheat nitrogen status and crop dry mass using a sensor with a wavelength centred on 532nm. Using sensors of this wavelength also enable more accurate biomass estimation, as separating returns from the green crop and the soil can be achieved using a simple threshold (Eitel et al. 2011). These methods allow a fine-grained characterisation of vegetation stress and vigour using TLS. Multi-wavelength systems offer the potential to improve this by enabling the derivation of vegetation indices indicative of crop biophysical characteristics.

In addition to using the intensity values of the returned pulse to characterise the reflectance of the crop canopy the light emitted by the sensor can also be used to induce fluorescence. Light absorbed by the plant as part of the photosynthetic process is re-emitted at different wavelengths. This is explored in detail in chapter 9. lidar systems designed to exploit this use a single excitation wavelength (usually 400nm or 532nm) and a spectrometer to record the intensity of light emitted across multiple wavelengths (Saito et al. 1998). This enables the accurate estimation of both chlorophyll content and the metabolic state of the plant using the $\frac{F_v}{F_m}$ ratio (Gitelson et al. 1999). Although imaging fluorescence sensors exist they are generally designed to measure small areas with a limited IFOV rather than wide areas of crop canopy, however, developments in sensor technology mean that measurement of fluorescence using TLS at this scale should become viable in the near future (Magney et al. 2014).

4.2.2.2 Airborne lidar

Scale is the chief difficulty in using airborne LiDAR sensors for the sensing of properties of arable crops using airborne sensors, as the crop is not high enough for the sensor to resolve both the ground surface and the canopy. Cui et al. (2010) successfully estimated both LAI and vegetation height using topographic returns from airborne lidar by estimating crop height using the minimum and maximum returns in each cell of a 10x10m grid over test plots of corn. The likelihood of individual minimal pulses in each cell being from the ground surface is high. However, the large size of each cell means that ground height is easily distorted by local changes in topography. In addition, although suitable for the monitoring of agricultural crops on a field level this approach is problematic when applied to looking for localised differences of a scale related to archaeological features.

4.2.3 ALS in archaeological prospection

ALS is widely used in archaeology for the detection of archaeological features (Crutchley & Crow 2010, Crutchley 2013, Opitz & Cowley 2013). Currently, the emphasis of this work has been on visualising the data in a way that enable an interpreter to confidently identify these features as changes in topographic relief, and offers a number of distinct advantages over passive airborne imagers, where detecting these features requires the images be acquired during low-solar zenith angle conditions so that the highlights and shadows provide definition, meaning that the result is highly dependant on the illumination conditions. In addition, the ability of lidar sensors to penetrate vegetation canopies means that forested areas can be investigated, where previously it was difficult or impossible to detect features using conventional imaging surveys.

ALS is less widely utilised as a means for detecting vegetation marks or other forms of proxy measurement in areas where protracted arable cultivation has resulted in very little remaining topographic definition of the features. However, the potential of using intensity measurements from both conventional and multi-spectral systems has been investigated. This has lead to the widespread adoption of ALS survey methodologies over the last decade by both researchers and curatorial bodies across Europe.

4.2.3.1 Topographic archaeological ALS techniques

Detecting features in topographic ALS data depends on emphasising relatively subtle changes in topography that are difficult to perceive in a stretched DSM (Digital Surface Model). Simple approaches to this problem use hill-shading algorithms to model

the shadows cast by a simulated light source at different angles and elevations (Crutchley & Crow 2010). However, if the feature and the light source are close to parallel orientation the features will not be detectable, meaning that to be used effectively a number of different light source orientations must be considered. Analytical hill-shading uses a combination of hill-shaded DSMs weighted by the aspect of the slope. However, these methods can still lead to features being obscured by larger topographic variations in the landscape (Štular et al. 2012, Zakšek et al. 2011).

Local Relief Modelling (LRM) or Residual Relief (RR) separation seeks to resolve this by removing the general trend of the topography from the DSM, emphasising features below a certain size (Doneus & Briese 2006, Hesse 2010, Hiller & Smith 2008). To achieve this the DSM is smoothed using a low-pass or median filter, which is subtracted from the original DSM. The size of the features in relation to the initial low-pass filter is critical, as if too large or small a filter is selected the features will be obscured. Doneus & Briese (2006) applied residual relief separation to improve detection of features in a forested environment by re-sampling the DSM to a lower spatial resolution as opposed to smoothing it. They note that doing this can result in the creation of spurious features, as the generalisation of the down-sampled model create changes in elevation around the edges of substantial features. Hesse (2010) has used the LRM technique successfully in the heavily forested landscapes of Baden-Württemberg in Germany to detect thousands of potential archaeological sites that would not otherwise have been identifiable. Hesse's approach uses an additional step, where contours are derived from the residual relief model. The values in the DSM at the vertices of the 0m contours are then used to derive a new DSM with the small scale features removed, which is then subtracted from the original DSM. This produces a model less influenced by larger features at the expense of contextual information. In addition, the derivation of the and interpolation of the contour-derived DSM is problematic in areas where there a high frequency of variation, for example, in a crop canopy. Humme et al. (2006) used residual relief to detect Celtic field systems in the Netherlands using Factorial Kriging to separate and filter components of different scale. This approach is more sophisticated than using low-pass or median filters, but is significantly more computationally intensive.

Sky-view factor seeks to quantify how much of the sky as a notional hemisphere is visible at each pixel of the DSM. Changes in relief constrain this, so features defined by topographic changes are thus detectable (Zakšek et al. 2011, Kidd & Chapman 2012, Kokalj et al. 2012). These techniques have been successfully and extensively applied

in Slovenia to detect archaeological activity in complex multi-period landscapes (Štular et al. 2012, Kokalj et al. 2011, 2012).

4.2.3.2 Archaeological soil and vegetation mark detection using ALS

Intensity values are less widely used for the detection of archaeological features than topographic measurements. Challis et al. (2011*b*), Challis & Howard (2013) examined the potential of using intensity data to assess the preservation potential of geo-archaeological features, and attempted to correlate soil moisture, organic content and earth resistance measurements with LiDAR intensity measurements. The surface vegetation made the correlation between the soil properties difficult. In addition, intensity measurements were also used to identify vegetation marks that associated with known archaeological features. For the latter it was found that the features were expressed as a change in intensity, but were not differentiated in terms of elevation values (Challis et al. 2011*a*, Challis & Howard 2013). The performance of the intensity measurements did not compare favourably to conventional aerial photography, however, the LiDAR surveys may not have been acquired under ideal conditions for contrast in the crop canopy (Brown et al. 2007, Carey et al. 2006). Briese, Doneus & Verhoeven (2013) use calibrated intensity measurements derived from full-waveform to record substantial archaeological vegetation marks related to the Roman city of Carnuntum in Austria. At the same site Briese, Pfennigbuar, Ullrich & Doneus (2013) found that using a multi-spectral lidar instrument recording calibrated reflectance at 532nm, 1064nm and 1550nm provided better results, with the data recorded at 1550nm being best able to identify the the cropmarks as it is highly sensitive to variations in leaf water content.

Despite the ability of full-waveform sensors to provide more nuanced intensity measurements there has been relatively little investigation of their capability for detecting vegetation marks outside of the work at Carnuntum. Applications of the technology have instead mostly focussed on providing cleaner DTMs in forested areas, as the sensor provides a greater ability to discriminate between understory vegetation and the ground surface. Examples of this work are Doneus & Briese (2006) and Lasaponara et al. (2011). This has limited applications in defining vegetation marks in arable areas, as in cereal crops the distance between the crop canopy and the ground is so short compared to the ability of the sensor to resolve it (Cui et al. 2010).

Stott et al. (2013) evaluated using both multi-temporal vegetation height and the width and magnitude of the full waveforms for a small subset of the data considered here. This indicated that width of the returned pulse was usable to detect archaeological features, but did not perform as well as either hyper-spectral derived NDVI or crop height. This work (Stott et al. 2015) also demonstrated the utility of the multi-temporal crop surface model, which was shown to provide more contrast than both the aerial photographs and the full-waveform ALS data. This approach was adapted by Verhoeven & Vermeulen (2016) to digital surface models derived from photogrammetric modelling of aerial photographs. The authors used a wide range of archival imagery to produce an optimised canopy surface model, and used residual relief modelling to enhance the local contrast of the archaeological features. These methods have also been employed in precision agriculture (Bendig et al. 2014)

4.3 Methodology

4.3.1 Data Collection

ALS data was collected for the DART project by NERC ARSF in conjunction with high-resolution ortho-photography and Eagle and Hawk hyperspectral. Table 4.1 summarises when these data were collected.

Flight	Provider	Sensor	Hits p/M	Full-waveform?
14/06/2011*	NERC ARSF	Leica ALS50	12	No
23/03/2012	NERC ARSF	Leica ALS50	12	Yes
20/06/2012	NERC ARSF	Leica ALS50	12	Yes

Table 4.1: Table summarising RGB imagery used in this study. (* Note: 2011/06/14 Diddington only).

The data were collected at 100m altitude, which means the footprint of each pulse on the ground's surface is approximately 0.22m. The data were supplied in the LAS 1.3 format and were filtered of spurious returns and converted to ASCII using the LAS-Tools software package. The discrete data were then interpolated to a 0.4m grid using the GDAL software library to produce a DSM for each image using inverse distance weighted interpolation.

The ALS data were collected over the DART project study sites at Diddington, in the South-East of England and at Harnhill, in the South-West. Both areas encompass free-draining and heavy clay soils, but the westernmost sites experience significantly more rainfall. At Diddington, fields T1 and T2 the soils are free-draining alluvial gravels, and the Clay Field is boulder clay. At Harnhill, Cherry Copse is located on free draining fragmented limestone. Quarry Field contains a significant depth of clay. Table 4.2 outlines the state of these fields when the ALS data was collected.

Site	Date	Crop	Condition	PSMD	Biomass contrast (T,P)
Diddington T1	2011/06/14	Winter wheat	Flowering	57mm	$T26.21$ $P < 0.05$
Diddington T1	2012/03/23	Oilseed rape	Stem elongation	-9mm	$T - 2.8$ $P > 0.05$
Diddington T1	2012/06/20	Oilseed rape	Fruiting	-10mm	<i>Not measured</i>
Diddington Clay Field	2011/06/14	Oilseed rape	Fruiting	57mm	<i>Not measured</i>
Diddington Clay Field	2012/03/23	Winter wheat	Tillers formed	-7mm	$T - 7.3$ $P < 0.05$
Diddington Clay Field	2012/06/20	Winter wheat	Flowering	-6.7mm	$T - 1.65$ $P > 0.05$
Harnhill Quarry Field	2012/03/23	Bare Soil	Drilled	-0.5mm	<i>No crop</i>
Harnhill Quarry Field	2012/06/20	Spring Wheat	Flowering	0mm	$T3.2$ $P < 0.05$
Harnhill Cherry Copse	2012/03/23	Pasture	Mature meadow	-0.5mm	$T0.2$ $P > 0.5$
Harnhill Cherry Copse	2012/06/20	Pasture	Heavily grazed	-3.3mm	$T6.4$ $P < 0.05$

Table 4.2: State of study sites during data acquisition.

Archaeological features were identified using fluxgate gradiometer magnetometer survey, using either a Bartington Grad 601-2 or a Geoscan FM256. Data were collected in 30m

grids located using RTK GNSS with 1m traverses and a reading every 0.125m along the traverse. These were then digitised as vector polygon features. These polygons were then used to classify pixels in the DEM, using the rasterize function of GDAL to create a mask used to overlay the interpolated DSMs. These masks were used to extract subsets of the point cloud for analysis.

4.3.2 Analysis rationale

In chapter 3 it was demonstrated that archaeological vegetation marks are strongly correlated with changes in both biomass, measured using both the average height of the crop canopy and LAI (Leaf area Index), particularly at DDT1 during 2011 and HHQF during 2012. It should thus be possible to detect the vegetation marks using the topographic returns from the ALS data, as the physical structure of the crop canopy will be detected as topographic variations.

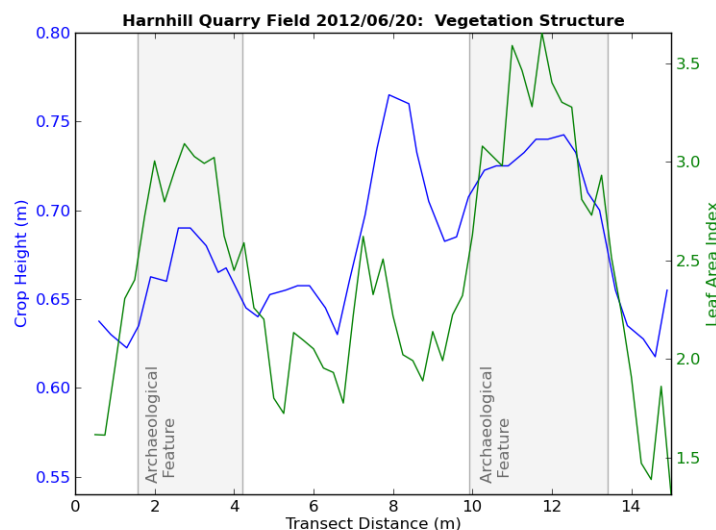


Figure 4.1: Leaf area index and vegetation height (measured to tip of flag leaf) in a mature wheat crop. Harnhill Quarry Field , June 20th, 2012.

Figure 4.1 demonstrates that the LAI over the archaeological features, measured using an Accupar LP-80 canopy ceptometer is significant in comparison to the height of the vegetation. Increased LAI should mean that any given pulse from the sensor has a greater probability of being intercepted before it reaches the ground surface, as the vegetation is more dense.

4.3.3 Full-waveform analysis

The full waveforms were extracted and analysed using Python software written for the purpose to extract the relevant portions of the waveform. For ecological applications where there are many peaks in the return from the canopy, understory and ground the most common approach is to use Gaussian fitting techniques to identify the peaks (Persson et al. 2005, Wagner et al. 2007, Doneus et al. 2008, Mallet & Bretar 2009b, Lin et al. 2010). This approach provided poor results and proved needlessly complex for the low arable crops considered here. There is generally only a single peak in these data, and the width of the base of the peak is more more important than the overall number and relative lateral position of the peaks.

The approach adopted here smoothed the raw waveforms using a univariate spline to remove minor high-frequency noise. The single peaks in the in the waveform were identified by applying a threshold at slightly above and below zero in the first derivative of the smoothed waveform. From this the sum of intensity within the peak, the maximum intensity of the peak and the overall width of the peak were extracted. The overall area and width of the peak should be capable of resolving differences in biomass, as attenuation of the signal by increased biomass should diffuse and attenuate the return. In previous studies this has been evaluated using the FWHM of the peak (Mallet & Bretar 2009b), but examination of the data from this study showed that most variation occurred below the FWHM (figure 4.3.3). Thus, the basal width of the peak was used. The resultant measurements were then interpolated using an inverse distance weighted method to raster images with a 0.4m spatial resolution using the GDAL software library.

4.3.4 Multi-temporal crop biomass modelling

Subtracting the height of the ground surface from the crop canopy could be used to produce a model of the density of the crop canopy. The low cereal crops are characterised as a single return in the discrete ALS surveys. Thus it is not possible to separate the crop canopy and the ground surface. To enable this, rather than using discrete data from a single survey, the data acquired over bare soil or low crop in March was subtracted from that acquired in June over a mature crop canopy (equation 4.1):

$$CSM = DSM - DTM \quad (4.1)$$

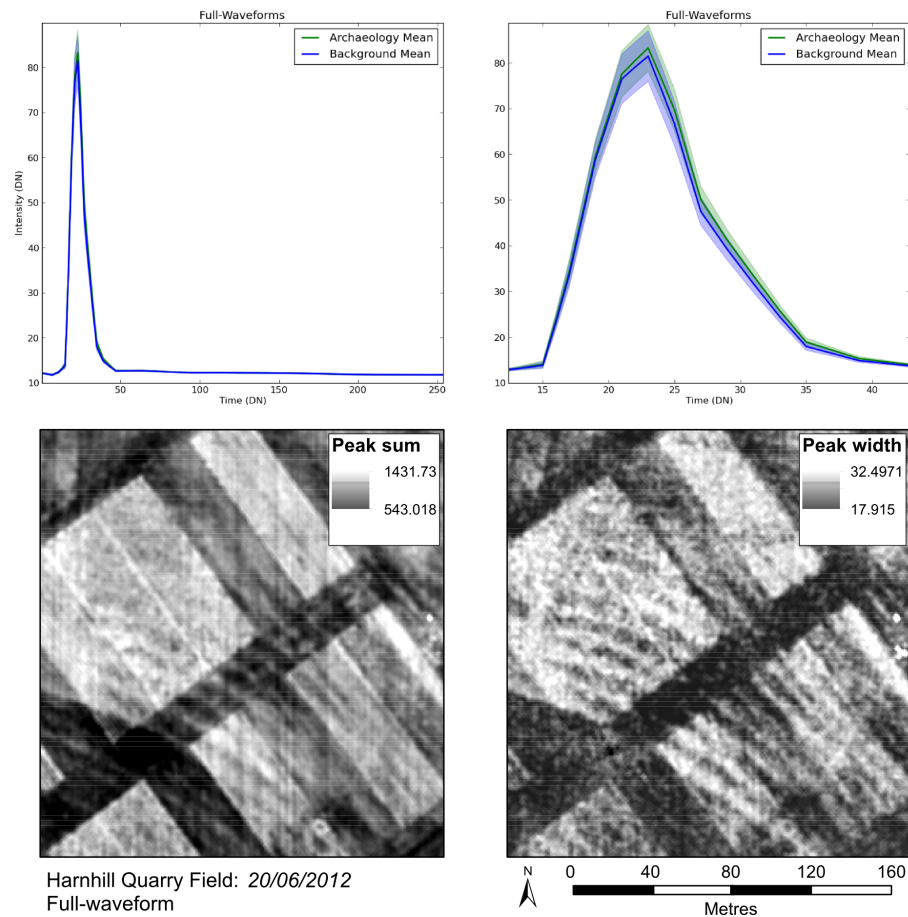


Figure 4.2: Mean full waveforms shown alongside interpolated rasters, Harnhill Quarry Field, June 20th, 2012. *Top left* shows the entire waveform, demonstrating that only a single peak is recorded over a mature cereal crop. *Top right* shows this peak in detail, demonstrating that there is a slightly shallower gradient and wider peak over the archaeology than the background. *Bottom left and right* show the sum of the peak intensities and peak width respectively. Medieval ridge and furrow cultivation is clearly visible.

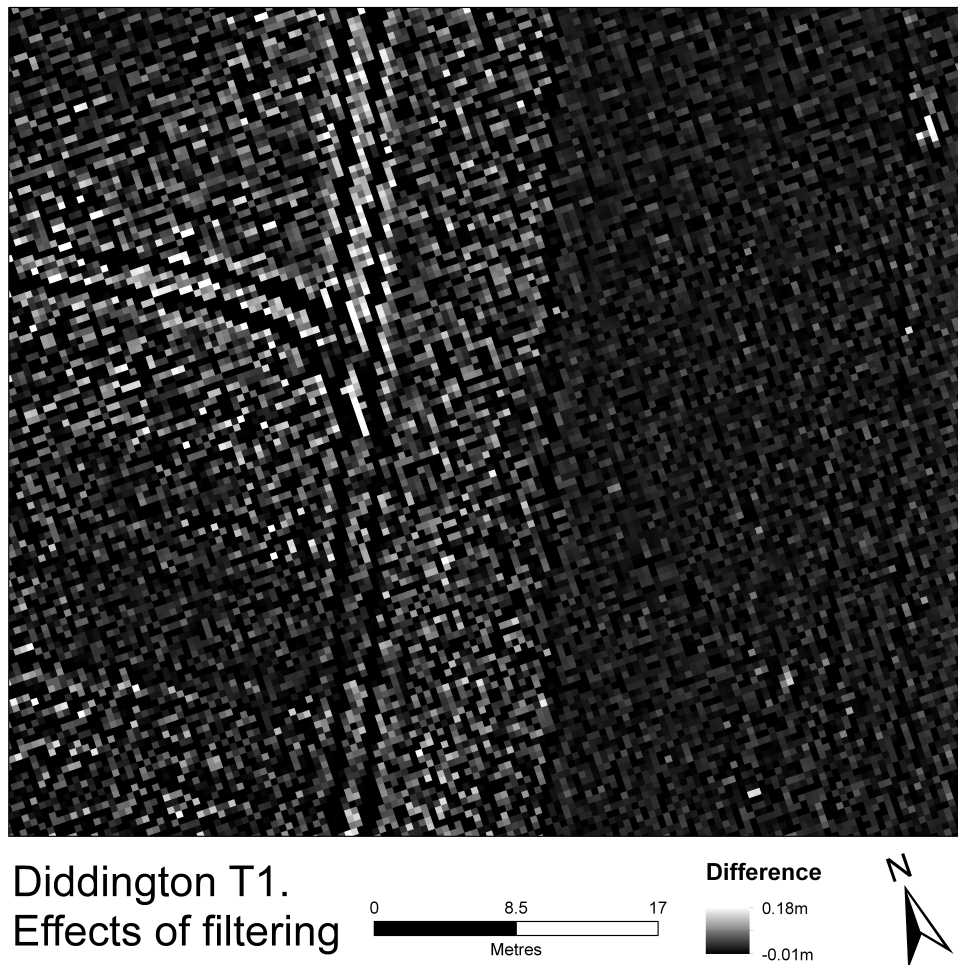


Figure 4.3: Effects of filtering on bare soil DTM, showing difference between filtered and unfiltered DTM. on *Left*: immature oilseed rape crop 10-15cm tall *Right*: Harrowed and drilled bare soil.

Where *DSM* is the digital surface model recorded over the crop and *DTM* is the digital terrain model acquired over bare soil. To achieve this the points were interpolated to the same grid using GDAL. The crop DSM was filtered using a median filter with a 3x3 kernel size to filter noise and small scale variations in the crop canopy. The 'bare soil' model was filtered using a uniform low-pass filter with an 11x11 kernel size. This was chosen to smooth out variations in the cultivated surface caused by tillage and the texture of the immature crop, that can produce spurious anomalies in the resultant model (figure 4.3).

4.3.4.1 Residual relief contrast enhancement

An residual relief model was derived for each of the datasets and the multi-temporal crop height models to investigate whether contrast in the crop canopy is improved using

this technique. In theory, the vegetation marks correspond to the positive and negative elevation changes this technique emphasises, regardless of whether these relate to changes in topography or changes in vegetation height. This was performed using Python to both the multi-temporal DSM and the individual DSMs. Rather than the uniform low-pass filter used by Hesse (2010), where the size of the filter in relation to the features is critical, or the scale invariant Kriging used by Humme et al. (2006), which uses a complex and computationally intensive method that requires *a priori* knowledge about the scale of the features, two Gaussian filters were used (equation 4.2), the first, *Surface* to remove small variations and noise from the DSM, the second, *Trend* to remove features approximating the scale of those we're interested in:

$$RR = \left(S(x, y) = A^e \left(-\frac{(x-x_0)^2 + (y-y_0)^2}{2\sigma^2} \right) \right) - \left(T(x, y) = A^e \left(-\frac{(x-x_0)^2 + (y-y_0)^2}{2\sigma^2} \right) \right) \quad (4.2)$$

Where A^e is the amplitude, x_0 and y_0 are the centre and σ is the x and y spread of the function. By varying the σ parameter to change the extent to which the DSMs are smoothed can be varied (Shapiro & Stockman n.d.). For the *S* or *Surface* DSM a σ value of 1 was used, for the *T* or *Trend* DSM a value of 10 was used. The advantage of this method is that due to the weighting of the kernel using the Gaussian distribution, coherent features smaller than the spread of the function are preserved, meaning that the *Surface* DSM is less prone to over-smoothing than when using a uniform low-pass or median filter (Babaud et al. 1986, Kokalj et al. 2012).

4.3.4.2 Analysis of contrast

The returns over the archaeological features were compared to those of the background using a Welch's T-test (Welch 1947, Zimmerman & Zumbo 1993). Evaluating contrast across the whole image gave poor results, largely due to the variability in the background caused by differences in the soil and cultivation practices. To avoid this the test was applied to a localised area of each dataset. Each pixel in the raster classified as archaeology was used as the centre of a 3.3x3.3m kernel forming the subset of values for each T-test (Dietterich 1998). The resultant T and P values were then plotted as geo-referenced rasters to show the spatial variability of the contrast in each dataset. The T values demonstrate the overall strength of the contrast, whereas the P values indicate the statistical significance of the contrast. P values below the 95% confidence level indicate .

4.4 Results

4.4.1 Summary

The results from the analysis of the ALS data demonstrate that these techniques can be used to identify significant contrast in crop biomass for proxy detection of archaeological vegetation marks. The multi-temporal methods provided the best over-all results, but the residual relief methods also indicate that detection of contrast in biomass is possible without the need for a bare-soil model. The results of the full waveform analyses from Harnhill Quarry Field during June 2012 also provided significant contrast, especially using the peak width method. In general the ALS results reflected the groundbased measurements, in that sites that exhibited significant contrast in biomass also did in the groundbased data. However, the strong contrasts detected in vegetation coverage at Diddington Clay Field during March 2012 were not detectable, likely as a result of the immature vegetation being smaller than the sensor can resolve. In addition, the results from Harnhill Quarry Field from June 2012 showed greater contrast in the ALS data than indicated by the groundbased survey.

4.4.2 Full-waveform

The full waveform data was only available for the surveys in 2012. The only significant results were from Harnhill Quarry Field in June, where both the peak sum and peak width measures show statistically significant variations between the archaeology and the background. The results from Diddington Clay Field during this period also indicate a significant contrast, but these are likely erroneous, and are probably the result of the archaeological features and the patterns of cultivation in the field being closely aligned. The results from Harnhill Cherry Copse in June 2012 show little contrast, despite a significant variation in biomass being recorded in the ground-based survey. This may be explained by the very dense vegetation (mean LAI $5.1 \text{ m}^2 \text{ m}^{-2}$), meaning it may have been impossible for the emitted pulse to travel through the crop canopy.

4.4.3 Crop Surface Model

The crop surface model proved successful means of detecting biomass variations. Again, this was most successful in Harnhill Quarry field during June 2012, where the medieval ridge and furrow field systems and ditch are clearly visible. The data from the ground based survey from June 2011 showed significant contrast in vegetation height (figure

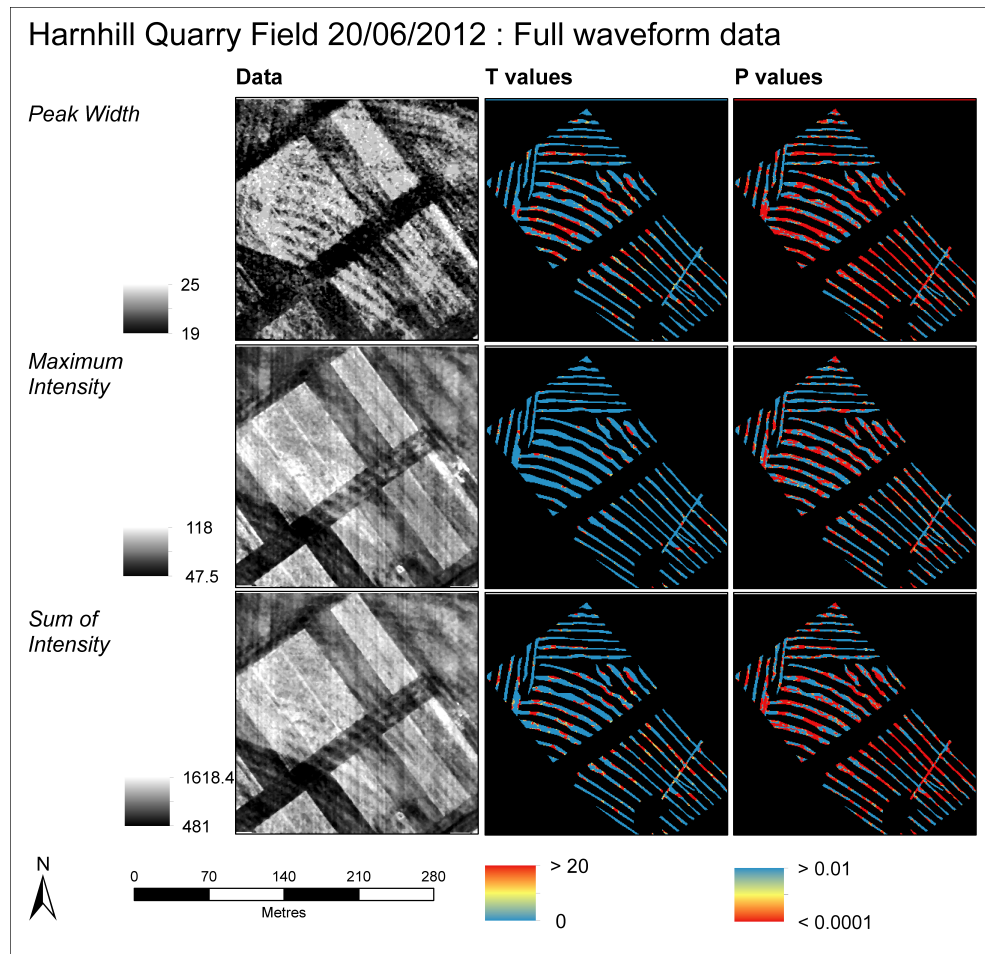


Figure 4.4: Full waveform results from HHQF, June 2012, showing a grayscale plot of each measure (*left column*), strength of the contrast (*middle column*) and the statistical significance of the contrast (*right column*).

3.11, page 81). This is reflected in the results from the crop surface model, where the features are clearly visible. However, the image lacks the definition observed in the aerial photograph (figure 4.6). This is potentially the result of the bare surface model being acquired over the low oilseed rape crop, causing variations in the height of the surface that are not related to the ground surface despite the initial filtering of the DSM.

The feature in Cherry Copse showed significant contrast in biomass and vegetation height, but the full waveform results failed to resolve much contrast over the ditch. The CSM results (figure 4.7) show that over parts of the ditch contrast is much improved. Examination of the grayscale image shows that although parts of the ditch do not exhibit much contrast the larger linear features running SW-NE outside the area of interest are clearly visible. These are the result of rearing outdoor pigs in 2007, and define part of a radial system of pens.

4.4.4 Residual relief

The residual relief model was applied to both the original DSM and the CSM. This largely agreed with the results of the other surveys, so only the results from HHQF June 2012 are presented here as an example. The results from the DSM (figure 4.8) show that the variations in the height of the crop can be discerned, that the contrast possesses a high level of statistical significance.

The results from the residual relief model applied to the CSM (figure 4.9) are not significantly different those derived from the DSM. However, the contrast in the CSM itself is clearer. This indicates that the residual relief model is an appropriate technique for resolving contrast in a DSM when no DTM is available to derive a CSM.

4.5 Discussion and further work

The most best performing technique was the CSM. This method can distinguish subtle contrasts in LAI and vegetation height, as demonstrated in the results from HHQF. While this model is effective, it requires the extra expense of acquiring the 'bare earth' DSM. This should be optimally acquired under minimal vegetation coverage, as demonstrated by the difference in the acuity between the results from Harnhill Quarry Field in June 2012 and Didditngton T1 in June 2011. The former was acquired from bare, harrowed and drilled soil, whereas the latter was acquired from a young oilseed rape crop. This

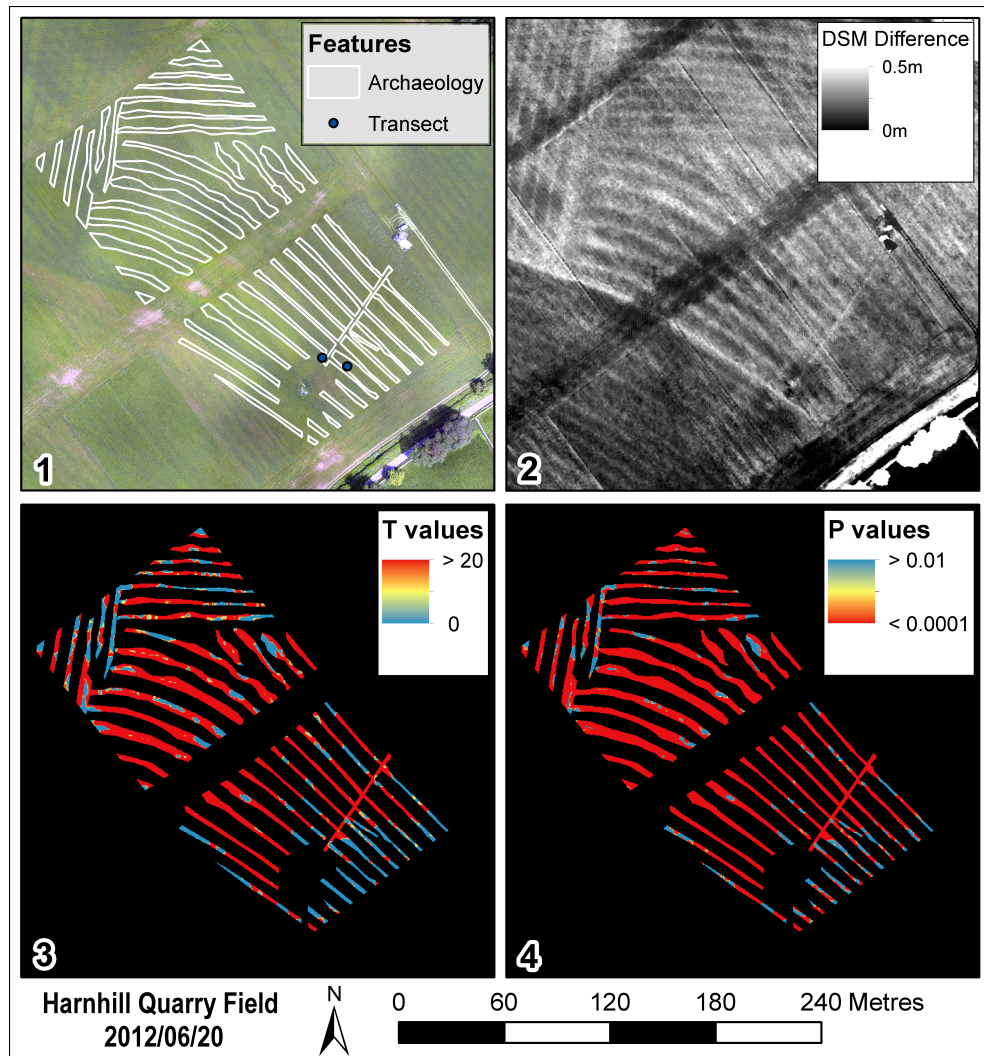


Figure 4.5: CSM results from HHQF, June 2012. The *top left* image shows the features against the background of the co-collected ortho photography. The *top right* image shows a gray-scale plot of the CSM, *bottom left* shows the strength of the contrast and *bottom right* the statistical significance of the contrast.

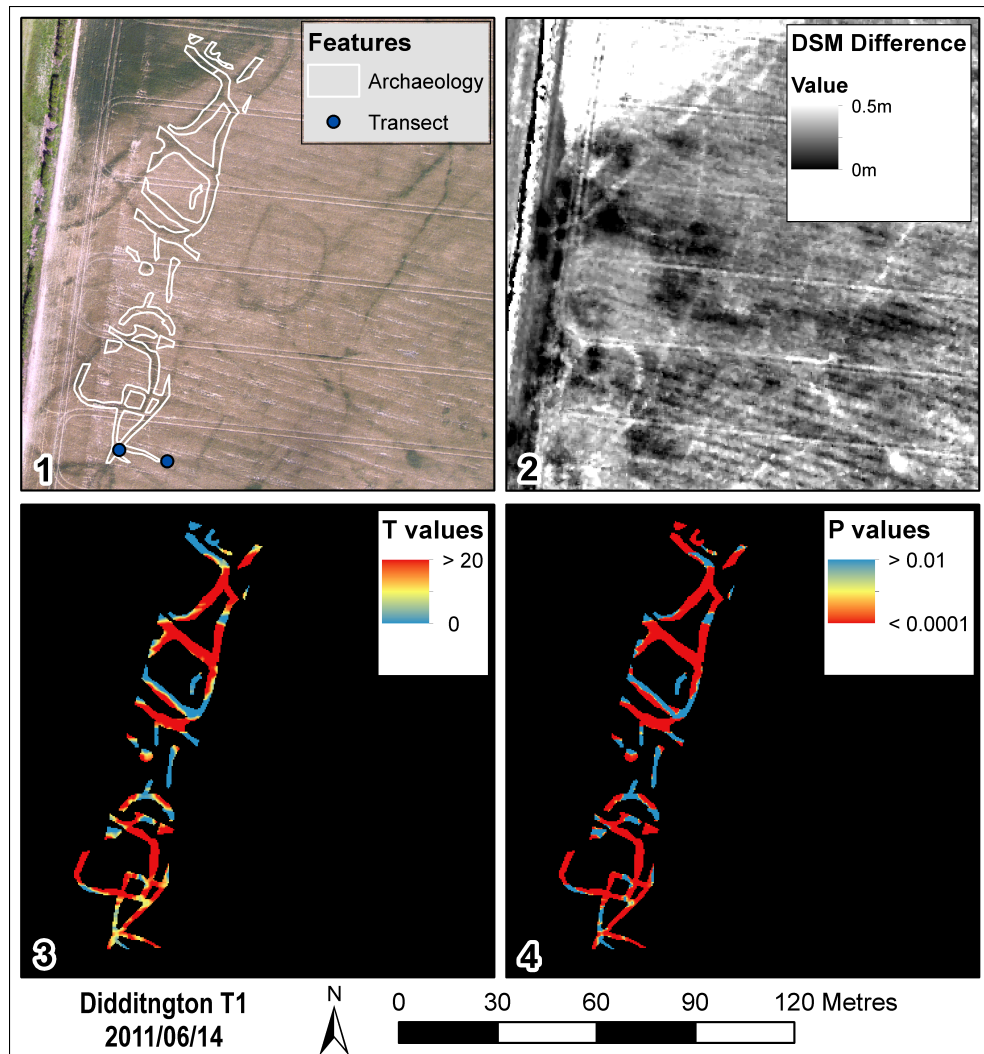


Figure 4.6: CSM results from DDT1, June 2011. The *top left* image shows the features against the background of the co-collected ortho photography. The *top right* image shows a gray-scale plot of the CSM, *bottom left* shows the strength of the contrast and *bottom right* the statistical significance of the contrast.

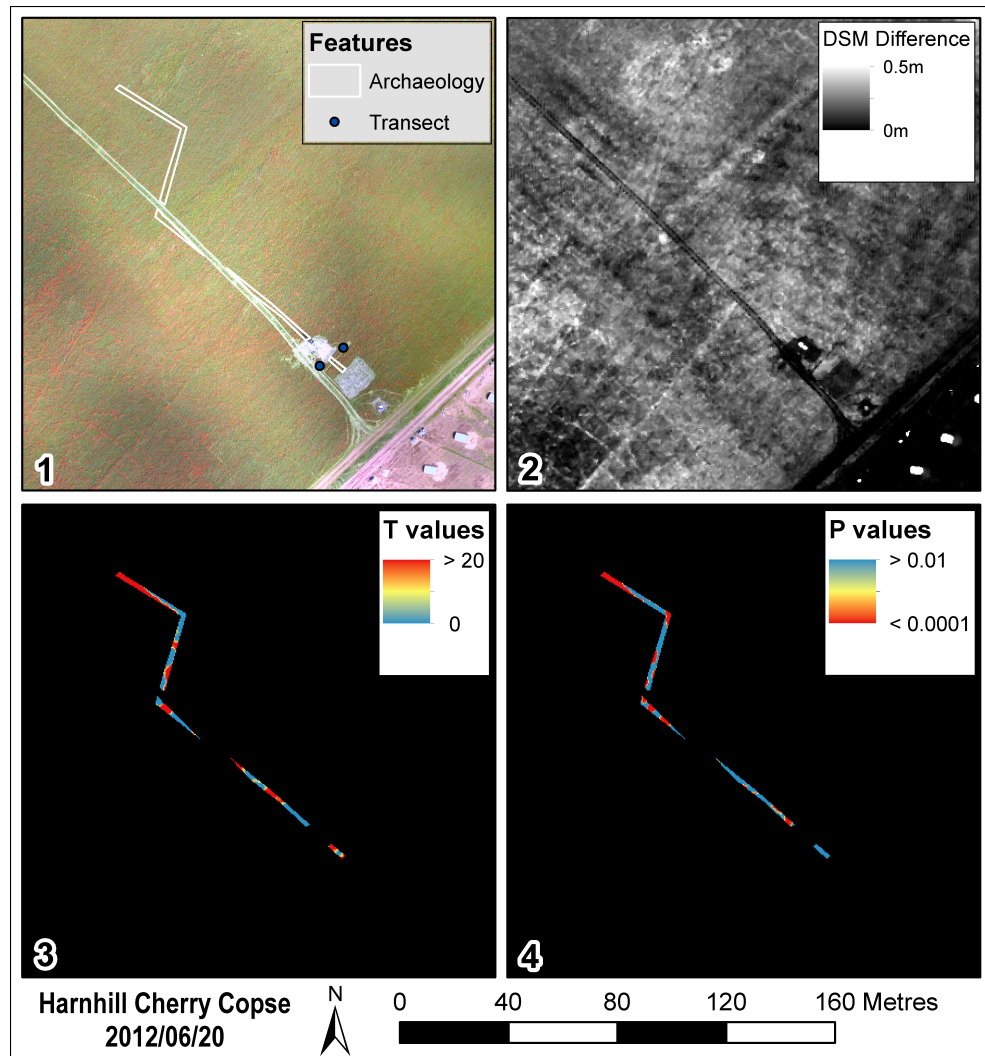


Figure 4.7: CSM results from HHCC, June 2012. The *top left* image shows the features against the background of the co-collected ortho photography. The *top right* image shows a gray-scale plot of the CSM, *bottom left* shows the strength of the contrast and *bottom right* the statistical significance of the contrast.

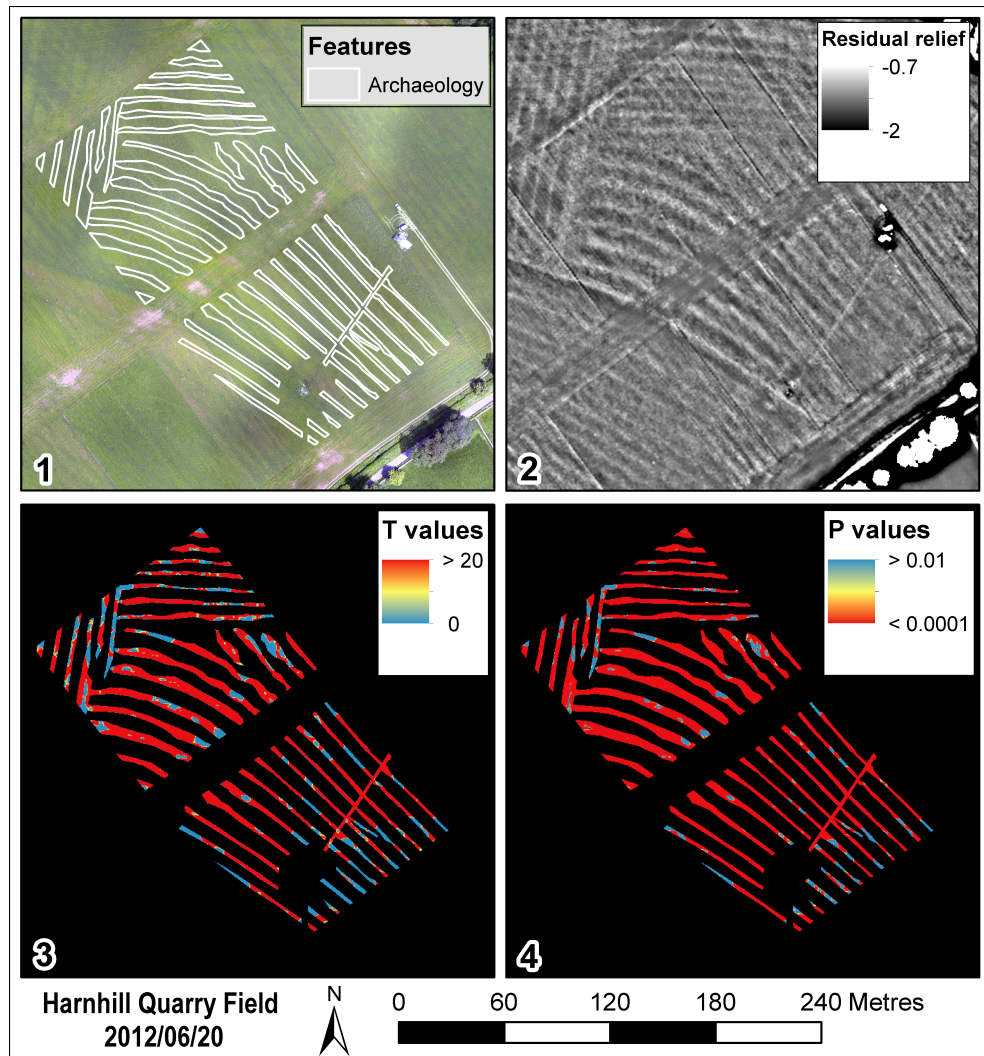


Figure 4.8: Residual relief model derived from first return DSM, HHQF June 2012. The *top left* image shows the features against the background of the co-collected ortho photography. The *top right* image shows a gray-scale plot of the CSM, *bottom left* shows the strength of the contrast and *bottom right* the statistical significance of the contrast.

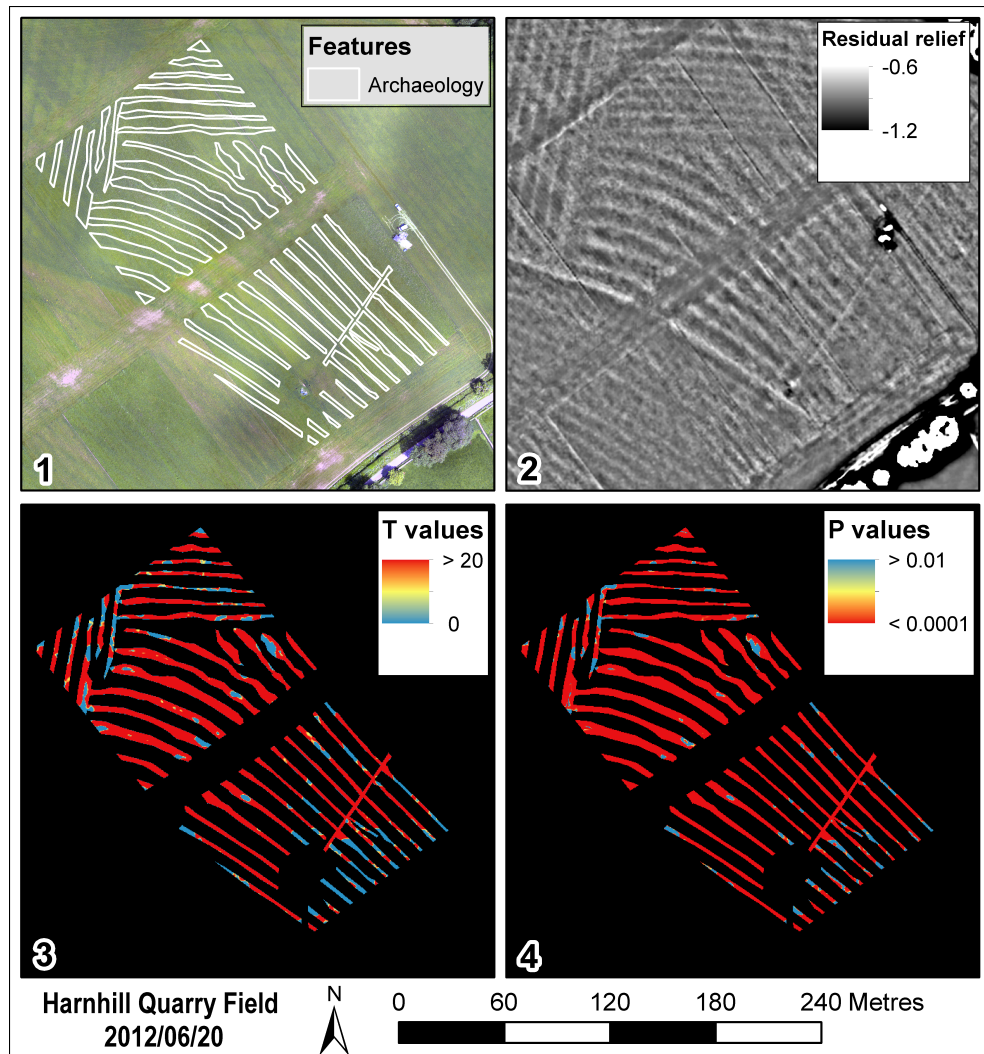


Figure 4.9: Residual relief model derived from Crop surface model, HHQF June 2011. The *top left* image shows the features against the background of the co-collected ortho-photography. The *top right* image shows a gray-scale plot of the CSM, *bottom left* shows the strength of the contrast and *bottom right* the statistical significance of the contrast.

creates variations in the DSM that are not related to the topography of the ground surface, meaning that the resultant model is erroneous. This could be improved using the method using the minimal returns for arbitrary areas to interpolate the DSM suggested by Cui et al. (2010), but this entails a significant loss in spatial resolution. It is thus suggested that the best time to acquire this model would be late autumn rather than the spring, as many fields will have been sown for winter crops and the stubble on those left for spring crops is of a more consistent length. The additional expense of acquiring the bare earth DTM is mitigated somewhat by the fact that the same model could be used for a number of years before the surface changed significantly. Verhoeven & Vermeulen (2016) and Bendig et al. (2014) demonstrate that the CSM can be successfully generated using surface models derived from aerial photography using photogrammetric techniques. This has some advantages, namely that a large quantity of archival imagery is available (Sevara 2013, Risbøl et al. 2015) and that the DSMs can be generated at very high spatial resolutions. However, using ALS for deriving the CSM has some advantages over this approach, namely that resultant DSM is not purely dependant on vegetation height, and is more strongly correlated with LAI (figure 4.10). In dense canopies the pulse from the sensor is more likely to be intercepted and reflected by the vegetation before it reaches the ground (Wagner et al. 2008). Additionally, using the photogrammetric workflow to produce accurate surface models is time consuming, and finding control points to provide vertical control on the images can be problematic, especially for archival imagery. Applying residual relief modelling was found to produce little additional contrast in this study. However, this may be a useful technique where it is not possible to obtain a bare surface DSM.

The full-waveform data are also capable of resolving biomass differences, however the sensors are not as capable of resolving contrasts in low cereal crops as the using CSM or residual relief methods. This may be due to the resolution at which the returning pulse is digitised, and this technique may become more tenable as sensor technology improves. The availability of multi-spectral full waveform sensors in particular have the potential to extend the utility of these techniques.

4.6 Conclusions

The work presented in this chapter tested two novel methods for the remote sensing of contrast in archaeological vegetation marks expressed as biomass variation using both

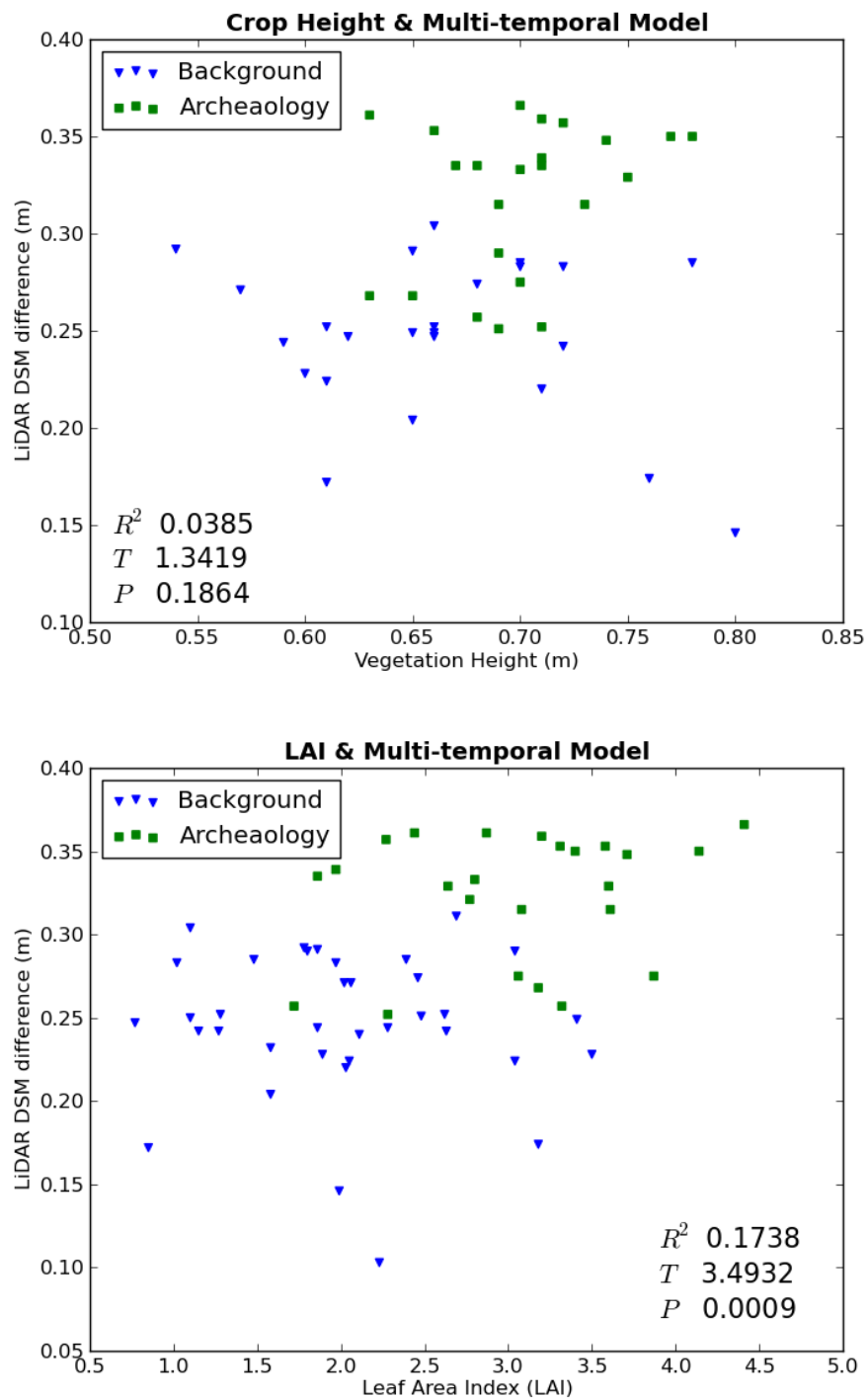


Figure 4.10: Correlation between ALS derived CSM and vegetation height (top) and LAI (bottom) from Harnhill Quarry Field. The CSM is more strongly correlated with LAI.

discrete and full waveform ALS data. This has interesting implications, as ALS is an active instrument that emits radiation, rather than relying on reflected solar illumination, meaning that the sensor can be used in sub-optimal lighting conditions or a times of day where trees or the topography shade the areas of interest. Additionally the technique could prove invaluable in crops where significant biomass variations are present but where there is little or no spectral contrast, for example in the senescent wheat crop at Diddington T1 during July 2011.

Chapter 5

Getting the most out of RGB images

5.1 Introduction

This chapter is an exploration of different methods of getting the most out of RGB images for vegetation mark detection. While widely used for aerial prospection in archaeology, standard RGB images are rarely processed beyond basic contrast enhancement techniques such as histogram stretching. This means that some extent the aerial archaeological community has not been exploiting these images to their full potential, as RGB cameras are in effect multi-spectral imaging devices, and can potentially be used to provide qualitative information on the state of vegetation and thus improve contrast usable for detection (Meyer et al. 1999, Lukina et al. 1999, Meyer et al. 2004, Jr et al. 2005, Meyer & Neto 2008). This can be achieved using simple ratios and slope transformations between the blue and red absorption maxima and the absorption minima in the green band (Rabatel et al. 2011).

The work presented here tests a variety of RGB vegetation indices currently employed in computer vision systems for precision agriculture to identify crop rows and individual plants for automated crop treatment machinery. The application of these techniques for archaeological detection is novel. If successful the impact of this work is potentially high, as these are the cheapest, highest spatial resolution, and most widely used sensors available for vegetation mark detection in archaeology. In addition, normalised difference indices can be used to mitigate the effects of variations in illumination and shadow caused by clouds or topography (Meyer et al. 2004) present at the time of image acquisition. This is especially important when using composite ortho-photographic mosaics, as these are by their nature composed of images acquired at different times, and thus are susceptible to changes in illumination making the resulting mosaics difficult to interpret. The results

demonstrate that RGB ratios have the potential to both maximise contrast and correct for these illumination differences.

5.2 Background

5.2.1 What are RGB images and how are they made?

The RGB colour space is the most widely used means of capturing and displaying digital colour images. This relies on the concept of additive colour mixing of the primary colours to produce a gamut of hues, broadly analogous to the function of the cone receptors in the human eye (Hunt 2005, pp. 10–18). These images are captured by recording three separate images in each primary colour by filtering the light entering a panchromatic sensor. In early analogue systems prisms were used to separate and filter light falling on photographic emulsions or video pickup tubes.

Since the 1990s most digital imaging systems have relied on on CMOS or CCD sensors to produce images. These sensors use two dimensional arrays of photo-detectors to produce a current which is then converted to a digital value. These sensors are panchromatic, with broadband sensitivity from the near ultraviolet to the near infra-red. To record colour in the visible wavelengths two different kinds of filtration are employed; a 'hot mirror' filter, that excludes light from the non-visible wavelengths, and a colour filter array (CFA) that separates the light falling on each detector into either red, green or blue (Adams et al. 1998, Ritchie et al. 2008, Tetley & Young 2007). These filters are generally applied directly to the surface of the sensor. The mostly widely used CFAs are 2-dimensional arrays such as the Bayer filter (Bayer 1976). These use a regularly spaced grid of RGB colour filters, with twice as many green elements as red or blue. This is because the M and L cone receptors in the retina, used for luminance perception in daylight, are most sensitive to green light (Kaiser & Boynton 1996, Watson & Null 1997). To obtain an RGB image de-mosaicking and interpolation algorithms are used to produce an RGB value for each pixel. In contrast to 2D CFAs the Fovonon X3 sensor uses a stacked array of three separate CCDs of different spectral sensitivities to produce a colour value at each detector site. These sensors offer considerable advantages over sensors using CFAs in terms of sensitivity and resolution as the resultant images are not interpolated (Guttosch et al. 2002, Hubel 2005)

Spectral properties of RGB sensors and vegetation

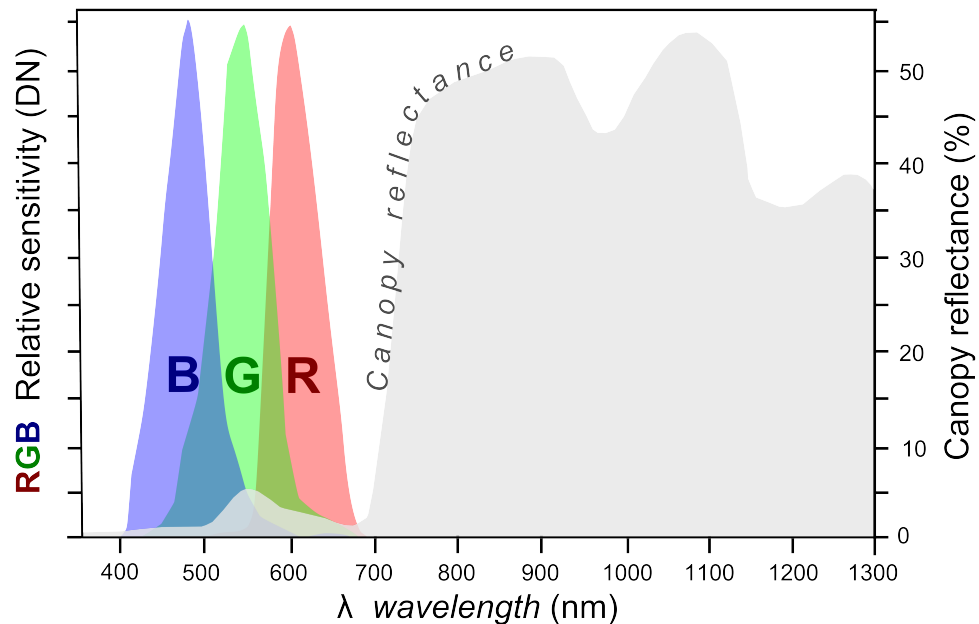


Figure 5.1: Sensitivities of a typical RGB Bayer filter CCD sensor shown against reflectance of a vegetation canopy

5.2.2 RGB cameras as multispectral sensors

Standard RGB cameras use three broad wavelength bands to record a colour image. These bands overlap with spectral features in the visible wavelengths that correspond with chlorophyll and green biomass. In healthy vegetation we expect increased reflectance in the green and increased absorption in the green and blue regions of the spectrum. This means that we can use the relationship between these bands to investigate the properties of the vegetation irrespective of variations in exposure and illumination given sufficient radiometric resolution.

Figure 5.1 demonstrates this by showing the sensitivity of each of the three bands against the reflectance of a typical vegetation canopy recorded by the ASD FieldSpec Pro. The peak of reflectance of in the visible spectrum at 550nm is coincident with the peak sensitivity of the green pixels in the Bayer filter. The red and blue bands are located in the absorption features on either side of this peak.

5.2.3 RGB methods for vegetation analysis

RGB band ratios and transformations are widely used in precision agriculture for automated identification of weeds and plant stress and vigour variations (Prez et al. 2000),

and their potential has been explored for the analysis of phenology from CCTV cameras (Morris et al. 2013). It has yet to be widely used for the identification of archaeological features despite the potential advantages outlined above. This is partially due to the fact that most of the precision agriculture approaches are focused on threshold for the automatic identification of plants and plant species, emphasising binary discrimination as opposed to detecting subtle contrasts across a continuously varying field. This is explored in chapter 3 as a means of identifying the proportion of the ground surface covered by an immature crop.

5.2.3.1 Simple indices

Simple indices are a ratio between one band and another. These simple indices are not widely utilised as they are more sensitive to illumination variation than normalised difference indices and slope transformations.

$$GB = \frac{G}{B} \quad (5.1)$$

$$RB = \frac{R}{B} \quad (5.2)$$

$$GR = \frac{G}{B} \quad (5.3)$$

$$ARI = \frac{G}{R} \quad (5.4)$$

The indices considered here are the Green Blue index (GB, 5.1), The Red Blue (RB, 5.2), the Green Red index (GR, 5.3) and the Anthocyanin Reflectance Index (ARI, 5.4). Of these only the ARI is widely used as it is highly sensitive to anthocyanin, a biochemical related to flowering and the red colouring in some algae and tree leaves (Gamon & Surfus 1999), however this is of limited utility for detecting contrast in largely green arable crops.

5.2.3.2 Normalised difference indices

Normalised difference indices are more widely used using the red and infrared bands of multi and hyper-spectral imagers, as there is a marked increase in reflectance in the infrared region of the spectrum. These are widely used to both identify areas of green vegetation and to quantify biomass (Guyot et al. 1990, Gausman 1985).

These indices are less commonly utilised in the visible spectrum, mostly because the absorption minima in the green region is not as pronounced as the rapid increase in reflectance after the red-edge in the near infrared. In addition, where there is lesser density of vegetation in terms of LAI the reflectance of the soil may mask the reflectance minima in the red region of the spectrum (Huete 1988, Baret & Guyot 1991). This can be used to our advantage, however, as this potentially makes indices reliant on the red band more sensitive to biomass variations. The methods considered here are:

$$NDGRI = \frac{G - R}{G + R} \quad (5.5)$$

$$NDGBI = \frac{G - B}{G + B} \quad (5.6)$$

$$NDRBI = \frac{R - B}{R + B} \quad (5.7)$$

Of these the most useful is the Normalised Difference Green Red Index (NDGRI, 5.5), as the most distinct difference between vegetation is between the green absorption minima and red bands (Gitelson, Kaufman, Stark & Rundquist 2002, Zakaluk & Sri Ranjan 2008). As discussed above, however, this may be susceptible to interference from the reflectance of the soil. In these instances the Normalised Difference Green Blue Index (NDGBI, 5.6) may provide more useful information.

$$VARI = \frac{G - R}{G + R - B} \quad (5.8)$$

The Visible Atmospherically Resistant Index (VARI, 5.8) was an attempt to produce an atmospheric self correction compared to the indices above, however, it was found to be more sensitive to biomass variations than the NDGRI (Gitelson, Kaufman, Stark & Rundquist 2002), and as such may improve contrast for archaeological detection

5.2.3.3 Slope derived indices

Slope transformations use the difference in reflectance between two bands normalised by the difference between the peak wavelength of the sensor at each band (Zakaluk & Sri Ranjan 2008). The methods considered here are:

$$GBS = \frac{G - B}{\lambda G - \lambda B} \quad (5.9)$$

$$GRS = \frac{G - R}{\lambda G - \lambda R} \quad (5.10)$$

$$RBS = \frac{R - B}{\lambda R - \lambda B} \quad (5.11)$$

Green Red Slope (GRS, 5.10) should be the most productive of these methods, however, in sparse vegetation or senescent vegetation Green Blue Slope (GBS, 5.9) may provide greater contrast.

$$GA\angle = 180 - (\arctan GBS + \arctan |GRS|) \quad (5.12)$$

Green Angle (GA, 5.12) is an attempt to resolve this by assuming that the green band forms the peak of a triangle, the angle of which can be resolved using GBS and GRS. This method should be more resistant to reduced contrast in the red region of the spectrum caused by interference from the soil line and senescent vegetation.

5.2.3.4 Chromatic transformations

RGB chromaticity transformations have been used in remote sensing to provide a method of suppressing illumination variation across an image caused by cloud or topographic shadows by normalising the reflectance at each band as a ratio across all bands (Gillespie et al. 1987). The methods considered here are:

$$r = \frac{R}{R + G + B} \quad (5.13)$$

$$g = \frac{G}{R + G + B} \quad (5.14)$$

$$b = \frac{B}{R + G + B} \quad (5.15)$$

These transformations provide the basis of a number of indices widely used in precision agriculture for automated plant identification, and have been found to out-perform normalised difference indices (Meyer & Neto 2008). These are:

$$ExG = 2g - r - b \quad (5.16)$$

$$ExR = 1.4r - g \quad (5.17)$$

$$ExGR = ExG - ExR \quad (5.18)$$

The Excess Green index (ExG, 5.16) is a measure of greenness developed as one of the basic methods of isolating leaves from their background in machine vision applications (Woebbecke et al. 1995). This, in common with other RGB ratios may be distorted by reflected red light from the soil, so the Excess Red index (ExR, 5.17) was proposed by Meyer et al. (2004), but did not perform well in later studies, leading to the development of the Excess Green minus Excess Red index (ExGR, 5.18), which exhibits better accuracy than either index individually (Meyer & Neto 2008, Romeo et al. 2013).

5.3 Methodology

5.3.1 Data collection and preparation

The data here considered were collected over the DART project study sites at Diddington in South-East England and Harnhill in the South-West. They comprise both ortho-photographic images acquired by NERC ARSF and the Geomatics Group Ltd and oblique, observer-directed photography acquired by Rog Palmer. See table 5.1 for a summary of the different surveys used in this section.

Flight	Provider	Sensor	Spatial resolution	Radiometric resolution
14/06/2011	NERC ARSF	Leica RCD105	0.1m	16 bit
20/06/2011	Rog Palmer	Nikon D700	0.25m	14 bit
27/06/2011	Geomatics Group Ltd	Unknown	0.25m	8 bit
14/06/2011	NERC ARSF	Leica RCD105	0.1m	16 bit
27/01/2012	Rog Palmer	Nikon D700	0.25m	14 bit
23/03/2012	NERC ARSF	Leica RCD105	0.1m	16 bit
20/06/2012	NERC ARSF	Leica RCD105	0.1m	16 bit

Table 5.1: Table summarising RGB imagery used in this study

5.3.1.1 Data preparation

The NERC ARSF survey photographs were located using the event file containing RTK GNSS coordinates co-collected with the photographs. These were used to create an ortho-photographic mosaic using the AgiSoft PhotoScan SFM (Structure from Motion) package (AgiSoft 2013), and output as a 16 bit *.tiff file. This was then re-projected and the georeferencing was improved using the Geomatics Group ortho-image as a base map using the Quantum GIS package (QGIS 2011). The resultant orthomosaic had a 0.08m spatial resolution and a spatial accuracy of +/-0.1m. The Geomatics Group imagery was acquired pre-processed as a ortho-rectified mosaics.

The oblique aerial images were rectified using the AirPhoto SE package using the ortho-mosaics as ground control. Due to the low angle of view and uncorrected distortions the geometric accuracy of the rectified images is +/- 0.5m. This was subsequently improved using polynomial transformations in QGIS to +/- 0.2m.

5.3.2 Data analysis

Subsets of the images were then produced corresponding with areas containing known archaeological features identified using fluxgate gradiometer survey. Then, using the Python programming language a multi-band raster image was produced using the vegetation analysis methods discussed above. Each band of the resultant image was then filtered using both Gaussian (Lee 1980) and median (Sun & Neuvo 1994) filters, as it was difficult to interpret changes in the canopy in the unfiltered results from the high spatial resolution images due to high frequency variation. This is likely caused by the sensor being able to resolve detail from individual plants, rather than the properties of the canopy as a whole. The properties of the filter kernels were determined using equation 5.19 below.

$$K_{px,py} = \frac{T_m}{(X_m + Y_m)/2} \quad (5.19)$$

Where $K_{px,py}$ is the size in pixels of the kernel, T_m is the size of the target in metres and X_m, Y_m are the size of the geo-referenced pixels in metres. A value of 1 was used for T_m , as this closely approximates the size of the archaeological features. Due to the constraints required by the implementation of these filters the nearest odd integer to the value $K_{px,py}$ was then used.

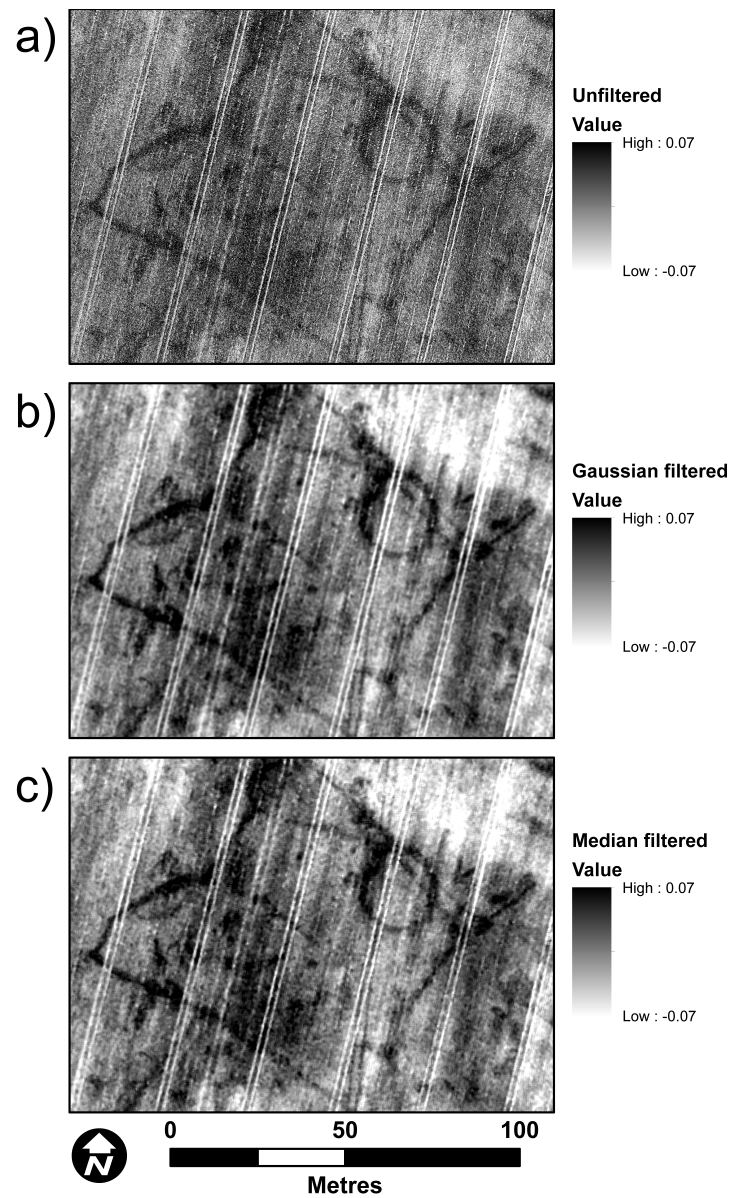


Figure 5.2: Filters applied to an NDGRI image derived from 0.1m spatial resolution NERC ARSF ortho-imagery acquired in June 2011. Filtering the image results in a marked increase in contrast compared to the unfiltered image

The pixels in each image were then classified using the extents of the features interpreted from the magnetic survey data. These were recorded as polygons and then used to classify each pixel in the processed image as either background, archaeological feature or natural feature. Each variable in each class was then compared to the others. This was initially attempted using T-tests as for the other airborne surveys, but it was found that it was not possible to differentiate between methods given the very large number of samples (Sullivan & Feinn 2012). To better resolve the differences between the classes Earth Mover's Distance (EMD) was used. EMD is a measure of the lowest cost of turning one probability distribution into the other, and as such can be used to provide a quantitative measure of the contrast between two normalised histograms or probability density functions (Cohen & Guibas 1997, Cohen & Guibasm 1999, Rubner et al. 2000, Rubner & Tomasi 2001). It is equivalent to the 1st Mallow's Distance (Levina & Bickel 2001) or 1st Wasserstein Distance (Sandler & Lindenbaum 2011) between the two distributions, and can be considered a transportation problem. It is widely used to compare the similarity of images in image and document databases (Rubner et al. 1998, Fu et al. 2006)

The method used is proposed by Rubner et al. (2000). Assuming that distribution P has m clusters with $P = \{(p_1, w_{p_1}), \dots, (p_m, w_{p_m})\}$, where p_i is the cluster and w_{p_i} is the weight of the cluster. To compare this to distribution $Q = \{(q_1, w_{q_1}), \dots, (q_n, w_{q_n})\}$ with n clusters the optimal flow $\mathbf{F} = [f_{ij}]$ between the two distributions must be found, where $f_{i,j}$ is the flow between p_i and p_j , minimising the overall cost:

$$\text{WORK}(P, Q, \mathbf{F}) = \sum_{i=1}^m \sum_{j=1}^n f_{ij} d_{ij} \quad (5.20)$$

Where $d_{i,j}$ is the ground distance between the clusters p_i and p_j . This is subject to constraints:

$$f_{ij} \geq 0 \quad 1 \leq i \leq m, 1 \leq j \leq n \quad (5.21)$$

$$\sum_{j=1}^n f_{ij} \leq w_{p_i} \quad 1 \leq i \leq m \quad (5.22)$$

$$\sum_{i=1}^m f_{ij} \leq w_{q_j} \quad 1 \leq j \leq n \quad (5.23)$$

$$\sum_{i=1}^m \sum_{j=1}^n f_{ij} = \min\left(\sum_{i=1}^m w_{p_i}, \sum_{j=1}^n w_{q_j}\right) \quad (5.24)$$

The first constraint (equation 5.21) is that the flow must only be between P and Q . The second (equation 5.22) is that the flow from P is limited by its weights, and the third (equation 5.23) is that the flow to Q does not exceed its weights. The fourth (equation 5.24) is that the maximum possible flow must be achieved. This is equal to the total weights of the smaller signature. Once the optimal flow F has been found the EMD can be defined as the work normalised by the total flow ((equation 5.25):

$$\text{EMD}(P, Q) = \frac{\sum_{i=1}^m \sum_{j=1}^n f_{ij} d_{ij}}{\sum_{i=1}^m \sum_{j=1}^n f_{ij}}. \quad (5.25)$$

To use the EMD properly the histograms for each variable in each class were computed. This was done using the combined range of values for both classes for binning, so that the histograms could be directly compared. In addition, the scale of the histograms were normalised so that the different classes were comparable despite different value ranges. These were then used to compute EMD for each variable. This provided a robust statistical method of comparing contrast between classes and between the different variables. The results were validated using data acquired over bare soil as control where there should be little or no discernible contrast, and over a flowering crop where vegetation marks were evident. This showed that over bare soil EMD showed little or no contrast between classes ($\text{EMD} \leq 1$), whereas over the mature crop with visible vegetation marks usable contrasts were identified ($\text{EMD} \geq 2$).

5.4 Results

5.4.1 Diddington Clay Field

The ground based survey (figure 3.8, page 78) indicated little contrast during the periods where the images were taken. However, the results of the RGB image analysis indicate particularly strong contrasts. These are erroneous, and are the result of the patterns of cultivation in the field being closely aligned with the archaeological features.

5.4.2 Diddington Transect 1

The results from the ground based survey (figure 3.11, page 81) during 2011 indicated strong contrasts expressed both as variations in biomass and foliar biochemical content. On the 14th of June the contrast is most strongly expressed by the individual bands of the RGB image, intensity and the gradient of reflectance between the red and blue bands.

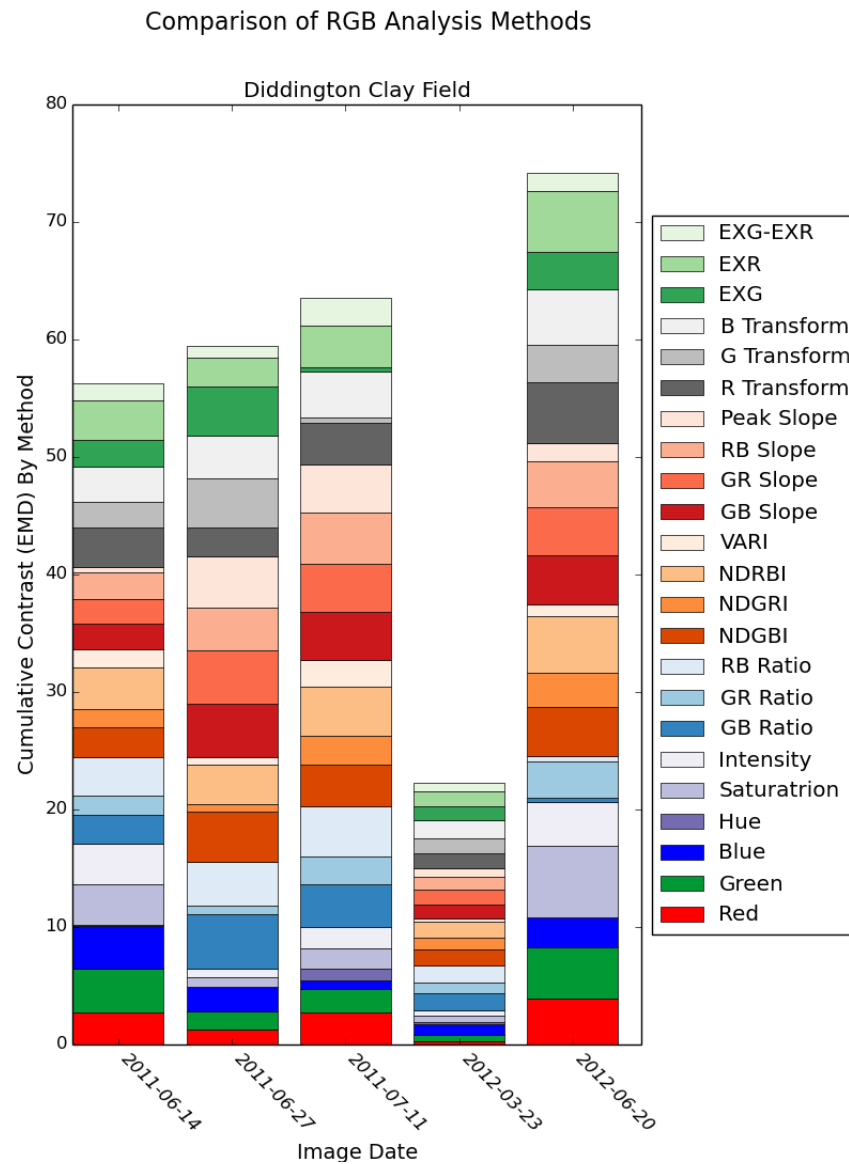


Figure 5.3: Summary of contrast from Diddington Clay Field, using different RGB analysis methods, expressed as earth mover's distance. Columns represent each image, with individual methods shown as subdivisions of the column.

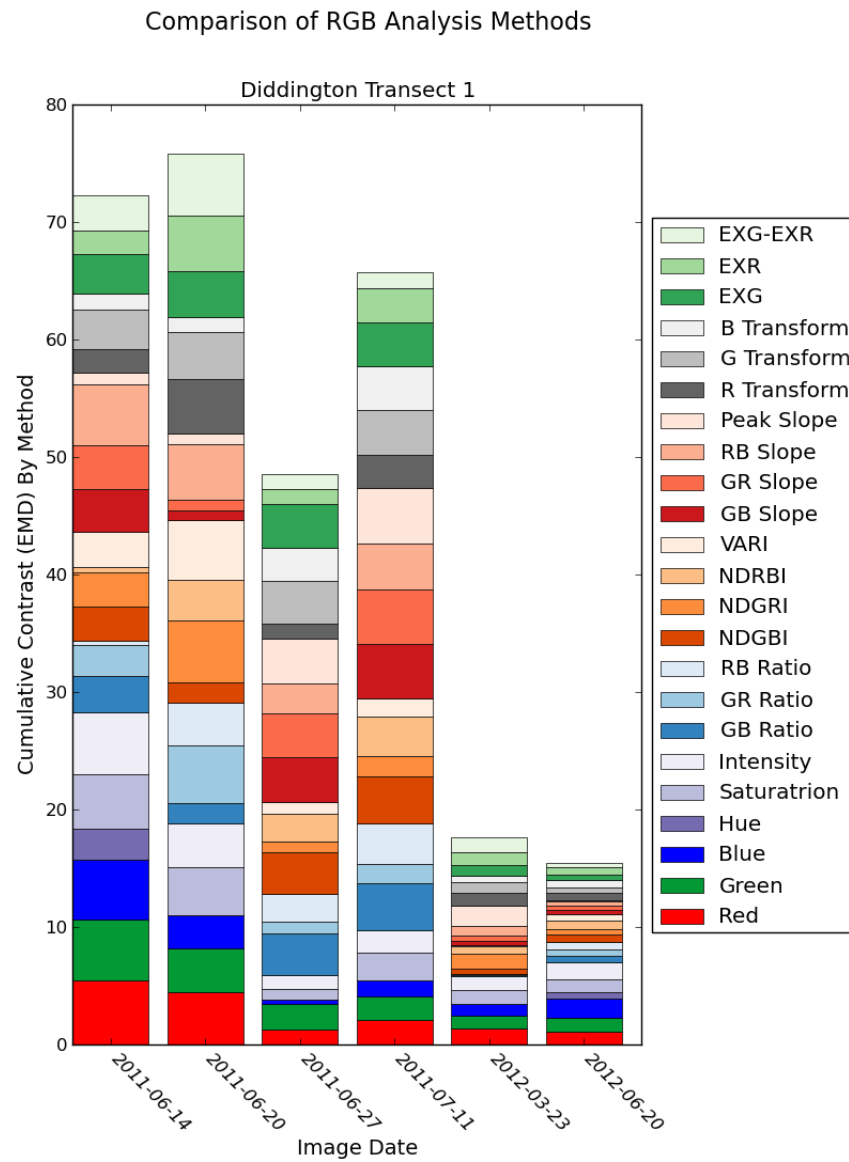


Figure 5.4: Summary of contrast from Diddington Transect 1, using different RGB analysis methods, expressed as earth mover's distance. Columns represent each image, with individual methods shown as subdivisions of the column.

These indicate that the expression of the vegetation marks expressed as biomass is significant, as there is greater absorption across the visible spectrum.

On the 20th of June no ground-based data were recorded. This image was taken in between the green crop observed in on the 14th and the ripening crop observed on the 27th. The methods that use the relationship between the red and green bands show the greatest contrast, including the GR ratio, NDGRI, GR slope, EXR and EXG-EXR methods. This indicates that there is a significant difference in the photosynthetic activity between the crop growing over the archaeology, as the ratio between absorption in the red and reflectance in the green bands is characteristic of greater photosynthetic activity. The contrast observed is thus probably a conflation of the observed biomass variation and foliar biochemical content.

On the 27th of June the total contrast observed is less than on the preceding and following images. This is likely as a result of the image being recorded as an 8 bit image, meaning that the radiometric resolution of the sensor is less able to resolve subtle differences between the archaeology and the background. On this date a variation in senescence between the archaeology and the background was observed in the ground-based survey, with the crop over the archaeological features ripening faster than the stressed vegetation over the background. The contrast expressed in the RGB images is strongest in the GB ratio, NDGBI, GB slope, green transform and EXG indices. These measures are sensitive to variations in greenness, which reflects the nature of the contrasts on the ground. These methods also outperform the individual RGB bands.

On the 11th of July the crop was senescent and ripening. No ground measurements were acquired on this date. The survey on the 15th showed that although photosynthesis had largely ceased, measures that returned a gradient of reflectance indicated that the differences in overall brightness resultant from biomass provided significant contrast. The indices derived from the RGB images confirm this, with slope and gradient based methods demonstrating the greatest contrast.

The images acquired during 2012 show little or no contrast between the archaeology and the background. This is supported by the ground-based measurements, where little significant contrast was recorded during this period, where a combination of the crop and the weather conditions made detection unlikely.

5.4.3 Harnhill Quarry Field

The results from Harnhill Quarry Field again largely confirmed the general trend of the ground-based surveys (figure 3.16, page 87). In June 2011 little appreciable contrast was observed in the mature winter wheat crop. This may be due to the decreased radiometric resolution of the 8-bit sensor. During March, when the field was under bare soil there is little slightly more variation. The contrast in March is observable in the gradient based methods, indicating tonal differences in the exposed soil.

During June 2012 significant biomass variations were observed both in the data from the ground-based survey and the ALS data (fig 4.5, page 122). In addition, significant spectral variations resultant from foliar biochemistry were recorded. These are reflected in the results from the analysis of the RGB images, where measures sensitive to absorption in the red region show the most difference. In particular the EXR, red transform, RB slope, NDGRI and GR ratio showed better contrast than the individual RGB bands.

5.4.4 Harnhill Cherry Copse

The strongest contrasts observed in Cherry Copse were over the spring wheat crop in June 2011. These were associated with significant biomass variations, visible on the ground. Indices responsive to relative absorption in the blue band showed the greatest sensitivity, especially those that utilise both the blue and red bands, such as the NDRBI, RB ratio and RB slope. Those that consider reflectance from the green and red bands showed slightly worse performance. This may indicate that overall greenness is not the best indicator of contrast on this date, and that increased absorption in the blue region, possibly due to the concentration of assistive pigments was responsible for the greatest contrast. Unfortunately spectroscopic measurements could not be acquired on this date to confirm this.

During March 2012 the area was under low grass, and the ground-based surveys (figure 3.18, page 90) indicated little contrast in terms of biomass variations and subtle contrasts in the red-edge and vegetation indices. The best contrast in the RGB images was observable in measures that examine reflectance in the red band relative to reflectance in the blue band.

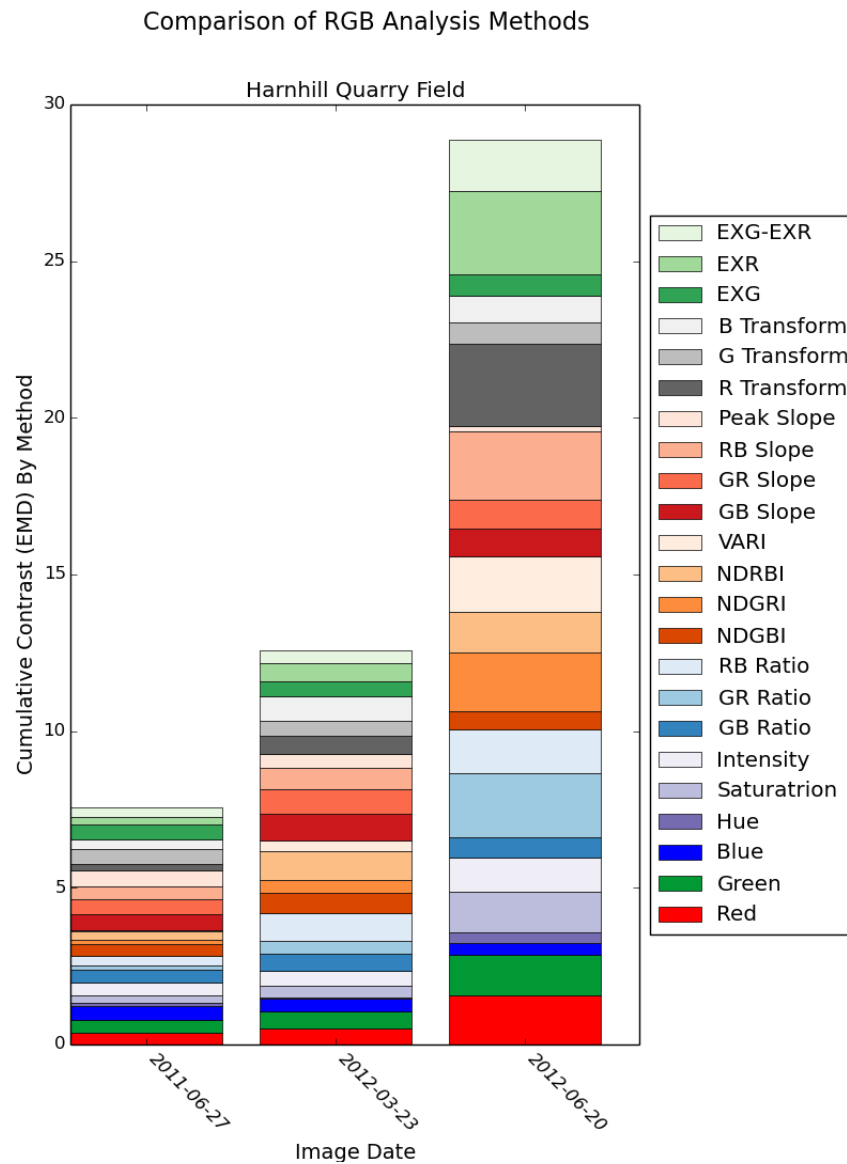


Figure 5.5: Summary of contrast from Harnhill Quarry Field, using different RGB analysis methods, expressed as earth mover's distance. Columns represent each image, with individual methods shown as subdivisions of the column.

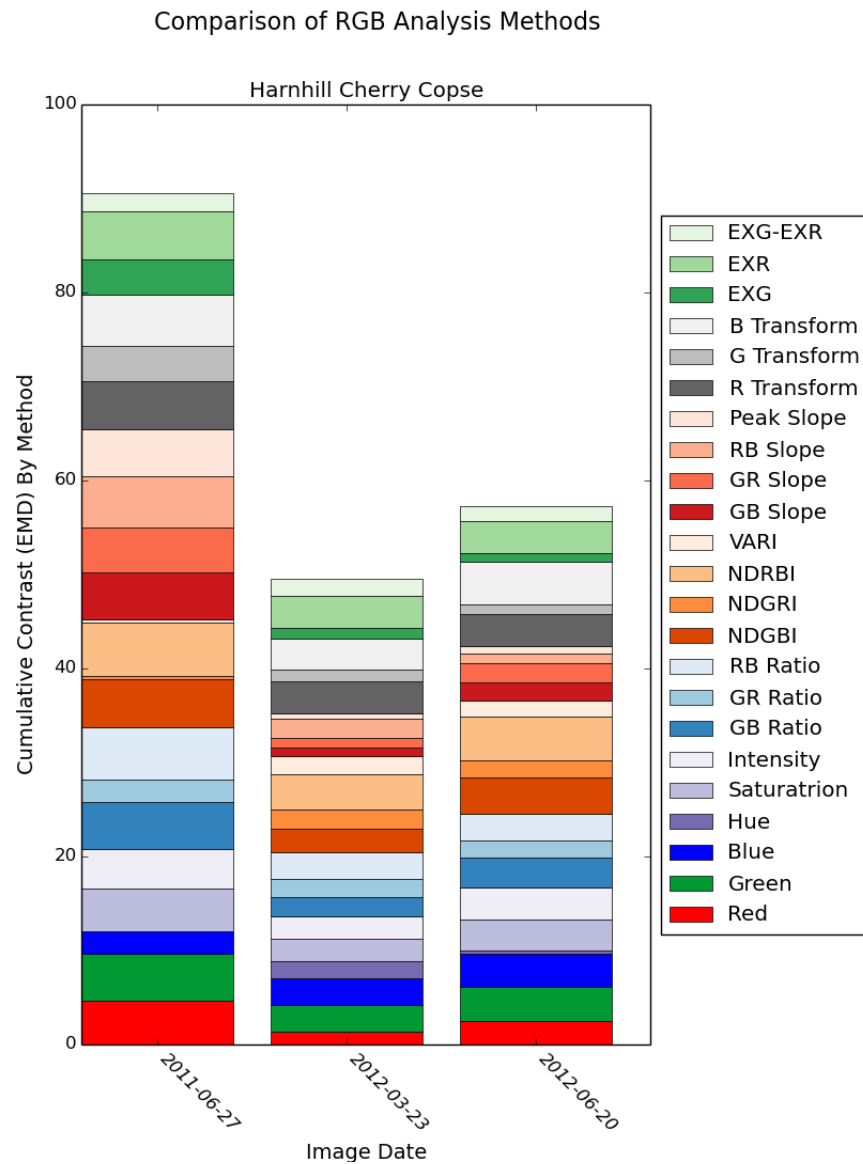


Figure 5.6: Summary of contrast from Harnhill Cherry Copse, using different RGB analysis methods, expressed as earth mover's distance. Columns represent each image, with individual methods shown as subdivisions of the column.

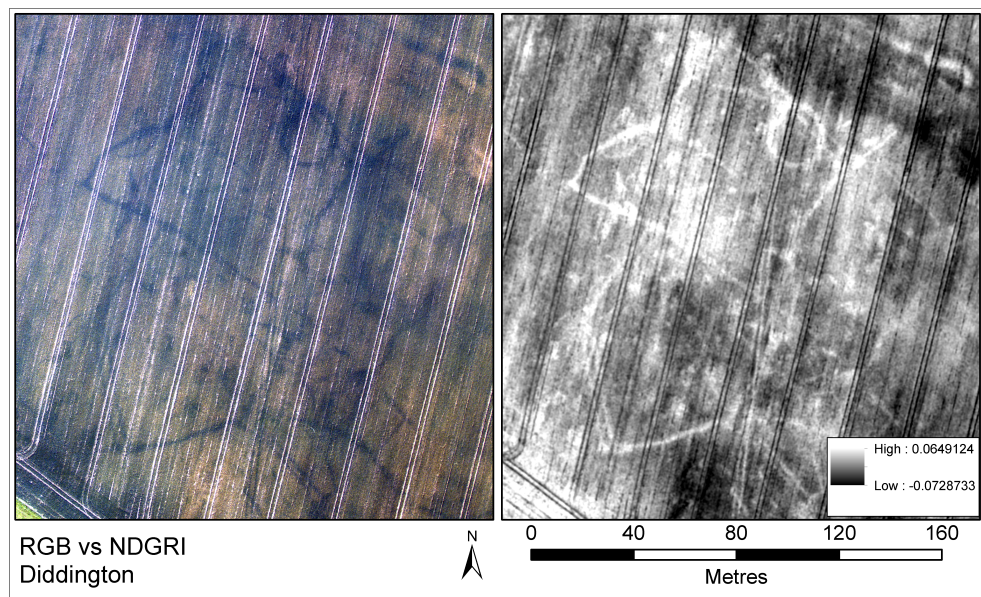


Figure 5.7: Comparison between RGB and NDGRI images, derived from the NERC ARSF ortho image 14/06/2011. The vegetation marks are a probable prehistoric settlement located 500m W of DDT1. Both images are stretched to two standard deviations. While the features are visible in both images the NDGRI has greater initial clarity, and some features visible on this are not readily discernible in the RGB image. Note that the NDGRI has saturated at the centre of the image. A different stretch reveals more detail in this region

In June 2012 significant variations were visible in the ground-based surveys both in biomass and chlorophyll fluorescence. On this date the greatest sensitivity is exhibited by normalised difference indices sensitive to the blue band and the blue transform.

5.5 Discussion

5.5.1 Do RGB ratios improve contrast?

On every image with detectable vegetation marks apart from DDT1 on the 14th of June the RGB indices provided more contrast than the individual bands of the image, and hue saturation and intensity. This is because the indices provide a relative measure of absorption using the gradient or difference between bands. However, RGB images are rarely used as single bands, rather they are generally displayed as colour composites and thus will display more contrast when viewed as such. Figure 5.7 demonstrates this. While the composite image provides additional contrast this is often qualitatively not as clear as the indices viewed as greyscale images.

The contrast resolved by the different indices varies with the state of the crop and the nature of the contrast expressed on the ground. In green crops methods that use the relationship between absorption in the red and blue bands provide the best contrasts. In mature and ripening crops methods that used the relationship between absorption in the red and reflectance in the green band provide the best resolution of contrast. In bare soil and senescent vegetation, where the characteristic absorption patterns of vegetation are not present ratios that capture the gradient of reflectance or slope based methods provide the best results. In addition, the radiometric resolution of the sensor is essential to the extent contrast can be resolved. This can be seen in the images from DDT1, where the 8 bit image acquired on the 27th of June demonstrates considerably less contrast than the preceding and following images.

5.5.2 Do RGB ratios correct for illumination differences?

The normalised RGB indices also provide correction for illumination variations in reflectance by normalising the relationships between absorption and reflectance. The images considered in this work were acquired in as close to optimum illumination properties as possible, so there were few images exhibiting variations in illumination across the image, meaning that this aspect of RGB image analysis is not fully explored. Figure 5.8 shows a possible enclosure and trackway located c.500m south of Diddington Clay Field, and is derived from one of the few images showing significant cloud shadow. It clearly demonstrates that the normalised difference indices can reduce the impact of shadows and illumination on the interpretation of the image. This may prove important, not just for variations in illumination caused by atmospheric effects, but also shadows cast by terrain in mountainous areas. In addition, ortho-photographic mosaics may be composed of hundreds of individual images taken at different times, meaning that it is unlikely that all the images can be acquired under the same illumination conditions. gain, radiometric resolution is an important consideration. If the sensor is not capable of resolving the full range of variation in both the pixels obscured by shadow and those under full illumination it is unlikely these techniques will provide any benefit.

5.6 Conclusions

The enhancement of RGB images using indices and ratios of band reflectance has significant potential to improve archaeological detection. By treating RGB sensors as multi-

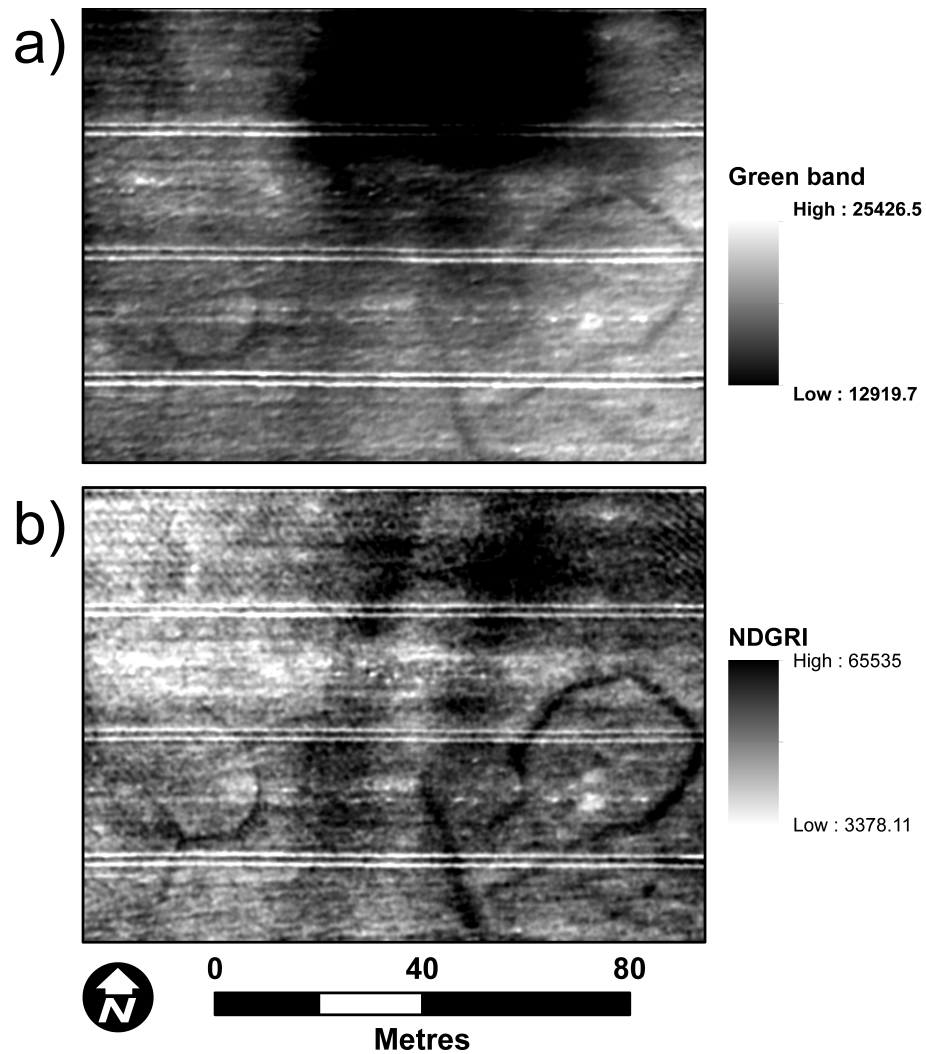


Figure 5.8: Image showing the ability of RGB ratios to correct for illumination variations. Diddington, 14/06/2011. *a)* shows the green band of the RGB image, where shadow from a cloud obscures much of the detail of the trackway running N-S across the image. *b)* shows the NDGRI derived from the same image

spectral sensors it is possible to infer information on foliar properties, and thus contrast in the crop canopy. In addition the normalising effects of the indices can both enhance detail in areas obscured by shadow and correct for differences in illumination between images. Given the prevalence of RGB sensors in aerial archaeology these advances represent a significant contribution.

Chapter 6

Airborne imaging spectroscopy

6.1 Introduction

This chapter examines the detection of archaeological features with Airborne Imaging Spectroscopy (AIS), using Speccim EAGLE and CASI visible to near-infrared scanners. Chapters 3 demonstrated that hyper-spectral data can be exploited for the detection of contrasts in the structure and health of the vegetation for the study sites considered here. However, extending the observations made in the field spectroscopy to the airborne surveys is not straightforward.

The lower spectral resolution of the airborne data means that the detection of contrasts based on the relationships between nearly adjacent bands, for example in the MTBVI and fluorescence indices, may not be possible in the airborne data. Additionally, the distance from the ground means that the achievable spatial resolution is reduced and the influence of atmospheric noise is increased. The results from this chapter indicate that contrast is more weakly expressed than in the ground-based data, likely as a result of the lower spatial resolution of the sensors. However, usable contrasts are still present in the images. At Diddington Transect 1 during June 2011 and Harnhill Quarry Field during June 2012 a wide range of methods were successful. On sites where contrasts are less evident, for example those under oilseed rape or cereals in period of low soil moisture deficits continuum removed reflectance and the MTBVI provided usable contrasts where the other, more commonly used methods were unsuccessful. As such this chapter demonstrates that

the novel approaches to detecting archaeological vegetation marks introduced in chapter 3 can be successfully applied to the airborne data.

6.2 Background

6.2.1 How the scanners work

The hyper-spectral scanners considered here are push-broom scanners. These use a 2-dimensional array of photodetectors. One dimension provides the spatial dimension across the travel of the aircraft, the second providing the spectral dimension. The scanner is thus reliant on the movement of the aircraft to provide data in the second spatial dimension (Gupta & Hartley 1997, Fricker & Rohrbach 2005). The signals produced by the array are sampled over the integration time of the sensor. These are located spatially using RTK GNSS and an Inertial Measurement Unit (IMU) to produce view vectors for each measurement, which record the footprint of each measurement on the ground from each pixel during the time they were acquired. The view vectors and sensor data are then interpolated to produce a gridded raster dataset (Awange & Kiema 2013, Toth & Józków 2016). The achievable spatial resolution is governed by the IFOV of the sensor and the altitude of the aircraft. The altitude that the aircraft can acquire data at is limited by the relative air-ground speed, which increases at lower altitudes, meaning that slower aircraft are capable of flying lower and thus acquiring data at a higher spatial resolution Lillesand et al. 2004, pp. 241-243,

6.2.2 AIS and archaeology

Hyper-spectral imaging spectroscopy has been applied to vegetation mark archaeology by many previous studies. For these studies the impetus is on providing the greatest contrast, and visualising it so that the archaeological vegetation marks can be interpreted. This is challenging given the large number of redundant bands present in the hyper-spectral data, so approaches such as vegetation indices, PCA (Principal Components Analysis) and the REIP are used to summarise information contained in multiple bands. These methods are more fully investigated in chapters 2 and 3.

6.3 Methodology

6.3.1 Data

The DART project received a data grant from the NERC ARSF (National Environmental Research Council) for three surveys during 2011 and 2012. In addition, the project commissioned an additional survey from the Geomatics Group Ltd during June 2011. The data were acquired at approximately 1000m altitude, limiting spatial resolution to 1m. Table 6.1 summarises the surveys.

Survey	Sensor	Provider	Bands	Range(nm)	Nominal Spatial resolution
Diddington 14/06/2011	Speccim Eagle	NERC ARSF	253	400-1000	1m
Diddington 27/06/2011	CASI	Geomatics Group Ltd	96	400-1000	1m
Harnhill 27/06/2011	CASI	Geomatics Group Ltd	96	400-1000	1m
Diddington 23/03/2012	Speccim Eagle	NERC ARSF	123	400-1000	1m
Harnhill 23/03/2012	Speccim Eagle	NERC ARSF	253	400-1000	1m
Diddington 20/06/2012	Speccim Eagle	NERC ARSF	253	400-1000	1m
Harnhill 20/06/2012	Speccim Eagle	NERC ARSF	253	400-1000	1m

Table 6.1: Table showing AIS surveys undertaken for this work.

6.3.1.1 Data Processing

The data supplied by NERC ARSF were processed to NASA level 1b (Parkinson et al. 2006), meaning that the sensor data are supplied with the associated view vectors required to produce the geo-referenced rasters. This was done for each flightline using the NERC APLCORR and APLTRAN software in conjunction with the co-collected ALS derived DEMs (Warren et al. 2014). The flightlines were merged using ESRI's ArcGIS mosaic routines (Xu & Becker 2012). The geo-referencing was then improved manually using the QGIS software package using the 27th of June 2011 ortho-photography as a backdrop.

Atmospheric correction of was conducted using MODTRAN correction algorithm with field spectra collected over dark (asphalt) and light (lawns) targets using the ENVI software package (Kneizys et al. 1996, Adler-Golden et al. 1998, Matthew et al. 2002, Cooley et al. 2002). However, the discrepancy in illumination between the different flightlines caused by cloud shadow made a robust correction impossible. Despite this, the relative differences used for detection of vegetation marks means that the methods that normalise reflectance such as indices and continuum removal are still appropriate for comparison.

In addition, the calibration of the Eagle sensor between March and June 2012 drifted by up to 18% in the 400-500nm region of the sensor's sensitivity. No calibration data were made available for the CASI sensor.

6.3.2 Data analyses

Subsets of the data from each of the test sites were extracted using the extents of features verified by fluxgate gradiometer survey in each field. The vegetation indices, red-edge inflection point (REIP), fluorescence indices, continuum removal for the 670nm absorption feature, and the MTBVI used in Chapter 3 were applied to the subsets and the archaeological contrast evaluated using the zonal statistics method used in chapter 4. A kernel size of 10x10 pixels was used for evaluation.

6.3.2.1 Vegetation Indices

Where appropriate to the VIS-NIR range of the sensor the methods used in chapter 3 were used to analyse the airborne spectra. In the ground-based surveys there were found to provide less contrast than the MTBVI and fluorescence indices. However, they provide a useful benchmark for comparison with methods adopted in other studies. Table 6.2 summarises the indices applied to these datasets.

6.3.2.2 Fluorescence Indices

The fluorescence indices for reflectance (page 47) and derivative of reflectance (page 47) applied in chapter 3 have been applied here. In the ground based data these were observed to provide significant contrast under a wide variety of conditions.

Index	Page	Sensitive to
SR 700 800	36	Biomass, red-edge
NDVI 705 750	36	Red-edge
NDVI 700 800	36	Biomass, red-edge
NDVI 694 760	36	Red-edge
NDVI 695 805	36	Biomass
NPCI	42	Chlorophyll
NPQI	43	Chlorophyll
RDVI	37	Chlorophyll, red-edge
SAVI	38	Biomass
MSAVI	39	Biomass
MSR	38	Red-edge, biomass
MSRVI	38	Red-edge, biomass
MDVI	40	Red-edge, biomass
TVI	40	Chlorophyll, biomass
MTVI	40	Chlorophyll, biomass
MTVI2	40	Chlorophyll, biomass
VOG1	41	Red-edge
VOG2	41	Red-edge
PRSI	42	Senescence
PRI	43	Light use efficiency
SIPI	43	Light use efficiency
CARI	39	Chlorophyll, biomass
MCARI1	39	Chlorophyll, biomass
MCARI2	39	Chlorophyll, biomass
CRI1	42	Carotenoids
CRI2	42	Carotenoids
ARI1	43	Anthocyanins
ARI2	43	Anthocyanins
WBI	41	Canopy water content

Table 6.2: Vegetation indices with the airborne data, showing page references to definitions and the foliar constituents the indices are correlated with.

6.3.2.3 The Red-edge

In chapter 3 it was demonstrated that often contrast attributed to the red-edge inflection point is often conflated with peaks in the first derivative of reflectance caused by chlorophyll fluorescence. By using Cho's extrapolation technique it was possible to remove the influence of fluorescence from the derivation of the red-edge. This method was applied to the AIS data.

6.3.2.4 The MTBVI

To investigate whether the successful MTBVI method outlined in chapter 3 could be applied to the AIS data. This was run using a range of 630-750nm in the red and 700-850nm in the NIR portion of the spectrum. These wavelengths were chosen to cover the entire 670nm absorption feature, including regions appropriate to the detection of chlorophyll fluorescence and the red-edge inflection point.

6.3.2.5 Continuum Removal

Continuum removal was performed for the 670nm absorption feature, as this is within the range of the sensors. The 470nm absorption feature, while within the range of the sensor was rejected, as it provided poor results given the erroneous sensor calibration for this region of the spectrum for the Eagle data. The 1200nm and 970nm absorption features were outside the range of the sensor.

6.4 Results

6.4.1 Summary

The results obtained using AIS confirmed those from previous chapters, in that the sites exhibiting the strongest statistically significant contrasts across a wide variety methods were detected in cereal crops at Diddington T1 during summer 2011 and at Harnhill Quarry field during June 2012. However, significant contrasts using a few methods were detected in the mature oilseed rape crop at Diddington clay field in summer 2011 and in the immature pasture at Harnhill Cherry Copse in spring 2012. As in chapter 3 the most consistent methods were chlorophyll fluorescence indices and the MTBVI at wavelengths related to the red-edge inflection point and fluorescence. However, under 'difficult' conditions continuum removal also provided good results.

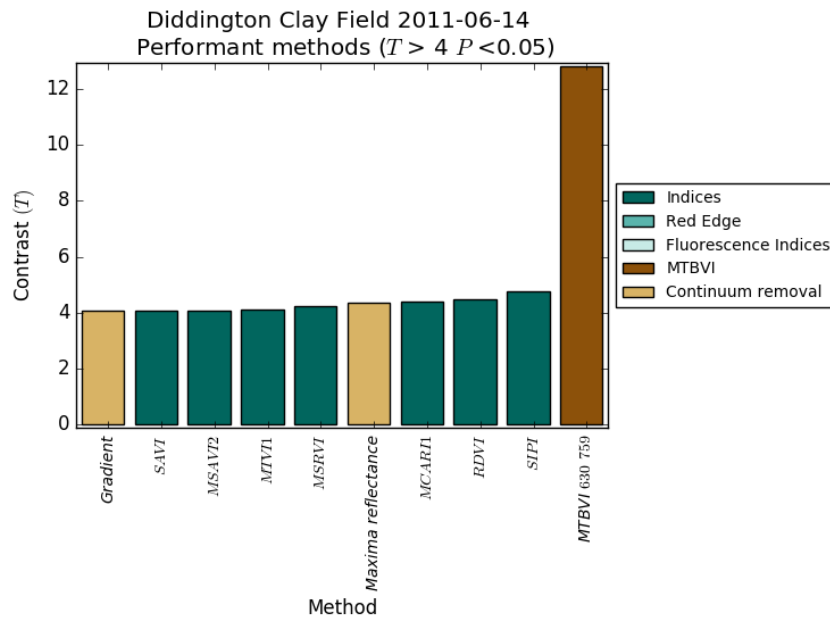


Figure 6.1: Significant results from Diddington Clay Field 14/06/2011.

6.4.2 Diddington Clay Field

6.4.2.1 2011

During 2011 DDCF was under oilseed rape. The mature crop is not generally considered conducive to vegetation mark expression. This, combined with the clay soil meant that little archaeological contrast was expected. However, the results from the 14th of June (figure 6.1) indicate strong, significant contrast in the MTBVI using wavelengths at 630nm 769nm. Reflectance at 630nm is strongly correlated with chlorophyll absorption (Gitelson, Zur, Chivkunova & Merzlyak 2002). Continuum removed reflectance at the absorption maxima and the gradient of the continuum line also indicated significant contrast. In addition, indices sensitive to chlorophyll content and biomass also detected contrast. This indicates differences in the maturity of the ripening crop, with the strong positive correlation between the MTBVI and senescence sensitive indices, indicating that the regions of greater biomass are more stressed by a shortfall in soil moisture as a result of the greater demand imposed by the higher biomass in these areas. No ground-based data were collected in this field during this period.

While encouraging, these results should be approached with caution. A number of the possible archaeological features identified as linear anomalies in the fluxgate gradiometer data are closely aligned with the cultivation patterns in the field, leading to an

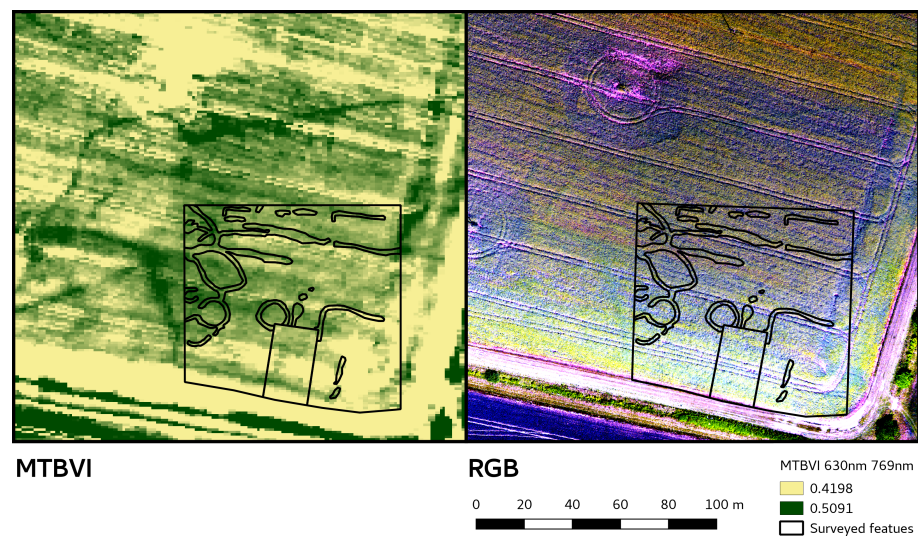


Figure 6.2: Comparison of MTBVI at 630nm & 769nm and RGB image with features from geophysical survey. In the MTBVI image further enclosure ditches are clearly visible to the north and west of the surveyed area as dark lines. Very little contrast is exhibited in the RGB image.

over-emphasis of contrast. Examination of the images in relation to the possible features confirms this. However, strong contrast is visible in relation to the features in the western part of the area. These contrasts are diffuse, and would be difficult to interpret correctly as archaeological features, likely as a result of the low spatial resolution of the sensor and low planting density of oilseed rape. More coherent features, possibly indicative of substantial enclosure ditches are visible in outside the area covered by the geophysical survey (figure 6.2).

On the 27th of June 2011 the crop was senescent and ripening. Very few methods indicated significant contrast, apart from the MTBVI using bands at 673nm and 698nm. Contrast at these wavelengths indicate chlorophyll fluorescence (Meroni et al. 2009). This probably reflects variations in the senescence of the crop, with that over the background ripening and maturing faster than that over the archaeology.

6.4.2.2 2012

During 2012 no significant contrast was observed in the AIS data in the winter wheat crop and low soil moisture deficits. This confirms the results of the ground-based data, where no significant contrast was observed for the June data and a subtle contrast in crop coverage was observed in the immature crop. As with the other airborne sensors this contrast was not resolved in the AIS data.

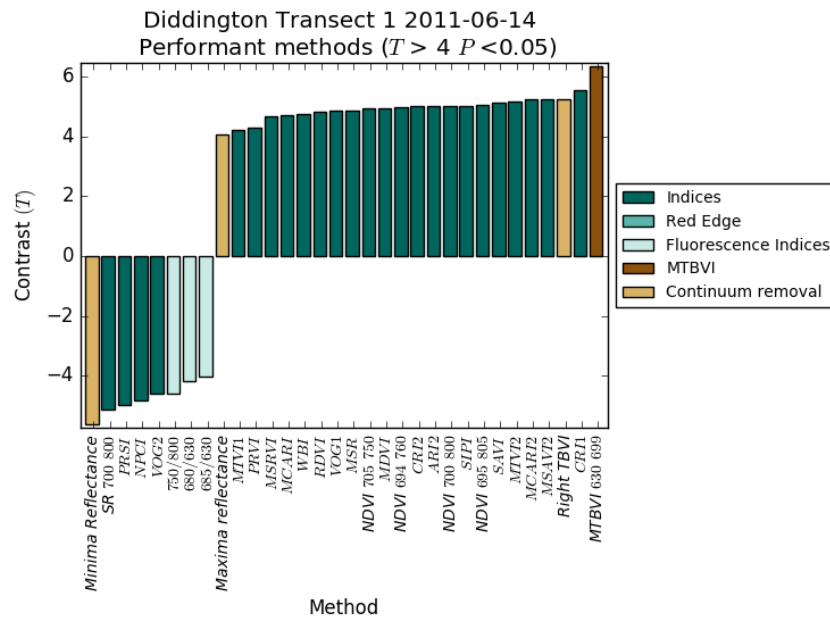


Figure 6.3: Significant results from Diddington Transect 1 14/06/2011.

6.4.3 Diddington Transect 1

6.4.3.1 2011

As with the other datasets the combination of cereal crops and high potential soil moisture deficits in June 2011 led to the expression of strong contrasts at Diddington transect 1 (figure 6.3). These contrasts were detectable using a wide variety of methods, with the MTBVI at 630 and 699nm giving the greatest significant contrast. These bands indicate the chlorophyll absorption maxima Gitelson et al. (1999). This is interesting, as the ground-based data showed the greatest contrast in the MTBVI at bands at 712nm and 714nm, indicative of shifts in the red-edge inflection point and thus chlorophyll content. This could be explained by the airborne data sampling a greater variety of features, whereas the ground-based measurements targeted only a single feature.

The airborne data was acquired closer to solar noon than the ground-based data, when the water demand of the crop, and thus also fluorescence is at its highest. The 750/800, 680/630 and 685/630 fluorescence indices all indicated significant contrasts in the AIS data. Vegetation indices sensitive to chlorophyll content, biomass, pigments and water content all demonstrated significant contrast. The index demonstrating the highest contrast was the CRI1 (Carotenoid reflectance index 1, page 39), which is sensitive to

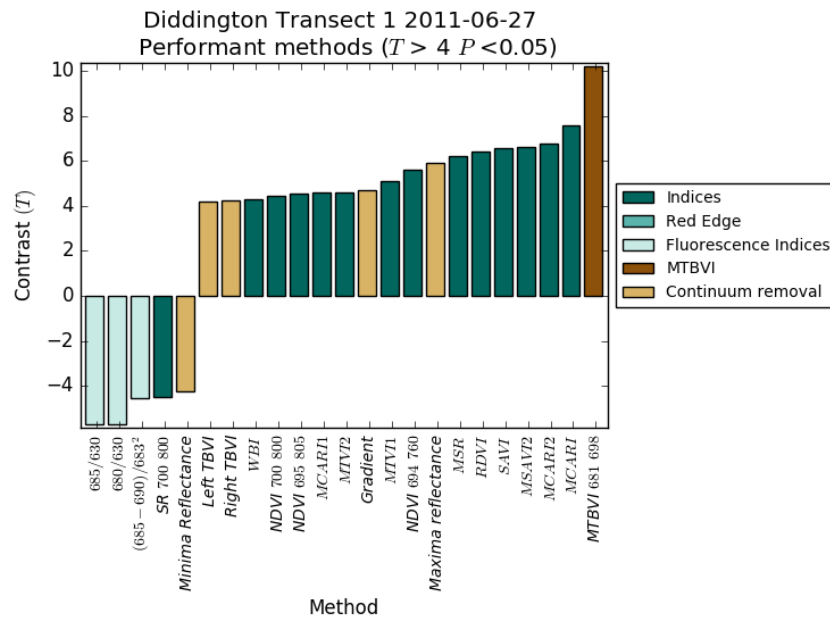


Figure 6.4: Significant results from Diddington Transect 1 27/06/2011.

carotenoid content. Carotenoids play an essential role as anti-oxidative pigments, protecting chlorophyll from photo damage, in addition to acting as accessory photosynthetic pigments (Cogdell 1978, Gitelson, Zur, Chivkunova & Merzlyak 2002). Continuum removed reflectance also performed well, with the reflectance at the absorption minima and maxima and the right TBVI all expressing significant contrasts.

On the 27th of June 2011 the ground-based data indicated less spectral contrast than the preceding survey. However, a significant biomass variation and the 'reversal' of the vegetation mark was noted, where the vegetation over the features had matured and started to ripen faster than that over the background (Riley 1987, pp. 33–35, Darvill 1996). This was not observed in the ALS data, where significant contrasts in fluorescence and biomass sensitive indices indicate that there is still a greater quantity of photosynthetic foliage over the archaeological features. The strongest contrast is again indicated by the MTBVI, this time at bands centred on 681 and 698nm, bands indicative of chlorophyll fluorescence (Meroni et al. 2009).

6.4.3.2 2012

During 2012 no contrast was visible in the oilseed rape crop in either March or June. This confirmed the results of the other survey methods, which did not find any significant

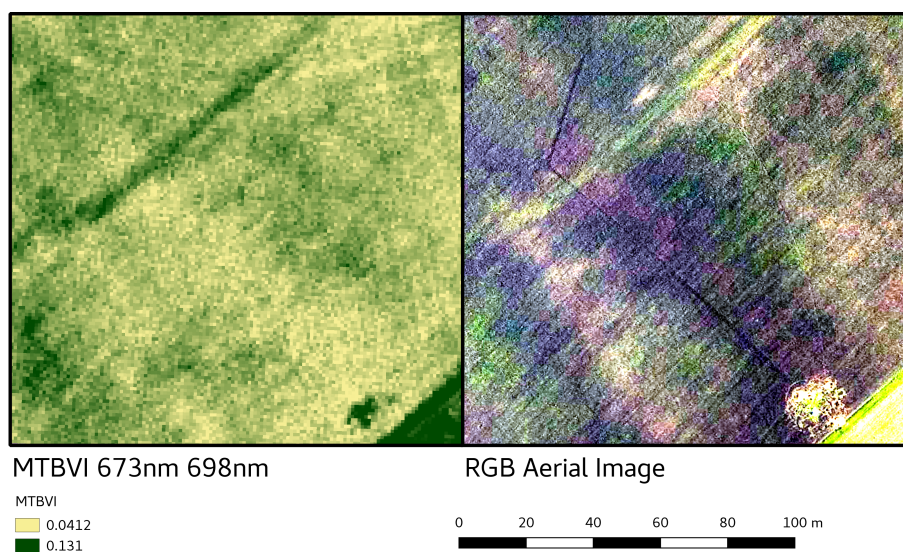


Figure 6.5: Comparison between aerial photograph and MTBVI at 673nm & 698nm. The ditch, running SE-NW through the images, is clearly visible in the RGB image, but is not observable in the hyperspectral image.

contrast other than in the spectroradiometry data from May 2012.

6.4.4 Harnhill Cherry Copse

6.4.4.1 2011

During June 2011 Cherry Copse was under spring wheat. Although no ground-based measurements could be acquired in the field a significant contrast in biomass was observed both on the ground, and in the aerial photography (see chapter 5) recorded on the same day. However, little significant contrast was observed in the AIS imagery of the wheat crop during June 2011. This is likely due to the spatial resolution of the sensor impacting its ability to resolve the feature. In the aerial photography the vegetation mark is only 0.75-1m wide, smaller than the nominal pixel size of the the interpolated imagery (figure 6.5).

6.4.4.2 2012

In March 2012 Cherry Copse was under closely grazed pasture. The ground-based survey indicated minor contrast in biomass sensitive indices, with the greatest contrast observed in the NDII index, sensitive to canopy water content. The greatest contrast was encountered in the MTBVI at 711 and 712nm, wavelengths associated with the REIP. In the airborne data the only significant contrast in the MTBVI is seen at 734 and 756nm, wave-

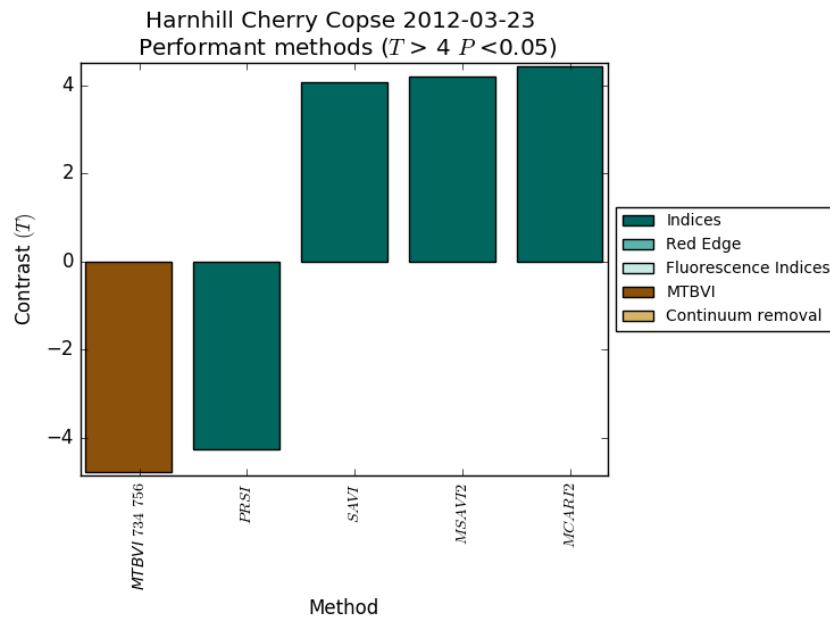


Figure 6.6: Significant results from Harnhill Cherry Copse 23/03/2012.

lengths associated with fluorescence.

In June 2012 the field was under mature pasture, with a diverse crop of grasses and flowering poppies. In the ground-based survey the strongest contrasts were observed as biomass variations, but were only detectable in the airborne data using the MTBVI at 634 and 701nm, again correlated with chlorophyll absorption. While significant contrasts were recorded for both the 2012 surveys it is again difficult to resolve the boundaries of the ditch, similar to the data for 2011. This is likely due to the spatial resolution of the sensor being too low relative to the size of the ditch.

6.4.5 Harnhill Quarry field

6.4.5.1 2011

During 2011 Quarry Field was under Spring wheat. While no ground-based survey was conducted during this period, vegetation marks from rig and furrow cultivation were detectable in the aerial photography. These marks were also detectable in the AIS data, significantly in the MTBVI at 735 and 832 nm, and in the 750/800 fluorescence index (Zarco-Tejada et al. 2012).

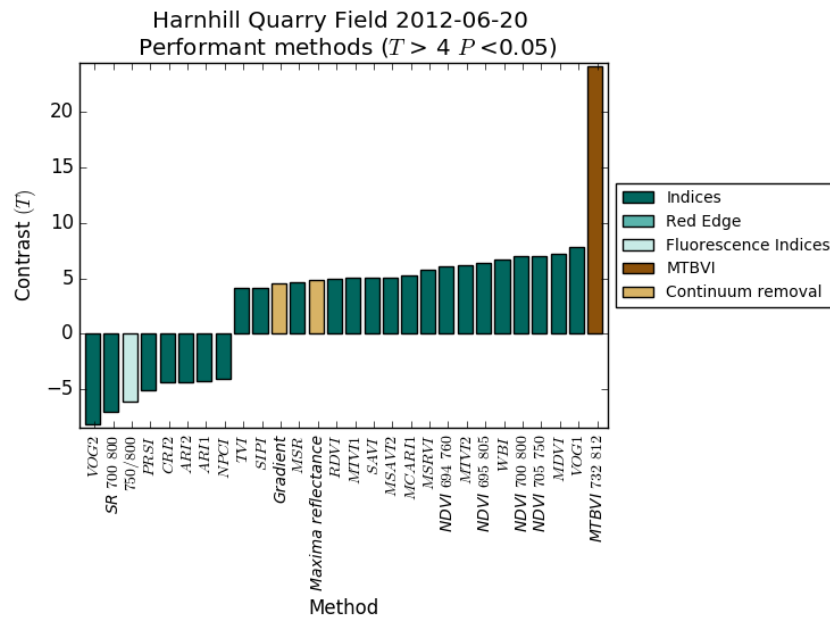


Figure 6.7: Significant results from Harnhill Quarry Field 20/06/2012.

6.4.5.2 2012

During March 2012 the site was bare soil, sown on the preceding day. Therefore there was no apparent contrast in the vegetation. During June 2012 the field was under spring wheat, with test areas of different tillage methodologies. In the ground-based data contrast was detected across a wide variety of methods, with the strongest contrast being exhibited as a positive correlation between fluorescence and the field drain measured by the transects. This correlation was not observed in the airborne data, likely as a result of a wider variety of features being recorded in the image and the field spectroscopy being recorded further from solar noon than the ALS data. In the AIS data the strongest contrast was observed in the MTBVI at 732 and 812nm, correlated with fluorescence (Meroni et al. 2009), but significant contrasts were also recorded across a wide variety of red-edge and biomass sensitive indices. In addition, significant variations in biomass were observed in the multi-temporal ALS data and biomass sensitive RGB indices.

6.5 Discussion

6.5.1 Resolution

In the introduction to this chapter it was suggested that the successful methods identified in chapter 3 for ground-based spectroscopy would not be applicable to the ALS datasets due to their lower spectral and spatial resolution. While spatial resolution limits the extent to which features can be successfully identified in the airborne data, as seen at Harnhill Cherry Copse, the lower spectral resolution seems to be less of a limiting factor to detection, and enables detection of features not observed in other datasets, as at Diddington Clay Field in June 2011. Methods reliant on near-adjacent bands in the ground-based surveys like the MTBVI were also successful. However, rather than the near adjacent bands observed to be successful for the MTBVI in the ground-based work, more widely spaced band combinations were successful here (table: 6.3).

Survey	Ground-based wavelengths	ALS wavelengths
DDT1 14/06/2011	712.0 714.0	630.0 699.0
DDT1 29/06/2011	681.0 718.0	681.0 699.0
HHCC 23/03/2012	711.0 712.0	734.0 756.0
HHCC 20/06/2012	634.0 712.0	634.0 701.0
HHQF 20/06/2012	749.0 785.0	732.0 812.0

Table 6.3: Comparison between the most successful wavelengths used for deriving the MTBVI from the ground-based and airborne data.

It should also be noted that rarely do the common NDVI combinations identified in the literature perform as well as the MTBVI, and that there is a demonstrable benefit to using a locally optimised MTBVI to obtain the best contrast in the images. However, for mapping large areas testing every combination of wavelengths in this region is not practical, as it results in a large number redundant of bands. To avoid this it is suggested that the best combinations for localised contrast are obtained for each field within in an image by first using spectral and spatial classification of the image to identify contiguous areas of the same crop. Then, within each of these the full set of MTBVI combinations are derived for sample of pixels. These are then evaluated to determine the which set of combinations produces the most heterogeneous data for each field. This workflow will be explored more thoroughly in the following chapter.

Fluorescence indices do not rely on closely spaced band combinations, but they do require bands specific enough to define the narrow emission features centred around 680 and 740nm (Meroni et al. 2009). Despite this, the broader bands from the ALS data still produced significant results. In particular, the lower spectral resolution CASI sensor produced usable contrast for indices related to the 690nm emission feature.

6.5.2 Further work

Despite the success of the airborne hyperspectral methods, using them successfully presents a number of challenges before they can be adopted widely for archaeological detection. Foremost of these is the availability of the sensors. Large area, aircraft deployed surveys are expensive, and because the systems are in high demand availability and access is limited. Given that timing is everything for vegetation mark detection this makes the airborne survey platforms operated by bodies such as NERC ARSF and Geomatics Group Ltd less than ideal for acquiring AIS data for these purposes, despite the advantage of it being possible to acquire these data in conjunction with ALS and aerial photographic imagery. However, the increasing availability of relatively inexpensive, small hyperspectral scanners capable of being deployed by Unmanned Aerial Vehicles (UAVs) could go some way to solving this problem (Aasen et al. 2015, Bareth et al. 2015, Zarco-Tejada et al. 2016), as these could be rapidly deployed according to conditions on the ground.

This would also address the second major challenge with AIS survey for archaeology, that of spatial resolution (figure 6.8). These sensors can be used at much lower altitudes than survey aircraft, and can be flown at much slower speeds. This means that data can be acquired at scales more appropriate to archaeological detection than the nominal minimum 1m spatial resolution attainable in this study. However, even fixed-wing UAVs do not have the range capable of mapping the extensive geographic areas achievable by aircraft (Colomina & Molina 2014). Therefore, it is suggested that these methods can be used in conjunction, with the lower spatial resolution datasets being used to detect sites of interest and UAVs being used to provide more detailed mapping at times when contrast is likely to be higher. Because the data considered here are co-collected with higher spatial resolution ALS and aerial photographic data it is also possible to enhance the spatial resolution of the ALS imagery by using pan-sharpening techniques, where other, spatially and spectrally correlated datasets are used to improve the spatial resolution of the ALS dataset (Cetin & Musaoglu 2009, Loncan et al. 2015). This is explored more fully in the next chapter.

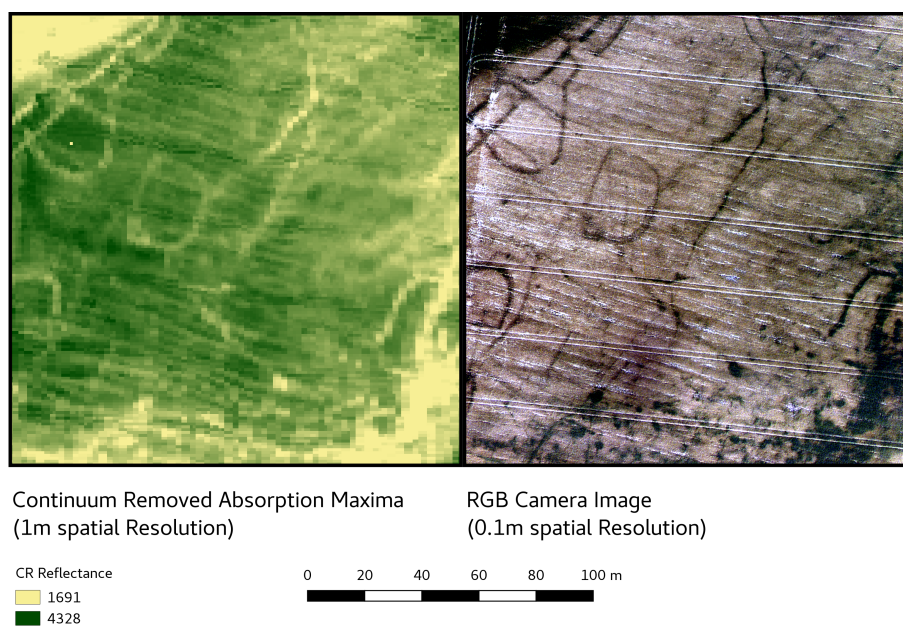


Figure 6.8: Comparison between Continuum removed reflectance at absorption maxima and the aerial photograph from Diddington Transect 1. Although some of the larger features are visible in the hyperspectral image fewer of the smaller features visible in the aerial photograph are visible.

6.6 Conclusions

This chapter has tested the novel methods successfully applied to the ground-based field spectroscopy in chapter three and tested them using the AIS data provided to the project. While these techniques provide demonstrably significant contrasts in conditions where other techniques do not, for at example Diddington Clay Field During June 2011, their utility is limited by the spatial resolution of the sensor being too low in relation to the size of the features being investigated.

Chapter 7

Conclusions

7.1 Introduction

The results of this work prove that it is possible to extend the temporal window for the detection of contrast in archaeological vegetation marks by applying the novel methods outlined in the preceding chapters. Multi-temporal biomass detection using ALS sensors and enhancement of the aerial photography using RGB reflectance ratios provide the ability to discriminate subtle contrasts resulting from feedforward responses to long-term environmental conditions. However, the greatest gains are evident in ground-based and airborne spectroscopic data, where the ability to resolve subtle differences in foliar biochemistry and metabolic processes mean that these sensors are capable of resolving contrasts that cannot be detected by other methods (figure 7.1). In particular, the ability to detect emissions resulting from chlorophyll fluorescence is important, as these are responses to short-term stresses imposed by water availability that are apparent before contrasts resulting from the regulation of vegetation structure by feedforward responses and degradation of pigments (Chaves et al. 2002, Dobrowski et al. 2005, Zarco-Tejada et al. 2009).

This concluding chapter will evaluate the results of the methods introduced in the preceding chapters, and explore how they can be integrated to further improve contrast. It will then investigate how they can be used in practice for vegetation mark detection, with specific focus on how to locally optimise the application of methods on a field by field ba-

sis. The further work section will provide recommendations for future studies of contrast, and go on to propose the development of survey systems that are specifically designed for the detection of short-term stress responses.

7.2 Evaluation of results

SITE	Date	Biomass	Chl absorption	Fluorescence	Water	Other
DDCF	14/06/11					
DDCF	27/06/11					
DDCF	20/03/12					
DDCF	24/07/12					
DDT1	06/08/11					
DDT1	14/06/11					
DDT1	29/06/11					
DDT1	15/07/11					
DDT1	16/02/12					
DDT1	22/05/12					
HHCC	27/06/11					
HHCC	17/12/11					
HHCC	14/02/12					
HHCC	23/03/12					
HHCC	24/05/12					
HHCC	19/06/12					
HHCC	25/07/12					
HHQF	27/06/11					
HHQF	29/09/11					
HHQF	20/06/12					



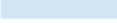
KEY:
 Significant contrast 
 Contrast expected 
 Contrast unexpected 

Figure 7.1: Summary of significant results from all sites. Dates highlighted in blue indicate sites where contrast was not (PSMD above 50mm for free draining sites and 150mm on clay soils). Indices and the MTBVI at wavelengths sensitive to chlorophyll fluorescence provide the most consistent results over a wider variety of conditions.

7.2.1 How are vegetation marks expressed?

These results show that the most consistent contrasts are detectable in feedforward responses to environmental conditions and fluorescence. While other methods provide useful contrasts, these are mostly only visible at the same times as contrasts in biomass or fluorescence. All sensors provided significant contrast, but it is evident from the ground-based and airborne spectroscopy that the hyper-spectral data shows the greatest potential to extend the temporal window for detection by permitting detection under conditions when they are not detectable with the other sensors.

7.2.1.1 Detecting environmental adaptation

Feedforward responses are the crop's means of regulating growth to avoid exceeding the capacity of its immediate environment to support the crop (Passioura 2002, Demmig-Adams et al. 2014). This means that because the soil over the archaeological features is capable of providing a greater quantity of resources, and can support a greater quantity of biomass over the archaeological features than over the unmodified subsoil when over the long term limitations are imposed by weather conditions on the the growth of the crop. This occurs during periods of high Potential Soil Moisture Deficit (PSMD) over the early part of the growth season, and creates variations in biomass.

While these have been long understood as a primary method of vegetation mark expression (Jones & Evans 1975, Evans & Jones 1977), this study has refined methods for their detection, especially using the multi-temporal Canopy Surface Model (CSM) introduced in chapter 4. This provides greater definition of these contrasts than either the aerial photography or the hyperspectral data, and given the independence of the method from illumination conditions it represents a useful addition to the range of techniques available to archaeologists. However, where these variations are visible in the ALS data they are also accompanied by contrasts in in the spectral data, other than in senescent crops. The utility of this technique appears to be limited in very dense canopies, such as the hay meadow at Harnhill Cherry Copse and the oilseed rape crop at Diddington Clay Field during 2011, despite contrast being evident in biomass sensitive spectral measurements.

While lacking the clarity of the CSM method, spectral detection of biomass contrast in both the RGB and ALS imagery provide useful contrasts. in particular continuum removed reflectance of the 670nm absorption feature and indices sensitive to chlorophyll absorption. While contrast from biomass using these methods is conflated with pigment contents and red-edge effects they provide a useful means of detecting contrast in Leaf Area Index (LAI) if other methods are not available (Carlson & Ripley 1997, Broge & Leblanc 2001).

7.2.1.2 Detecting short-term stress responses

Fluorescence sensitive methods afford the opportunity to detect short-term responses to resource availability, providing the opportunity to detect contrast before feedforward responses regulate growth or long-term damage occurs to photosynthetic capacity of the crop (Carter & Miller 1994, Zarco-Tejada et al. 2000, Meroni et al. 2009, Zarco-Tejada

et al. 2003, 2009). This is important, as it extends the potential of vegetation mark detection in soils and crops where other contrasts are not evident. The locally optimised MTBVI index performed particularly well under these conditions, returning significant contrasts at wavelengths relate to fluorescence even when indices designed for detecting chlorophyll fluorescence did not.

While the application of fluorescence sensitive indices to archaeological detection in this study is novel, a number of previous studies using principal components analyses and first derivative methods have identified bands that overlap with wavelengths related to chlorophyll fluorescence as being effective for detection without identifying causation Challis et al. (2009). In particular, contrast identified as being resultant from shifts in the red-edge inflection point using first derivative spectra potentially conflate red-edge reflectance and fluorescence emissions.

Adopting fluorescence as a method for archaeological detection requires a fundamental rethink of the how the fundamental principles of remote sensing are applied to vegetation marks. Most studies examine the problem in terms of reflectance and absorption by pigments and expressions of stress and vigour (Bennett et al. 2013, Doneus et al. 2014, Agapiou et al. 2013), however, the complexity of active biological process mean this is an oversimplification of the problem. Understanding that instead contrast using this method is the result of emissions indicative of the metabolic responses of plants to their environment affords possibilities to expand the utility of this method by refining the design of affordable systems designed especially for detecting short term, transient contrasts.

7.2.1.3 Detecting long-term damage

Long-term damage to the photosynthetic capability of the crop occurs when a paucity of resources lead to damage and impaired synthesis of pigments in the foliage and the initiation of protective mechanisms such as the xanthophyll cycle (Peuelas et al. 1994, Kov et al. 2013). The latter are detectable in the 470nm absorption feature and in indices designed for their detection. Impaired photosynthesis as a result of long term damage to the photosynthetic pigments is expressed in the position of the REIP and reflectance in this region. The REIP and indices designed for its detection have been identified as one the best ways of detecting contrast in vegetation marks (Agapiou et al. 2010, Verhoeven & Doneus 2011, Verhoeven et al. 2013, Doneus et al. 2014), however, as discussed above this may be because it is conflated with chlorophyll fluorescence (Cho & Skidmore 2006). Contrast indicative of longer-term stress is only visible during fairly extreme conditions,

in particular at Diddinton T1 during June 2011. While these contrasts are usable, they are accompanied by stronger contrasts in biomass, indicating that by the time these stresses are manifest feedforward responses have already affected development of the crop.

7.2.2 Limitations

This study has a number of limitations that must be addressed. Foremost among these is the lack of comparability between the different study sites. Measurements were recorded over different features, crops, soils and weather without enough temporal depth to record contrasts in a way that makes comparison between these different casual factors possible. Although this was not the main focus of this work, this is problematic, as it does not enable a broad enough variety of conditions to be investigated and compared. A better experimental design would plant strips of different crops across the same features under different soil conditions. This would enable evaluation of contrast in different crops under similar soil and weather conditions. Obviously this is would be expensive, as it essentially requires land management practices to be dictated by the requirements of the archaeological investigations.

The second limitation was time. Greater temporal depth would enable a better, more comprehensive investigation across a greater variety of weather conditions. The two seasons measured were respectively extremes of dry and wet weather, and cannot be considered representative of normal conditions. In addition, more intensive temporal sampling would have enabled the investigation of short duration contrasts in greater detail. However, this was not possible given the requirements of site access and weather conditions. The latter is particularly a problem for recording spectral data, as these require perfect weather conditions rarely encountered in temperate climates.

As demonstrated in the previous chapter, the low spatial resolution and restricted availability of the AIS sensors is a limitation to their utility for archaeological detection. To be truly useful for these purposes either better sensors or slower aircraft are required. These also need to be available at short notice, so that they can be deployed rapidly in response to favourable conditions.

7.3 Further work

7.3.1 Optimising contrast in the airborne datasets

So far this work has considered how to maximise contrast for individual datasets. This was achieved by identifying the techniques providing the best contrast over known archaeological features. These results show that locally optimising contrast to specific crop and soil conditions is essential. To be useful for detection in areas where there are no known features it is not practical to examine every technique without *a-priori* knowledge, especially with the many permutations of the MTBVI. In addition, thus far only one sensor at a time has been considered, but by integrating data from different techniques it may be possible to improve contrast further.

7.3.1.1 Local optimisation

Assessing where the best contrasts are likely to be found in the data requires examining the data at a local scale. Deriving every permutation of every technique for high-spectral resolution datasets represents a high degree of unnecessary computation. In addition, choosing the best method from such a large number of datasets is not trivial. It is suggested that this is addressed by processing subsets of from the data, and evaluating each for variability to select the appropriate methods for evaluating contrast over the entire dataset. Given the complexity and variation of contrast in images as a result of crops and soils it is proposed that this be performed on a field level. Figure 7.2 details a proposed workflow for this process.

First, within each field a number of random points are generated within the field. These are then buffered with a spatial extent appropriate the spatial resolution of the source data. These are used to extract spectra using the intersection between the source raster and the buffered points, and then processed using all the available processing techniques. The variance of values in each technique is then evaluated, as the best technique is the one likely to provide the greatest heterogeneity in the crop canopy. The best techniques are then applied to the the full image. Figure 7.3 demonstrates how this can be applied to identify MTBVI values in areas where little is known about archaeological features.

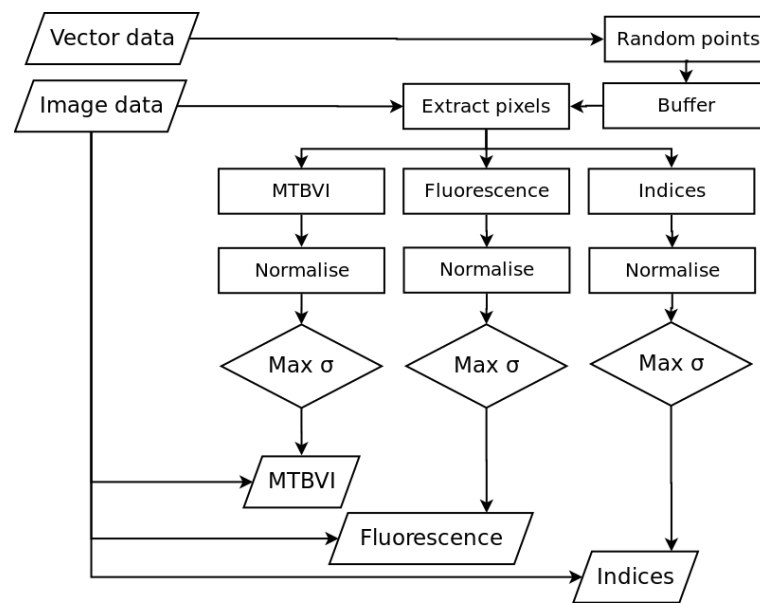


Figure 7.2: Suggested workflow for optimisation of AIS data. The full range of methods are applied to randomly sampled points within each field. These are then normalised and the methods with the highest variance in the subsets are used to select and process methods for archaeological detection.

7.3.1.2 Data fusion

Each of the different sensors reveal different properties of the crop, emphasising different foliar properties. This makes interpretation complex, as none of the datasets individually provides all the information pertinent to detection. This can be addressed by applying data fusion techniques, which enable different datasets to be integrated and displayed simultaneously for qualitative rather than quantitative interpretation. False-colour composites are the most commonly applied techniques for achieving this for spectral data, where a combination of wavelength bands are mapped to the RGB channels of the computer display (Haack & Jampoler 1995, Du et al. 2008). In addition, overlay of datasets can be achieved using transparency and vector layers derived from further datasets, such as contours and hill shading (Kvamme 2006).

Data fusion techniques can be also used to address the shortcomings for individual sensors, for example, the low spectral resolution of the AIS imagery can be supplemented using the higher resolution ALS and RGB imagery. This technique, designated as pan-sharpening, is commonly used in satellite remote sensing to improve lower spatial resolution multi-spectral bands with a higher spatial resolution panchromatic band sensitive to a broad range of wavelengths (Loncan et al. 2015). These techniques have been applied

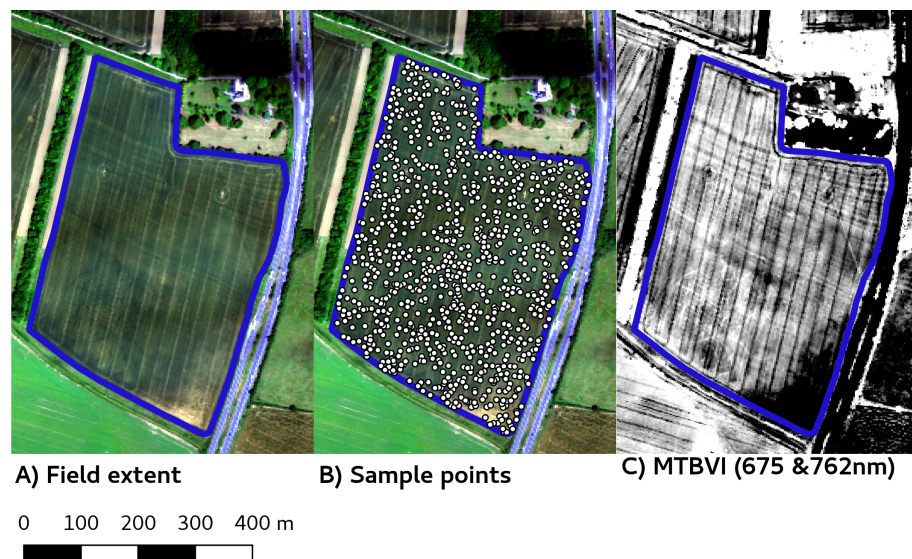


Figure 7.3: Optimisation workflow applied to field at Diddington 14/06/2011. An extent polygon for the field (A) is used to contain 1000 random points, to which are applied a 5m buffer (B). The pixels intersecting the buffered points are used to derive the MTBVI, and the band combinations showing the greatest variance are used to derive the MTBVI for the whole field (C).

for archaeological prospection, mostly for improving the spatial resolution of satellite imagery (Beck, Philip, Abdulkarim & Donoghue 2007, De Laet et al. 2009, Lasaponara & Masini 2012, Noviello et al. 2013). While the techniques are useful, they can introduce both spatial and spectral distortions in the data, and the various methods used represent a trade-off between spatial acuity and spectral accuracy (Du et al. 2007, Ehlers et al. 2010, Loncan et al. 2015, Vivone et al. 2015). The simplest application of these methods simply transform three bands of the image using an Hue Saturation Intensity (HSI) transformation for the lower spatial resolution dataset and substitute the intensity with the panchromatic image (Winter & Winter 2002, Rahmani et al. 2010). To preserve the original number of bands in the original spectral image more complex methods are used to correlate reflectance in each of the bands with the intensity of the panchromatic image, including wavelet transformations (Pradhan et al. 2006, Zhang et al. 2009) and PCA decomposition (Shah et al. 2008, Licciardi et al. 2012, Palsson et al. 2015).

Further data fusion techniques for emphasising contrast for the interpretation of archaeological datasets from diverse sources are proposed by Kvamme (2006). These are applied to various geophysical and airborne data, and considerably improve the interpretability of

data from various sources using both boolean and continuous methods. For the former, binary thresholds are applied to the individual datasets to identify possible features above predetermined minima. The sums of these binary datasets can be used to indicate consensus between the different datasets. The continuous methods use normalised data from the sensors together to present a wider range of values. The methods suggested were sum of values, value at each pixel, the product of the values, PCA and logistic regression classifiers.

In the work considered here the focus is on recording variability in the vegetation canopy. This means that the methods used for investigating contrast are, in general highly correlated, and this makes them highly suitable for the application of these approaches. However, approaches using thresholding and classification are not suitable, given the variability of the contrast in the same field. Using false-colour composites of pan-sharpened AIS, ALS derived CSM data and RGB ratios provide means of both enhancing contrast and preserving the continuous range of variation across the image. For example, at Harnhill Quarry field in June 2011 the strongest contrast in the AIS data was observed in the MTBVI. This was most strongly correlated with the VARI index in the RGB data, so this was used to pan-sharpen the MTBVI (table 7.1. This, the ALS derived CSM and the NGRI were then mapped to separate colour channels of the image. The resulting composite demonstrates contrasts not visible in the individual datasets (figure 7.4).

	MTBVI	CSM	NDGRI	VARI
MTBVI	1	0.55	0.68	0.69
CSM	0.55	1	0.35	0.39
NDGRI	0.68	0.35	1	0.98
VARI	0.67	0.39	0.98	1

Table 7.1: R values from Spearman's Rank correlation between methods used for data fusion. Harnhill Quarry Field 20/06/2012.

7.3.2 Designing better systems

The low spatial resolution and temporal inflexibility of the hyperspectral data considered here mean it is not practical for detection, as both higher resolutions and greater responsiveness to changing conditions are required. However, the results from this study have demonstrated that the full spectral resolution of the hyperspectral sensor is not required

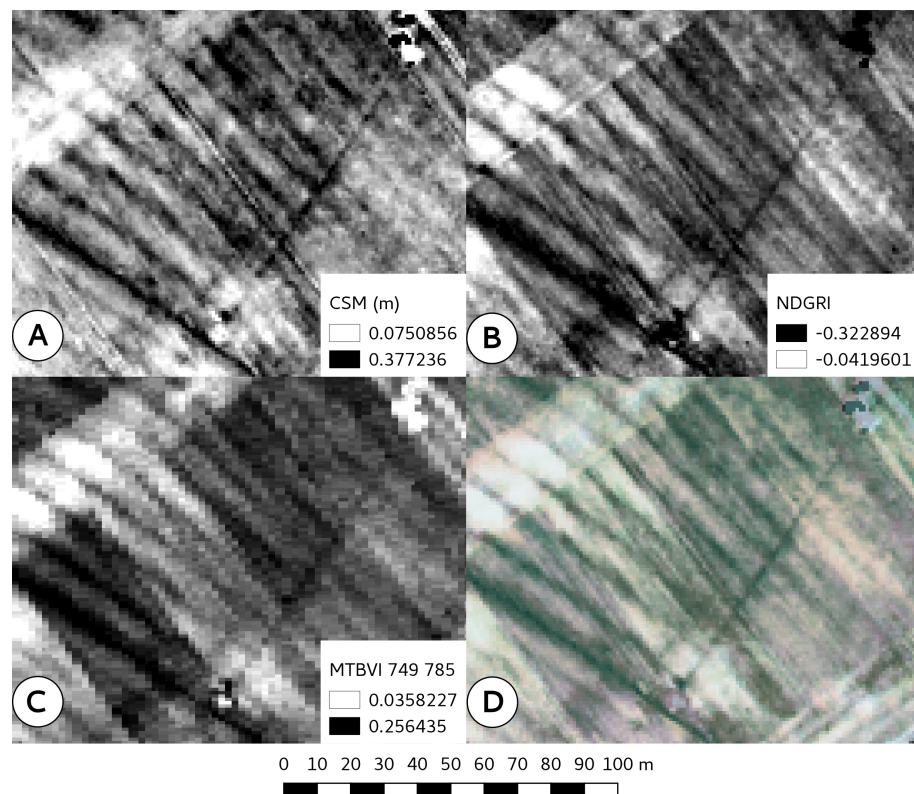


Figure 7.4: Example of the application of data fusion techniques to the methods considered here. *A)* ALS derived CSM. *B)* RGB derived NDGRI. *C)* AIS derived MTBVI. Note the variability of contrast in the crop in all three methods. *D)* False colour composite. Red is the MTBVI pan-sharpened using the VARI index applied to the RGB image, Green is the ALS derived CSM up-sampled to the same spatial resolution as the the RGB image and Blue is the RGB derived NDGRI.

for archaeological detection. Only a few bands are required to detect variations in chlorophyll fluorescence and biomass.

This afford the opportunity for smaller, more inexpensive systems capable of being deployed using Uanmanned Aerial Vehicles (UAVs) or light aircraft at short notice. There are two approaches to this. The first uses consumer cameras adapted for sensitivity in the red and near-infrared by applying interference filtering to provide relatively narrow spectral bands in the near infrared. This approach has been adotped by Verhoeven & Sevara (2016), who suggest 30nm wide bands centred on 550nm, 705nm, and 820nm in addition to broad-band RGB reflectance. These are sensitive to the green peak, the red-edge and the near-infrared shoulder respectively. However, the results of work indicate the fluorescence affords the greatest opportunity to improve the temporal flexibility of detection. Therefore it is suggested that bands sensitive to fluorescence centred on the

peaks at 690nm and 740nm are used instead, with a third band centred on 720nm used to provide sensitivity to the red-edge at a wavelength not sensitive to fluorescence (see figure 3.24, page 97).

The second approach to vegetation monitoring is to use a lightweight hyperspectral imaging system. High demand for these systems in recent years has led to decreasing cost (Hill & Clemens 2015, Tiwari & Dixit 2015, Bareth et al. 2015). For example, the BaySpec OCI-UAV camera is capable of recording 100 bands at wavelengths between 600 and 1000nm in a 2048 pixel wide swath, with a total system weight under 500g (BaySpec Inc. 2016). These developments have led to a large number of recent studies using these sensors on UAVs for environmental monitoring (e.g. Aasen et al. 2015, Bareth et al. 2015, Tailanián et al. 2015, Constantin et al. 2015). A number of studies have assessed the utility of these sensors for detection of fluorescence (Zarco-Tejada et al. 2013, 2016, Calderón Madrid et al. 2013). These systems have great potential for archaeological detection, but their comparatively low spatial resolution necessitates flying at lower altitudes, limiting the areas that can be covered with the sensors.

In addition to the possibility of using these sensors to record spectral properties the integration of frame cameras in these system means that deriving CSMs is possible using structure from motion and related imaging techniques (Bendig et al. 2014, 2015, Verhoeven & Vermeulen 2016), enabling detailed recording of contrasts in biomass.

7.3.2.1 Extending the spectral range

The airborne component of this study has considered sensors operating in the visible to near-infrared regions of the spectrum. However, the ground-based work also indicates that contrast is expressed in the Shortwave Infrared (SWIR) in absorption features sensitive to canopy water content (Clevers et al. 2008). These could be further exploited in the airborne data. NIR-SWIR Hawk hyperspectral imaging was collected as a part of this study, however, the nominal spatial resolution of 15m mean that the spatial resolution of the data was too coarse for archaeological detection.

Thermal infrared imaging could also provide a useful means of detecting contrast, as this can be used as a measure of transpiration, which may be useful as a further short-term stress indicator (Chaerle et al. 2007, Grant et al. 2007, Jones et al. 2009, Alchanatis et al.

2010). This has been used for the detection archaeological vegetation marks by Poirier et al. (2013).

Bibliography

- Aasen, H., Burkart, A., Bolten, A. & Bareth, G. (2015), 'Generating 3d hyperspectral information with lightweight uav snapshot cameras for vegetation monitoring: From camera calibration to quality assurance', *ISPRS Journal of Photogrammetry and Remote Sensing* **108**, 245–259.
- Adams, J., Parulski, K. & Spaulding, K. (1998), 'Color processing in digital cameras', *IEEE micro* **18**(6), 20–30.
- Adler-Golden, S., Berk, A., Bernstein, L., Richtsmeier, S., Acharya, P., Matthew, M., Anderson, G., Allred, C., Jeong, L. & Chetwynd, J. (1998), Flaash, a modtran4 atmospheric correction package for hyperspectral data retrievals and simulations, in 'Proc. 7th Ann. JPL Airborne Earth Science Workshop', pp. 9–14.
- Agache, R. (1962), *Vues aériennes de la Somme et recherche du passé*, Société Préhistorique du Nord.
- Agache, R. (1964), 'La prospection aérienne sur sols nus et l'inventaire archéologique de la somme', *Actes du colloque international d'archéologie aérienne* pp. 49–58.
- Agache, R. (1968), 'Essai d'utilisation aérienne et au sol de démodulations spectrozonales, dites infrarouges couleurs', *Bulletin de la Société Préhistorique Française* **65**, 198–200.
- Agapiou, A., Hadjimitsis, D. & Alexakis, D. (2012), 'Evaluation of broadband and narrowband vegetation indices for the identification of archaeological crop marks', *Remote Sensing* **4**(12), 3892–3919.
- Agapiou, A., Hadjimitsis, D. G., Sarris, A., Georgopoulos, A. & Alexakis, D. D. (2013), 'Optimum temporal and spectral window for monitoring crop marks over archaeological remains in the mediterranean region', *Journal of Archaeological Science* **40**(3), 1479–1492.

- Agapiou, A., Hadjimitsis, D., Sarris, A., Themistocleous, K. & Papadavid, G. (2010), Hyperspectral ground truth data for the detection of buried architectural remains, *in* 'Digital Heritage', Springer, pp. 318–331.
- Agisoft, L. (2013), 'Agisoft photoscan user manual. professional edition, version 0.9. 0'.
- Aiken, R. & Smucker, A. (1996), 'Root system regulation of whole plant growth 1', *Annual review of phytopathology* **34**(1), 325–346.
- Alam, S. M. (1999), 'Nutrient uptake by plants under stress conditions', *Handbook of plant and crop stress* **2**, 285–313.
- Alberte, R. S., Thornber, J. P. & Fiscus, E. L. (1977), 'Water stress effects on the content and organization of chlorophyll in mesophyll and bundle sheath chloroplasts of maize', *Plant Physiology* **59**(3), 351–353.
- Alchanatis, V., Cohen, Y., Cohen, S., Moller, M., Sprinstin, M., Meron, M., Tsipris, J., Saranga, Y. & Sela, E. (2010), 'Evaluation of different approaches for estimating and mapping crop water status in cotton with thermal imaging', *Precision Agriculture* **11**(1), 27–41.
- Allen, G. W., Bradford, J., Crawford, O., RILEY, D. & EDWARDS, D. (1984), 'Discovery from the air', *Aerial Archaeology East Dereham* **10**, 1–92.
- Almeida, T. I. R. & Filho, D. S. (2004), 'Principal component analysis applied to feature-oriented band ratios of hyperspectral data: A tool for vegetation studies', *International Journal of Remote Sensing* **25**(22), 5005–5023.
- Analytical Spectral Devices, I. (2002), 'FieldSpec Pro User's Guide'.
URL: <http://support.asdi.com/Document/FileGet.aspx?f=600000.PDF>
- Andjar, D., Escol, A., Rosell-Polo, J. R., Fernandez-Quintanilla, C. & Dorado, J. (2013), 'Potential of a terrestrial LiDAR-based system to characterise weed vegetation in maize crops', *Computers and Electronics in Agriculture* **92**, 11–15.
- Aqduş, S. A., Drummond, J. & Hanson, W. S. (2008), 'Discovering archaeological cropmarks: a hyperspectral approach', *Int. Arch. Photogramm. Remote Sens. Spat. Inf. Sci* pp. 361–366.
- Aqduş, S. A., Hanson, W. S. & Drummond, J. (2012), 'The potential of hyperspectral and multi-spectral imagery to enhance archaeological cropmark detection: a comparative study', *Journal of Archaeological Science* **39**(7), 1915–1924.

- Armbrust, D. (1990), 'Rapid measurement of crop canopy cover', *Agronomy Journal* **82**(6), 1170–1171.
- Armitage, R. P., Alberto Ramirez, F., Mark Danson, F. & Ogunbadewa, E. Y. (2013), 'Probability of cloud-free observation conditions across great britain estimated using MODIS cloud mask', *Remote Sensing Letters* **4**(5), 427–435.
- Ashraf, M. & Harris, P. J. C. (2013), 'Photosynthesis under stressful environments: An overview', *Photosynthetica* **51**(2), 163–190.
- Asner, G. P. & Lobell, D. B. (2000), 'A biogeophysical approach for automated swir unmixing of soils and vegetation', *Remote sensing of environment* **74**(1), 99–112.
- Asrar, G., Fuchs, M., Kanemasu, E. & Hatfield, J. (1984), 'Estimating absorbed photosynthetic radiation and leaf area index from spectral reflectance in wheat', *Agronomy journal* **76**(2), 300–306.
- Atkinson, C. J., Fitzgerald, J. D. & Hipps, N. A. (2010), 'Potential mechanisms for achieving agricultural benefits from biochar application to temperate soils: a review', *Plant and Soil* **337**(1-2), 1–18.
- Atkinson, R. (1957), 'Worms and weathering', *Antiquity* **31**(124), 219–233.
- Atwell, B. J. (1990), 'The effect of soil compaction on wheat during early tillering', *New Phytologist* **115**(1), 29–35.
- Awange, J. L. & Kiema, J. B. K. (2013), Optical remote sensing, in 'Environmental Geoinformatics', Springer, pp. 119–132.
- Babaud, J., Witkin, A. P., Baudin, M. & Duda, R. O. (1986), 'Uniqueness of the gaussian kernel for scale-space filtering', *IEEE Transactions on pattern analysis and machine intelligence* (1), 26–33.
- Baltsavias, E. P. (1999), 'Airborne laser scanning: basic relations and formulas', *ISPRS Journal of photogrammetry and remote sensing* **54**(2), 199–214.
- Barber, C. B., Dobkin, D. P. & Huhdanpaa, H. (1996), 'The quickhull algorithm for convex hulls', *ACM Transactions on Mathematical Software (TOMS)* **22**(4), 469–483.
- Barber, M. (2014), *Stonehenge World Heritage Site Landscape Project: 'Restoring' Stonehenge 1881-1939*, English Heritage.

- Baret, F. & Guyot, G. (1991), 'Potentials and limits of vegetation indices for LAI and APAR assessment', *Remote sensing of environment* **35**(2), 161–173.
- Bareth, G., Aasen, H., Bendig, J., Gnyp, M. L., Bolten, A., Jung, A., Michels, R. & Soukkamäki, J. (2015), 'Low-weight and uav-based hyperspectral full-frame cameras for monitoring crops: Spectral comparison with portable spectroradiometer measurements', *Photogrammetrie-Fernerkundung-Geoinformation* **2015**(1), 69–79.
- Barken, L. R., Bsrresen, T. & Njss, A. (1987), 'Effect of soil compaction by tractor traffic on soil structure, denitrification, and yield of wheat (*triticum aestivum* l.)', *Journal of Soil Science* **38**(3), 541–552.
- Barker, A. V. & Pilbeam, D. J. (2010), *Handbook of plant nutrition*, Vol. 117, CRC press.
- Barnes, J. D., Balaguer, L., Manrique, E., Elvira, S. & Davison, A. W. (1992), 'A reappraisal of the use of DMSO for the extraction and determination of chlorophylls a and b in lichens and higher plants', *Environmental and Experimental Botany* **32**(2), 85–100.
- Barraclough, P. B. (1989), 'Root growth, macro-nutrient uptake dynamics and soil fertility requirements of a high-yielding winter oilseed rape crop', *Plant and Soil* **119**(1), 59–70.
- Bates, L. & Hall, A. (1981), 'Stomatal closure with soil water depletion not associated with changes in bulk leaf water status', *Oecologia* **50**(1), 62–65.
- Batey, T. & McKenzie, D. (2006), 'Soil compaction: identification directly in the field', *Soil Use and Management* **22**(2), 123–131.
- Bayer, B. E. (1976), 'Color imaging array'. US Patent 3,971,065.
- BaySpec Inc. (2016), 'OCI UAV Airborne Hyperspectral Camera - BaySpec'.
URL: <http://www.bayspec.com/spectroscopy/oci-uav-hyperspectral-camera/>
- Beck, A. (2011), 'Archaeological applications of multi/hyper-spectral data—challenges and potential', *Remote sensing for archaeological heritage management* pp. 87–97.
- Beck, A., Philip, G., Abdulkarim, M. & Donoghue, D. (2007), 'Evaluation of corona and ikonos high resolution satellite imagery for archaeological prospection in western syria', *Antiquity* **81**(311), 161–175.

- Beck, A. R. (2007), Archaeological site detection: the importance of contrast, *in* 'Proceedings of the 2007 Annual Conference of the Remote Sensing and Photogrammetry Society'.
- Beck, A., Wilkinson, K. & Philip, G. (2007), Some techniques for improving the detection of archaeological features from satellite imagery, *in* 'Remote Sensing', pp. 674903–674903.
- Bendig, J., Bolten, A., Bennertz, S., Broscheit, J., Eichfuss, S. & Bareth, G. (2014), 'Estimating biomass of barley using crop surface models (csms) derived from uav-based rgb imaging', *Remote Sensing* **6**(11), 10395–10412.
- Bendig, J., Yu, K., Aasen, H., Bolten, A., Bennertz, S., Broscheit, J., Gnyp, M. L. & Bareth, G. (2015), 'Combining uav-based plant height from crop surface models, visible, and near infrared vegetation indices for biomass monitoring in barley', *International Journal of Applied Earth Observation and Geoinformation* **39**, 79–87.
- Bennett, R. (2011), Archaeological Remote Sensing: Visualisation and analysis of grass-dominated environments using airborne laser scanning and digital spectra data, PhD thesis, Bournemouth University.
- Bennett, R., Welham, K., Hill, R. A. & Ford, A. (2011), 'Making the most of airborne remote sensing techniques for archaeological survey and interpretation', *Remote Sensing for Archaeological Heritage Management* pp. 99–107.
- Bennett, R., Welham, K., Hill, R. A. & Ford, A. (2013), 'Airborne spectral imagery for archaeological prospection in grassland environments an evaluation of performance', *Antiquity* **87**(335), 220–236.
- Bennett, R., Welham, K., Hill, R. A. & Ford, A. L. J. (2012), 'The application of vegetation indices for the prospection of archaeological features in grass-dominated environments: Application of vegetation indices in grass-dominated environments', *Archaeological Prospection* **19**(3), 209–218.
- Berry, P., Cook, S., Ellis, S., Gladders, P. & Roques, S. (2014), The oilseed rape growth guide, Technical report, Home Grown Cereals Association.
- Bewley, B. (2001), 'Understanding England's historic landscapes: an aerial perspective', *Landscapes* **2**(1), 74–84.

- Bewley, R. (1993), Aerial photography for archaeology, in J. Hunter & I. Ralston, eds, 'Archaeological Research Management in the UK', Alan Sutton/IFA, pp. 197–204.
- Bewley, R. (1999a), *Archiving aerial photography and remote sensing data: a guide to good practice*, Vol. 2, Oxbow Books Limited.
- Bewley, R. H. (1999b), 'Understanding englands landscapes: An aerial survey approach to a national mapping programme for england', *BAR INTERNATIONAL SERIES* **750**, 185–188.
- Blankenship, R. E. (2008), *Molecular Mechanisms of Photosynthesis*, Wiley.
- Boddice, D. (2015), Changing geophysical contrast between archaeological features and surrounding soil, PhD thesis, University of Birmingham.
- Bonham-Carter, G. F. (1988), 'Numerical procedures and computer program for fitting an inverted gaussian model to vegetation reflectance data', *Computers & Geosciences* **14**(3), 339–356.
- Boochs, F., Kupfer, G., Dockter, K. & KHbauch, W. (1990), 'Shape of the red edge as vitality indicator for plants', *International Journal of Remote Sensing* **11**(10), 1741–1753.
- Bourgeois, J., Roovers, I., Meganck, M., Semey, J., Pelegrin, R. & Lodewijckx, M. (2002), Flemish aerial archaeology in the last 20 years: past and future perspectives, in 'NATO Advanced Research Workshop on Aerial Archaeology', Vol. 337, IOS Press, pp. 76–83.
- Braasch, O. (2014), 'Daten und gedanken zur luftbildarchäologie in baden-württemberg', *Denkmalpflege in Baden-Württemberg-Nachrichtenblatt der Landesdenkmalpflege* **19**(4), 149–155.
- Briese, C., Doneus, M. & Verhoeven, G. (2013), Radiometric calibration of als data for archaeological interpretation, in 'Wolfgang Neubauer, Immo Trinks, Roderick B. Salisbury und Christina Einwgerer (Hg.): Archaeological Propection. Proceedings of the 10th International Conference-Vienna. Wien: Verl. der sterr. Akad. d. Wiss., S', pp. 427–429.
- Briese, C., Pfennigbuar, M., Ullrich, A. & Doneus, M. (2013), Multi-wavelength airborne laser scanning for archaeological prospection, in 'International Archives of the Photogrammetry, Remote Sensing and Spatial Information Sciences, Volume XL-5/W2-

2013. XXIV International CIPA Symposium 2-6 September 2013, Strasbourg, France', pp. 119–124.
- Broge, N. H. & Leblanc, E. (2001), 'Comparing prediction power and stability of broadband and hyperspectral vegetation indices for estimation of green leaf area index and canopy chlorophyll density', *Remote Sensing of Environment* **76**(2), 156–172.
- Brophy, K. (2005), 'Subjectivity, bias and perception in aerial archaeology'.
- Brown, A. G., Carey, C., Challis, K., Howard, A., Kincey, M., Tetlow, E. & Cooper, L. (2007), 'Predictive modelling of multi-period geoarchaeological resources at a river confluence', *Phase II Report. PNUM* **3357**.
- Brown, J. S. (1983), 'A new evaluation of chlorophyll absorption in photosynthetic membranes', *Photosynthesis research* **4**(1), 375–383.
- Buddenbaum, H., Seeling, S. & Hill, J. (2013), 'Fusion of full-waveform lidar and imaging spectroscopy remote sensing data for the characterization of forest stands', *International Journal of Remote Sensing* **34**(13), 4511–4524.
- Buhtz, A., Pieritz, J., Springer, F. & Kehr, J. (2010), 'Phloem small rnas, nutrient stress responses, and systemic mobility', *BMC plant biology* **10**(1), 64.
- Bukovac, M. & Wittwer, S. (1957), 'Absorption and mobility of foliar applied nutrients.', *Plant physiology* **32**(5), 428.
- Burt, T. & Butcher, D. (1985), 'Topographic controls of soil moisture distributions', *Journal of Soil Science* **36**(3), 469–486.
- Butzer, K. W. (1982), *Archaeology as human ecology: method and theory for a contextual approach*, Cambridge University Press.
- Calder, I. R., Harding, R. J. & Rosier, P. T. W. (1983), 'An objective assessment of soil-moisture deficit models', *Journal of Hydrology* **60**(1), 329–355.
- Calderón Madrid, R., Navas Cortés, J. A., Lucena León, C. & Zarco-Tejada, P. J. (2013), 'High-resolution hyperspectral and thermal imagery acquired from uav platforms for early detection of verticillium wilt using fluorescence, temperature and narrow-band indices'.
- Campbell, J. B. & Wynne, R. H. (2011), *Introduction to remote sensing*, Guilford Press.

- Canadell, J., Jackson, R. B., Ehleringer, J. B., Mooney, H. A., Sala, O. E. & Schulze, E.-D. (1996), 'Maximum rooting depth of vegetation types at the global scale', *Oecologia* **108**(4), 583–595.
- Canti, M. G. (2003), 'Earthworm activity and archaeological stratigraphy: a review of products and processes', *Journal of Archaeological Science* **30**(2), 135–148.
- Carey, C. J., Brown, T. G., Challis, K. C., Howard, A. J. & Cooper, L. (2006), 'Predictive modelling of multiperiod geoarchaeological resources at a river confluence: a case study from the TrentSoar, UK', *Archaeological Prospection* **13**(4), 241–250.
- Carlson, T. N. & Ripley, D. A. (1997), 'On the relation between ndvi, fractional vegetation cover, and leaf area index', *Remote sensing of Environment* **62**(3), 241–252.
- Carter, G. A., Jones, J. H., Mitchell, R. J. & Brewer, C. H. (1996), 'Detection of solar-excited chlorophyll a fluorescence and leaf photosynthetic capacity using a fraunhofer line radiometer', *Remote Sensing of Environment* **55**(1), 89–92.
- Carter, G. A. & Miller, R. L. (1994), 'Early detection of plant stress by digital imaging within narrow stress-sensitive wavebands', *Remote Sensing of Environment* **50**(3), 295–302.
- Carter, G., Theisen, A. & Mitchell, R. (1990), 'Chlorophyll fluorescence measured using the fraunhofer line-depth principle and relationship to photosynthetic rate in the field', *Plant, Cell & Environment* **13**(1), 79–83.
- Carver, M. (2013), *Archaeological investigation*, Routledge.
- Castro-Esau, K., Sánchez-Azofeifa, G. & Caelli, T. (2004), 'Discrimination of lianas and trees with leaf-level hyperspectral data', *Remote Sensing of Environment* **90**(3), 353–372.
- Cavalli, R. M., Colosi, F., Palombo, A., Pignatti, S. & Poscolieri, M. (2007), 'Remote hyperspectral imagery as a support to archaeological prospection', *Journal of Cultural Heritage* **8**(3), 272–283.
- Ceraudo, G. (2003), '105 years of archaeological aerial photography in Italy (1899–2004)', *Aerial Photography and Archaeology* pp. 73–86.
- Cetin, M. & Musaoglu, N. (2009), 'Merging hyperspectral and panchromatic image data: qualitative and quantitative analysis', *International Journal of Remote Sensing* **30**(7), 1779–1804.

- Chaerle, L., Leinonen, I., Jones, H. G. & Van Der Straeten, D. (2007), 'Monitoring and screening plant populations with combined thermal and chlorophyll fluorescence imaging', *Journal of Experimental Botany* **58**(4), 773–784.
- Challis, K., Carey, C., Kincey, M. & Howard, A. J. (2011a), 'Airborne lidar intensity and geoarchaeological prospection in river valley floors', *Archaeological Prospection* **18**(1), 1–13.
- Challis, K., Carey, C., Kincey, M. & Howard, A. J. (2011b), 'Assessing the preservation potential of temperate, lowland alluvial sediments using airborne lidar intensity', *Journal of Archaeological Science* **38**(2), 301–311.
- Challis, K. & Howard, A. (2013), 'The role of lidar intensity data in interpreting environmental and cultural archaeological landscapes', *Interpreting archaeological topography: 3D data, visualisation and observation. Oxford Books, Oxford* pp. 161–170.
- Challis, K., Kincey, M. & Howard, A. J. (2009), 'Airborne remote sensing of valley floor geoarchaeology using daedalus ATM and CASI', *Archaeological Prospection* **16**(1), 17–33.
- Challis, K., Kokalj, Z., Kincey, M., Moscrop, D. & Howard, A. J. (2008), 'Airborne lidar and historic environment records', *Antiquity* **82**(318), 1055–1064.
- Chapman, H. P. (2002), 'Global warming the implications for sustainable archaeological resource management', *Conservation and management of archaeological sites* **5**(4), 241–245.
- Chaves, M. M., Pereira, J. S., Maroco, J., Rodrigues, M. L., Ricardo, C. P. P., Osrio, M. L., Carvalho, I., Faria, T. & Pinheiro, C. (2002), 'How plants cope with water stress in the field? photosynthesis and growth', *Annals of Botany* **89**(7), 907–916.
- Chen, J. M. (1996), 'Evaluation of vegetation indices and a modified simple ratio for boreal applications', *Canadian Journal of Remote Sensing* **22**(3), 229–242.
- Chew, Y. H., Smith, R. W., Jones, H. J., Seaton, D. D., Grima, R. & Halliday, K. J. (2014), 'Mathematical models light up plant signaling', *The Plant Cell* **26**(1), 5–20.
- Cho, M. A., Skidmore, A., Corsi, F., van Wieren, S. E. & Sobhan, I. (2007), 'Estimation of green grass/herb biomass from airborne hyperspectral imagery using spectral indices and partial least squares regression', *International Journal of Applied Earth Observation and Geoinformation* **9**(4), 414–424.

- Cho, M. A. & Skidmore, A. K. (2006), 'A new technique for extracting the red edge position from hyperspectral data: The linear extrapolation method', *Remote Sensing of Environment* **101**(2), 181–193.
- Cho, M. A., Skidmore, A. K. & Atzberger, C. (2008), 'Towards rededge positions less sensitive to canopy biophysical parameters for leaf chlorophyll estimation using properties optiques spectrales des feuilles (PROSPECT) and scattering by arbitrarily inclined leaves (SAILH) simulated data', *International Journal of Remote Sensing* **29**(8), 2241–2255.
- Cho, M. A., Sobhan, I., Skidmore, A. K. & de Leeuw, J. (2008), 'Discriminating species using hyperspectral indices at leaf and canopy scales', *The International Archives of the Spatial Information Sciences* pp. 369–376.
- Christensen, L. (1974), 'Crop-marks revealing large-scale patterned ground structures in cultivated areas, southwestern jutland, denmark', *Boreas* **3**(4), 153–180.
- Clark, C. (2002), 'Measured and estimated evaporation and soil moisture deficit for growers and the water industry', *Meteorological Applications* **9**(1), 85–93.
- Clark, O. A. & Clark, A. (2003), *Seeing beneath the soil: prospecting methods in archaeology*, Routledge.
- Clark, R. N. & Roush, T. L. (1984), 'Reflectance spectroscopy: Quantitative analysis techniques for remote sensing applications', *Journal of Geophysical Research: Solid Earth (19782012)* **89**(B7), 6329–6340.
- Clevers, J., De Jong, S. M., Epema, G. F., Van Der Meer, F. D., Bakker, W. H., Skidmore, A. K. & Scholte, K. H. (2002), 'Derivation of the red edge index using the MERIS standard band setting', *International Journal of Remote Sensing* **23**(16), 3169–3184.
- Clevers, J. G. (1994), Imaging spectrometry in agriculture-plant vitality and yield indicators, in 'Imaging spectrometry A tool for environmental observations', Springer, pp. 193–219.
- Clevers, J., Kooistra, L. & Schaepman, M. (2008), 'Using spectral information from the NIR water absorption features for the retrieval of canopy water content', *International Journal of Applied Earth Observation and Geoinformation* **10**(3), 388–397.
- Cogdell, R. J. (1978), 'Carotenoids in photosynthesis', *Philosophical Transactions of the Royal Society B: Biological Sciences* **284**(1002), 569–579.

- Cohen, S. & Guibas, L. (1997), The earth mover's distance: Lower bounds and invariance under translation, Technical report, DTIC Document.
- Cohen, S. & Guibas, L. (1999), The earth mover's distance under transformation sets, in 'Computer vision, 1999. The proceedings of the seventh IEEE international conference on', Vol. 2, IEEE, pp. 1076–1083.
- Cohen, S., Rao, R. S. & Cohen, Y. (1997), 'Canopy transmittance inversion using a line quantum probe for a row crop', *Agricultural and Forest Meteorology* **86**(3), 225–234.
- Colgan, M. S., Baldeck, C. A., Féret, J.-B. & Asner, G. P. (2012), 'Mapping savanna tree species at ecosystem scales using support vector machine classification and brdf correction on airborne hyperspectral and lidar data', *Remote Sensing* **4**(11), 3462–3480.
- Colomina, I. & Molina, P. (2014), 'Unmanned aerial systems for photogrammetry and remote sensing: A review', *ISPRS Journal of Photogrammetry and Remote Sensing* **92**, 79–97.
- Constantin, D., Rehak, M., Akhtman, Y. & Liebisch, F. (2015), Hyperspectral remote sensing of crop properties with unmanned aerial vehicles, in '9th EARSeL SIG Imaging Spectroscopy workshop', number EPFL-CONF-207795.
- Cooley, T., Anderson, G., Felde, G., Hoke, M., Ratkowski, A., Chetwynd, J., Gardner, J., Adler-Golden, S., Matthew, M., Berk, A. et al. (2002), Flaash, a modtran4-based atmospheric correction algorithm, its application and validation, in 'Geoscience and Remote Sensing Symposium, 2002. IGARSS'02. 2002 IEEE International', Vol. 3, IEEE, pp. 1414–1418.
- Cornish, P. S. (1993), 'Soil macrostructure and root growth of establishing seedlings', *Plant and Soil* **151**(1), 119–126.
- Cowley, D. C. (2002), 'A case study in the analysis of patterns of aerial reconnaissance in a lowland area of southwest scotland', *Archaeological Prospection* **9**(4), 255–265.
- Cowley, D. C. & Dickson, A. L. (2007), 'Clays and difficult soils in eastern and southern scotland: dealing with the gaps', *Populating Clay Landscapes: Recent advances in archaeology on difficult soils (Stroud: Tempus)* pp. 43–54.
- Crawford, O. (1954), 'A century of air-photography', *Antiquity* **28**(112), 206–210.
- Crawford, O. G. S. (1923), 'Air survey and archaeology', *Geographical Journal* pp. 342–360.

- Crook, M. & Ennos, A. (1995), 'The effect of nitrogen and growth regulators on stem and root characteristics associated with lodging in two cultivars of winter wheat', *Journal of Experimental Botany* **46**(8), 931–938.
- Crutchley, S. (2013), 'Using lidar data—drawing on 10 years experience at english heritage [w:] interpreting archaeological topography, airborne laser scanning, 3d data and ground observation, red. rs opitz, dc cowley'.
- Crutchley, S. & Crow, P. (2010), *The Light Fantastic: Using airborne lidar in archaeological survey*, English Heritage Swindon.
- Cui, Y., Zhao, K., Fan, W. & Xu, X. (2010), Using airborne lidar to retrieve crop structural parameters, in 'Geoscience and Remote Sensing Symposium IGARSS, 2010 IEEE International', IEEE, pp. 2107–2110.
- Curran, P. J. (1989), 'Remote sensing of foliar chemistry', *Remote Sensing of Environment* **30**(3), 271–278.
- Curran, P. J., Dungan, J. L., Macler, B. A. & Plummer, S. E. (1991), 'The effect of a red leaf pigment on the relationship between red edge and chlorophyll concentration', *Remote Sensing of Environment* **35**(1), 69–76.
- Curran, P. J., Dungan, J. L. & Peterson, D. L. (2001), 'Estimating the foliar biochemical concentration of leaves with reflectance spectrometry: Testing the kokaly and clark methodologies', *Remote Sensing of Environment* **76**(3), 349–359.
- Curran, P. J., Windham, W. R. & Gholz, H. L. (1995), 'Exploring the relationship between reflectance red edge and chlorophyll concentration in slash pine leaves', *Tree physiology* **15**(3), 203–206.
- Darvill, T. (1996), *Prehistoric Britain from the air: a study of space, time and society*, Cambridge University Press.
- Darvill, T. (2014), *Ancient monuments in the countryside: an archaeological management review*, English Heritage Publishing.
- Daughtry, C. S. T., Walthall, C. L., Kim, M. S., De Colstoun, E. B. & McMurtrey Iii, J. E. (2000), 'Estimating corn leaf chlorophyll concentration from leaf and canopy reflectance', *Remote sensing of Environment* **74**(2), 229–239.
- Davies, W. J. & Zhang, J. (1991), 'Root signals and the regulation of growth and development of plants in drying soil', *Annual review of plant biology* **42**(1), 55–76.

- Dawson, T. P. & Curran, P. J. (1998), 'Technical note a new technique for interpolating the reflectance red edge position', *International Journal of Remote Sensing* **19**(11), 2133–2139.
- De Laet, V., Paulissen, E., Meuleman, K. & Waelkens, M. (2009), 'Effects of image characteristics on the identification and extraction of archaeological features from ikonos-2 and quickbird-2 imagery: case study sagalassos (southwest turkey)', *International Journal of Remote Sensing* **30**(21), 5655–5668.
- Decagon Devices Inc. (2014), 'AccuPAR LP-80 User Manual'.
- Deegan, A. (2007), 'Archaeology on the boulder clay in northamptonshire: some results from the northamptonshire national mapping programme project', *Populating Clay Landscapes* pp. 104–119.
- Deegan, A. & Foard, G. (2013), *Mapping Ancient Landscapes in Northamptonshire*, English Heritage.
- Demmig-Adams, B., Stewart, J. J. & Adams, W. W. (2014), 'Multiple feedbacks between chloroplast and whole plant in the context of plant adaptation and acclimation to the environment', *Philosophical Transactions of the Royal Society B: Biological Sciences* **369**(1640), 20130244.
- D'Entremont, R. P. & Thomason, L. W. (1987), 'Interpreting meteorological satellite images using a color-composite technique', *Bulletin of the American Meteorological Society* **68**(7), 762–768.
- Developers, N. (2014), 'Numpy documentation. 2013'.
- Dietterich, T. G. (1998), 'Approximate statistical tests for comparing supervised classification learning algorithms', *Neural computation* **10**(7), 1895–1923.
- Dobrowski, S., Pushnik, J., Zarcotejada, P. & Ustin, S. (2005), 'Simple reflectance indices track heat and water stress-induced changes in steady-state chlorophyll fluorescence at the canopy scale', *Remote Sensing of Environment* **97**(3), 403–414.
- Donahue, R. L., Shickluna, J. C. & Robertson, L. S. (1972), 'Soils, an introduction to soils and plant growth', *Soil Science* **114**(6), 497.
- Doneus, M. (1997), 'On the archaeological use of vertical photographs', *AARGnews* **15**, 23–27.

- Doneus, M. (2000), 'Vertical and oblique photographs', *AARG News* **20**, 33–39.
- Doneus, M. (2001), 'Precision mapping and interpretation of oblique aerial photographs', *Archaeological Prospection* **8**(1), 13–27.
- Doneus, M. & Briese, C. (2006), 'Full-waveform airborne laser scanning as a tool for archaeological reconnaissance', *BAR International Series* **1568**, 99.
- Doneus, M., Briese, C., Fera, M. & Janner, M. (2008), 'Archaeological prospection of forested areas using full-waveform airborne laser scanning', *Journal of Archaeological Science* **35**(4), 882–893.
- Doneus, M., Verhoeven, G., Atzberger, C., Wess, M. & Ruš, M. (2014), 'New ways to extract archaeological information from hyperspectral pixels', *Journal of Archaeological Science* **52**, 84–96.
- Donoghue, D. & Shennan, I. (1988), 'The application of remote sensing to environmental archaeology', *Geoarchaeology* **3**(4), 275–285.
- Downton, W., Loveys, B. & Grant, W. (1988), 'Non-uniform stomatal closure induced by water stress causes putative non-stomatal inhibition of photosynthesis', *New Phytologist* **110**(4), 503–509.
- Du, Q., Raksuntorn, N., Cai, S. & Moorhead, R. J. (2008), 'Color display for hyperspectral imagery', *IEEE Transactions on Geoscience and Remote Sensing* **46**(6), 1858–1866.
- Du, Q., Younan, N. H., King, R. & Shah, V. P. (2007), 'On the performance evaluation of pan-sharpening techniques', *IEEE Geoscience and Remote Sensing Letters* **4**(4), 518–522.
- Dubayah, R., Knox, R., Hofton, M., Blair, J. B. & Drake, J. (2000), 'Land surface characterization using lidar remote sensing', *Spatial information for land use management* pp. 25–38.
- Edgeworth, M. (2014), 'The relationship between archaeological stratigraphy and artificial ground and its significance in the anthropocene', *Geological Society, London, Special Publications* **395**(1), 91–108.
- Ehlers, M., Klonus, S., Johan Åstrand, P. & Rosso, P. (2010), 'Multi-sensor image fusion for pansharpening in remote sensing', *International Journal of Image and Data Fusion* **1**(1), 25–45.

- Ehlert, D., Adamek, R. & Horn, H.-J. (2009), 'Vehicle based laser range finding in crops', *Sensors* **9**(5), 3679–3694.
- Ehlert, D. & Heisig, M. (2013), 'Sources of angle-dependent errors in terrestrial laser scanner-based crop stand measurement', *Computers and Electronics in Agriculture* **93**, 10–16.
- Ehlert, D., Horn, H.-J. & Adamek, R. (2008), 'Measuring crop biomass density by laser triangulation', *Computers and Electronics in Agriculture* **61**(2), 117–125.
- Eitel, J. U. H., Magney, T. S., Vierling, L. A., Brown, T. T. & Huggins, D. R. (2014), 'Li-DAR based biomass and crop nitrogen estimates for rapid, non-destructive assessment of wheat nitrogen status', *Field Crops Research* **159**, 21–32.
- Eitel, J. U. H., Vierling, L. A., Long, D. S. & Hunt, E. R. (2011), 'Early season remote sensing of wheat nitrogen status using a green scanning laser', *Agricultural and Forest Meteorology* **151**(10), 1338–1345.
- Elvidge, C. D. (1990), 'Visible and near infrared reflectance characteristics of dry plant materials', *Remote Sensing* **11**(10), 1775–1795.
- Evans, R. (2007), 'The weather and other factors controlling the appearance of crop marks on clay and difficultsoils', *Populating clay landscapes* pp. 16–27.
- Evans, R. & Catt, J. A. (1987), 'Causes of crop patterns in eastern england', *Journal of Soil Science* **38**(2), 309–324.
- Evans, R. & Jones, R. (1977), 'Crop marks and soils at two archaeological sites in britain', *Journal of Archaeological Science* **4**(1), 63–76.
- Farquhar, G. D. & Sharkey, T. D. (1982), 'Stomatal conductance and photosynthesis', *Annual review of plant physiology* **33**(1), 317–345.
- Filella, I. & Penuelas, J. (1994), 'The red edge position and shape as indicators of plant chlorophyll content, biomass and hydric status.', *International Journal of Remote Sensing* **15**(7), 1459–1470.
- Fisher, J., Baumbach, M. M., Bowles, J. H., Grossmann, J. M. & Antoniadis, J. A. (1998), Comparison of low-cost hyperspectral sensors, in 'SPIE's International Symposium on Optical Science, Engineering, and Instrumentation', International Society for Optics and Photonics, pp. 23–30.

- Flexas, J., Escalona, J. M., Evain, S., Gulías, J., Moya, I., Osmond, C. B. & Medrano, H. (2002), 'Steady-state chlorophyll fluorescence (fs) measurements as a tool to follow variations of net co2 assimilation and stomatal conductance during water-stress in c3 plants', *Physiologia plantarum* **114**(2), 231–240.
- Fourty, T., Baret, F., Jacquemoud, S., Schmuck, G. & Verdebout, J. (1996), 'Leaf optical properties with explicit description of its biochemical composition: Direct and inverse problems', *Remote Sensing of Environment* **56**(2), 104–117.
- Fricker, P. & Rohrbach, A. (2005), Pushbroom scanners provide highest resolution earth imaging information in multispectral bands, in 'IPSRS Hannover Workshop: High Resolution Earth Imaging for Geospatial Information: Proceedings'.
- Fry, R. J. (2014), Time-lapse Geophysical Investigations over Known Archaeological Features Using Electrical Resistivity Imaging and Earth Resistance, PhD thesis, University of Bradford.
- Fu, A. Y., Wenyin, L. & Deng, X. (2006), 'Detecting phishing web pages with visual similarity assessment based on earth mover's distance (emd)', *IEEE transactions on dependable and secure computing* **3**(4), 301–311.
- Gaffney, C. F. & Gater, J. (2006), *Revealing the buried past: geophysics for archaeologists*, Tempus.
- Galloway, J. N., Dentener, F. J., Capone, D. G., Boyer, E. W., Howarth, R. W., Seitzinger, S. P., Asner, G. P., Cleveland, C. C., Green, P. A., Holland, E. A., Karl, D. M., Michaels, A. F., Porter, J. H., Townsend, A. R. & Vosmarty, C. J. (2004), 'Nitrogen cycles: Past, present, and future', *Biogeochemistry* **70**(2), 153–226.
- Gamon, J. A., Penuelas, J. & Field, C. B. (1992), 'A narrow-waveband spectral index that tracks diurnal changes in photosynthetic efficiency', *Remote Sensing of environment* **41**(1), 35–44.
- Gamon, J. A., Serrano, L. & Surfus, J. S. (1997), 'The photochemical reflectance index: an optical indicator of photosynthetic radiation use efficiency across species, functional types, and nutrient levels', *Oecologia* **112**(4), 492–501.
- Gamon, J. A. & Surfus, J. S. (1999), 'Assessing leaf pigment content and activity with a reflectometer', *New Phytologist* **143**(1), 105–117.

- Gao, B.-C. (1995), Normalized difference water index for remote sensing of vegetation liquid water from space, in 'SPIE's 1995 Symposium on OE/Aerospace Sensing and Dual Use Photonics', International Society for Optics and Photonics, pp. 225–236.
- Garab, G. (1998), *Photosynthesis: Mechanisms and Effects*, Springer Science & Business Media.
- Gausman, H. W. (1985), 'Plant leaf optical properties in visible and near-infrared light', *Graduate studies/Texas Tech University (USA)* .
- Genty, B., Briantais, J.-M. & Baker, N. R. (1989), 'The relationship between the quantum yield of photosynthetic electron transport and quenching of chlorophyll fluorescence', *Biochimica et Biophysica Acta (BBA)-General Subjects* **990**(1), 87–92.
- Gillespie, A. R., Kahle, A. B. & Walker, R. E. (1987), 'Color enhancement of highly correlated images. II. channel ratio and chromaticity transformation techniques', *Remote Sensing of Environment* **22**(3), 343–365.
- Gimp, G. (2008), 'Image manipulation program', *User Manual, Edge-Detect Filters, Sobel, The GIMP Documentation Team* **8**(2), 8–7.
- Gitelson, A. A., Buschmann, C. & Lichtenthaler, H. K. (1999), 'The chlorophyll fluorescence ratio F735/F700 as an accurate measure of the chlorophyll content in plants', *Remote Sensing of Environment* **69**(3), 296–302.
- Gitelson, A. A., Kaufman, Y. J., Stark, R. & Rundquist, D. (2002), 'Novel algorithms for remote estimation of vegetation fraction', *Remote Sensing of Environment* **80**(1), 76–87.
- Gitelson, A. A., Merzlyak, M. N. & Chivkunova, O. B. (2001), 'Optical properties and nondestructive estimation of anthocyanin content in plant leaves', *Photochemistry and Photobiology* **74**(1), 38–45.
- Gitelson, A. & Merzlyak, M. N. (1994), 'Spectral reflectance changes associated with autumn senescence of *Aesculus hippocastanum* L. and *Acer platanoides* L. leaves. spectral features and relation to chlorophyll estimation', *Journal of Plant Physiology* **143**(3), 286–292.
- Gitelson, A., Zur, Y., Chivkunova, O. & Merzlyak, M. (2002), 'Assessing carotenoid content in plant leaves with reflectance spectroscopy', *Photochemistry and Photobiology* **75**(3), 272–281.

- Glaser, B. & Birk, J. J. (2012), 'State of the scientific knowledge on properties and genesis of anthropogenic dark earths in central amazonia (terra preta de índio)', *Geochimica et Cosmochimica Acta* **82**, 39–51.
- Gojda, M. (1997), 'The contribution of aerial archaeology to european landscape studies: Past achievements, recent developments and future perspectives', *Journal of European Archaeology* **5**(2), 91–104.
- Gojda, M. & Hejcman, M. (2012), 'Cropmarks in main field crops enable the identification of a wide spectrum of buried features on archaeological sites in central europe', *Journal of Archaeological Science* **39**(6), 1655–1664.
- Gowing, D. J. G., Davies, W. J. & Jones, H. G. (1990), 'A positive root-sourced signal as an indicator of soil drying in apple, *malus x domestica* borkh.', *Journal of Experimental Botany* **41**(12), 1535–1540.
- Grady, D. (2007), 'Cropmarks on clay, getting the timing right', *Mills and Palmer, Populating Clay Landscapes, Tempus, Stroud*.
- Grant, O. M., Tronina, E., Jones, H. G. & Chaves, M. M. (2007), 'Exploring thermal imaging variables for the detection of stress responses in grapevine under different irrigation regimes', *Journal of Experimental Botany* **58**(4), 815–825.
- Grave, P. & Kealhofer, L. (1999), 'Assessing bioturbation in archaeological sediments using soil morphology and phytolith analysis', *Journal of Archaeological Science* **26**(10), 1239–1248.
- Gupta, R. & Hartley, R. I. (1997), 'Linear pushbroom cameras', *IEEE Transactions on pattern analysis and machine intelligence* **19**(9), 963–975.
- Guttosch, R. J. et al. (2002), 'Investigation of color aliasing of high spatial frequencies and edges for bayer-pattern sensors and foveon x3® direct image sensors', *Foveon Inc.*
- Guyot, G., Baret, F. & Jacquemoud, S. (1992), 'Imaging spectroscopy for vegetation studies', *Imaging spectroscopy: fundamentals and prospective application* **2**, 145–165.
- Guyot, G., Steven, M., Clark, J. et al. (1990), 'Optical properties of vegetation canopies.', *Applications of remote sensing in agriculture*. pp. 19–43.
- Haack, B. & Jampoler, S. (1995), 'Colour composite comparisons for agricultural assessments', *International journal of remote sensing* **16**(9), 1589–1598.

- Haboudane, D. (2004), 'Hyperspectral vegetation indices and novel algorithms for predicting green LAI of crop canopies: Modeling and validation in the context of precision agriculture', *Remote Sensing of Environment* **90**(3), 337–352.
- Haldenby, D. & Richards, J. D. (2010), 'Charting the effects of plough damage using metal-detected assemblages', *Antiquity* **84**(326), 1151.
- Hampton, J. (1974), 'An experiment in multispectral air photography for archaeological research', *The Photogrammetric Record* **8**(43), 37–64.
- Hampton, J. N., Palmer, R. & Clark, A. J. (1977), 'Implications of aerial photography for archaeology: Geophysical and chemical assessment of air photograph sites', *Archaeological Journal* **134**(1), 157–193.
- Hansen, P. & Schjoerring, J. (2003), 'Reflectance measurement of canopy biomass and nitrogen status in wheat crops using normalized difference vegetation indices and partial least squares regression', *Remote sensing of environment* **86**(4), 542–553.
- Hanson, J. A. (1978), 'The application of remotely sensed imagery to the prehistory of central arizona'.
- Hanson, W. S. (2005), 'Sun, sand and see: creating bias in the archaeological record', *From the air. Understanding aerial archaeology* pp. 73–86.
- Hardisky, M. A., Klemas, V. & Smart, M. (1983), 'The influence of soil salinity, growth form, and leaf moisture on the spectral radiance of', *Spartina alterniflora* pp. 77–83.
- Harper, F. R. & Berkenkamp, B. (1975), 'Revised growth-stage key for brassica campestris and b. napus', *Canadian Journal of Plant Science* **55**(2), 657–658.
- Harris, E. C., Brown, M. R. & Brown, G. J. (1993), *Practices of archaeological stratigraphy*, Academic Press.
- Heinzel, J. & Koch, B. (2011), 'Exploring full-waveform LiDAR parameters for tree species classification', *International Journal of Applied Earth Observation and Geoinformation* **13**(1), 152–160.
- Hesse, R. (2010), 'LiDAR-derived local relief models—a new tool for archaeological prospection', *Archaeological Prospection* **17**(2), 67–72.

- Hill, S. L. & Clemens, P. (2015), Miniaturization of high spectral spatial resolution hyperspectral imagers on unmanned aerial systems, *in* 'SPIE Sensing Technology+ Applications', International Society for Optics and Photonics, pp. 94821E–94821E.
- Hiller, J. K. & Smith, M. (2008), 'Residual relief separation: digital elevation model enhancement for geomorphological mapping', *Earth Surface Processes and Landforms* **33**(14), 2266–2276.
- Hinnrichs, M. & Massie, M. A. (1997), New approach to imaging spectroscopy using diffractive optics, *in* 'Optical Science, Engineering and Instrumentation'97', International Society for Optics and Photonics, pp. 194–205.
- Höfle, B., Hollaus, M. & Hagenauer, J. (2012), 'Urban vegetation detection using radiometrically calibrated small-footprint full-waveform airborne LiDAR data', *ISPRS Journal of Photogrammetry and Remote Sensing* **67**, 134–147.
- Hopkins, W. G. & Hner, N. P. (1995), *Introduction to plant physiology*, Vol. 355, Wiley New York.
- Horler, D. N. H., Dockray, M. & Barber, J. (1983), 'The red edge of plant leaf reflectance', *International Journal of Remote Sensing* **4**(2), 273–288.
- Horne, P. (2009), 'A strategy for the national mapping programme', *English Heritage* .
- Hosoi, F. & Omasa, K. (2009), 'Estimating vertical plant area density profile and growth parameters of a wheat canopy at different growth stages using three-dimensional portable lidar imaging', *ISPRS Journal of Photogrammetry and Remote Sensing* **64**(2), 151–158.
- Hu, Y. & Schmidhalter, U. (2005), 'Drought and salinity: a comparison of their effects on mineral nutrition of plants', *Journal of Plant Nutrition and Soil Science* **168**(4), 541–549.
- Hubel, P. M. (2005), Foveon technology and the changing landscape of digital cameras, *in* 'Color and Imaging Conference', Vol. 2005, Society for Imaging Science and Technology, pp. 314–317.
- Huete, A. R. (1988), 'A soil-adjusted vegetation index (SAVI)', *Remote Sensing of Environment* **25**(3), 295–309.
- Huete, A. R. (2005), 'Estimation of soil properties using hyperspectral vis/ir sensors', *Encyclopedia of Hydrological Sciences* .

- Humme, A., Lindenbergh, R. & Sueur, C. (2006), Revealing celtic fields from lidar data using kriging based filtering, *in* 'Proceedings of the ISPRS Commission V Symposium'.
- Hunt Jr, E. R. & Rock, B. N. (1989), 'Detection of changes in leaf water content using near-and middle-infrared reflectances', *Remote sensing of environment* **30**(1), 43–54.
- Hunt, R. W. G. (2005), *The reproduction of colour*, John Wiley & Sons.
- Hunter, J. D. et al. (2007), 'Matplotlib: A 2d graphics environment', *Computing in science and engineering* **9**(3), 90–95.
- Jackson, R. D., Moran, M. S., Slater, P. N. & Biggar, S. F. (1987), 'Field calibration of reference reflectance panels', *Remote Sensing of Environment* **22**(1), 145–158.
- Jackson, R., Slater, P. & Pinter, P. (1983), 'Discrimination of growth and water stress in wheat by various vegetation indices through clear and turbid atmospheres', *Remote sensing of environment* **13**(3), 187–208.
- Jacquemoud, S., Baret, F. & Hanocq, J. (1992), 'Modeling spectral and bidirectional soil reflectance', *Remote sensing of Environment* **41**(2), 123–132.
- Jaleel, C. A., Manivannan, P., Wahid, A., Farooq, M., Al-Juburi, H. J., Somasundaram, R., Panneerselvam, R. & others (2009), 'Drought stress in plants: a review on morphological characteristics and pigments composition', *Int. J. Agric. Biol* **11**(1), 100–105.
- Johnson, D. L. (2002), 'Darwin would be proud: bioturbation, dynamic denudation, and the power of theory in science', *Geoarchaeology* **17**(1), 7–40.
- Jones, E., Oliphant, T., Peterson, P. et al. (2001), 'Open source scientific tools for python'.
- Jones, E., Oliphant, T., Peterson, P. et al. (2014), 'SciPy: Open source scientific tools for Python'. [Online; accessed 2014-08-29].
URL: <http://www.scipy.org/>
- Jones, H. G., Serraj, R., Loveys, B. R., Xiong, L., Wheaton, A. & Price, A. H. (2009), 'Thermal infrared imaging of crop canopies for the remote diagnosis and quantification of plant responses to water stress in the field', *Functional Plant Biology* **36**(11), 978–989.
- Jones, R. J. A. & Evans, R. (1975), 'Soil and crop marks in the recognition of archaeological sites by air photography', *Aerial reconnaissance for archaeology* pp. 1–11.

- Jr, E. R. H., Cavigelli, M., Daughtry, C. S. T., Iii, J. E. M. & Walthall, C. L. (2005), 'Evaluation of digital photography from model aircraft for remote sensing of crop biomass and nitrogen status', *Precision Agriculture* **6**(4), 359–378.
- Kaiser, P. K. & Boynton, R. M. (1996), 'Human color vision'.
- Kaiser, W. M. (1987), 'Effects of water deficit on photosynthetic capacity', *Physiologia Plantarum* **71**(1), 142–149.
- Kalacska, M. E., Bell, L. S., Arturo Sanchez-Azofeifa, G. & Caelli, T. (2009), 'The application of remote sensing for detecting mass graves: An experimental animal case study from costa rica*', *Journal of Forensic Sciences* **54**(1), 159–166.
- Kidd, C. & Chapman, L. (2012), 'Derivation of sky-view factors from lidar data', *International Journal of Remote Sensing* **33**(11), 3640–3652.
- Kim, M. S., Daughtry, C. S. T., Chappelle, E. W., McMurtrey, J. E. & Walthall, C. L. (1994), 'The use of high spectral resolution bands for estimating absorbed photosynthetically active radiation (a par)'.
- Knapp, A. B. & Ashmore, W. (1999), 'Archaeological landscapes: constructed, conceptualized, ideational', *Archaeologies of landscape: contemporary perspectives* pp. 1–30.
- Kneizys, F., Abreu, L., Anderson, G., Chetwynd, J., Shettle, E., Berk, A., Bernstein, L., Robertson, D., Acharya, P., Rothman, L. et al. (1996), 'The modtran 2/3 report and lowtran 7 model', *Phillips Laboratory, Hanscom AFB, MA* **1731**.
- Kokalj, Ž., Zakšek, K. & Oštir, K. (2012), 'Visualizations of lidar derived relief models', *Interpreting archaeological topography* pp. 100–114.
- Kokalj, ., Zakek, K. & Otir, K. (2011), 'Application of sky-view factor for the visualisation of historic landscape features in lidar-derived relief models.', *Antiquity* **85**(327).
- Kokaly, R. F. & Clark, R. N. (1999), 'Spectroscopic determination of leaf biochemistry using band-depth analysis of absorption features and stepwise multiple linear regression', *Remote Sensing of Environment* **67**(3), 267–287.
- Kov, D., Malenovsk, Z., Urban, O., punda, V., Kalina, J., A, A., Kaplan, V. & Hanu, J. (2013), 'Response of green reflectance continuum removal index to the xanthophyll deoxidation cycle in norway spruce needles', *Journal of Experimental Botany* p. ert069.

- Kramer, P. J. et al. (1969), 'Plant and soil water relationships: a modern synthesis.', *Plant and soil water relationships: a modern synthesis*. .
- Krause, G. H. & Weis, E. (1984), 'Chlorophyll fluorescence as a tool in plant physiology', *Photosynthesis Research* **5**(2), 139–157.
- Krause, G. & Weis, E. (1991), 'Chlorophyll fluorescence and photosynthesis: the basics', *Annual review of plant biology* **42**(1), 313–349.
- Kristiansen, K. (2009), 'Contract archaeology in europe: an experiment in diversity', *World archaeology* **41**(4), 641–648.
- Krouk, G., Ruffel, S., Gutiérrez, R. A., Gojon, A., Crawford, N. M., Coruzzi, G. M. & Lacombe, B. (2011), 'A framework integrating plant growth with hormones and nutrients', *Trends in plant science* **16**(4), 178–182.
- Kumar, L., Schmidt, K., Dury, S. & Skidmore, A. (2002), Imaging spectrometry and vegetation science, in 'Imaging spectrometry', Springer, pp. 111–155.
- Kvamme, K. L. (2006), 'Integrating multidimensional geophysical data', *Archaeological Prospection* **13**(1), 57–72.
- Large, E. C. (1954), 'Growth stages in cereals illustration of the feekes scale', *Plant pathology* **3**(4), 128–129.
- Lasaponara, R., Coluzzi, R. & Masini, N. (2011), 'Flights into the past: full-waveform airborne laser scanning data for archaeological investigation', *Journal of Archaeological Science* **38**(9), 2061–2070.
- Lasaponara, R. & Masini, N. (2012), Pan-sharpening techniques to enhance archaeological marks: an overview, in 'Satellite Remote Sensing', Springer, pp. 87–109.
- Leberl, F., Gruber, M., Ponticelli, M., Bernoegger, S. & Perko, R. (2003), The ultracam large format aerial digital camera system, in 'Proceedings of the American Society For Photogrammetry & Remote Sensing', pp. 5–9.
- Lebourgeois, V., Bégué, A., Labbé, S., Mallavan, B., Prévot, L. & Roux, B. (2008), 'Can commercial digital cameras be used as multispectral sensors? a crop monitoring test', *Sensors* **8**(11), 7300–7322.
- Lee, J.-S. (1980), 'Digital image enhancement and noise filtering by use of local statistics', *IEEE transactions on pattern analysis and machine intelligence* (2), 165–168.

- Legleiter, C. J., Marcus, W. & Lawrence, R. (2002), 'Effects of sensor resolution on mapping instream habitats', *Photogrammetric Engineering and Remote Sensing* **68**(8), 801–807.
- Lehmann, J. & Joseph, S. (2009), *Biochar for environmental management: science and technology*, Earthscan.
- Levina, E. & Bickel, P. (2001), The earth mover's distance is the mallows distance: some insights from statistics, in 'Computer Vision, 2001. ICCV 2001. Proceedings. Eighth IEEE International Conference on', Vol. 2, IEEE, pp. 251–256.
- Liang, B., Lehmann, J., Solomon, D., Kinyangi, J., Grossman, J., O'neill, B., Skjemstad, J. O., Thies, J., Luizao, F. J., Petersen, J. & others (2006), 'Black carbon increases cation exchange capacity in soils', *Soil Science Society of America Journal* **70**(5), 1719–1730.
- Liang, S. & Strahler, A. H. (1993), 'An analytic BRDF model of canopy radiative transfer and its inversion', *Geoscience and Remote Sensing, IEEE Transactions on* **31**(5), 1081–1092.
- Licciardi, G. A., Khan, M. M., Chanussot, J., Montanvert, A., Condat, L. & Jutten, C. (2012), 'Fusion of hyperspectral and panchromatic images using multiresolution analysis and nonlinear pca band reduction', *EURASIP Journal on Advances in Signal processing* **2012**(1), 1–17.
- Lillesaeter, O. (1982), 'Spectral reflectance of partly transmitting leaves: laboratory measurements and mathematical modeling', *Remote Sensing of Environment* **12**(3), 247–254.
- Lillesand, T. M., Kiefer, R. W., Chipman, J. W. & others (2004), *Remote sensing and image interpretation.*, John Wiley & Sons Ltd.
- Lin, Y.-C., Mills, J. & Smith-Voysey, S. (2010), 'Rigorous pulse detection from full-waveform airborne laser scanning data', *International Journal of Remote Sensing* **31**(5), 1303–1324.
- Lisá, L., Komoróczy, B., Vlach, M., Válek, D., Bajer, A., Kovárník, J., Rajtár, J., Hüssen, C. & Šumberová, R. (2015), 'How were the ditches filled? sedimentological and micro-morphological classification of formation processes within graben-like archaeological objects', *Quaternary International* **370**, 66–76.

- Loncan, L., de Almeida, L. B., Bioucas-Dias, J. M., Briottet, X., Chanussot, J., Dobigeon, N., Fabre, S., Liao, W., Licciardi, G. A., Simoes, M. et al. (2015), 'Hyperspectral pansharpening: a review', *IEEE Geoscience and remote sensing magazine* **3**(3), 27–46.
- Long, D. S. & McCallum, J. D. (2013), 'Mapping straw yield using on-combine light detection and ranging (lidar)', *International Journal of Remote Sensing* **34**(17), 6121–6134.
- Lukina, E., Stone, M. & Raun, W. (1999), 'Estimating vegetation coverage in wheat using digital images', *Journal of Plant Nutrition* **22**(2), 341–350.
- M., O. (2005), 'Patterns of aerial photography in the central midlands of england: evaluating biases in past programs of aerial reconnaissance and their potential impact', *From the air. Understanding aerial archaeology* pp. 141–151.
- Mackinney, G. (1941), 'Absorption of light by chlorophyll solutions', *J. biol. Chem* **140**(2), 315–322.
- Magney, T. S., Eusden, S. A., Eitel, J. U., Logan, B. A., Jiang, J. & Vierling, L. A. (2014), 'Assessing leaf photoprotective mechanisms using terrestrial LiDAR: towards mapping canopy photosynthetic performance in three dimensions', *New Phytologist* **201**(1), 344–356.
- Mallet, C. & Bretar, F. (2009a), 'Full-waveform topographic lidar: State-of-the-art', *ISPRS Journal of photogrammetry and remote sensing* **64**(1), 1–16.
- Mallet, C. & Bretar, F. (2009b), 'Full-waveform topographic lidar: State-of-the-art', *ISPRS Journal of Photogrammetry and Remote Sensing* **64**(1), 1–16.
- Malvar, H. S., He, L. & Cutler, R. (2004), High-quality linear interpolation for demosaicing of bayer-patterned color images, in 'Acoustics, Speech, and Signal Processing, 2004. Proceedings.(ICASSP'04). IEEE International Conference on', Vol. 3, IEEE, pp. iii–485.
- Mather, P. M. & Koch, M. (2011), 'Remote sensing platforms and sensors', *Computer Processing of Remotely-Sensed Images: An Introduction, Fourth Edition* pp. 29–66.
- Matthew, M. W., Adler-Golden, S. M., Berk, A., Felde, G., Anderson, G. P., Gorodetzky, D., Paswaters, S. & Shippert, M. (2002), Atmospheric correction of spectral imagery:

- evaluation of the flash algorithm with aviris data, in 'Applied Imagery Pattern Recognition Workshop, 2002. Proceedings. 31st', IEEE, pp. 157–163.
- Matthews, W., French, C. A., Lawrence, T., Cutler, D. F. & Jones, M. K. (1997), 'Microstratigraphic traces of site formation processes and human activities', *World archaeology* **29**(2), 281–308.
- Maxwell, K. & Johnson, G. N. (2000), 'Chlorophyll fluorescence practical guide', *Journal of experimental botany* **51**(345), 659–668.
- McCoy, R. M. (2005), *Field Methods in Remote Sensing*, Guilford Press.
- Melillo, J. M., Aber, J. D. & Muratore, J. F. (1982), 'Nitrogen and lignin control of hardwood leaf litter decomposition dynamics', *Ecology* **63**(3), 621–626.
- Meroni, M., Rossini, M., Guanter, L., Alonso, L., Rascher, U., Colombo, R. & Moreno, J. (2009), 'Remote sensing of solar-induced chlorophyll fluorescence: Review of methods and applications', *Remote Sensing of Environment* **113**(10), 2037–2051.
- Merzlyak, M. N., Gitelson, A. A., Chivkunova, O. B. & Rakitin, V. Y. (1999), 'Non-destructive optical detection of pigment changes during leaf senescence and fruit ripening', *Physiologia plantarum* **106**(1), 135–141.
- Meyer, G. E., Camargo Neto, J., Jones, D. D. & Hindman, T. W. (2004), 'Intensified fuzzy clusters for classifying plant, soil, and residue regions of interest from color images', *Computers and Electronics in Agriculture* **42**(3), 161–180.
- Meyer, G. E., Hindman, T. W. & Laksmi, K. (1999), Machine vision detection parameters for plant species identification, Vol. 3543, pp. 327–335.
- Meyer, G. E. & Neto, J. C. (2008), 'Verification of color vegetation indices for automated crop imaging applications', *Computers and Electronics in Agriculture* **63**(2), 282–293.
- Mills, J. (2005), 'Bias and the world of the vertical aerial photograph', *From the Air: Understanding Aerial Archaeology* pp. 117–126.
- Milton, E. (1987), 'Review article principles of field spectroscopy', *Remote Sensing* **8**(12), 1807–1827.
- Milton, E. J., Schaepman, M. E., Anderson, K., Kneubühler, M. & Fox, N. (2009), 'Progress in field spectroscopy', *Remote Sensing of Environment* **113**, S92–S109.

- Monteith, J. L. & Moss, C. J. (1977), 'Climate and the efficiency of crop production in Britain [and discussion]', *Philosophical Transactions of the Royal Society of London. B, Biological Sciences* **281**(980), 277–294.
- Morris, D. E., Boyd, D. S., Crowe, J. A., Johnson, C. S. & Smith, K. L. (2013), 'Exploring the potential for automatic extraction of vegetation phenological metrics from traffic webcams', *Remote Sensing* **5**(5), 2200–2218.
- Murata, N., Takahashi, S., Nishiyama, Y. & Allakhverdiev, S. I. (2007), 'Photoinhibition of photosystem II under environmental stress', *Biochimica et Biophysica Acta (BBA) - Bioenergetics* **1767**(6), 414–421.
- Murphy, P., Thackray, D. & Wilson, E. (2009), 'Coastal heritage and climate change in England: assessing threats and priorities', *Conservation and management of Archaeological Sites* **11**(1), 9–15.
- Mutanga, O. & Skidmore, A. K. (2004), 'Narrow band vegetation indices overcome the saturation problem in biomass estimation', *International Journal of Remote Sensing* **25**(19), 3999–4014.
- Mutanga, O. & Skidmore, A. K. (2007), 'Red edge shift and biochemical content in grass canopies', *ISPRS Journal of Photogrammetry and Remote Sensing* **62**(1), 34–42.
- Myneni, R. & Asrar, G. (1994), 'Atmospheric effects and spectral vegetation indices', *Remote Sensing of Environment* **47**(3), 390–402.
- Nagler, P., Daughtry, C. & Goward, S. (2000), 'Plant litter and soil reflectance', *Remote Sensing of Environment* **71**(2), 207–215.
- Nagler, P. L., Inoue, Y., Glenn, E. P., Russ, A. L. & Daughtry, C. S. T. (2003), 'Cellulose absorption index (CAI) to quantify mixed soilplant litter scenes', *Remote Sensing of Environment* **87**(2–3), 310–325.
- Nicodemus, F. E. (1965), 'Directional reflectance and emissivity of an opaque surface', *Applied Optics* **4**(7), 767–775.
- Nielsen, N. H. & Kristiansen, S. M. (2014), 'Identifying ancient manuring: traditional phosphate vs. multi-element analysis of archaeological soil', *Journal of Archaeological Science* **42**, 390–398.

- Nijland, W., De Jong, R., De Jong, S. M., Wulder, M. A., Bater, C. W. & Coops, N. C. (2014), 'Monitoring plant condition and phenology using infrared sensitive consumer grade digital cameras', *Agricultural and forest meteorology* **184**, 98–106.
- Noomen, M. F., Skidmore, A. K., van der Meer, F. D. & Prins, H. H. T. (2006), 'Continuum removed band depth analysis for detecting the effects of natural gas, methane and ethane on maize reflectance', *Remote Sensing of Environment* **105**(3), 262–270.
- Noviello, M., Ciminale, M. & De Pasquale, V. (2013), 'Combined application of pan-sharpening and enhancement methods to improve archaeological cropmark visibility and identification in quickbird imagery: Two case studies from apulia, southern italy', *Journal of Archaeological Science* **40**(10), 3604–3613.
- Novotny, E. H., Hayes, M. H., Madari, B. E., Bonagamba, T. J., Azevedo, E. R. d., Souza, A. A. d., Song, G., Nogueira, C. M. & Mangrich, A. S. (2009), 'Lessons from the terra preta de índios of the amazon region for the utilisation of charcoal for soil amendment', *Journal of the Brazilian Chemical Society* **20**(6), 1003–1010.
- Nuijs, A. M., van Gorkom, H. J., Plijter, J. J. & Duysens, L. N. (1986), 'Primary-charge separation and excitation of chlorophyll a in photosystem ii particles from spinach as studied by picosecond absorbance-difference spectroscopy', *Biochimica et Biophysica Acta (BBA)-Bioenergetics* **848**(2), 167–175.
- Olesen, L. H. (2004), 'Aerial Archaeology in Denmark', *Useful reminders..?* p. 28.
- Oonk, S., Slomp, C., Huisman, D. et al. (2009), 'Geochemistry as an aid in archaeological prospection and site interpretation: current issues and research directions', *Archaeological Prospection* **16**(1), 35–51.
- Opitz, R. S. & Cowley, D. (2013), *Interpreting archaeological topography: airborne laser scanning, 3D data and ground observation*, Oxbow Books.
- Otsu, N. (1975), 'A threshold selection method from gray-level histograms', *Automatica* **11**(285-296), 23–27.
- Oussible, M., Crookston, R. K. & Larson, W. E. (1992), 'Subsurface compaction reduces the root and shoot growth and grain yield of wheat', *Agronomy Journal* **84**(1), 34–38.
- Palmer, R. (2005), 'If they used their own photographs they wouldnt take them like that', *From the air. Understanding aerial archaeology* pp. 94–116.

- Palmer, R. (2007), 'Seventy-five years v. ninety minutes: implications of the 1996 bedfordshire vertical aerial survey on our perceptions of clayland archaeology', *Populating Clay Landscapes* pp. 88–103.
- Palsson, F., Sveinsson, J. R., Ulfarsson, M. O. & Benediktsson, J. A. (2015), 'Model-based fusion of multi- and hyperspectral images using pca and wavelets', *IEEE transactions on Geoscience and Remote Sensing* **53**(5), 2652–2663.
- Parkinson, C., Ward, A. & King, M. (2006), 'Earth science reference handbook: a guide to nasas earth science program and earth observing satellite missions', *National Aeronautics and Space Administration* p. 277.
- Passioura, J. B. (1983), 'Roots and drought resistance', *Agricultural water management* **7**(1), 265–280.
- Passioura, J. B. (2002), 'soil conditions and plant growth', *Plant, Cell & Environment* **25**(2), 311–318.
- Penuelas, J., Baret, F. & Filella, I. (1995), 'Semi-empirical indices to assess carotenoids/chlorophyll a ratio from leaf spectral reflectance', *Photosynthetica* **31**(2), 221–230.
- Persson, Å., Söderman, U., Töpel, J. & Ahlberg, S. (2005), 'Visualization and analysis of full-waveform airborne laser scanner data', *International Archives of Photogrammetry, Remote Sensing and Spatial Information Sciences* **36**(3/W19), 103–108.
- Peuelas, J., Filella, I., Biel, C., Serrano, L. & Save, R. (1993), 'The reflectance at the 950/970 nm region as an indicator of plant water status', *International journal of remote sensing* **14**(10), 1887–1905.
- Peuelas, J., Gamon, J. A., Fredeen, A. L., Merino, J. & Field, C. B. (1994), 'Reflectance indices associated with physiological changes in nitrogen- and water-limited sunflower leaves', *Remote Sensing of Environment* **48**(2), 135–146.
- Pinar, A. & Curran, P. J. (1996), 'Technical note grass chlorophyll and the reflectance red edge', *International Journal of Remote Sensing* **17**(2), 351–357.
- Pohl, C. & Van Genderen, J. L. (1998), 'Review article multisensor image fusion in remote sensing: concepts, methods and applications', *International journal of remote sensing* **19**(5), 823–854.

- Poirier, N., Hautefeuille, F. & Calastrenc, C. (2013), 'Low altitude thermal survey by means of an automated unmanned aerial vehicle for the detection of archaeological buried structures', *Archaeological Prospection* **20**(4), 303–307.
- Porter, T. & Duff, T. (1984), Compositing digital images, in 'ACM Siggraph Computer Graphics', Vol. 18, ACM, pp. 253–259.
- Pradhan, P. S., King, R. L., Younan, N. H. & Holcomb, D. W. (2006), 'Estimation of the number of decomposition levels for a wavelet-based multiresolution multisensor image fusion', *IEEE Transactions on Geoscience and Remote Sensing* **44**(12), 3674–3686.
- Prospere, K., McLaren, K. & Wilson, B. (2014), 'Plant species discrimination in a tropical wetland using in situ hyperspectral data', *Remote sensing* **6**(9), 8494–8523.
- Prez, A. J., Lpez, F., Benlloch, J. V. & Christensen, S. (2000), 'Colour and shape analysis techniques for weed detection in cereal fields', *Computers and Electronics in Agriculture* **25**(3), 197–212.
- QGIS, D. (2011), 'Quantum gis geographic information system', *Open Source Geospatial Foundation Project* **45**.
- Qi, J., Chehbouni, A., Huete, A. R., Kerr, Y. H. & Sorooshian, S. (1994), 'A modified soil adjusted vegetation index', *Remote Sensing of Environment* **48**(2), 119–126.
- Qi, J., Kerr, Y. & Chehbouni, A. (1994), External factor consideration in vegetation index development, in 'Proceedings of 6th International Symposium on Physical Measurements and Signatures in Remote Sensing; p 723-730'.
- Rabatel, G., Gorretta, N. & Labbé, S. (2011), Getting ndvi spectral bands from a single standard rgb digital camera: a methodological approach, in 'Conference of the Spanish Association for Artificial Intelligence', Springer, pp. 333–342.
- Rahmani, S., Strait, M., Merkurjev, D., Moeller, M. & Wittman, T. (2010), 'An adaptive ihs pan-sharpening method', *IEEE Geoscience and Remote Sensing Letters* **7**(4), 746–750.
- Rama Rao, N., Garg, P. & Ghosh, S. (2007), 'Evaluation of radiometric resolution on land use/land cover mapping in an agricultural area', *International Journal of Remote Sensing* **28**(2), 443–450.
- Raven, J. & Edwards, D. (2001), 'Roots: evolutionary origins and biogeochemical significance', *Journal of Experimental Botany* **52**(suppl 1), 381–401.

- Renfrew, C. & Bahn, P. (1991), 'Archaeology: Theory, method and practice'.
- Richards, L. A. (1928), 'The usefulness of capillary potential to soil moisture and plant investigators', *J. Agric. Res* **37**(12), 719–742.
- Richards, L. & Wadleigh, C. (1952), 'Soil water and plant growth', *Soil physical conditions and plant growth* **2**, 74–253.
- Riley, D. (1986), 'The frequency of occurrence of cropmarks in relation to soils', *C.B.A Research Reports* **49**, 59–73.
- Riley, D. N. (1944), 'The technique of air-archaeology', *Archaeological Journal* **101**(1), 1–16.
- Riley, D. N. (1987), *Air photography and archaeology*, Duckworth.
- Risbøl, O., Briese, C., Doneus, M. & Nesbakken, A. (2015), 'Monitoring cultural heritage by comparing dems derived from historical aerial photographs and airborne laser scanning', *Journal of Cultural Heritage* **16**(2), 202–209.
- Ritchie, G., Sullivan, D., Perry, C., Hook, J. & Bednarz, C. (2008), 'Preparation of a low-cost digital camera system for remote sensing', *Applied engineering in agriculture* **24**(6), 885–894.
- Rollin, E., Milton, E. & Emery, D. (2000), 'Reference panel anisotropy and diffuse radiation-some implications for field spectroscopy', *International Journal of Remote Sensing* **21**(15), 2799–2810.
- Romeo, J., Pajares, G., Montalvo, M., Guerrero, J. M., Guijarro, M. & de la Cruz, J. M. (2013), 'A new expert system for greenness identification in agricultural images', *Expert Systems with Applications* **40**(6), 2275–2286.
- Roujean, J.-L. & Breon, F.-M. (1995), 'Estimating PAR absorbed by vegetation from bidirectional reflectance measurements', *Remote Sensing of Environment* **51**(3), 375–384.
- Rouse, J. W., Haas, R. H., Schell, J. A. & Deering, D. W. (1974), 'Monitoring vegetation systems in the great plains with ERTS', *NASA special publication* **351**, 309.
- Rubner, Y. & Tomasi, C. (2001), The earth movers distance, in 'Perceptual Metrics for Image Database Navigation', Springer, pp. 13–28.

- Rubner, Y., Tomasi, C. & Guibas, L. J. (1998), A metric for distributions with applications to image databases, *in* 'Computer Vision, 1998. Sixth International Conference on', IEEE, pp. 59–66.
- Rubner, Y., Tomasi, C. & Guibas, L. J. (2000), 'The earth mover's distance as a metric for image retrieval', *International journal of computer vision* **40**(2), 99–121.
- Russell, R. S. et al. (1977), *Plant root systems: their function and interaction with the soil.*, McGraw-Hill Book Company (UK) Limited.
- Saeyns, W., Lenaerts, B., Craessaerts, G. & De Baerdemaeker, J. (2009), 'Estimation of the crop density of small grains using lidar sensors', *Biosystems Engineering* **102**(1), 22–30.
- Saito, Y., Kanoh, M., Hatake, K.-i., Kawahara, T. D. & Nomura, A. (1998), 'Investigation of laser-induced fluorescence of several natural leaves for application to lidar vegetation monitoring', *Applied optics* **37**(3), 431–437.
- Sandler, R. & Lindenbaum, M. (2011), 'Nonnegative matrix factorization with earth mover's distance metric for image analysis', *IEEE Transactions on Pattern Analysis and Machine Intelligence* **33**(8), 1590–1602.
- Sandmeier, S., Mller, C., Hosgood, B. & Andreoli, G. (1998), 'Physical mechanisms in hyperspectral BRDF data of grass and watercress', *Remote Sensing of Environment* **66**(2), 222–233.
- Schaepman-Strub, G., Schaepman, M., Painter, T., Dangel, S. & Martonchik, J. (2006), 'Reflectance quantities in optical remote sensing definitions and case studies', *Remote sensing of environment* **103**(1), 27–42.
- Schiffer, M. B. (1996), *Formation processes of the archaeological record*, University of Utah Press Salt Lake City.
- Schofield, A. (1989), 'Understanding early medieval pottery distributions: cautionary tales and their implications for further research', *Antiquity* **63**(240), 460–470.
- Schreiber, U., Bilger, W. & Neubauer, C. (1995), Chlorophyll fluorescence as a non-intrusive indicator for rapid assessment of in vivo photosynthesis, *in* 'Ecophysiology of photosynthesis', Springer, pp. 49–70.

- Schreiber, U., Schliwa, U. & Bilger, W. (1986), 'Continuous recording of photochemical and non-photochemical chlorophyll fluorescence quenching with a new type of modulation fluorometer', *Photosynthesis research* **10**(1-2), 51–62.
- Scollar, I. (1964), Physical conditions tending to produce crop sites in the rhineland, in 'Proceedings Colloque International D'Archaeologie Aerienne. 31 Aug–3 Sept, 1963', SEVPEN Paris, pp. 39–47.
- Scollar, I., Tabbagh, A., Hesse, A. & Herzog, I. (1990), *Archaeological prospecting and remote sensing*, Cambridge University Press.
- Serrano, L., Penuelas, J. & Ustin, S. L. (2002), 'Remote sensing of nitrogen and lignin in mediterranean vegetation from AVIRIS data: Decomposing biochemical from structural signals', *Remote sensing of Environment* **81**(2), 355–364.
- Sevara, C. (2013), 'Top secret topographies: recovering two and three-dimensional archaeological information from historic reconnaissance datasets using image-based modelling techniques', *International Journal of Heritage in the Digital Era* **2**(3), 395–418.
- Shah, V. P., Younan, N. H. & King, R. L. (2008), 'An efficient pan-sharpening method via a combined adaptive pca approach and contourlets', *IEEE transactions on geoscience and remote sensing* **46**(5), 1323–1335.
- Shapiro, L. G. & Stockman, G. C. (n.d.), *Computer Vision, March 2000*, ISBN-10.
- Sharpe, L. (2004), Geophysical, geochemical and arable crop responses to archaeological sites in the Upper Clyde Valley, Scotland, PhD thesis, University of Glasgow.
- Shotton, F. W. (1960), 'Large scale patterned ground in the valley of the worcestershire avon', *Geological Magazine* **97**(05), 404–408.
- Sims, D. A. & Gamon, J. A. (2002), 'Relationships between leaf pigment content and spectral reflectance across a wide range of species, leaf structures and developmental stages', *Remote sensing of environment* **81**(2), 337–354.
- Smith, K., Steven, M. & Colls, J. (2004), 'Use of hyperspectral derivative ratios in the red-edge region to identify plant stress responses to gas leaks', *Remote Sensing of Environment* **92**(2), 207–217.

- Smith, M. J., Chandler, J. & Rose, J. (2009), 'High spatial resolution data acquisition for the geosciences: kite aerial photography', *Earth Surface Processes and Landforms* **34**(1), 155–161.
- St. Joseph, J. (1945), 'Air photography and archaeology', *The Geographical Journal* **105**(1/2), 47–59.
- St Joseph, J. (1969), 'Air reconnaissance: recent results, 18', *Antiquity* **43**, 314–315.
- Stanjek, H. & Fassbinder, J. (1995), 'Soil aspects affecting archaeological details in aerial photographs', *Archaeological Prospection* **2**, 91–102.
- Stevenson, F. J. (1965), Origin and distribution of nitrogen in soil, in 'Soil nitrogen', American Society of Agronomy, pp. 1–42.
- Stott, D., Boyd, D., Beck, A. & Cohn, A. (2013), Hyperspectral detection dynamics of archaeological vegetation marks and enhancement using full waveform LiDAR data, in 'Geoscience and Remote Sensing Symposium (IGARSS), 2013 IEEE International', pp. 2829–2831.
- Stott, D., Boyd, D. S., Beck, A. & Cohn, A. G. (2015), 'Airborne lidar for the detection of archaeological vegetation marks using biomass as a proxy', *Remote Sensing* **7**(2), 1594–1618.
- Strahler, A. H. (1997), 'Vegetation canopy reflectance modeling recent developments and remote sensing perspectives', *Remote Sensing Reviews* **15**(1-4), 179–194.
- Strunk-Lichtenberg, G. (1965), 'Bodenkundliche untersuchungen an archäologischen objekten, die durch luftbild-aufnahmen entdeckt wurden', *Archaeo-Physica* **15**, 175–202.
- Štular, B., Kokalj, Ž., Oštir, K. & Nuninger, L. (2012), 'Visualization of lidar-derived relief models for detection of archaeological features', *Journal of Archaeological Science* **39**(11), 3354–3360.
- Sullivan, G. M. & Feinn, R. (2012), 'Using effect size-or why the p value is not enough', *Journal of graduate medical education* **4**(3), 279–282.
- Sun, T. & Neuvo, Y. (1994), 'Detail-preserving median based filters in image processing', *Pattern Recognition Letters* **15**(4), 341–347.
- Svensson, H. (1988), 'Ice-wedge casts and relict polygonal patterns in scandinavia', *Journal of Quaternary Science* **3**(1), 57–67.

- Sylvester-Bradley, R., Berry, P., Blake, J., Kindred, D., Spink, J., Bingham, I., McVittie, J. & Foulkes, J. (2008), The wheat growth guide, Technical report, Home Grown Cereals Association.
- Tailanián, M., Castiglioni, E., Musé, P., Flores, G. F., Lema, G., Mastrángelo, P., Almansa, M., Liñares, I. F. & Liñares, G. F. (2015), Early pest detection in soy plantations from hyperspectral measurements: a case study for caterpillar detection, *in* 'SPIE Remote Sensing', International Society for Optics and Photonics, pp. 96372I–96372I.
- Tajima, J. (1983), 'Uniform color scale applications to computer graphics', *Computer Vision, Graphics, and Image Processing* **21**(3), 305–325.
- Tardieu, F., Bruckler, L. & Lafolie, F. (1992), 'Root clumping may affect the root water potential and the resistance to soil-root water transport', *Plant and Soil* **140**(2), 291–301.
- Tartaglia, L. J. (1977), 'Infrared archaeological reconnaissance', *Remote Sensing Techniques in Archaeology. Albuquerque, NM, Chaco Center* pp. 35–50.
- Tenhunen, J., Lange, O., Gebel, J., Beyschlag, W. & Weber, J. (1984), 'Changes in photosynthetic capacity, carboxylation efficiency, and co₂ compensation point associated with midday stomatal closure and midday depression of net co₂ exchange of leaves of quercus suber', *Planta* **162**(3), 193–203.
- Tetley, C. & Young, S. (2007), 'Digital infrared and ultraviolet imaging part 1: infrared', *Journal of visual communication in medicine* **30**(4), 162–171.
- Thorup-Kristensen, K., Salmern Cortasa, M. & Loges, R. (2009), 'Winter wheat roots grow twice as deep as spring wheat roots, is this important for n uptake and n leaching losses?', *Plant and Soil* **322**(1-2), 101–114.
- Tiwari, A. & Dixit, A. (2015), 'Unmanned aerial vehicle and geospatial technology pushing the limits of development', *American Journal of Engineering Research* **4**, 16–21.
- Toet, A. & Walraven, J. (1996), 'New false color mapping for image fusion', *Optical Engineering* **35**(3), 650–658.
- Torrance, K. E. & Sparrow, E. M. (1967), 'Theory for off-specular reflection from roughened surfaces', *JOSA* **57**(9), 1105–1112.
- Toth, C. & Józków, G. (2016), 'Remote sensing platforms and sensors: A survey', *ISPRS Journal of Photogrammetry and Remote Sensing* **115**, 22–36.

- Tucker, C. J. (1980), 'Radiometric resolution for monitoring vegetation how many bits are needed?', *International Journal of Remote Sensing* **1**(3), 241–254.
- van der Tol, C., Verhoef, W. & Rosema, A. (2009), 'A model for chlorophyll fluorescence and photosynthesis at leaf scale', *Agricultural and Forest Meteorology* **149**(1), 96–105.
- Veihmeyer, F. & Hendrickson, A. (1927), 'The relation of soil moisture to cultivation and plant growth', *Proc. 1st Intern. Congr. Soil Sci* **3**, 498–513.
- Verhoeven, G. (2008), 'Imaging the invisible using modified digital still cameras for straightforward and low-cost archaeological near-infrared photography', *Journal of Archaeological Science* **35**(12), 3087–3100.
- Verhoeven, G. & Doneus, M. (2011), 'Balancing on the borderline - a low-cost approach to visualize the red-edge shift for the benefit of aerial archaeology: Balancing on the red-edge borderline', *Archaeological Prospection* **18**(4), 267–278.
- Verhoeven, G., Doneus, M., Atzberger, C., Wess, M., Rus, M., Pregesbauer, M. & Briese, C. (2013), New approaches for archaeological feature extraction of airborne imaging spectroscopy data, in '10th International Conference on Archaeological Prospection', pp. 13–15.
- Verhoeven, G. J. (2009), 'Providing an archaeological bird's-eye view—an overall picture of ground-based means to execute low-altitude aerial photography (laap) in archaeology', *Archaeological Prospection* **16**(4), 233–249.
- Verhoeven, G. J. (2011), 'Near-infrared aerial crop mark archaeology: From its historical use to current digital implementations', *Journal of Archaeological Method and Theory* **19**(1), 132–160.
- Verhoeven, G., Nowak, M. & Nowak, R. (2016), Pixel-level image fusion for archaeological interpretative mapping, in '8th International Congress on Archaeology, Computer Graphics, Cultural Heritage and Innovation (ARQUEOLÓGICA 2.0)', Editorial Universitat Politècnica de València, pp. 404–407.
- Verhoeven, G. & Sevara, C. (2016), 'Trying to break new ground in aerial archaeology', *Remote Sensing* **8**(11), 918.
- Verhoeven, G., Smet, P., Poelman, D. & Vermeulen, F. (2009), 'Spectral characterization of a digital still camera's NIR modification to enhance archaeological observation', *IEEE Transactions on Geoscience and Remote Sensing* **47**(10), 3456–3468.

- Verhoeven, G. & Vermeulen, F. (2016), 'Engaging with the canopy multi-dimensional vegetation mark visualisation using archived aerial images', *Remote Sensing* **8**(9), 752.
- Vivone, G., Alparone, L., Chanussot, J., Dalla Mura, M., Garzelli, A., Licciardi, G. A., Restaino, R. & Wald, L. (2015), 'A critical comparison among pansharpening algorithms', *IEEE Transactions on Geoscience and Remote Sensing* **53**(5), 2565–2586.
- Vogelmann, J. E., Rock, B. N. & Moss, D. M. (1993), 'Red edge spectral measurements from sugar maple leaves', *International Journal of Remote Sensing* **14**(8), 1563–1575.
- Vosselman, G. & Maas, H.-G. (2010), *Airborne and terrestrial laser scanning*, Whittles Publishing.
- Wagner, W., Hollaus, M., Briese, C. & Ducic, V. (2008), '3d vegetation mapping using small-footprint full-waveform airborne laser scanners', *International Journal of Remote Sensing* **29**(5), 1433–1452.
- Wagner, W., Roncat, A., Melzer, T. & Ullrich, A. (2007), 'Waveform analysis techniques in airborne laser scanning', *International Archives of Photogrammetry and Remote Sensing* **36**(3), 413–418.
- Wagner, W., Ullrich, A., Melzer, T., Briese, C. & Kraus, K. (2004), 'From single-pulse to full-waveform airborne laser scanners: potential and practical challenges', *International Archives of Photogrammetry and Remote Sensing* **35**(B3), 201–206.
- Wallace, A. M., McCarthy, A., Nichol, C. J., Ren, X., Morak, S., Martinez-Ramirez, D., Woodhouse, I. H. & Buller, G. S. (2014), 'Design and evaluation of multispectral lidar for the recovery of arboreal parameters', *IEEE Transactions on Geoscience and Remote Sensing* **52**(8), 4942–4954.
- Wang, F.-m., Wang, Y. & Huang, J.-f. (2004), 'Spectra characteristics of rape canopy at different nitrogen levels [j]', *Remote Sensing Technology and Application* **2**, 002.
- Warren, M. A., Taylor, B. H., Grant, M. G. & Shutler, J. D. (2014), 'Data processing of remotely sensed airborne hyperspectral data using the airborne processing library (apl): Geocorrection algorithm descriptions and spatial accuracy assessment', *Computers & Geosciences* **64**, 24–34.
- Watson, A. B. & Null, C. H. (1997), 'Digital images and human vision', *NASA Technical Reports* .

- Wehr, A. & Lohr, U. (1999), 'Airborne laser scanning introduction and overview', *ISPRS Journal of photogrammetry and remote sensing* **54**(2), 68–82.
- Weiss, M. & Baret, F. (1999), 'Evaluation of canopy biophysical variable retrieval performances from the accumulation of large swath satellite data', *Remote sensing of environment* **70**(3), 293–306.
- Welch, B. L. (1947), 'The generalization of 'student's' problem when several different population variances are involved', *Biometrika* **34**(1/2), 28.
- Welles, J. M. & Cohen, S. (1996), 'Canopy structure measurement by gap fraction analysis using commercial instrumentation', *Journal of Experimental Botany* **47**(9), 1335–1342.
- White, J. G. & Zasoski, R. J. (1999), 'Mapping soil micronutrients', *Field crops research* **60**(1), 11–26.
- White, R. G. & Kirkegaard, J. A. (2010), 'The distribution and abundance of wheat roots in a dense, structured subsoil—implications for water uptake', *Plant, cell & environment* **33**(2), 133–148.
- Wilkinson, K., Tyler, A., Davidson, D. & Grieve, I. (2006), 'Quantifying the threat to archaeological sites from the erosion of cultivated soil', *Antiquity* **80**(309), 658–670.
- Wilkinson, M. T., Richards, P. J. & Humphreys, G. S. (2009), 'Breaking ground: pedological, geological, and ecological implications of soil bioturbation', *Earth-Science Reviews* **97**(1), 257–272.
- Wilson, C. A., Davidson, D. A. & Cresser, M. S. (2008), 'Multi-element soil analysis: an assessment of its potential as an aid to archaeological interpretation', *Journal of Archaeological Science* **35**(2), 412–424.
- Wilson, D. (1975), 'Photographic techniques in the air', *Aerial reconnaissance for archaeology* **12**, 12–31.
- Wilson, D. R. (1982), *Air photo interpretation for archaeologists*, Batsford London.
- Winter, M. E. & Winter, E. M. (2002), Physics-based resolution enhancement of hyperspectral data, in 'Proceedings of SPIE', Vol. 4725, pp. 580–587.

- Winterbottom, S. J. & Dawson, T. (2005), 'Airborne multi-spectral prospection for buried archaeology in mobile sand dominated systems', *Archaeological Prospection* **12**(4), 205–219.
- Winton, H., Horne, P., Olesen, L. H., Stoker, A., Palmer, R., Deegan, A., Musson, C., Radcliffe, F. F., Burks, J., Bacilieri, C. et al. (2010), 'Mapping archaeology', *Landscapes through the Lens: Aerial Photographs and Historic Environment* **2**, 7.
- Woebbecke, D. M., Meyer, G. E., Von Bargen, K. & Mortensen, D. A. (1995), 'Color indices for weed identification under various soil, residue, and lighting conditions', *Transactions of the ASAE* **38**(1), 259–269.
- Woodcock, C. E. & Strahler, A. H. (1987), 'The factor of scale in remote sensing', *Remote sensing of Environment* **21**(3), 311–332.
- Wozencraft, J. & Millar, D. (2005), 'Airborne lidar and integrated technologies for coastal mapping and nautical charting', *Marine Technology Society Journal* **39**(3), 27–35.
- Xu, H. & Becker, P. (2012), 'Arcgis data models for managing and processing imagery', *ISPRS-International Archives of the Photogrammetry, Remote Sensing and Spatial Information Sciences* **39**.
- Yorston, R. M., Gaffney, V. L. & Reynolds, P. J. (1990), 'Simulation of artefact movement due to cultivation', *Journal of Archaeological Science* **17**(1), 67–83.
- Yuen, P. W. & Richardson, M. (2010), 'An introduction to hyperspectral imaging and its application for security, surveillance and target acquisition', *The Imaging Science Journal* **58**(5), 241–253.
- Zakaluk, R. & Sri Ranjan, R. (2008), 'Predicting the leaf water potential of potato plants using RGB reflectance', *Canadian Biosciences Engineering* **50**, 7–1.
- Zakšek, K., Oštir, K. & Kokalj, Ž. (2011), 'Sky-view factor as a relief visualization technique.', *Remote Sensing* **3**(2).
- Zarco-Tejada, P., Berni, J., Surez, L., Sepulcre-Cant, G., Morales, F. & Miller, J. (2009), 'Imaging chlorophyll fluorescence with an airborne narrow-band multispectral camera for vegetation stress detection', *Remote Sensing of Environment* **113**(6), 1262–1275.
- Zarco-Tejada, P., González-Dugo, M. & Fereres, E. (2016), 'Seasonal stability of chlorophyll fluorescence quantified from airborne hyperspectral imagery as an indicator of net

- photosynthesis in the context of precision agriculture', *Remote Sensing of Environment* **179**, 89–103.
- Zarco-Tejada, P., Gonzalez-Dugo, V. & Berni, J. (2012), 'Fluorescence, temperature and narrow-band indices acquired from a UAV platform for water stress detection using a micro-hyperspectral imager and a thermal camera', *Remote Sensing of Environment* **117**, 322–337.
- Zarco-Tejada, P. J., Catalina, A., González, M. & Martín, P. (2013), 'Relationships between net photosynthesis and steady-state chlorophyll fluorescence retrieved from airborne hyperspectral imagery', *Remote Sensing of Environment* **136**, 247–258.
- Zarco-Tejada, P. J., Miller, J. R., Mohammed, G. H. & Noland, T. L. (2000), 'Chlorophyll fluorescence effects on vegetation apparent reflectance: I. leaf-level measurements and model simulation', *Remote Sensing of Environment* **74**(3), 582–595.
- Zarco-Tejada, P. J., Pushnik, J. C., Dobrowski, S. & Ustin, S. L. (2003), 'Steady-state chlorophyll fluorescence detection from canopy derivative reflectance and double-peak red-edge effects', *Remote Sensing of Environment* **84**(2), 283–294.
- Zhang, J. & Davies, W. J. (1989), 'Abscisic acid produced in dehydrating roots may enable the plant to measure the water status of the soil', *Plant, Cell & Environment* **12**(1), 73–81.
- Zhang, Y., De Backer, S. & Scheunders, P. (2009), 'Noise-resistant wavelet-based bayesian fusion of multispectral and hyperspectral images', *IEEE Transactions on Geoscience and Remote Sensing* **47**(11), 3834–3843.
- Zhimin, Z., Tianqiao, Z., Dongzhou, K. & Jianfang, Y. (2002), 'False color composite of multi-spectral rs images and its application in environmental geography', *Image Technology* **1**, 010.
- Zimmerman, D. W. & Zumbo, B. D. (1993), 'Rank transformations and the power of the student t test and welch t'test for non-normal populations with unequal variances.', *Canadian Journal of Experimental Psychology/Revue canadienne de psychologie expérimentale* **47**(3), 523.

Appendices

Appendix A

Data and code

A.1 Data

All data considered in this project are hosted on the DART project repository as part of the project's commitment to open science. In addition to the remote sensing data presented here the data from the excavations, soil analyses, monitoring equipment and geophysical surveys. This can be found at <http://dartportal.leeds.ac.uk/group>

A.2 Code

All Python programs used in the analysis of the data for this work are hosted on GitHub under an MIT license. While this code works, it should be considered a proof of concept, as it has not been optimised for performance or tested on a variety of systems. A brief description of each follows.

A.3 Spectral analyses

https://github.com/dav-stott/phd-thesis/blob/master/spectra_thesis2.py

This code is used to derive the vegetation indices, fluorescence indices, MTBVI, and continuum removal. These are accessible through classes for each group of methods, with individual spectral analyses callable as methods of the class. Input spectra must be accompanied by a CSV file denoting the wavelength of each input band.

<https://github.com/dav-stott/phd-thesis/blob/master/>


```
spectra_thesis_analysis2.py
```

This code is for the statistical analysis of the archaeological features. It is used to perform Welch's T-Test on observations classified as either archaeology or background.

```
https://github.com/dav-stott/phd-thesis/blob/master/spectra\_thesis\_ais.py
```

This is for the analysis of contrast in the AIS images. These are mostly a duplication of the classes and methods used in the code for examining the field spectroscopy data discussed above. Input images should be accompanied by a wavelength definition file

```
https://github.com/dav-stott/phd-thesis/blob/master/MTBVI\_AIS.py
```

Code for deriving the MTBVI from hyperspectral imagery. Input images should be accompanied by a wavelength definition file

```
//github.com/dav-stott/phd-thesis/blob/master/asd\_result\_plotting2.py
```

Code for producing plots from the field spectroscopy.

A.4 Raster Analyses

```
https://github.com/dav-stott/phd-thesis/blob/master/raster\_analysis\_ais3.py
```

Code for the estimation of contrast in remote sensing images. This rasterizes a polygon shapefile to the same grid parameters as the input raster, so that pixels can be easily classified for analysis in the output images.

```
https://github.com/dav-stott/phd-thesis/blob/master/ais\_zonal3.py
```

Derives the zonal statistics by applying a T-Test to pixels in an input kernel for all pixels classified as archaeology.

A.5 ALS data

`https://github.com/dav-stott/phd-thesis/blob/fullwaveform_3.py`

Code to extract the full waveforms from ascii data and derive the metrics discussed in chapter 4. This uses a univariate spline to remove high frequency, low magnitude noise, and identifies the maximal cross section of the return from the maximum first derivative of the return.

A.6 RGB images

`https://github.com/dav-stott/phd-thesis/blob/master/specrgb.py`

Code to derive the RGB indices discussed in chapter 5. Accepts RGB images with three bands.

Appendix B

Transect survey results

B.1 Transect Survey conditions

These tables summarise the conditions of the fields during the transect surveys.

Date	Ground cover	PSMD	Spectroradiometry
28/09/2011	Winter Wheat: Feekes 1	56mm	No
26/11/2011	Winter wheat: Feekes 2	46mm	No
23/01/2012	Winter wheat: Feekes 3	-9mm	Yes
16/02/2012	Winter wheat: Feekes 3	-9mm	Yes
20/03/2012	Winter wheat: Feekes 4	-5mm	Yes
25/04/2012	Winter wheat: Feekes 5	-10mm	No
16/05/2013	Winter wheat: Feekes 7	-5mm	Yes
23/05/2012	Winter wheat: Feekes 8	0mm	No
27/06/2012	Winter wheat: Feekes 10.5	-4mm	Yes
24/07/2012	Winter wheat: Feekes 11	2mm	Yes

Table B.1: DDCF transect survey summary

Date	Ground cover	PSMD	Spectroradiometry
08/06/2011	Winter wheat: Feekes 10.1 (heading)	58mm	Yes
14/06/2011	Winter wheat: Feekes 10.5 (flowering)	56mm	Yes
29/06/2011	Winter wheat: Feekes 11 (ripening)	52mm	Yes
15/07/2011	Winter wheat: Feekes 11 (ripening-senescent)	57mm	Yes
24/08/2011	Oilseed rape. Harper stage 0 (pre-emergence)	71mm	Yes
25/10/2011	Oilseed rape. Harper stage 2 (rosette formation)	68mm	Yes
17/11/2011	Oilseed rape. Harper stage 2.1 (rosette growth)	54mm	No
17/12/2011	Oilseed rape. Harper stage 2.4 (rosette growth)	27mm	No
23/01/2012	Oilseed rape. Harper stage 2.6 (rosette growth)	-10mm	No
16/02/2012	Oilseed rape. Harper stage 3.1 (rosette growth)	-9mm	Yes
21/03/2012	Oilseed rape. Harper stage 3.2 (budding)	-8mm	Yes
23/04/2012	Oilseed rape. Harper stage 4.1 (flowering)	-10mm	No
22/05/2012	Oilseed rape. Harper stage 4.2 (flowering)	-1mm	Yes
27/06/2012	Oilseed rape. Harper stage 5.5 (ripening)	-2mm	No

Table B.2: DDT1 Transect Survey summary

Date	Ground cover	PSMD	Spectroradiometry
29/09/2011	Fallow, clover and grasses.	160mm	Yes
16/11/2011	Fallow, clover and grasses.	154mm	No
17/12/2011	Fallow, clover and grasses.	56mm	No
25/01/2012	Fallow, clover and grasses.	-10mm	No
15/02/2012	Fallow, clover and grasses.	-10mm	No
23/03/2012	Spring wheat drilled: Feekes 0	-0.5	Yes
25/04/2012	Spring wheat: Feekes 3	8mm	No
24/05/2012	Spring wheat: Feekes 6	21mm	Yes
20/06/2012	Spring wheat: Feekes 10	-3mm	Yes
26/07/2012	Spring wheat: Feekes 11	28mm	Yes
23/08/2012	Spring wheat: Feekes 11	9.7mm	Yes

Table B.3: HHQF Transect Survey summary

Date	Ground cover	PSMD	Spectroradiometry
27/06/2011	Spring wheat: Feekes 10.5	110mm	No
29/09/2011	Pasture, drilled with grass and clover mix	160mm	Yes
28/10/2011	Pasture, grazed by sheep	171mm	Yes
17/12/2011	Pasture, grazed by sheep	56mm	Yes
25/01/2012	Pasture, grass and clover.	-10mm	No
14/02/2012	Pasture, grass and clover.	-10mm	Yes
20/03/2012	Hay meadow, grass, wildflowers and clover	0mm	Yes
24/04/2012	Hay meadow, grass, wildflowers and clover	8mm	No
24/05/2012	Hay meadow, grass, wildflowers and clover	21mm	Yes
19/06/2012	Hay meadow, grass, wildflowers and clover	-4mm	Yes
25/07/2012	Hay meadow. Mown.	28mm	Yes
22/08/2012	Pasture. Regenerated grass and clover	10mm	Yes
27/09/2012	Pasture. Regenerated grass and clover	-9mm	Yes

Table B.4: HHCC Transect Survey summary

B.2 Transect survey plots

This section contains full results for the transect surveys undertaken in chapter 3. These are grouped by field and ordered by date.

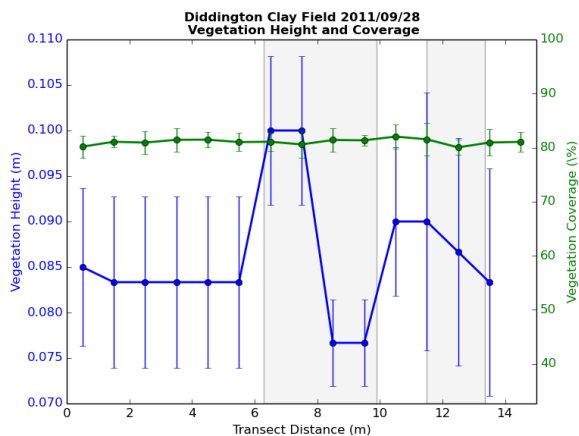


Figure B.1: Physical vegetation properties DDCF 28/09/2011

Figure B.2: Physical vegetation properties DDCF 23/01/2012

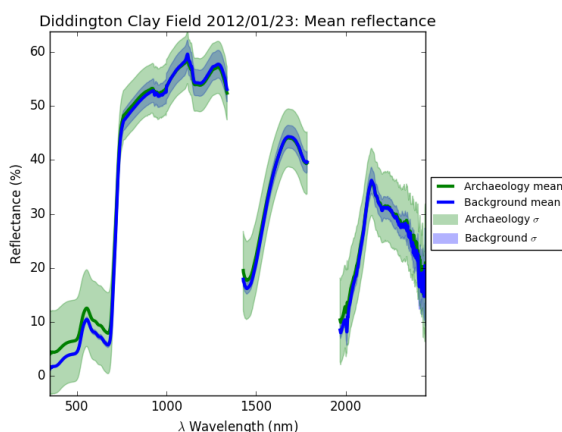


Figure B.3: Spectra from DDCF 23/01/2012

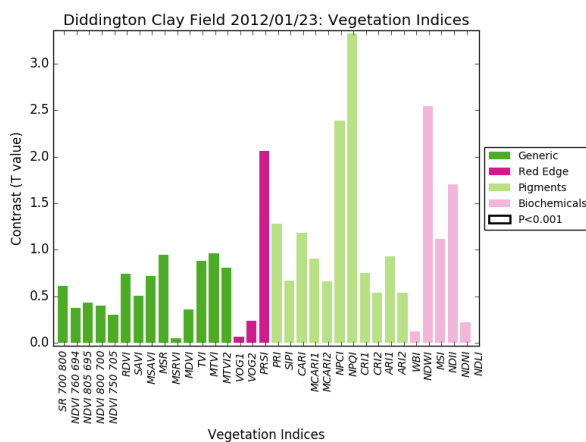


Figure B.4: Vegetation indices DDCF 23/01/2012

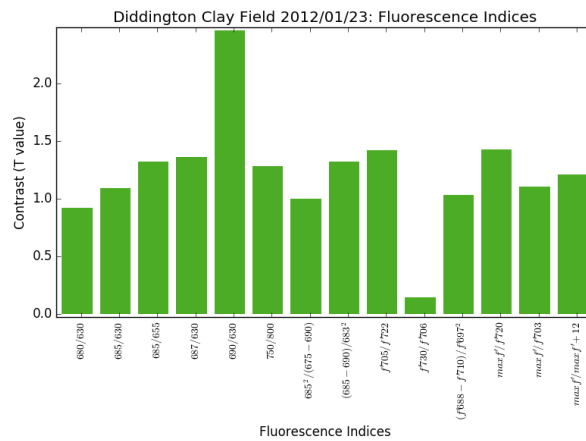


Figure B.5: Fluorescence Indices DDCF 23/01/2012

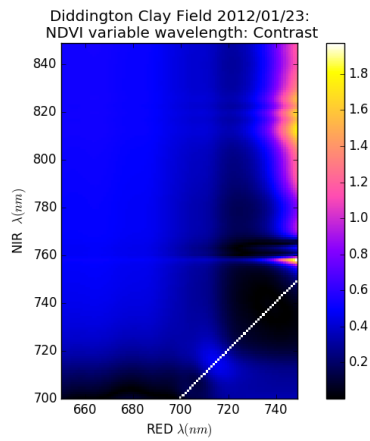


Figure B.6: MTBVI DDCF 23/01/2012

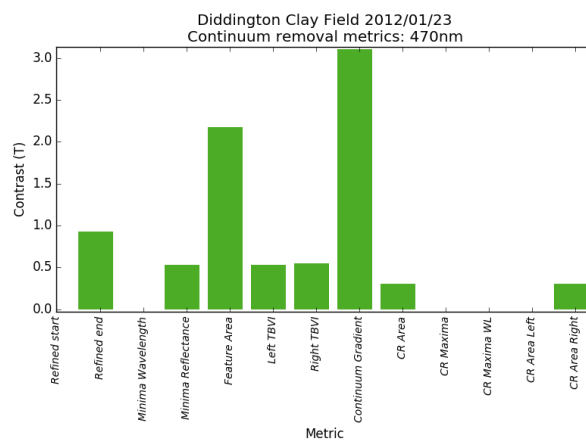


Figure B.7: Continuum removed metrics 470nm DDCF 23/01/2012

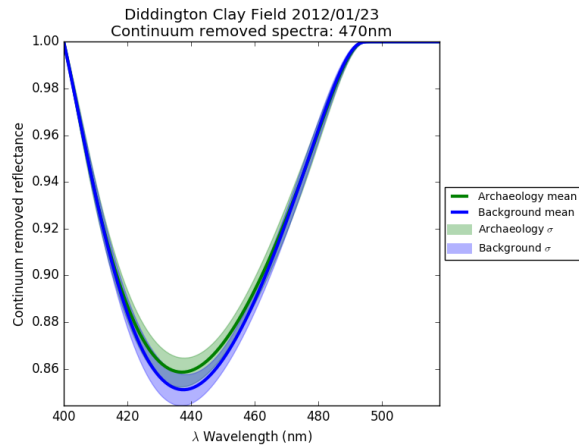


Figure B.8: Continuum removed reflectance 470nm DDCF 23/01/2012

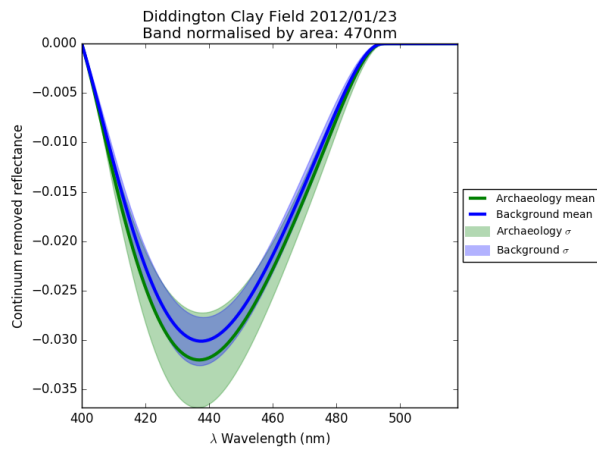


Figure B.9: Continuum removed reflectance band normalised by area 470nm DDCF 23/01/2012

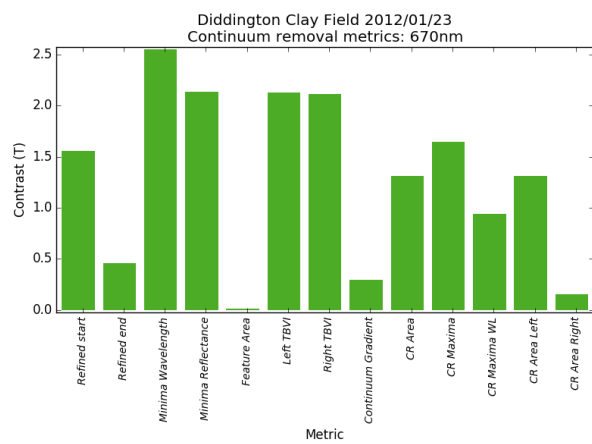


Figure B.10: Continuum removed metrics 670nm DDCF 23/01/2012

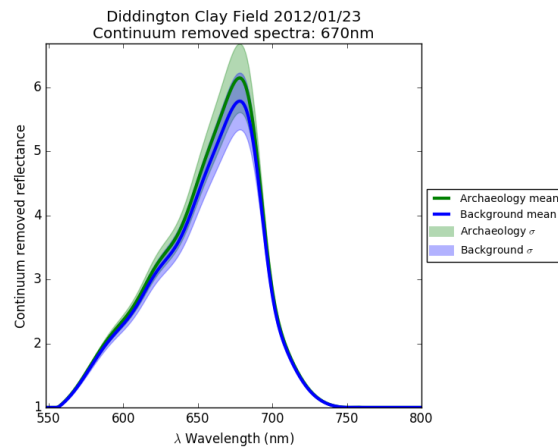


Figure B.11: Continuum removed reflectance 670nm DDCF 23/01/2012

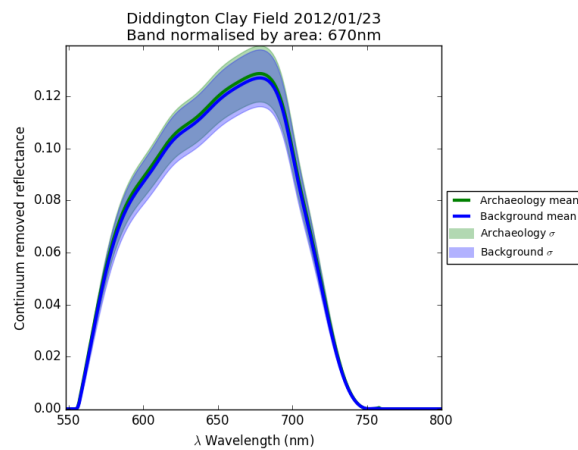


Figure B.12: Continuum removed reflectance band normalised by area 670nm DDCF 23/01/2012

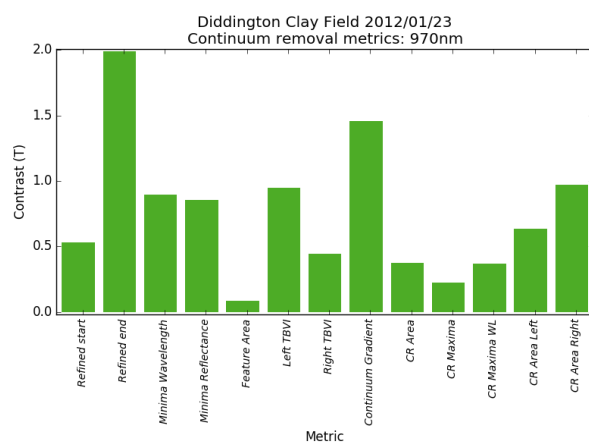


Figure B.13: Continuum removed metrics 970nm DDCF 23/01/2012

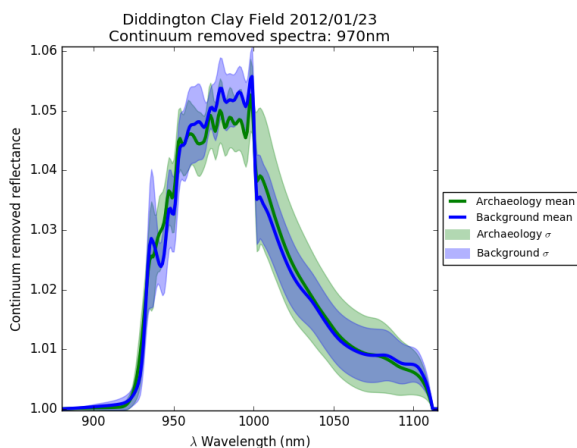


Figure B.14: Continuum removed reflectance 970nm DDCF 23/01/2012

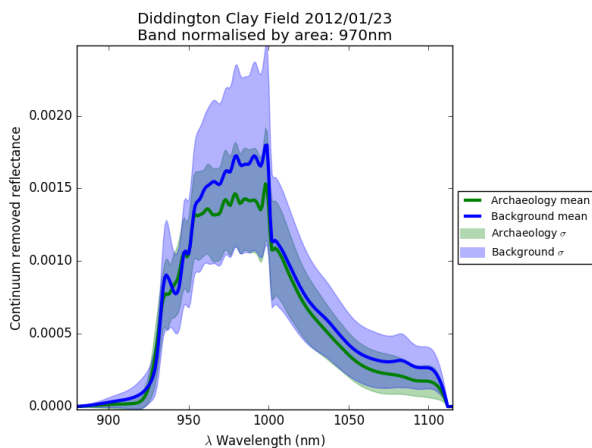


Figure B.15: Continuum removed reflectance band normalised by area 970nm DDCF 23/01/2012

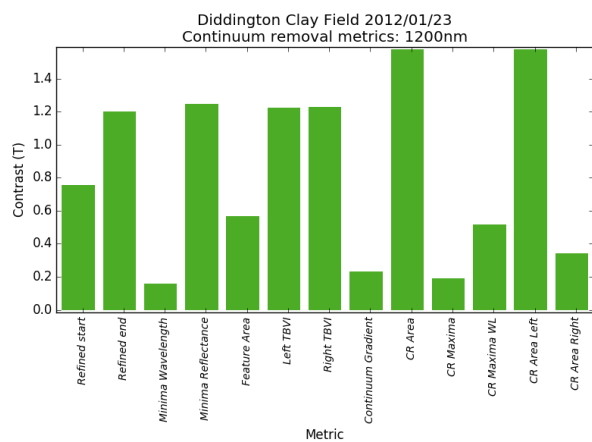


Figure B.16: Continuum removed metrics 1200nm DDCF 23/01/2012

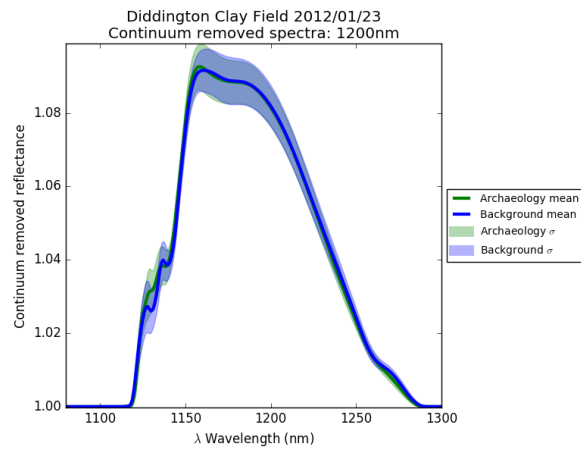


Figure B.17: Continuum removed reflectance 1200nm DDCF 23/01/2012

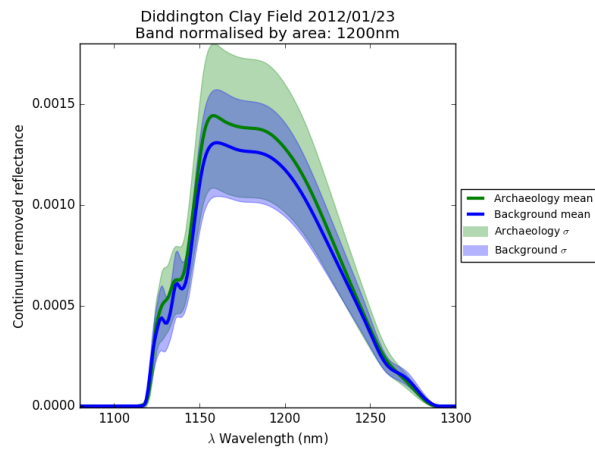


Figure B.18: Continuum removed reflectance band normalised by area 1200nm DDCF 23/01/2012

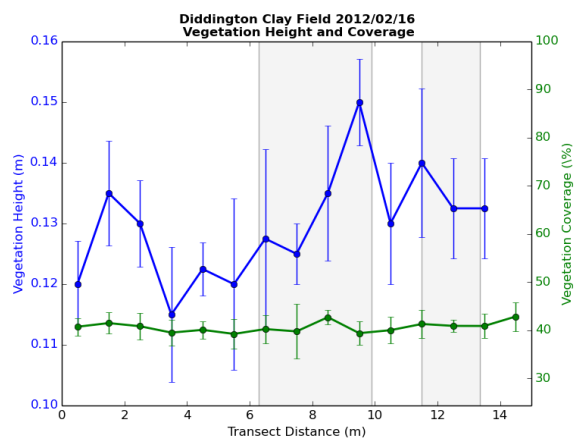


Figure B.19: Physical vegetation properties DDCF 16/02/2012

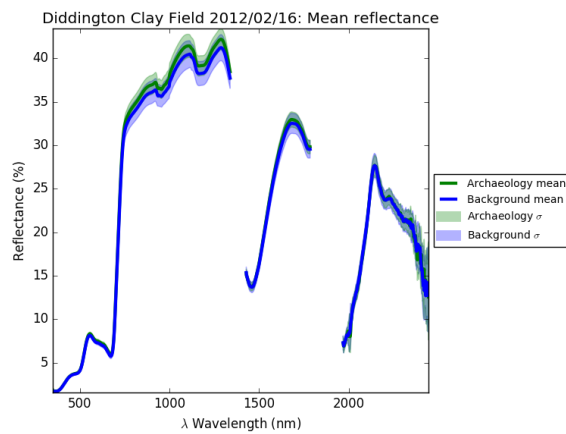


Figure B.20: Spectra from DDCF 16/02/2012

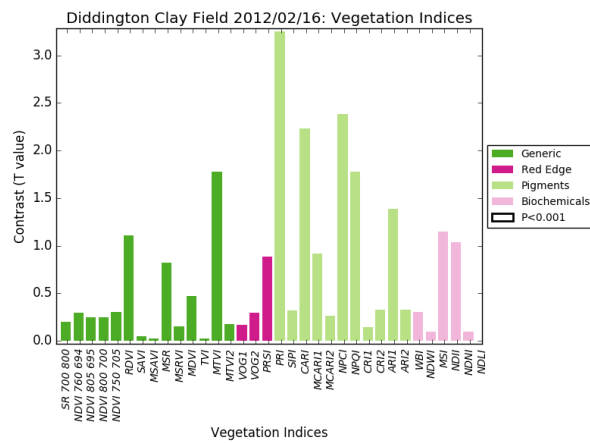


Figure B.21: Vegetation indices DDCF 16/02/2012

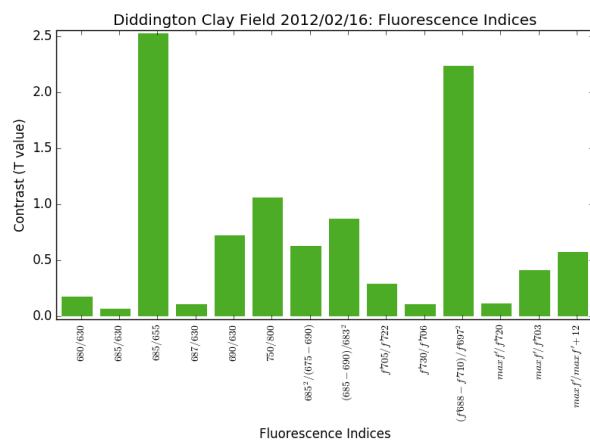


Figure B.22: Fluorescence Indices DDCF 16/02/2012

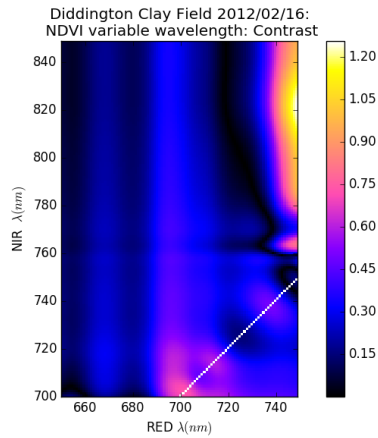


Figure B.23: MTBVI DDCF 16/02/2012

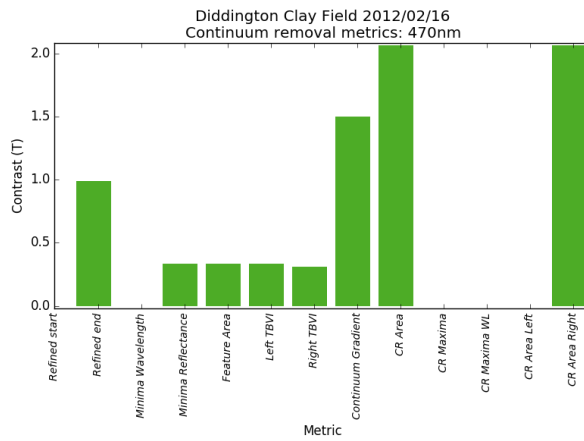


Figure B.24: Continuum removed metrics 470nm DDCF 16/02/2012

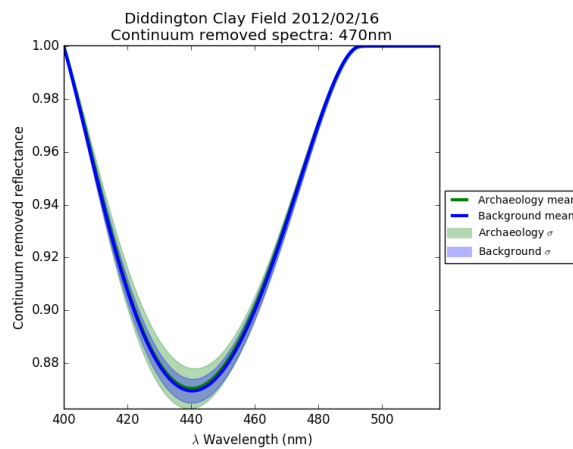


Figure B.25: Continuum removed reflectance 470nm DDCF 16/02/2012

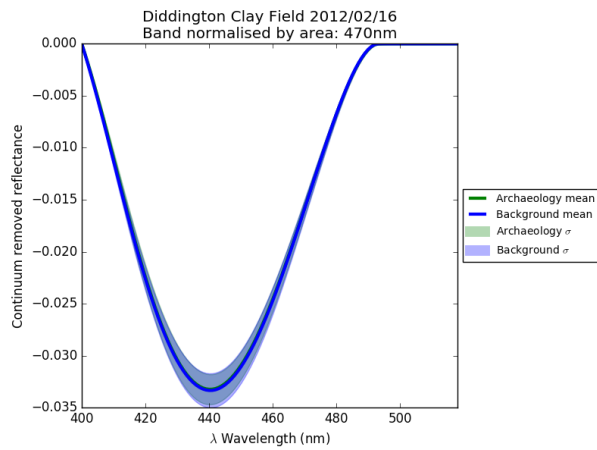


Figure B.26: Continuum removed reflectance band normalised by area 470nm DDCF 16/02/2012

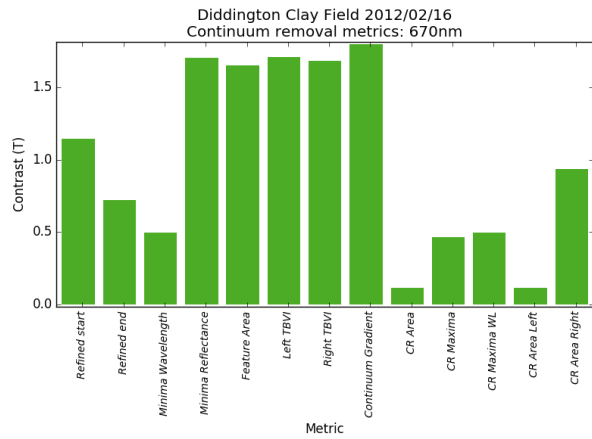


Figure B.27: Continuum removed metrics 670nm DDCF 16/02/2012

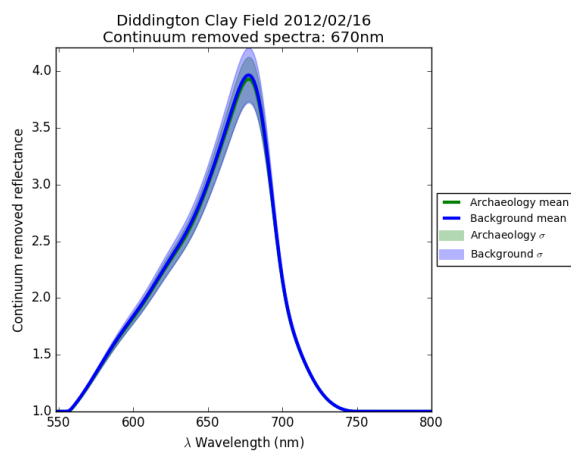


Figure B.28: Continuum removed reflectance 670nm DDCF 16/02/2012

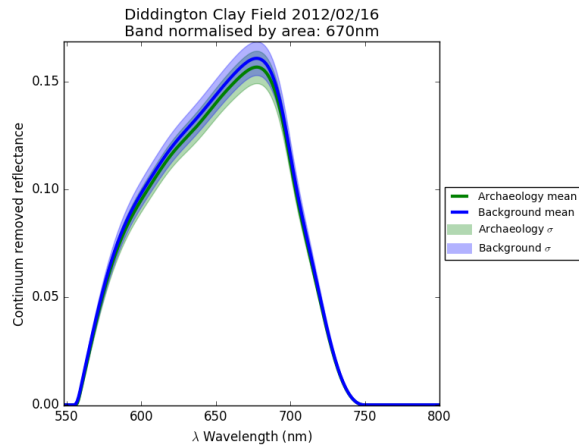


Figure B.29: Continuum removed reflectance band normalised by area 670nm DDCF 16/02/2012

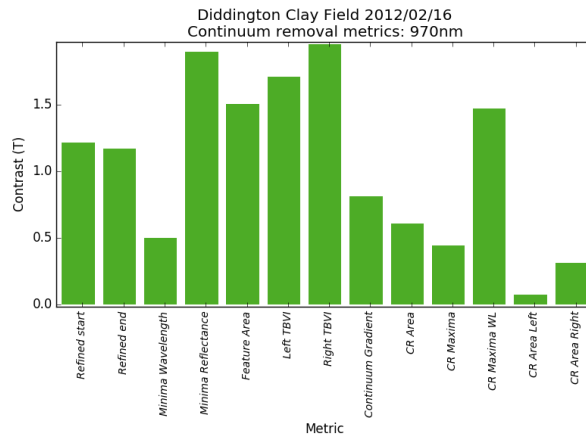


Figure B.30: Continuum removed metrics 970nm DDCF 16/02/2012

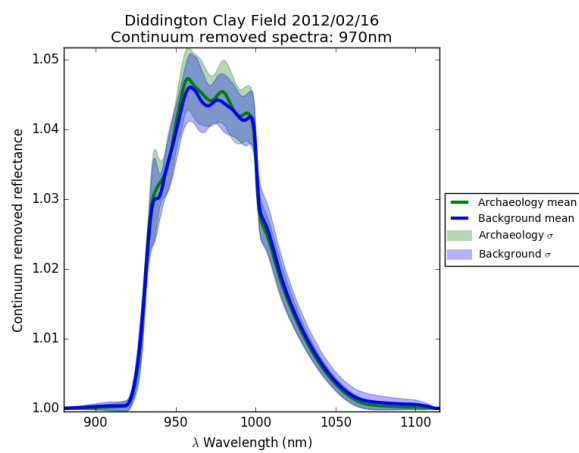


Figure B.31: Continuum removed reflectance 970nm DDCF 16/02/2012

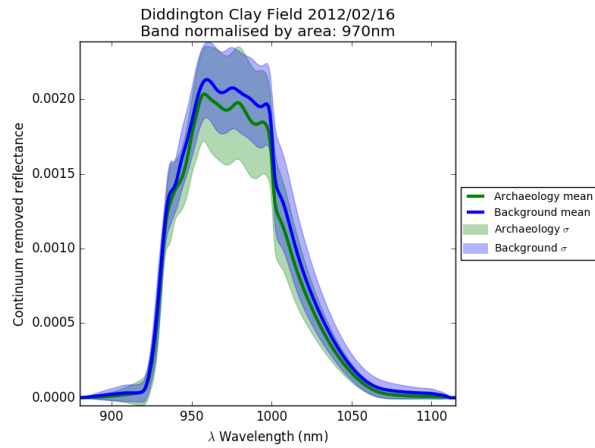


Figure B.32: Continuum removed reflectance band normalised by area 970nm DDCF 16/02/2012

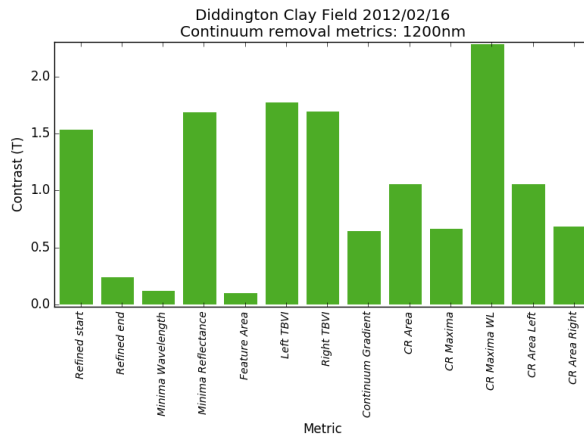


Figure B.33: Continuum removed metrics 1200nm DDCF 16/02/2012

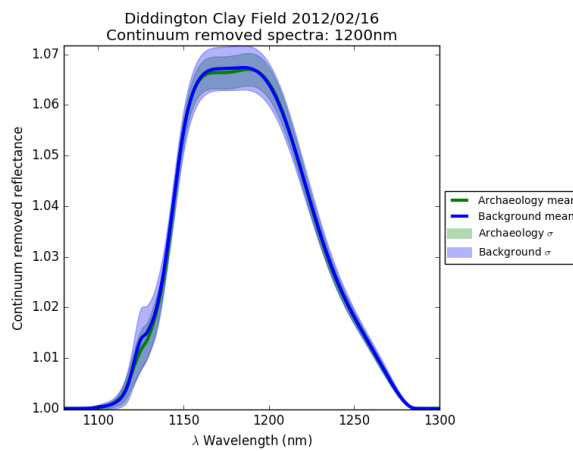


Figure B.34: Continuum removed reflectance 1200nm DDCF 16/02/2012

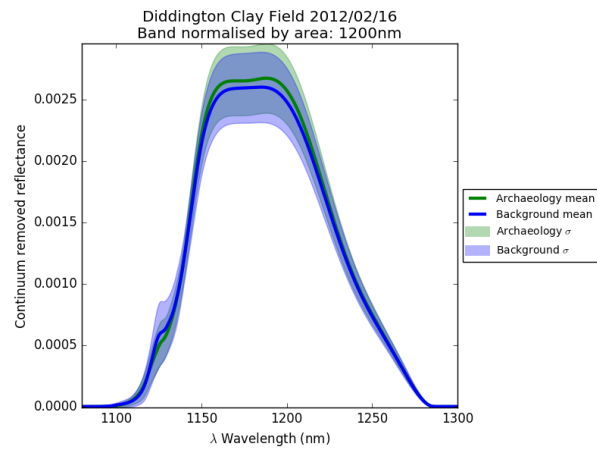


Figure B.35: Continuum removed reflectance band normalised by area 1200nm DDCF 16/02/2012

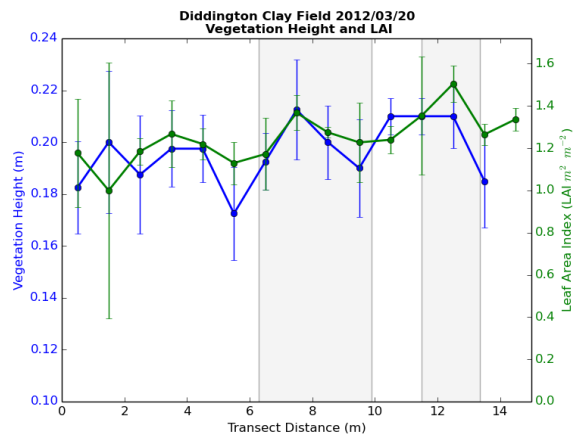


Figure B.36: Physical vegetation properties DDCF 20/03/2012

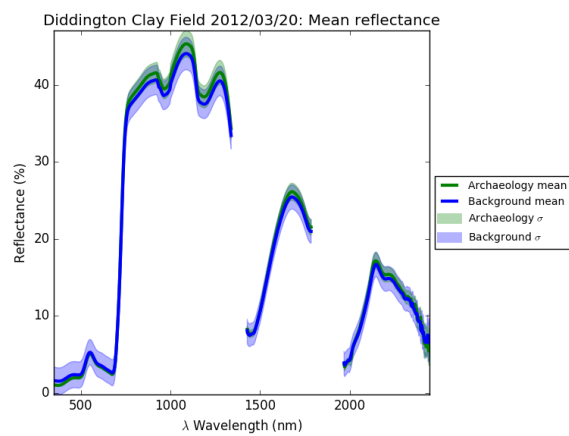


Figure B.37: Spectra from DDCF 20/03/2012

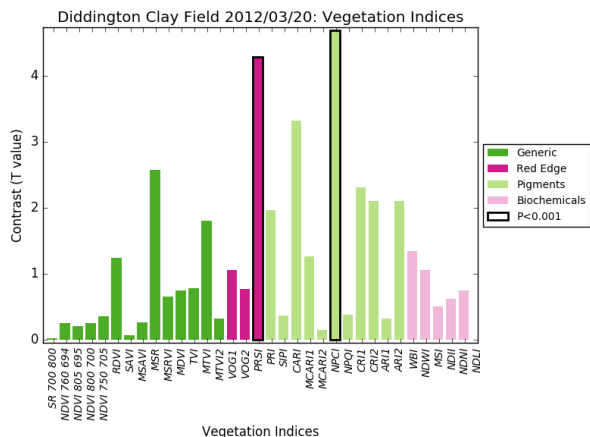


Figure B.38: Vegetation indices DDCF 20/03/2012

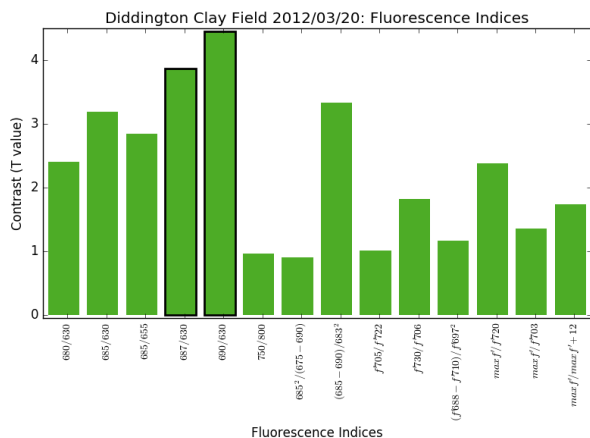


Figure B.39: Fluorescence Indices DDCF 20/03/2012

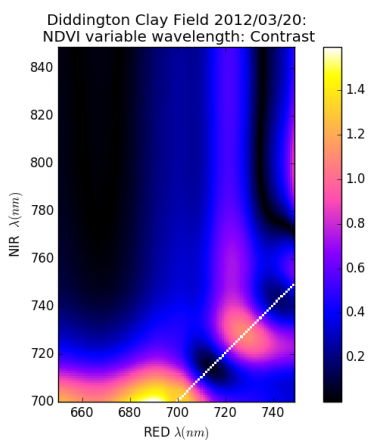


Figure B.40: MTBVI DDCF 20/03/2012

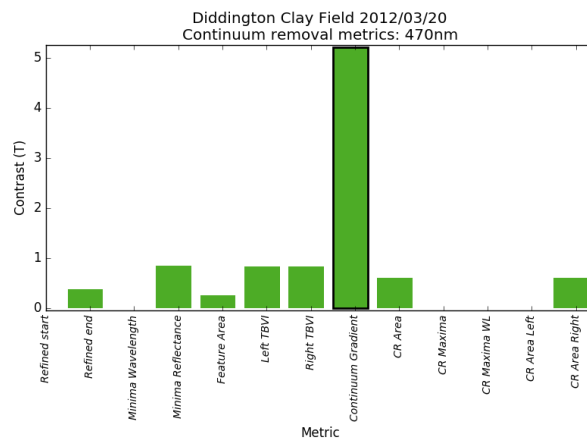


Figure B.41: Continuum removed metrics 470nm DDCF 20/03/2012

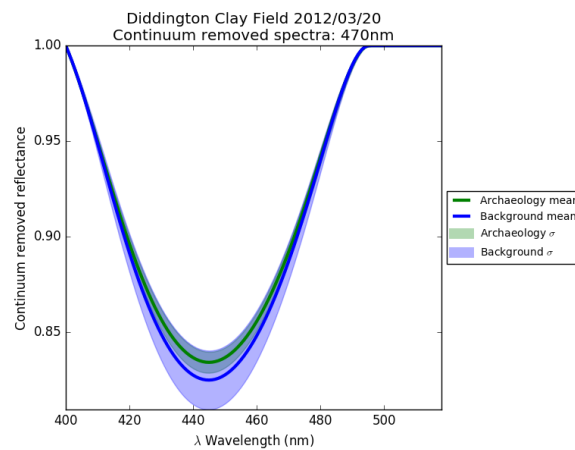


Figure B.42: Continuum removed reflectance 470nm DDCF 20/03/2012

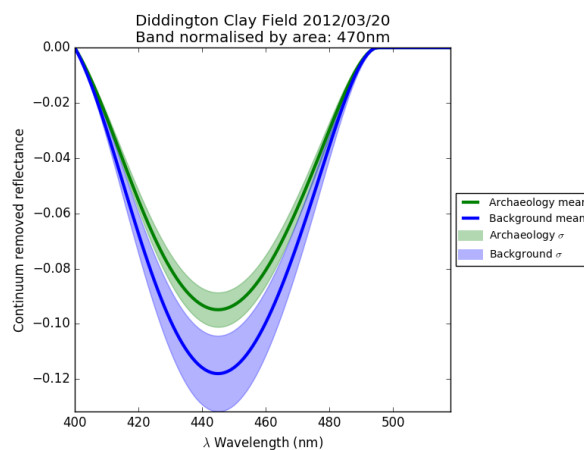


Figure B.43: Continuum removed reflectance band normalised by area 470nm DDCF 20/03/2012

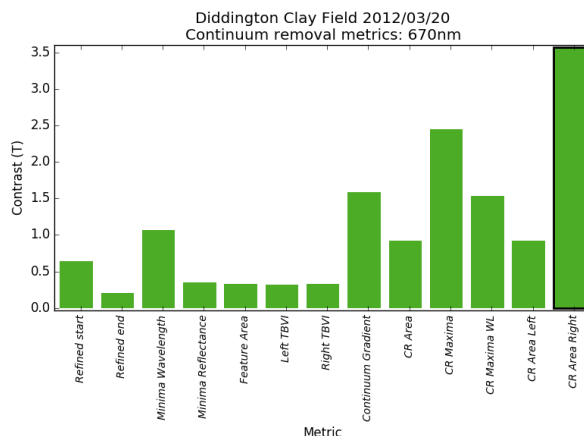


Figure B.44: Continuum removed metrics 670nm DDCF 20/03/2012

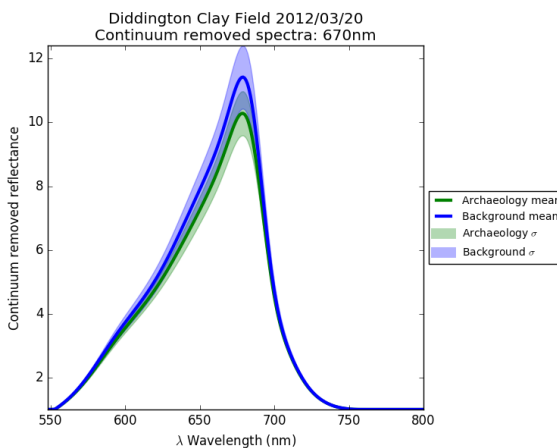


Figure B.45: Continuum removed reflectance 670nm DDCF 20/03/2012

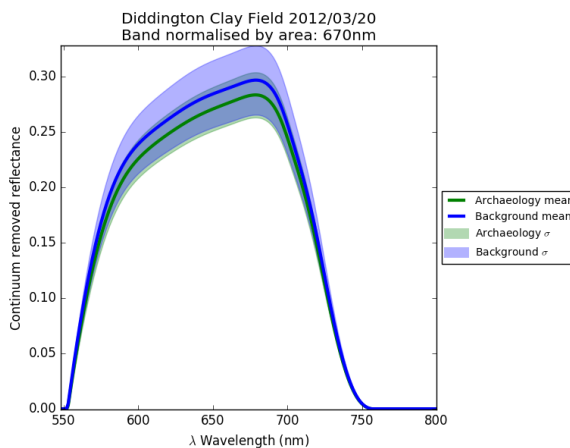


Figure B.46: Continuum removed reflectance band normalised by area 670nm DDCF 20/03/2012

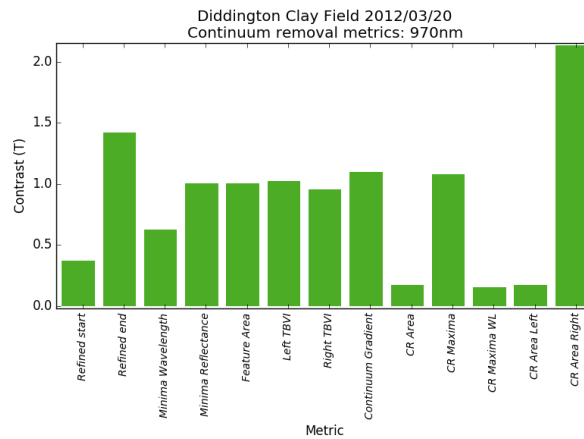


Figure B.47: Continuum removed metrics 970nm DDCF 20/03/2012

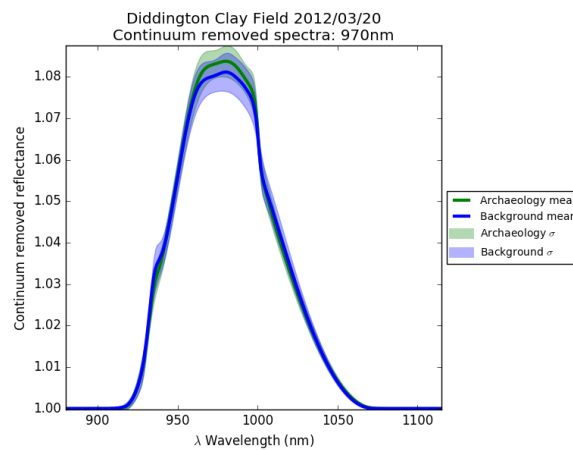


Figure B.48: Continuum removed reflectance 970nm DDCF 20/03/2012

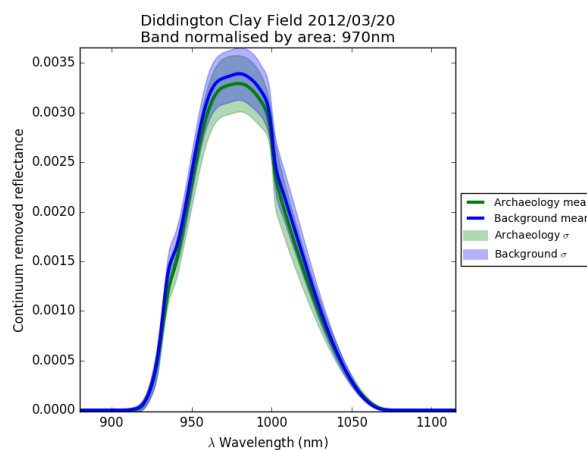


Figure B.49: Continuum removed reflectance band normalised by area 970nm DDCF 20/03/2012

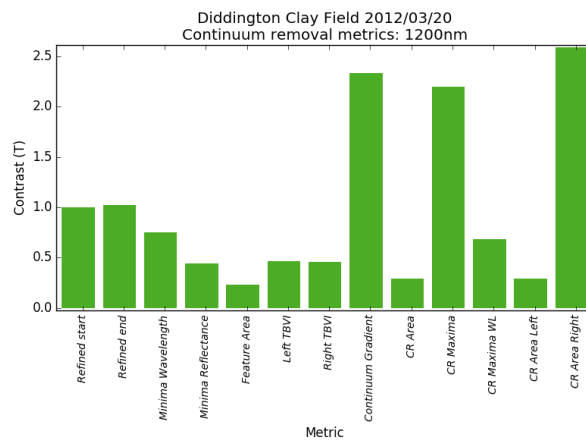


Figure B.50: Continuum removed metrics 1200nm DDCF 20/03/2012

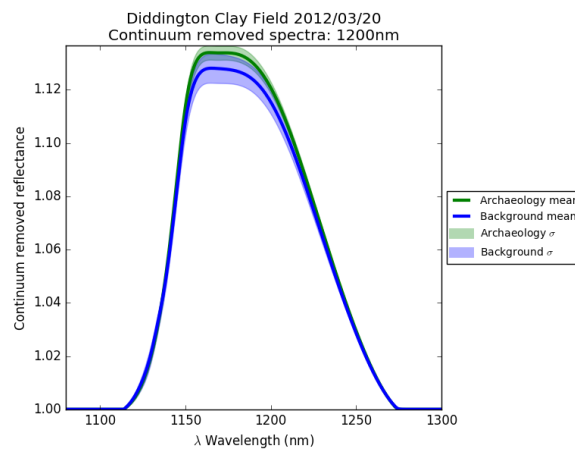


Figure B.51: Continuum removed reflectance 1200nm DDCF 20/03/2012

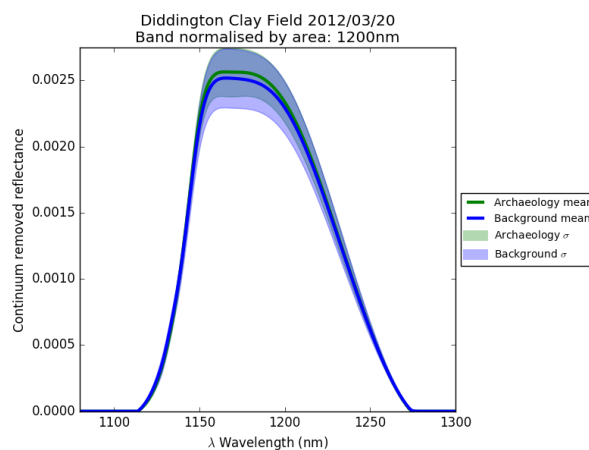


Figure B.52: Continuum removed reflectance band normalised by area 1200nm DDCF 20/03/2012

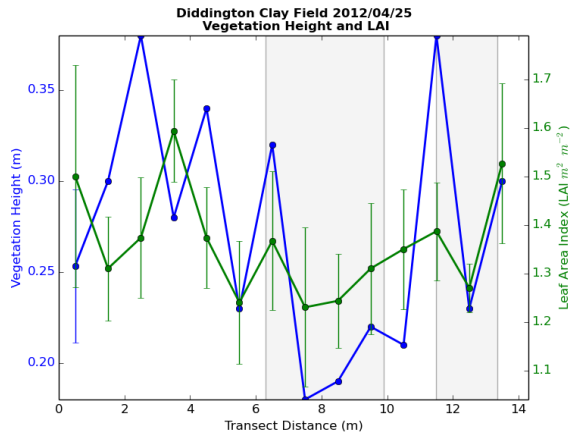


Figure B.53: Physical vegetation properties DDCF 25/04/2012

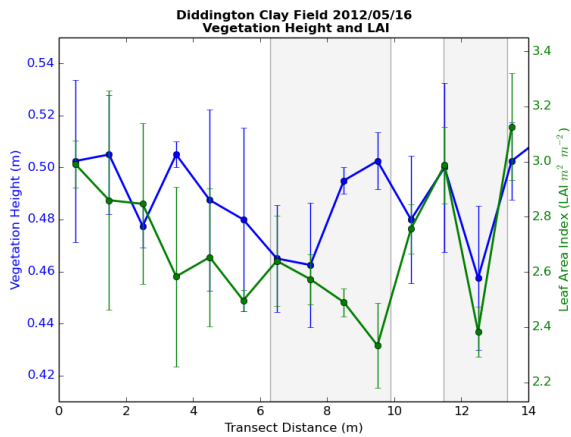


Figure B.54: Physical vegetation properties DDCF 16/05/2012

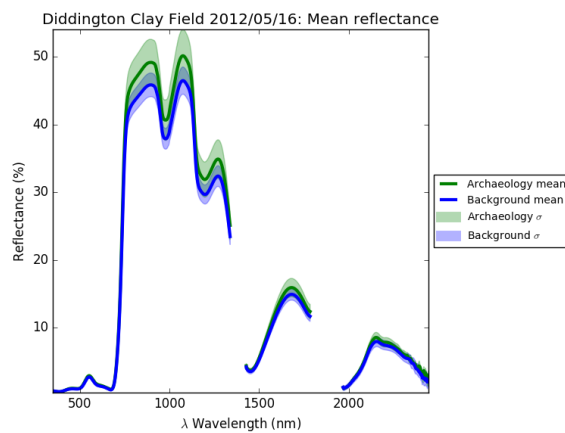


Figure B.55: Spectra from DDCF 16/05/2012

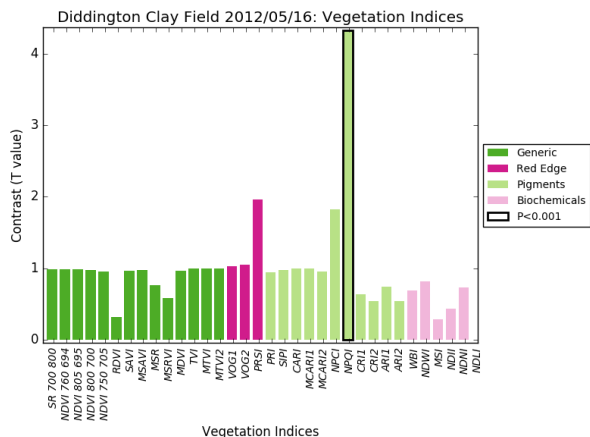


Figure B.56: Vegetation indices DDCF 16/05/2012

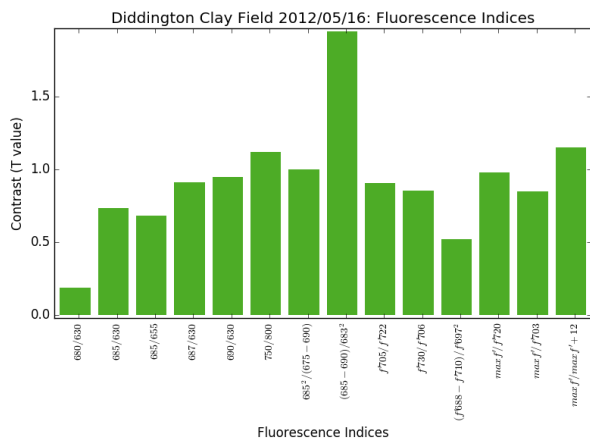


Figure B.57: Fluorescence Indices DDCF 16/05/2012

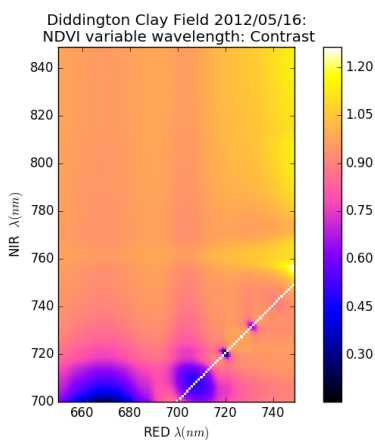


Figure B.58: MTBVI DDCF 16/05/2012

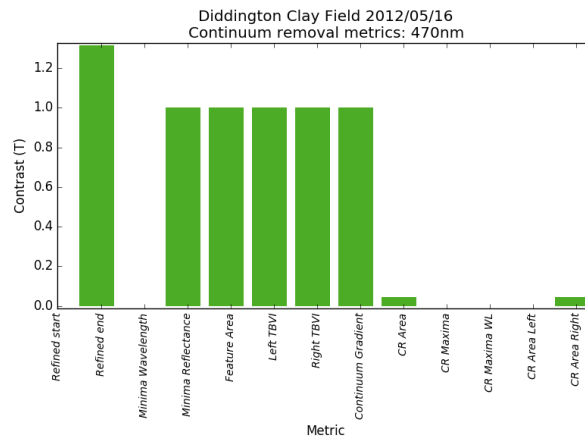


Figure B.59: Continuum removed metrics 470nm DDCF 16/05/2012

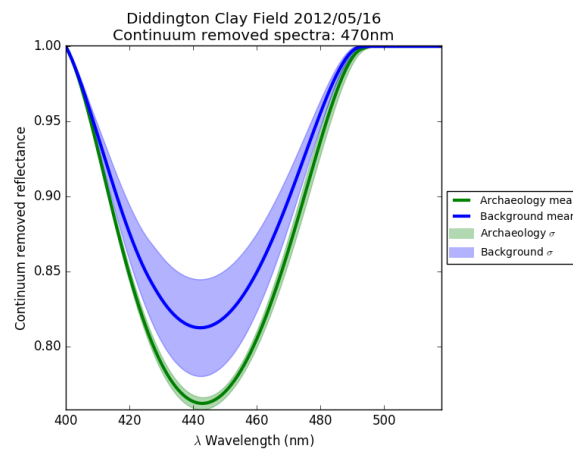


Figure B.60: Continuum removed reflectance 470nm DDCF 16/05/2012

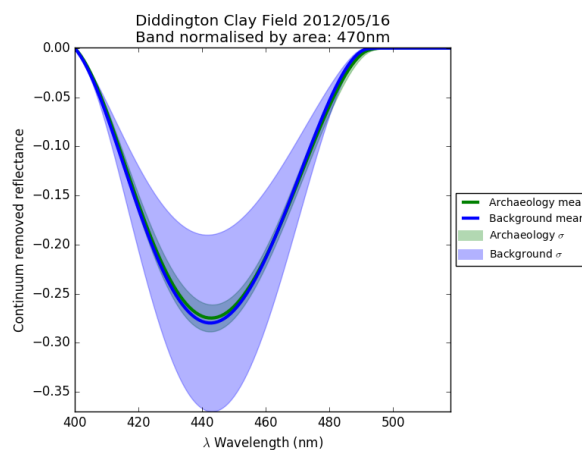


Figure B.61: Continuum removed reflectance band normalised by area 470nm DDCF 16/05/2012

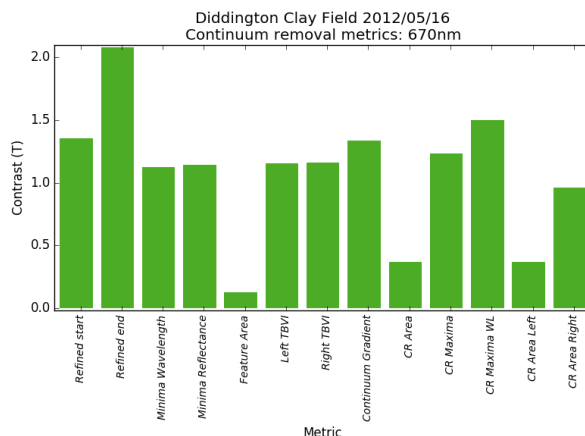


Figure B.62: Continuum removed metrics 670nm DDCF 16/05/2012

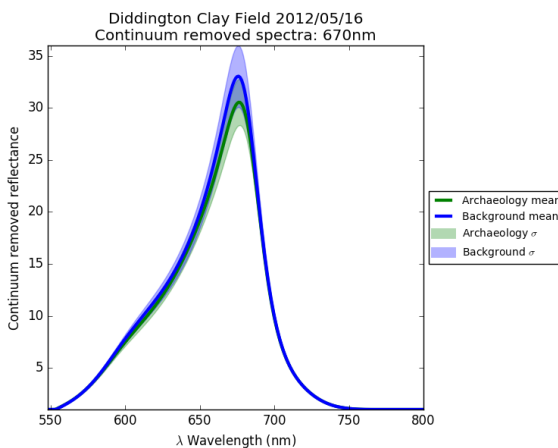


Figure B.63: Continuum removed reflectance 670nm DDCF 16/05/2012

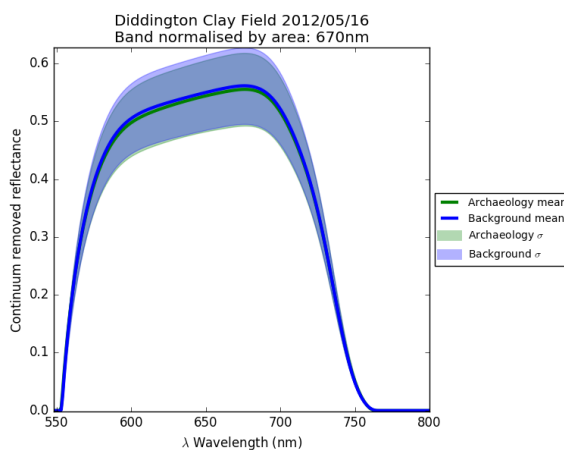


Figure B.64: Continuum removed reflectance band normalised by area 670nm DDCF 16/05/2012

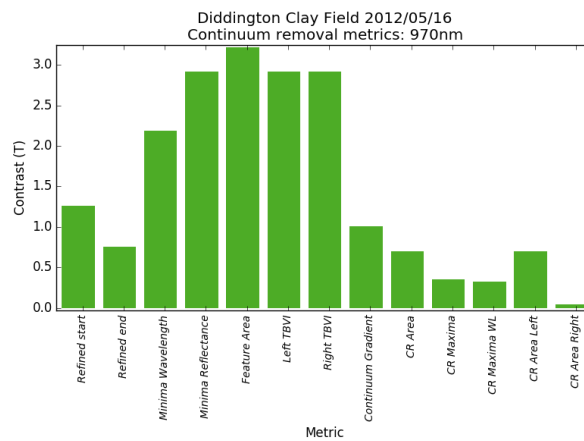


Figure B.65: Continuum removed metrics 970nm DDCF 16/05/2012

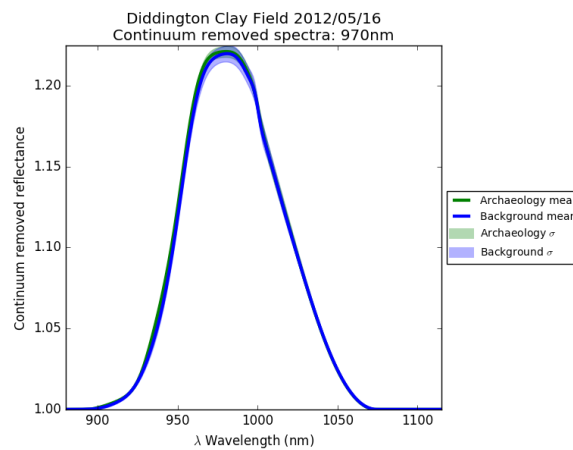


Figure B.66: Continuum removed reflectance 970nm DDCF 16/05/2012

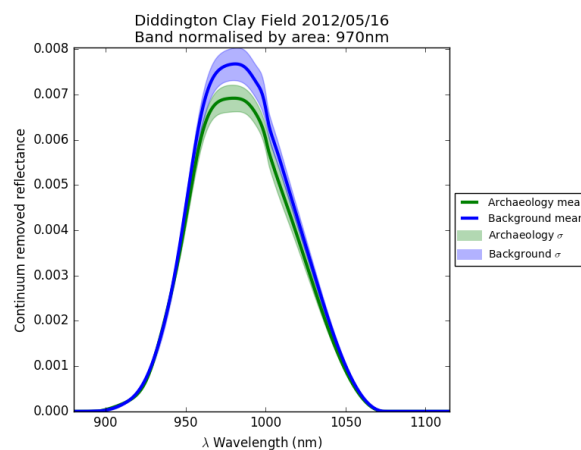


Figure B.67: Continuum removed reflectance band normalised by area 970nm DDCF 16/05/2012

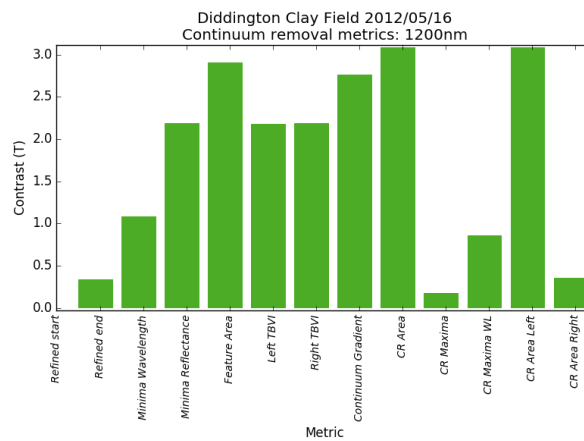


Figure B.68: Continuum removed metrics 1200nm DDCF 16/05/2012

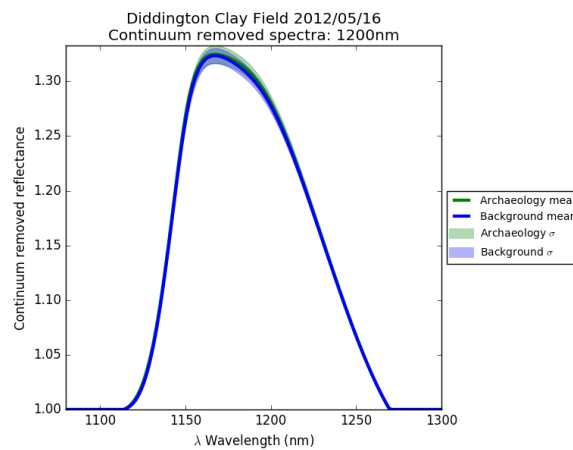


Figure B.69: Continuum removed reflectance 1200nm DDCF 16/05/2012

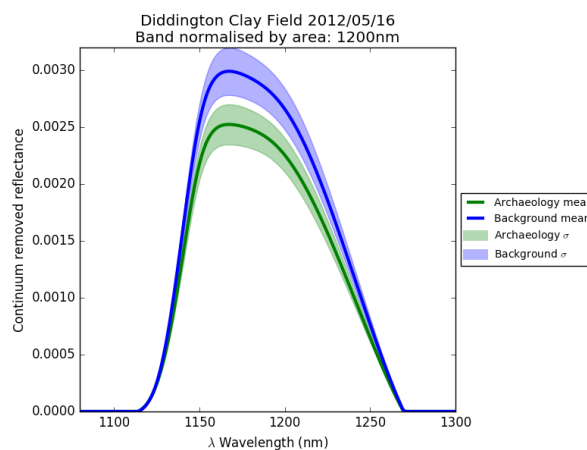


Figure B.70: Continuum removed reflectance band normalised by area 1200nm DDCF 16/05/2012

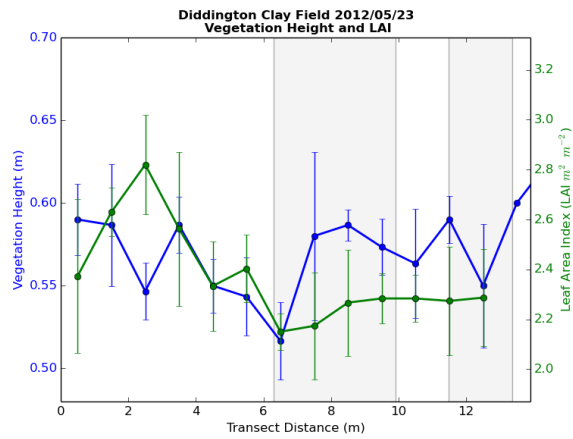


Figure B.71: Physical vegetation properties DDCF 23/05/2012

Figure B.72: Physical vegetation properties DDCF 26/06/2012

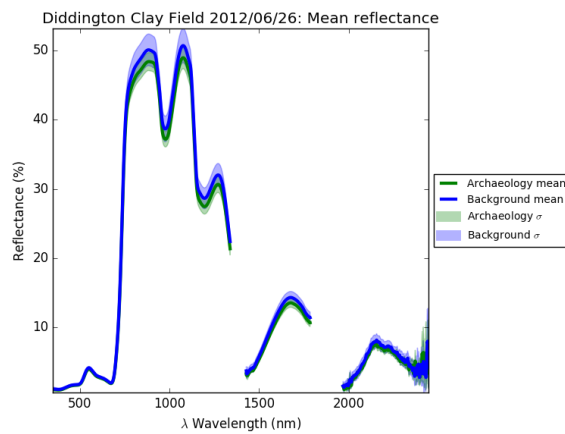


Figure B.73: Spectra from DDCF 26/06/2012

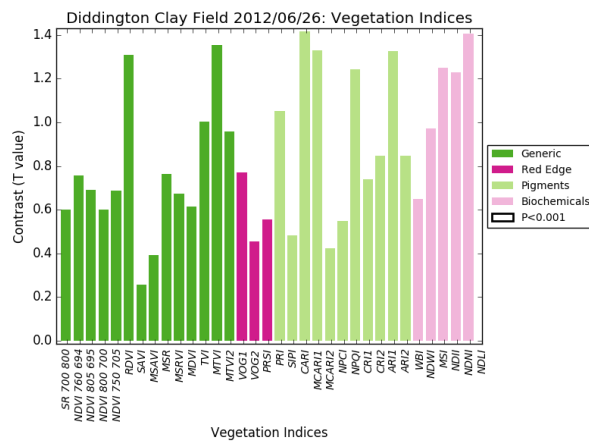


Figure B.74: Vegetation indices DDCF 26/06/2012

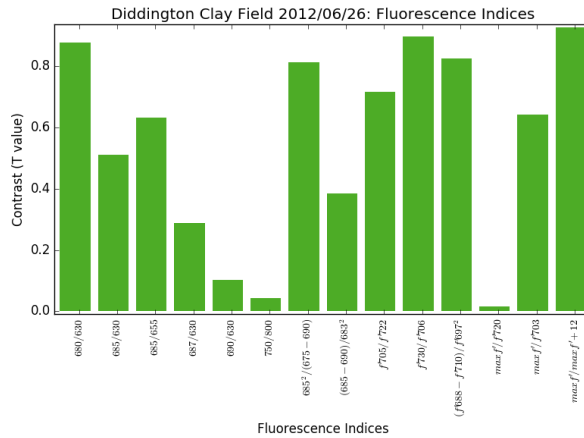


Figure B.75: Fluorescence Indices DDCF 26/06/2012

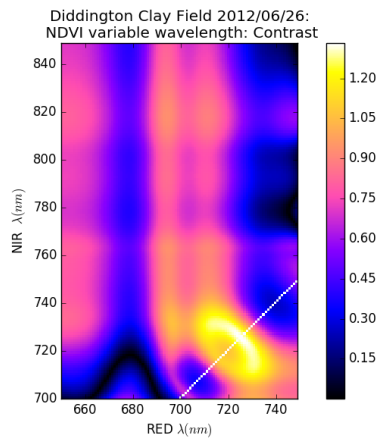


Figure B.76: MTBVI DDCF 26/06/2012

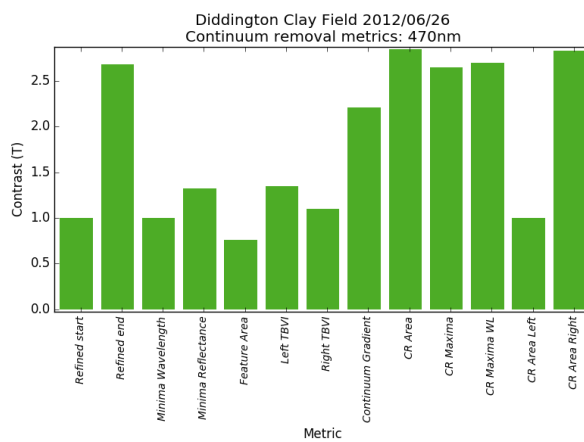


Figure B.77: Continuum removed metrics 470nm DDCF 26/06/2012

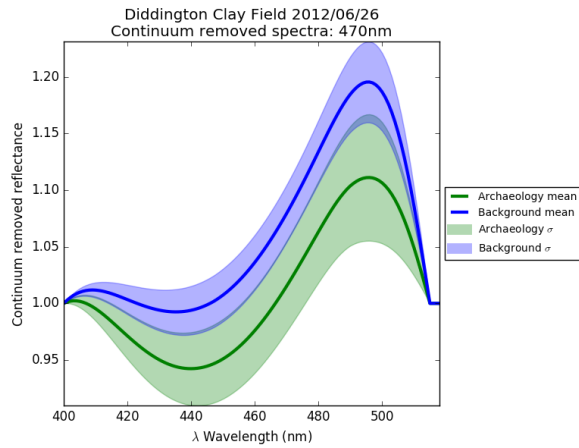


Figure B.78: Continuum removed reflectance 470nm DDCF 26/06/2012

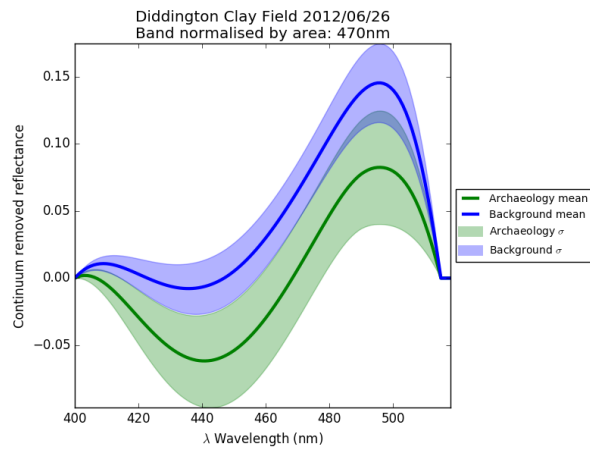


Figure B.79: Continuum removed reflectance band normalised by area 470nm DDCF 26/06/2012

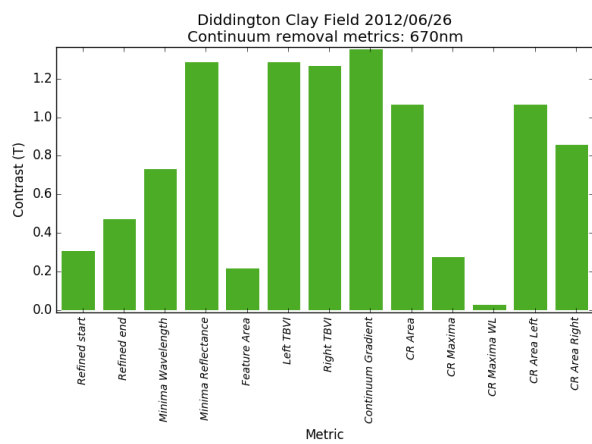


Figure B.80: Continuum removed metrics 670nm DDCF 26/06/2012

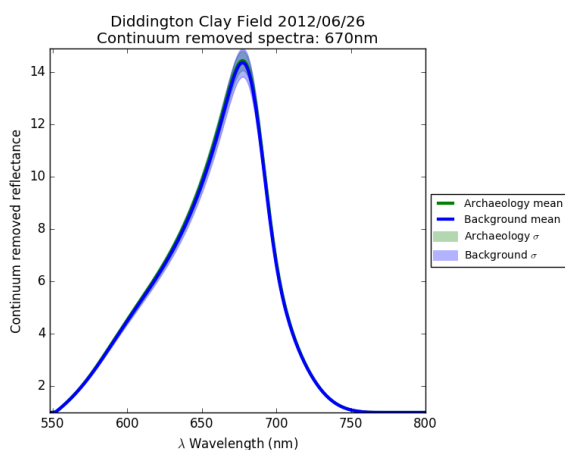


Figure B.81: Continuum removed reflectance 670nm DDCF 26/06/2012

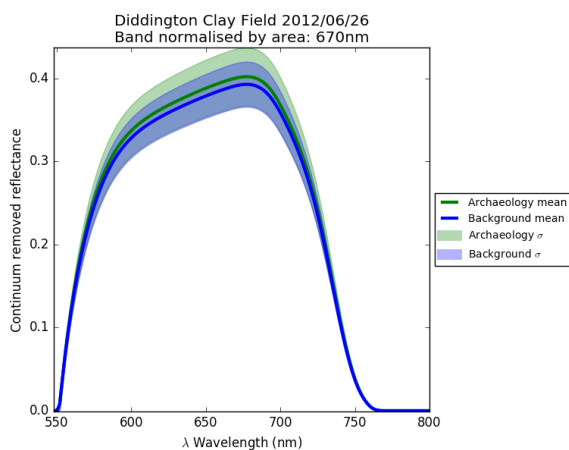


Figure B.82: Continuum removed reflectance band normalised by area 670nm DDCF 26/06/2012

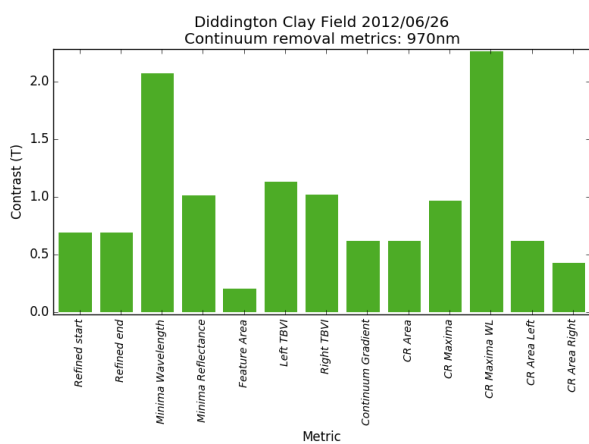


Figure B.83: Continuum removed metrics 970nm DDCF 26/06/2012

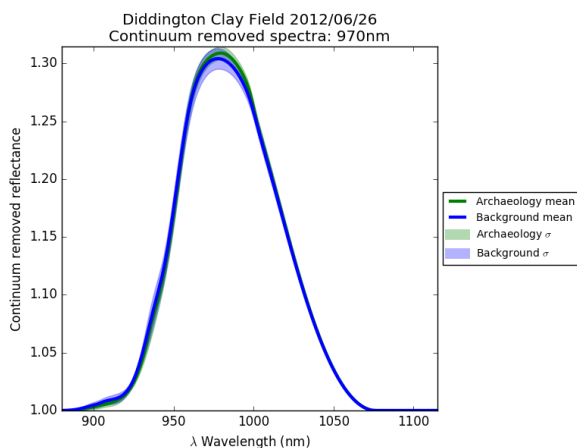


Figure B.84: Continuum removed reflectance 970nm DDCF 26/06/2012

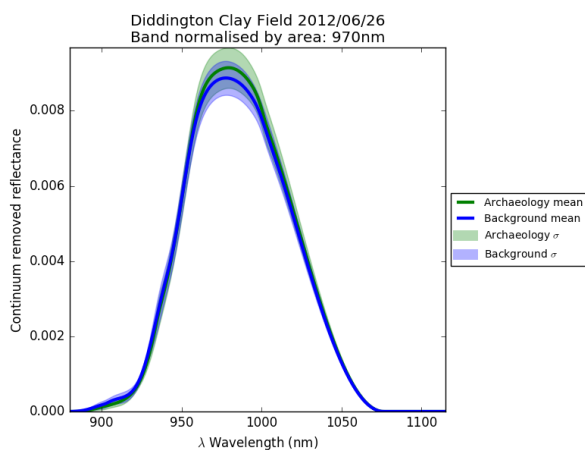


Figure B.85: Continuum removed reflectance band normalised by area 970nm DDCF 26/06/2012

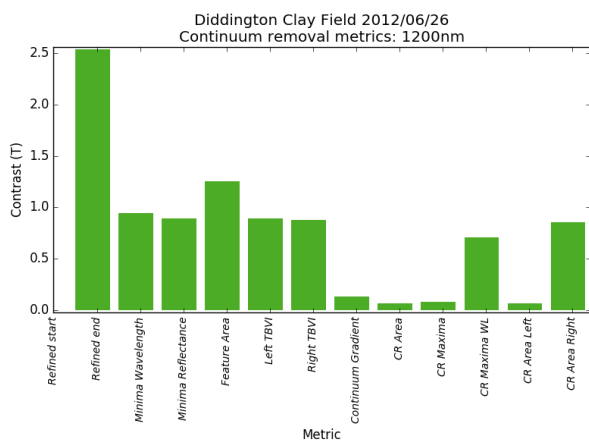


Figure B.86: Continuum removed metrics 1200nm DDCF 26/06/2012

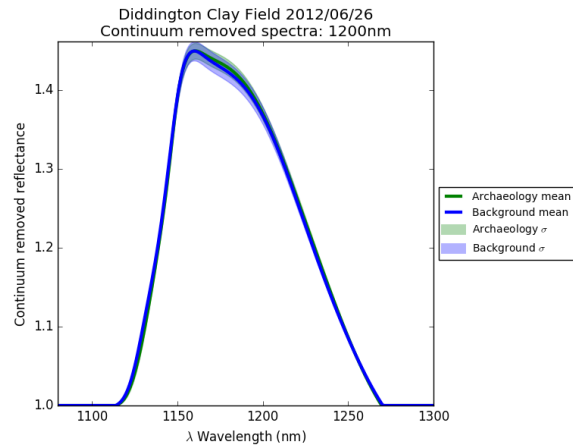


Figure B.87: Continuum removed reflectance 1200nm DDCF 26/06/2012

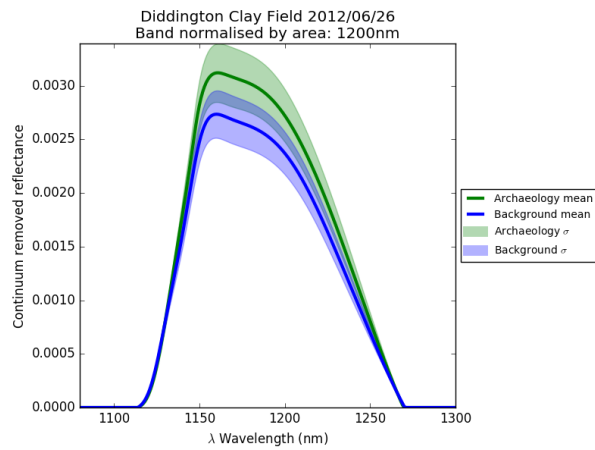


Figure B.88: Continuum removed reflectance band normalised by area 1200nm DDCF 26/06/2012

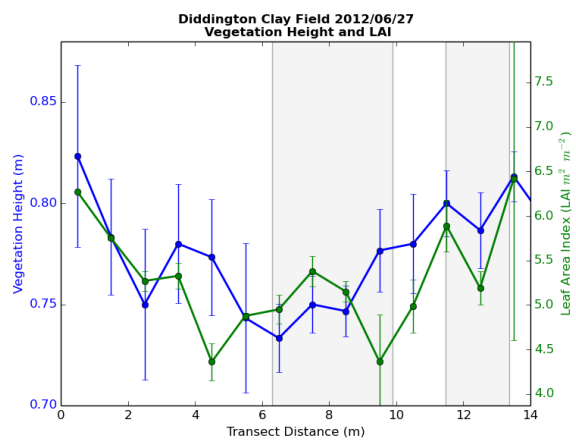


Figure B.89: Physical vegetation properties DDCF 27/06/2012

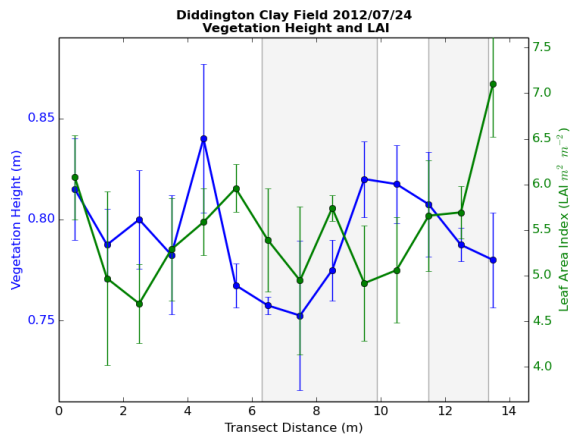


Figure B.90: Physical vegetation properties DDCF 24/07/2012

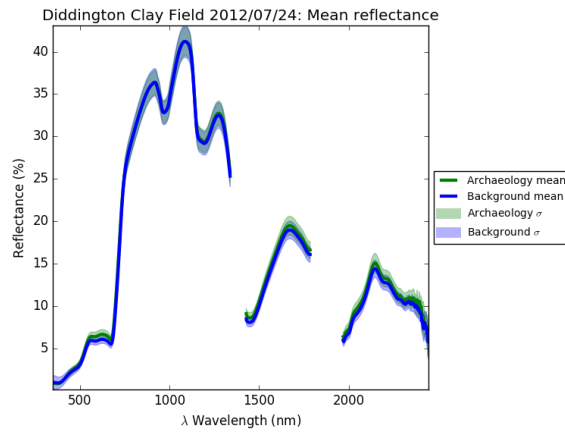


Figure B.91: Spectra from DDCF 24/07/2012

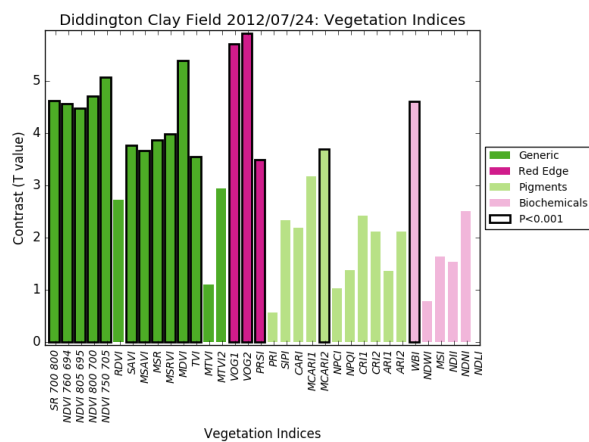


Figure B.92: Vegetation indices DDCF 24/07/2012

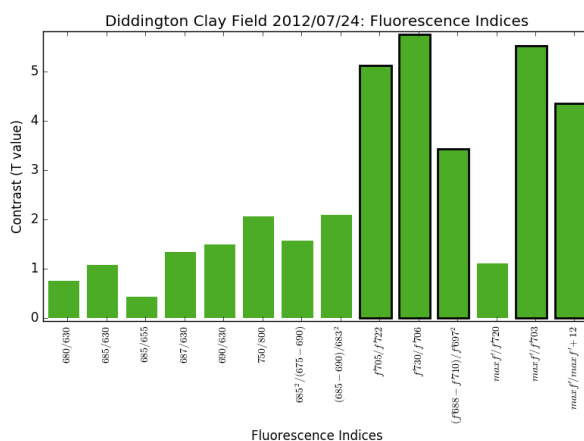


Figure B.93: Fluorescence Indices DDCF 24/07/2012

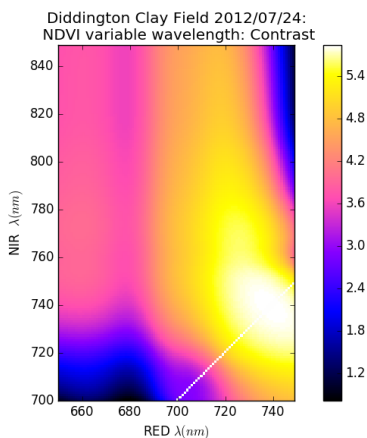


Figure B.94: MTBVI DDCF 24/07/2012

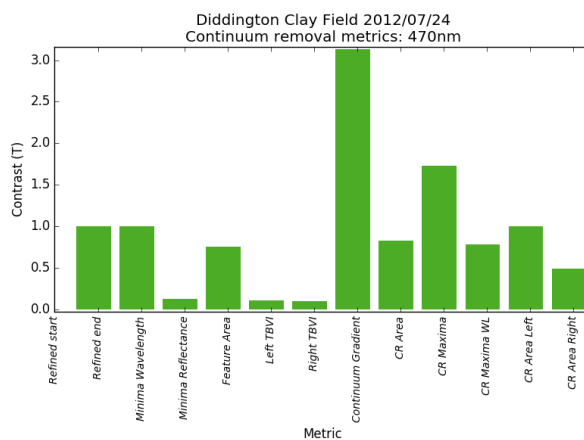


Figure B.95: Continuum removed metrics 470nm DDCF 24/07/2012

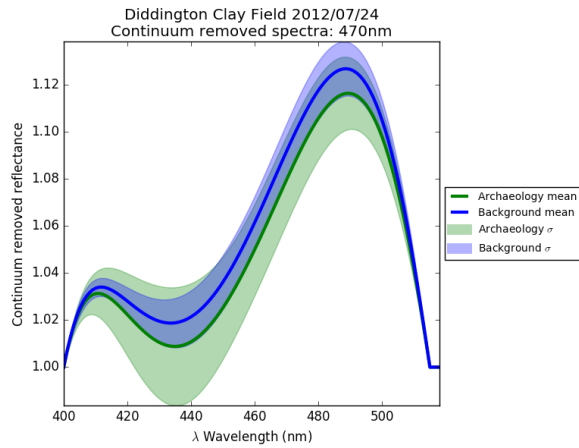


Figure B.96: Continuum removed reflectance 470nm DDCF 24/07/2012

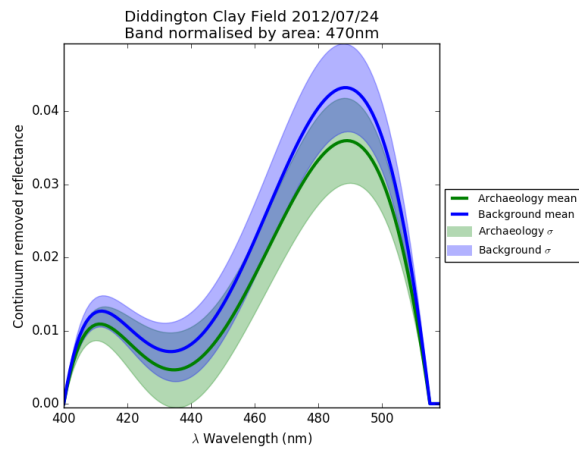


Figure B.97: Continuum removed reflectance band normalised by area 470nm DDCF 24/07/2012

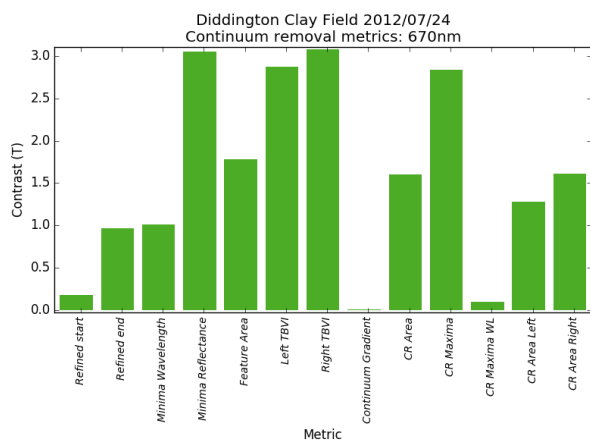


Figure B.98: Continuum removed metrics 670nm DDCF 24/07/2012

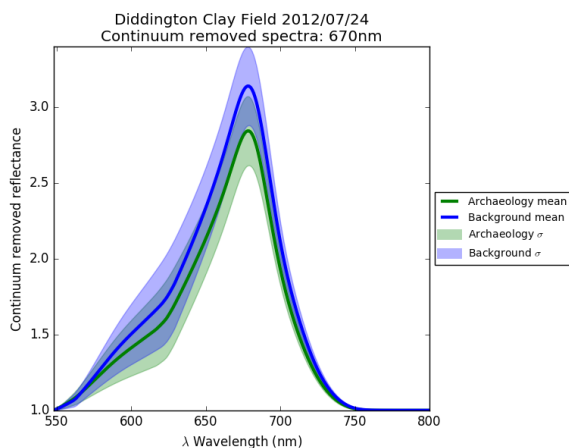


Figure B.99: Continuum removed reflectance 670nm DDCF 24/07/2012

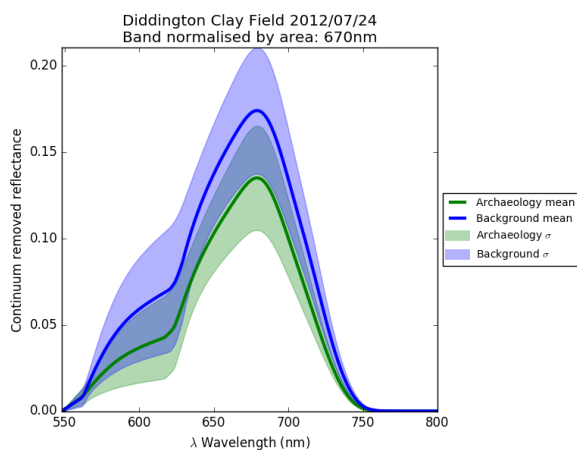


Figure B.100: Continuum removed reflectance band normalised by area 670nm DDCF 24/07/2012

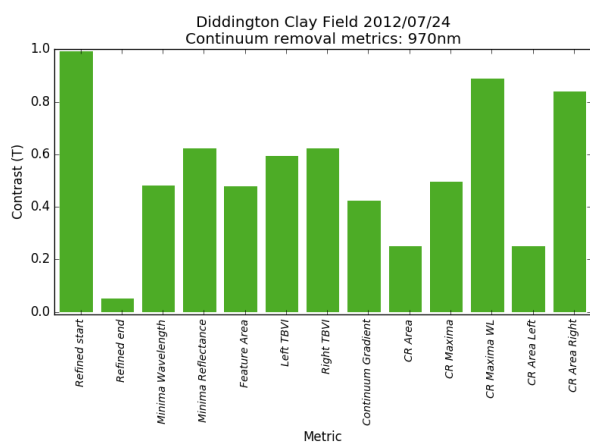


Figure B.101: Continuum removed metrics 970nm DDCF 24/07/2012

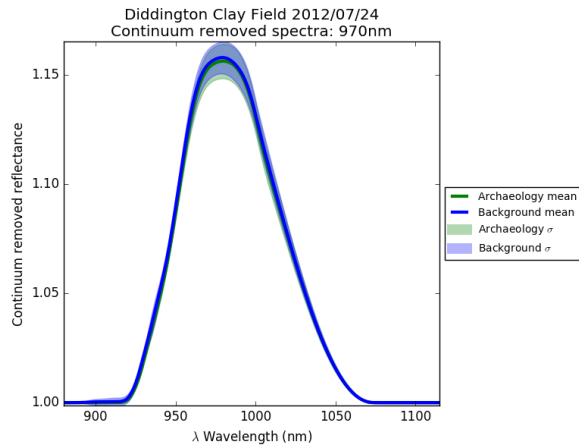


Figure B.102: Continuum removed reflectance 970nm DDCF 24/07/2012

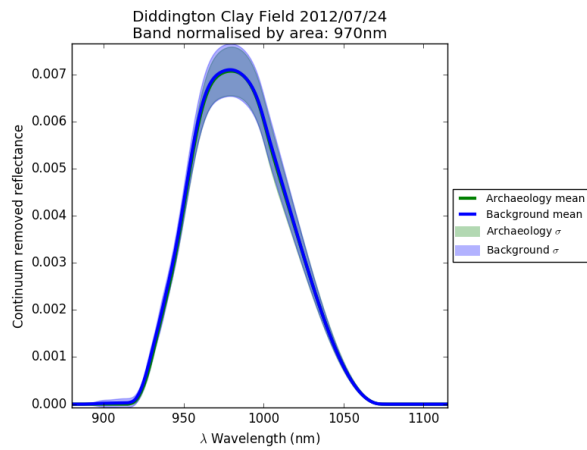


Figure B.103: Continuum removed reflectance band normalised by area 970nm DDCF 24/07/2012

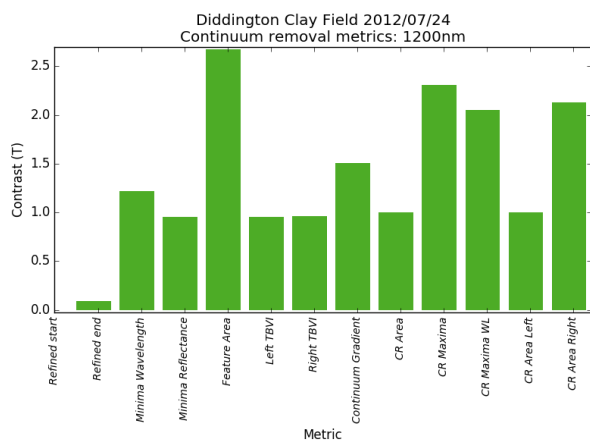


Figure B.104: Continuum removed metrics 1200nm DDCF 24/07/2012

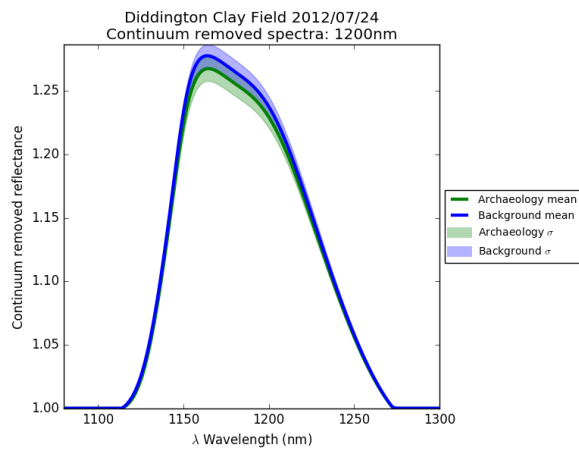


Figure B.105: Continuum removed reflectance 1200nm DDCF 24/07/2012

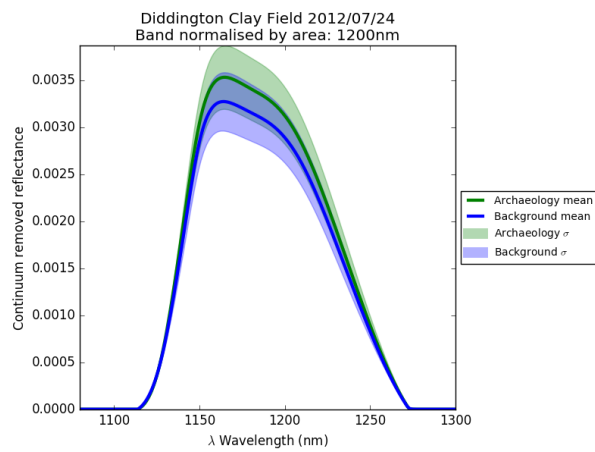


Figure B.106: Continuum removed reflectance band normalised by area 1200nm DDCF 24/07/2012

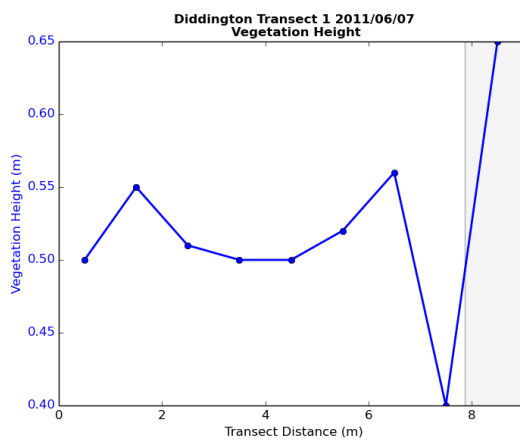


Figure B.107: Physical vegetation properties DDT1 07/06/2011

Figure B.108: Physical vegetation properties DDT1 08/06/2011

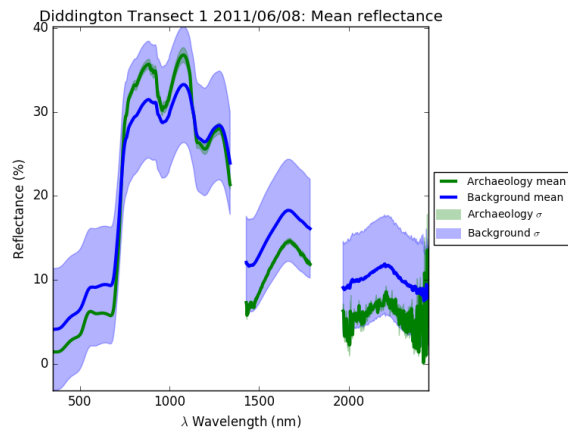


Figure B.109: Spectra from DDT1 08/06/2011

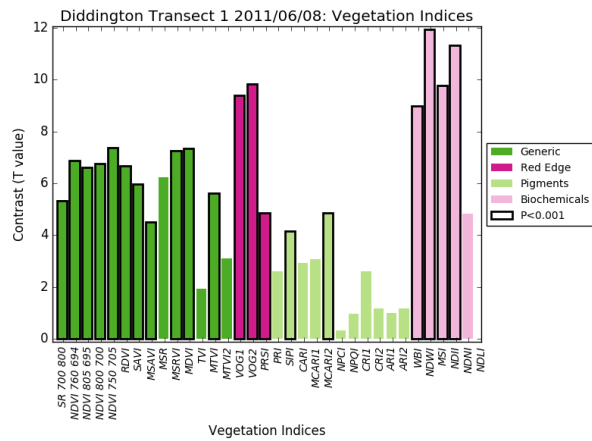


Figure B.110: Vegetation indices DDT1 08/06/2011

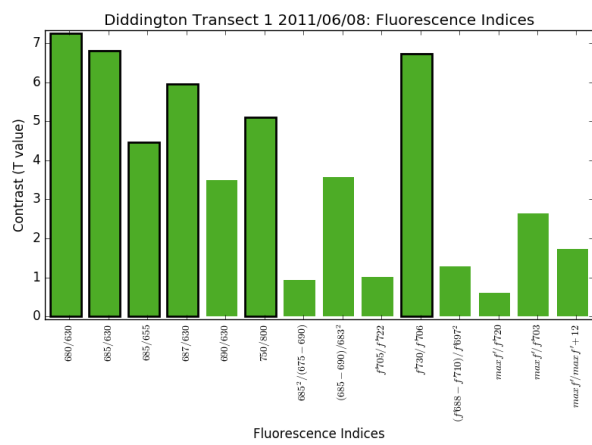


Figure B.111: Fluorescence Indices DDT1 08/06/2011

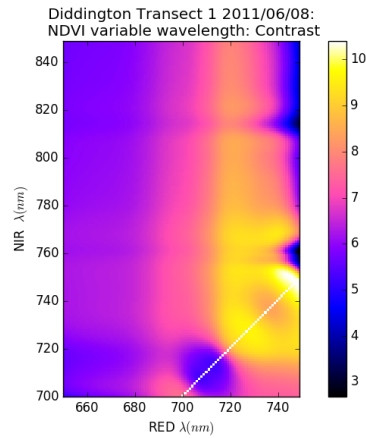


Figure B.112: MTBVI DDT1 08/06/2011

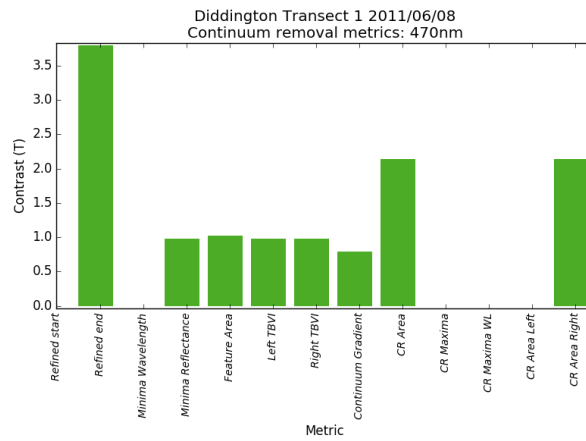


Figure B.113: Continuum removed metrics 470nm DDT1 08/06/2011

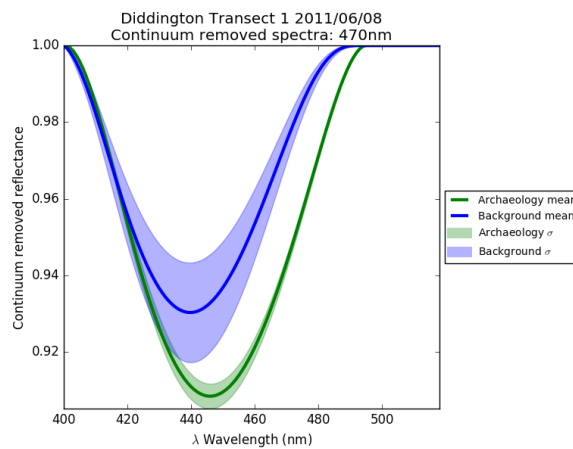


Figure B.114: Continuum removed reflectance 470nm DDT1 08/06/2011

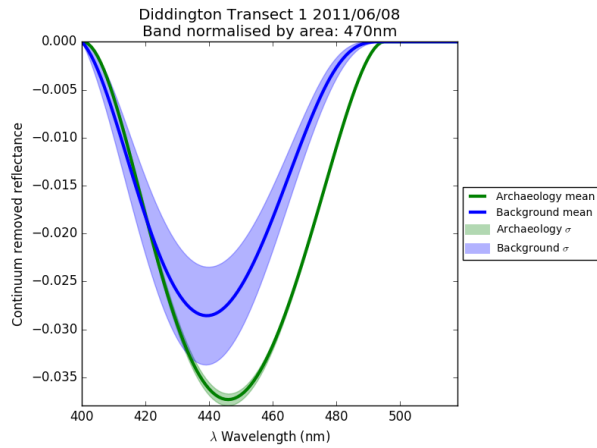


Figure B.115: Continuum removed reflectance band normalised by area 470nm DDT1 08/06/2011

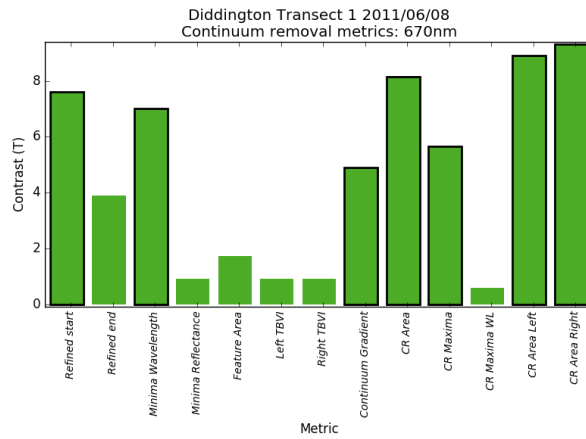


Figure B.116: Continuum removed metrics 670nm DDT1 08/06/2011

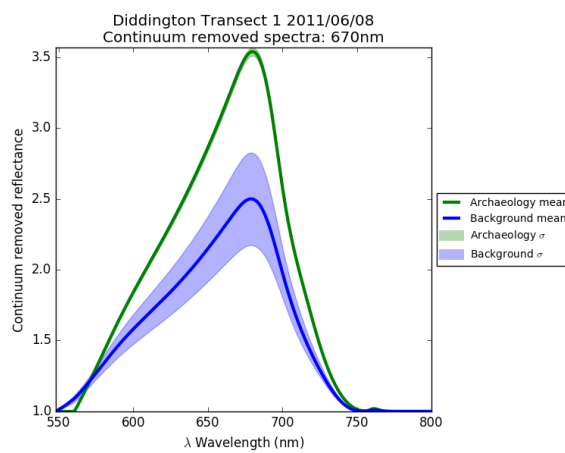


Figure B.117: Continuum removed reflectance 670nm DDT1 08/06/2011

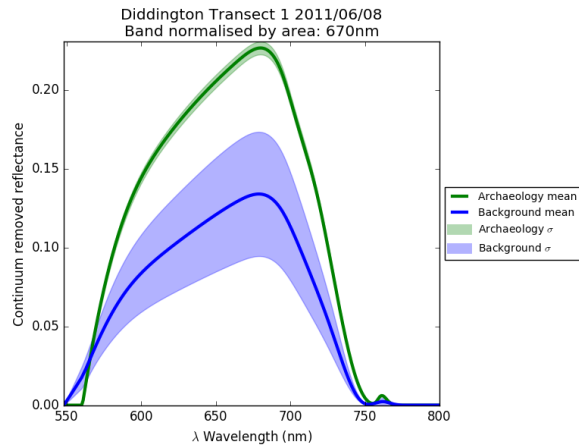


Figure B.118: Continuum removed reflectance band normalised by area 670nm DDT1 08/06/2011

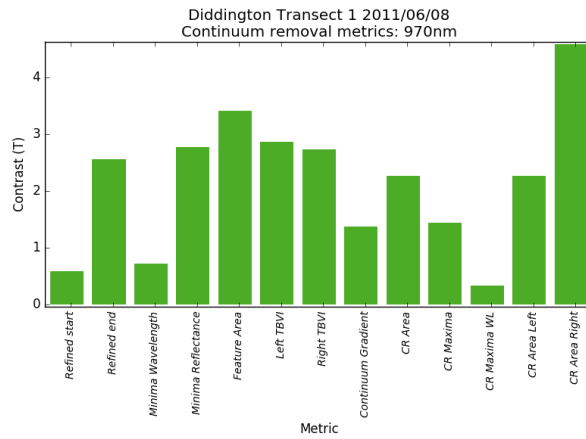


Figure B.119: Continuum removed metrics 970nm DDT1 08/06/2011

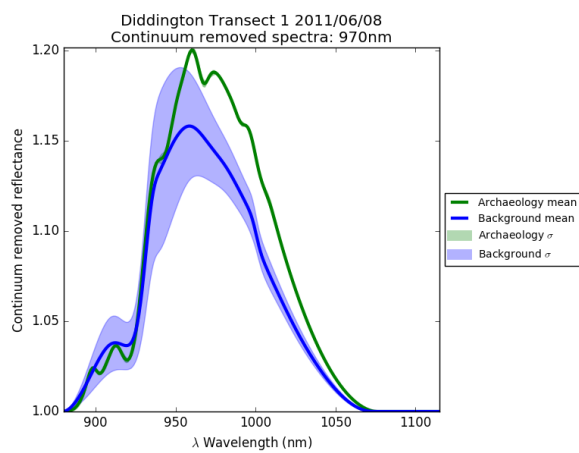


Figure B.120: Continuum removed reflectance 970nm DDT1 08/06/2011

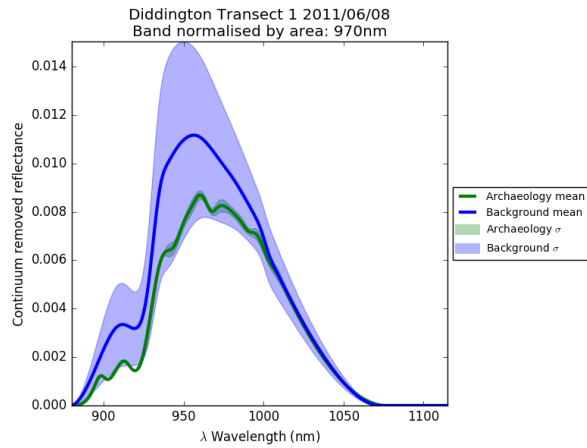


Figure B.121: Continuum removed reflectance band normalised by area 970nm DDT1 08/06/2011

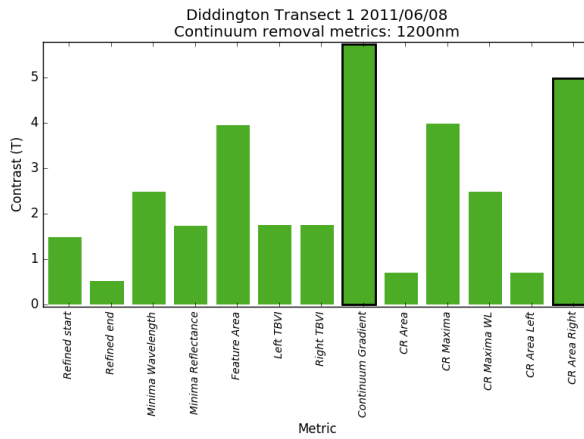


Figure B.122: Continuum removed metrics 1200nm DDT1 08/06/2011

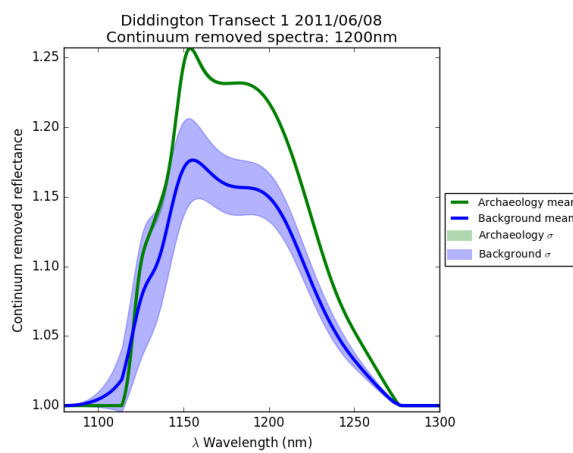


Figure B.123: Continuum removed reflectance 1200nm DDT1 08/06/2011

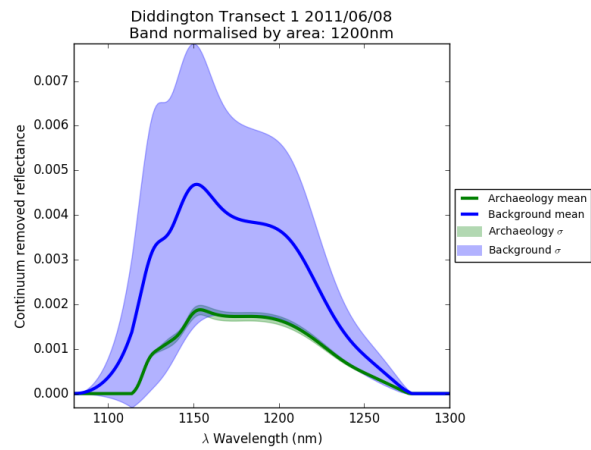


Figure B.124: Continuum removed reflectance band normalised by area 1200nm DDT1 08/06/2011

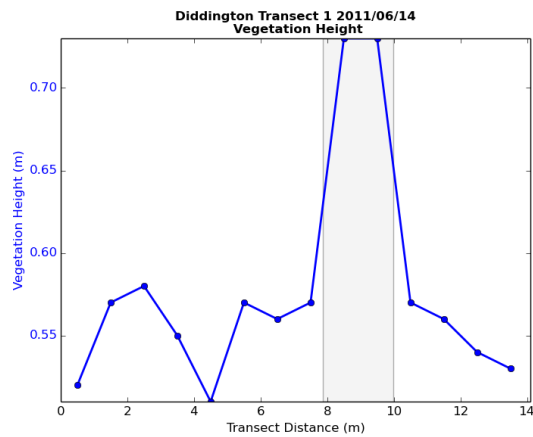


Figure B.125: Physical vegetation properties DDT1 14/06/2011



Figure B.126: Spectra from DDT1 14/06/2011

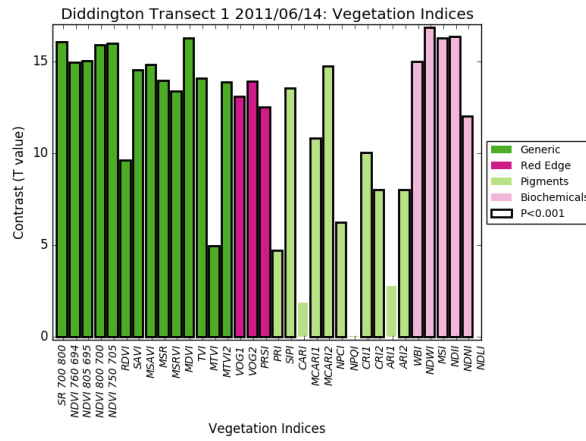


Figure B.127: Vegetation indices DDT1 14/06/2011

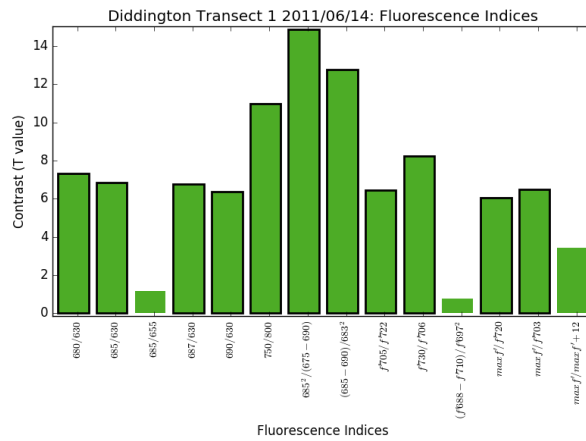


Figure B.128: Fluorescence Indices DDT1 14/06/2011

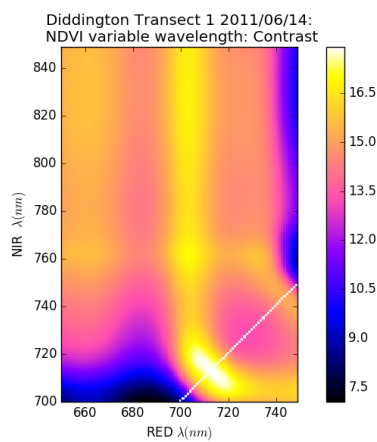


Figure B.129: MTBVI DDT1 14/06/2011

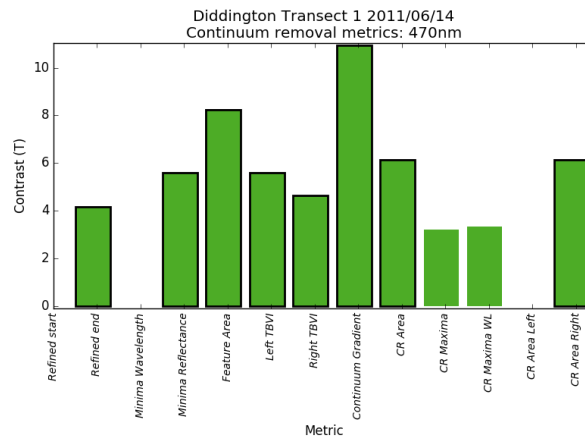


Figure B.130: Continuum removed metrics 470nm DDT1 14/06/2011

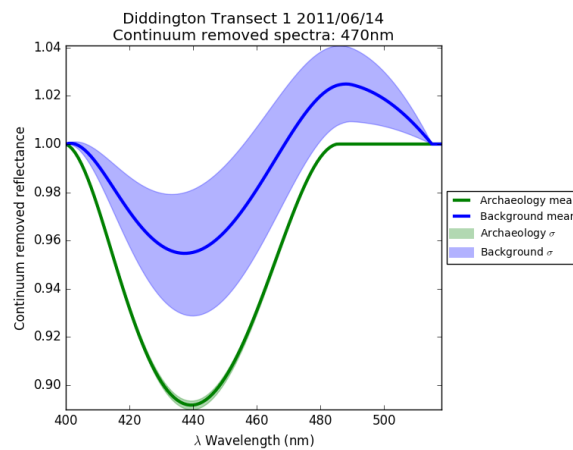


Figure B.131: Continuum removed reflectance 470nm DDT1 14/06/2011

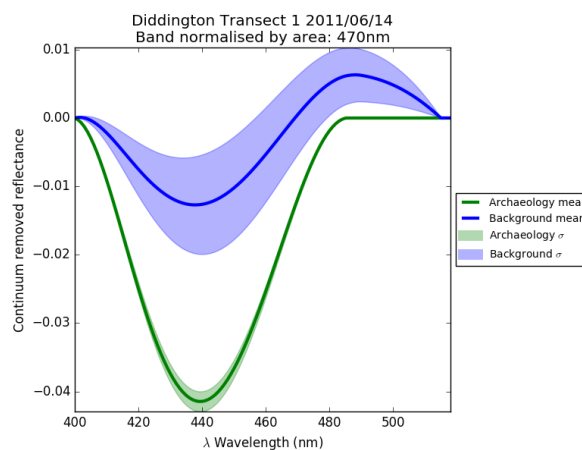


Figure B.132: Continuum removed reflectance band normalised by area 470nm DDT1 14/06/2011

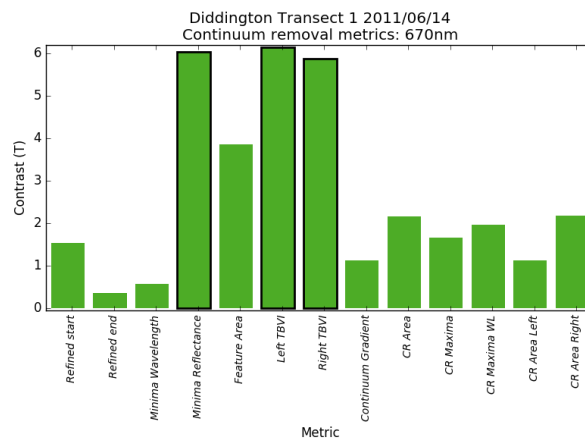


Figure B.133: Continuum removed metrics 670nm DDT1 14/06/2011

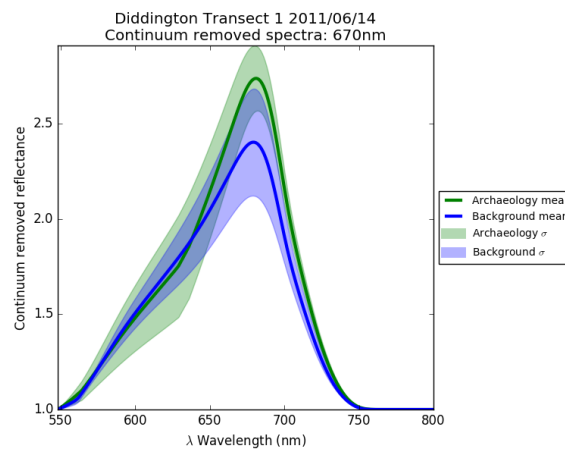


Figure B.134: Continuum removed reflectance 670nm DDT1 14/06/2011

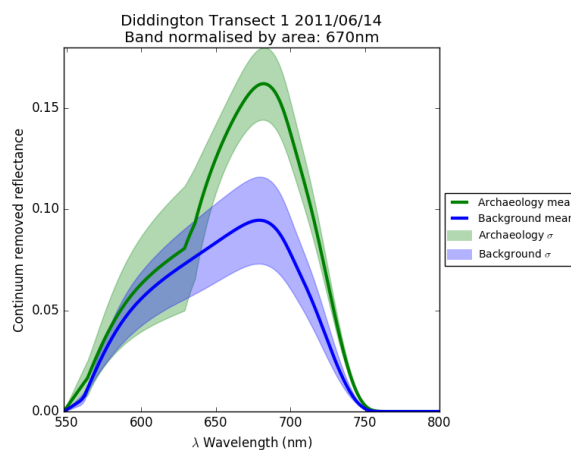


Figure B.135: Continuum removed reflectance band normalised by area 670nm DDT1 14/06/2011

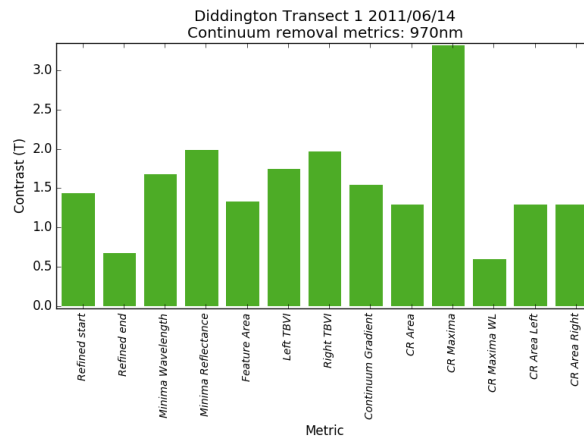


Figure B.136: Continuum removed metrics 970nm DDT1 14/06/2011

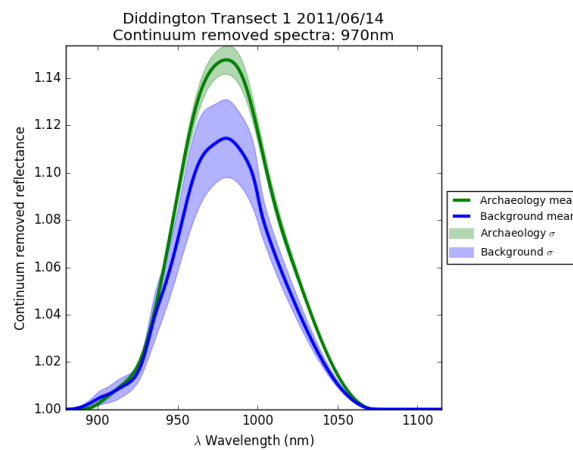


Figure B.137: Continuum removed reflectance 970nm DDT1 14/06/2011

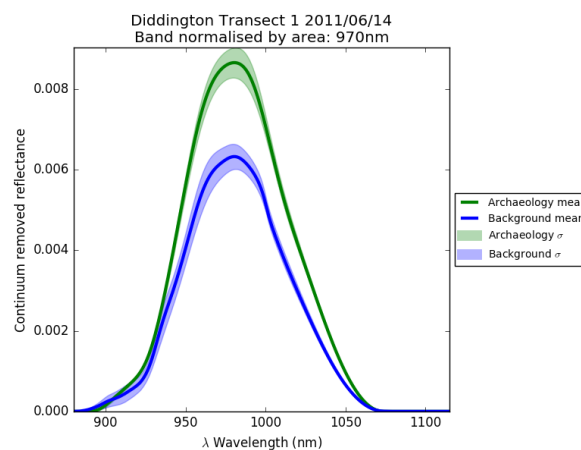


Figure B.138: Continuum removed reflectance band normalised by area 970nm DDT1 14/06/2011

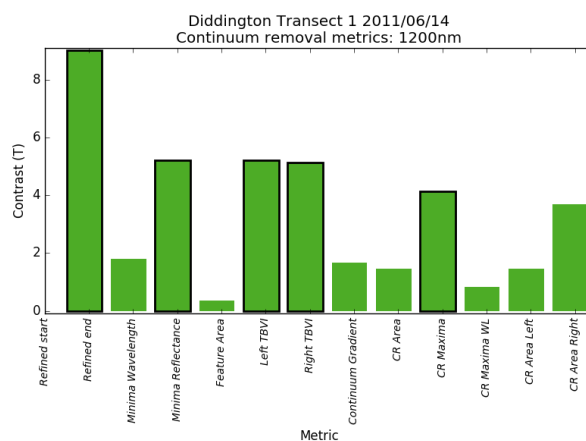


Figure B.139: Continuum removed metrics 1200nm DDT1 14/06/2011

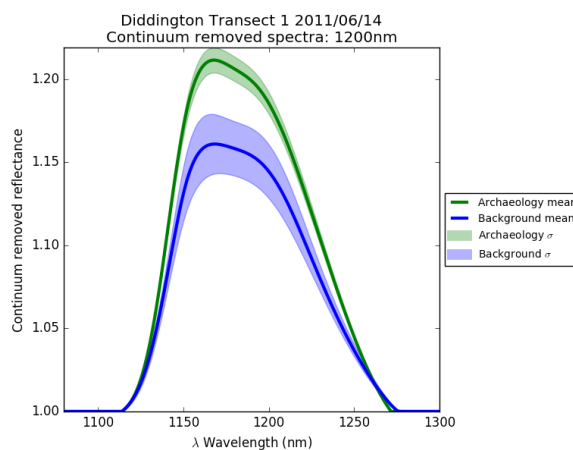


Figure B.140: Continuum removed reflectance 1200nm DDT1 14/06/2011

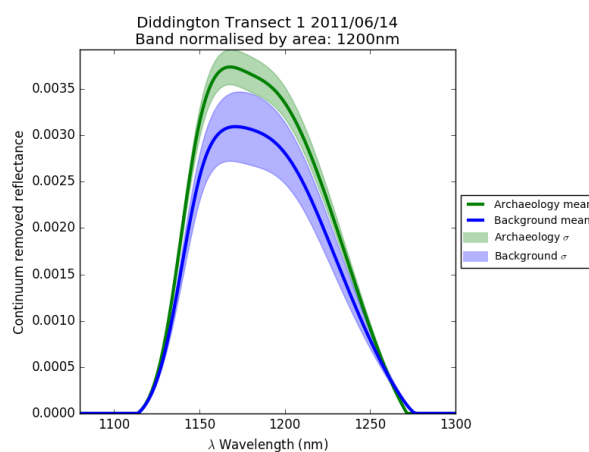


Figure B.141: Continuum removed reflectance band normalised by area 1200nm DDT1 14/06/2011

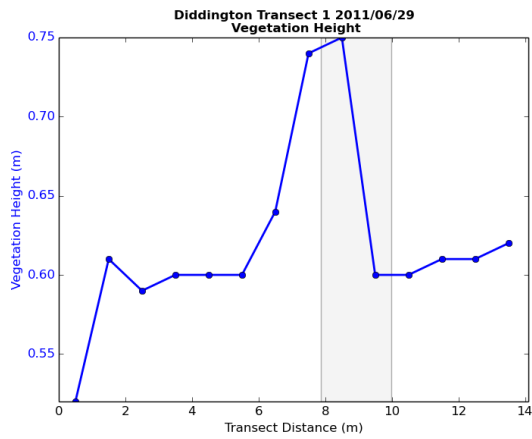


Figure B.142: Physical vegetation properties DDT1 29/06/2011

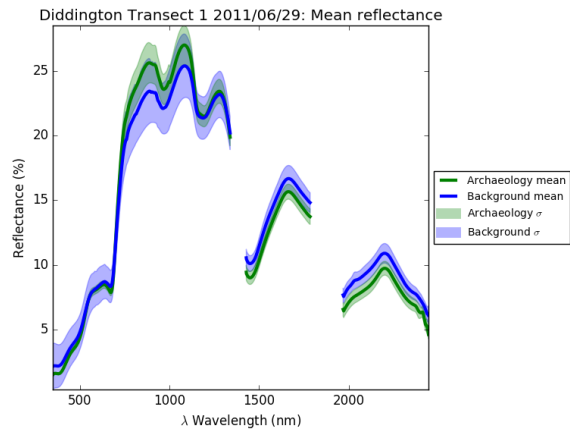


Figure B.143: Spectra from DDT1 29/06/2011

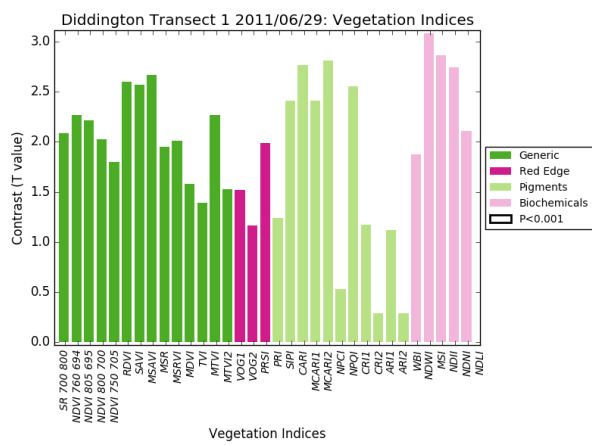


Figure B.144: Vegetation indices DDT1 29/06/2011

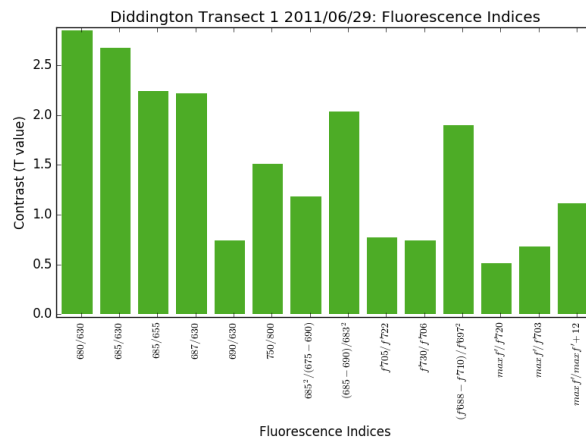


Figure B.145: Fluorescence Indices DDT1 29/06/2011

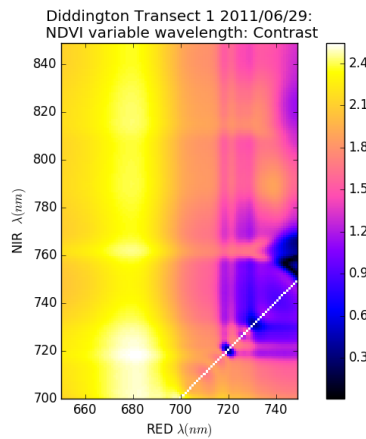


Figure B.146: MTBVI DDT1 29/06/2011

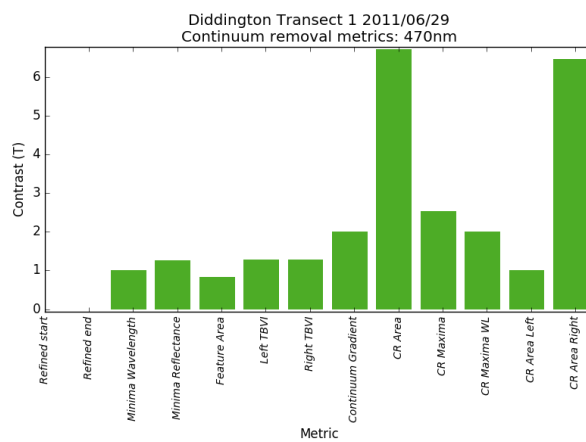


Figure B.147: Continuum removed metrics 470nm DDT1 29/06/2011

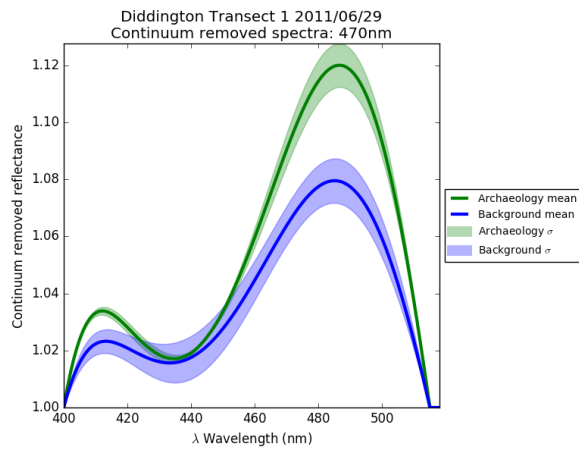


Figure B.148: Continuum removed reflectance 470nm DDT1 29/06/2011

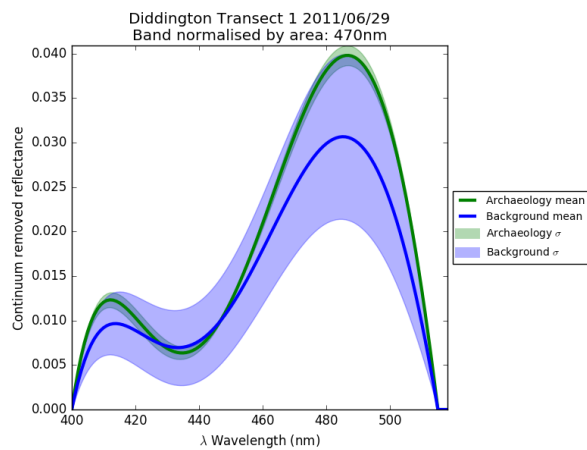


Figure B.149: Continuum removed reflectance band normalised by area 470nm DDT1 29/06/2011

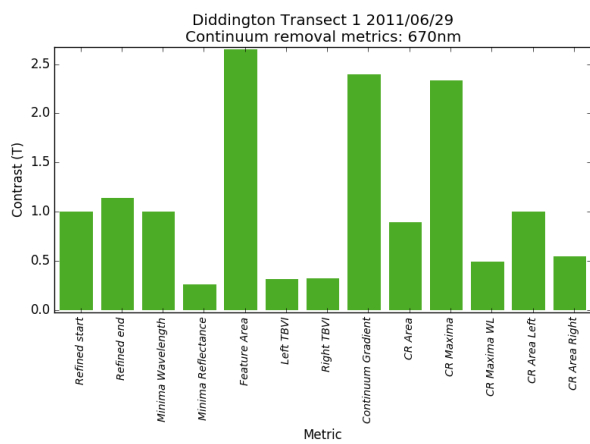


Figure B.150: Continuum removed metrics 670nm DDT1 29/06/2011

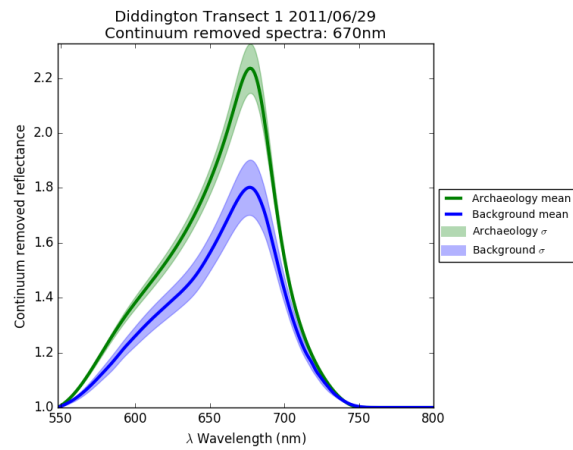


Figure B.151: Continuum removed reflectance 670nm DDT1 29/06/2011

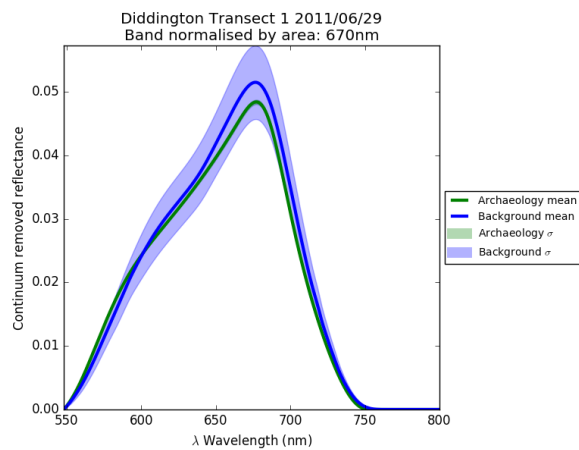


Figure B.152: Continuum removed reflectance band normalised by area 670nm DDT1 29/06/2011

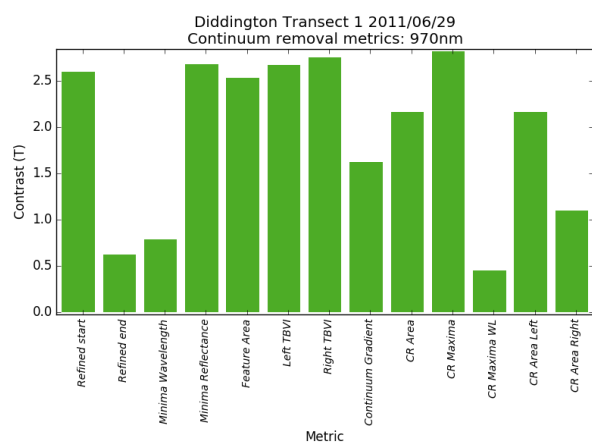


Figure B.153: Continuum removed metrics 970nm DDT1 29/06/2011

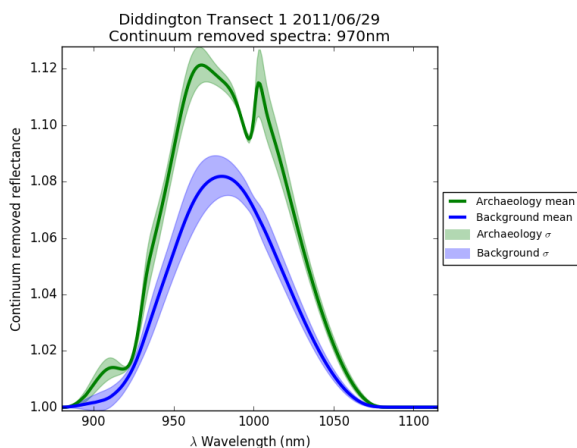


Figure B.154: Continuum removed reflectance 970nm DDT1 29/06/2011

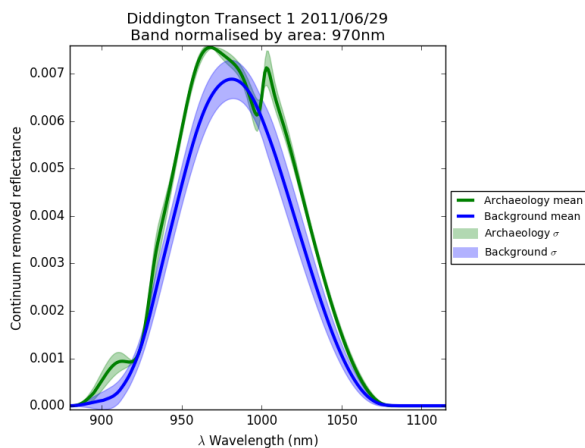


Figure B.155: Continuum removed reflectance band normalised by area 970nm DDT1 29/06/2011

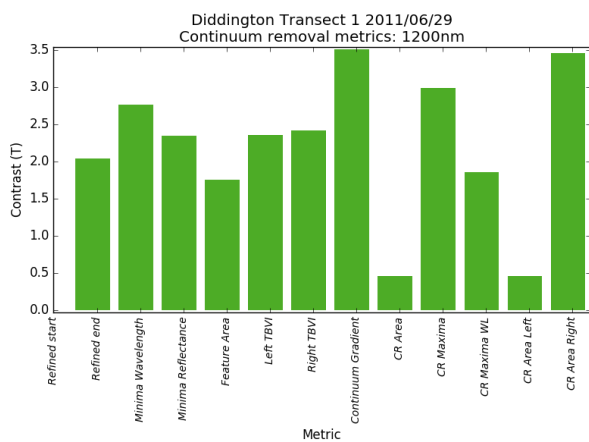


Figure B.156: Continuum removed metrics 1200nm DDT1 29/06/2011

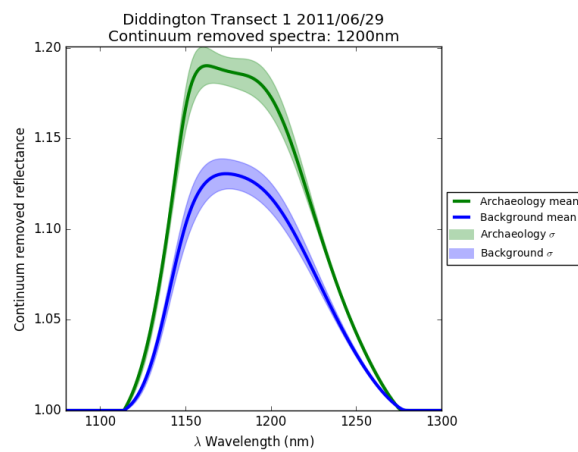


Figure B.157: Continuum removed reflectance 1200nm DDT1 29/06/2011

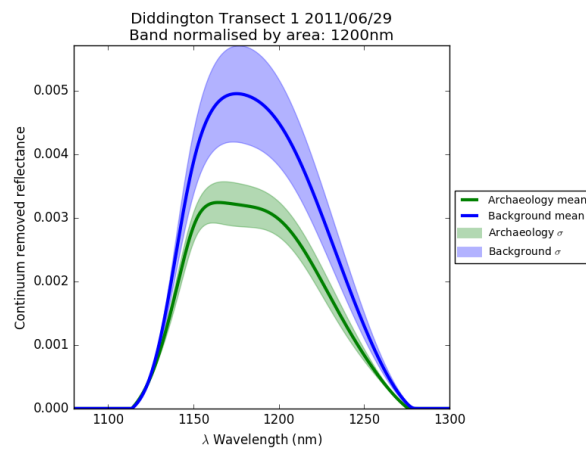


Figure B.158: Continuum removed reflectance band normalised by area 1200nm DDT1 29/06/2011

Figure B.159: Physical vegetation properties DDT1 15/07/2011

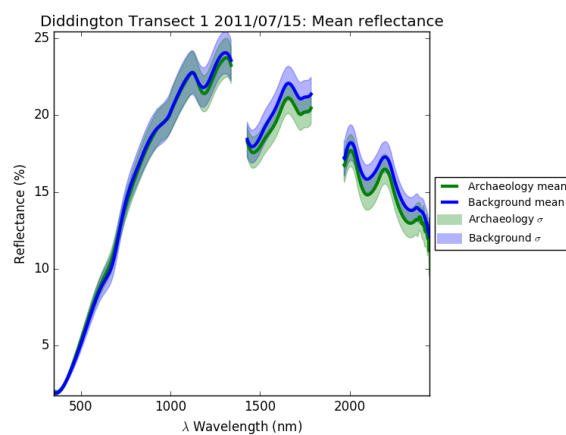


Figure B.160: Spectra from DDT1 15/07/2011

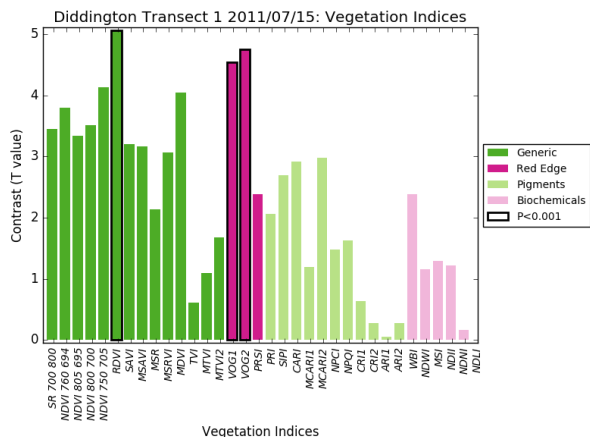


Figure B.161: Vegetation indices DDT1 15/07/2011

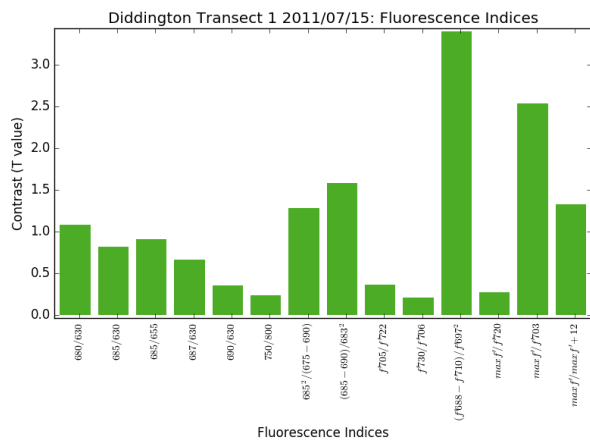


Figure B.162: Fluorescence Indices DDT1 15/07/2011

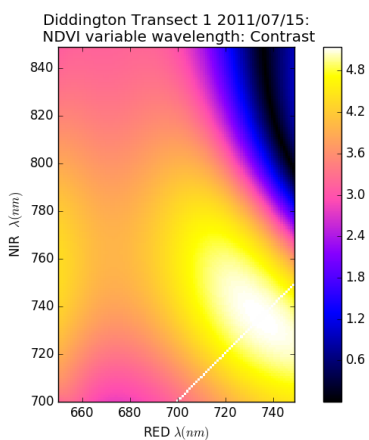


Figure B.163: MTBVI DDT1 15/07/2011

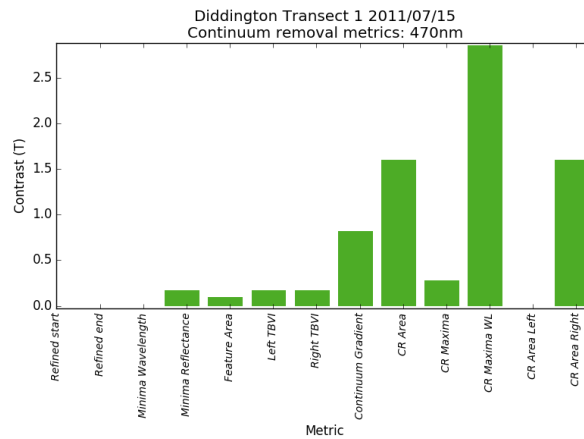


Figure B.164: Continuum removed metrics 470nm DDT1 15/07/2011

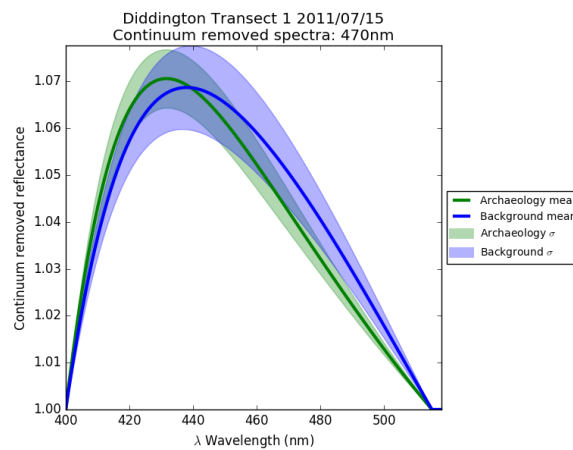


Figure B.165: Continuum removed reflectance 470nm DDT1 15/07/2011

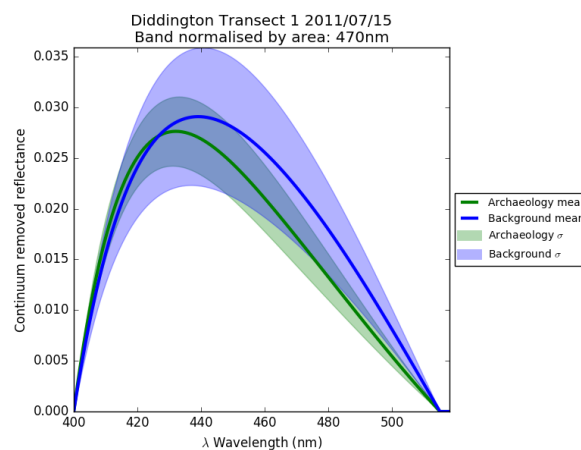


Figure B.166: Continuum removed reflectance band normalised by area 470nm DDT1 15/07/2011

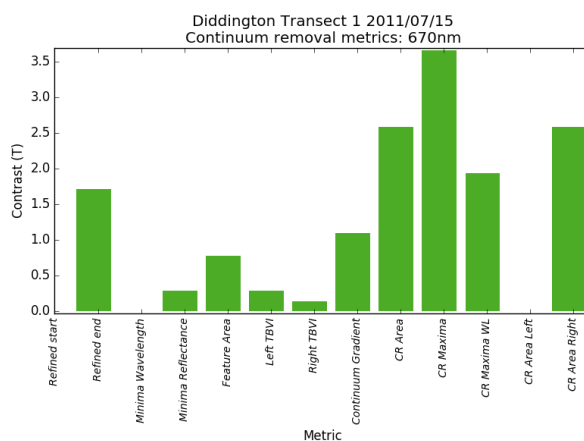


Figure B.167: Continuum removed metrics 670nm DDT1 15/07/2011

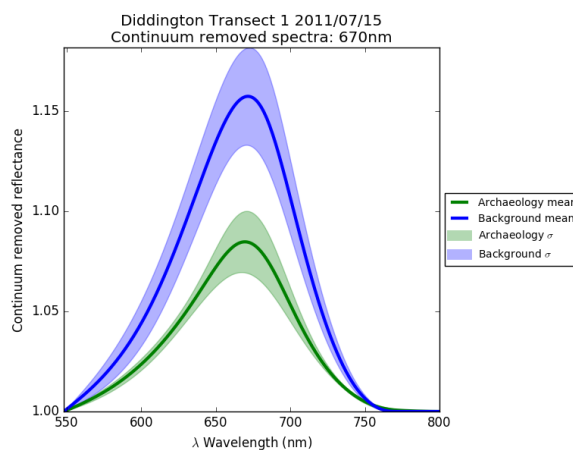


Figure B.168: Continuum removed reflectance 670nm DDT1 15/07/2011

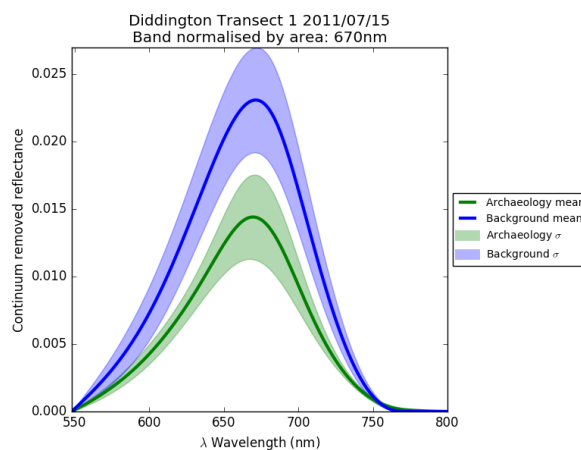


Figure B.169: Continuum removed reflectance band normalised by area 670nm DDT1 15/07/2011

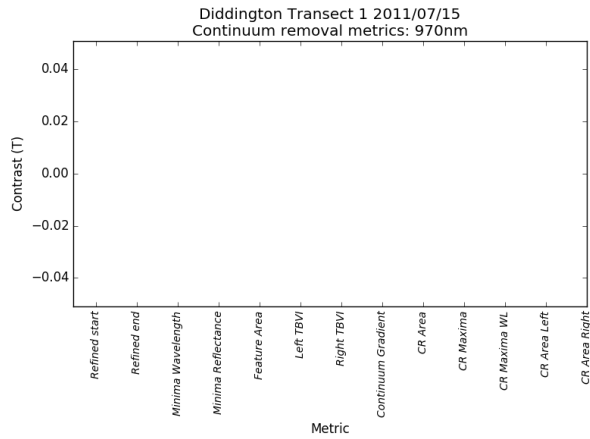


Figure B.170: Continuum removed metrics 970nm DDT1 15/07/2011

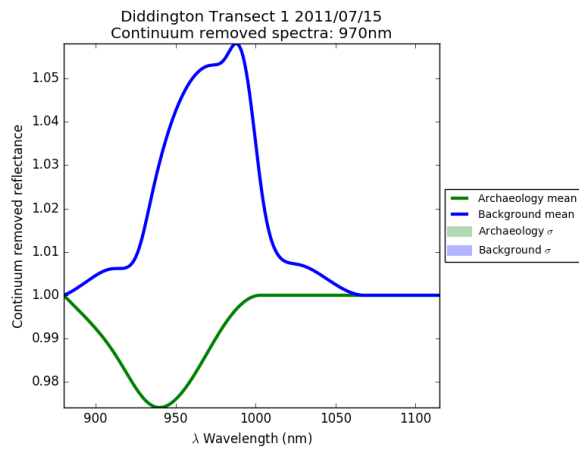


Figure B.171: Continuum removed reflectance 970nm DDT1 15/07/2011

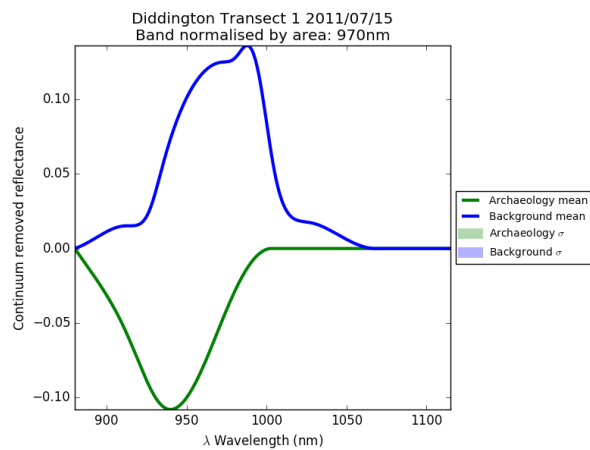


Figure B.172: Continuum removed reflectance band normalised by area 970nm DDT1 15/07/2011

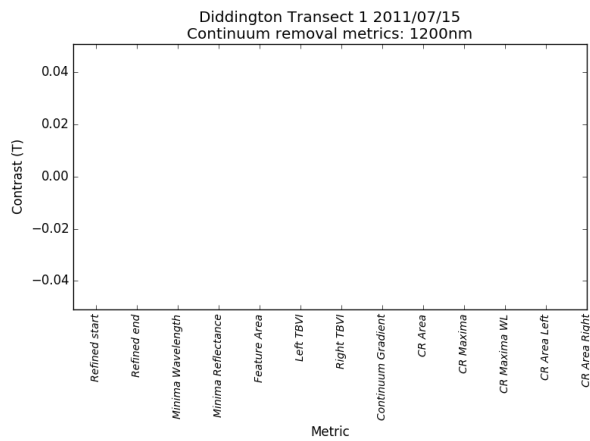


Figure B.173: Continuum removed metrics 1200nm DDT1 15/07/2011

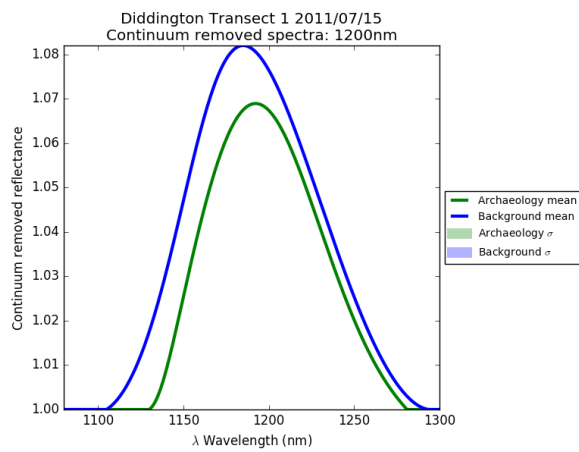


Figure B.174: Continuum removed reflectance 1200nm DDT1 15/07/2011

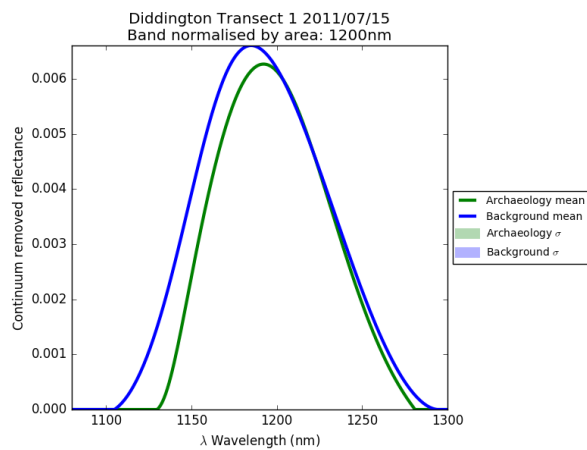


Figure B.175: Continuum removed reflectance band normalised by area 1200nm DDT1 15/07/2011

Figure B.176: Physical vegetation properties DDT1 24/08/2011

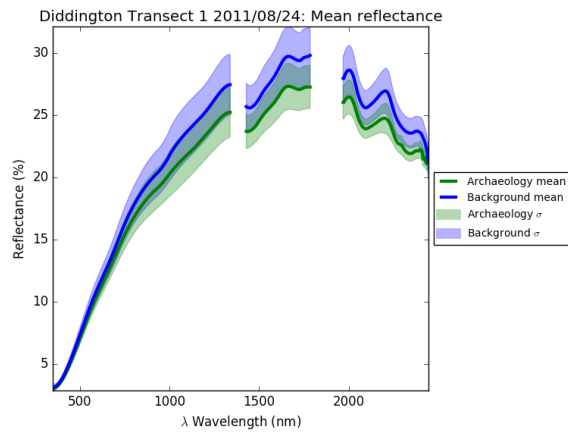


Figure B.177: Spectra from DDT1 24/08/2011

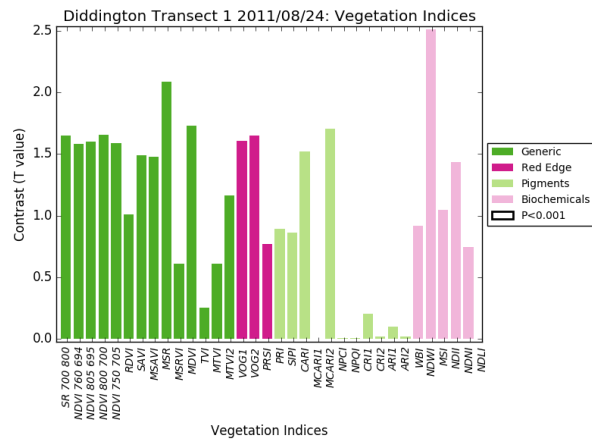


Figure B.178: Vegetation indices DDT1 24/08/2011

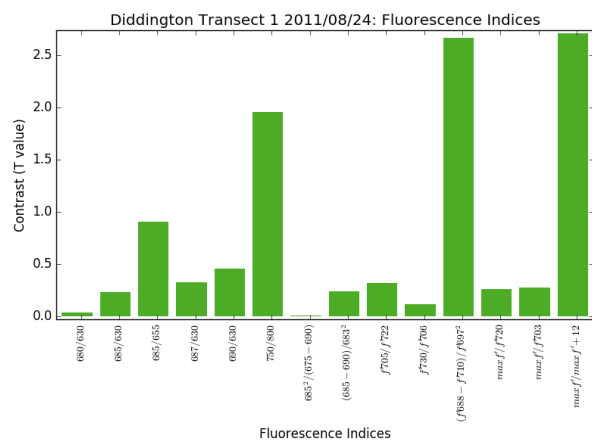


Figure B.179: Fluorescence Indices DDT1 24/08/2011

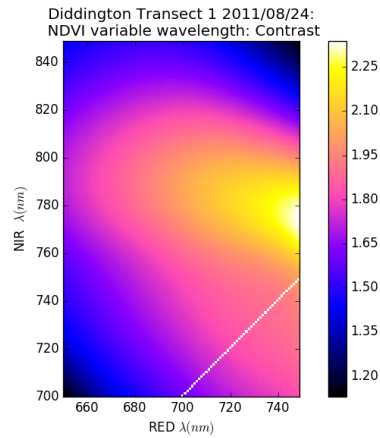


Figure B.180: MTBVI DDT1 24/08/2011

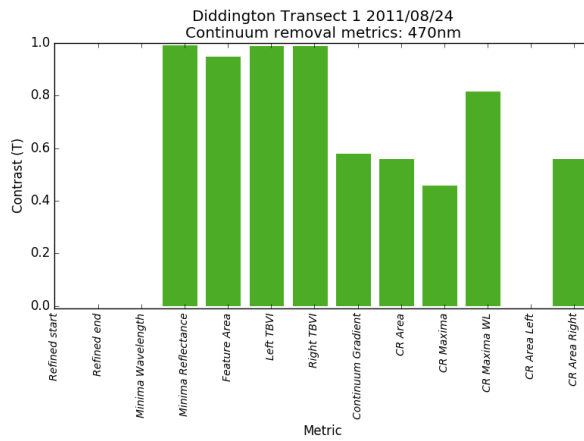


Figure B.181: Continuum removed metrics 470nm DDT1 24/08/2011

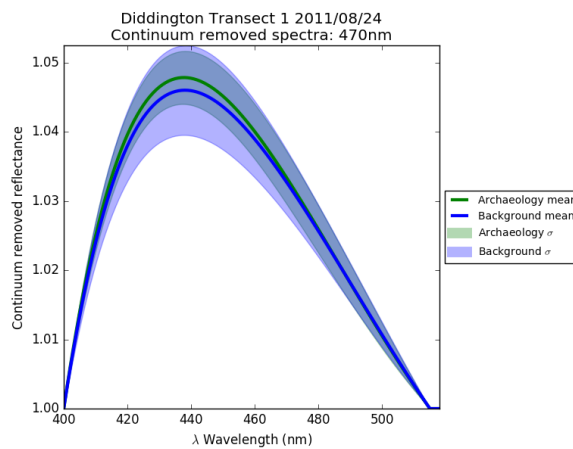


Figure B.182: Continuum removed reflectance 470nm DDT1 24/08/2011

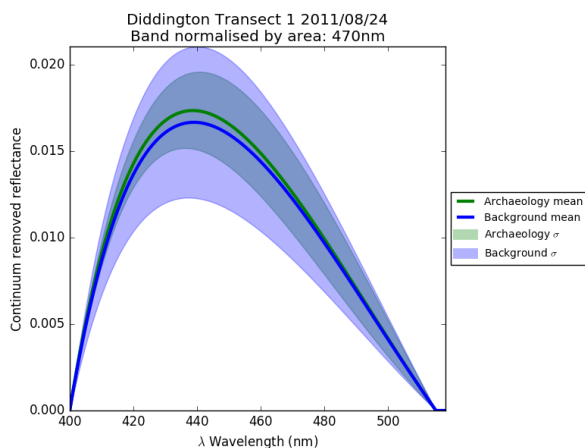


Figure B.183: Continuum removed reflectance band normalised by area 470nm DDT1 24/08/2011

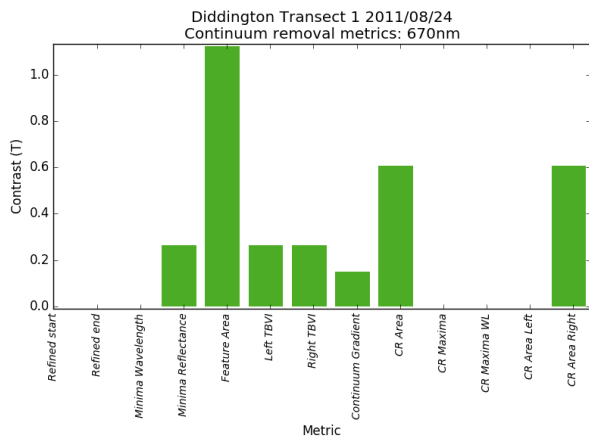


Figure B.184: Continuum removed metrics 670nm DDT1 24/08/2011

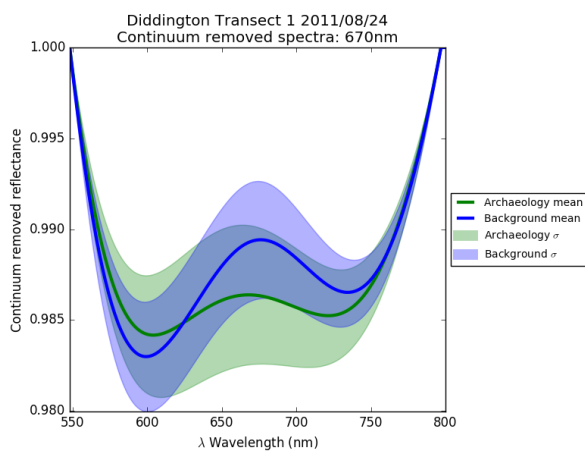


Figure B.185: Continuum removed reflectance 670nm DDT1 24/08/2011

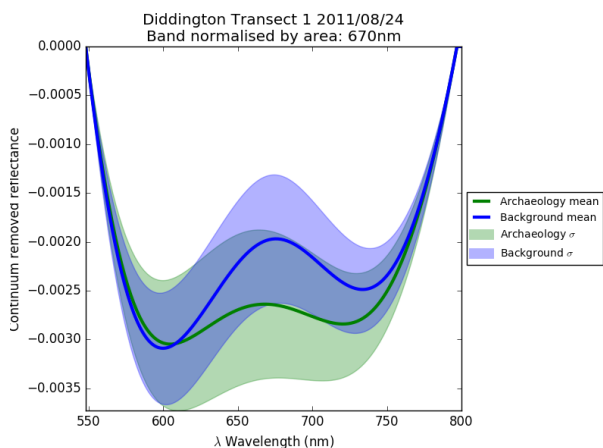


Figure B.186: Continuum removed reflectance band normalised by area 670nm DDT1 24/08/2011

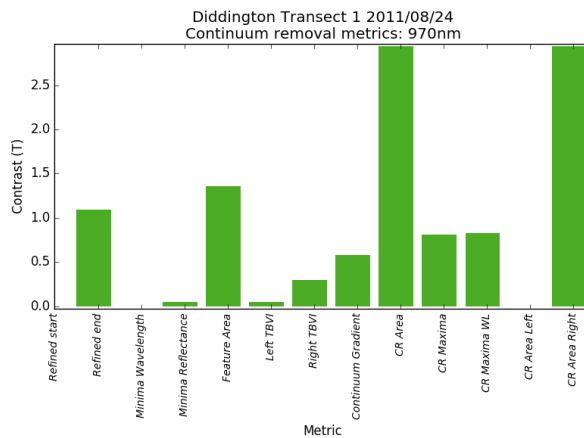


Figure B.187: Continuum removed metrics 970nm DDT1 24/08/2011

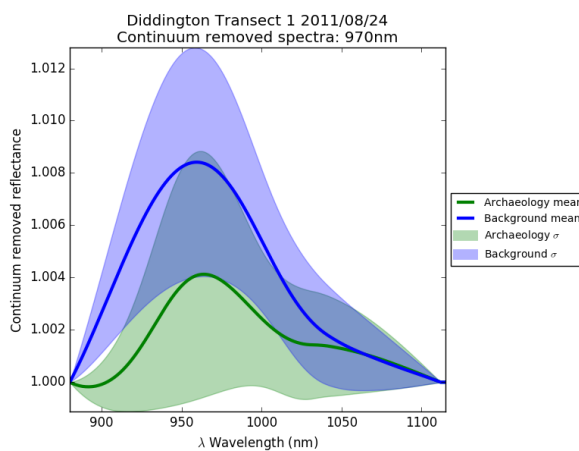


Figure B.188: Continuum removed reflectance 970nm DDT1 24/08/2011

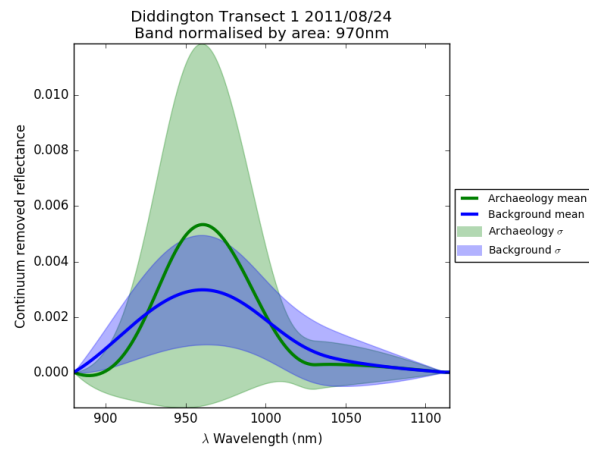


Figure B.189: Continuum removed reflectance band normalised by area 970nm DDT1 24/08/2011

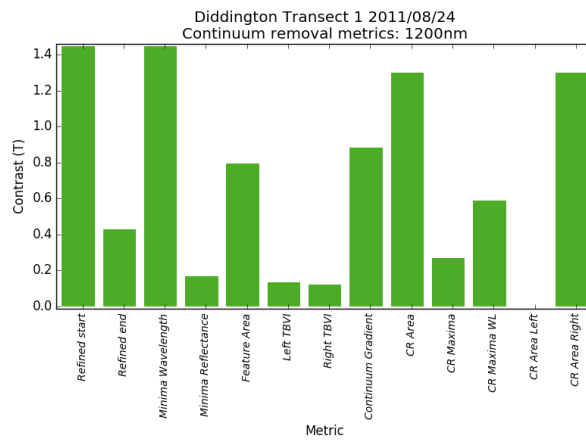


Figure B.190: Continuum removed metrics 1200nm DDT1 24/08/2011

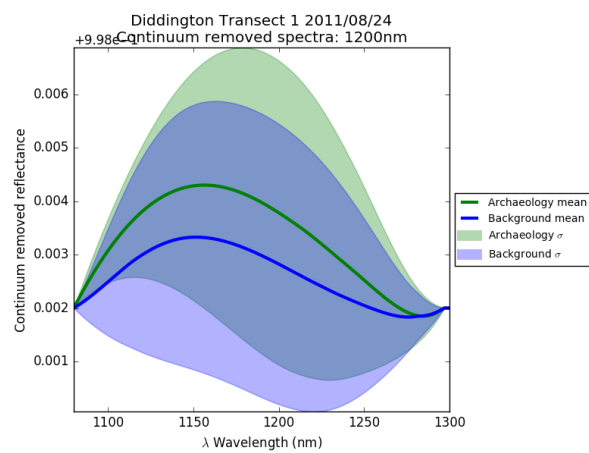


Figure B.191: Continuum removed reflectance 1200nm DDT1 24/08/2011

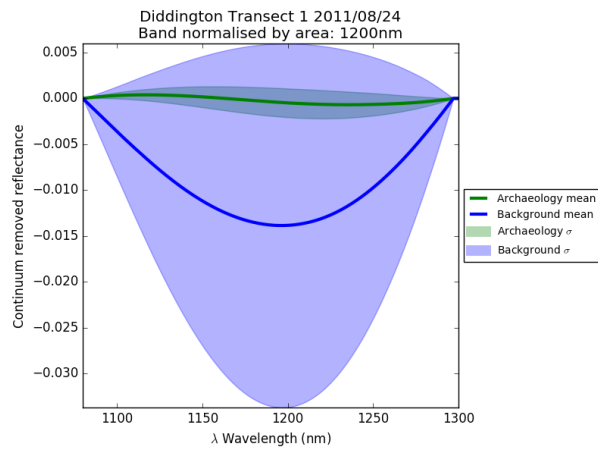


Figure B.192: Continuum removed reflectance band normalised by area 1200nm DDT1 24/08/2011

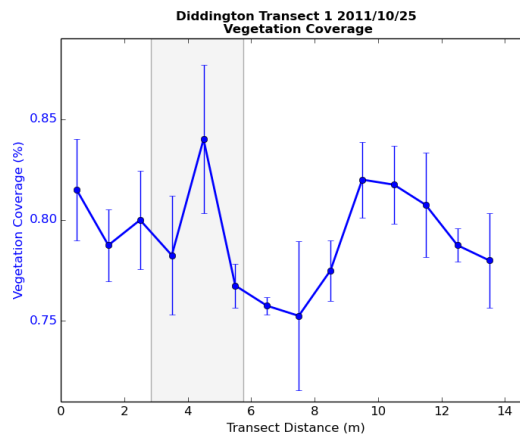


Figure B.193: Physical vegetation properties DDT1 25/10/2011

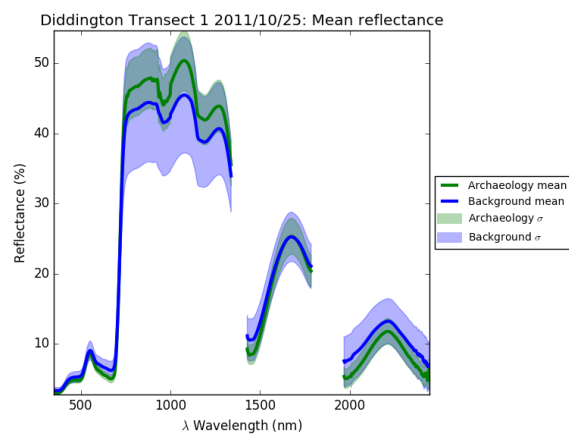


Figure B.194: Spectra from DDT1 25/10/2011

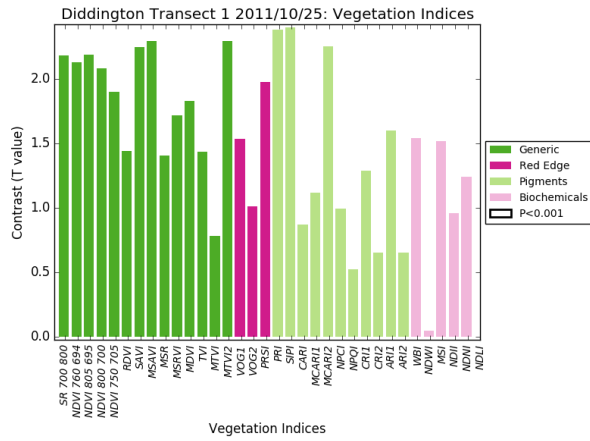


Figure B.195: Vegetation indices DDT1 25/10/2011

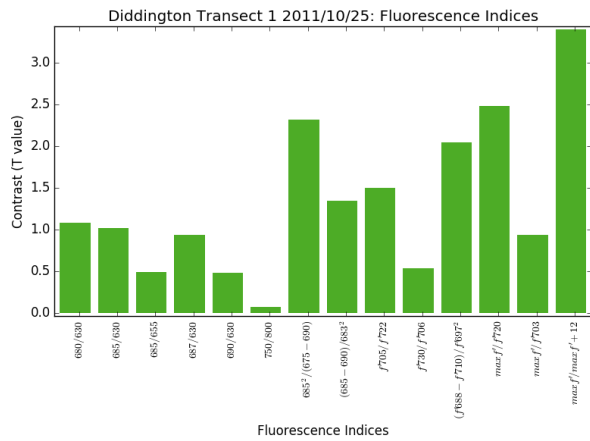


Figure B.196: Fluorescence Indices DDT1 25/10/2011

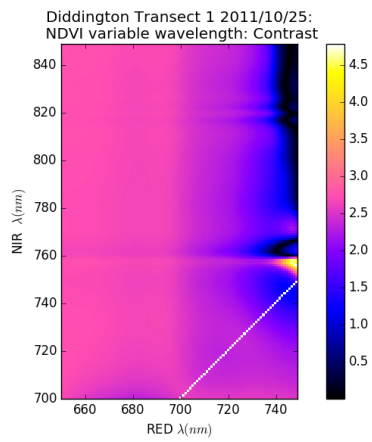


Figure B.197: MTBVI DDT1 25/10/2011

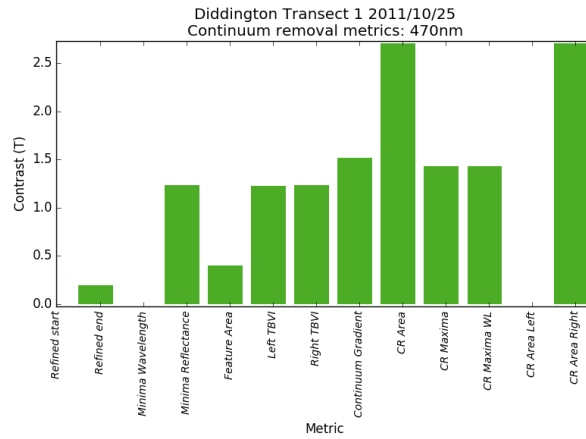


Figure B.198: Continuum removed metrics 470nm DDT1 25/10/2011

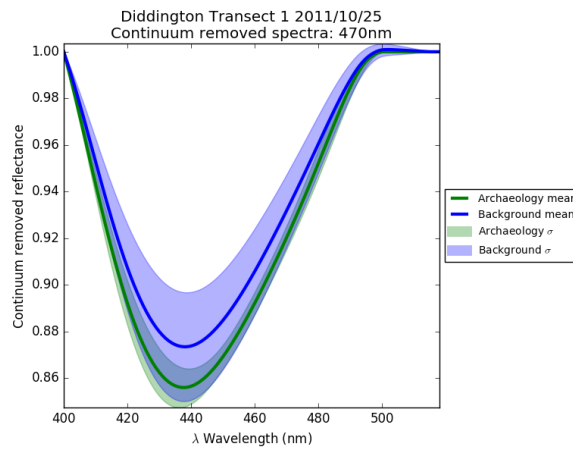


Figure B.199: Continuum removed reflectance 470nm DDT1 25/10/2011

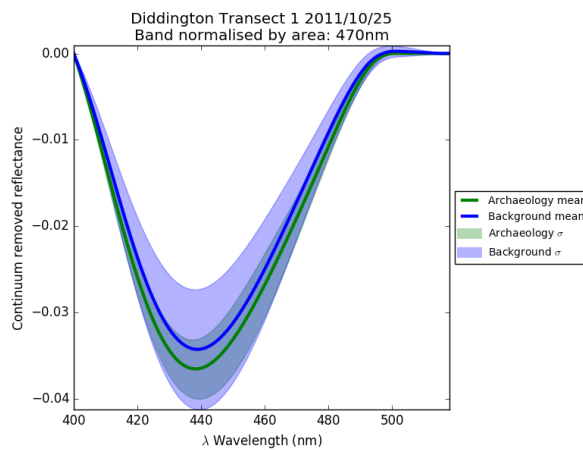


Figure B.200: Continuum removed reflectance band normalised by area 470nm DDT1 25/10/2011

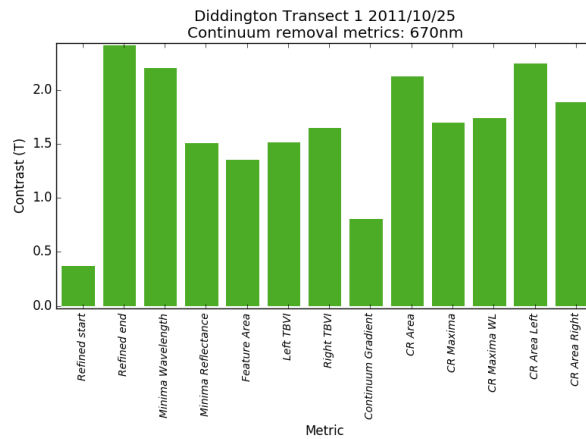


Figure B.201: Continuum removed metrics 670nm DDT1 25/10/2011

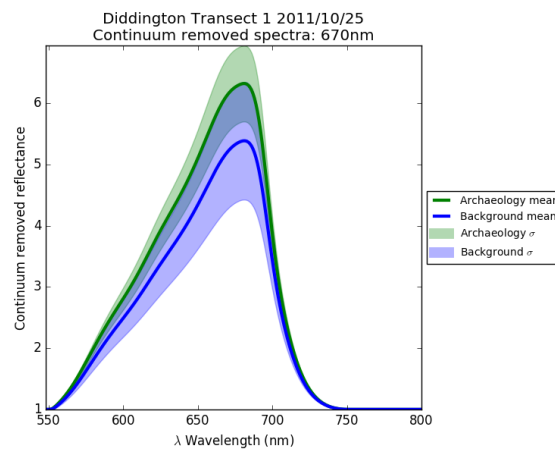


Figure B.202: Continuum removed reflectance 670nm DDT1 25/10/2011

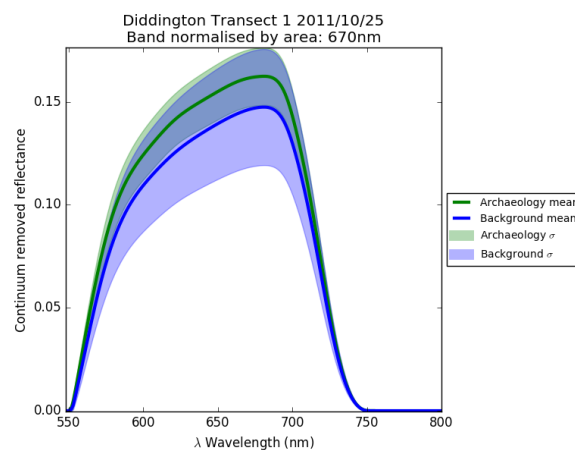


Figure B.203: Continuum removed reflectance band normalised by area 670nm DDT1 25/10/2011

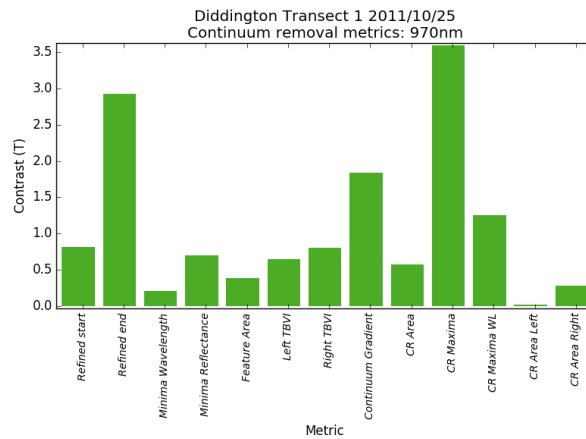


Figure B.204: Continuum removed metrics 970nm DDT1 25/10/2011

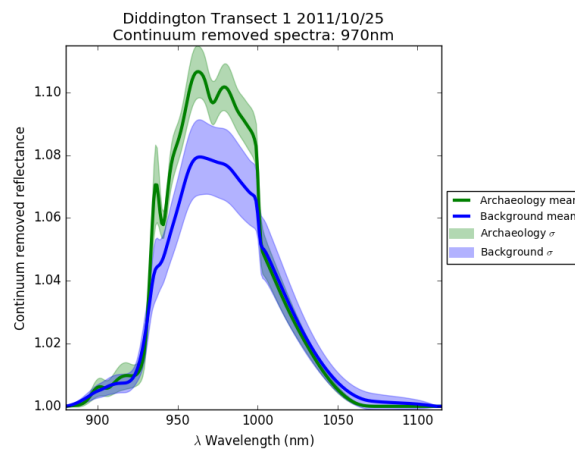


Figure B.205: Continuum removed reflectance 970nm DDT1 25/10/2011

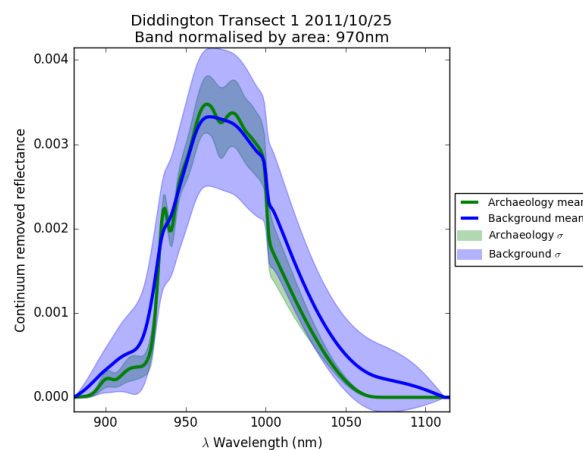


Figure B.206: Continuum removed reflectance band normalised by area 970nm DDT1 25/10/2011

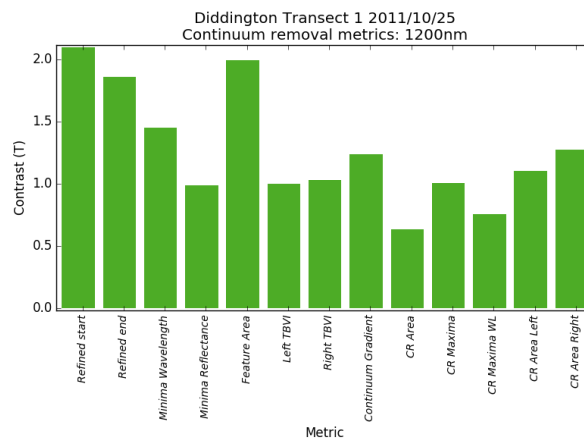


Figure B.207: Continuum removed metrics 1200nm DDT1 25/10/2011

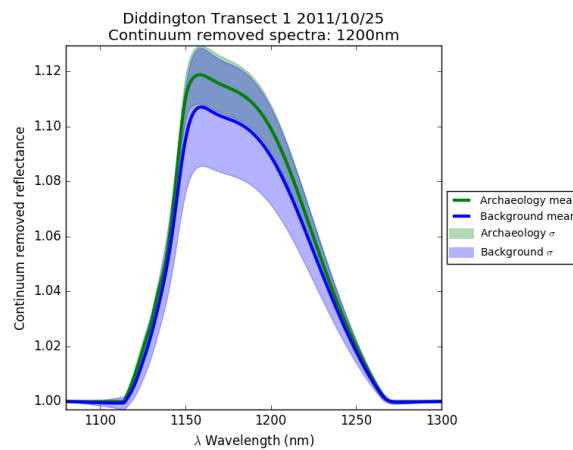


Figure B.208: Continuum removed reflectance 1200nm DDT1 25/10/2011

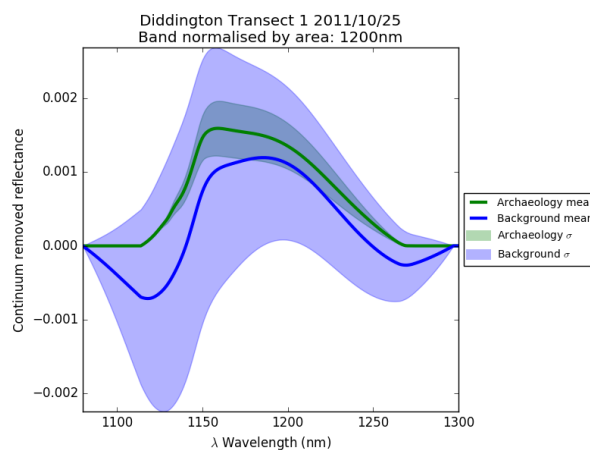


Figure B.209: Continuum removed reflectance band normalised by area 1200nm DDT1 25/10/2011

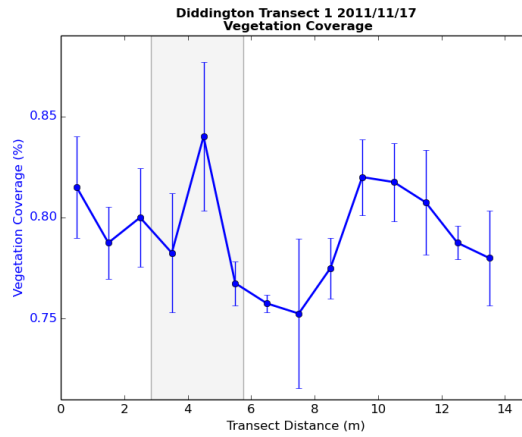


Figure B.210: Physical vegetation properties DDT1 17/11/2011

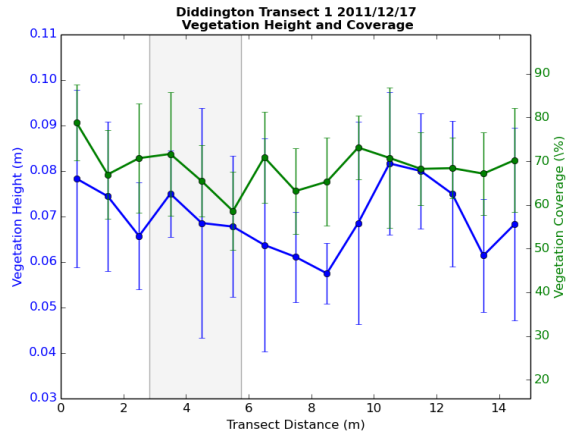


Figure B.211: Physical vegetation properties DDT1 17/12/2011

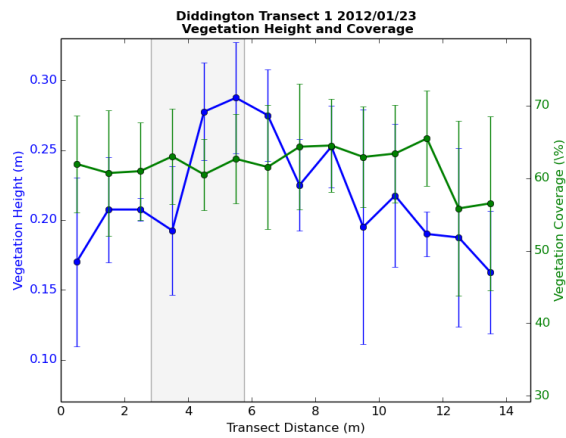


Figure B.212: Physical vegetation properties DDT1 23/01/2012

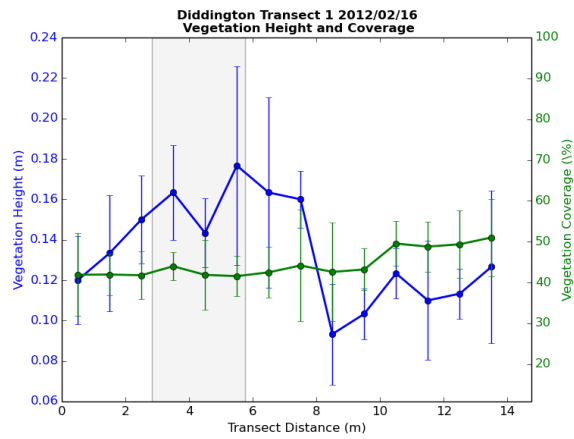


Figure B.213: Physical vegetation properties DDT1 16/02/2012

Figure B.214: Physical vegetation properties DDT1 20/03/2012

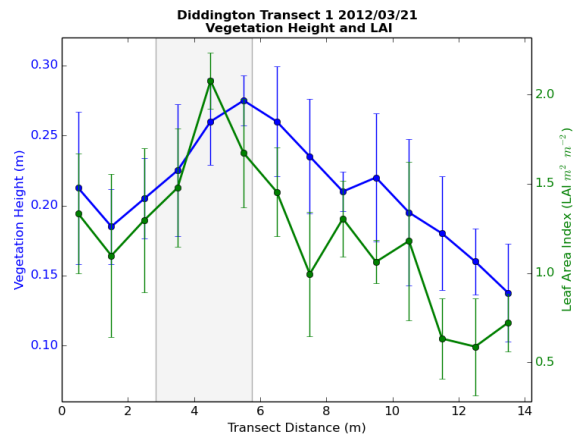


Figure B.215: Physical vegetation properties DDT1 21/03/2012

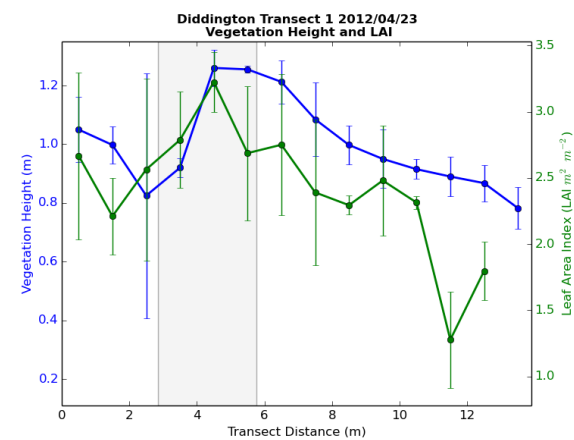


Figure B.216: Physical vegetation properties DDT1 23/04/2012

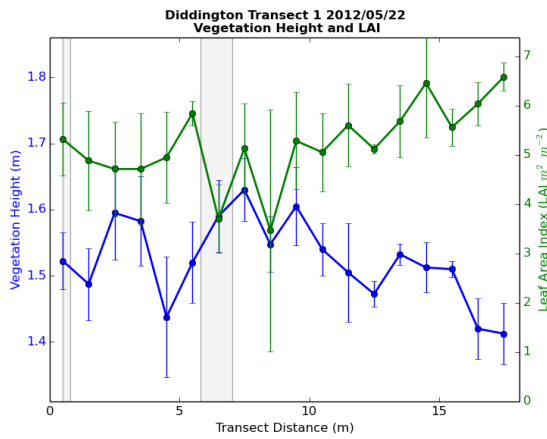


Figure B.217: Physical vegetation properties DDT1 22/05/2012

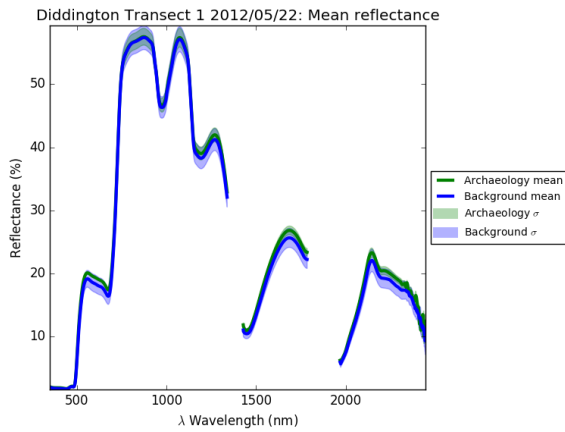


Figure B.218: Spectra from DDT1 22/05/2012

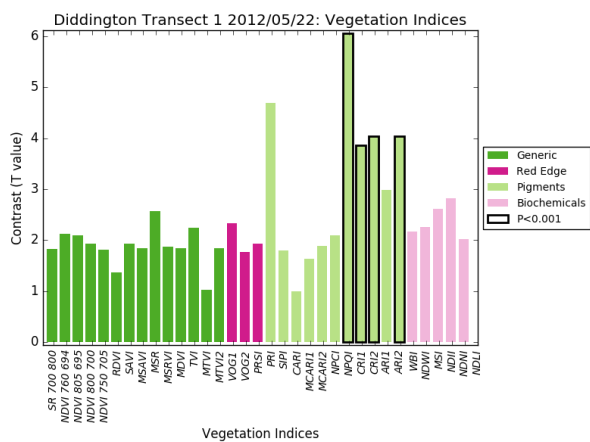


Figure B.219: Vegetation indices DDT1 22/05/2012

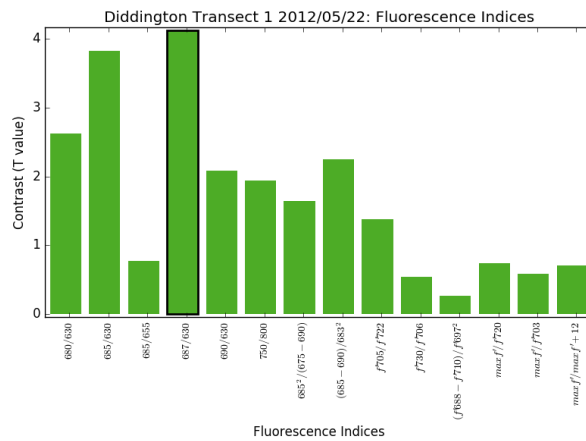


Figure B.220: Fluorescence Indices DDT1 22/05/2012

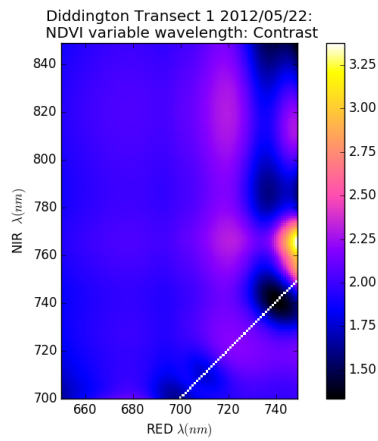


Figure B.221: MTBVI DDT1 22/05/2012

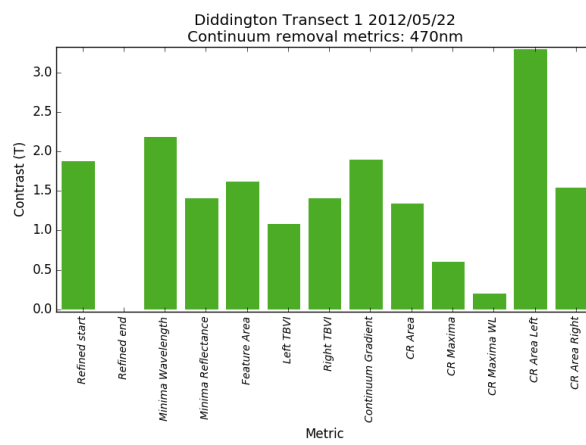


Figure B.222: Continuum removed metrics 470nm DDT1 22/05/2012

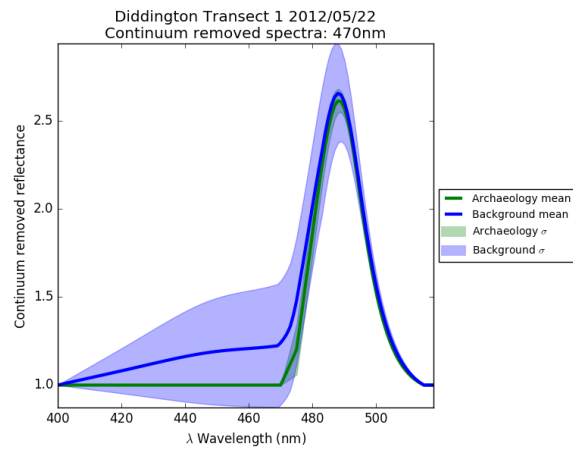


Figure B.223: Continuum removed reflectance 470nm DDT1 22/05/2012

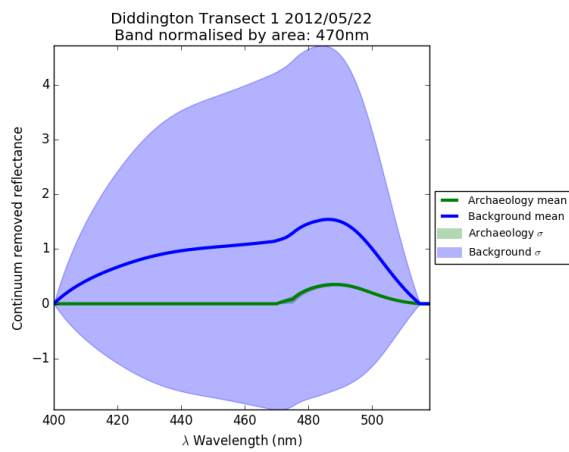


Figure B.224: Continuum removed reflectance band normalised by area 470nm DDT1 22/05/2012

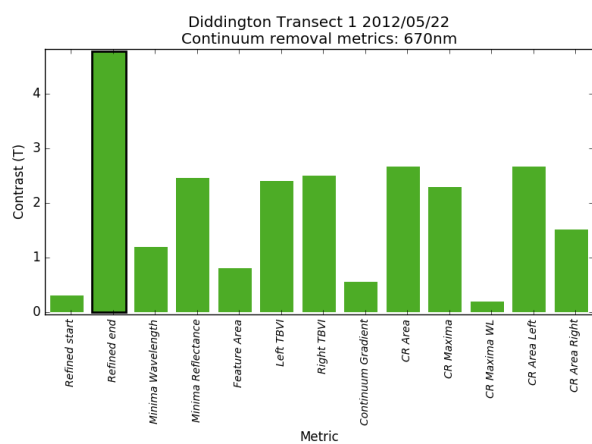


Figure B.225: Continuum removed metrics 670nm DDT1 22/05/2012

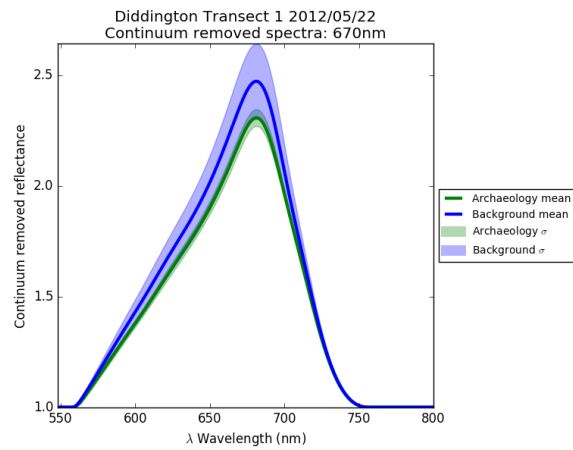


Figure B.226: Continuum removed reflectance 670nm DDT1 22/05/2012

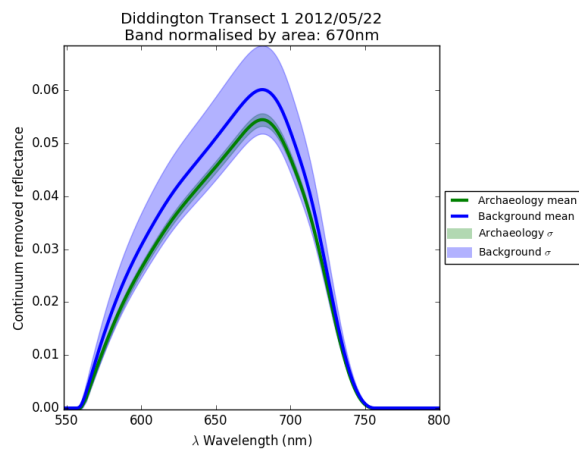


Figure B.227: Continuum removed reflectance band normalised by area 670nm DDT1 22/05/2012

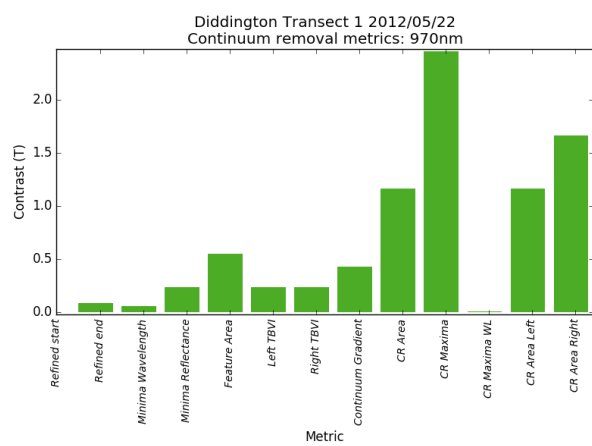


Figure B.228: Continuum removed metrics 970nm DDT1 22/05/2012

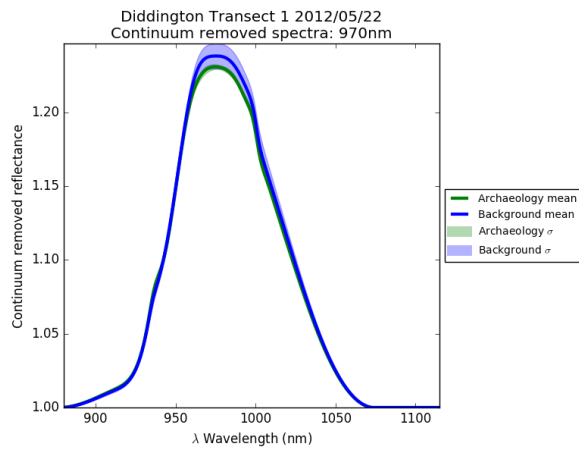


Figure B.229: Continuum removed reflectance 970nm DDT1 22/05/2012

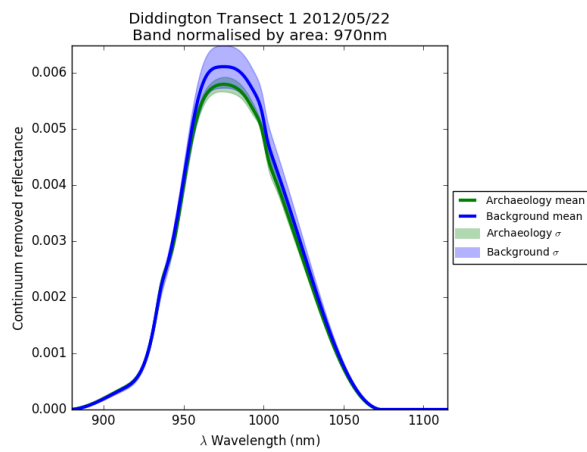


Figure B.230: Continuum removed reflectance band normalised by area 970nm DDT1 22/05/2012

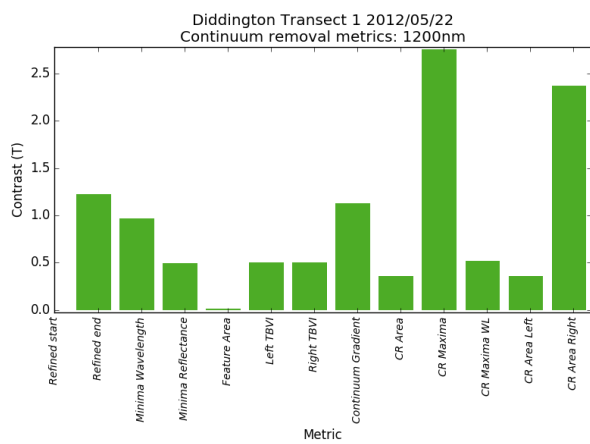


Figure B.231: Continuum removed metrics 1200nm DDT1 22/05/2012

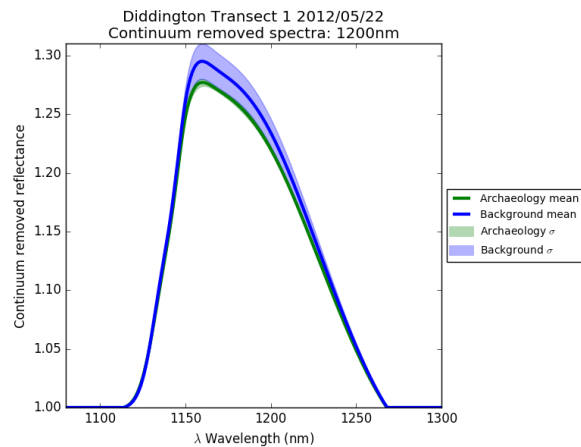


Figure B.232: Continuum removed reflectance 1200nm DDT1 22/05/2012

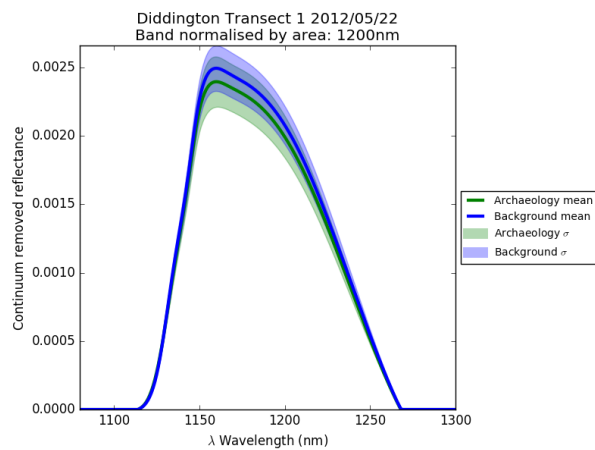


Figure B.233: Continuum removed reflectance band normalised by area 1200nm DDT1 22/05/2012

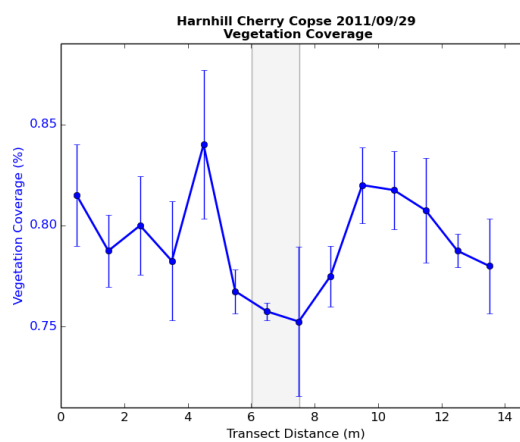


Figure B.234: Physical vegetation properties HHCC 29/09/2011

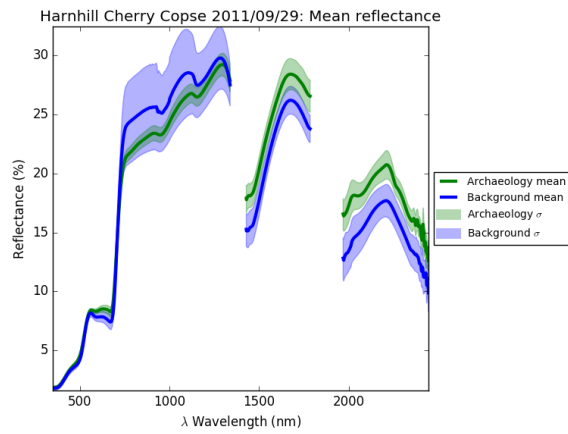


Figure B.235: Spectra from HHCC 29/09/2011

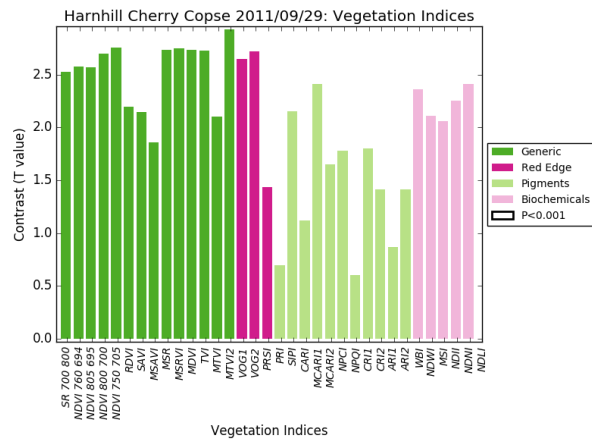


Figure B.236: Vegetation indices HHCC 29/09/2011

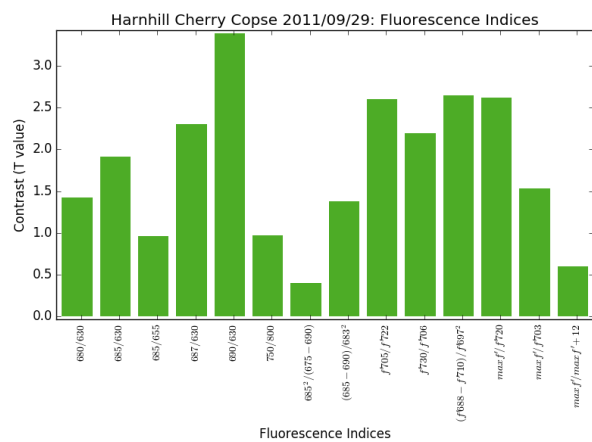


Figure B.237: Fluorescence Indices HHCC 29/09/2011

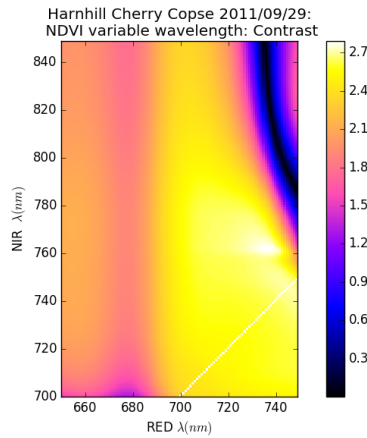


Figure B.238: MTBVI HHCC 29/09/2011

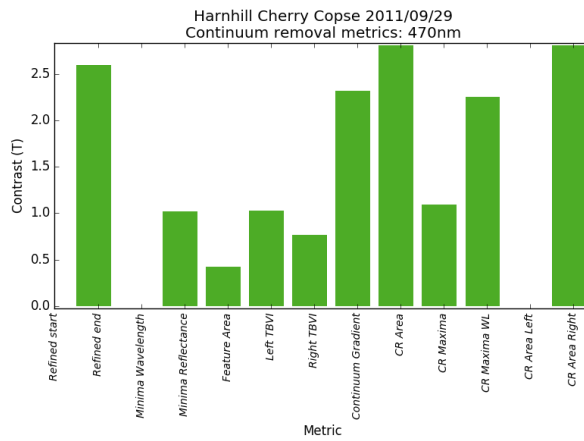


Figure B.239: Continuum removed metrics 470nm HHCC 29/09/2011

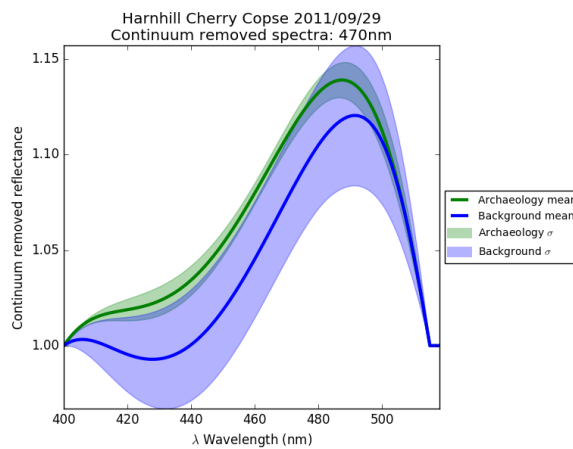


Figure B.240: Continuum removed reflectance 470nm HHCC 29/09/2011

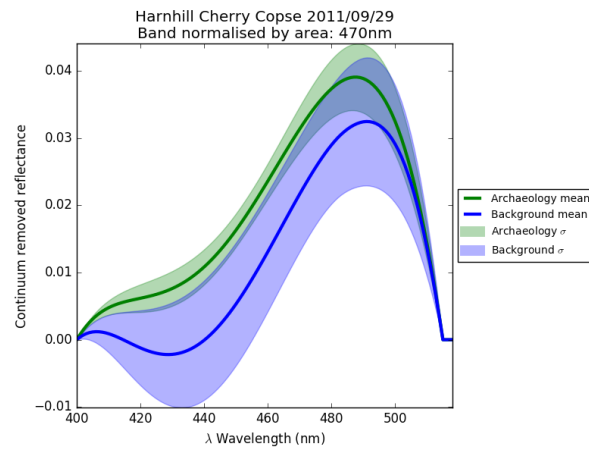


Figure B.241: Continuum removed reflectance band normalised by area 470nm HHCC 29/09/2011

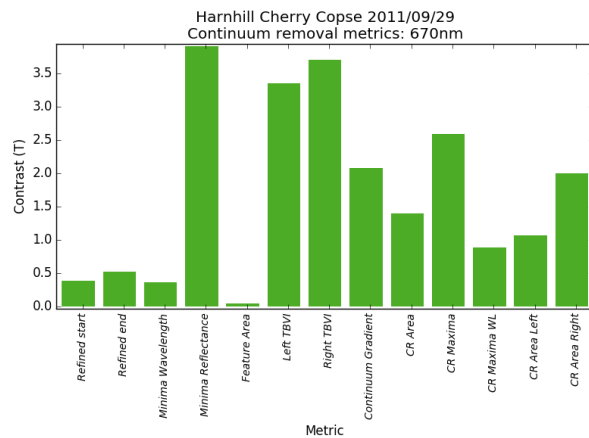


Figure B.242: Continuum removed metrics 670nm HHCC 29/09/2011

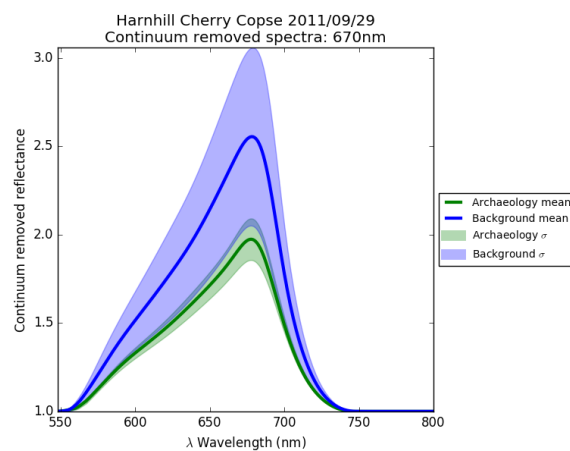


Figure B.243: Continuum removed reflectance 670nm HHCC 29/09/2011

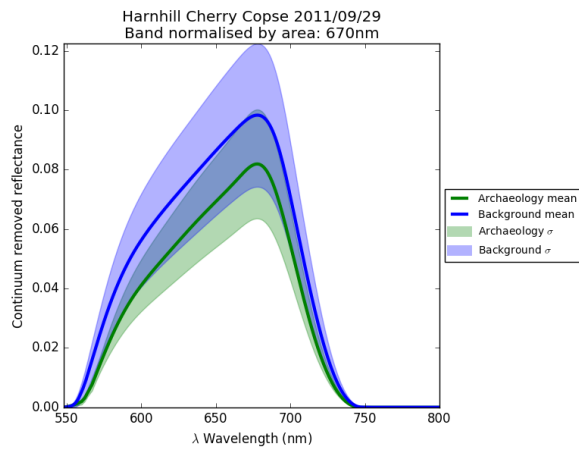


Figure B.244: Continuum removed reflectance band normalised by area 670nm HHCC 29/09/2011

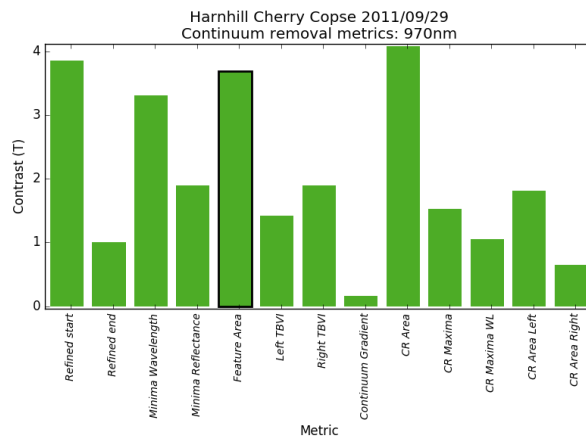


Figure B.245: Continuum removed metrics 970nm HHCC 29/09/2011

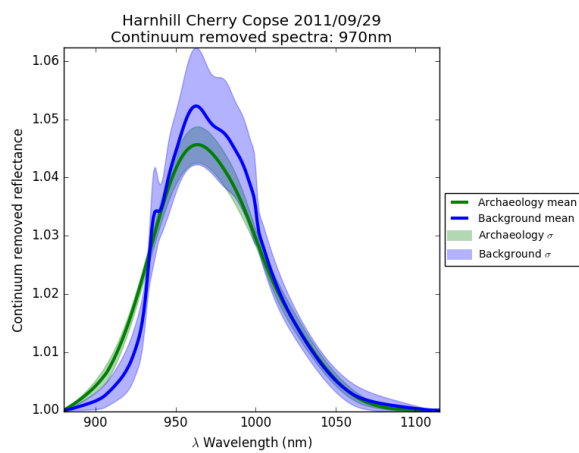


Figure B.246: Continuum removed reflectance 970nm HHCC 29/09/2011

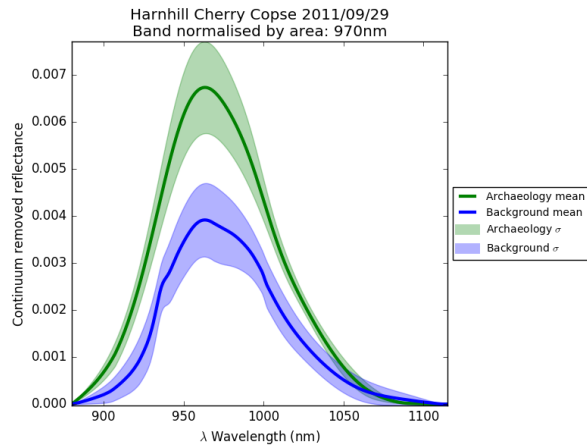


Figure B.247: Continuum removed reflectance band normalised by area 970nm HHCC 29/09/2011

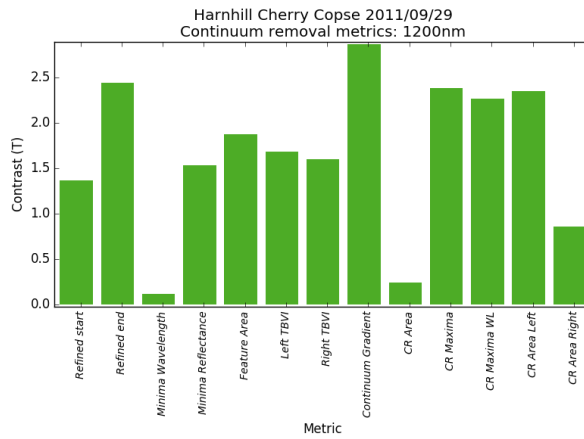


Figure B.248: Continuum removed metrics 1200nm HHCC 29/09/2011

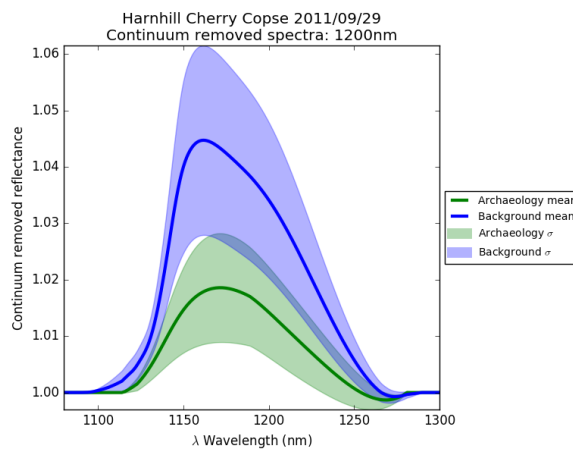


Figure B.249: Continuum removed reflectance 1200nm HHCC 29/09/2011

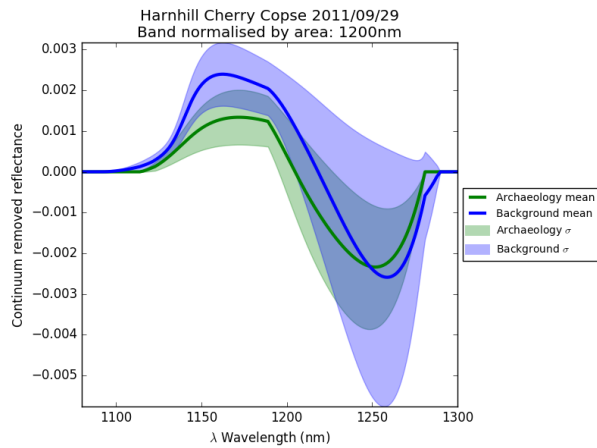


Figure B.250: Continuum removed reflectance band normalised by area 1200nm HHCC 29/09/2011

Figure B.251: Physical vegetation properties HHCC 28/10/2011

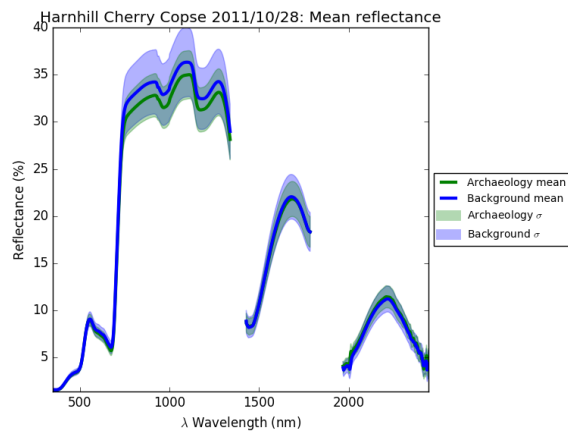


Figure B.252: Spectra from HHCC 28/10/2011

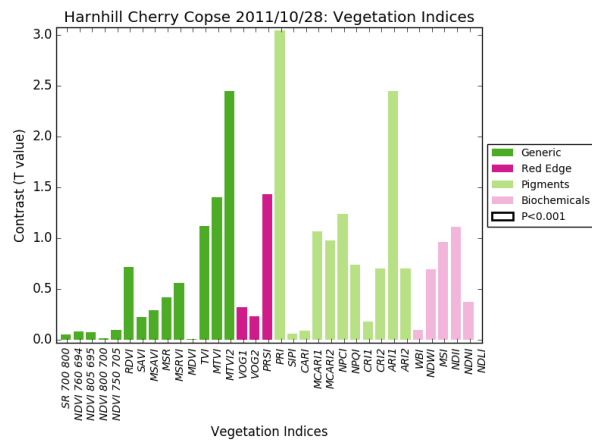


Figure B.253: Vegetation indices HHCC 28/10/2011

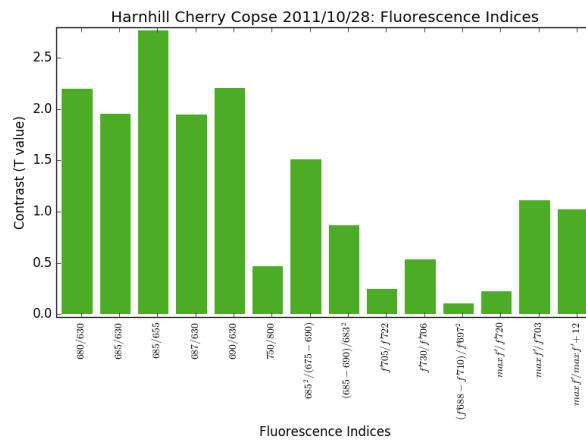


Figure B.254: Fluorescence Indices HHCC 28/10/2011

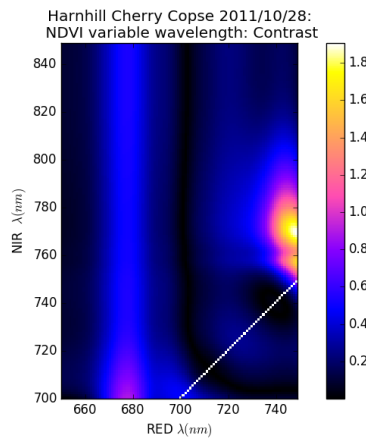


Figure B.255: MTBVI HHCC 28/10/2011

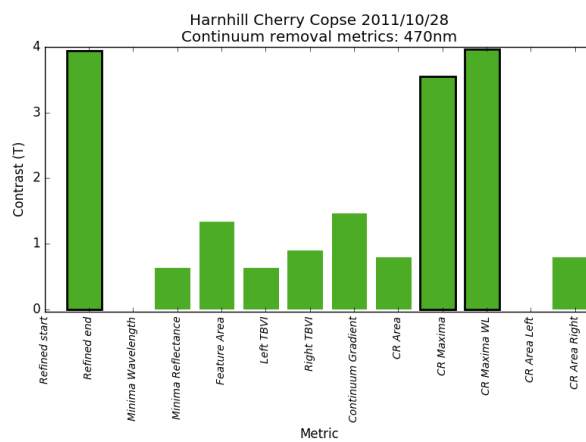


Figure B.256: Continuum removed metrics 470nm HHCC 28/10/2011

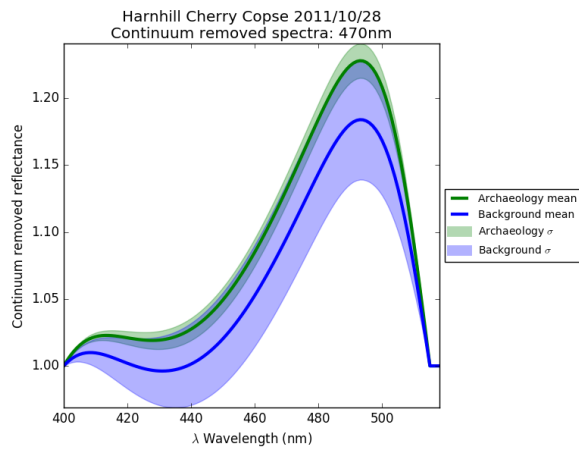


Figure B.257: Continuum removed reflectance 470nm HHCC 28/10/2011

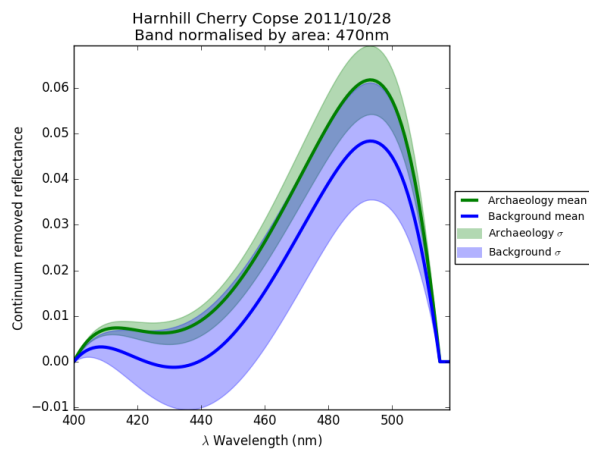


Figure B.258: Continuum removed reflectance band normalised by area 470nm HHCC 28/10/2011

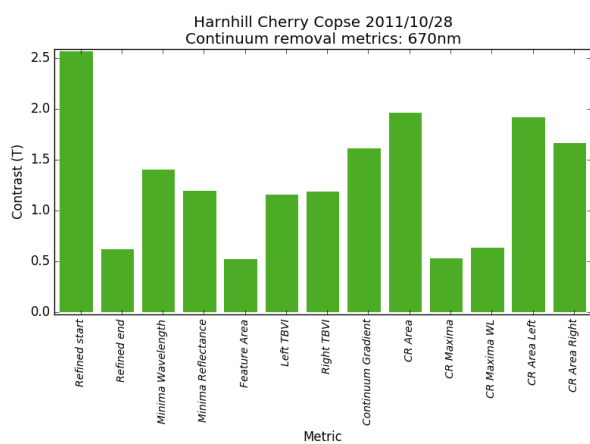


Figure B.259: Continuum removed metrics 670nm HHCC 28/10/2011

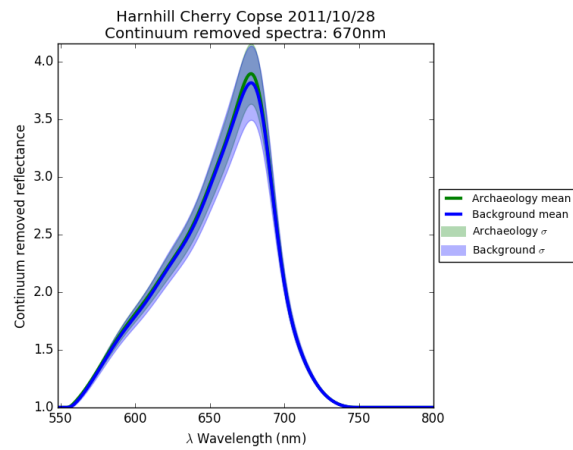


Figure B.260: Continuum removed reflectance 670nm HHCC 28/10/2011

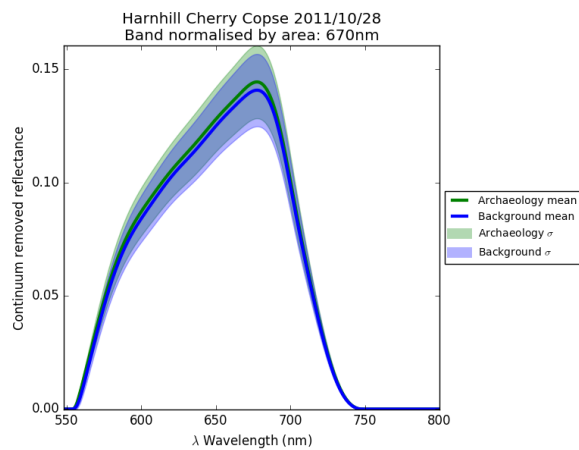


Figure B.261: Continuum removed reflectance band normalised by area 670nm HHCC 28/10/2011

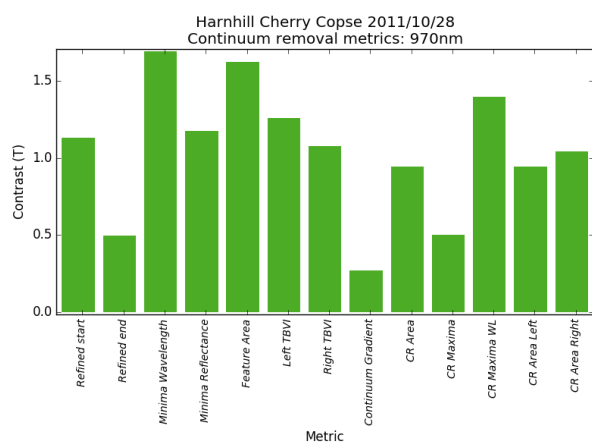


Figure B.262: Continuum removed metrics 970nm HHCC 28/10/2011



Figure B.263: Continuum removed reflectance 970nm HHCC 28/10/2011

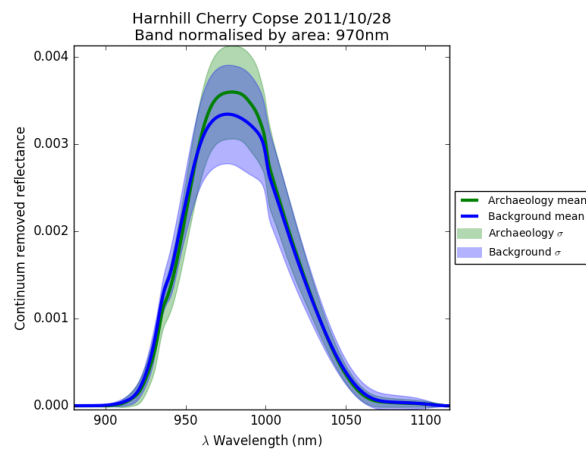


Figure B.264: Continuum removed reflectance band normalised by area 970nm HHCC 28/10/2011

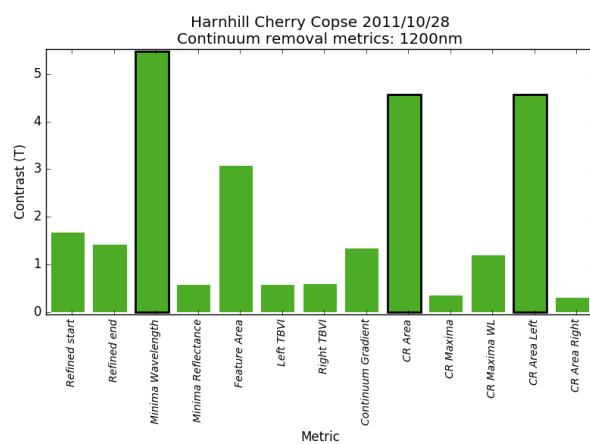


Figure B.265: Continuum removed metrics 1200nm HHCC 28/10/2011

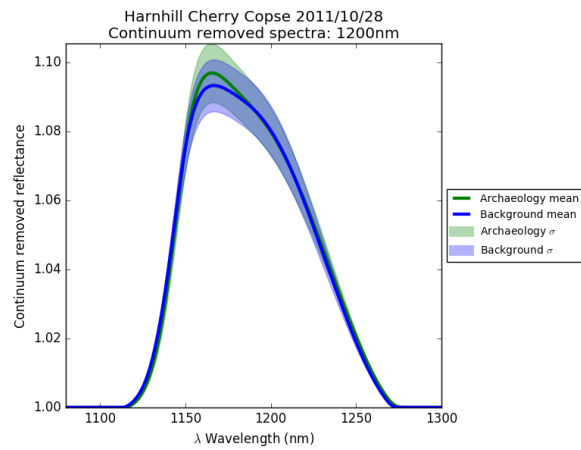


Figure B.266: Continuum removed reflectance 1200nm HHCC 28/10/2011

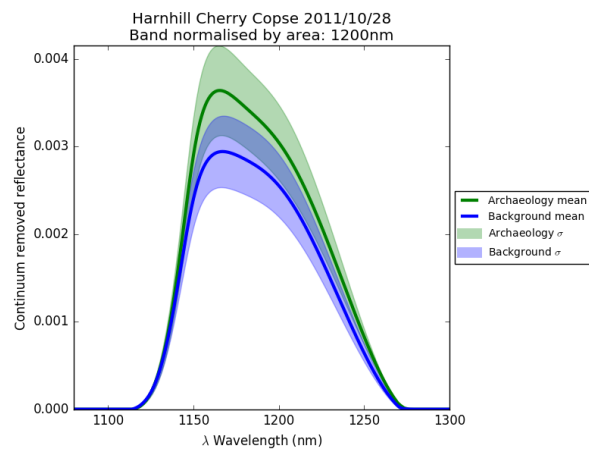


Figure B.267: Continuum removed reflectance band normalised by area 1200nm HHCC 28/10/2011

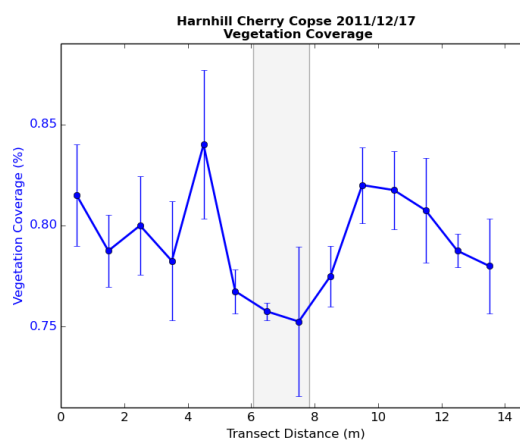


Figure B.268: Physical vegetation properties HHCC 17/12/2011

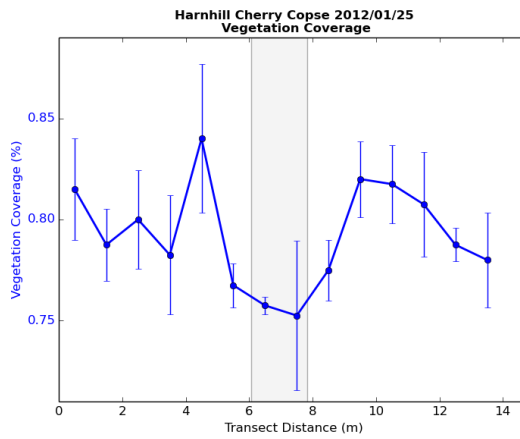


Figure B.269: Physical vegetation properties HHCC 25/01/2012

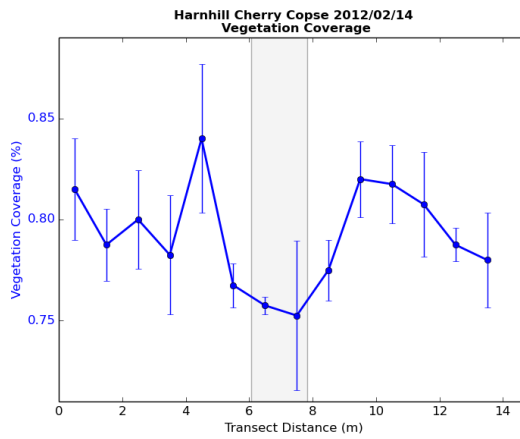


Figure B.270: Physical vegetation properties HHCC 14/02/2012

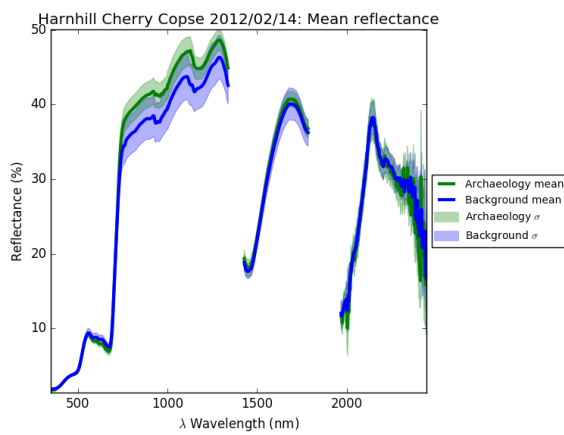


Figure B.271: Spectra from HHCC 14/02/2012

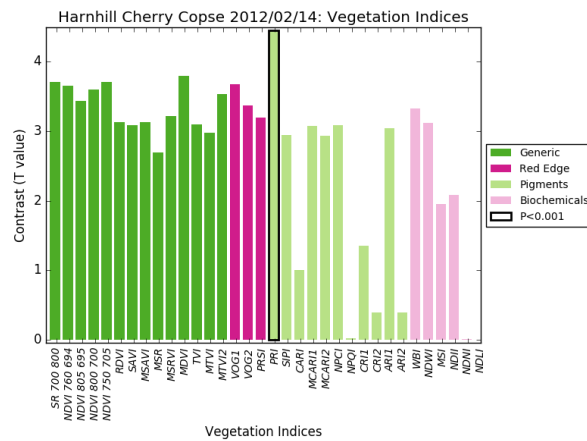


Figure B.272: Vegetation indices HHCC 14/02/2012

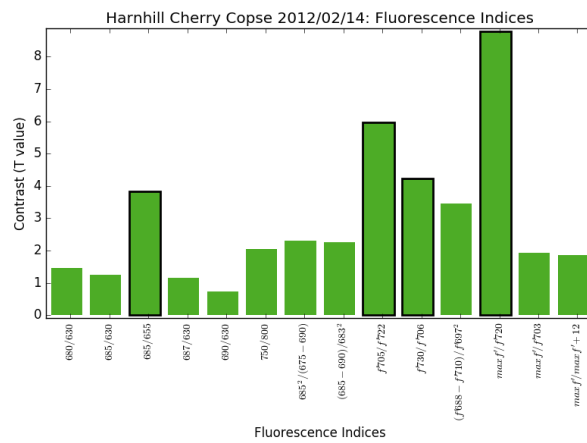


Figure B.273: Fluorescence Indices HHCC 14/02/2012

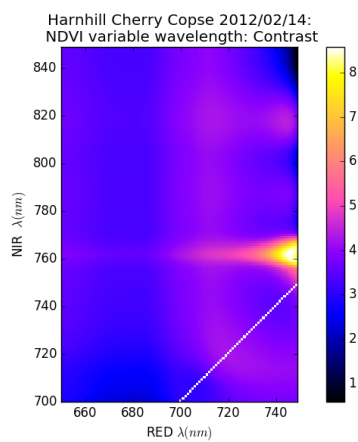


Figure B.274: MTBVI HHCC 14/02/2012

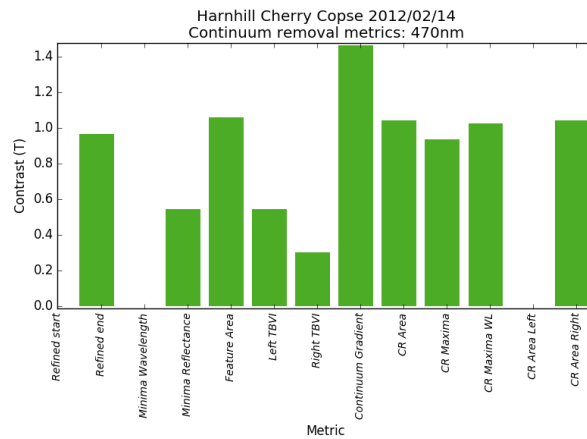


Figure B.275: Continuum removed metrics 470nm HHCC 14/02/2012

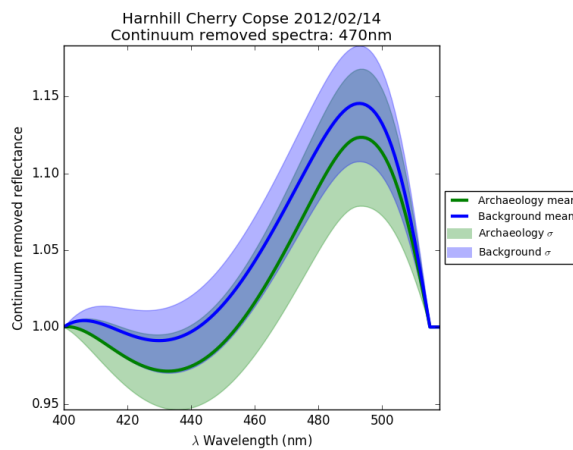


Figure B.276: Continuum removed reflectance 470nm HHCC 14/02/2012

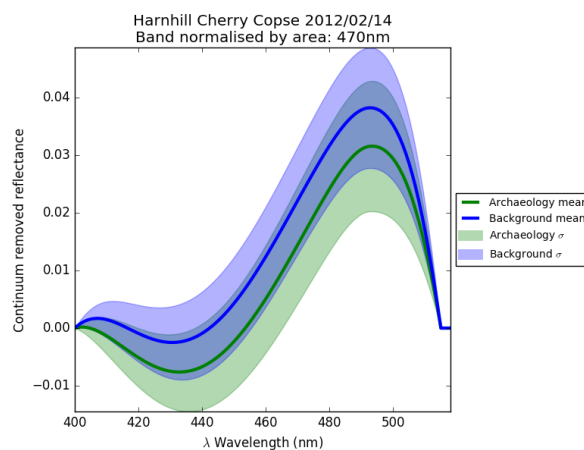


Figure B.277: Continuum removed reflectance band normalised by area 470nm HHCC 14/02/2012

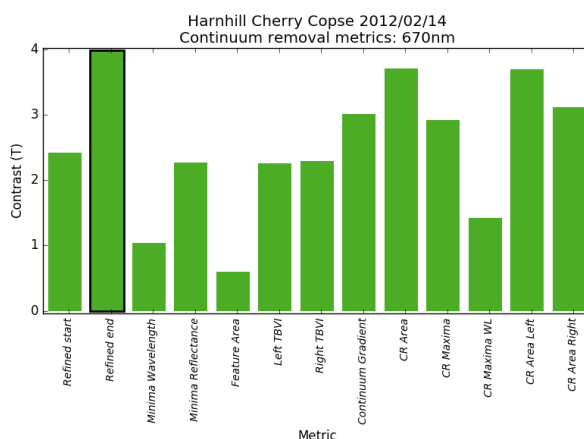


Figure B.278: Continuum removed metrics 670nm HHCC 14/02/2012

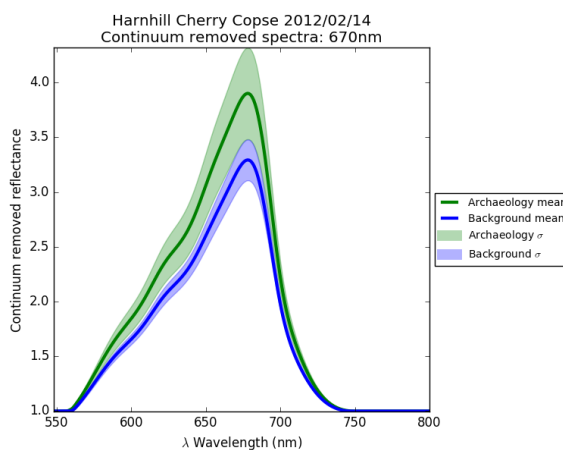


Figure B.279: Continuum removed reflectance 670nm HHCC 14/02/2012

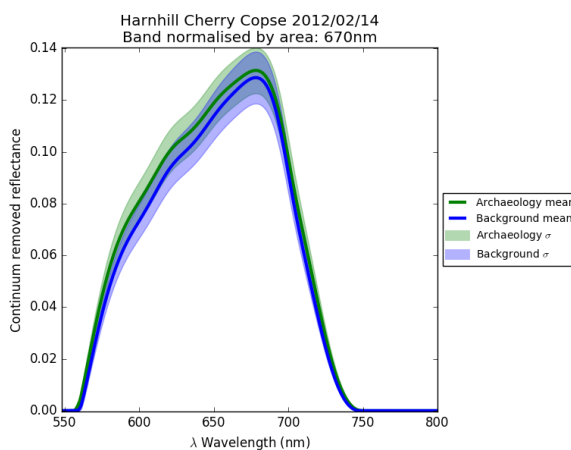


Figure B.280: Continuum removed reflectance band normalised by area 670nm HHCC 14/02/2012

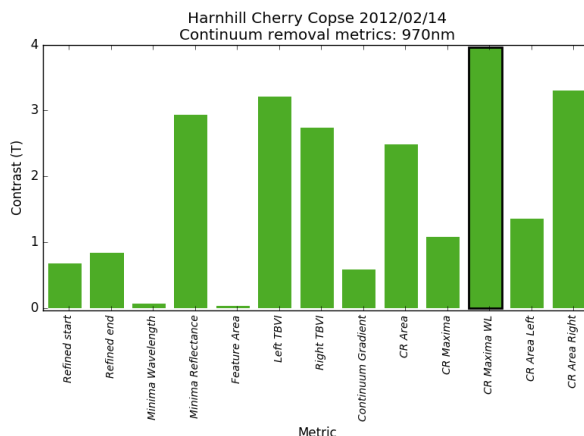


Figure B.281: Continuum removed metrics 970nm HHCC 14/02/2012

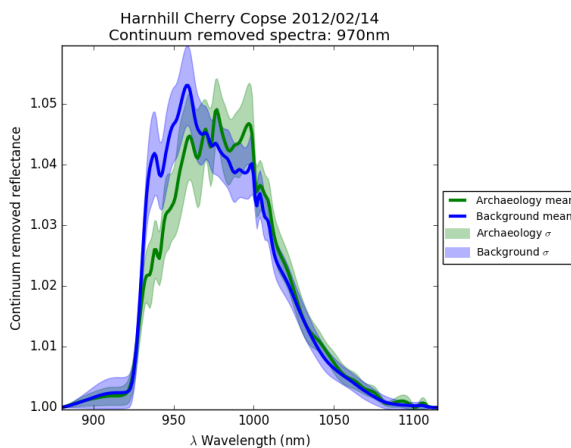


Figure B.282: Continuum removed reflectance 970nm HHCC 14/02/2012

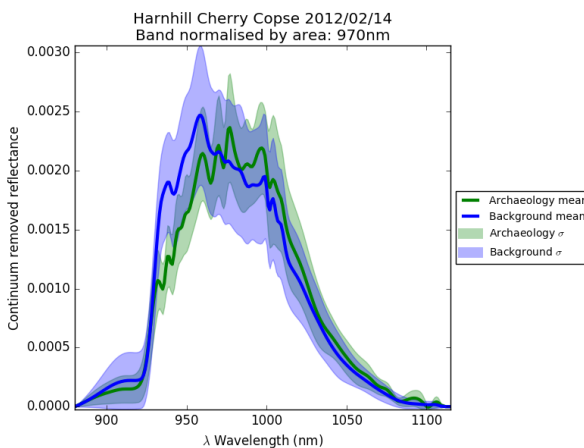


Figure B.283: Continuum removed reflectance band normalised by area 970nm HHCC 14/02/2012

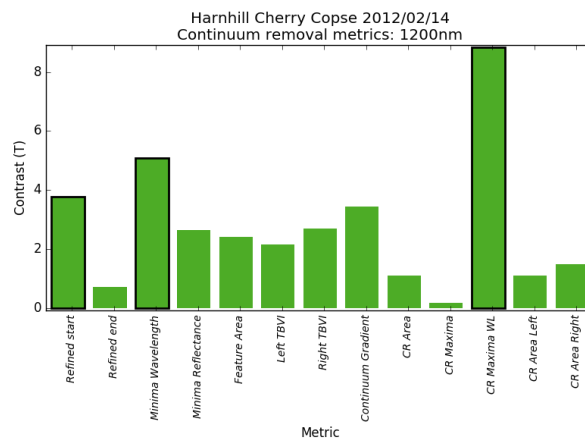


Figure B.284: Continuum removed metrics 1200nm HHCC 14/02/2012

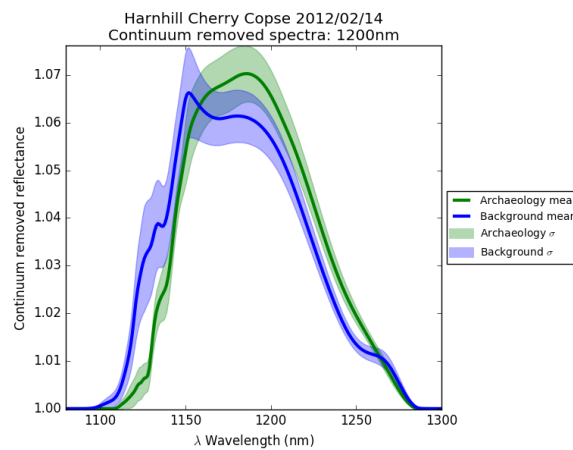


Figure B.285: Continuum removed reflectance 1200nm HHCC 14/02/2012

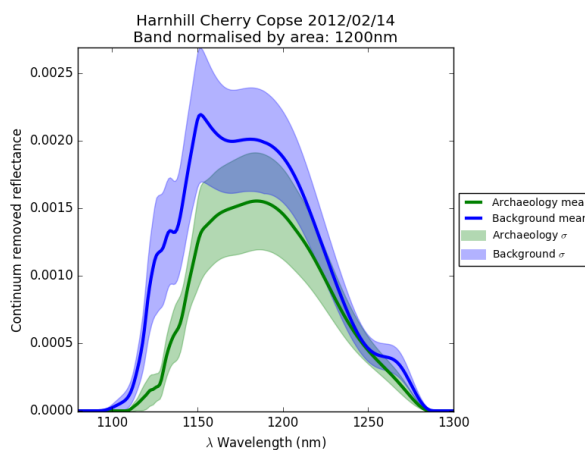


Figure B.286: Continuum removed reflectance band normalised by area 1200nm HHCC 14/02/2012

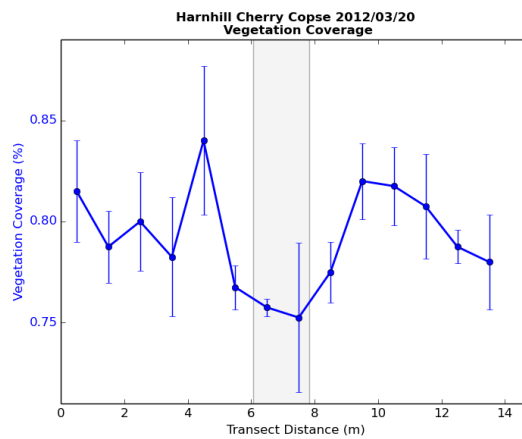


Figure B.287: Physical vegetation properties HHCC 20/03/2012

Figure B.288: Physical vegetation properties HHCC 22/03/2012

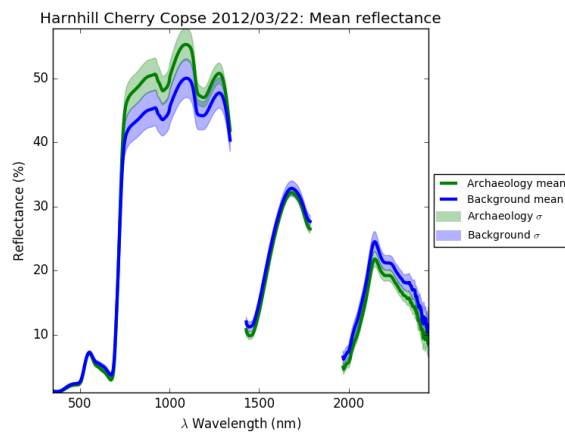


Figure B.289: Spectra from HHCC 22/03/2012

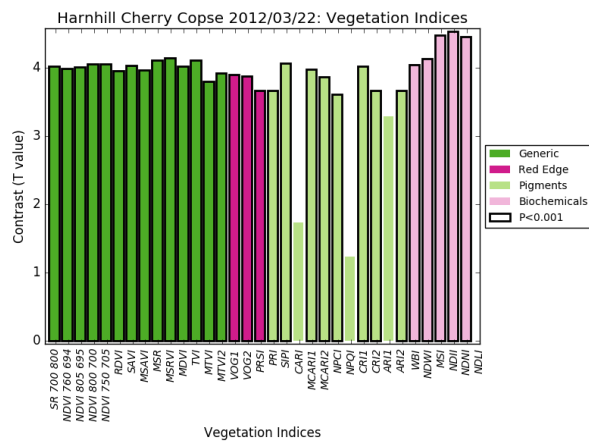


Figure B.290: Vegetation indices HHCC 22/03/2012

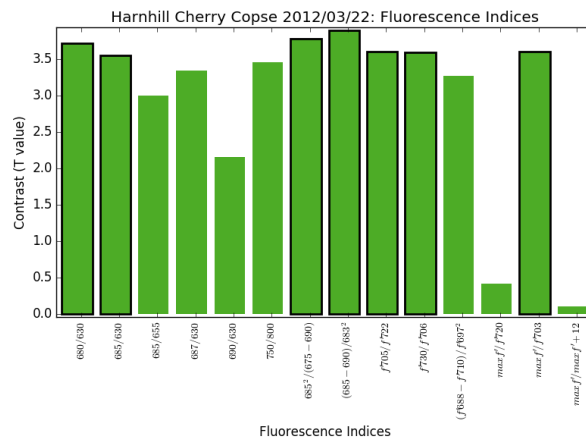


Figure B.291: Fluorescence Indices HHCC 22/03/2012

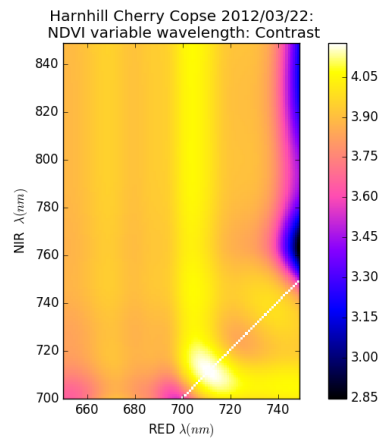


Figure B.292: MTBVI HHCC 22/03/2012

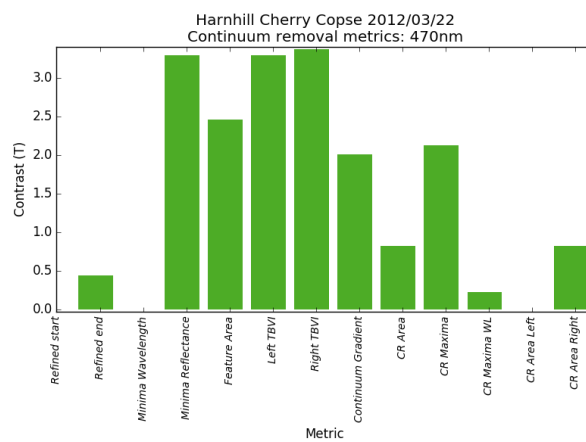


Figure B.293: Continuum removed metrics 470nm HHCC 22/03/2012

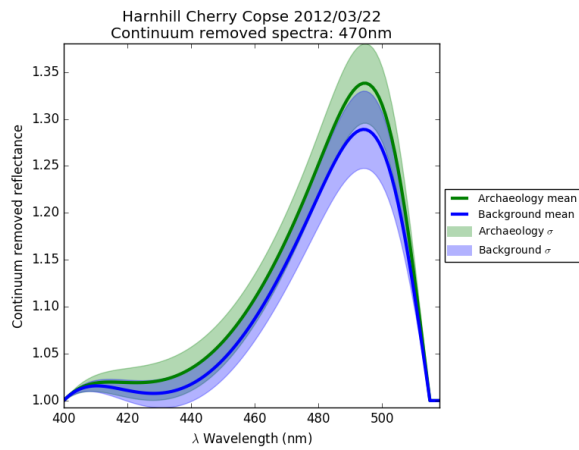


Figure B.294: Continuum removed reflectance 470nm HHCC 22/03/2012

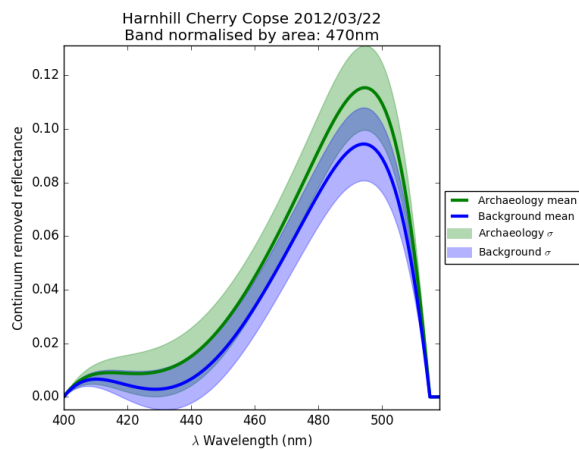


Figure B.295: Continuum removed reflectance band normalised by area 470nm HHCC 22/03/2012

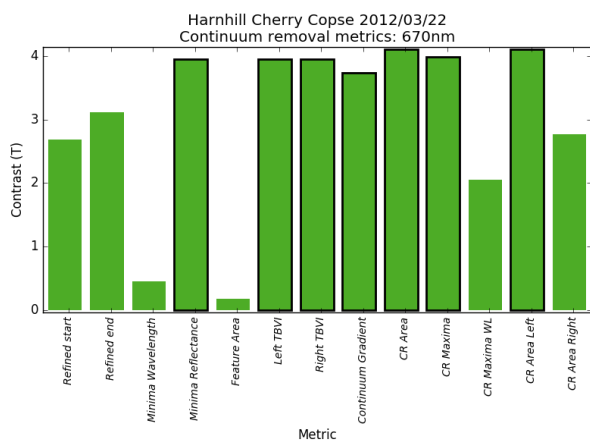


Figure B.296: Continuum removed metrics 670nm HHCC 22/03/2012

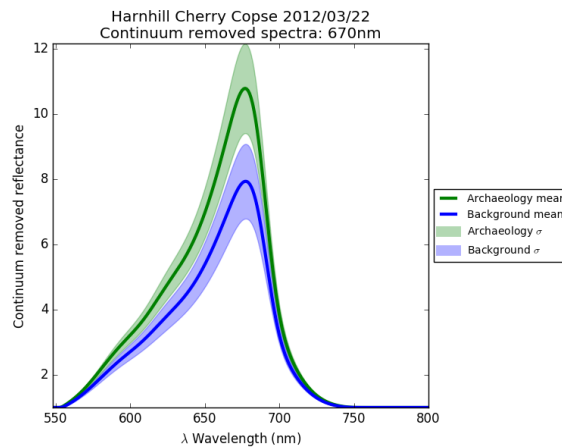


Figure B.297: Continuum removed reflectance 670nm HHCC 22/03/2012

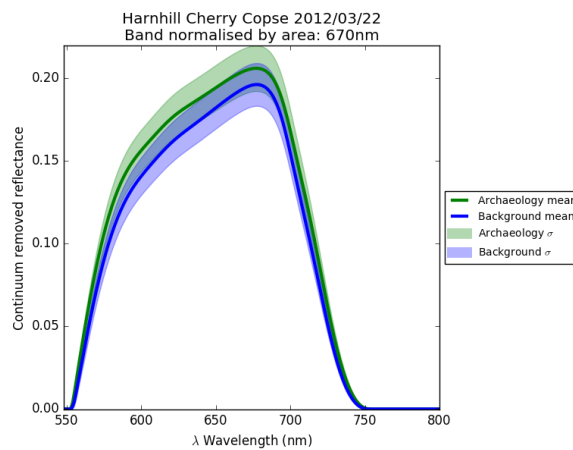


Figure B.298: Continuum removed reflectance band normalised by area 670nm HHCC 22/03/2012

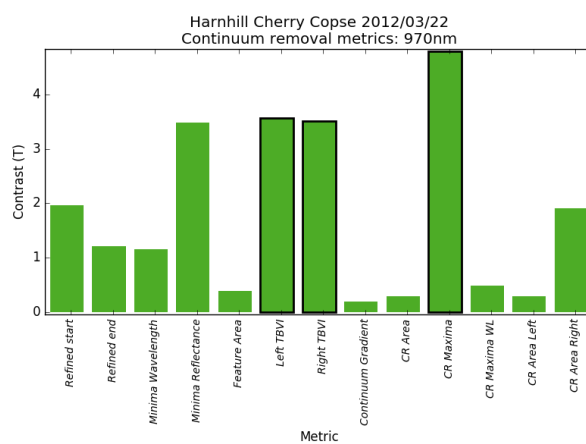


Figure B.299: Continuum removed metrics 970nm HHCC 22/03/2012

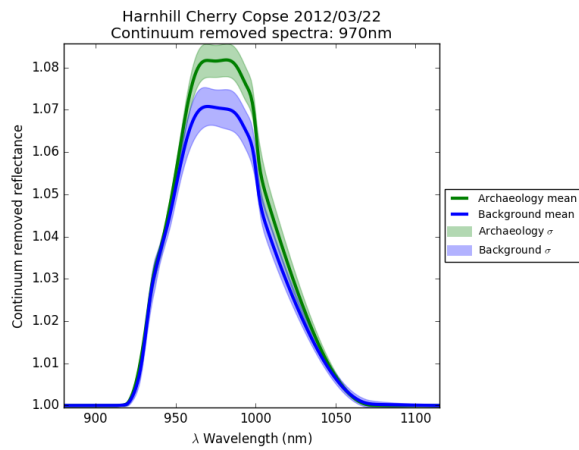


Figure B.300: Continuum removed reflectance 970nm HHCC 22/03/2012

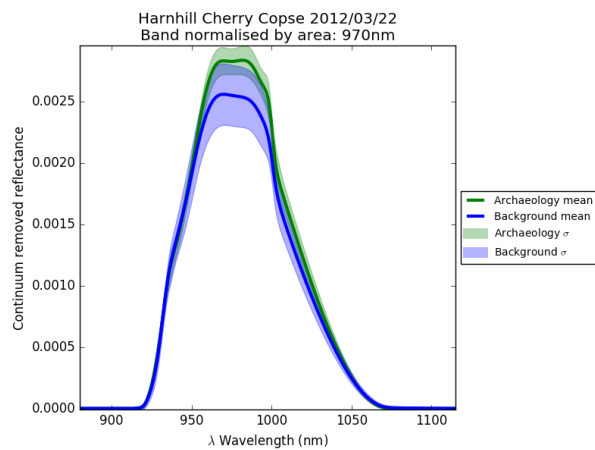


Figure B.301: Continuum removed reflectance band normalised by area 970nm HHCC 22/03/2012

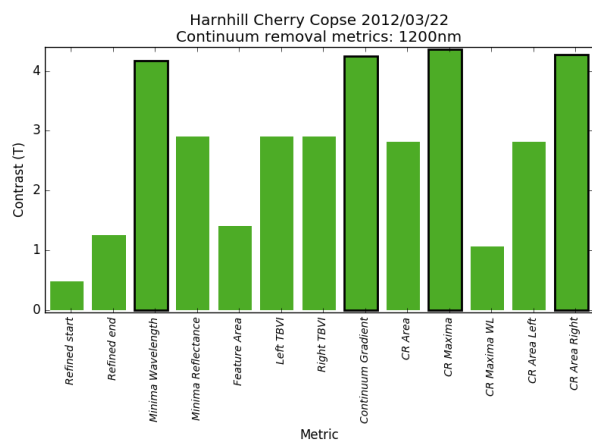


Figure B.302: Continuum removed metrics 1200nm HHCC 22/03/2012

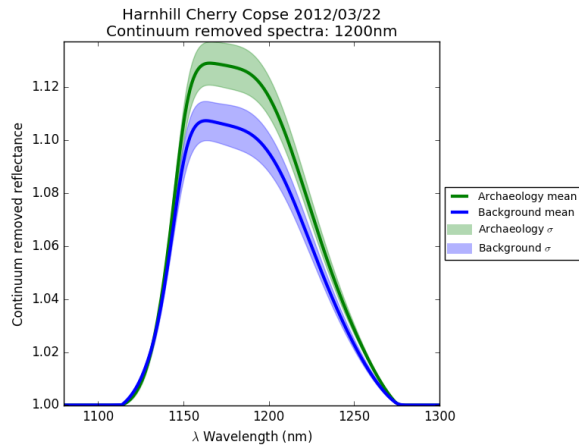


Figure B.303: Continuum removed reflectance 1200nm HHCC 22/03/2012

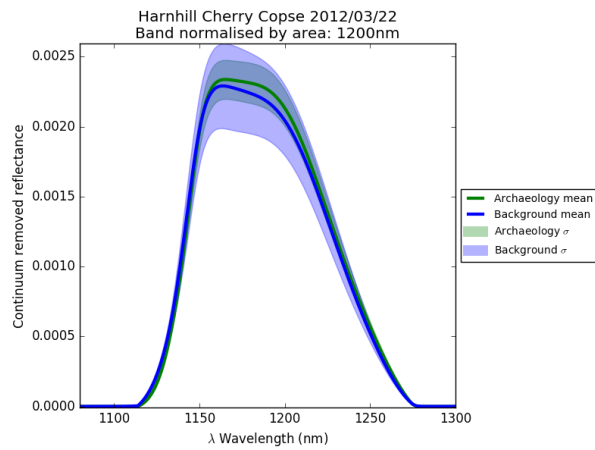


Figure B.304: Continuum removed reflectance band normalised by area 1200nm HHCC 22/03/2012

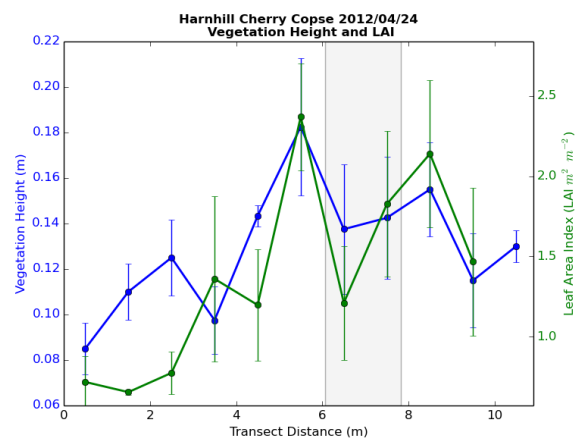


Figure B.305: Physical vegetation properties HHCC 24/04/2012

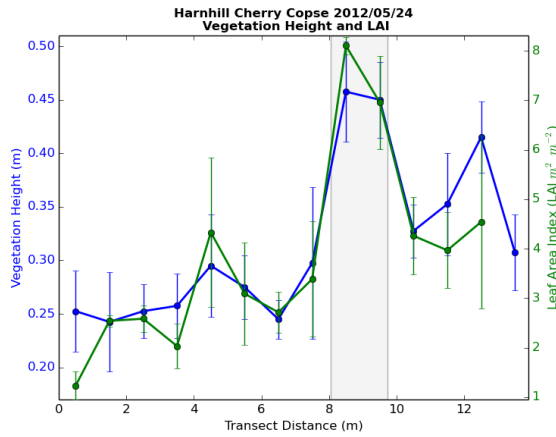


Figure B.306: Physical vegetation properties HHCC 24/05/2012

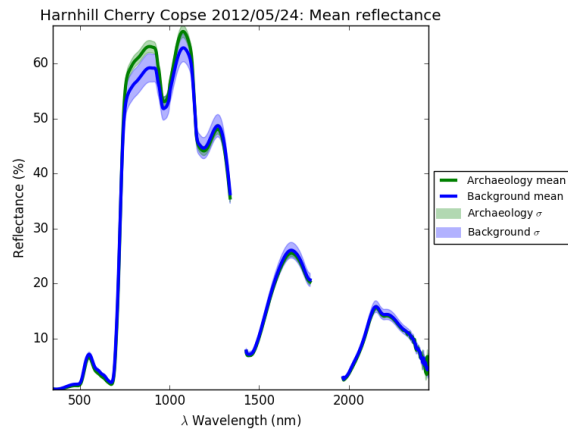


Figure B.307: Spectra from HHCC 24/05/2012

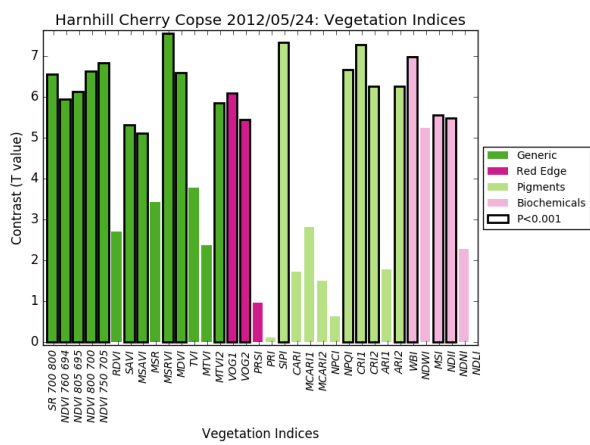


Figure B.308: Vegetation indices HHCC 24/05/2012

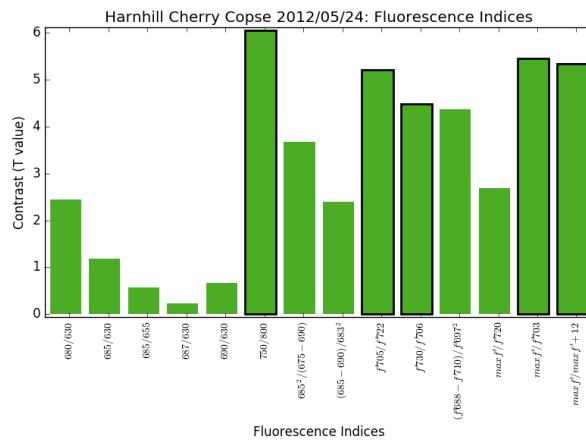


Figure B.309: Fluorescence Indices HHCC 24/05/2012

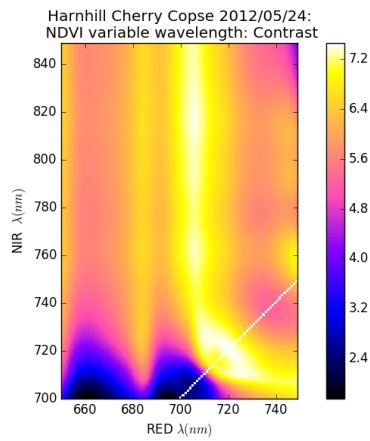


Figure B.310: MTBVI HHCC 24/05/2012

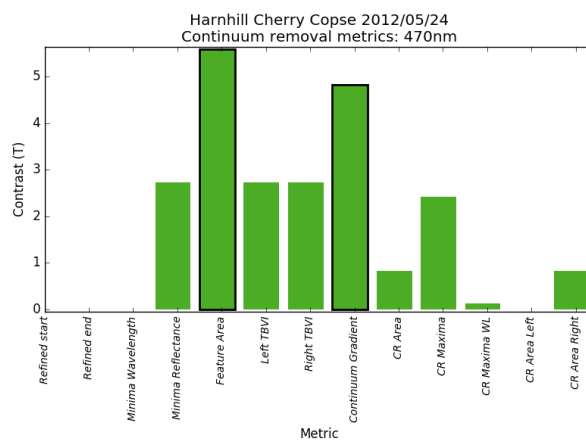


Figure B.311: Continuum removed metrics 470nm HHCC 24/05/2012

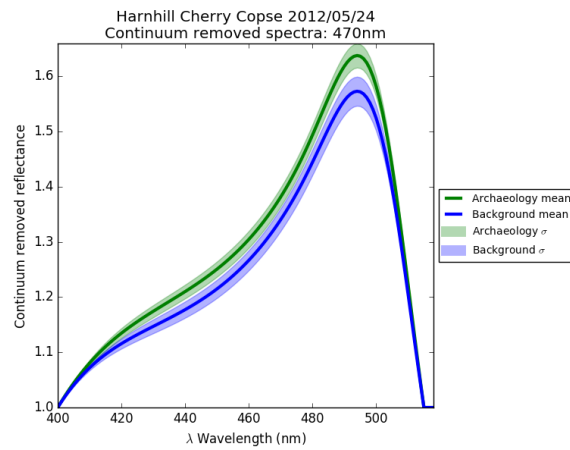


Figure B.312: Continuum removed reflectance 470nm HHCC 24/05/2012

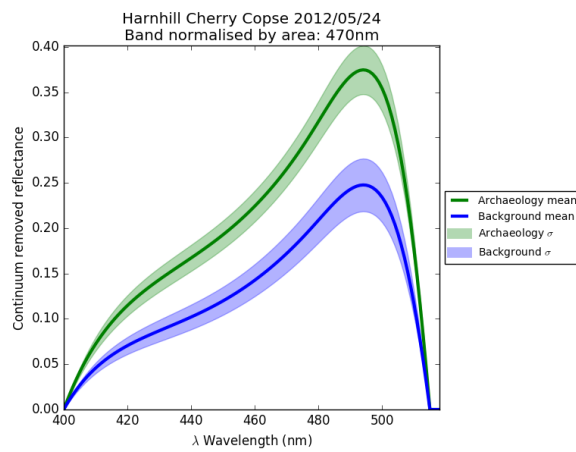


Figure B.313: Continuum removed reflectance band normalised by area 470nm HHCC 24/05/2012

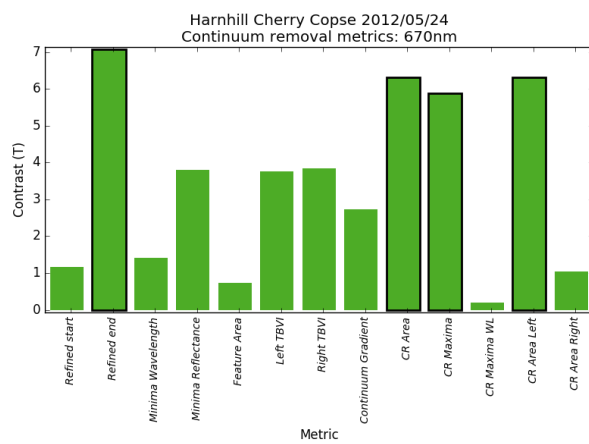


Figure B.314: Continuum removed metrics 670nm HHCC 24/05/2012

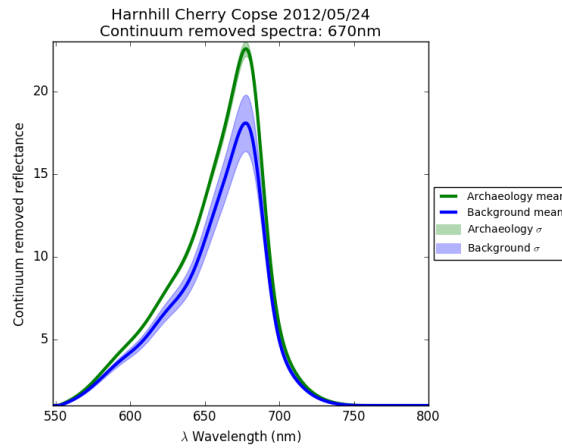


Figure B.315: Continuum removed reflectance 670nm HHCC 24/05/2012

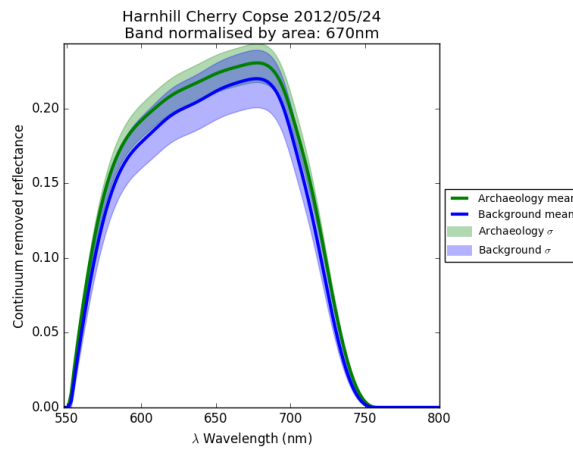


Figure B.316: Continuum removed reflectance band normalised by area 670nm HHCC 24/05/2012

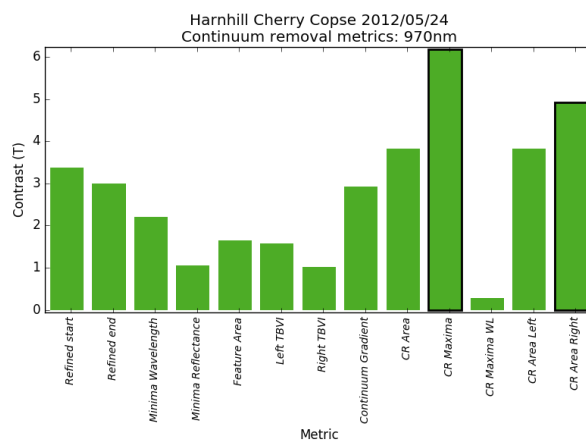


Figure B.317: Continuum removed metrics 970nm HHCC 24/05/2012

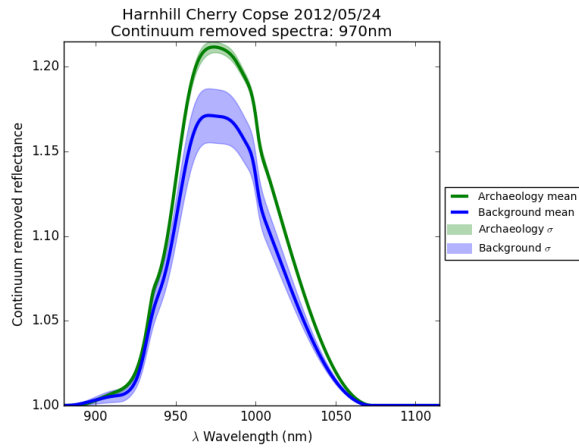


Figure B.318: Continuum removed reflectance 970nm HHCC 24/05/2012

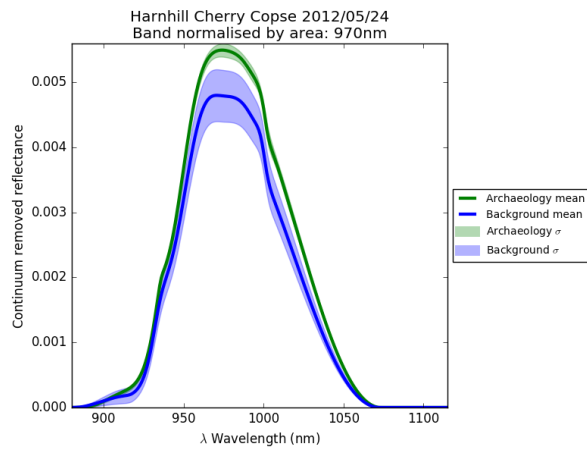


Figure B.319: Continuum removed reflectance band normalised by area 970nm HHCC 24/05/2012

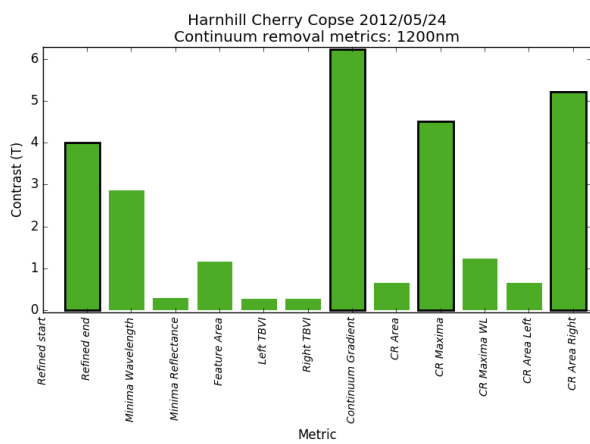


Figure B.320: Continuum removed metrics 1200nm HHCC 24/05/2012

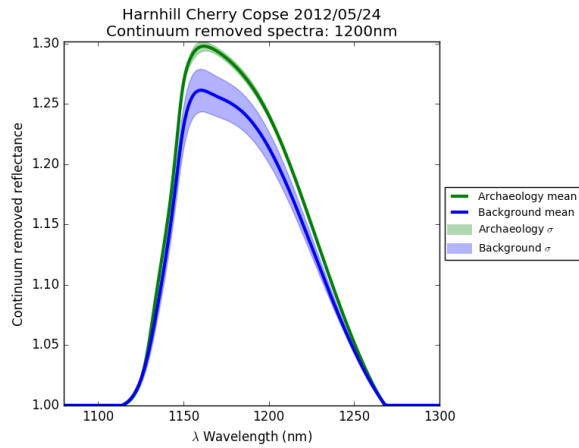


Figure B.321: Continuum removed reflectance 1200nm HHCC 24/05/2012

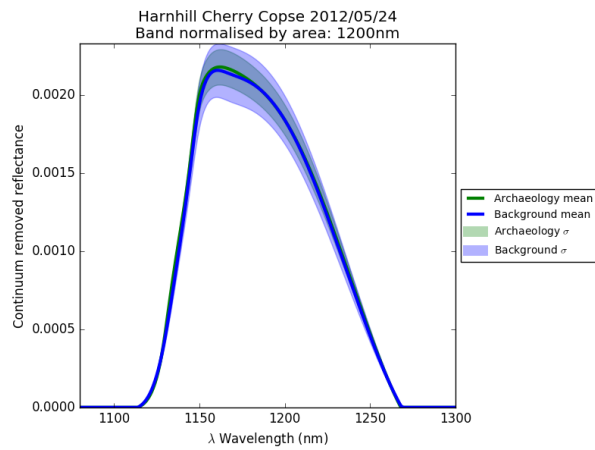


Figure B.322: Continuum removed reflectance band normalised by area 1200nm HHCC 24/05/2012

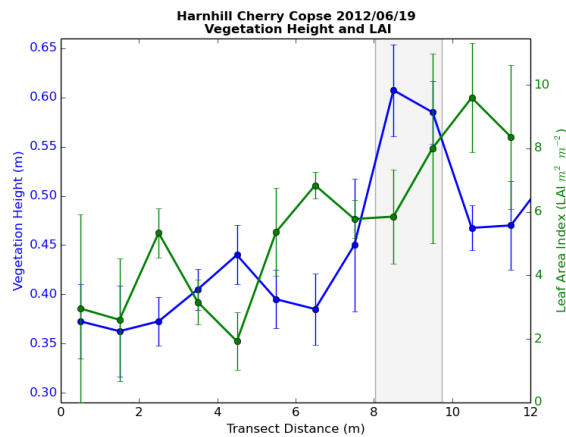


Figure B.323: Physical vegetation properties HHCC 19/06/2012

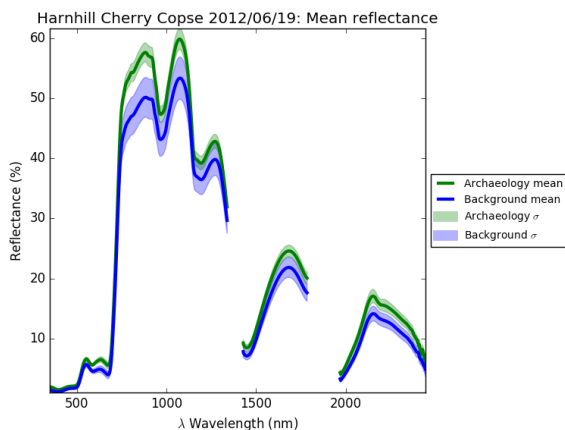


Figure B.324: Spectra from HHCC 19/06/2012

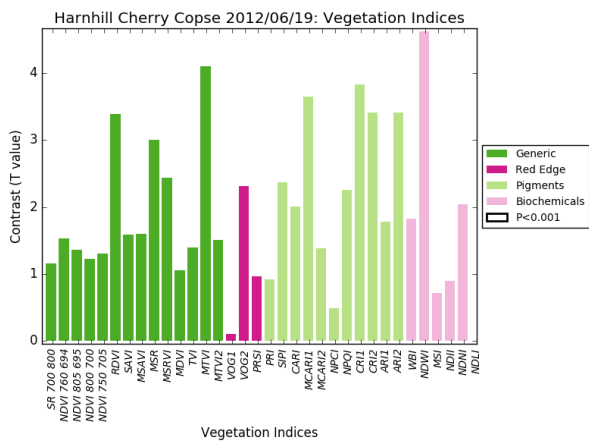


Figure B.325: Vegetation indices HHCC 19/06/2012

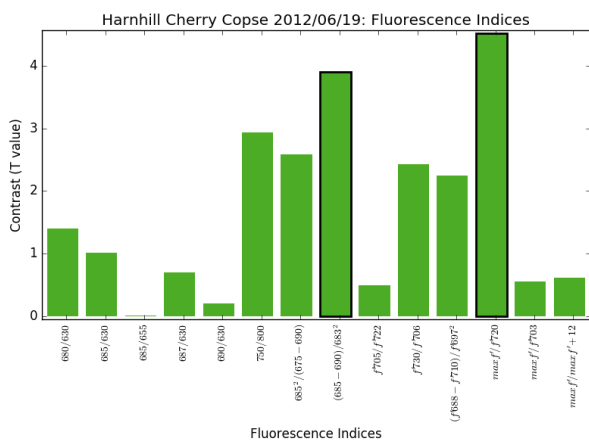


Figure B.326: Fluorescence Indices HHCC 19/06/2012

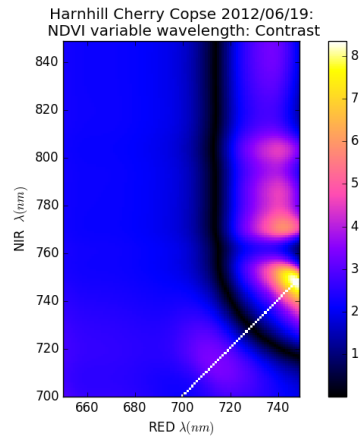


Figure B.327: MTBVI HHCC 19/06/2012

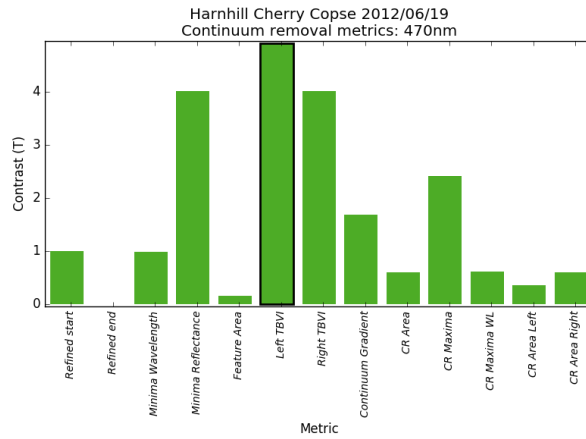


Figure B.328: Continuum removed metrics 470nm HHCC 19/06/2012

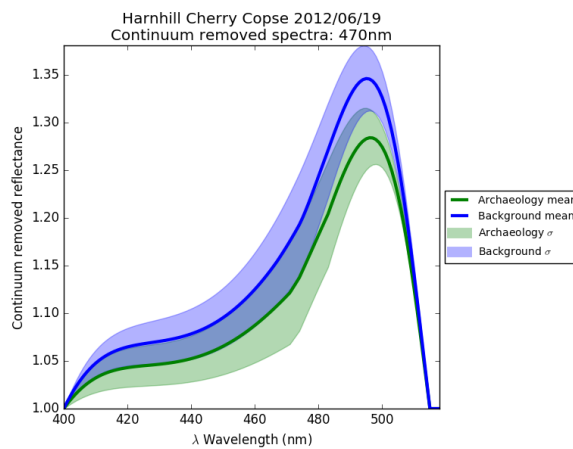


Figure B.329: Continuum removed reflectance 470nm HHCC 19/06/2012

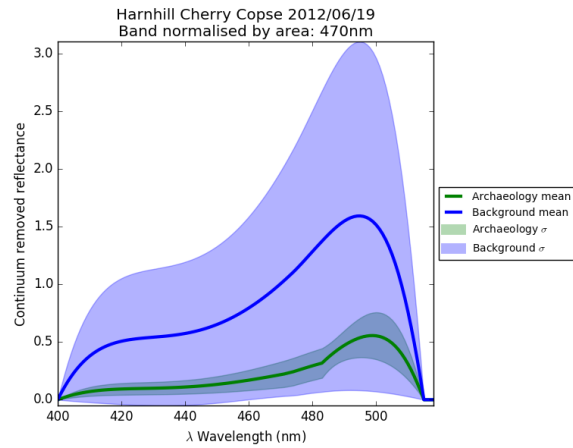


Figure B.330: Continuum removed reflectance band normalised by area 470nm HHCC 19/06/2012

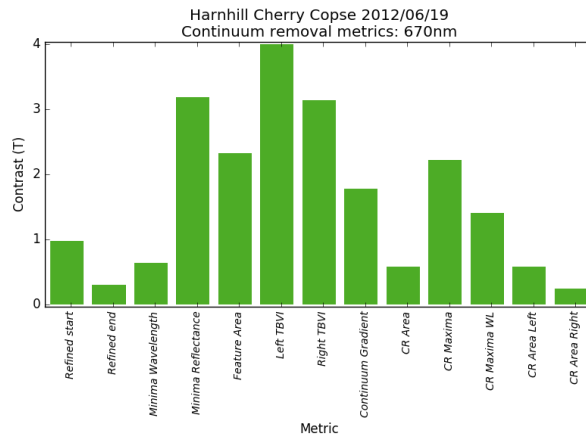


Figure B.331: Continuum removed metrics 670nm HHCC 19/06/2012

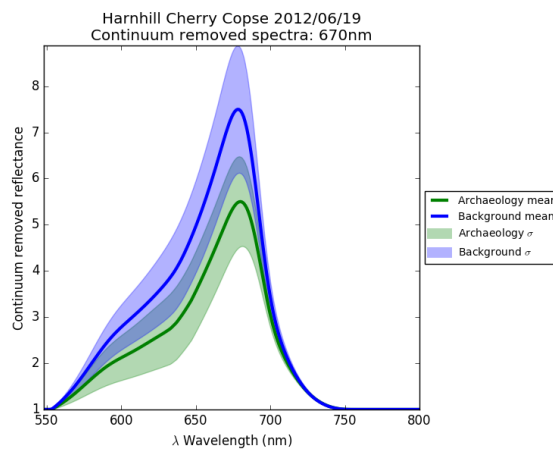


Figure B.332: Continuum removed reflectance 670nm HHCC 19/06/2012

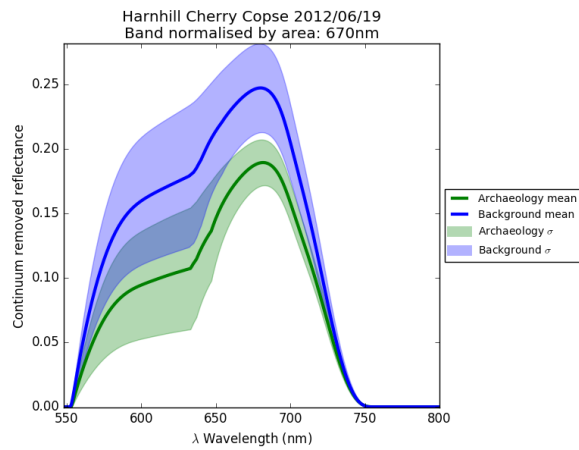


Figure B.333: Continuum removed reflectance band normalised by area 670nm HHCC 19/06/2012

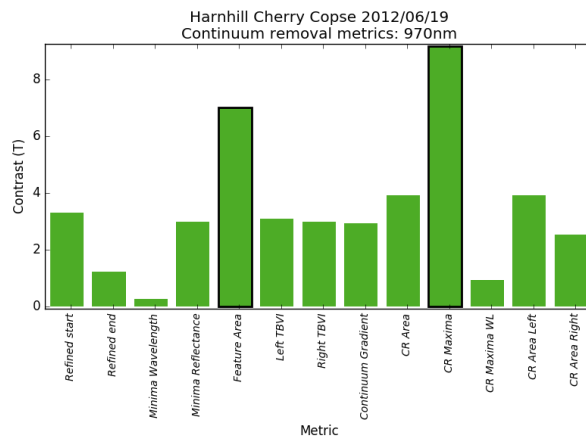


Figure B.334: Continuum removed metrics 970nm HHCC 19/06/2012

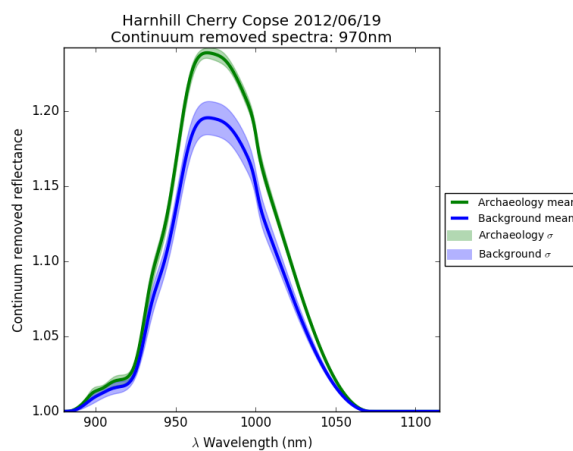


Figure B.335: Continuum removed reflectance 970nm HHCC 19/06/2012

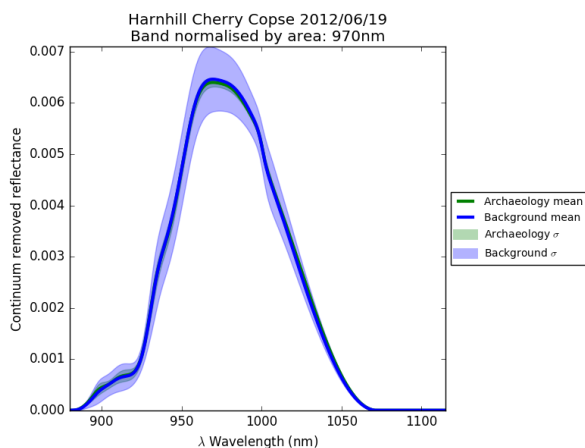


Figure B.336: Continuum removed reflectance band normalised by area 970nm HHCC 19/06/2012

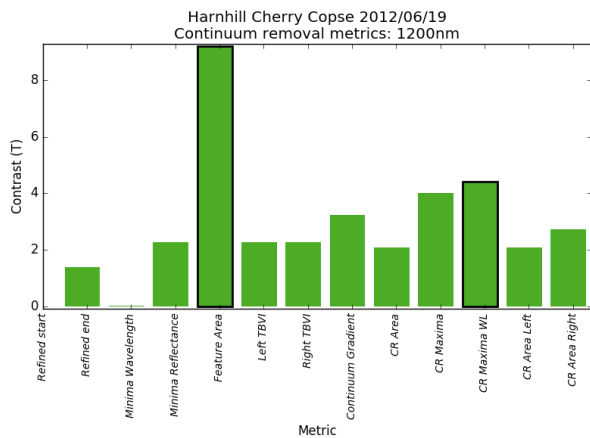


Figure B.337: Continuum removed metrics 1200nm HHCC 19/06/2012

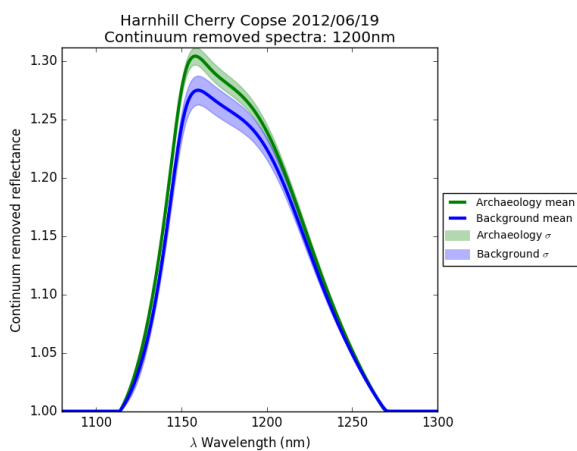


Figure B.338: Continuum removed reflectance 1200nm HHCC 19/06/2012

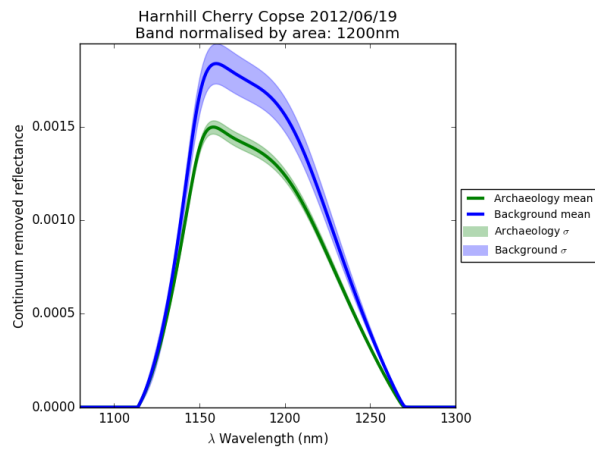


Figure B.339: Continuum removed reflectance band normalised by area 1200nm HHCC 19/06/2012

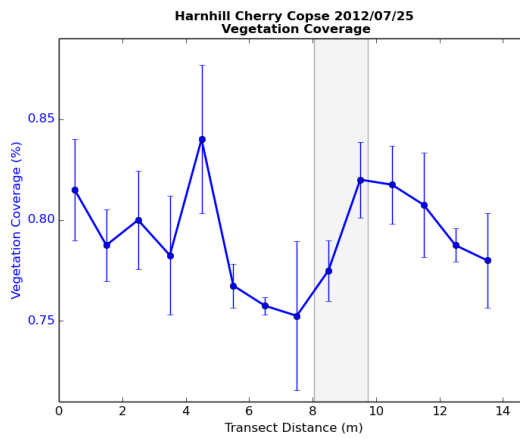


Figure B.340: Physical vegetation properties HHCC 25/07/2012

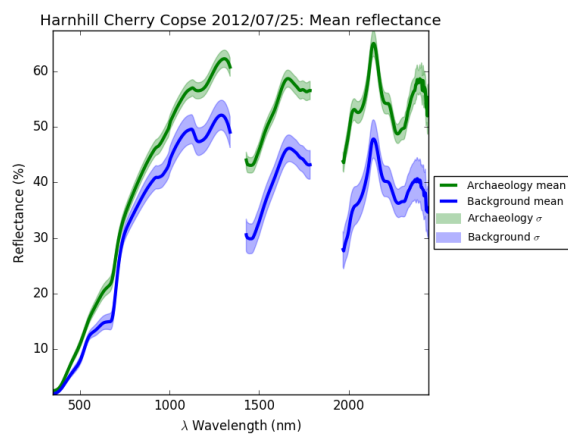


Figure B.341: Spectra from HHCC 25/07/2012

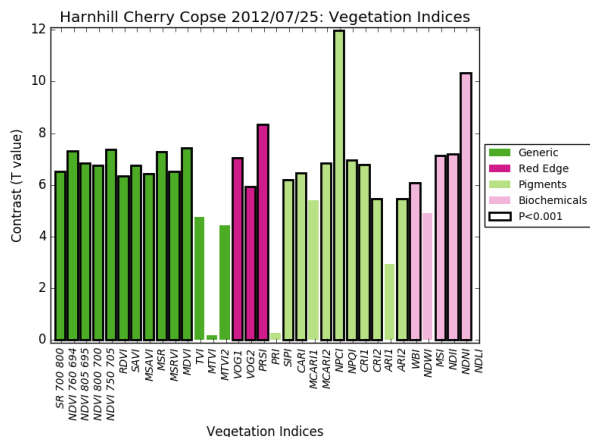


Figure B.342: Vegetation indices HHCC 25/07/2012

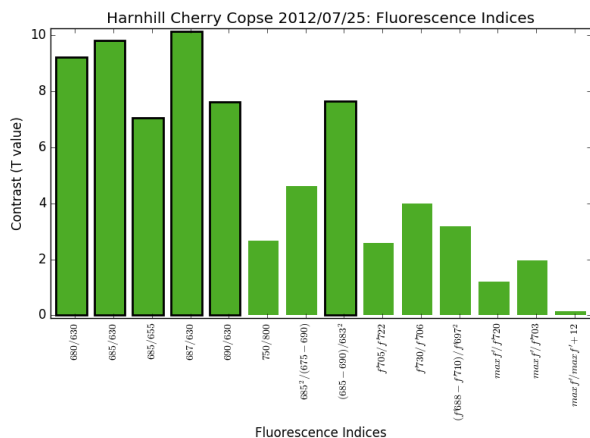


Figure B.343: Fluorescence Indices HHCC 25/07/2012

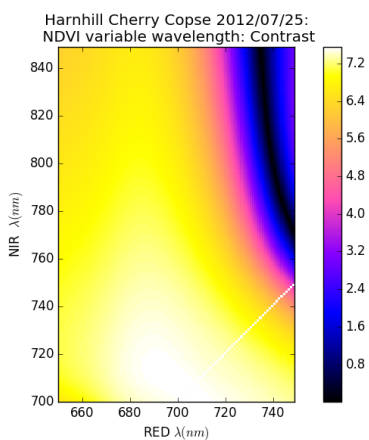


Figure B.344: MTBVI HHCC 25/07/2012

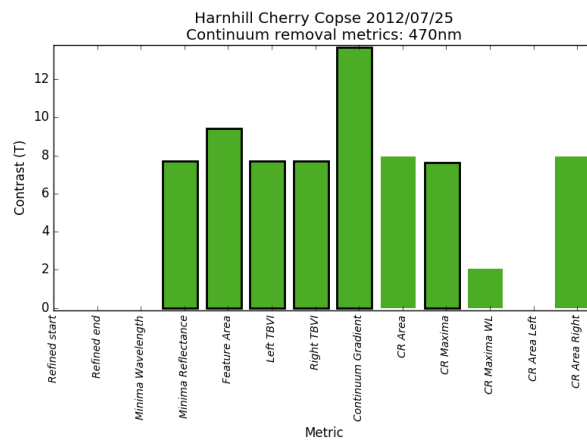


Figure B.345: Continuum removed metrics 470nm HHCC 25/07/2012

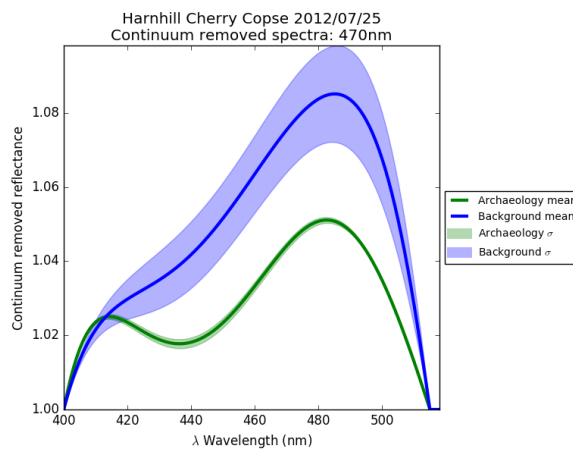


Figure B.346: Continuum removed reflectance 470nm HHCC 25/07/2012

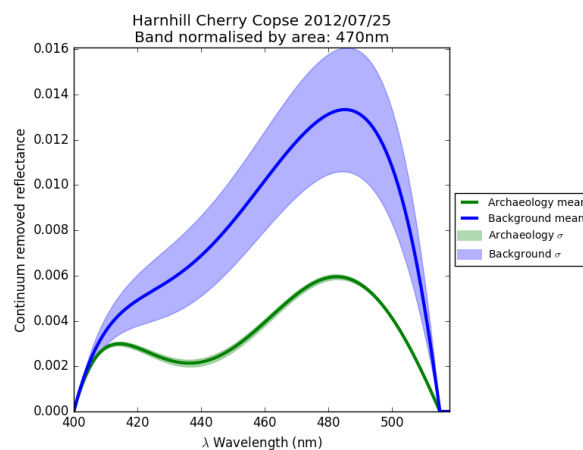


Figure B.347: Continuum removed reflectance band normalised by area 470nm HHCC 25/07/2012

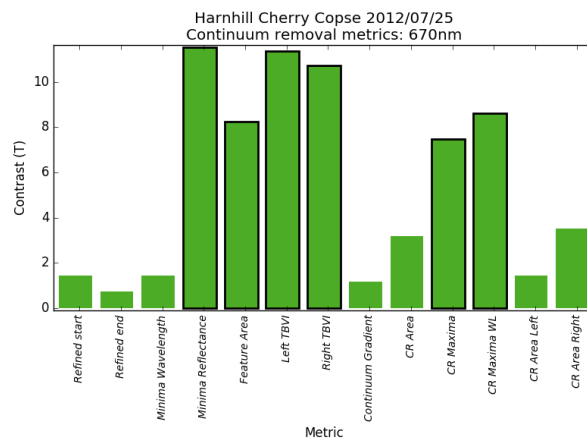


Figure B.348: Continuum removed metrics 670nm HHCC 25/07/2012

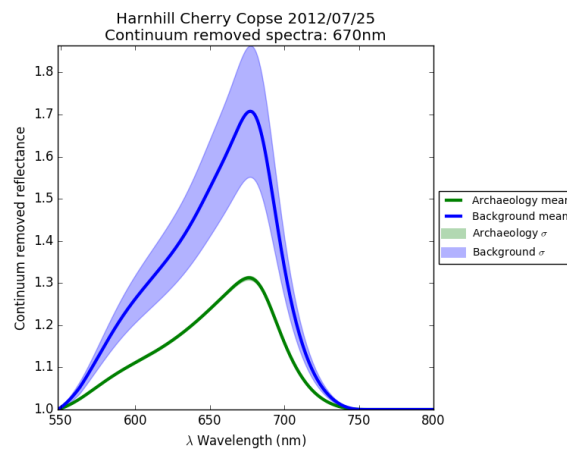


Figure B.349: Continuum removed reflectance 670nm HHCC 25/07/2012

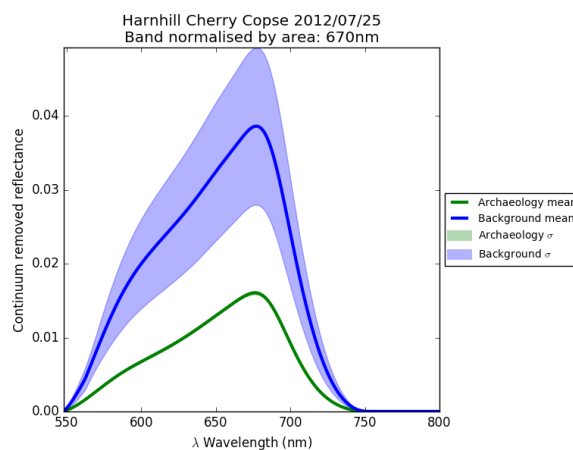


Figure B.350: Continuum removed reflectance band normalised by area 670nm HHCC 25/07/2012

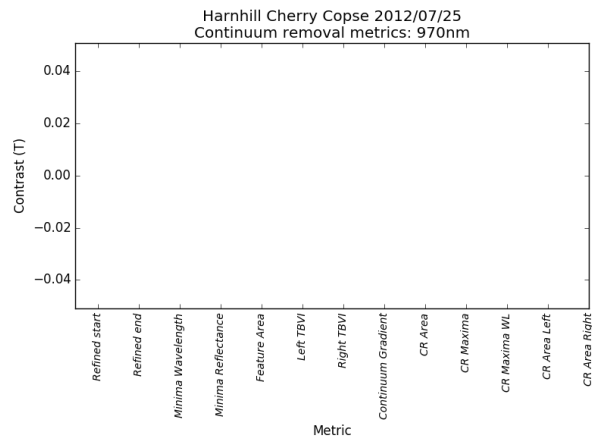


Figure B.351: Continuum removed metrics 970nm HHCC 25/07/2012

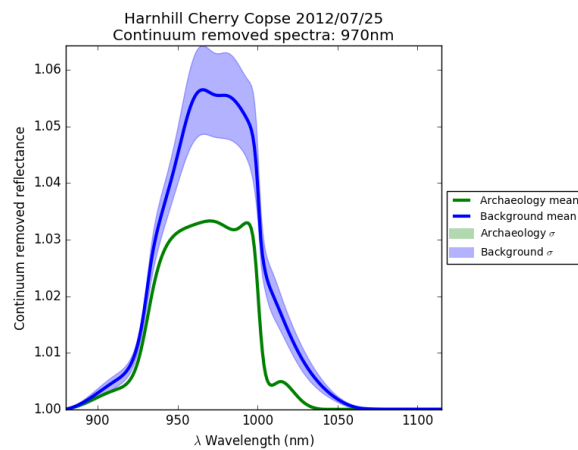


Figure B.352: Continuum removed reflectance 970nm HHCC 25/07/2012

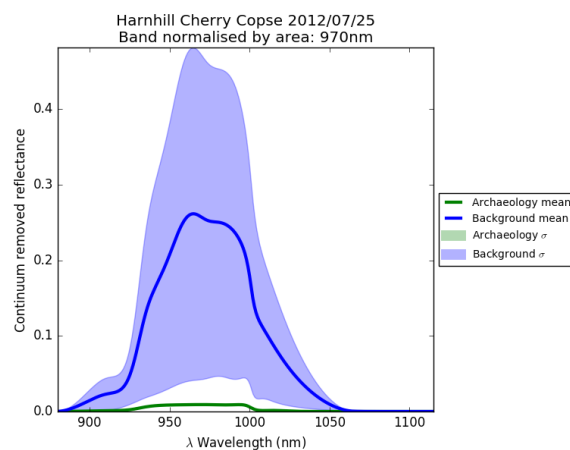


Figure B.353: Continuum removed reflectance band normalised by area 970nm HHCC 25/07/2012

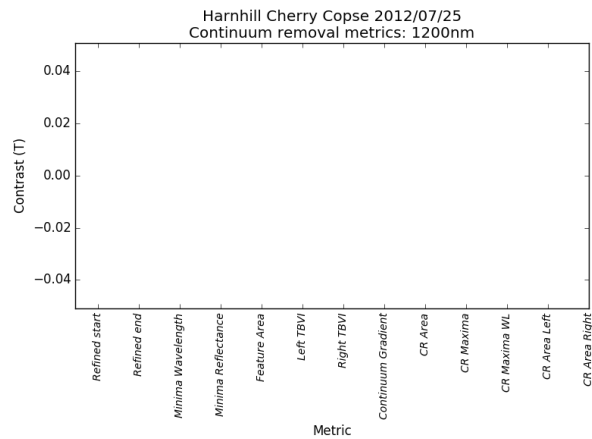


Figure B.354: Continuum removed metrics 1200nm HHCC 25/07/2012

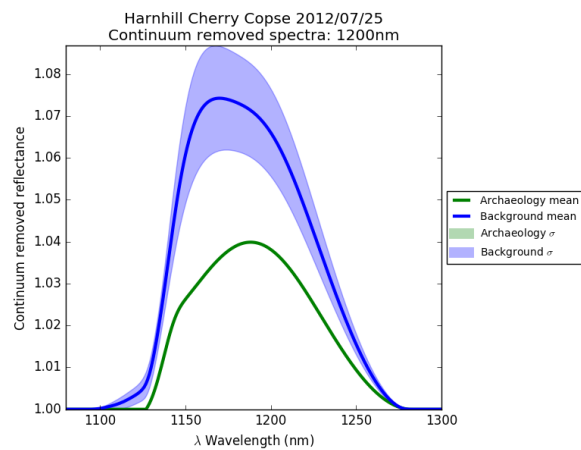


Figure B.355: Continuum removed reflectance 1200nm HHCC 25/07/2012

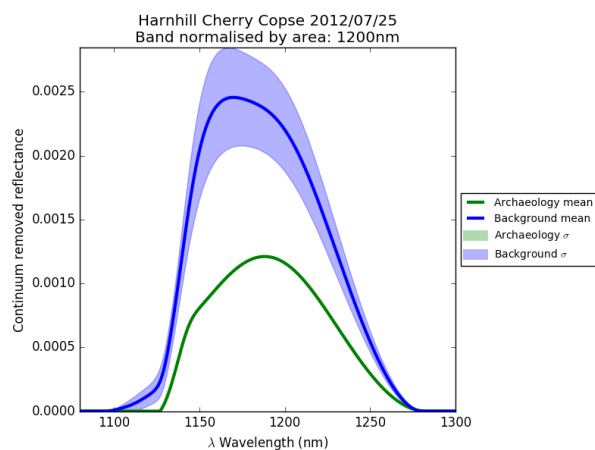


Figure B.356: Continuum removed reflectance band normalised by area 1200nm HHCC 25/07/2012

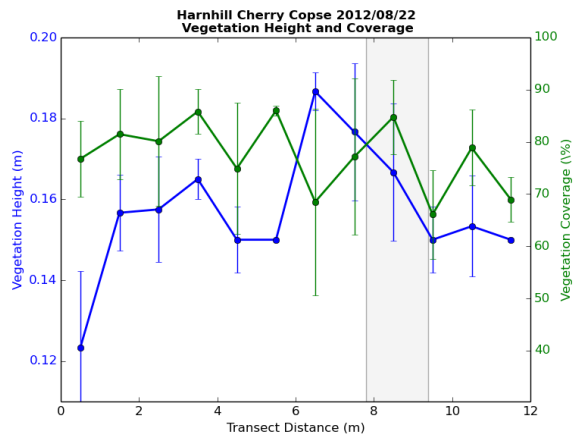


Figure B.357: Physical vegetation properties HHCC 22/08/2012

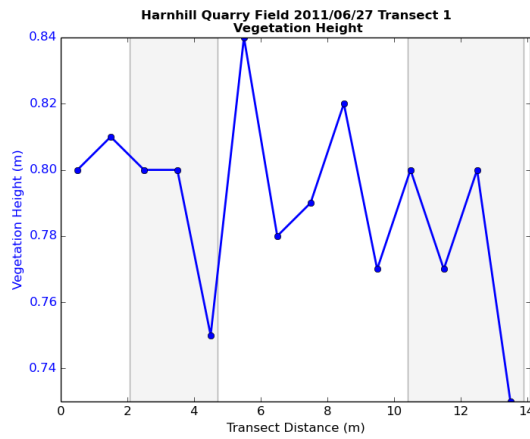


Figure B.358: Physical vegetation properties HHQF 27/06/2011

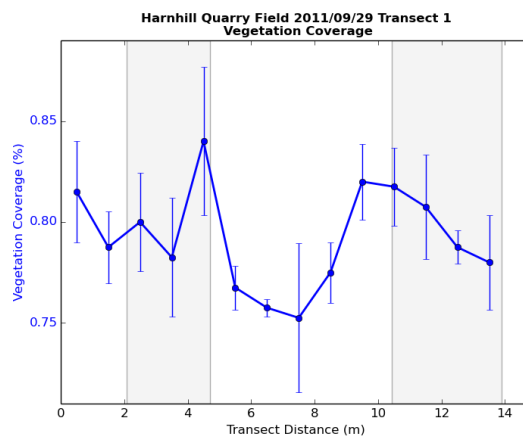


Figure B.359: Physical vegetation properties HHQF 29/09/2011

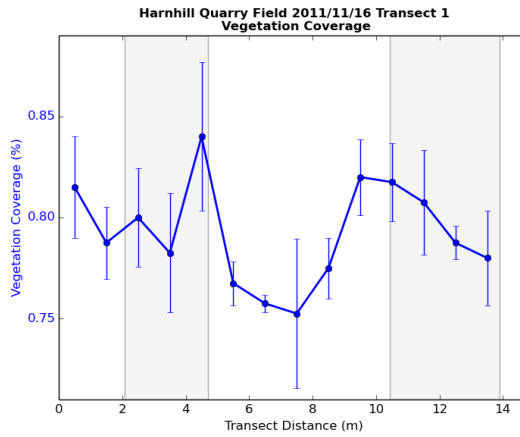


Figure B.360: Physical vegetation properties HHQF 16/11/2011

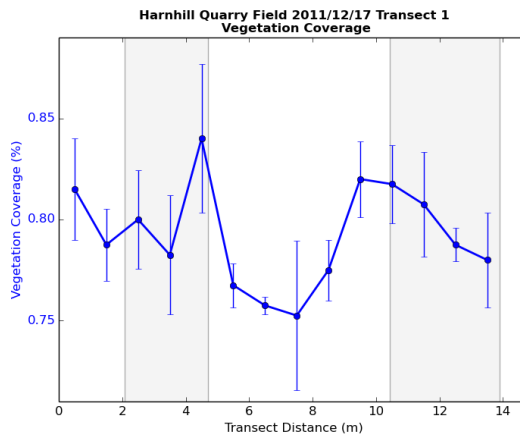


Figure B.361: Physical vegetation properties HHQF 17/12/2011

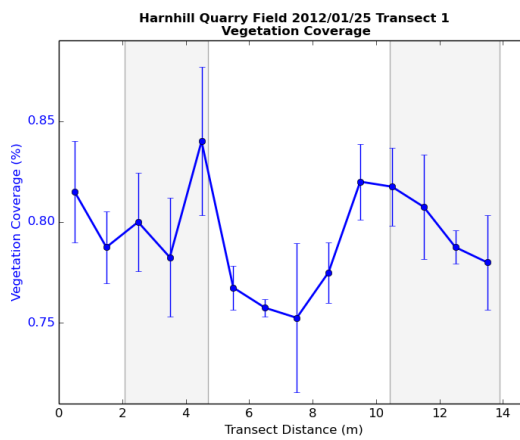


Figure B.362: Physical vegetation properties HHQF 25/01/2012

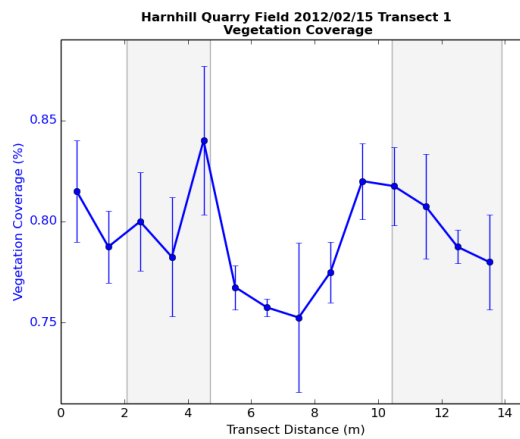


Figure B.363: Physical vegetation properties HHQF 15/02/2012

Figure B.364: Physical vegetation properties HHQF 21/03/2012

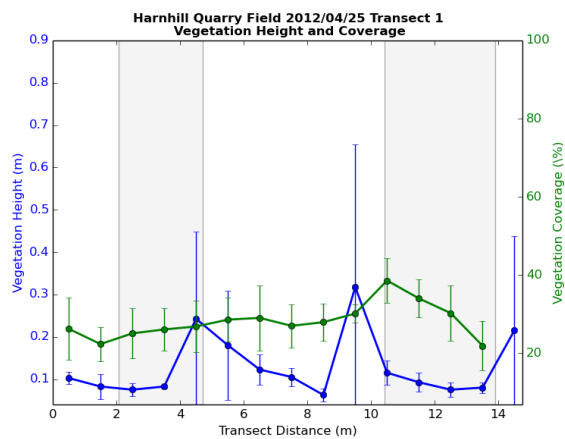


Figure B.365: Physical vegetation properties HHQF 25/04/2012

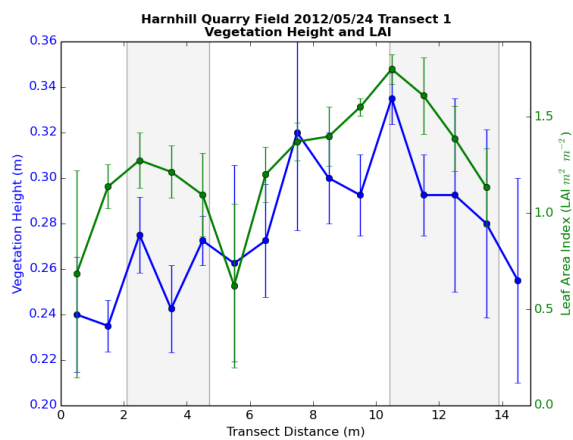


Figure B.366: Physical vegetation properties HHQF 24/05/2012